The Small-World of "Le Petit Prince": revisiting the word frequency distribution

D. Gamermann[*1], C. Moret-Tatay[2], E. Navarro-Pardo[3], and P. Fernandez de Córdoba Castellá[4]

[1]Department of Physics, Universidade Federal do Rio Grande do Sul (UFRGS) - Instituto de Física , Av. Bento Gonçalves 9500 - Caixa Postal 15051 - CEP 91501-970 - Porto Alegre, RS, Brasil.
[2]Departamento de Neuropsicobiología, Metodología y Psicología Social - Facultad de Psicología, Magisterio y Ciencias de la Educación, Sede de San Juan Bautista. Universidad Católica de Valencia, San Vicente Mártir - Calle Guillem de Castro 175, 46008- Valencia, Spain.
[3]Department of Developmental and Educational Psychology - Faculty of Psychology, Universitat de València. Av. Blasco Ibáñez, 21 46010 - Valencia, Spain.
[4]Instituto Universitario de Matemática Pura y Aplicada, Universitat Politècnica de València. Camino de Vera, s/n 46022 - Valencia, Spain.

March 6, 2018

Abstract

Many complex systems are naturally described through graph theory and different kinds of systems described as networks present certain important characteristics in common. One of these features is the so called scale-free distribution for its node's connectivity, which means that the degree distribution for the network's nodes follows a power law. Scale-free networks are usually refered to as small-world because the average distance between their nodes do not scale linearly with the size of the network, but logarithmically. Here we present a mathematical analysis on linguistics: the word frequency effect for different translations of the "Le Petit Prince" in different languages. Comparison of word association networks with random networks makes evident the discrepancy between the random Erdös-Rény model for graphs and real world networks.

Key words: Small-world, word frequency, Zipf's law

Many objects of study in different interdisciplinary fields find a natural mathematical description as graphs. A graph is simply an object formed by two different sets: a set of nodes and a set of edges connecting these nodes. For many decades the mathematical study of graphs has been guided by the Erdös-Rény model for random graphs Erdös, P. and Rényi, A. (1960). In this model a (random) graph is constructed from a set of N nodes by connecting or not each one of the $\frac{N(N-1)}{2}$ pairs of nodes with a probability p. A random graph will, therefore, have on average

---

[*]danielg@if.ufrgs.br

$p\frac{N(N-1)}{2}$ links and the degree distribution of its nodes will follow a Poisson distribution. Another characteristic of random graphs is the fact that its size (average node distance) scales linearly with the number of nodes in the graph.

As graph theory started being applied to many real systems such as metabolic or protein networks, neural networks, the Internet, social networks, food-chains, among many others Rives & Galitski (2003), Haykin (1994), Pastor-Satorras et al. (2001), Crucitti et al. (2003), a discrepancy between these real-world graphs and the random Erdös-Rény graphs became evident. The node's degree distribution in real-world graphs do not follow a Poisson distribution, instead they follow a power-law distribution and thus became known as scale-free. As a consequence, the average distance between two nodes in such networks grows slowly with the the number of N nodes in the network and this characteristic is known as small-world behavior Amaral et al. (2000).

It has been observed that the word frequency distribution in a language also follows a scale-free distribution and many explanations for this phenomenon have been given. In linguistics, this observation is known as Zipf's law. It states that the proportion of words P (in a text, for example) with a given frequency k follows a power law: $P(k) \sim k^{-\gamma}$ where γ is generally a number between 2 and 3. This law shows that few words present very high frequency and, conversely, many words present low frequency. A particular and appealing explanation for this could be achieved via concepts from statistical mechanics where one tries to minimize an energy function based on the balance between the efforts of the speaker and the listener which is defined by the word frequency and ambiguity, as shown in Cancho & Solé (2003).

One traditional way to examine differences between languages is by variables such as frequency, morphological complexity, evolution and cultural transmission. All these aspects can be related in a complex adaptive system Beckner et al. (2009). In particular, the word frequency is a classical effect in cognitive psychology characterized by its robustness: high frequency words are recognized quicker and remembered better Sternberg & Powell (1983). Therefore, a large body of research has employed the word frequency as an approach of word difficulties Dufau et al. (2011), Esteves et al. (2015), Moreno-Cid et al. (2015), Moret-Tatay & Perea (2011b,a), Navarro-Pardo et al. (2013), Perea, Moret-Tatay & Carreiras (2011), Perea, Comesaña, Soares & Moret-Tatay (2012), Perea, Gatt, Moret-Tatay & Fabri (2012), Perea, Moret-Tatay & Gómez (2011). According to Breland (1996), the logic of this is that low frequency words are more difficult because they appear less often in print. Moreover, (van Heuven et al. (2014)) proposed the Zipf-scale as a better standardized measure of word frequency. Given the ease with which word counts can be collected at the present time, a useful tool on contrastive linguistics is a lexical corpus of a language. In other words, a large collection of texts in the electronic form supplemented by linguistic annotation that has become an important tool in linguistic studies. Not surprisingly, several databases for Computing Statistics and Psycholinguistic in several languages have been developed for this objective Coltheart (1981), Davis (2005). However, according to Perea et al. (2013), Yap et al. (2011), other variables might be involved in word recognition, in particular in word frequency, such as the number of contexts in which a word appears.

In the present work we focus on the analysis of a single linguistic material (the Little Prince by Saint-Exupéry) in several different languages. To this propose, we have studied statistical properties of the text and networks (graphs) associated with this text. In the different languages we studied the word frequency distribution on one hand and then we constructed different networks by word associations. For each network we built, we evaluated its main properties, like its average clustering coefficient, nodes distances and its degree distribution. In the next

2

section we present the methodology we used and the mathematics behind our analyses, in the Results section we describe our findings and in the Conclusions section we present the main aspects of our results and a brief overview.

1 Methods

1.1 Materials

The Little Prince text was obtained from the Internet in eight different languages: Spanish, English, Dutch, Greek, Basque, Italian, Portuguese and (of course) French.

In order to analyze the text, python scripts were written. The computer codes were run in a computer with a i7 quadcore processor and 8Gb of RAM memory. The scripts first stored all text in the computer RAM memory. Then, it used punctuation in order to slice the text in its sentences and then removed all punctuation and numerals (0, 1, 2, ...) from the raw text. It then identified the different words as the strings left which were separated by spaces. As an example, below one can see the first 300 characters from the French text:

`Antoine de Saint-Exupéry`

`LE PETIT PRINCE`

`1943`

`PREMIER CHAPITRE`

`Lorsque j'avais six ans j'ai vu, une fois, une magnifique image, dans un livre sur la Forêt Vierge qui s'appelait « Histoires Vécues ».  Ça représentait un serpent boa qui avalait un fauve. Voilà la copie du dessin.  On disai`

Through our scripts, the extract above becomes the list of words: `antoine, de, saint, exupéry, le, petit, prince, premier, chapitre, lorsque, j, avais, six, ans, j, ai, vu, une, fois, une, magnifiqu image, dans, un, livre, sur, la, forêt, vierge, qui, s, appelait, histoires, vecues, ça, représenta un, serpent, boa, qui, avalait, un, fauve, voilà, la, copie, du, dessin, on, disait`.

Once the python script transforms the whole text in a raw list of words (15612 in the case of the French text), it counts the number of different words (2600 in the French text) and counts also the number of times that each single word is repeated in the text. For the construction of networks, we will link words based on their relative distance in the text. For this, one needs to keep track of the sentences in which the text is divided and which words appear in each sentence. So our script actually first creates a list of sentences, by slicing the text when it finds a punctuation symbol, and after that a list of single words, by slicing the sentences in its blank spaces.

1.2 Analysis

The word frequency distribution $P(k)$ is a function that, for each natural number k, tells how many words appeared in the text k times. In the case of the French text, for example, 1516 different words appeared only once ($P(1) = 1516$), one of these is the word "`réjouir`", that appears in the whole text only once. On the other hand, the word "`et`" was the fifth most frequent word, appearing 306 times ($k = 306$) and this is the only word

3

that appeared this number of times, consequently $P(306) = 1$. The most frequent word was the article "le" that appeared 465 times and is the only word appearing 465 times in the text ($P(465) = 1$).

Typically, for a text, many words appear only a few times, while a few words are repeated constantly along the text. As a consequence, the function $P(k)$ is a decreasing function. A mathematical function that often fits $P(k)$ in a text is the power-law distribution:

$$P(k) = Ak^{-\gamma}, \tag{1}$$
$$\log(P(k)) = \log(A) - \gamma \log(k) \tag{2}$$

where A is a proportionality constant that can be evaluated by the total number of words. The fact that the frequency distribution follows a power-law (or scale-free) distribution is known as the Zipf law. Note from equation (2) that, in a log-log plot, the distribution will follow a straight line.

For real texts, the tail (large values of k) of the $P(k)$ distribution will be very noisy, because only a handful of large values of k will be populated and then by a single word. In figure 1 we show the function $P(k)$ (in logarithmic scale) for the French text. One can clearly see the noise in the right tail.

Figure 1: Word frequency distribution for the French text with a noisy right tail.


4
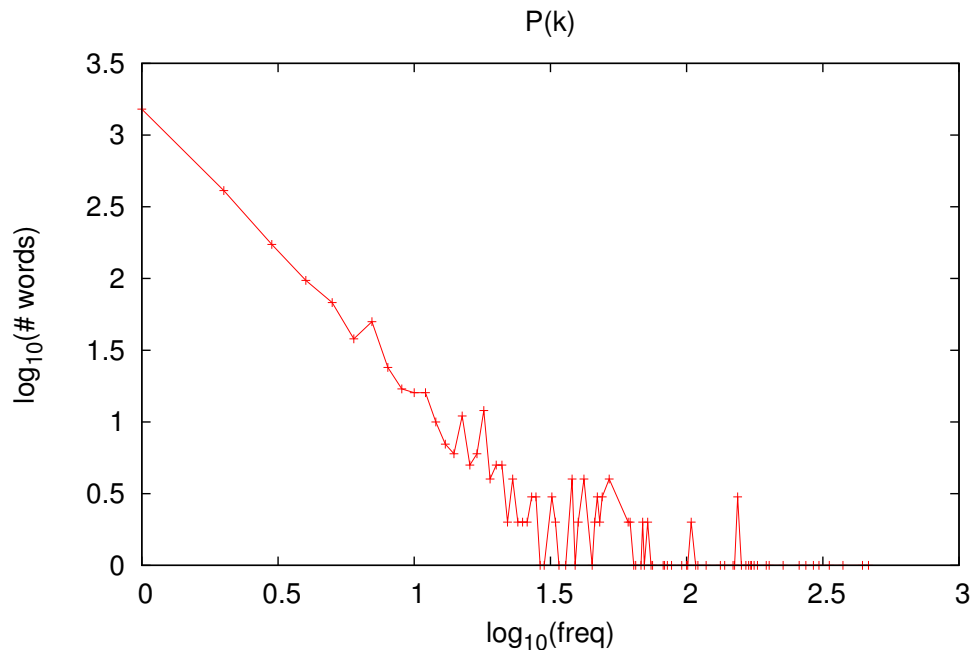
In order to fit the distribution avoiding the noisy tail, one can use the right-cumulative distribution:

$$P_c(k) = \int_k^\infty P(k')dk' = \frac{A}{\gamma - 1}k^{-(\gamma-1)} \tag{3}$$

$$\log(P_c(k)) = \log\left(\frac{A}{\gamma - 1}\right) - (\gamma - 1)\log(k). \tag{4}$$

In figure 2 one can see the distribution $P_c(k)$ (in logarithmic scale) for the French text. This curve is much smoother than the raw $P(k)$ distribution and it is always decreasing.

Figure 2: Word frequency cumulative distribution for the French text.
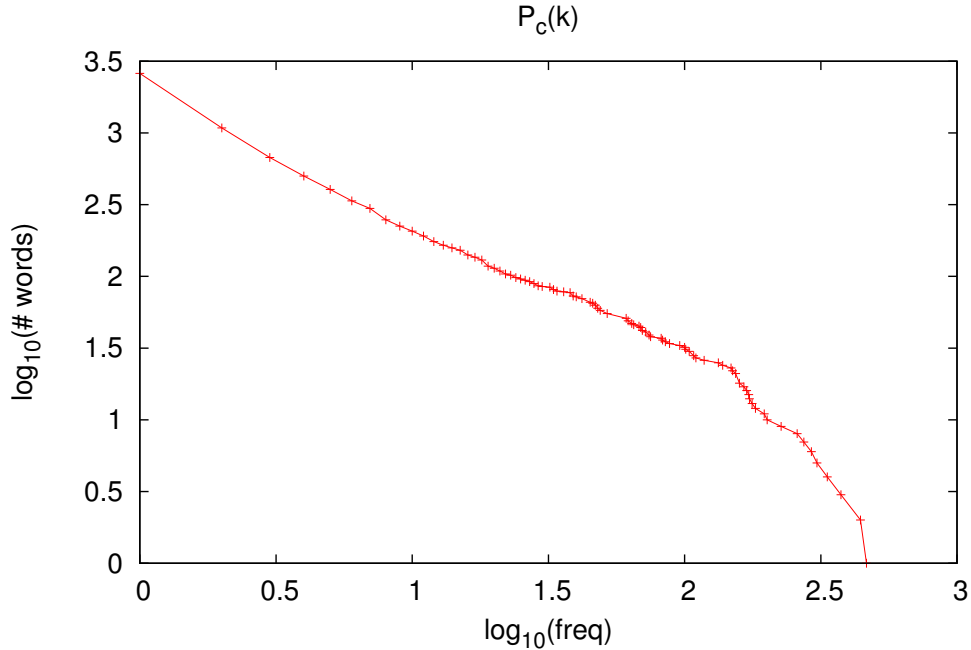

From equations (2) and (4) it is clear that the plot of $\log(P)$ or $\log(P_c)$ versus $\log(k)$ will follow a straight line if the distribution $P(k)$ follows the power-law in equation (1). So fitting lines to the empirical data collected from the texts, one can determine the parameters A and γ. The parameter A divided by $\gamma - 1$ is just the total number of different words in a text. One can realize this by noticing that $P_c(1) = \#$total of words.

Apart from measuring and fitting the word frequency distribution, we analyzed networks of words association built from the texts. In order to build a network from the texts in each language, we set each word as a node and

we built two different networks by following two different rules in order to set the links between words. In the first network we define a link between two words if they appear side by side in at least one sentence in the text. In the second network a link is defined between two words if there is a third word between the two in at least one sentence in the text. In figure 3 we show examples of the two networks based on a single sentence in the text: "My drawing was not a picture of a hat!"

Figure 3: Example of the two networks. Network 1 on the left and network 2 on the right.

Network 1   Network 2
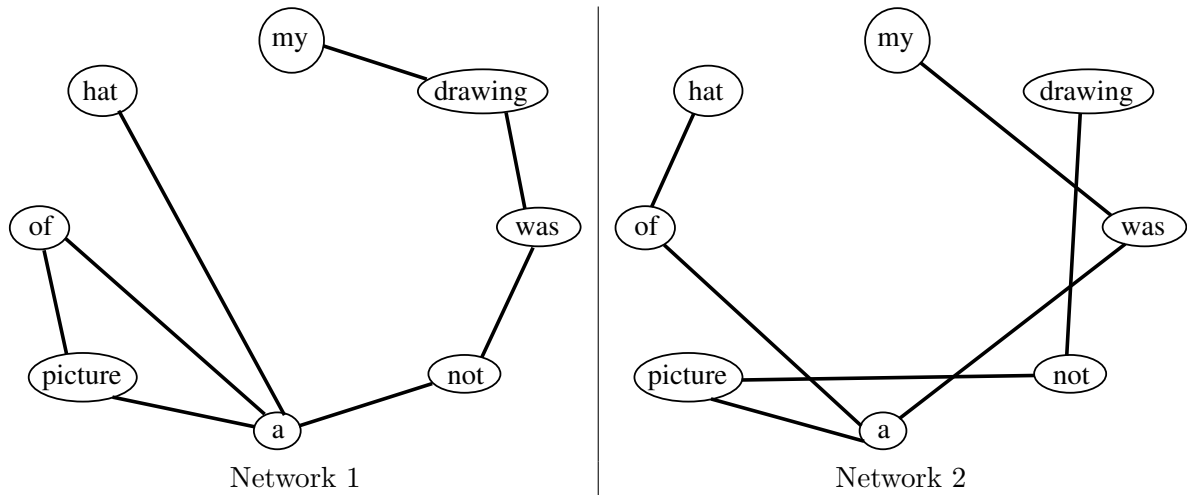
An important structure in order to analyze a graph is its adjacency matrix, this is a symmetric $N \times N$ matrix, where N is the number of nodes in the graph and the elements M_{ij} are equal to one if there is a link between nodes i and j and zero otherwise. From this matrix, one can directly obtain the degree (number of neighbors or connections) for any given node in the graph: $k_i = \sum_{j=1}^{N} M_{ij}$.

The number of nodes (words) in each network constructed from the texts maybe less than the total number of different words in each whole text because we remove non-connected components (sets of nodes from which it is not possible the reach a bigger set of nodes following the links within the set) from the graphs. For each network we performed three analyzes: we fitted a power-law to its degree distribution, we calculated the average clustering coefficient and the average distance between two nodes.

The fitting of a power-law follows the same steps done in order to fit word frequencies (but now looking at degree for each node in the network). The clustering coefficient of a node is given by Ravasz & Barabasi (2003):

$$C_i \quad = \quad \frac{2E_i}{k_i(k_i - 1)} \tag{5}$$

where k_i is the degree of node i and E_i is the number of connections between the neighbors of node i. The average

clustering $\bar{C}$ of a network can now be calculated straightforward as the average value of the C_i's for all nodes in the network.

The distance between two nodes is defined as the minimum number of links one has to go through in order to travel from one node to the other. The average distance between every one of the $\frac{N(N-1)}{2}$ different pairs of nodes in each network was calculated using Dijkstra's algorithm Dijkstra (1959) via the PyNetMet package Gamermann et al. (2014). The average of the distances between every pair is the network's average distance $\bar{d}$.

We compared the average clustering and average distance in every network with results from random networks. For this purpose, for each network, we built an ensemble with twenty random networks with the same number of nodes and the same number of links, but with random topology. The input for a network is its adjacency matrix M. So, for building a random network we use the following algorithm:

(1) Start with an $N \times N$ matrix where all its elements are zero. (One has here N nodes and zero links ($\ell = 0$) between them.

(2) While the number of links (ℓ) is less than the desired number of links in the network, repeat:

(2.1) Chose two different integer random numbers (i and j) between 1 and N.

(2.2) If M_{ij} is zero, change M_{ij} and M_{ji} to one and increase in one unit the number of links ($\ell \to \ell + 1$).

(3) Check if any node (i) has been left unconnected. If so, randomly choose a node (j) to connect it (i) to and randomly break an existing connection of node j.

(4) Repeat step (3) until no node is left unconnected.

Steps (3) and (4) are actually optional, but throughout our calculations, we have chosen to work with fully connected graphs. This algorithm returns a randomly generated adjacency matrix representing a connected network with a predefined number of nodes and links.

Using this algorithm, for each network obtained from a text, we generate an ensemble of twenty random networks with the same number of nodes and links. For each random network in the ensemble the average clustering and average distance is calculated and then the average inside each ensemble is evaluated.

2   Results

In figure 4 the distributions for all the eight languages in log-log scale are supper-posed showing the tendency they have to follow a straight line. In figure 5 the distribution for each individual language is shown with the best line fitted using the least squares method. In the title of each plot one finds the equation fitted.

In table 1 we show the values of γ, $\frac{A}{\gamma-1}$, total number of words and the $\frac{\chi^2}{dof}$ for the best fit for each language. The value for χ^2 (minimized by the least square method) is calculated as:

$$\chi^2 \quad = \quad \sum_{k=1}^{k_{max}} \frac{\left(\log(P_c(k)) - \log(P_{c_{obs,k}})\right)^2}{\epsilon_k} \tag{6}$$

7

Figure 4: Cumulative word frequency distribution for all texts.
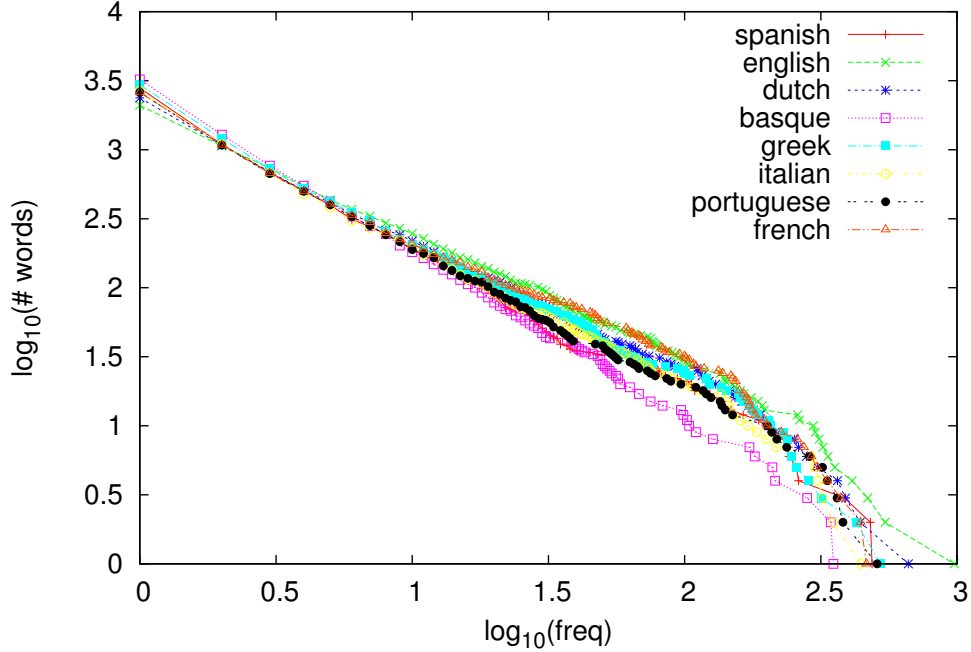
where $P_{c_{obs,k}}$ is the observed value for the right-cumulative distribution of words at frequency k, ϵ_k is the error associated to $\log(P_{c_{obs,k}})$ and the sum is made for all k's for which $P_{obs,k}$ is different from zero [1]. Since $P_{c_{obs,k}}$ is an absolute frequency, the error associated to it is its square-root and, therefore, one evaluates the logarithmic[2] error $\epsilon_k = \frac{1}{\ln(10)\sqrt{P_{c_{obs,k}}}}$.

The results for the networks analysis can be found in tables 2 and 3. In figure 6 we show, for the Network 1 constructed from the Portuguese text, its degree distribution, the best fitted line to it and the degree distribution for a random network with the same number of nodes and links ($N = 2424$ and $\ell = 6175$). From this figure, one can clearly see the difference between the distribution obtained from a "real" network (power-law distribution) and the one obtained from a completely random network (Poisson distribution). In a power-law distribution there is a sensible probability of observing nodes with a higher (much bigger than average) degree, while in a Poisson distribution this probability drops to zero very fast.

---

[1]Note that $P_{c_{obs,k}}$ is the right cumulative distribution so, if $P_{obs,k}$ is zero for a given value of k, $P_{c_{obs,k}}$ will be a constant for all $k's$ after this, until reaching a new k where $P_{obs,k}$ is not zero, and therefore, these points would not bring any new information to the analysis.

[2]In all our equations log is the base 10 logarithm and ln is the natural (base e) logarithm.

Figure 5: Cumulative word frequency distribution for all texts with the best line fitted.

$\log_{10}(P_c) = -0.951297 \log_{10}(k) + 3.325550$

$\log_{10}(P_c) = -1.040888 \log_{10}(k) + 3.393484$

$\log_{10}(P_c) = -1.216154 \log_{10}(k) + 3.485592$

$\log_{10}(P_c) = -0.995365 \log_{10}(k) + 3.337836$

$\log_{10}(P_c) = -0.937050 \log_{10}(k) + 3.327242$

$\log_{10}(P_c) = -1.056252 \log_{10}(k) + 3.362926$

$\log_{10}(P_c) = -1.067550 \log_{10}(k) + 3.364569$

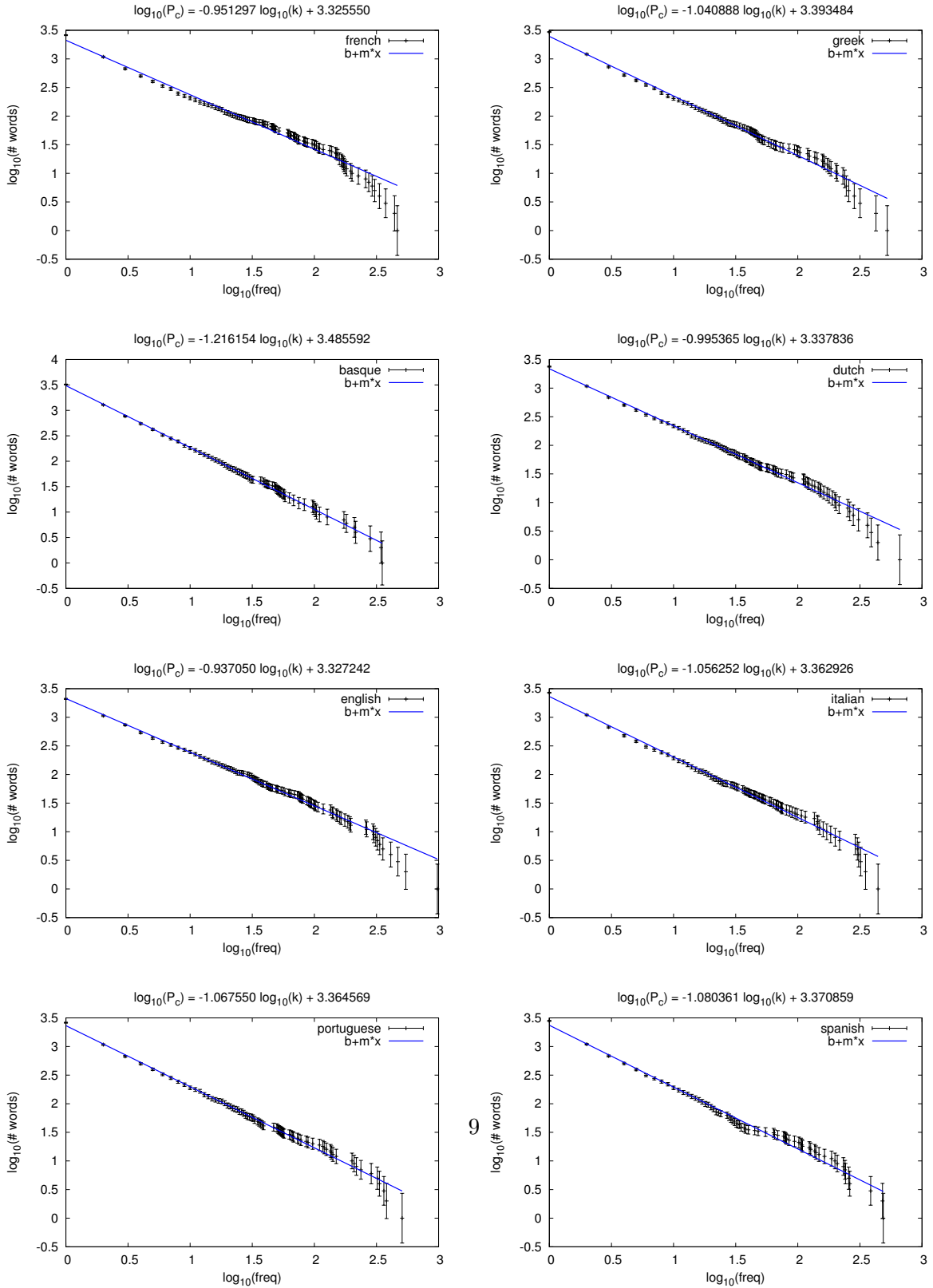$\log_{10}(P_c) = -1.080361 \log_{10}(k) + 3.370859$

9

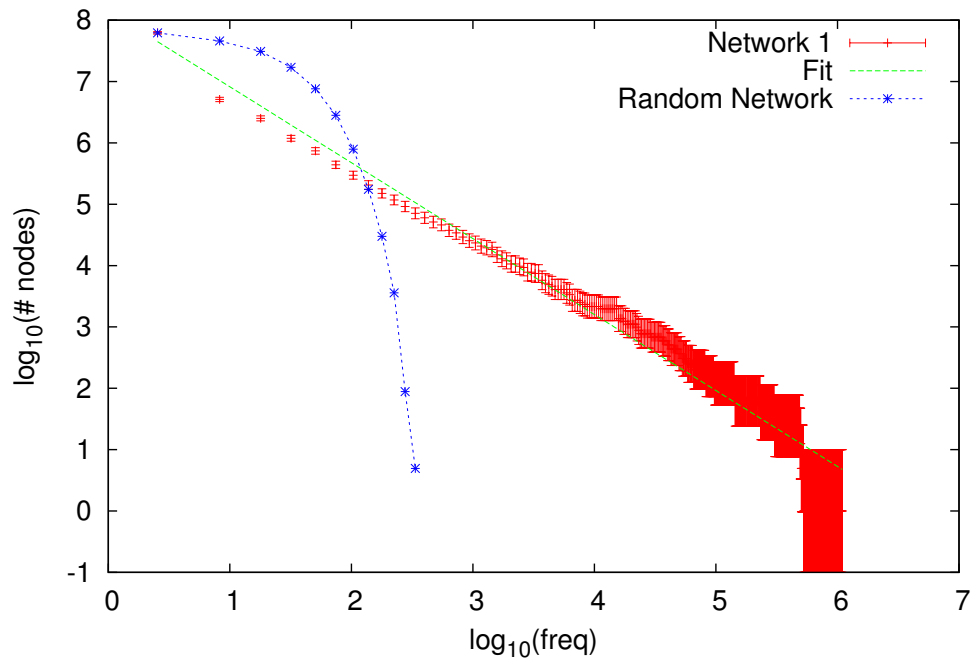Figure 6: Degree distribution for the Network 1 obtained from the Portuguese text compared with a random network.

Table 1: Summary of the fits.

Language	# words	$\frac{A}{\gamma-1}$	γ	$\frac{\chi^2}{dof}$
SPANISH	2801	2348.87	2.08	0.078
ENGLISH	2098	2124.43	1.94	0.041
DUTCH	2375	2176.89	2.00	0.040
BASQUE	3226	3059.09	2.22	0.016
GREEK	2951	2474.48	2.04	0.063
ITALIAN	2689	2306.35	2.06	0.045
PORTUGUESE	2607	2315.10	2.07	0.031
FRENCH	2600	2116.17	1.95	0.112

The properties calculated for the two types of networks (1 and 2) are very similar, but they differ significantly from the properties calculated for random networks. The average node distance in the random networks are, on average, around two units bigger than in the language networks and they present a much smaller standard deviation in the case of random networks. The second interesting difference between random and language networks is the average clustering coefficient, which is very close to zero in the case of random networks. In language networks, words tend to form clusters because of the language structure (they will share either context, grammatical or semantic function, ...) and this feature is reflected in the clustering coefficient calculated from eq. (5).

3 Conclusions

Here we present a mathematical analysis on linguistics: the word frequency effect for different translations of the same book ("Le Petit Prince") in eight different languages. The interest of these studies is that the occurrence of words in sentences reflects the language's organization. Apart from the word frequency distribution, we also performed analyzes of different networks built based on word associations in the text and compared these to random networks.

As expected, word frequency presented a scaling law. The results suggest small differences on language volume for the same material. In particular, the γ parameter varied slightly across the different languages. Moreover, our study shows how different languages tend to slightly differ in formal aspects. Comparison of word association networks with random networks makes evident the discrepancy between the random Erdös-Rény model for graphs and real world networks. A real network follows a specific design principle and therefore its nodes are connected in an organized way. This becomes evident from the clustering coefficient of the networks which have a high value for networks 1 and 2, but is very close to zero for the random networks. Another interesting difference between the real and random networks is the observation of the small-world effect in real networks: its average node's distance is much smaller than in random networks.

Finally, one can conclude that these results show how different languages tend to slightly differ in formal aspects

Table 2: Network 1 parameters for the different languages. N is the number of nodes and ℓ is the number of links, γ is the parameter obtained fitting a power-law to the degree distribution for the nodes, $\bar{C}$ is the average clustering, $\bar{d}$ is the average nodes distances. The parameters with a subscript R refer to the the averages in the random networks and the uncertainties shown are the standard deviations for the calculated averages (in the case $\bar{C}_R$ and $\bar{d}_R$, it is the standard deviation within the ensemble and not the average standard deviation within networks).

Language	N	ℓ	γ	$\bar{C}$	$\bar{d}$	$\bar{C}_R$	$\bar{d}_R$
SPANISH	2705	6912	2.223	0.203 ± 0.343	3.240 ± 0.416	0.002 ± 0.000	4.988 ± 0.015
ENGLISH	1950	6770	2.260	0.248 ± 0.358	3.026 ± 0.379	0.004 ± 0.001	4.123 ± 0.006
DUTCH	2236	7048	2.201	0.294 ± 0.440	3.156 ± 0.413	0.003 ± 0.001	4.388 ± 0.006
BASQUE	3100	7017	2.481	0.069 ± 0.219	3.915 ± 0.657	0.001 ± 0.000	5.408 ± 0.021
GREEK	2745	6990	2.273	0.210 ± 0.349	3.287 ± 0.494	0.002 ± 0.000	5.005 ± 0.013
ITALIAN	2559	6566	2.258	0.153 ± 0.302	3.363 ± 0.446	0.002 ± 0.000	4.946 ± 0.014
PORTUGUESE	2311	5786	2.240	0.198 ± 0.365	3.292 ± 0.442	0.002 ± 0.000	4.945 ± 0.020
FRENCH	2230	6004	2.327	0.207 ± 0.362	3.231 ± 0.391	0.002 ± 0.001	4.737 ± 0.017

when the context is controlled. In particular, these results are of interest to other applied fields. Bear in mind that, in recent decades, the cognitive psychology has paid particular interest to examining factors influencing the recognition of printed words, i.e., frequency, familiarity, word length, age of acquisition among others, according to Andrews (2006). There remain some empirical underlying questions, regarding the question of measuring the word frequency for different languages, from printed manuals to even subtitles. Even if more research is needed here, the comparison between these sources is beyond the scope of this study. Here, we offer a comparison employing different translations of the same printed material in different languages. That allows us to compare differences of word frequency in the same context. Regarding this topic, Perea et al. (2013), Yap et al. (2011) stated that other variables must have a role on frequency, such as the number of contexts in which a word appears. That correspond with the nature of our results. Furthermore, some researchers (van Heuven et al. (2014)) proposed the Zipf-scale as a better standardized measure of word frequency, giving also examples of printed words with various Zipf values. The authors also claimed that an alternative Zipf scale presented in their work is better suited for research in word recognition. Here, we follow the same logic. Thus, these results might offer some insights in to the role of the word frequency effect for print words, but more research in this field is necessary.

Acknowledgment

Table 3: Network 2 parameters for the different languages. N is the number of nodes and ℓ is the number of links, γ is the parameter obtained fitting a power-law to the degree distribution for the nodes, $\bar{C}$ is the average clustering, $\bar{d}$ is the average nodes distances. The parameters with a subscript R refer to the the averages in the random networks and the uncertainties shown are the standard deviations for the calculated averages (in the case $\bar{C}_R$ and $\bar{d}_R$, it is the standard deviation within the ensemble and not the average standard deviation within networks).

Language	N	ℓ	γ	$\bar{C}$	$\bar{d}$	$\bar{C}_R$	$\bar{d}_R$
SPANISH	2682	6418	2.233	0.262 ± 0.518	3.413 ± 0.644	0.002 ± 0.001	5.164 ± 0.017
ENGLISH	1927	6499	2.277	0.332 ± 0.513	3.129 ± 0.506	0.003 ± 0.000	4.167 ± 0.009
DUTCH	2218	6577	2.213	0.370 ± 0.611	3.145 ± 0.560	0.003 ± 0.001	4.515 ± 0.010
BASQUE	3035	6064	2.439	0.157 ± 0.416	3.792 ± 0.948	0.001 ± 0.000	5.784 ± 0.024
GREEK	2703	6266	2.321	0.221 ± 0.481	3.438 ± 0.803	0.002 ± 0.000	5.250 ± 0.018
ITALIAN	2537	6203	2.283	0.163 ± 0.367	3.478 ± 0.654	0.002 ± 0.001	5.068 ± 0.019
PORTUGUESE	2260	5064	2.285	0.232 ± 0.476	3.425 ± 0.792	0.002 ± 0.000	5.230 ± 0.016
FRENCH	2191	5290	2.298	0.202 ± 0.447	3.366 ± 0.712	0.002 ± 0.001	5.007 ± 0.015

References

Amaral, L. A., Scala, A., Barthelemy, M. & Stanley, H. E. (2000), 'Classes of small-world networks', *Proc. Natl. Acad. Sci. U.S.A.* **97**(21), 11149–11152.

Andrews, S. (2006), 'All about words: A lexicalist perspective on reading', *From inkmarks to ideas: Current issues in lexical processing* p. 318.

Beckner, C., Blythe, R., Bybee, J., Christiansen, M. H., Croft, W., Ellis, N. C., Holland, J., Ke, J., Larsen-Freeman, D. & Schoenemann, T. (2009), 'Language is a complex adaptive system: Position paper', *Language learning* **59**(s1), 1–26.

Breland, H. M. (1996), 'Word frequency and word difficulty: A comparison of counts in four corpora', *Psychological Science-Cambridge-* **7**, 96–99.

Cancho, R. F. & Solé, R. V. (2003), 'Least effort and the origins of scaling in human language', *Proceedings of the National Academy of Sciences* **100**(3), 788–791.

Coltheart, M. (1981), 'The mrc psycholinguistic database', *The Quarterly Journal of Experimental Psychology* **33**(4), 497–505.

Crucitti, P., Latora, V., Marchiori, M. & Rapisarda, A. (2003), 'Efficiency of scale-free networks: error and attack tolerance', *Physica A: Statistical Mechanics and its Applications* **320**, 622–642.

Davis, C. J. (2005), 'N-watch: A program for deriving neighborhood size and other psycholinguistic statistics', *Behavior research methods* **37**(1), 65–70.

Dijkstra, E. (1959), 'A note on two problems in connexion with graphs', *Numerische Mathematik* **1**(1), 269–271.
URL: *http://dx.doi.org/10.1007/BF01386390*

Dufau, S., Duñabeitia, J. A., Moret-Tatay, C., McGonigal, A., Peeters, D., Alario, F.-X., Balota, D. A., Brysbaert, M., Carreiras, M., Ferrand, L. et al. (2011), 'Smart phone, smart science: how the use of smartphones can revolutionize research in cognitive science', *PloS one* **6**(9), e24974.

Erdös, P. and Rényi, A. (1960), On the Evolution of Random Graphs, *in* 'Publication of the mathematical institute of the hungarian academy of sciences', , pp. 17–61.

Esteves, C. S., Oliveira, C. R., Moret-Tatay, C., Navarro-Pardo, E., Carli, G. A. D., Silva, I. G., Irigaray, T. Q. & Argimon, I. I. d. L. (2015), 'Phonemic and semantic verbal fluency tasks: normative data for elderly brazilians', *Psicologia: Reflexão e Crítica* **28**(2), 350–355.

Gamermann, D., Montagud, A., Jaime Infante, R., Triana, J., Urchueguía, J. & Fernández de Córdoba, P. (2014), 'Pynetmet: Python tools for efficient work with networks and metabolic models', *Computational and Mathematical Biology* (3), 1–11.

Haykin, S. (1994), *Neural Networks: A Comprehensive Foundation*, 1st edn, Prentice Hall PTR, Upper Saddle River, NJ, USA.

Moreno-Cid, A., Moret-Tatay, C., Irigaray, T. Q., Argimon, I. I., Murphy, M., Szczerbinski, M., Martínez-Rubio, D., Beneyto-Arrojo, M. J., Navarro-Pardo, E. & Fernández, P. (2015), 'The role of age and emotional valence in word recognition: An ex-gaussian analysis', *Studia Psychologica* **57**(2), 83–94.

Moret-Tatay, C. & Perea, M. (2011*a*), 'Do serifs provide an advantage in the recognition of written words?', *Journal of Cognitive Psychology* **23**(5), 619–624.

Moret-Tatay, C. & Perea, M. (2011*b*), 'Is the go/no-go lexical decision task preferable to the yes/no task with developing readers?', *Journal of experimental child psychology* **110**(1), 125–132.

Navarro-Pardo, E., Navarro-Prados, A. B., Gamermann, D. & Moret-Tatay, C. (2013), 'Differences between young and old university students on a lexical decision task: Evidence through an ex-gaussian approach', *The Journal of General Psychology* **140**(4), 251–268.

Pastor-Satorras, R., Vazquez, A. & Vespignani, A. (2001), 'Dynamical and correlation properties of the internet', *Phys. Rev. Lett.* **87**(25), 258701.

Perea, M., Comesaña, M., Soares, A. P. & Moret-Tatay, C. (2012), 'On the role of the upper part of words in lexical access: Evidence with masked priming', *The Quarterly Journal of Experimental Psychology* **65**(5), 911–925.

Perea, M., Gatt, A., Moret-Tatay, C. & Fabri, R. (2012), 'Are all semitic languages immune to letter transpositions? the case of maltese', *Psychonomic bulletin & review* **19**(5), 942–947.

Perea, M., Moret-Tatay, C. & Carreiras, M. (2011), 'Facilitation versus inhibition in the masked priming same–different matching task', *The Quarterly Journal of Experimental Psychology* **64**(10), 2065–2079.

Perea, M., Moret-Tatay, C. & Gómez, P. (2011), 'The effects of interletter spacing in visual-word recognition', *Acta psychologica* **137**(3), 345–351.

Perea, M., Soares, A. P. & Comesaña, M. (2013), 'Contextual diversity is a main determinant of word identification times in young readers', *Journal of experimental child psychology* **116**(1), 37–44.

Ravasz, E. & Barabasi, A. L. (2003), 'Hierarchical organization in complex networks', *Phys Rev E Stat Nonlin Soft Matter Phys* **67**(2 Pt 2), 026112.

Rives, A. W. & Galitski, T. (2003), 'Modular organization of cellular networks', *Proc. Natl. Acad. Sci. U.S.A.* **100**(3), 1128–1133.

Sternberg, R. J. & Powell, J. S. (1983), 'Comprehending verbal comprehension.', *American Psychologist* **38**(8), 878.

van Heuven, W. J., Mandera, P., Keuleers, E. & Brysbaert, M. (2014), 'Subtlex-uk: A new and improved word frequency database for british english', *The Quarterly Journal of Experimental Psychology* **67**(6), 1176–1190.

Yap, M. J., Tan, S. E., Pexman, P. M. & Hargreaves, I. S. (2011), 'Is more always better? effects of semantic richness on lexical decision, speeded pronunciation, and semantic classification', *Psychonomic Bulletin & Review* **18**(4), 742–750.
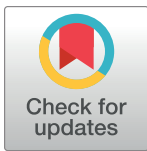
Large scale evaluation of differences between network-based and pairwise sequence-alignment-based methods of dendrogram reconstruction

Daniel Gamermann[1], Arnau Montagud[2,3], J. Alberto Conejero[4]*, Pedro Fernández de Córdoba[4], Javier F. Urchueguía[5]

1 Instituto de Física, Universidade Federal do Rio Grande do Sul (UFRGS), Av. Bento Gonçalves 9500, CP 15051, 91501-970 Porto Alegre RS, Brazil, **2** Institut Curie, PSL Research University, INSERM, U900, 26 rue d'Ulm, F-75005, Paris, France, **3** Barcelona Supercomputing Centre (BSC), C/ Jordi Girona 29, E-08034, Barcelona, Spain, **4** Instituto Universitario de Matemática Pura y Aplicada - IUMPA, Universidad Politécnica de Valencia, E-46022 Valencia, Spain, **5** Instituto Universitario de las Telecomunicaciones Avanzadas - ITACA, Universidad Politécnica de Valencia, E-46022 Valencia, Spain

* aconejero@upv.es

Abstract

Dendrograms are a way to represent relationships between organisms. Nowadays, these are inferred based on the comparison of genes or protein sequences by taking into account their differences and similarities. The genetic material of choice for the sequence alignments (all the genes or sets of genes) results in distinct inferred dendrograms. In this work, we evaluate differences between dendrograms reconstructed with different methodologies and for different sets of organisms chosen at random from a much larger set. A statistical analysis is performed to estimate fluctuations between the results obtained from the different methodologies that allows us to validate a systematic approach, based on the comparison of the organisms' metabolic networks for inferring dendrograms. This has the advantage that it allows the comparison of organisms very far away in the evolutionary tree even if they have no known ortholog gene in common. Our results show that dendrograms built using information from metabolic networks are similar to the standard sequence-based dendrograms and can be a complement to them.

Introduction

Dendrograms are a way to represent relationships among entities, such as species, proteins, coding genes, exons, etc In our case, for a given dendrogram we will consider two types of nodes: leaves (a node connected with another single node) represent species, either current or extincted, and the rest of nodes (connected with more than one node) represent a common ancestor of the nodes hanging from it.

These dendrograms can only be inferred based on data of currently living species or, in a few cases, using fossil records. Currently, the most common methodology to construct (infer)

such dendrograms is to infer the distance of two organisms to their common ancestor based on the comparison (alignment and scoring) of their genetic sequences.

Alignments between sequences are not unique, as the scoring of the alignments can differ. As a consequence, different dendrograms will be reconstructed for the same set of organisms when applying different methodologies (e.g. distance matrix, maximum parsimony, maximum likelihood, Bayesian inference,. . .) in the reconstruction. Even the same methodology may result in different dendrograms depending on the material used to study, e.g. a single gene, a set of genes, amino acid sequences or whole genomes. Therefore, it is important to obtain a dendrogram and compare it to others. In other words, measurements to compare several dendrograms and their fluctuations are relevant. An accepted such metric is the Robinson-Foulds [1] also known as the symmetric difference metric on dendrograms, which evaluates the cost needed to modify one dendrogram to obtain the other. For further information, see also [2–4].

Closely related species share many genes in common, while distant species share very few traits. Traditionally, phylogenetic relationships among distant species have been computed using the small subunit ribosomal RNA (16S) sequences in the comparisons [5]. Some works have used other conserved sequences, such as a subset of genes [6] or a combination of these [7]. In the last years it has been increasingly feasible to perform these studies using whole genome alignments [8–12]. Studies have underlined the importance of considering only sets of genes [13], but they have been mixed about the usefulness of filtering the genome sequences that are compared [14]. Thus, which is the perfect set of sequences, if any, to obtain a dendrogram that includes very distant species is still a matter of debate [7].

Recently, a new approach based on the comparison of metabolic networks was proposed to infer the distance between two organisms [15]. Metabolic networks are graphs where every metabolite in an organism's metabolome represents a node and pairs of nodes are connected whenever a chemical reaction in the organism's metabolism connects the two metabolites as substrate-product. Metabolic networks' properties have been extensively studied [16] and present many characteristics in common (e.g. approximate scale-free distribution of their node's degrees, high clustering coefficient, small-world structure), which indicate a common internal organization of the studied metabolisms.

A metabolic network is reconstructed using the information of all enzymes contained in an organism. Therefore, it contains the information of a large subset of this organism's genome. Moreover, even organisms far away in the evolutionary tree will share important pathways; also, many metabolites (nodes) are ubiquitous and will be present in all species. This explains that differences and similarities can always be established between two given metabolisms. In fact, is has been published that the comparison of metabolic networks represents a valuable tool to infer phylogenetic relationships [15, 17, 18].

In this work, we systematically construct and compare dendrograms built from different sets of organisms using different genes, proteins or networks. We present evidences that dendrograms reconstructed using only information from metabolic networks are comparable to more traditional gene-based dendrograms in terms of accuracy and comprehensiveness.

The work is organized as follows: In the *Materials and Methods* section, we explain in detail how we obtained and processed our data to reconstruct the dendrograms, how the sequence alignments were performed and the scoring systems and methods we used to obtain the distance matrices and, lastly, how to evaluate the distances among dendrograms. We also explain the graph-theoretical aspects used in the network comparison, how the "network" dendrograms were constructed and how the dendrograms' differences were evaluated. In the *Results and Discussion* section we explain the statistical analysis performed and discuss our results. We also included an appendix with mathematical details on how the Pagerank algorithm is

used to determine the relative importance of every metabolite in an organism based on their connections to the rest of the metabolic network.

Materials and methods

Dataset used to build the dendrograms

We retrieved from the KEGG database [19] a large set of organisms' genes, and we identified those associated with enzymes. For each enzyme in a given organism, we identified all the chemical reactions associated with that enzyme, such that, for each organism we were able to build a list of all identified chemical reactions potentially present in its metabolism. Moreover, for each gene we obtained their corresponding nucleic acid and amino acid sequences. Details on the procedures used to obtain information from KEGG can be found in [20].

Separately, for each prokaryotic organism in our dataset, we searched the NCBI database for its 16S rRNA subunit sequence using an automatized script including the terms `Genus species[Orgn] AND 16S ribosomal RNA[Titl] NOT partial sequence [Titl]`, where `Genus species` was the binomial nomenclature of each organism in the dataset obtained from KEGG. In this way, only complete sequences were considered and partial ones discarded.

Our original data set built with KEGG's information comprised 4803 organisms. From these, the metabolic networks of 3972 organisms were completed, whereby NCBI searches retrieved 16S rRNA subunit sequences for 1537 of them. The intersection of all these sets resulted in a dataset with 1506 prokaryote organisms for which we had complete information, *i.e.* we had all sequences for their enzymes, the complete list of chemical reactions and 16S rRNA nucleotide sequences.

Definition and construction of dendrograms

Our analysis is based on three categories of dendrograms, referred to as *gene-based dendrograms*, *network dendrograms*, and *random dendrograms*. Gene-based dendrograms are those constructed with sequence alignments. We compute three different gene-based dendrograms, the difference between them coming from the sequence (or sequences) used in the alignments: either a large set of proteins (amino acid sequences); a single protein from this set; or the 16S rRNA subunit nucleic-acid sequences. Metabolic network dendrograms are those constructed via comparison of metabolic networks reconstructed from the list of chemical reactions that is obtained from the annotation of the organism's genome. Finally, random dendrograms are constructed by linking the organisms in a set at random.

Given a set of N organisms the first step in our proposed dendrogram reconstruction is the evaluation of a symmetric $N \times N$ distance matrix (D), where each element element D_{ij} is a measure of the distance between organism i and j. The evaluation of this matrix follows different methodologies that are described in the following subsections. Here we explain the reconstruction of the dendrogram once the D matrix is calculated, following the same procedure as in [15].

The matrix D can be viewed as a complete weighted graph $G = (V, E, w)$. The set of nodes V stands for all the organisms in the dataset. Each pair of different organisms are linked by an edge in E. A non-negative function $w : E \rightarrow \mathbb{R}_0^+$ associates a weight to each edge, according to the distance between the organisms connected by that edge. Once this weighted graph is generated, we apply Kruskal algorithm to obtain a minimum spanning tree. A *spanning tree* is an acyclic and connected subgraph $G' = (V'E', w')$ of G such that $V' = V$ and $E' \subset E$. The edges in E' have the same weights as the corresponding ones in E. Among all the spanning trees of a

given graph G, a *minimum spanning tree* is a spanning tree such that the sum of the weights associated to their edges is minimum respect to all the admissible spanning trees of G. Further information on trees and graphs can be found in [21]. From this minimum spanning tree a *dendrogram* is obtained that represents the relationships among the given set of N organisms. The lengths of the branches in the *dendrogram* are proportional to the distances in the matrix D.

Gene-based dendrogram construction

Gene-based dendrograms are based on pairwise alignment of nucleotides or amino acid sequences, *i.e.* the matrix distance D for the organisms present in a set is evaluated from the result obtained from sequence alignments done using the *Needleman-Wunsch* algorithm [22] with affine gap penalty. The algorithm inserts gaps in the sequences to create the alignment that maximizes some score S. In the scoring of an alignment the opening of a gap subtracts 10 points from S and every extension of the gap subtracts 0.5 points. In the nucleotide alignments every match of nucleotides adds 5 points and a mismatch subtracts 4 points, while for the alignment of amino acid sequences, different standard matrices are used (BLOSUM and PAM). Given the alignment score S we define the parameter P as:

$$P \quad = \quad 1 - \frac{S}{M} \tag{1}$$

were M is the maximum score possible (the score which would be obtained with no mismatches and no gaps in the alignment). The smaller P is, the closer the two sequences are. Typically, P is a value between 0 and 1 but, for very bad alignments, a P larger than 1 is possible, meaning that gaps and mismatches in the alignment subtracted more points than matches added.

In the comparison of two organisms $1 \le i, j \le N$, if each organism has only one sequence to be compared, the distance D_{ij} between both of them is just the result for P in (1) obtained from the alignment of this sequence. If one or both organisms in a comparison have more than one sequence corresponding to the same gene we match each sequence from the organism with the least number of sequences to its best alignment with sequences from the other organism. Then, we set the distance D_{ij} as the average $\bar{P}$ for the values of P obtained from each possible alignment.

Three different gene-based dendrograms were constructed for each set of organisms, called *DRIBO*, *DENZS* and *D1ENZ*:

- *DRIBO* is a dendrogram constructed using the rRNA sequences for the 16S ribosomal subunit.

- *DENZS* is a dendrogram constructed using the amino acid sequences of all proteins associated to all EC numbers common to all organisms in a set. (The average number of common EC numbers among all organisms in a set, for the organisms sets we worked with, was 40.15 ± 20.73.)

- *D1ENZ* is a dendrogram constructed using the amino acid sequences associated to a single EC number taken at random from all EC numbers common to all the organisms in the set.

Network dendrogram construction

For the construction of dendrograms based on networks, the matrix distance D is obtained from the comparison of the metabolic networks of each pair of organisms in the set following [15]. In this previous work, a parameter (ζ) is defined as the result of the comparison of two

networks. This parameter depends on weighted averages over different sets of metabolites (common or not to each pair of organisms), where the weights of the metabolites are evaluated according to their connectivity degree. In present work, we will test an array of parameters, including this ζ, to establish the one that produces dendrograms that are closer to the ones produced by the other methodologies.

Given two arbitrary organisms $1 \leq i, j \leq N$, we consider the metabolic networks of each one of these organisms as weighted graphs. In these graphs, nodes stand for metabolites and edges between a pair of nodes indicate the presence of a chemical reaction in the corresponding organism's metabolism linking the two metabolites as substrate and product.

A successful approach to measure the importance of a node in a network can be obtained using the Pagerank algorithm [23]. This was inspired by the eigenvalue problem on scientometrics and successfully used in the former versions of the Google browser and afterwards, Pagerank has been extensively used in network theory for different purposes. For instance, in computational biology it has been used to determine which are the key species in a food web that can cause the collapse of the entire system [24] or to improve outcome prediction for cancer patients [25]. In our work, Pagerank is used to assign weights to the edges of the graph that results of the union of the metabolic networks of all organisms in a set. For further details, please refer to the S1 File.

From the metabolic network of organisms i and j, let us define the sets of edges A_{ij}, B_{ij} and C_{ij}, where A_{ij} is the set of edges present in organism i but not in j, B_{ij} is the set of edges present in organism j but not in i, and C_{ij} is the set of edges present simultaneously in both networks of organisms i and j.

Given these three sets, A_{ij}, B_{ij}, and C_{ij} let us define the following parameters:

$$\alpha_{ij} = \sum_{l \subset A_{ij}} w_l \tag{2}$$

$$\beta_{ij} = \sum_{l \subset B_{ij}} w_l \tag{3}$$

$$\gamma_{ij} = \sum_{l \subset C_{ij}} w_l \tag{4}$$

where the sums are made for the weights w_l, given by the Pagerank, of all edges l in each set. Details of the evaluation of weights are discussed in the S1 File. Defined as such, the parameters α_{ij} and β_{ij} represent measures of the differences between the networks i and j in respect to each other, while the parameter γ_{ij} is a measurement of the similarity between them (Fig 1).

Different network dendrograms were constructed for each set of organisms, based on different choices of parameters for the distance matrix D:

- *DS1* is obtained when the distance matrix is given by $D_{ij} = |n_i - n_j|$ where n_i is the number of nodes in each network.

- *DS2* is obtained if $D_{ij} = |e_i - e_j|$, where e_i is the number of links in each network.

- *DNET1* is obtained if $D_{ij} = \frac{n_{tot}}{\gamma_{ij}}$, where n_{tot} is the number of common metabolites in networks i and j.

- *DNET2* is obtained if $D_{ij} = \alpha_{ij} + \beta_{ij}$, where α_{ij} and β_{ij} are defined in (2) and (3).

- *DNET3* is obtained if $D_{ij} = \frac{\alpha_{ij} + \beta_{ij}}{\gamma_{ij}}$, where α_{ij}, β_{ij} and γ_{ij} are defined in (2)–(4).
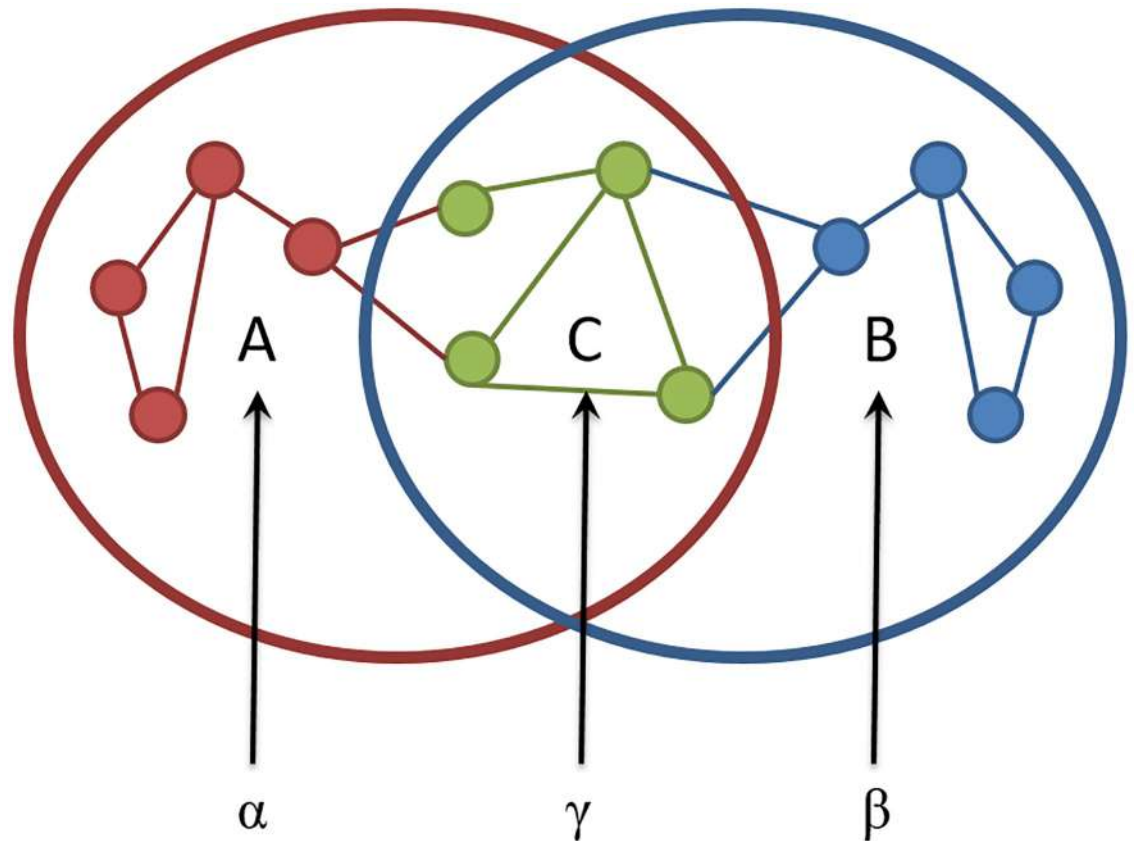
Fig 1. Network dendrogram construction parameters. Schematic representation of A, B and C sets and their parameters of the network dendrogram construction.

- *DNET4* is obtained if $D_{ij} = \zeta_{ij}$, with ζ_{ij} calculated varying the procedure presented in [15]. In [15], parameters α, β and γ were evaluated following the same principles as in present work, but the sums in (2)–(4) were made over nodes and not over links and the weights of the nodes were related to their connectivity. Finally, the parameter ζ_{ij} is the equivalent to the parameter used in *DNET3* above, but using nodes and not links in the evaluation.

Note that *DS1* and *DS2* are two different ways of comparing the difference in size of two given networks, while the other dendrograms in this list take into account different measurements of the importance of the links and/or nodes which are either common to both networks or particular to only one of them. Additionally to these dendrograms, we also consider dendrograms build linking the different species at random, termed RAND in Table 1 and DRAND in Tables 2 and 3 and Figs 2 and 3. These random dendrograms are produced by generating a symmetrical distance matrix whose elements are uniformly distributed random numbers.

Dendrogram comparisons

Since different methods have been proposed for generating dendrograms from the same set of organisms, a measure is needed to compare them. Robinson-Foulds metric, introduced in [1], allows to measure similarity among two dendrograms. This metric has been widely used since it is not limited to binary trees and is based on counting elementary operations which

Table 1. Comparison of DENZS dendrograms built using different scoring matrices for the first ensemble (10 sets of 20 organisms in each set).

DENDROGRAMS	BLO 55	BLO 62	BLO 90	PAM 60	PAM 120	PAM 250	RAND
BLO 45	0.055 ± 0.025	0.524 ± 0.038	1.219 ± 0.071	2.082 ± 0.137	1.146 ± 0.104	0.462 ± 0.113	15.237 ± 0.463
BLO 55		0.516 ± 0.036	1.210 ± 0.068	2.064 ± 0.136	1.135 ± 0.108	0.480 ± 0.114	15.246 ± 0.462
BLO 62			0.721 ± 0.062	1.581 ± 0.123	0.662 ± 0.098	0.805 ± 0.133	15.733 ± 0.493
BLO 90				0.897 ± 0.080	0.305 ± 0.075	1.479 ± 0.152	16.383 ± 0.536
PAM 60					1.021 ± 0.084	2.344 ± 0.183	17.213 ± 0.596
PAM 120						1.368 ± 0.150	16.318 ± 0.554
PAM 250							15.088 ± 0.480
RAND							

https://doi.org/10.1371/journal.pone.0221631.t001

transform one dendrogram into another. The lower the difference between two dendrograms is, the more similar the two dendrograms are. A more detailed description can be found in the S1 File. Several algorithms have been described to efficiently compute this metric [2, 3], but in this work we have considered the implementation in the Python library DendroPy [26].

Two ensembles were constructed by randomly choosing organisms from the 1506 organisms set for which there was complete information. The first ensemble contains 10 sets of organisms, each set containing 20 organisms. The second ensemble contains 10 sets of 30 organisms. S2 File contains the organisms in each set in each ensemble. In the additional files, each organism is identified by its KEGG code (usually a 3 letter code).

Table 2. Comparison of different gene-based and network dendrograms for the first ensemble (10 sets of 20 organisms in each set).

DENDROGRAMS	D1ENZ	DRIBO	DS1	DS2	DNET1	DNET2	DNET3	DNET4	DRAND
DENZS	3.796 ± 1.471	4.631 ± 1.706	13.062 ± 0.402	13.036 ± 0.380	5.345 ± 1.348	5.612 ± 1.076	8.432 ± 1.345	7.189 ± 1.427	15.156 ± 0.417
D1ENZ		4.918 ± 1.964	12.022 ± 1.742	11.999 ± 1.872	5.687 ± 1.991	5.698 ± 1.642	7.936 ± 2.592	6.782 ± 1.888	14.200 ± 1.933
DRIBO			9.883 ± 1.430	9.848 ± 1.493	4.910 ± 0.678	5.497 ± 0.874	5.931 ± 1.612	5.504 ± 1.110	12.091 ± 1.532
DS1				3.147 ± 1.209	9.673 ± 1.901	9.987 ± 1.878	6.762 ± 1.771	8.455 ± 1.494	9.150 ± 0.480
DS2					9.614 ± 1.753	9.902 ± 1.365	6.656 ± 1.682	8.362 ± 1.408	9.148 ± 0.423
DNET1						3.968 ± 0.513	3.929 ± 0.635	4.361 ± 1.307	12.254 ± 1.293
DNET2							5.982 ± 1.165	5.379 ± 0.963	12.728 ± 1.127
DNET3								3.953 ± 0.888	9.938 ± 1.085
DNET4									11.050 ± 1.109

https://doi.org/10.1371/journal.pone.0221631.t002

Table 3. Comparison of different gene-based and network dendrograms for the second ensemble (10 sets of 30 organisms in each set).

| DENDROGRAMS	D1ENZ	DRIBO	DS1	DS2	DNET1	DNET2	DNET3	DNET4	DRAND
DENZS	4.482 ± 1.040	6.635 ± 1.524	18.157 ± 0.709	18.202 ± 0.747	7.925 ± 2.445	8.458 ± 0.700	12.380 ± 1.701	10.129 ± 1.827	22.456 ± 0.835
D1ENZ		6.625 ± 1.752	17.028 ± 2.314	17.028 ± 2.379	8.333 ± 2.739	8.735 ± 0.874	11.728 ± 2.983	9.750 ± 2.659	21.295 ± 2.334
DRIBO			14.118 ± 1.629	14.140 ± 1.641	7.532 ± 1.480	8.392 ± 1.509	8.859 ± 2.307	7.123 ± 1.825	18.479 ± 1.452
DS1				5.046 ± 1.076	13.342 ± 2.805	15.033 ± 1.702	8.645 ± 1.449	11.584 ± 1.408	12.970 ± 0.897
DS2					13.328 ± 2.625	15.078 ± 1.717	8.700 ± 1.317	11.622 ± 1.253	13.028 ± 0.917
DNET1						6.347 ± 2.633	6.035 ± 1.762	5.976 ± 1.099	18.153 ± 2.231
DNET2							9.536 ± 2.679	8.036 ± 2.136	19.841 ± 1.785
DNET3								5.391 ± 1.401	14.121 ± 0.940
DNET4									16.337 ± 0.933

https://doi.org/10.1371/journal.pone.0221631.t003
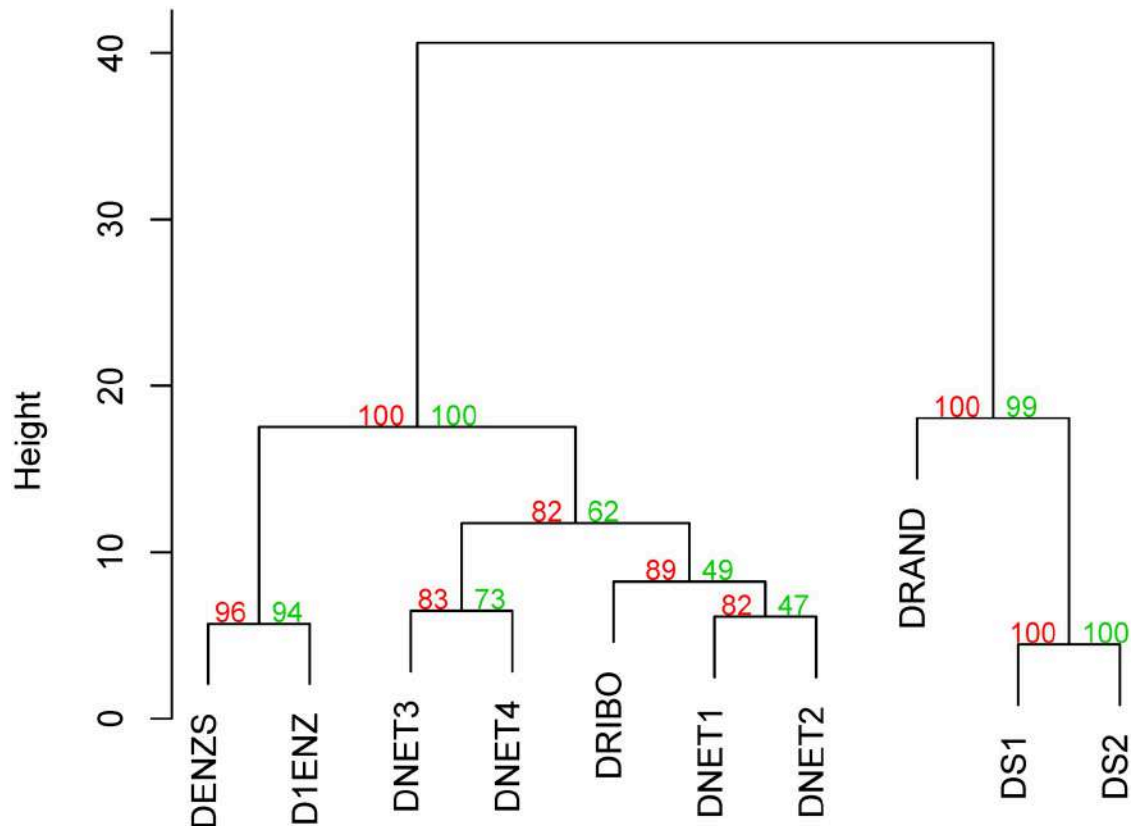
Fig 2. Cluster of dendrograms built with different methodologies for the first ensemble of organisms. Ward's minimum variance method was used for the agglomerative hierarchical clustering using Euclidean distances. P-values are shown in green for approximately unbiased (AU) and in red for bootstrap probability (BP).

https://doi.org/10.1371/journal.pone.0221631.g002

The procedure adopted is the following: given an ensemble, for each organisms' set in the ensemble, the different distance matrices are calculated and gene-based and network dendrograms are constructed. So, for each set, 9 distance matrices (3 gene-based and 6 based on networks) are evaluated and the corresponding 9 dendrograms are constructed. Each dendrogram is compared to the rest of dendrograms using the Robinson-Foulds metric, totaling 36 comparisons (as there are 36 possible combinations of 9 elements two by two). This is repeated for each set in the ensemble and the resulting comparisons are averaged over all sets.

Note that the distance parameter in each methodology has arbitrary units. For comparing the dendrograms, we rescale the distances in the dendrograms such that the biggest distance is always 1. Also note that distances do not have a direct correspondence to any real unit, only the relative distance has a meaning. Therefore, a rescaling of the numbers in a dendrogram should not result in any bias in the comparisons.

Fig 4 illustrates the workflow adopted: we have picked at random the sets of organisms to build up both ensembles, then we have compared their sequences and we have built dendrograms using Kruskal algorithm. Then we have compared the different dendrograms using Robinson-Foulds metric.

Results and discussion

We have worked with two ensembles of organism information, all constructed by randomly selecting these from the 1506 organisms dataset for which we had complete information
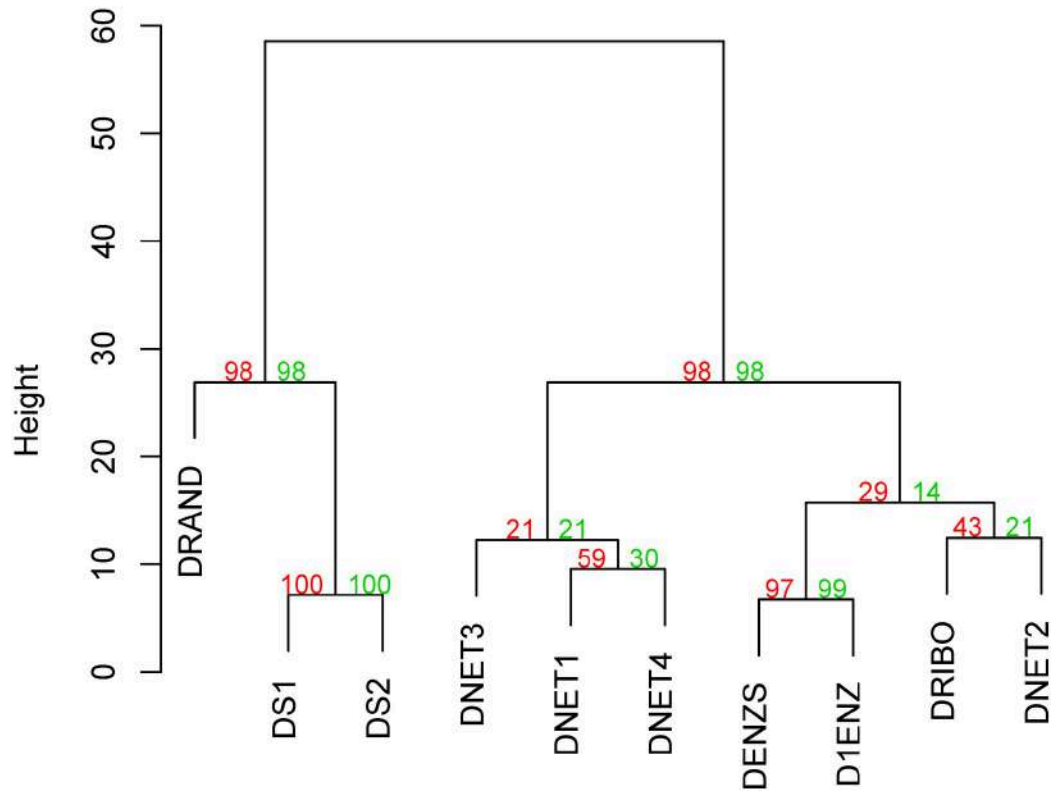
Fig 3. Cluster of dendrograms built with different methodologies for the second ensemble of organisms. Ward's minimum variance method was used for the agglomerative hierarchical clustering using Euclidean distances. P-values are shown in green for approximately unbiased (AU) and in red for bootstrap probability (BP).

(sequence information of the enzymes and their 16S rRNA and the complete list of chemical reactions, see the aforementioned dataset subsection). The first ensemble contained ten organisms sets with twenty organisms in each set while the second ensemble contained ten organisms sets with thirty organisms in each set.
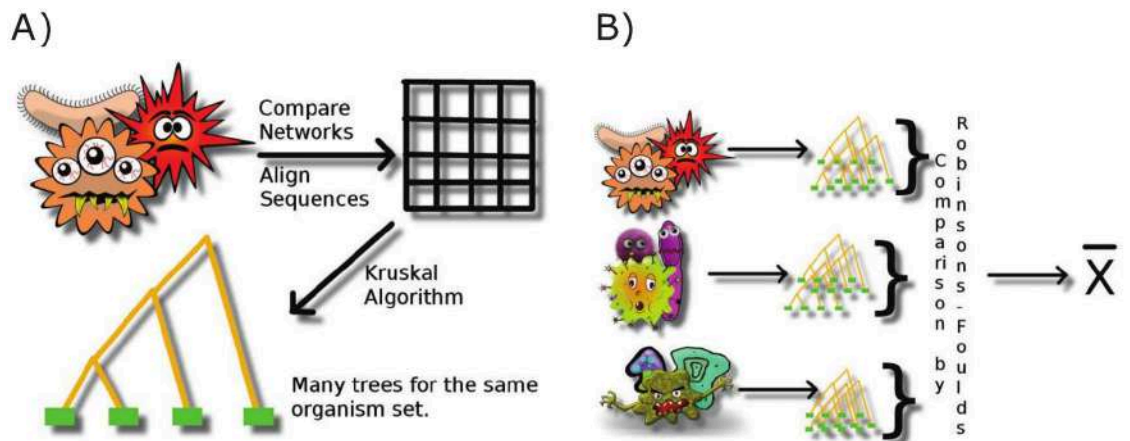
Fig 4. Workflow for evaluating and comparing dendrograms. A) We first obtain dendrogram for a given organism set. B) We compare the difference between dendrograms for many sets. Bacteria cartoons from https://pixabay.com/.

For each set in a given ensemble, we constructed 3 gene-sequence-based dendrograms (denoted by DRIBO that includes information of 16S rRNA, DENZS that includes information of all the enzymes in common among the species of the dendrogram and D1ENZ that includes information of one randomly-chosen enzyme in common among the species of the dendrogram), 6 network-based dendrograms (denoted by DS1 that includes information of the nodes, DS2 that includes information of the links and DNET1, DNET2, DNET3 and DNET4 that include information of the metabolic network) and 100 random dendrograms (DRAND).

Then we compared each dendrogram with the rest by calculating the symmetric differences among them, *i.e.* the Robinson-Foulds metric. We evaluated the average and standard deviation for every pair of dendrograms for each organisms set in each ensemble, so that all comparisons were covered.

We were interested in comparing dendrograms built using very different types of information. For this, we have used the randomly-generated dendrograms (DRAND) as the worst-case example to which dissimilarity was expected to be maximal and have used a set of examples of different dendrograms that use the same information as the best-case examples among which dissimilarity was expected to be minimal. We have used DRIBO as a common standard for sequence alignment as 16S rRNA is universally present, rarely subjected to horizontal gene transfer and have broad coverage of taxa between domain and species. D1ENZ and DENZS have been used considered as examples of enzyme sequence data use, while DS1 and DS2 as examples of use of network properties. Finally, DNET1, DNET2, DNET3 and DNET4 have been considered as examples of use of metabolic network data).

We wanted to compare our dendrograms built with enzyme sequences information with well-known distances of amino acid substitutions. Thus, we compared the DENZS, a dendrogram constructed using amino acids sequences from all enzymes common to the organisms considered, built using different scoring matrices, such as BLOSUM and PAM matrices. BLOSUM matrices are amino acids substitution matrices based on observed alignments [27]. BLOSUM45 is used for distantly-related proteins and BLOSUM62 for midrange-related proteins. On the other hand, PAM amino acids substitution matrices' observations are extrapolated from comparisons of closely related proteins, as they look for point accepted mutations (PAM) [28]. These consist on the replacement of a single amino acid in the protein sequence with another single amino acid. For instance, PAM250 matrix was calculated based on 1572 observed mutations in 71 families of proteins with alignments that were more than 85% identical [29]. Unsurprisingly, Table 1 shows small distances between DENZS dendrograms built with different substitution matrices and, thus, the resulting dendrograms are very similar. This is due to the fact that PAM and BLOSUM matrices have equivalences, for instance, PAM250 retrieves very similar results as BLOSUM45 [29] and, thus, dendrograms built with equivalent substitution matrices will be similar. From this diversity of DENZS dendrograms, we chose to use for the following comparison only the DENZS built with the BLOSUM55 matrix.

The results of the dissimilarity averages are in Tables 1–3 with the standard deviation depicted as uncertainty. The smaller the value in an element in one of these tables is, the more similar the corresponding dendrograms are. In S3 File, we provide all 9 dendrograms obtained for each set of each ensemble.

In order to visualize the comparison of results, dendrograms were built from the tables using *pvclust* R package [30] using Ward.D2 clustering method and Euclidean distance on the Robinson-Foulds values for each dendrogram pair. Two different methods of significance are shown: approximately unbiased p-value (AU, in green) and bootstrap probability value (BP, in red). AU p-value is computed by multiscale bootstrap resampling and is generally a better approximation to unbiased p-value than BP value that is computed by normal bootstrap resampling [30].

Results for the first ensemble with ten sets of twenty organisms each (Table 2 and Fig 2) were similar to the ones for the second ensemble with ten sets of thirty organisms each (Table 3 and Fig 3). In Tables 2 and 3, DRAND dendrograms can be seen to have the greatest dissimilarity values to the rest of the dendrograms, leaving the smallest values to dendrograms built using similar type of information. This can be seen in Figs 2 and 3, where DS1 and DS2, D1ENZ and DENZS and the different DNETs, cluster together. DRIBO, constructed using 16S rRNA sequences and used as our common standard, clusters with DNET1 and DNET2 on the first ensemble and with DNET2 in the second ensemble. In fact, in the second ensemble DNET2 cluster with DRIBO before clustering with the rest of the DNETs dendrograms. In both ensembles dendrograms built using metabolic network (DNET1, DNET2, DNET3 and DNET4) and enzymes (D1ENZ and DENZS) information are closer to DRIBO than dendrograms built using information on number of nodes (DS1) or links (DS2) or randomly built (DRAND). In fact, in both ensembles DRAND, DS1 and DS2 are an outgroup of the sequence-based and metabolic network dendrograms (Figs 2 and 3).

The proximity of DNETs dendrograms to DRIBO and their distance to DRAND supports our claim that the use of metabolic network information can complement the established dendrograms built using sequence data. DNETs dendrograms are closer than D1ENZ and DENZS to DRIBO in one ensemble, but not in the other. Thus, our results show that gene sequence- and metabolic-network-based dendrograms are equally distant from the 16S rRNA standard DRIBO. Also, expectedly, values in Tables 2 and 3 are higher than in Table 1 where the only difference in the construction of the dendrograms was the scoring matrices used in the alignments.

Conclusions

Building dendrograms is an approximation to capture distances and relationships among different species. Present work targets the potential of using the species' metabolic topologies to find distances as a complementary method to pair-wise sequence comparison of enzymes. The results of the two ensembles suggest that, in some cases, network comparison might be even better than amino acid sequence alignment of enzymes to infer relationships between organisms. On the other hand, considering networks' size as a distance between organisms is a very poor way to capture the relationship among organisms, as can be seen with the results for dendrograms DS1 (number of nodes in the network) and DS2 (number of links), that are closer to DRAND than to gene-based dendrograms.

The last decade has provided researchers with loads of sequences from a wide variety of organisms, promoting the development of new tools and the renewal of old ones. Hereby, we have shown the possibility to incorporate topological information in these studies, as well as to compare dendrograms built with very different methodologies and to study their ability to capture the relationship among species comparing them with the alignment of the 16S subunit of ribosomal RNA. This shows the potential of network studies to explain and complement sequence alignment methodologies and contributes to build methodologies in which distances and relationships among species may be calculated considering very different sources of information, such as a recent work where metabolic networks and evolution have been shown to give very interesting insights into one another [31].

Supporting information

S1 File. The Pagerank algorithm. A brief explanation of the Pagerank algorithm used in present work.
(PDF)

S2 File. Ensembles of organisms. The file `ensembles.txt` contains the organisms (referred to by their KEGG code) in each set in each ensemble used in this work. (TXT)

S3 File. Dendrograms of each ensemble. The file `trees.txt` contains all dendrograms generated for each set in each ensemble in `newick` format. (TXT)

Acknowledgments

We thank Salvador Capella-Gutiérrez for helpful discussions on the topic.

Author Contributions

Conceptualization: Pedro Fernández de Córdoba, Javier F. Urchueguía.

Data curation: Daniel Gamermann.

Formal analysis: Daniel Gamermann, J. Alberto Conejero.

Funding acquisition: J. Alberto Conejero, Pedro Fernández de Córdoba, Javier F. Urchueguía.

Investigation: Arnau Montagud.

Methodology: Daniel Gamermann, J. Alberto Conejero.

Validation: Arnau Montagud.

Writing – original draft: Daniel Gamermann, Arnau Montagud, J. Alberto Conejero.

Writing – review & editing: Daniel Gamermann, Arnau Montagud, J. Alberto Conejero, Pedro Fernández de Córdoba, Javier F. Urchueguía.

References

1. Robinson DF, Foulds LR. Comparison of phylogenetic trees. Mathematical Biosciences. 1981; 53(1–2):131—147. http://dx.doi.org/10.1016/0025-5564(81)90043-2.

2. Day WE. Optimal algorithms for comparing trees with labeled leaves. Journal of Classification. 1985; 2(1):7–28. https://doi.org/10.1007/BF01908061

3. Pattengale ND, Gottlieb EJ, Moret BME. Efficiently computing the Robinson-Foulds metric. J Comput Biol. 2007; 14(6):724–735 (electronic). https://doi.org/10.1089/cmb.2007.R012 PMID: 17691890

4. Böcker S, Canzar S, Klau G. The Generalized Robinson-Foulds Metric. In: Darling A, Stoye J, editors. Algorithms in Bioinformatics. vol. 8126 of Lecture Notes in Computer Science. Springer Berlin Heidelberg; 2013. p. 156–169. Available from: http://dx.doi.org/10.1007/978-3-642-40453-5_13.

5. Woese CR, Fox GE. Phylogenetic structure of the prokaryotic domain: the primary kingdoms. Proc Natl Acad Sci USA. 1977; 74(11):5088–5090. https://doi.org/10.1073/pnas.74.11.5088 PMID: 270744

6. Ciccarelli FD, Doerks T, von Mering C, Creevey CJ, Snel B, Bork P. Toward automatic reconstruction of a highly resolved tree of life. Science. 2006; 311(5765):1283–1287. https://doi.org/10.1126/science.1123061 PMID: 16513982

7. Lienau EK, DeSalle R, Allard M, Brown EW, Swofford D, Rosenfeld JA, et al. The mega-matrix tree of life: using genome-scale horizontal gene transfer and sequence evolution data as information about the vertical history of life. Cladistics. 2010; 27(4):417–427. https://doi.org/10.1111/j.1096-0031.2010.00337.x

8. Wu M, Eisen JA. A simple, fast, and accurate method of phylogenomic inference. Genome Biol. 2008; 9(10):R151. https://doi.org/10.1186/gb-2008-9-10-r151 PMID: 18851752

9. Wu D, Hugenholtz P, Mavromatis K, Pukall R, Dalin E, Ivanova NN, et al. A phylogeny-driven genomic encyclopaedia of Bacteria and Archaea. Nature. 2009; 462(7276):1056–1060. https://doi.org/10.1038/nature08656 PMID: 20033048

10. Dewey CN. In: Anisimova M, editor. Whole-Genome Alignment. Totowa, NJ: Humana Press; 2012. p. 237–257. Available from: https://doi.org/10.1007/978-1-61779-582-4_8.

11. Mai H, Lam TW, Ting HF. A simple and economical method for improving whole genome alignment. BMC Genomics. 2017; 18(4):362. https://doi.org/10.1186/s12864-017-3734-2 PMID: 28589863

12. Feng B, Lin Y, Zhou L, Guo Y, Friedman R, Xia R, et al. Reconstructing Yeasts Phylogenies and Ancestors from Whole Genome Data. Scientific Reports. 2017; 7(1):15209. https://doi.org/10.1038/s41598-017-15484-5 PMID: 29123238

13. Rokas A, Williams BL, King N, Carroll SB. Genome-scale approaches to resolving incongruence in molecular phylogenies. Nature. 2003; 425(6960):798–804. https://doi.org/10.1038/nature02053 PMID: 14574403

14. Jeffroy O, Brinkmann H, Delsuc F, Philippe H. Phylogenomics: the beginning of incongruence? Trends Genet. 2006; 22(4):225–231. https://doi.org/10.1016/j.tig.2006.02.003 PMID: 16490279

15. Gamermann D, Montagud A, Conejero JA, Urchueguia JF, de Cordoba PF. New approach for phylogenetic tree recovery based on genome-scale metabolic networks. J Comput Biol. 2014; 21(7):508–519. https://doi.org/10.1089/cmb.2013.0150 PMID: 24611553

16. Jeong H, Tombor B, Albert R, Oltvai ZN, Barabasi AL. The large-scale organization of metabolic networks. Nature. 2000; 407(6804):651–654. https://doi.org/10.1038/35036627 PMID: 11034217

17. Clemente JC, Satou K, Valiente G. Phylogenetic reconstruction from non-genomic data. Bioinformatics. 2007; 23(2):e110–115. https://doi.org/10.1093/bioinformatics/btl307 PMID: 17237077

18. Deyasi K, Banerjee A, Deb B. Phylogeny of metabolic networks: A spectral graph theoretical approach. Journal of Biosciences. 2015; 40(4):799–808. https://doi.org/10.1007/s12038-015-9562-0 PMID: 26564980

19. Kanehisa M, Goto S. KEGG: kyoto encyclopedia of genes and genomes. Nucleic Acids Res. 2000; 28(1):27–30. https://doi.org/10.1093/nar/28.1.27 PMID: 10592173

20. Reyes R, Gamermann D, Montagud A, Fuente D, Triana J, Urchueguia JF, et al. Automation on the generation of genome-scale metabolic models. J Comput Biol. 2012; 19(12):1295–1306. https://doi.org/10.1089/cmb.2012.0183 PMID: 23210477

21. Gross JL, Yellen J, Zhang P. Handbook of Graph Theory, Second Edition. 2nd ed. Chapman & Hall/CRC; 2013.

22. Needleman SB, Wunsch CD. A general method applicable to the search for similarities in the amino acid sequence of two proteins. J Mol Biol. 1970; 48(3):443–453. https://doi.org/10.1016/0022-2836(70)90057-4 PMID: 5420325

23. Brin S, Page L. The anatomy of a large-scale hypertextual Web search engine. Computer Networks and ISDN Systems. 1998; 30(1–7):107–117. http://dx.doi.org/10.1016/S0169-7552(98)00110-X.

24. Allesina S, Pascual M. Googling Food Webs: Can an Eigenvector Measure Species' Importance for Coextinctions? PLoS Comput Biol. 2009; 5(9):e1000494. https://doi.org/10.1371/journal.pcbi.1000494 PMID: 19730676

25. Winter C, Kristiansen G, Kersting S, Roy J, Aust D, Knösel T, et al. Google Goes Cancer: Improving Outcome Prediction for Cancer Patients by Network-Based Ranking of Marker Genes. PLoS Comput Biol. 2012; 8(5):e1002511. https://doi.org/10.1371/journal.pcbi.1002511 PMID: 22615549

26. Sukumaran J, Holder MT. DendroPy: a Python library for phylogenetic computing. Bioinformatics. 2010; 26(12):1569–1571. https://doi.org/10.1093/bioinformatics/btq228 PMID: 20421198

27. Henikoff S, Henikoff JG. Amino acid substitution matrices from protein blocks. Proc Natl Acad Sci USA. 1992; 89(22):10915–10919. https://doi.org/10.1073/pnas.89.22.10915 PMID: 1438297

28. Dayhoff MO, Schwartz RM. Chapter 22: A model of evolutionary change in proteins. In: in Atlas of Protein Sequence and Structure; 1978.

29. Pearson WR. In: Selecting the Right Similarity-Scoring Matrix. John Wiley & Sons, Inc.; 2002. Available from: http://dx.doi.org/10.1002/0471250953.bi0305s43.

30. Suzuki R, Shimodaira H. Pvclust: an R package for assessing the uncertainty in hierarchical clustering. Bioinformatics. 2006; 22(12):1540–1542. https://doi.org/10.1093/bioinformatics/btl117 PMID: 16595560

31. Plata G, Henry CS, Vitkup D. Long-term phenotypic evolution of bacteria. Nature. 2015; 517(7534):369–372. https://doi.org/10.1038/nature13827 PMID: 25363780

An analysis of the temperature field of the workpiece in dry continuous grinding

**J. L. González–Santander · J. Pérez ·
P. Fernández de Córdoba · J. M. Isidro**

Abstract   The recent model for heat transfer during intermittent grinding described in Skuratov, Ratis, Selezneva, Pérez, Fernández de Córdoba and Urchueguía (Appl Math Model 31:1039–1047, 2007) is considered. This model is particularized to the case of continuous dry grinding, where an alternative solution is obtained in the steady state. This alternative solution is analytically equivalent to the well-known formula of Jaeger (Proc R Soc NSW 76:204–224, 1942) for the steady–state temperature field created by an infinite moving source of heat and proves to be very useful for evaluating the maximum point of the temperature.

Keywords   Dirac delta representation · Dry grinding process · Jaeger's formula

1 Introduction

Two relevant contributions on mathematical modelling of the grinding problem [1,2] use coupled systems of two-dimensional partial differential equations to calculate the evolution of the temperature fields in the wheel, the workpiece and the grinding fluid. These models are nonlinear in that they allow for temperature-dependent contact heat source and heat-exchanger coefficients. These works extend an improved model allowing heat-flux variation along the grinding zone [3]. Recently, a simplified mathematical model was proposed in terms of a two-dimensional boundary-value problem where the interdependence among the grinding wheel, the workpiece and the coolant was described by two-variable functions in the boundary condition [4]. An analytical expression for the evolution of the workpiece temperature field during intermittent wet grinding was given. The heat partitioning to other heat sinks [5] is then fully decoupled. A numerical analysis of this solution was presented in [6]. In the present paper, we show that the solution of the mathematical problem [4] for the particular case of dry continuous grinding and in the steady-state is given by an expression that is analytically equivalent to the well-known integral formula of Jaeger [7]. The proof of the equivalence of both expressions (3.6) and (4.8), is derived from the uniqueness of the solution of the problem (see Sect. 5.2)

Our setup is depicted in Fig. 1. The workpiece moves at a constant speed v_d and is assumed to be infinite along Ox and Oz, and semiinfinte along Oy. The plane $y = 0$ is the surface being ground. The contact area between

J. L. González–Santander · J. Pérez · P. F. de Córdoba · J. M. Isidro (✉)
Instituto Universitario de Matemática Pura y Aplicada, IUMPA Departamento de Matemática Aplicada, Universidad Politécnica de Valencia, Camino de Vera s/n, Valencia 46022, Spain
e-mail: joissan@mat.upv.es
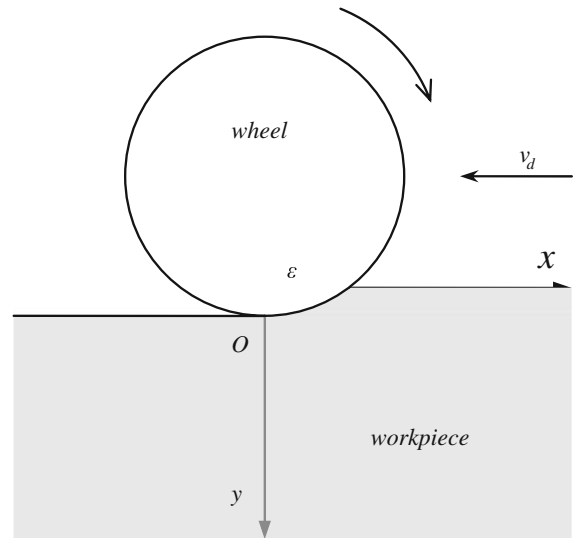
the wheel and the workpiece is an infinitely long strip of width ε located parallel to the Oz-axis and on the plane $y = 0$. Both the wheel and the workpiece are assumed rigid. Although our equations below allow for the case of wet and intermittent grinding, we will mostly consider the case of dry and continuous grinding.

This paper is organized as follows. Section 2 presents the differential equations governing our problem which are extracted from [4]. Section 3 gives a brief summary of the steady-state solution to the these equations following [7]. The time-dependent thermal field is derived in Sect. 4 and analyzed in detail in Sect. 5. Emphasis is laid on determining the maximum of the temperature for the workpiece that takes place in the steady-state. Our conclusions are summarized in Sect. 6.

2 Problem formulation

Our problem is modelled by the heat equation in the presence of a convective term [4]

$$\partial_t T(t, x, y) = k \left[\partial_{xx} T(t, x, y) + \partial_{yy} T(t, x, y) \right] - v_d \partial_x T(t, x, y), \tag{2.1}$$

subject to the initial condition

$$T(0, x, y) = 0, \tag{2.2}$$

and to the boundary condition

$$k_0 \partial_y T(t, x, 0) = b(t, x) T(t, x, 0) + d(t, x), \tag{2.3}$$

where $-\infty < x < \infty$ and $t \geq 0$, $y \geq 0$. Above, $b(t, x)$ is the heat exchange coefficient between the workpiece and the grinding wheel, and $d(t, x)$ is the heat generated by friction between the two. Under the assumption of dry grinding, the workpiece is thermally insulated, and $b(t, x) = 0$. In this case we have that $d(t, x)$ equals the heat flux ϕ between the wheel and the workpiece. Now the heat flux ϕ across the plane $y = 0$ is

$$\phi = \rho c (k \nabla T + T \mathbf{v}_d) \cdot \mathbf{n}, \tag{2.4}$$

where $\mathbf{n}$ is the unit normal to the plane $y = 0$, pointing in the direction of $y > 0$. Since $\mathbf{v}_d \cdot \mathbf{n} = 0$ we have

$$\phi = \rho c k \left. \frac{\partial T}{\partial y} \right|_{y=0}. \tag{2.5}$$

3 The steady-state solution

We will first review the steady-state solution to (2.1)–(2.3) as given in [7]. In the absence of lubrication fluid, the workpiece is assumed to be thermally isolated form the environment, so we can set

$$b(t, x) = 0. \tag{3.1}$$

Moreover, in the case of continuous grinding, we may assume that the physical contact between the wheel and the workpiece extends over an interval $x \in (0, \varepsilon)$, friction being zero outside. This can be modeled as

$$d(t, x') = -Q_s H(x') H(\varepsilon - x'), \tag{3.2}$$

where Q_s is the frictional heat-generation source term into the workpiece and $H(x)$ is a step function. For the details of parameter Q_s see references [6,8]. That is, the heat flux due to friction is localized exactly on the contact area (an infinitely long strip of width ε) between the wheel and the workpiece. This solution is constructed from the expression for the Green function corresponding to (2.1) when $v_d = 0$. For a point source of heat power Q_p located at (x', y', z'), this function is given by

$$T(t, x, y, z; x', y', z') = \frac{Q_p}{8(\pi k t)^{3/2}} \exp\left\{-\frac{1}{4kt}\left[(x - x')^2 + (y - y')^2 + (z - z')^2\right]\right\}. \tag{3.3}$$

The superposition principle is applied to (3.3). This is first done for $v_d = 0$. The temperature field $T(x, y)$ corresponding to an infinite linear source along the z-axis on the plane $y = 0$ can be obtained by superposition of point sources such as (3.3). Then the motion of the source along the Ox-axis, with a speed v_d, is modeled by changing coordinates to a moving reference frame. In the stationary state, when $t \to \infty$, one finds that an infinitely long, infinitely thin linear source causes a temperature field within the medium given by

$$T(x, y) = \frac{Q_l}{2\pi \rho c k} \exp\left(-\frac{v_d x}{2k}\right) K_0\left(\left|\frac{v_d}{2k}\right| \sqrt{x^2 + y^2}\right), \tag{3.4}$$

where Q_l is the heat power of the infinite linear source and $K_0(x)$ is the modified Bessel function of order zero [9, Sect. 9.6].

Further, applying the superposition principle to (3.4), one obtains the temperature field created by an infinitely long source of finite width ε moving exactly as above. If the band releases heat at a rate Q_s, then the steady-state temperature field is found to be given by

$$T(x, y)_{\text{infinite}} = \frac{Q_s}{\pi \rho c v_d} \int\limits_{-v_d x/2k}^{-v_d (x-\varepsilon)/2k} e^u K_0\left(\sqrt{u^2 + \left(\frac{v_d y}{2k}\right)}\right) du. \tag{3.5}$$

Equation 3.5 gives the steady-state temperature field created by an infinitely long flat band of width ε located on the plane $y = 0$ along the z-axis, within an *infinite* medium along the axis Oy. This implies that the temperature field (3.5) does *not* solve the boundary-value problem (2.1)–(2.3). In order to obtain the temperature field created by grinding a *semi-infinite* workpiece (above called medium) in contact with a grinding wheel (above called source), without lubrication, we multiply the temperature field (3.5) by a factor of 2:

$$T(x, y)_{\text{semi-infinite}} = 2T(x, y)_{\text{infinite}} = \frac{2Q_s}{\pi \rho c v_d} \int\limits_{-v_d x/2k}^{-v_d (x-\varepsilon)/2k} e^u K_0\left(\sqrt{u^2 + \left(\frac{v_d y}{2k}\right)^2}\right) du. \tag{3.6}$$

Now (3.6) does solve the boundary-value problem (2.1)–(2.3) along with (3.1)–(3.2). We can verify that the thermal flux across $y = 0$, Eq. 2.5, indeed is nonzero only on the contact area. In order to compute the thermal flux corresponding to (3.6), we first introduce the dimensionless variables $X := v_d x/2k$ and $Y := v_d y/2k$. We can also extend the integral (3.6) to the whole line if we include the appropriate Heaviside functions $H(u)$:

$$T(X, Y)_{\text{semi-infinite}} = \frac{2Q_s}{\pi \rho c v_d} \int\limits_{-\infty}^{\infty} H(X - u) H(u - X + \Delta) e^{-u} K_0\left(\sqrt{u^2 + Y^2}\right) du, \tag{3.7}$$

where $\Delta = v_d \varepsilon / 2k$. This allows one to compute the derivative at $y = 0$ if one uses the representation of the Dirac δ-function given in (5.13), to be derived in Sect. 5.3. We find

$$\phi(x, y = 0) = -Q_s H(x) H(\varepsilon - x), \tag{3.8}$$

as expected.

4 The time-dependent solution

For the time-dependent solution to (2.1)–(2.3) we refer to [4]; what follows is a brief summary thereof. We apply a number of integral transformations on the variables x, y, t; this will turn the differential equation (2.1) into an algebraic equation that can be readily solved. Transforming back into the original variables will yield the solution. Since $t \geq 0$ and $y \geq 0$, the natural transformation to apply on them will be Laplace's. On the other hand, x varies on the whole real line $\mathbb{R}$, so it will be Fourier-transformed. Details can be found in [4]. The result is

$$T(t, x, y) = \frac{1}{4\pi} \int_0^t \frac{\exp\left(-\frac{y^2}{4ks}\right)}{s} \left(\int_{-\infty}^{\infty} \exp\left[-\frac{(x' - x - v_d s)^2}{4ks} \right] \right.$$
$$\left. \times \left[\left(\frac{y}{2ks} - \frac{b(t - s, x')}{k_0} \right) T(t - s, x', 0) - \frac{d(t - s, x')}{k_0} \right] dx' \right) ds. \tag{4.1}$$

Equation 4.1 solves the boundary-value problem (2.1–2.3) along with (3.1, 3.2) exactly. If the workpiece had an initial temperature T_0, then T_0 is to be added as a constant to the above.

Equation 4.1 splits into two summands,

$$T(t, x, y) = T^{(0)}(t, x, y) + T^{(1)}(t, x, y), \tag{4.2}$$

where

$$T^{(0)}(t, x, y) = -\frac{1}{4\pi k_0} \int_0^t \frac{\exp\left(-\frac{y^2}{4ks}\right)}{s} \left(\int_{-\infty}^{\infty} d(t - s, x') \exp\left[-\frac{(x' - x - v_d s)^2}{4ks} \right] dx' \right) ds, \tag{4.3}$$

and

$$T^{(1)}(t, x, y) = \frac{1}{4\pi} \int_0^t \frac{\exp\left(-\frac{y^2}{4ks}\right)}{s} \left(\int_{-\infty}^{\infty} T(t - s, x', 0) \right.$$
$$\left. \times \left[\frac{y}{2ks} - \frac{b(t - s, x')}{k_0} \right] \exp\left[-\frac{(x' - x - v_d s)^2}{4ks} \right] dx' \right) ds. \tag{4.4}$$

Neither $T^{(0)}$ nor $T^{(1)}$ separately is a solution to the boundary-value problem (2.1)–(2.3), but their sum is.

For convenience we will use the notations

$$T(x, y) = \lim_{t \to \infty} T(t, x, y), \tag{4.5}$$

$$T^{(0)}(x, y) = \lim_{t \to \infty} T^{(0)}(t, x, y), \tag{4.6}$$

$$T^{(1)}(x, y) = \lim_{t \to \infty} T^{(1)}(t, x, y) \tag{4.7}$$

for the temperature field in the steady state, so (4.2) simplifies to

$$T(x, y) = T^{(0)}(x, y) + T^{(1)}(x, y). \tag{4.8}$$

5 Analysis of the solution

Following [10, http://hdl.handle.net/10251/4769, Chap.5], next we analyze the solution (4.2)–(4.4). As compared with that found in Sect. 4, the solution (4.2)–(4.4) is more general: it is valid in the transient regime, when t is finite; it also allows for wet and/or pulsed grinding. However, for comparison purposes with the solution of Sect. 4, we will make some simplifying assumptions.

5.1 Continuous dry grinding in the steady state

The simplifying assumptions (3.1) and (3.2) reduce (4.3) and (4.4) to

$$T^{(0)}(t, x, y) = \frac{Q_s}{4\pi k_0} \int_0^t \frac{\exp\left(-\frac{y^2}{4ks}\right)}{s} \left(\int_0^\varepsilon \exp\left[-\frac{y^2 + (x' - x - v_d s)^2}{4ks} \right] dx' \right) ds, \tag{5.1}$$

and

$$T^{(1)}(t, x, y) = \frac{y}{8\pi k} \int_0^t \frac{\exp\left(-\frac{y^2}{4ks}\right)}{s^2} \left(\int_{-\infty}^\infty T(t - s, x', 0) \exp\left[-\frac{y^2 + (x' - x - v_d s)^2}{4ks} \right] dx' \right) ds. \tag{5.2}$$

It will be useful to re-express (5.1) as

$$T^{(0)}(t, x, y) = \frac{Q_s}{4\pi k_0} \int_0^t \frac{\exp\left(-\frac{y^2}{4ks}\right)}{s} F(x, s) \, ds, \tag{5.3}$$

with

$$F(x, s) = \int_0^\varepsilon \exp\left(-\frac{(x' - x - v_d s)^2}{4ks} \right) dx'. \tag{5.4}$$

In the steady state, some manipulations reduce (5.3) to

$$T^{(0)}(x, y) = \frac{Q_s}{\pi \rho c v_d} \int_{-v_d x/2k}^{-v_d(x-\varepsilon)/2k} e^u K_0\left(\sqrt{u^2 + \left(\frac{v_d y}{2k}\right)^2} \right) du, \tag{5.5}$$

or, equivalently, to

$$T^{(0)}(x, y) = \frac{Q_s}{4k_0\sqrt{\pi}} \int_0^\infty \exp\left(-\frac{y^2}{\sigma^2} \right) \left[\text{erf}\left(\frac{x}{\sigma} + \frac{v_d \sigma}{4k} \right) - \text{erf}\left(\frac{x - \varepsilon}{\sigma} + \frac{v_d \sigma}{4k} \right) \right] d\sigma. \tag{5.6}$$

Equation 5.5 is useful in showing the complete agreement with the solution (3.5) for a workpiece stretching along the whole axis Oy. Incidentally, this shows again that (3.5) cannot be an exact solution to the boundary-value problem (2.1)–(2.3), because the term $T^{(1)}(x, y)$ does not vanish identically.

Concerning $T^{(1)}(t, x, y)$, we can rewrite (5.2) as

$$T^{(1)}(t, x, y) = \frac{y}{8\pi k} \int_0^t \frac{\exp\left(-\frac{y^2}{4ks}\right)}{s^2} G(x, t, s) \, ds, \tag{5.7}$$

with

$$G(x, t, s) = \int_{-\infty}^\infty T(t - s, x', 0) \exp\left(-\frac{(x' - x - v_d s)^2}{4ks} \right) dx'. \tag{5.8}$$

Passing again to the steady state, one may reduce (5.7) to

$$T^{(1)}(x, y) = \frac{y v_d^2}{8\pi k^2} \int_{-\infty}^{\infty} T(x', 0) \exp\left(\frac{v_d(x' - x)}{2k}\right) K_1\left(\frac{|v_d|}{2k}\sqrt{y^2 + (x - x')^2}\right) \frac{2k/|v_d|}{\sqrt{y^2 + (x - x')^2}} dx'. \quad (5.9)$$

In the dimensionless variables $X' = v_d x'/2k$, $X = |v_d|x/2k$ and $Y = |v_d|y/2k$ one finds

$$T^{(1)}(X, Y) = \frac{Y}{2\pi} \int_{-\infty}^{\infty} T(X', 0)\, e^{X'-X} \frac{K_1\left(\sqrt{Y^2 + (X' - X)^2}\right)}{\sqrt{Y^2 + (X' - X)^2}} dX'. \quad (5.10)$$

The above integral contains the kernel function

$$N(X - X', Y) := Y \frac{K_1\left(\sqrt{Y^2 + (X' - X)^2}\right)}{\sqrt{Y^2 + (X' - X)^2}}. \quad (5.11)$$

Below we prove that this kernel behaves like a Dirac δ-function on the workpiece surface,

$$\lim_{Y \to 0^+} N(X - X', Y) = \pi \delta(X - X'), \quad (5.12)$$

as one approaches $y = 0$ from above. Equivalently we can write (5.12) as

$$\lim_{y \to 0^\pm} \frac{y}{\pi} \frac{K_1\left(\sqrt{y^2 + u^2}\right)}{\sqrt{y^2 + u^2}} = \pm\delta(u). \quad (5.13)$$

Then by (5.12) in (5.10) we find

$$T^{(1)}(X, 0) = \lim_{Y \to 0^+} \frac{1}{2\pi} \int_{-\infty}^{\infty} T(X', 0)\, e^{X'-X} N(X - X', Y) dX'$$

$$= \frac{1}{2} \int_{-\infty}^{\infty} T(X', 0)\, e^{X'-X} \delta(X - X') dX' = \frac{1}{2} T(X, 0). \quad (5.14)$$

This is an important result: the surface temperature $T(X, 0)$ is twice the value of $T^{(1)}(X, 0)$,

$$T(X, 0) = 2T^{(1)}(X, 0). \quad (5.15)$$

Substitution in (4.8) leads to another important conclusion:

$$T^{(0)}(X, 0) = T^{(1)}(X, 0). \quad (5.16)$$

5.2 Uniqueness of the solution

We can generalize our result (5.16) if we impose further assumptions. In the case of continuous dry grinding, and in the steady state, the boundary-value problem posed in Sect. 2 has a unique solution.[1] By the method of Sect. 3, in the steady state our equation reads

$$\nabla^2 T(x, y) = 0, \quad (5.17)$$

subject to the boundary conditions

$$k_0 \partial_y T(x, 0) = -Q_s H(x) H(\varepsilon - x), \quad \lim_{x \to \pm\infty} T(x, 0) = 0. \quad (5.18)$$

Now non-constant harmonic functions can only attain their extrema on the boundary of their domain [11, Chap. X, Sect. 1], and a standard argument establishes that the solution is unique. We conclude that, under the assumption of continuous dry grinding, the steady-state solutions of Sects. 3 and 4 must be equal:

$$T(x, y)_{\text{semi-infinite}} = 2T^{(0)}(x, y). \quad (5.19)$$

This is stronger than our previous result (5.16), at the cost of imposing the additional assumption that $\lim_{x \to \pm\infty} T(x, 0) = 0$, which was not required to derive (5.16).

---

[1] Of course, the solution may also be unique under more general assumptions than continuous dry grinding in the steady state, but here we are interested in this case only.

5.3 Proof of (5.12)

In (5.11) we have, for $X' \neq X$,

$$\lim_{Y \to 0^+} N(X - X', Y) = 0. \tag{5.20}$$

However, when $X = X'$, we have

$$\lim_{Y \to 0^+} N(0, Y) = \lim_{Y \to 0^+} K_1(|Y|) = \infty, \tag{5.21}$$

because of the singularity of the Bessel function K_1 at the origin. This behavior is reminiscent of the Dirac δ-function. It remains to compute the integral of the kernel function (5.11) and to prove that it is finite, in order to conclude that N is indeed a multiple of the Dirac δ-function. Let us therefore consider the integral

$$I_N := \lim_{Y \to 0^+} \int_{-\infty}^{\infty} N(X - X', Y) \mathrm{d}X'. \tag{5.22}$$

Performing the change of variables $\chi = X' - X$ and remembering that the integrand is even, we can write

$$I_N = 2 \lim_{Y \to 0^+} Y \int_0^{\infty} \frac{K_1\left(\sqrt{Y^2 + \chi^2}\right)}{\sqrt{Y^2 + \chi^2}} \mathrm{d}\chi. \tag{5.23}$$

Now the substitution $u = \sqrt{Y^2 + \chi^2}$ leads to

$$I_N = 2 \lim_{Y \to 0^+} Y \int_Y^{\infty} \frac{K_1(u)}{\sqrt{u^2 - Y^2}} \mathrm{d}u. \tag{5.24}$$

Finally, setting $u = Y \cosh z$, we find

$$I_N = 2 \lim_{Y \to 0^+} Y \int_0^{\infty} K_1(Y \cosh z) \mathrm{d}z. \tag{5.25}$$

A useful expression for K_1 reads [12, Eq. 5.7.11]

$$K_1(x) = \frac{1}{x} + \frac{1}{2} \sum_{k=0}^{\infty} \frac{(x/2)^{2k+1}}{k!(k+1)!} \left[2 \log\left(\frac{x}{2}\right) - \psi(k+1) - \psi(k+n+1) \right], \tag{5.26}$$

where $\psi(x) = \Gamma'(x)/\Gamma(x)$ is the logarithmic derivative of the Euler Gamma function. Hence

$$\lim_{Y \to 0^+} x K_1(\lambda x) = \frac{1}{\lambda}. \tag{5.27}$$

Substitution of (5.27) in (5.25) gives

$$I_N = 2 \int_0^{\infty} \frac{\mathrm{d}z}{\cosh z}. \tag{5.28}$$

This integral is readily evaluated by applying the change of variables $\zeta = \tanh z$, with the result that

$$I_N = \pi, \tag{5.29}$$

and (5.12) follows immediately.

5.4 The maximal temperature as a function of time

We claim that the maximal temperature as a function of the time is attained in the steady state. In order to prove it we observe that, since the integrand of (5.3) is positive and $Q_s > 0$, the integral (5.3) is a monotonically increasing function of the time. We have

$$T^{(0)}(t, x, y) < T^{(0)}(x, y), \quad \forall t \in (0, \infty), \tag{5.30}$$

and the maximum value of $T^{(0)}$ is attained in the steady state. Analogous arguments apply to (5.7), so

$$T^{(1)}(t, x, y) < T^{(1)}(x, y), \quad \forall t \in (0, \infty), \tag{5.31}$$

and again the maximum value of $T^{(1)}$ is reached in the steady state. Altogether, Eqs. 5.30 and 5.31 imply that

$$T(t, x, y) < T(x, y), \quad \forall t \in (0, \infty), \tag{5.32}$$

with $T(t, x, y)$ being a monotonically increasing function of the time. Hence the maximum temperature, as a function of time, is reached in the steady-state, as claimed.

5.5 The maximal temperature as a function of space

By the maximum principle for harmonic functions [11, Chap X, Sect. 1], the maximal temperature must be reached on the boundary, $y = 0$ in our case. Let us analyze the maximum of the function $T(x, 0)$. By (5.15), (5.16) and (5.19) we need to compute the derivative $\partial T^{(0)}(x, 0)/\partial x$. This can be done with the help of (5.6):

$$\frac{\partial T^{(0)}(x, 0)}{\partial x} = \frac{Q_s}{2\pi k_0} \int_0^\infty \left\{ \exp\left[-\left(\frac{x}{\sigma} + \frac{v_d \sigma}{4k}\right)^2\right] - \exp\left[-\left(\frac{x - \varepsilon}{\sigma} + \frac{v_d \sigma}{4k}\right)^2\right]\right\} \frac{d\sigma}{\sigma} \tag{5.33}$$

where the derivative of the error function has been used. To further manipulate (5.33) let us consider the function

$$R(\chi) := \int_0^\infty \exp\left[-\left(\frac{\chi}{\sigma} + \frac{v_d \sigma}{4k}\right)^2\right] \frac{d\sigma}{\sigma}. \tag{5.34}$$

The change of variables $h = (v_d \sigma/4k)^2$ reduces (5.34) to

$$R(\chi) = \frac{1}{2} \exp\left(-\frac{v_d \chi}{2k}\right) \int_0^\infty \exp\left(-\frac{z^2}{4h} - h\right) \frac{dh}{h}, \quad z := \left|\frac{v_d \chi}{2k}\right|, \tag{5.35}$$

and this can be expressed in terms of the Bessel function K_0 as [12, Eq. 5.10.25]

$$R(\chi) = \exp\left(-\frac{v_d \chi}{2k}\right) K_0\left(\left|\frac{v_d \chi}{2k}\right|\right). \tag{5.36}$$

Therefore

$$\frac{\partial T^{(0)}(x, 0)}{\partial x} = \frac{Q_s}{2\pi k_0} \left[R(x) - R(x - \varepsilon)\right]. \tag{5.37}$$

Since $\lim_{x \to 0} K_0(x) = \infty$, we have

$$\lim_{x \to 0} \frac{\partial T^{(0)}(x, 0)}{\partial x} = \infty, \qquad \lim_{x \to \varepsilon} \frac{\partial T^{(0)}(x, 0)}{\partial x} = -\infty, \tag{5.38}$$

and we can limit our search for the zeroes of $\partial T^{(0)}(x, 0)/\partial x$ to the interval $(0, \varepsilon)$. A detailed analysis, supplemented with Bolzano's theorem, establishes the following. When $v_d > 0$, there exists a unique value $c_+ \in (0, \varepsilon)$ at which $T^{(0)}(x, 0)$ attains a maximum. When $v_d < 0$, there also exists a unique value $c_- \in (0, \varepsilon)$ at which $T^{(0)}(x, 0)$ attains a maximum. Moreover, the fact that the error function is odd implies that $c_- = \varepsilon - c_+$.

Table 1 Input data for numerical simulations

ε (m)	2.663×10^{-3}
v_d (m s^{-1})	0.53
Q_s (W m^{-2})	5.89×10^7
k_0 (W m^{-1} K^{-1})	13
k (m^2 s^{-1})	4.23×10^{-6}
T_0 (K)	300

Fig. 2 $T_0 + 2T^{(0)}(x, y)$ for $(x, y) \in (-\epsilon, \epsilon) \times (0, \epsilon/10)$
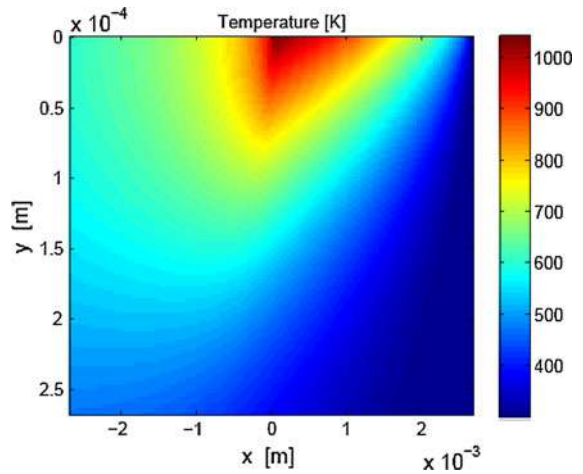
5.6 Numerical example

Very fast and simple numerical algorithms have been implemented in MATLAB to compute the maximum of the workpiece temperature in the steady-state, see Appendix E of reference [10, http://hdl.handle.net/10251/4769, Chap.5] for further details. These algorithms are based on formulas (5.5), (5.19) and (5.37) presented before. Assuming that the workpiece is a VT20 titanium alloy and using the values of the parameters tabulated in Table 1, see references [4,6], we show that the maximum point $c_+ = 0.0072\,\varepsilon$ m and that the maximum value of the temperature, reached on the workpiece surface, $T_{\max} = T_0 + 2T^{(0)}(c_+, 0) = 1042.23$ K. These values agree with the temperature field shown in Fig. 2.

6 Conclusions

Our first conclusion is the equality between the (apparently different) solutions for the temperature field given in the literature (and summarized here in Sects. 3 and 4). Beyond summarizing the existing approaches to the boundary-value problem (2.1)–(2.3), we have presented a detailed analysis of its exact solution in the case of dry grinding. For this purpose, a new representation of the Dirac delta distribution has been developed, involving a modified Bessel function; this new representation of the Dirac delta has not been tabulated in the literature yet.

From an applied point of view, the computation of the maximum temperature is the principal goal. According to this, it has been proved that this maximum is reached in the stationary state within the contact zone on the workpiece surface. It is shown that the numerical computation of this maximum is quite simple from the approach given in the Samara–Valencia model.

The maximal surface temperature, and also the maximal temperature as a function of the time, have been computed theoretically and numerically.

Our analysis can be generalized to the case of wet grinding [13] again considering the assumption of constant heat-transfer coefficient on the workpiece surface. One can expect the results concerning the maximal temperature to be quantitatively different from those of dry grinding. We expect to report on these issues soon.

References

1. Andrews KT, Shillor M, Wright S (1999) A model for heat transfer in grinding. Nonlinear Anal 35:233–246
2. Gu RJ, Shillor M, Barber GC, Jen T (2004) Thermal analysis of the grinding process. Math Comput Model 39:991–1003
3. Jen T-C, Lavine AS (1995) A variable heat flux model of heat transfer in grinding: model development. ASME J Heat Transf 117:473–478
4. Skuratov D, Ratis Y, Selezneva I, Pérez J, Fernández de Córdoba P, Urchueguía J (2007) Mathematical modelling and analytical solution for workpiece temperature in grinding. Appl Math Model 31:1039–1047
5. Lavine AS, Jen T-C (1991) Coupled heat transfer to workpiece, wheel, and fluid in grinding, and the occurrence of workpiece burn. Int J Heat Mass Transf 34:983–992
6. Pérez J, Hoyas S, Skuratov D, Ratis Y, Selezneva I, Fernández de Córdoba P, Urchueguía J (2008) Heat transfer analysis of intermittent grinding processes. Int J Heat Mass Transf 51:4132–4138
7. Jaeger JC (1942) Moving sources of heat and the temperature at sliding contacts. Proc R Soc NSW 76:204–224
8. Malkin S (1989) Grinding technology: theory and applications of machining with abrasives. Ellis Horwood Limited, England
9. Abramowitz M, Stegun I (1972) Handbook of mathematical functions. NBS Applied Mathematics Series 55, Washington
10. González–Santander J (2008) Master's thesis, Universidad Politécnica de Valencia
11. Conway J (2001) Functions of one complex variable I. Springer Graduate Texts in Mathematics, New York
12. Lebedev N (1965) Special functions and their applications. Dover, New York
13. Guo C, Malkin S (1992) Analysis of fluid flow through the grinding zone. J Eng Ind 114:427

Article

A Probabilistic Classification Procedure Based on Response Time Analysis Towards a Quick Pre-Diagnosis of Student's Attention Deficit

M. Hernaiz-Guijarro [1], J. C. Castro-Palacio [2,*], E. Navarro-Pardo [3] , J. M. Isidro [1] and P. Fernández-de-Córdoba [1]

[1] Instituto Universitario de Matemática Pura y Aplicada, Grupo de Modelización Interdisciplinar, InterTech, Universitat Politècnica de València, E-46022 Valencia, Spain; moihergu@doctor.upv.es (M.H.-G.); joissan@mat.upv.es (J.M.I.); pfernandez@mat.upv.es (P.F.-d.-C.)

[2] Institute of Nuclear Fusion, ETSII, Universidad Politécnica de Madrid, c/José Gutiérrez Abascal, 2, 28006 Madrid, Spain

[3] Departamento de Psicología Evolutiva y de la Educación, Grupo de Modelización Interdisciplinar, InterTech, Universitat de València, E-46010 Valencia, Spain; esperanza.navarro@uv.es

* Correspondence: juancarlos.castro@upm.es or juanccastro2007@yahoo.com

check for updates

Abstract: A classification methodology based on an experimental study is proposed towards a fast pre-diagnosis of attention deficit. Our sample consisted of school-aged children between 8 and 12 years from Valencia, Spain. The study was based on the response time (RT) to visual stimuli in computerized tasks. The process of answering consecutive questions usually follows an ex-Gaussian distribution of the RTs. Specifically, we seek to propose a simple automatic classification scheme of children based on the most recent evidence of the relationship between RTs and ADHD. Specifically, the prevalence percentage and reported evidence for RTs in relation to ADHD or to attention deficit symptoms were taken as reference in our study. We explain step by step how to go from the computer-based experiments and through the data analysis. Our desired aim is to provide a methodology to determine quickly those children who behave differently from the mean child in terms of response times and thus are potential candidates to be diagnosed for ADHD or any another cognitive disorder related to attention deficit. This is highly desirable as there is an urgent need for objective instruments to diagnose attention deficit symptomatology. Most of the methodologies available nowadays lead to an overdiagnosis of ADHD and are not based on direct measurement but on interviews of people related to the child such as parents or teachers. Although the ultimate diagnosis must be made by a psychologist, the selection provided by a methodology like ours could allow them to focus on assessing a smaller number of candidates which would help save time and other resources.

Keywords: attention deficit hyperactivity disorder (ADHD); reaction time; ex-Gaussian analysis

1. Introduction

Among cognitive disorders, attention deficit hyperactivity disorder (ADHD) common in children and can be present until an adult age in about 30–50% of cases [1,2]. It usually comes with problems paying attention, hyperactivity and impulsive behavior [3]. There are other elements associated with ADHD such as behavior problems, low academic performance, rejection, non-compliance with others, with others, and lack of social skills [4,5]. These educational and psychosocial consequences that come with ADHD and have long-term impact can be alleviated with early assessment and treatment [6]. An estimate of the world prevalence percentage of ADHD is 5–7% in school-aged children (American Psychiatric Association, 2013).

The process of diagnosing ADHD is somewhat long and tedious compared to the diagnosis of other mental disorders [7]. According to the American Academy of Child and Adolescent Psychiatry (AACAP), the assessment of ADHD should include collecting information from the parents, school, interviews with the child, and gathering information about the overall functioning of the child, including the child's medical, social, and family histories [8]. Given the fact that performing a good diagnosis of ADHD may be a difficult and long task to do, it is desirable to count on a methodology capable of determining quickly those children more likely to be diagnosed with ADHD. Based on this first screening, clinicians can make a more definite diagnosis. A methodology with these features may contribute enormously to saving resources and serve as a guide to psychologists.

Previous work [9] has reported that children suffering from ADHD can be impulsive and respond faster than other children. On the other hand, their performance is very slow in cognitive tasks. Their mean response times are higher independently from the specific ability being tested [10–12]. Overall, children with ADHD show both very fast and very slow responses and thus present a high intra-individual variability (IIV) [13].

Response time distribution are positively skewed [14] and thus are not properly described by standard central tendency estimators, for instance, the mean and standard deviation [15,16]. In this respect, the ex-Gaussian function has been proven to optimally fit the probability distribution curves of the RT [17,18]. This function results from a convolution of a Gaussian and an exponential function [19] from where, there interpretable parameters result: μ, σ, and τ [15,20]. Parameters μ and σ come from the Gaussian function and τ from the exponentially distributed component, which relates to the positive skew of the RT distribution. Where the data are represented by ex-Gaussian function, trimming of the data is not necessary which may lead to a subjective variation of the sample by removing extremely high RT values treated as outliers.

There are a number of works in the literature where the ex-Gaussian function is used to represent the RT data and interpret its parameters μ, σ, and τ in relation to cognitive disorders. For instance, parameters σ and τ, along with the standard deviation of the ex-Gaussian function have been found to be related to ADHD in adults. Similarly, correlation was found between τ and the rate of omission errors [17]. In the case of youth with ADHD, the ex-Gaussian analysis revealed larger standard deviation and parameter τ (of the exponential component) [21]. In Reference [22], the authors, studied ADHD and autism spectrum disorder (ASD) in children aged 7–10 years to gain insights into the attentional fluctuations, related to increased response time variability. The ex-Gaussian parameters are claimed to be clearly correlated with cognitive processes such as attention. The exponential component τ seems to be diagnostic of ADHD particularly in boys [23]. However, the authors in Reference [18] determined that this is not absolutely true, as the ex-Gaussian parameters may not correspond uniquely to specific cognitive processes. In this respect, they point out that researchers should be more careful when examining the changes in the ex-Gaussian parameters.

In summary, when it comes to interpreting the ex-Gaussian parameters, children showing a combination of higher μ values and low τ values are more likely to have slower response times. On the other hand, children showing lower values of the parameter μ and higher values of τ correlate with much faster or much lower responses. The representation of the data in terms of an ex-Gaussian distribution has been a common procedure whose benefits have been widely discussed in the literature [24–27].

The main advantage of the ex-Gaussian analysis consists of its three parameters may be correlated with cognitive processes [26], although there is a large debate about the functional interpretation of these parameters [21]. In this respect, τ seems to be the parameter attracting the most attention and has been described as a perceptual aspect of RT [28], related to decision [14] and in more recent works, as a defective effort control mechanism or attentional component [23]. In addition, there are plenty of works in the literature supporting the idea of interpreting the response time in computerized tasks in terms of ex-Gaussian parameters as a useful approach to gain access to a more sensitive and specific measure of variability in patients with ADHD [29].

In this work, a response time classification methodology based on an experimental study is proposed towards a quick pre-diagnosis of attention deficit or any another cognitive disorder related with it. Our sample consisted of school-aged children between 8 and 12 years from Valencia, Spain. Response times (RTs) were collected from computerized tasks based on visual stimuli.

First, we aimed to find the empirical probability distribution for the response time which can be considered the normative behavior of a child in the population that was explored. Subsequently, we proposed a classification methodology that identified those children lying furthest from the normative behavior of a child. The RT data were represented in terms of the ex-Gaussian function and its three parameters. Subsequently, the probability distributions of these parameters and of the mode were used to establish a classification methodology. The ex-Gaussian parameters were also considered in a more global approach as components of a vector, which is associated to each child through its norm definitions.

Our main hypothesis is that, taking into account the prevalence percentage of ADHD in general, childhood population, and the most recent evidence of the relationship between RTs and attention deficit in the literature, we should be able to establish a simple automated classification scheme of children with attention deficit based on their statistical RT distribution to visual stimuli.

We explain in detail all stages followed in the data analysis. Our ultimate aim was to provide a classification methodology to determine, without going through the entire diagnosis process, those children who may be behaving differently from the mean child regarding attention deficit and thus are potential candidates to be diagnosed with ADHD or any another cognitive disorders. This is the first part of a series of works on classification methodologies based on different representations of the RT data and their relationship with cognitive disorders.

2. Materials and Methods

2.1. Participants

A sample of 190 children (95 males and 95 females) with ages between 8 and 12 years. The age distribution of the sample is shown in panel a) of Figure 1. The overall mean age was 9.5 years, with a standard deviation (SD) of 1.3 years. The mean ages and standard deviations of females and males were 9.4 (SD = 1.3) and 9.7 (SD = 1.2) years, respectively. The differences were not statistically significant. The children who participated in the experiments attended a primary school in Valencia (Spain). This public school is located in the La Patacona District of Alboraia municipality. We obtained all necessary consents and authorizations at all necessary levels, namely, the children's parents, the Direction of the School, and the City Council. This study was carried out in accordance with the recommendations of the Secretariat of Education of the Valencian Community. The protocol was approved by the Government of Valencia (Generalitat Valenciana). The due written consent of the children's parents or legal guardians was obtained in accordance with the Declaration of Helsinki [30]. The children forming our sample were not previously diagnosed with ADHD. The children participating in the computerized experiments had never had any health issue, such as any seizures, brain injury or any other neurological damage, which could bias the results by mimicking ADHD. This information was obtained from parents and from school psychologists, who assessed all the children at the start of primary school and continued to assess them biannually.
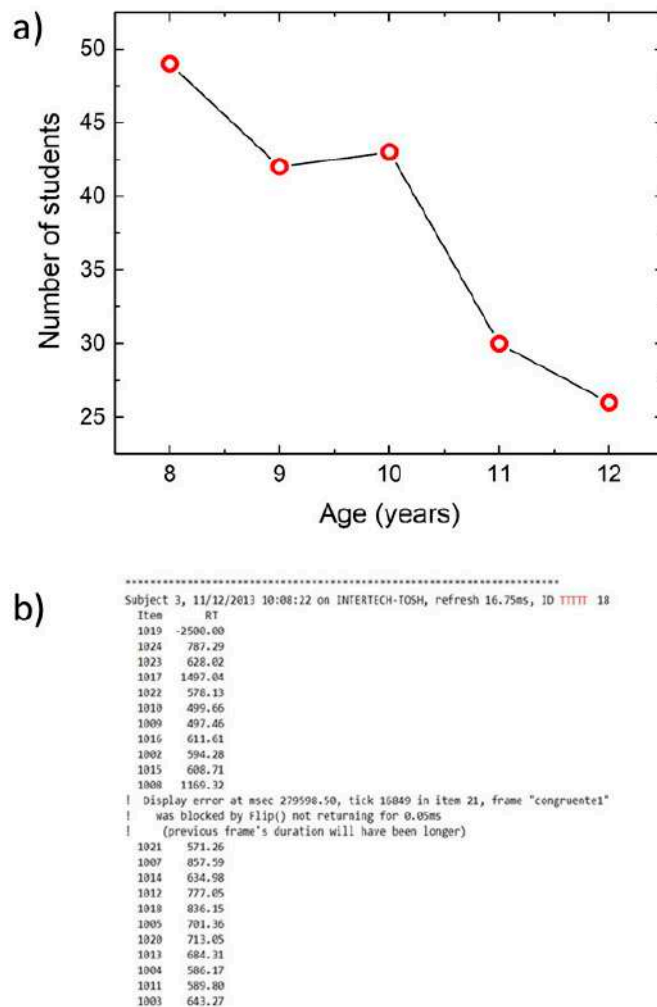
Figure 1. The age distribution of the sample is shown in panel (**a**) and a fragment of a *.azk output file in panel (**b**). In order to protect the privacy of the child who performed the experiment, the characters "TTTTT" have been used as a pseudonym for the actual name.

2.2. Experiments with DMDX

Computer-based experiments were carried out through the Windows program DMDX [31] widely used in the community of experimental and cognitive psychologists [26,32]. By means of this program, stimuli were presented to the participants and RTs recorded. The tasks applied in this work were designed by psychologists of the Interdisciplinary Modeling Group *InterTech* (www.intertech.upv.es), a team from both the Polytechnic University of Valencia and the University of Valencia, Spain. Experiments were carried out in a quiet classroom and using laptop computers bearing DMDX software. Each experiment lasted for 6–7 min and stimuli were presented randomly to avoid order presentation effects.

The experiments included an attention network task (ANT) [32] which seeks testing three attentional networks: alerting, orienting, and executive control. Alerting network is assessed by changes in reaction time as a result of a warning signal. Orienting is related with changes in the RT indicating where the target will take place. Finally, the efficiency of the executive control is carried out by asking the children to answer by pressing the keys in indicating left or right direction of an image placed at the center in between neutral, congruent or incongruent flankers. These three networks are very related among them [33,34]. Each stimulus consisted of 5 fish aligned horizontally looking at the right or the left (Figure 2a). The color is black and the background is white. The objective of the task was to identify, in each trial, the direction of the central fish. There were three cases depending on the

orientation of the fish around the central one. The neutral case was when there was only the central fish. The congruent case was where the surrounding fish were placed in the same direction as the central fish. The third case was where the surrounding fish were placed in the opposite direction in respect to the central one. If the central fish was facing right, the key labeled "M" should be pressed, if not, the key labeled "Z" should be pressed (Figure 2a). Four cue conditions anticipated the appearance of the target, namely, "no cue", "central cue", "spatial cue", and "double cue" which vary depending on the stimulus (Figure 2b). A total of 144 stimuli were presented in a random way and for a maximum of 2500 ms or until the child pressed a key.
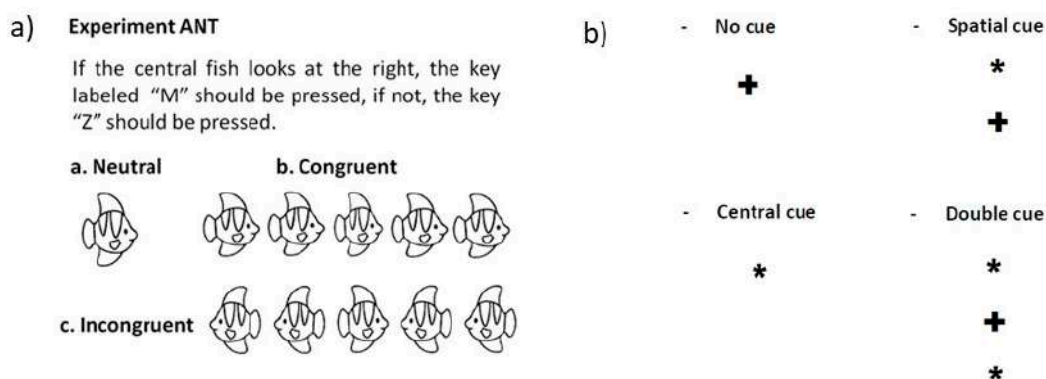
Figure 2. In panel (**a**), a visual example of the attention network task (ANT) carried out in this work is shown whereas in panel (**b**), the four cue conditions are included.

2.3. Procedure for the Data Analysis

The results of the experiments performed on DMDX software were saved out to a file with the extension *.azk. Figure 1b shows a fragment of this file. First, a heading with the computer and student data can be found. Just after, two columns are shown. The first named "ITEM" contains a number assigned to each item in the design of the experiments. The second column indicates the response time in milliseconds.

Two types of errors can be found in the output data. The first happens when the child does not react after the exposure time of the image (2500 ms) has passed. The second error takes place when the child does not respond correctly and presses the wrong key. Errors have not been analyzed in the present study, although they can correlate with attention deficit. This important aspect will be considered in full in a further article which is currently under way.

By using a home-made code written in FORTRAN, the output files (*.azk) were filtered such that records with errors were not included. The data were organized in the new file with three columns. The first column was a number identifying each trial (child), the second was the item number in the experiment, and the third was the response time.

Once the output files were cleaned by removing the undesired records, histograms of the response times were constructed for each trial. Different bin widths were tried out. The optimal bin size used to construct the histograms was 50 ms. Subsequently, probability distribution functions were calculated by means of dividing the counts per bin by the total number of counts. The probability distribution functions were the starting point for the statistical analysis carried out in this work. In a first part, descriptive statistics were used and in the second an ex-Gaussian analysis with the corresponding interpretation of the three parameters of this function.

3. Results and Discussions

Figure 3 summarizes the results from filtering the output data (.azk files) obtained with DMDX program for the tasks considered in this work. Specifically, it shows the averages over the probability density curves corresponding to the data obtained with each laptop computer used to carry out the

experiments. It can be seen that the DMDX program corrects properly the timing differences among the microprocessors. The number of response times included in each average is indicated between parentheses. It can be also noticed that all curves almost overlap and peak around 575 ms approximately.
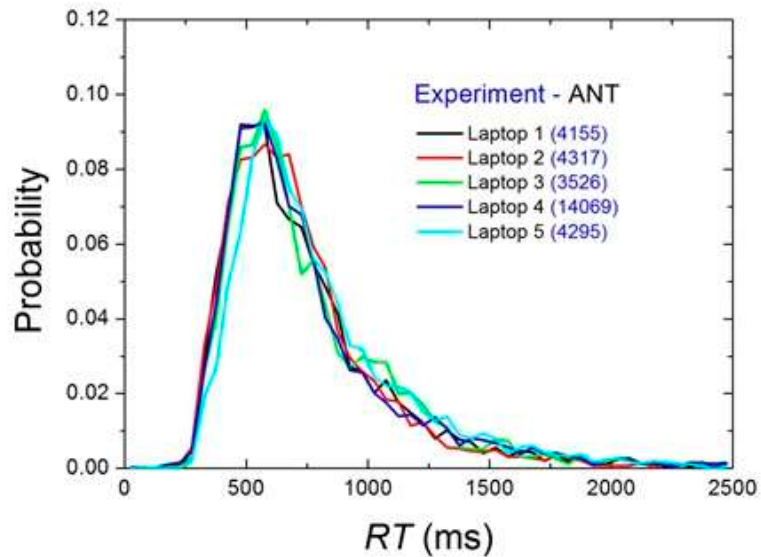

Figure 3. Comparison of the outputs from the different laptop computers used in the experiments.

The probability distributions of the RTs are shown in Figure 4. These curves where obtained from the histograms by dividing the number of counts corresponding to each bin over the total number of counts. The bin-by-bin average curve is represented along with the single curves. We worked with a sample of children who had not been diagnosed with ADHD before; however, there may occur a 7% prevalence rate within the sample. In any case, we assumed that this 7% would not significantly vary the mean curve shown in Figure 4, which represents the average child.
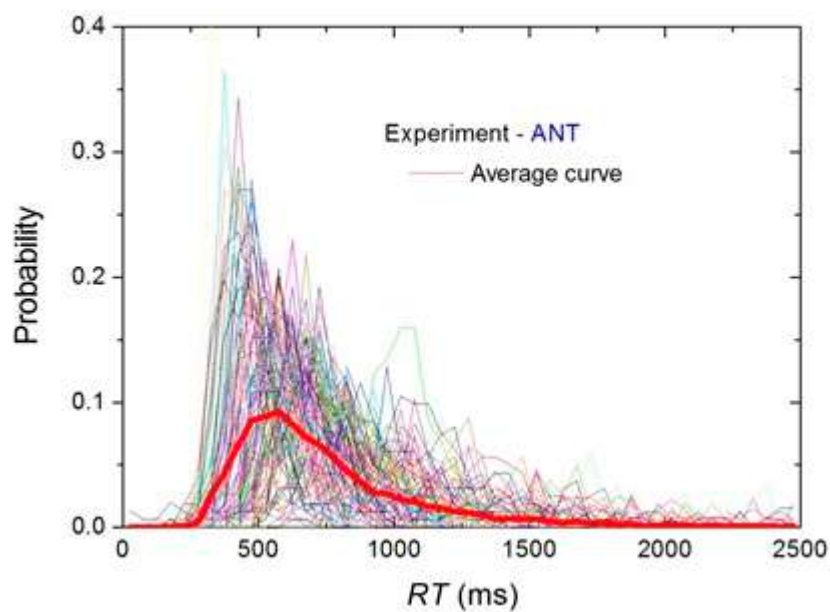

Figure 4. Probability distributions and average curve.

3.1. Ex-Gaussian Analysis

In order to represent the RT data, we have chosen the ex-Gaussian distribution which has proven to be a good fit in previous works [35,36]. Our sample size is in line with Ratcliff et al. [37], who have suggested that samples with at least 100 data points are considered reliable as for parameter estimates. As commented in the Introduction section, the ex-Gaussian distribution relates three parameters: μ (the mean of the Gaussian component), σ (the standard deviation of the Gaussian component), and τ, which is the decay constant of the exponential component. These parameters are claimed in multiple works to describe cognitive processes such as attention or effort control mechanism, although there is a big debate in the literature about their interpretation [21].

Among the different forms of the ex-Gaussian distribution we have chosen the following as this is the one incorporated in the professional software for data analysis, ORIGIN version 6.1 [https://www.originlab.com/], used here as a reference to test our FORTRAN code,

$$f(x) = y_0 + \frac{A}{t_0} e^{\frac{1}{2}(\frac{\omega}{t_0})^2 - \frac{x-x_c}{t_0}} \int_{-\infty}^{z} \frac{1}{\sqrt{2\pi}} e^{\frac{y^2}{2}} \, dy, \tag{1}$$

where $z = \frac{x-x_c}{\omega} - \frac{\omega}{t_0}$.

In Equation (1), the parameters can be identified as $\mu = x_C$, $\sigma = \omega$ y $\tau = t_0$, that is, in terms of the Gaussian and exponential functions parameters,

$$f_1(x) = \frac{A}{t_0} e^{-\frac{x}{t_0}}, \tag{2}$$

$$f_2(x) = \frac{1}{\sqrt{2\pi}\omega} e^{-\frac{(x-x_c)^2}{2\omega^2}}. \tag{3}$$

It should be pointed out that μ and σ do not represent the mean and the standard deviation of the ex-Gaussian distribution. Instead, the true mean of the distribution is $M = \mu + \tau$, the variance $S^2 = \sigma^2 + \tau^2$, and the skewness $2\tau^3/S^3$ [38]. In fact, one can characterize this distribution $f(x)$ through its moments. One can consider moments of this distribution centered either at the origin (raw moments), or centered at the corresponding average (central moments). Thus,

$$M \equiv \int_{-\infty}^{\infty} x \, f(x) \, dx, \tag{4}$$

is the raw moment of order one, whereas,

$$S^2 \equiv \int_{-\infty}^{\infty} (x - M)^2 \, f(x) \, dx, \tag{5}$$

is the variance, or second central moment, of the random variable x with probability distribution $f(x)$ and centered at M. The positive squared root of the above, S, is the standard derivation. On the other hand, the skewness t of the distribution is defined as

$$t \equiv 1/S^3 \int_{-\infty}^{\infty} (x - M)^3 \, f(x) \, dx. \tag{6}$$

That is, the centered moment of order three, divided by the standard deviation cubed. Altogether, an ex-Gaussian distribution can be characterized through its three moments,

$$a \equiv (M, S^2, t) \tag{7}$$

The fitting parameters and their uncertainties were obtained by the non-linear fitting algorithm of Levenberg–Marquardt [39,40], implemented in the ORIGIN version 6.1 data analysis software.

3.2. Classification Methodology

As stated above, the main objective of this work was to provide a methodology for a fast determination of the children whose time reaction differs from the mean and thus are potential candidates to be diagnosed with ADHD. To do so, evidence from the literature was used as criteria in our automatic methodology. The main criterion came from the world prevalence percentage, 7% for school-aged children according to the American Psychiatric Association (American Psychiatric Association, 2013). We would like to point out that any more specific prevalence percentages can be used if available. Then, the prevalence percentage was split between slow and fast response time regions in the probability distributions. Previous work indicates that children with ADHD are likely to manifest rather low and fast responses in the RT distributions [41].

There is another criterion which has not been considered here but could be also included along with the previous ones. ADHD occurs about three times more often in boys than in girls, although some authors claim that the disorder is often overlooked in girls due to their symptoms differing from those of boys [42].

For our analysis we have considered four parameters. The mode, which is the value that appears most often in a dataset which is derived from descriptive statistics. This is a better descriptor than the mean value as the ex-Gaussian is a skewed distribution where the mean would not have a useful interpretation. The other three parameters come from the ex-Gaussian representation of the data, μ, σ and τ, which have been widely related with ADHD in the literature [26,38].

To combine both criteria stated above in one, probability distributions have been built for each of the four parameters aforementioned, namely, for the mode and for ex-Gaussian distribution parameters. In order to account for the skewness of the probability distributions of each of the four parameters, the percentages of counts at both sides (left and right hand sides) of the mode, namely $x\_$"left" and $x\_$"right", are determined from the corresponding number of counts, $N\_$"left" and $N\_$"right". Then, the prevalence percentage (P) can be expressed as,

$$P = x_L + x_R = (N_{left}/N)100 + (N_{right}/N)100. \tag{8}$$

We took the world prevalence percentage, P = 7% [3] which is inclusive of both genders. We are aware that ADHD is more prevalent in males than females (4:1 ratio), and that this ratio tends to become 1:1 by the adult age [43]. This methodology as applied to our data, was reflected in Figures 5 and 6, where the probability distributions of the four parameters are shown along with the resulting splitting of the prevalence percentage for each case. The resulting candidates according to the split percentages were included in Table 1, and in Figures 7 and 8. It should be considered that those candidates with a very fast response time may also include skilled children who are able to answer the experiment's queries both correctly and quickly. If the fast-responding children make a considerable number of mistakes, that could be used as a complementary criterion for the selection of ADHD candidates.
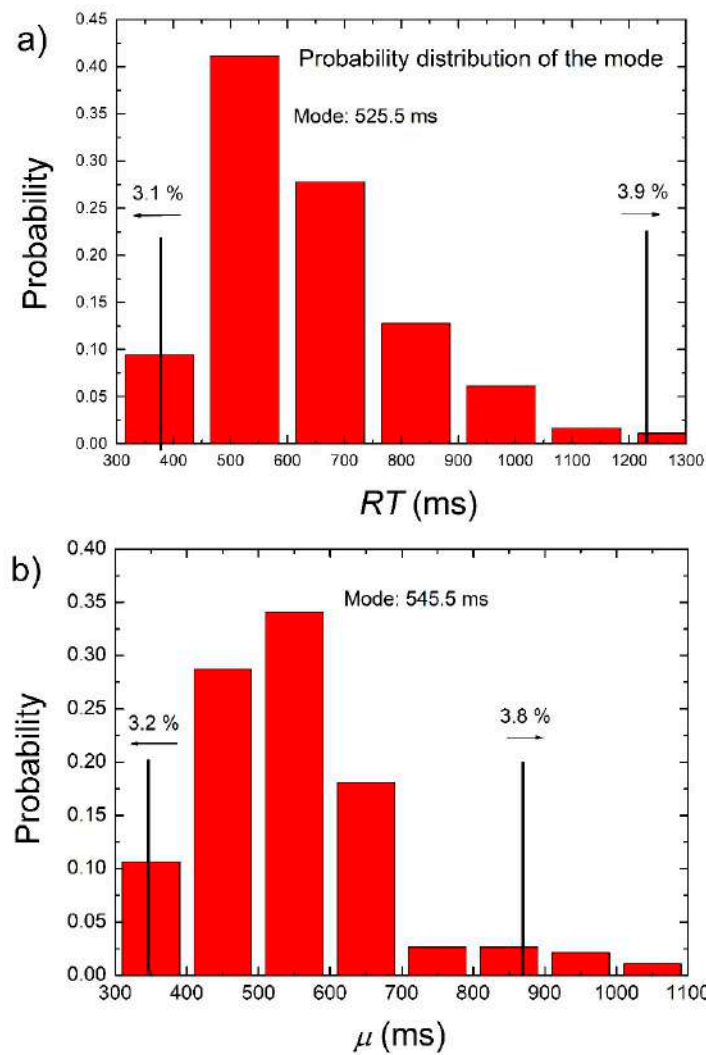
Figure 5. Probability distributions of the mode (**a**) and of μ parameter in an ex-Gaussian representation of the data (**b**).

Table 1. Results of the classification for the distribution of the mode, μ, σ and τ (columns from second to fifth) taking into account a 7% of world prevalence of ADHD in school-aged children. The rows show the mode, the probability percentages at both sides of the mode (%-PD), the splitting of the prevalence percentage (%-Prev.), corresponding number of children (No. Ch.), and the selected children in terms of labels.

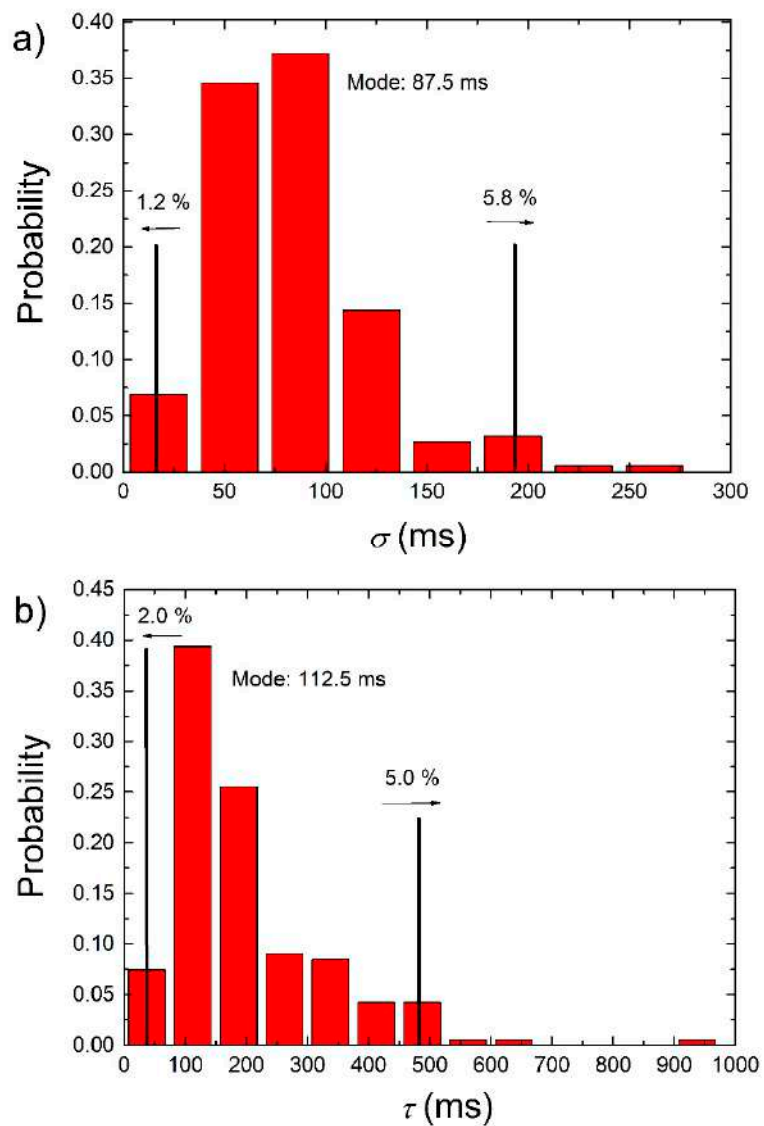|	Mode		μ		σ		τ	
Mode (ms)	**525.5**		**545.5**		**87.5**		**112.5**	
	L	R	L	R	L	R	L	R
%-PD	44.4	55.6	45.0	55.0	16.5	83.5	14.9	85.1
%-Prev.	3.1	3.9	3.2	3.8	1.2	5.8	2.0	5.0
No. Ch.	6	7	6	7	2	11	2	11
Selected children (labels)	2, 28, 34, 55, 77, 75, 130, 85, 102, 107, 134, 142, 159		28, 34, 55, 58, 75, 77, 80, 102, 106, 130, 163, 167, 184		5, 39, 41, 58, 71, 80, 85, 109, 130, 136, 141, 183, 184		5, 28, 34, 55, 58, 80, 109, 113, 133, 136, 163, 183, 187	

Figure 6. Probability distributions of σ (**a**) and τ (**b**) parameters in an ex-Gaussian representation of the data.

Previous work, where the ex-Gaussian function was used to represent the RT data in children with ADHD, seem to indicate that ADHD correlates with slow response times and high RT variability, namely, large values for **σ** and **τ** parameters [22,44]. This is one of the reasons why we are including here the probability distribution of the ex-Gaussian function parameters as well.
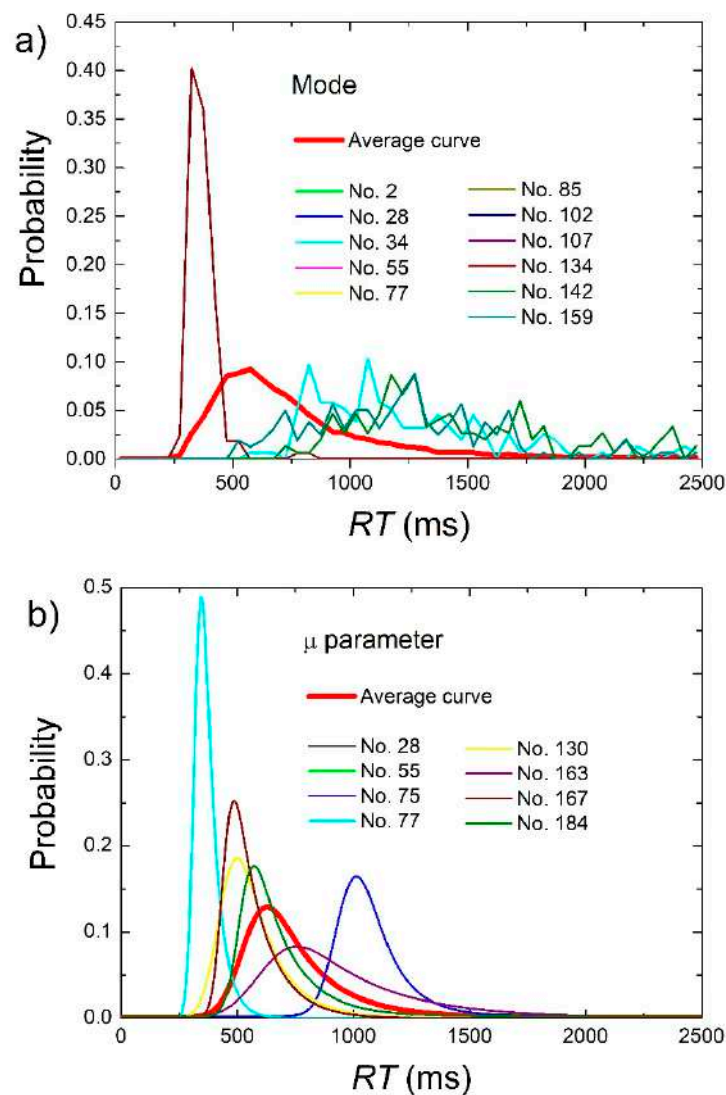
Figure 7. Probability distributions of the candidates resulting from the probability distribution of the mode in panel (**a**) and of the candidates resulting from the probability distribution of the parameter μ in panel (**b**). The average curve has also been included.

3.3. Vector Criterion Based on the Ex-Gaussian Parameters

A number of N=190 vectors, of three components each, was defined over the parameters of the ex-Gaussian distribution for each student. The components of each vector were calculated as the difference of each student's parameter (μ_i, σ_i, and τ_i) with respect to the mode of the corresponding parameter's probability distribution (M^μ, M^σ, and M^τ),

$$X_i = (\mu_i - M^\mu,\ \sigma_i - M^\sigma, \tau_i - M^\tau). \tag{9}$$

We will use two common norm definitions for the vector defined in Equation (9) such that each student can be identified globally by a single scalar. This is a transformation of the data from the separate parameters to a scalar number which can capture maybe a more complex relationship between response time and cognitive disorders. The first norm is the Euclidean defined as,

$$\|X_i\|_2 = ((\mu_i - M^\mu)^2 + (\sigma_i - M^\sigma)^2 + (\tau_i - M^\tau)^2)^{1/2}. \tag{10}$$

The second norm definition used here is the norm of the maximum,

$$\|\mathbf{X_i}\|_\infty = \max \left(\left|\mu_i - M^\mu\right|, \ |\sigma_i - M^\sigma|, |\tau_i - M^\tau|\right). \tag{11}$$

Figure 9 shows the curves for the norms defined above applied to the vector in Equation (8) as a function of the student label. The highest peaks in the plot represent the students whose ex-Gaussian parameters lie furthest from the respective modes. In this case, the students labeled as 5, 34, 41, 58, 80, 110, 131, 137, 142, 169, 185, 186, 189 represent the 13 students ranking highest (~7% of 190) for both norms.
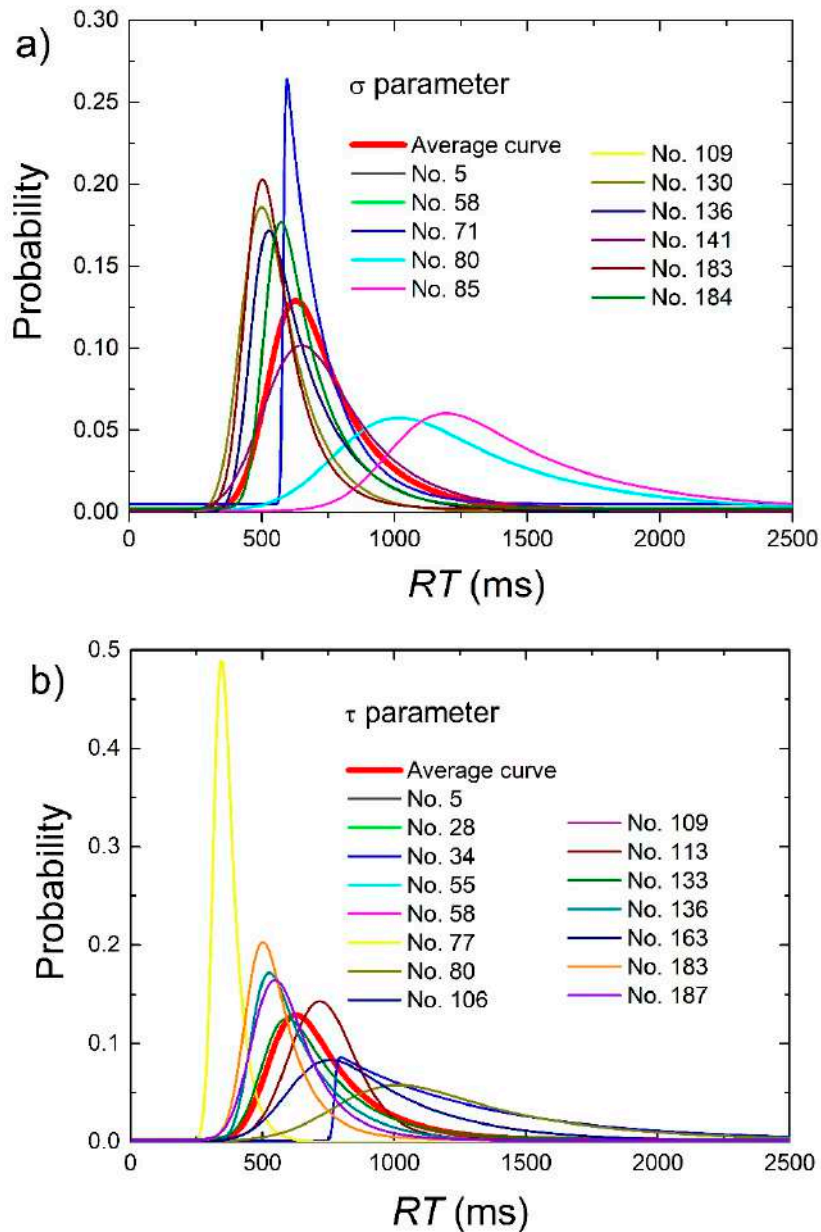
Figure 8. Probability distributions of the candidates resulting from the probability distribution of σ (**a**) and τ (**b**) parameters of the ex-Gaussian probability density. The average curve has also been included.
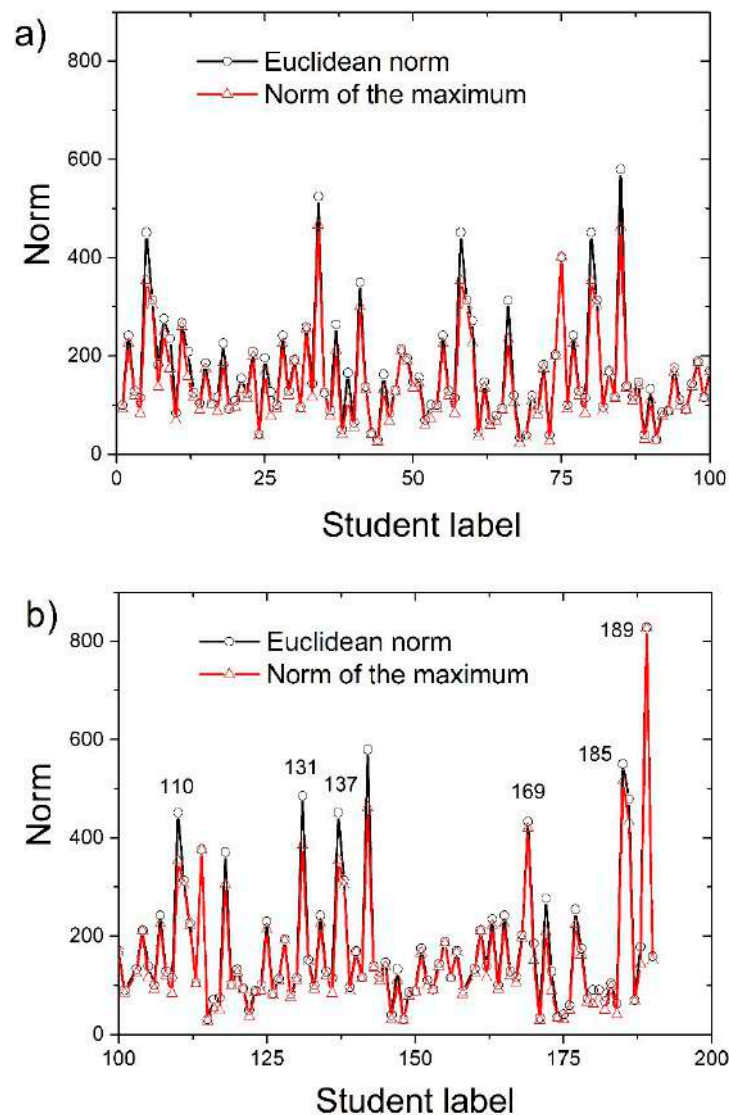
Figure 9. Euclidean norm and the norm of the maximum applied to the vector defined in Equation (8) as a function of the student label. In the upper panel, students from 1 to 100 are shown, and in the lower panel, students from 101 to 200. The students labeled as 110 (M), 131 (F), 137 (M), 169 (F), 185 (M), and 189 (F) appear in this classification only. The letter "M" between parentheses stands for male and the letter "F" for female.

4. Conclusions

A classification methodology based on response time data was proposed towards a quick pre-diagnosis of attention deficit or any another related cognitive disorder. The mode of the probability distributions of the RTs and the three parameters from an ex-Gaussian representation of the RT data were used to identify a number of children from the sample with non-normative behavior according to the world prevalence percentage of ADHD. Our methodology took into account the skewness of the probability distributions of the four parameters. The prevalence percentage was then split into the slow and fast RT regions proportionally to the percentage of counts at both sides of the mode of the probability distribution function. It should be pointed out that the candidates falling in the very fast region of the RT distribution may include skilled children who are able to respond fast and correctly. In general, a complementary criterion such as the number of mistakes made by the child can help select the candidates for ADHD among the fast-responding children. We provide a number of classification possibilities, all of them based on the prevalence percentage and the probability

distributions of the mode and ex-Gaussian parameters. Among them, a classification based on the distance of the ex-Gaussian parameters to their respective mode which constitute the components of a vector whose norm serves as a unique, global scalar identifier of each child. We would like to point out that the validity of this work is not limited to ADHD pre-diagnosis but to identifying children with attention and cognitive disorders in general. Our methodology could also be adapted to cognitive disorders in elderly people, as they clearly correlate with slower response time as well. The development of objective instruments is highly desirable as methodologies available nowadays are not based on direct measurements but on interviewing people related to the child, and are known to lead to an over-diagnosis of ADHD. Although the ultimate diagnosis must be made by a psychologist, the selection provided by our methodology will allow them to focus on assessing a smaller number of children that would help save time and other resources. We aimed to develop a simple, fast automated methodology based on the response time as another step towards the diagnosis of cognitive disorders.

Author Contributions: E.N.-P. conceived and designed the experiments; M.H.-G. and E.N.-P. performed the experiments; all authors analyzed the data; J.C.C.-P., J.M.I. and P.F.-d.-C. contributed to the development of analysis tools; J.C.C.-P. and E.N.-P. wrote the paper. All authors read and approved the final manuscript.

Conflicts of Interest: The authors declare no conflict of interest.

References

1. Sroubek, A.; Kelly, M.; Li, X. Inattentiveness in attention-deficit/hyperactivity disorder. *Neurosci. Bull.* **2013**, *29*, 103–110. [CrossRef] [PubMed]

2. Clauss-Ehlers, C.S. (Ed.) *Encyclopedia of Cross-Cultural School Psychology*; Springer Science & Business Media LLC: Boston, MA, USA, 2010.

3. American Psychiatric Association. *American Psychiatric Association Diagnostic and Statistical Manual of Mental Disorders*, 5th ed.; APA: Washington, DC, USA, 2013.

4. Barkley, R.A. *Attention Deficit Hyperactivity Disorder: A Handbook for Diagnosis and Treatment*, 3rd ed.; Guilford: New York, NY, USA, 2006.

5. DuPaul, G.J.; Volpe, R.J.; Jitendra, A.K.; Lutz, J.G.; Lorah, K.S.; Gruber, R. Elementary school students with AD/HD: Predictors of academic achievement. *J. Sch. Psychol.* **2004**, *42*, 285–301. [CrossRef]

6. Sonuga-Barke, E.; Koerting, J.; Smith, E.; McCann, D.C.; Thompson, M. Early detection and intervention for attention-deficit/hyperactivity disorder. *Expert Rev. Neurother.* **2011**, *11*, 557–563. [CrossRef] [PubMed]

7. Lavigne Cerván, R.; Romero-Pérez, J.F. *The Attention Deficit Hyperactivity Dissorder*; Ediciones Pirámide: Madrid, Spain, 2010; (In Spanish, EL TDAH).

8. Pliszka, S. Practice parameter for the assessment and treatment of children and adolescents with attention-deficit/hyperactivity disorder. *J. Am. Acad. Child Adolesc. Psychiatry* **2007**, *46*, 894–921. [CrossRef]

9. Tarantino, S.C.; Mogentale, C.; Bisiacchi, P.S. Time-on-Task in Children with ADHD: An ex-Gaussian Analysis. *Vincenza J. Int. Neuropsychol. Soc.* **2013**, *19*, 820–828. [CrossRef]

10. Klein, C.; Wendling, K.; Huettner, P.; Ruder, H.; Peper, M. Intra-subject variability in attention-deficit hyperactivity disorder. *Biol. Psychiatry* **2006**, *60*, 1088–1097. [CrossRef] [PubMed]

11. Nigg, J.T.; Willcutt, E.G.; Doyle, A.E.; Sonuga-Barke, E.J. Causal heterogeneity in attention-deficit/hyperactivity disorder: Do we need neuropsychologically impaired subtypes? *Biol. Psychiatry* **2005**, *57*, 1224–1230. [CrossRef] [PubMed]

12. Willcutt, E.G.; Doyle, A.E.; Nigg, J.T.; Faraone, S.V.; Pennington, B.F. Validity of the executive function theory of attention-deficit/hyperactivity disorder: A meta-analytic review. *Biol. Psychiatry* **2005**, *57*, 1336–1346. [CrossRef]

13. Castellanos, F.X.; Sonuga-Barke, E.J.; Scheres, A.; Di Martino, A.; Hyde, C.; Walters, J.R. Varieties of attention-deficit/hyperactivity disorder-related intra-individual variability. *Biol. Psychiatry* **2005**, *57*, 1416–1423. [CrossRef]

14. Luce, R.D. *Response Times: Their Role in Inferring Elementary Mental Organization*; Oxford University Press: New York, NY, USA, 1986.

15. Hockley, W.E.; Corballis, M.C. Test of serial scanning in item recognition. *Can. J. Psychol.* **1982**, *36*, 189–212. [CrossRef]

16. Ratcliff, R.; Murdock, B.B. Retrieval processes in recognition memory. *Psychol. Rev.* **1976**, *83*, 190–214. [CrossRef]

17. Gmehlin, D.; Fuermaier, A.B.M.; Walther, S.; Debelak, R.; Rentrop, M.; Westermann, C.; Sharma, A.; Tucha, L.; Koerts, J.; Tucha, O.; et al. Intraindividual Variability in Inhibitory Function in Adults with ADHD—An Ex-Gaussian Approach. *PLoS ONE* **2014**, *9*, e112298. [CrossRef]

18. Adamo, N.; Hodsoll, J.; Asherson, P.; Buitelaar, J.K.; Kuntsi, J. Ex-Gaussian, Frequency and Reward Analyses Reveal Specificity of Reaction Time Fluctuations to ADHD and Not Autism Traits. *J. Abnorm. Child Psychol.* **2019**, *47*, 557–567. [CrossRef]

19. Burbeck, S.L.; Luce, R.D. Evidence from auditory simple reaction times for both change and level detectors. *Percept. Psychophys.* **1982**, *32*, 117–133. [CrossRef]

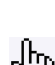20. Heathcote, A.; Popiel, S.J.; Mewhort, D.J.K. Analysis of response time distributions: An example using the Stroop task. *Psychol. Bull.* **1991**, *109*, 340–347. [CrossRef]

21. Matzke, D.; Wagenmakers, E.-J. Psychological interpretation of the ex-Gaussian and shifted Wald parameters: A diffusion model analysis. *Psychon. Bull. Rev.* **2009**, *16*, 798–817. [CrossRef]

22. Shahar, N.; Teodorescu, A.R.; Karmon-Presser, A.; Anholt, G.E.; Meiran, N. Memory for Action Rules and Reaction Time Variability in Attention-Deficit/Hyperactivity Disorder. *Biol. Psychiatry Cogn. Neurosci. Neuroimaging* **2016**, *1*, 132–140. [CrossRef]

23. Leth-Steensen, C.; King Elbaz, Z.; Douglas, V.I. Mean response times, variability, and skew in the responding of ADHD children: A response time distributional approach. *Acta Psychol.* **2000**, *104*, 167–190. [CrossRef]

24. Navarro-Pardo, E.; Navarro-Prados, A.B.; Gamermann, D. Moret-Tatay, C. Differences between younger and older university students on lexical decision task: Evidence through an ex-Gaussian approach. *J. Gen. Psychol.* **2013**, *140*, 251–268. [CrossRef]

25. Lemus-Zúñiga, L.G.; Navarro-Pardo, E.; Moret-Tatay, C.; Pocinho, R. Serious games for elderly continuous monitoring. In *Data Mining in Clinical Medicine*; Springer: New York, NY, USA, 2015; pp. 259–267. [CrossRef]

26. Moret-Tatay, C.; Moreno-Cid, A.; Argimon, I.I.D.L.; Quarti Irigaray, T.; Szczerbinski, M.; Murphy, M.; Vázquez-Martínez, A.; Vázquez-Molina, J.; Sáiz-Mauleon, B.; Navarro-Pardo, E.; et al. The effects of age and emotional valence on recognition memory: An ex-Gaussian components analysis. *Scand. J. Psychol.* **2014**, *55*, 420–426. [CrossRef] [PubMed]

27. Moret-Tatay, C.; Irigaray, T.Q.; Oliveira, C.; Argimon, I.I.D.L. Reaction Times as a dependent variable of memory: Future lines of research through an ex-Gaussian fit. *Horiz. Neurosci. Res.* **2015**, *17*, 60–71.

28. Hohle, R.H. Inferred components of reaction times as functions of foreperiod duration. *J. Exp. Psychol.* **1965**, *69*, 382–386. [CrossRef]

29. Borella, E.; de Ribaupierre, A.; Cornoldi, C.; Chicherio, C. Beyond interference control impairment in ADHD: Evidence from increased intraindividual variability in the color—Stroop test. *Child Neuropsychol.* **2012**, *19*, 495–515. [CrossRef] [PubMed]

30. World Medical Association. Declaration of Helsinki: Ethical Principles for Medical Research Involving Human Subjects. *J. Am. Med. Assoc.* **2013**, *310*, 2191–2194. [CrossRef]

31. Forster, K.I.; Forster, J.C. DMDX: A windows display program with millisecond accuracy. *Behav. Res. Methods Instrum. Comput.* **2003**, *35*, 116–124. [CrossRef]

32. Fan, J.; McCandliss, B.D.; Sommer, T.; Raz, A.; Posner, M.I. Testing the efficiency and independence of attentional networks. *J. Cogn. Neurosci.* **2002**, *14*, 340–347. [CrossRef]

33. Posner, M.I.; Dehaene, S. Attentional networks. *Trends Neurosci.* **1994**, *17*, 75–79. [CrossRef]

34. Posner, M.I.; Raichle, M.E. *Images of Mind*; Scientific American Library: New York, NY, USA, 1994.

35. Lacouture, Y.; Cousineau, D. How to use MATLAB to fit the ex-Gaussian and other probability functions to a distribution of response times. *Tutor. Quant. Methods Psychol.* **2008**, *4*, 35–45. [CrossRef]

36. Ratcliff, R.; McKoon, G. The diffusion decision model: Theory and data for two-choice decision tasks. *Neural Comput.* **2008**, *20*, 873–922. [CrossRef] [PubMed]

37. Ratcliff, R. Group reaction time distributions and an analysis of distribution statistics. *Psychol. Bull.* **1979**, *86*, 446–461. [CrossRef] [PubMed]

38. Moret-Tatay, C.; Gamermann, D.; Navarro-Pardo, E.; Fernández-de-Córdoba-Castellá, P. ExGUtils: A python package for statistical analysis with the ex-Gaussian probability density. *Front. Psychol.* **2018**, *9*, 1–11. [CrossRef]

39. Levenberg, K. A method for the solution of certain non-linear problems in least squares. *Q. Appl. Math.* **1944**, *2*, 164–168. [CrossRef]

40. Marquardt, D. An algorithm for least-squares estimation of nonlinear parameters. *J. Soc. Ind. Appl. Math.* **1963**, *11*, 431–441. [CrossRef]

41. Castellanos, F.X.; Sonuga-Barke, E.J.; Milham, M.P.; Tannock, R. Characterizing cognition in ADHD: Beyond executive dysfunction. *Trends Cogn. Sci.* **2006**, *10*, 117–123. [CrossRef]

42. Emond, V.; Joyal, C.; Poissant, H. Neuroanatomie structurelle et fonctionnelle du trouble déficitaire d'attention avec ou sans hyperactivité (TDAH) [Structural and functional neuroanatomy of attention-deficit hyperactivity disorder (ADHD)]. *Encephale* **2009**, *35*, 107–114. (In French) [CrossRef] [PubMed]

43. Reinhardt, M.C.; Reinhardt, C.A. Attention deficit-hyperactivity disorder, comorbidities, and risk situations. *J. Pediatr. (Rio. J.)* **2013**, *89*, 124–130. [CrossRef] [PubMed]

44. Hwang-Gu, S.L.; Chen, Y.C.; Liang, S.H.; Ni, H.C.; Lin, H.Y.; Lin, C.F.; Gau, S.S. Exploring the Variability in Reaction Times of Preschoolers at Risk of Attention-Deficit/Hyperactivity Disorder: An ex-Gaussian Analysis. *J. Abnorm. Child Psychol.* **2019**. [CrossRef] [PubMed]

Contenidos más descargados en DYNA

Mes / Año		*IdDoc*	*Título*		
5	1927	4239	LA ENERGIA ELECTRICA Y LA ENERGIA HIDRAULICA		**411** *Veces*
3	1967	3809	CONDUCTORES, AISLANTES Y SEMICONDUCTORES		**389** *Veces*
6	1926	1843	LA ENERGIA TERMICA Y LA ENERGIA HIDRAULICA (PARTE 1)		**332** *Veces*
4	2002	1535	APLICACIONES DE LA ROBOTICA: ULTIMAS TENDENCIAS Y NUEVAS PERSPECTIVAS		**329** *Veces*
3	2022	10212	BIOPLÁSTICO ELABORADO DE CÁSCARAS DE NARANJA		**325** *Veces*
9	2004	1163	LA INGENIERIA INDUSTRIAL		**264** *Veces*
3	2016	7572	RUEDA DE EMOCIONES DE GINEBRA+: INSTRUMENTO PARA LA VALORACIÓN EMOCIONAL DE LOS USUARIOS MIENTRAS PARTICIPAN EN UNA EVALUACIÓN DE SISTEMAS INTERACTIVOS		**250** *Veces*
1	2015	7174	UN PASO MÁS ALLÁ DEL TRIÁNGULO Y EL TETRAEDRO. EL MODELO QF7 PARA EL CONOCIMIENTO DEL FUEGO		**239** *Veces*
9	1998	1824	LA CERVEZA, SU HISTORIA PRODUCCION Y CARACTERISTICAS		**237** *Veces*
2	2006	511	LA ENERGIA EOLICA		**221** *Veces*
7	2013	5526	ANÁLISIS CRÍTICO DEL ESTANDAR INTERNACIONAL ISO 21500:2012, DE GUÍA EN LA DIRECCIÓN DE PROYECTOS		**213** *Veces*
2	2002	1540	LA CONSTRUCCION CON ESTRUCTURA DE ACERO		**207** *Veces*
10	2007	842	ECODISEÑO: Integración de criterios ambientales en la sistemática del diseño de productos industriales		**188** *Veces*

Mes / Año		IdDoc	Título		
5	2015	7205	EL GRAFENO. PARTE I: ESTRUCTURA, PROPIEDADES Y APLICACIONES		187 *Veces*
10	2004	1196	LA SEDIMENTACION EN EMBALSES		175 *Veces*
3	2021	9890	EL PAPEL DEL HIDRÓGENO VERDE EN LA TRANSICIÓN ENERGÉTICA DE LA INDUSTRIA		171 *Veces*
9	2008	1563	EL LANZAMIENTO DE NUEVOS PRODUCTOS: RENTABILIDAD, COMPETENCIA Y PATENTES		170 *Veces*
4	2004	1074	LA TRANSMUTACION NUCLEAR Y SU APLICACION A LA REDUCCION DEL IMPACTO AMBIENTAL Y ECONOMICO DE LOS RESIDUOS RADIACTIVOS PROCEDENTES DEL USO DE LA ENERGIA NUCLEAR DE FISION		167 *Veces*
12	2008	2411	ENERGIA SOLAR		166 *Veces*
9	2013	5658	LA NORMA ISO 14006 COMO GUÍA PARA EL ECODISEÑO		161 *Veces*
6	2003	377	LA PAPA, TESORO Y ENERGIA DE LOS INCAS		161 *Veces*
5	1998	1820	LA SEGURIDAD INDUSTRIAL		161 *Veces*
6	2004	1143	EL INGENIERO INDUSTRIAL Y LA ELECTRICIDAD		159 *Veces*
2	2000	1972	MANTENIMIENTO PREDICTIVO: UNA TECNICA QUE REDUCE O ELIMINA AVERIAS INESPERADAS		159 *Veces*
5	1999	1669	AVANCES TECNOLOGICOS EN EL SECTOR DE LA CONSTRUCCION		157 *Veces*
11	2014	7128	MOTORES SÍNCRONOS DE IMANES PERMANENTES PARA VEHÍCULOS HÍBRIDOS. EL TOYOTA PRIUS		157 *Veces*
9	2022	10540	PROPUESTA DE MARCO PARA EL DISEÑO DE SISTEMAS PRODUCTIVOS LEAN CIRCULARES A PARTIR DE CASOS DE ESTUDIO		157 *Veces*

Mes / Año		IdDoc	Título		
3	2012	4367	MODELOS DE GESTION DE PROYECTOS: DIRECCION DE PROYECTOS COMPATIBLE CON EL PENSAMIENTO LEAN.		**156** *Veces*
5	1997	1770	LAS MAQUINAS HIDRAULICAS Y DE FLUIDOS A LO LARGO DE LA HISTORIA		**156** *Veces*
11	2012	4709	SIMULANDO LA INYECCIÓN DE PLÁSTICOS. NUEVAS FORMAS DE APRENDER LOS PROCESOS.		**154** *Veces*
5	2021	10011	PROTOTIPO DE IDS PARA DETECCIÓN DE INTRUSIONES CON MODELOS DE MACHINE LEARNING EN SISTEMAS IOT DE LA INDUSTRIA 4.0		**154** *Veces*
3	1976	3205	ENSAYO SOBRE EL AHORRO DE ENERGIA		**153** *Veces*
1	2023	10625	ESTUDIO EXPERIMENTAL Y NUMÉRICO DE LA INFLUENCIA DE LOS PARÁMETROS DE FABRICACIÓN SOBRE EL COMPORTAMIENTO DE LAS CAPAS INTERMEDIAS DE LOS MATERIALES DE IMPRESIÓN 3D CON Y SIN FIBRAS DE REFUERZO		**153** *Veces*
10	2008	2214	EL SALARIO EMOCIONAL: CLAVE PARA REDUCIR EL ESTRES		**149** *Veces*
5	2017	8008	APLICACIÓN DE UN SISTEMA BUSINESS INTELLIGENCE EN UN CONTEXTO BIG DATA DE UNA EMPRESA INDUSTRIAL ALIMENTARIA		**149** *Veces*
11	2005	985	MECATRONICA		**148** *Veces*
6	2007	139	SISTEMAS INSTRUMENTADOS DE SEGURIDAD (SIS):CICLO DE VIDA		**147** *Veces*
10	1967	3836	LAS FIBRAS SINTETICAS		**146** *Veces*
10	2005	959	ADOBE ACROBAT 7.0 PROFESSIONAL		**145** *Veces*
1	2017	7990	DETECCIÓN Y DIAGNÓSTICO DE FALLOS EN SENSORES DE TEMPERATURA EN UNA COLUMNA DE DESTILACIÓN FRACCIONADA		**144** *Veces*
11	2016	7890	EVOLUCIÓN HISTÓRICA DEL MANTENIMIENTO INDUSTRIAL EN RELACIÓN A LA GESTIÓN DEL CONOCIMIENTO		**144** *Veces*

Mes / Año		IdDoc	Título		Veces
1	2015	6938	INTEGRACIÓN DE LA INGENIERÍA EN LA ODONTOLOGÍA		143 Veces
6	2008	1525	APLICACION DE LA CIBERNETICA ORGANIZACIONAL AL ESTUDIO DE LA VIABILIDAD DE LAS ORGANIZACIONES. PATOLOGIAS ORGANIZATIVAS FRECUENTES (1ª PARTE).		143 Veces
9	2022	10588	REVISIÓN DE LOS DISEÑOS DE LAS PRINCIPALES TECNOLOGÍAS PARA MICROGENERACIÓN HIDROELÉCTRICA		143 Veces
9	2016	7807	ESTADO DEL ARTE SOBRE DISPOSITIVOS ACTIVOS Y PASIVOS DE CONTROL DE FLUJO PARA TURBINAS EÓLICAS		142 Veces
3	2023	10718	ANÁLISIS DE LAS EMISIONES DEL SECTOR TRANSPORTE DESDE UNA PERSPECTIVA GLOBAL.		142 Veces
9	1998	1823	APLICACION DE NUEVAS TECNOLOGIAS EN LA CONSERVACION DE ALIMENTOS		140 Veces
9	2013	5543	LECTURA DE PLANOS INDUSTRIALES: UNA PROPUESTA DE ENSEÑANZA-APRENDIZAJE PARA LAS ESCUELAS DE INGENIERÍA		139 Veces
9	2010	3739	CADENAS DE SUMINISTRO TRADICIONALES Y COLABORATIVAS. ANÁLISIS DEL EFECTO LÁTIGO Y OTROS COSTES RELACIONADOS.		139 Veces
3	2013	5705	LA SUPERCONDUCTIVIDAD Y SUS APLICACIONES (PARTE 1)		138 Veces
5	2007	121	LAS 3 GARGANTAS: OTRO GRAN PROYECTO CHINO		138 Veces
1	2023	10651	REALIDAD AUMENTADA APLICADA A LA RECUPERACIÓN DEL PATRIMONIO HISTÓRICO		138 Veces
7	2022	10591	MOVILIDAD SOSTENIBLE. GESTIÓN DE LA DEMANDA DE TRANSPORTE		138 Veces
5	2017	8071	GESTION DE LAS RELACIONES CON EL CLIENTE (CRM) Y BIG DATA: UNA APROXIMACIÓN CONCEPTUAL Y SU INFLUENCIA SOBRE EL VALOR DE LOS DATOS APLICADOS A LA ESTRATEGIA DE VENTA		137 Veces
11	2021	10067	INTEGRACIÓN DE INTERNET DE LAS COSAS Y BLOCKCHAIN PARA AUMENTAR EL RENDIMIENTO DE LAS CADENAS DE SUMINISTRO DE AYUDA HUMANITARIA		137 Veces

Mes / Año		IdDoc	Título		
12	2007	183	VIBRACIONES MECÁNICAS QUE SON Y COMO SE EVALUA EL RIESGO		136 *Veces*
3	1997	1767	RESIDUOS SANITARIOS		136 *Veces*
5	2014	3908	APLICACIÓN DE UN SISTEMA DE GESTIÓN DEL MANTENIMIENTO BASADO EN UN RCM ADAPTADO		135 *Veces*
11	1997	1787	CALCULO DE PERDIDAS DE CARGA EN TUBERIAS		135 *Veces*
12	1998	1712	LA GESTION DE RESIDUOS EN DINAMARCA: EVOLUCION HISTORIA Y SITUACION ACTUAL		134 *Veces*
7	2014	7003	TECNOLOGIAS DE CAPTURA DE CO2		133 *Veces*
3	2003	279	CHARLES AUGUSTIN DE COULOMB		133 *Veces*
6	2004	1130	PARA NO PERDERNOS EN LA GLOBALIZACION: UNA REFLEXION DESDE LA ETICA		133 *Veces*
9	1996	1897	POSIBILIDADES Y PERSPECTIVAS DE LA ROBOTICA EN LA MEDICINA		133 *Veces*
5	2016	7781	EVOLUCIÓN HISTÓRICA DE LOS VEHICULOS AEREOS NO TRIPULADOS HASTA LA ACTUALIDAD		133 *Veces*
3	2021	9893	ANÁLISIS DE LOS REQUERIMIENTOS DE MATERIALES DE LA MOVILIDAD ELÉCTRICA MUNDIAL		133 *Veces*
10	2010	3871	ENERGÍA SOLAR TERMOELÉCTRICA. TECNOLOGÍA Y DESARROLLOS.		132 *Veces*
12	2005	1007	LAS DORSALES OCEANICAS: VULCANISMO, HIDROTERMALISMO Y YACIMIENTOS DE METALES DE MAÑANA		132 *Veces*
9	1996	1890	LA INGENIERIA INDUSTRIAL EN LA MEDICINA		132 *Veces*

Mes / Año		IdDoc	Título		Veces
9	2016	7822	DILEMA MORAL PARA EL DESARROLLO DE COMPETENCIAS ÉTICAS EN LOS ESTUDIOS DE INGENIERÍA INDUSTRIAL. APLICACIÓN A LA INGENIERÍA MECÁNICA		132 Veces
5	2021	10037	AUDITORÍA Y DIAGNÓSTICO EN GESTIÓN DE ACTIVOS Y MANTENIMIENTO APLICADO EN LA INDUSTRIA ELÉCTRICA		132 Veces
2	2007	65	transporte y logistica		131 Veces
5	2017	8089	RESPONSABILIDAD SOCIAL EMPRESARIAL EN LA INDUSTRIA MANUFACTURERA: ÁMBITOS SOCIAL Y ECONÓMICO		131 Veces
11	2000	2000	PERSPECTIVA HISTORICA DE LA INNOVACION		130 Veces
6	2008	1421	SISTEMA BALÍSTICO PARA EL CONTROL Y EXTINCIÓN DE INCENDIOS FORESTALES EN ZONAS INACCESIBLES		129 Veces
1	1968	3712	EL METODO DE MONTECARLO		129 Veces
1	2017	7942	LIDERAZGO Y CULTURA DE SEGURIDAD LABORAL: REVISIÓN DEL ESTADO DE LA CUESTIÓN		129 Veces
5	2016	7660	ANALISIS DE LA MOVILIDAD EN CAMPUS UNIVERSITARIOS INTEGRADOS EN ZONAS URBANAS		129 Veces
3	2023	10835	ESTRATEGIAS DE PRECIOS Y SERVICIOS EN UNA CADENA DE SUMINISTRO DE DOBLE CANAL CON INFORMACIÓN COMPARTIDA		129 Veces
1	2017	8024	VALORIZACIÓN DE LODOS PROCEDENTES DE PLANTAS DE TRATAMIENTO DE AGUA POTABLE. UNA APUESTA POR LA ECONOMÍA CIRCULAR Y SOSTENIBILIDAD		128 Veces
6	2011	3966	INGENIERÍA DE CONTROL Y PROTECCION DE SUBESTACIONES ELECTRICAS		127 Veces
7	2014	7009	BUSES Y PROTOCOLOS DE COMUNICACIÓN PARA INSTALACIONES DOMÓTICAS		127 Veces
5	2001	5533	APLICACIONES DE LA INFORMATICA EN LA INDUSTRIA		127 Veces

Mes / Año		IdDoc	Título		
6	2007	151	OHSAS 18000, GESTIÓN DE LA SEGURIDAD Y SALUD EN EL TRABAJO		127 *Veces*
7	2017	8169	APLICACIÓN DE LAS TECNOLOGÍAS DE LA INDUSTRIA 4.0 AL DISEÑO Y FABRICACIÓN DE PRODUCTOS ARTESANALES		127 *Veces*
6	2007	153	IMPACTO SOCIAL Y ECONOMICO DE LOS ACCIDENTES LABORALES		126 *Veces*
5	2003	337	REUNIONES DE TRABAJO, COMO HACERLAS PRODUCTIVAS		126 *Veces*
12	2003	478	UNA REFLEXION SOBRE LOS FUNDAMENTOS Y LA APLICABILIDAD DE CADENA CRITICA EN PROYECTOS		126 *Veces*
11	2017	8469	ANÁLISIS SOBRE LAS CARACTERÍSTICAS HIDRÁULICAS Y DE EMPUJE DE UNA BOMBA A PROPULSIÓN POR AGUA EN MINIATURA		126 *Veces*
5	2016	7685	METODOLOGÍA PARA AUDITAR LAS INSTALACIONES EXISTENTES DE ALUMBRADO PÚBLICO Y CONOCER SU POTENCIAL DE AHORRO, PROTECCIÓN DEL MEDIO AMBIENTE Y CONDICIONES DE SEGURIDAD		126 *Veces*
1	2014	5763	SEGUNDAS VIDAS PARA BATERÍAS DE COCHES ELÉCTRICOS: BUENAS IDEAS - MALOS NEGOCIOS		125 *Veces*
7	2018	8888	LA MUJER EN LA INGENIERIA INDUSTRIAL: DIFICULTADES A SUPERAR		124 *Veces*
11	2013	5846	MANTENIMIENTO PREDICTIVO EN PEQUEÑA Y MEDIANA EMPRESA		123 *Veces*
7	2013	5646	EFECTO DE LAS FIBRAS DE COCO SOBRE LA RESISTENCIA A LA FLEXIÓN DE MEZCLAS DE HORMIGÓN		123 *Veces*
10	2011	4060	DISEÑO DE UN SISTEMA DE PICKING PRODUCTO A OPERARIO. APLICACION DEL DISEÑO DE EXPERIMENTOS MEDIANTE SIMULACION DE EVENTOS DISCRETOS.		123 *Veces*
11	2012	4965	CÁLCULO DEL PERÍODO DE GARANTÍA TRAS LA REPARACIÓN DE UN ACTIVO INDUSTRIAL COMPLEJO, APLICANDO PROCESOS DE POISSON NO HOMOGÉNEOS		123 *Veces*
3	2013	4983	ASPECTOS AMBIENTALES A CONSIDERAR EN VERTEDEROS: UBICACIÓN Y EMISIONES DE BIOGÁS		123 *Veces*

Mes / Año		IdDoc	Título		
9	2012	5237	EVOLUCION: CADENAS DE SUMINISTRO TRADICIONALES Y COLABORATIVAS.		**123** *Veces*
12	2005	29	LA CONTAMINACION LUMINICA		**123** *Veces*
10	2009	3027	LA IMPORTANCIA DE LA ÉTICA EN LA PROFESIÓN DE INGENIERÍA		**123** *Veces*

The final publication is available at

https://dx.doi.org/10.1007/s11483-011-9215-2

Additional Information

WATER CONTENT-WATER ACTIVITY-GLASS TRANSITION TEMPERATURE RELATIONSHIPS OF SPRAY-DRIED BOROJÓ AS RELATED TO CHANGES IN COLOR AND MECHANICAL PROPERTIES

Luz Hicela Mosquera; Gemma Moraga; Pedro Fernández de Córdoba; Nuria Martínez-Navarrete.

ABSTRACT

The water content-water activity-glass transition temperature relationships of commercial spray-dried borojó powder, with and without maltodextrin, have been studied as related to changes in color and mechanical properties. The GAB and Gordon and Taylor models were well fitted to the sorption and glass transition data, respectively. The Boltzman equation adequately described the evolution of the mechanical parameter characterized in the samples with the difference between the experimental temperature and the glass transition temperature (T_g) of the sample. The color of the samples showed a sigmoid change with water activity. The changes in the mechanical properties of borojó powder related to collapse development started when the sample moved to the rubbery state and began to be significant at about 10 ºC above T_g. The increase in the molecular mobility from this point on also favors browning reactions. Maltodextrin presence slows the caking kinetics but induces color changes to spray-dried borojó powder.

Key Words: powdered borojó, maltodextrin, sorption isotherms, glass transition, compression test, CIEL*a*b* coordinates.

INTRODUCTION

Borojó represents one of the major consumer products in the department of Chocó (Colombia) and in much of South America, where the functional properties conferred by the traditional use of the fruit has encouraged its introduction in some international sectors. It is characterized by a high energy and nutritional capacity, especially a high fiber content, as well as the supposed properties attributed by the indigenous and black groups in the region who use it as medicine, to embalm cadavers and to prepare aphrodisiacal beverages. Current developments focus on the commercialization of borojó as energy drinks, jellies or jams, as the appearance and weight of the fruit (700 - 1000 g) make it difficult to distribute as a fresh product, besides its pulp is quite acid and viscous[1]. Extracts and juices obtained from plants and fruits are used more and more in both the pharmaceutical and the food industry for the manufacture of a large number of products. On the other hand, freeze-drying and spray-drying are used to obtain products in powdered form, which highly preserve the majority of the natural components present in the fresh products. Nevertheless, the presence of compounds such as sugars makes it difficult to dry these products by spray due to their adherence to the inner surfaces of the equipment, which leads to a poor performance when obtaining the final product[2]. The use of inert additives such as starch, cyclodextrin, lactose or maltodextrin favors the product recovery, acting as interveners of the drying[3].

The deteriorative phenomenon that occurs most frequently in the powdered products has been associated with the transition from a glassy to rubbery state. In these products, when a critical temperature, related to the glass transition temperature, is reached, a sequence of deleterious events occur[4]. Initially, stickiness is developed due to the formation of an incipient liquid state of lower viscosity on the particle surface. The

91 caking of sticky powders takes place because of interparticle bridging, eventually

92 forming agglomerations[5]. The extension of this phenomenon in the matrix leads to

93 structure collapse. To prevent the occurrence of this undesirable phenomenon, it is

94 important to keep the amorphous matrix in a glassy state[4]. The glass transition

95 temperature (T_g) of an amorphous matrix defines the temperature at which the

96 glassy/rubbery change occurs and depends on its water content; the greater the water

97 content, the lower the T_g. For this reason, during the processing, handling, storage and

98 distribution, powdered products may experience a deteriorative evolution due to

99 changes in temperature and environmental relative humidity. An increase in the product

100 temperature above the T_g will lead it to the unstable rubbery state. On the other hand, an

101 increase in the environmental relative humidity surrounding the powder of over 100

102 times its water activity will lead to the hydration of the powder, thus decreasing its T_g.

103 If the T_g falls below the storage temperature, the product will again change into the

104 rubbery state. The relationship between the water activity and the water content is given

105 by the water sorption isotherm. Structural changes caused by powder collapse, together

106 with the water content, may affect some physical properties such as color or mechanical

107 behavior[6-7]. From this point of view, it is important to maintain the glassy state in these

108 products.

109 The solid composition also affects the T_g, the greater the average molecular

110 weight, the greater the T_g. The carbohydrates present in fruits are normally low

111 molecular weight sugars, thus implying low T_g values in this kind of foods. For this

112 reason, high molecular weight solutes are usually added to fruit prior to spray-drying, to

113 improve not only the drying process but also the product stability of the obtained

114 powder. The effect of adding a solute will depend on the amount used and its average

115 molecular weight as related to that of the solids present in the fruit.

116   This work focused on studying the effect water uptake had on the stability of

117   spray-dried borojó, with and without added maltodextrin, related both to glass transition

118   and to changes in the mechanical properties and color.

119

MATERIAL AND METHODS

120

121   **1. Sorption isotherms and glass transition.**

122   The commercial products *Borojó Powder, Spray Dried* (B) and *Borojó Powder,*

123   *Spray Dried (Maltodextrin)* (BM) were acquired from Ecoflora Ltda. (Medellín,

124   Colombia). B and BM water content was 0.044 and 0.043 g water/100g product,

125   respectively and water activity was 0.315 and 0.312, respectively.

126   For sorption experiments, both B and BM spray-dried powder samples were

127   placed at 20ºC in hermetic chambers containing saturated salt solutions (LiCl,

128   CH_3COOK, $MgCl_2$, K_2CO_3, $Mg(NO_3)_2$, $CuCl_2$, $NaCl_2$ and KCl_2). Three replicates of

129   about 2 g each were placed in each chamber with different relative humidities (RH)

130   ranging between 11- 85 %[8]. The sample weights were controlled till a constant value

131   ($\Delta m < \pm 0.0005$ g) was reached, where the equilibrium between the sample and the

132   environment was assumed[9]. In this moment, the a_w of each sample was assumed to be

133   equal to the corresponding RH/100. In each equilibrated sample, the final water content

134   was obtained from both the initial water content data and the change in the registered

135   weight till the equilibrium. The initial water content of the samples was determined

136   from the loss of mass when drying the samples at 60 ± 1 °C under a pressure of < 100

137   mm Hg until constant weight. Water content (dry basis) and a_w values were used in

138   order to construct the sorption isotherms. Calorimetric analyses were carried out in each

139   equilibrated sample in order to determine the glass transition temperature (T_g) by means

140 of differential scanning calorimetry (DSC). About 10 mg of each sample were placed

141 into DSC pans (P/N SSC000C008, Seiko Instruments, Inc., Japan), sealed and analyzed

142 using a DSC 220CU-SSC5200 (Seiko instruments, Inc., Japan). The heating rate was 5

143 ºC/min and the temperature range varied between -100 and 200ºC, depending on the

144 sample water content and the kind of sample. The mid-point of the glass transition was

145 considered as the characteristic temperature of the transition.

146

2. Mechanical properties and color analyses

148

149 Different samples of about 1 g of B and BM were placed in cylindrical vials and

150 stored in hermetic chambers at relative humidities of between 23 % and 85 %, following

151 the same procedure described for sorption experiments. Every 3 days, for a period of 4

152 weeks, a vial of B and BM was weighed and its water content, mechanical properties

153 and color analyzed. The water content was calculated from the initial moisture content

154 and the sample mass change. For the analysis of the physical properties, the powder was

155 placed in a circular aluminum sample holder of 11 mm in diameter and 5.5 mm in

156 height. A reflectance glass (CR-A51, Minolta Camera, Japan) was placed between the

157 sample and the spectrophotometer lens (Colorimeter Minolta mod. CM-3600d, Japan.).

158 The measurement window was 6 mm in diameter and D65 illuminant/10º observer were

159 selected to obtain CIE L*a*b* color co-ordinates. After color measurement, a

160 mechanical compression test with a cylindrical probe of 10 mm in diameter was carried

161 out using a texture analyzer TA-XT Plus (Stable micro Systems, Ltd., UK). The sample

162 was compressed at a fixed distance of 3 mm at a constant rate of 0.05 mm/s. The

163   maximum force attained during the test was recorded as Fmax. Each color and

164   mechanical property measurement was carried out in quadruplicate.

165

3. Fitted models and statistical comparison of the different experimental series

167

168   In order to predict the water sorption behavior of samples, the GAB

169   (Guggenheim, Anderson and de Boer)[10] model (Eq. 1) was used.

170

$$w_e = \frac{w_o \cdot C \cdot K \cdot a_w}{\left(1 - K \cdot a_w\right) \cdot \left(1 + \left(C - 1\right) \cdot K \cdot a_w\right)}$$

171   Eq. 1

172   where:

173   w_e: water content (g water/ g solids).

174   a_w: water activity.

175   w_o: monolayer water content (g water/ g solids).

176   C: constant related to monolayer sorption heat.

177   K: constant related to multilayer sorption heat.

178

179   Experimental T_g (mid-point)–water content (g water/g product) data were fitted

180   to the Gordon and Taylor model[11], (Eq. 2).

181

$$T_g = \frac{\left(1 - x_w\right) \cdot T_{g(as)} + k \cdot x_w \cdot T_{g(w)}}{\left(1 - x_w\right) + k \cdot x_w}$$

182   Eq. 2

183   where:

184   x_w: mass fraction of water (g water/ g product).

185   T_g: glass transition temperature (°C).

186    $T_{g(w)}$: glass transition temperature for amorphous water: -135 °C[4].

187    $T_{g(as)}$: glass transition temperature for anhydrous solids (°C).

188   k: model constant.

189

190   The Boltzman function was fitted to correlate the sigmoid behavior described by

191   the mechanical parameter of samples with a different water content, referred to the

192   sample mass, (Fmax/m) as a function of its glass transition temperature (Eq. 3). In this

193   equation, F1 and F2 are the values of Fmax/m at the initial (upper) and final (lower)

194   asymptotes, respectively, λ_F is a parameter that describes the shape of the curve between

195   the upper and lower asymptotes, and ΔT_F is the value of T-T_g at which Fmax/m attains

196   the average value between F1 and F2[12].

197

$$F\max/m = \frac{F1 - F2}{1 + e^{(\Delta T - \Delta T_F)/\lambda_F}} + F2$$

198   Eq. 3.

199

200   To evaluate the differences between sample behavior (a_w or T_g changes with x_w

201   and Fmax/m with ΔT_F) as a function of the presence of maltodextrin (MD), the models

202   were fitted to each individual data series (B and BM) and to all the grouped data (B +

203   BM). The obtained results were statistically compared through the values of statistic E

204 (Eq. 4) which was compared with tabulated F-Snedecor as a function of the values of

205 DFDR and SFDRi at 99% significance level[13].

206

$$E = \frac{(RSSg - \sum_{i=1}^{n} RSSi)/DFDR}{\sum_{i=1}^{n} RSSi / \sum_{i=1}^{n} FDRi}$$

207   Eq. 4

208 where:

209 RSSg: residual square sum of the function fitted to a group of series.

210 RSSi: residual square sum of the function fitted to an individual series.

211 FDRg: freedom degrees of the residuals of the function fitted to a group of series.

212 FDRi: freedom degrees of the residuals of the function fitted to an individual series.

213 DFDR: difference between freedom degrees of the residuals of the function fitted to a

214 group of series (FDRg) and the sum of freedom degrees of the residuals of the

215 individual fittings of the series involved in the group (ΣFDRi),

216

217 **RESULTS AND DISCUSSION**

218 **1. Sorption isotherms and plasticizer effect of the water.**

219   Wall depositions of sticky products are a frequent problem during the spray-

220 drying of fruit juices, as the low molecular weight of the sugars present prevents

221 products from being obtained with a water content of under 5 %. The convenience of

222 adding maltodextrin to decrease the higroscopicity of fruit powders, thus improving the

223 handling during spray-drying, has been widely studied. Moreover, the high T_g value of

224 maltodextrins provides a good stability in powdered products[14, 15].

225   Figure 1 shows the sorption isotherm of B and BM. Experimental sorption data

226   were well fitted to the GAB model (table 1). On the other hand, the decrease in the T_g

227   observed when increasing the water content of the samples (figure 2) was fitted to the

228   Gordon and Taylor model (table 1). A non-linear fitting procedure (CHI^2)[16] using

229   OriginPro 6.1 software was applied. Both models were fitted individually to the B and

230   BM samples and to all the B+BM data. The statistical analysis performed by means of

231   the Snedecor test showed no significant differences either between the sorption behavior

232   of B and BM or in $T_g - x_w$ relationships (table 2), which suggests that adding

233   maltodextrin has no effect. The parameters of these models fitted to all the grouped data

234   appear in table 1.

235   The fact that this study found that maltodextrin had no significant effect on

236   water sorption and T_g do not coincide with what has been found when working on other

237   fruits, such as pineapple, camu camu or grapefruit[17,18,12] and even freeze-dried borojó.

238   This may be related to the different soluble solid composition of borojó as compared to

239   the other fruits and also to the amount of maltodextrin added to our product. Mosquera

240   et al.[1] have pointed to the high carbohydrate content of borojó (about 30 g / 100 g

241   borojó). Fructose, glucose and sucrose account for a very small fraction of these

242   carbohydrates (7.3 g / 100 g borojó), so the rest may be attributed to high molecular

243   weight carbohydrates, bearing in mind the total analyzed dietary fiber (23.58 g / 100 g

244   borojó) and pectin (2.62 g / 100 g borojó) content. Carbohydrates in pineapple and

245   grapefruit represent about 10 % of the fruit weight, being almost all of them sugars.

246   From this point of view, the average molecular weight of the solids present in borojó is

247   much greater and so its adsorption capacity is lower and its T_g is higher. So a greater

248   amount of maltodextrin will be needed to affect these aspects. Silva et. al.[18] noted that

249   the addition of 0.88 kg of maltodextrin (20 DE) / 1 kg of total solids can reduce the

250 moisture content in freeze-dried camu camu pulp from 15.8 % to 6.5 % (dry basis) and

251 increase the T_g. A similar effect was observed by Gabas et al.[17] and Telis & Martínez-

252 Navarrete[12] studying freeze-dried powdered pineapple pulp and freeze-dried grapefruit

253 when adding 0.2 and 1kg of maltodextrin / kg of total solids, respectively.

254 Mosquera et al.[1] also suggested the use of 0.55 kg of maltodextrin (16.5 - 19.5

255 DE) or arabic gum for each kg of total solids in freeze-dried borojó to significantly

256 affect the sorption behavior and T_g, although this effect was not so noticeable as in the

257 other fruit powders with high amount of low molecular weight carbohydrates. In our

258 study, as no effect of MD on water sorption and T_g of borojó was observed, the amount

259 of maltodextrin added to the fruit (not specified on the label) must be supposed to be

260 lower than 0.55 kg maltodextrin / kg total solids in the sample and not enough to reduce

261 the hygroscopicity of the powder and to increase the glass transition temperature. On

262 the other hand, in the mentioned study of Mosquera et al.[1], the critical water content

263 (CWC) for the glass transition of freeze-dried borojó at 20 ºC was increased from 0.059

264 to 0.085 when maltodextrin was added, which significantly improves the handling of

265 the powder. In our work, when considering the information of B and BM samples

266 together, the combined analysis of water sorption and T_g data, allowed us to obtain the

267 T_g-a_w-x_w relationships (figure 3). From this analysis, CWC and critical water activity

268 (CWA) for the glass transition at 20 °C were determined, these being 0.046 g water /g

269 product and 0.319, respectively. As deduced from this value and the measured water

270 content in newly spray-dried borojó products used as raw matter in the study (see

271 Material and methods section), both of them were in a glassy state at this temperature,

272 although very near to the critical values. The greater CWC of freeze-dried borojó as

273 compared to that of spray-dried borojó may be related to the different structure of the

274 obtained products. As referred by Haque and Roos[19], spray-dried particles are spherical

275   and of low porosity, while freeze-dried particles appear as porous flakes with a greater

276   surface area available for water adsorption. Therefore a spray-dried material may have

277   less hydrogen-bonding sites available for water molecules in sorption than freeze dried

278   materials. In our case, sorption and T_g behavior of freeze-dried and spray-dried borojó

279   powder seems to be different. The lower stability of the powders obtained by spray-

280   drying would recommend a greater amount of high molecular weight solute to be added

281   to them as compared to freeze-dried products.

282

283   *2*. **Mechanical properties and color**

284   As referred to in the introduction section, the collapse of food powders includes

285   time dependent structural changes related to four stages: bridging, agglomeration,

286   compaction and liquefaction[20]. Caking and/or stickiness of powdered products

287   developed during this process occur as a result of the viscous flow caused in the product

288   at over T_g and it lead changes in the mechanical properties[21]. The rate of caking is a

289   function of T_g, relative humidity and time. Relative humidities that allow the product to

290   be maintained in a glassy state at storage temperature do not provoke caking, while a

291   RH that implies a decrease of T_g to below the storage temperature does lead to caking;

292   the higher the RH, the faster the observed changes[5]. When a system is above its T_g, the

293   kinetics of caking and related phenomena, such as collapse and stickiness, vary as $10^{\Delta T}$,

294   where $\Delta T = T - T_g$[20,22].

295   The analysis of the shape of the curve force-distance and the maximum force

296   attained during the mechanical compression test used in this study have been proposed

297   by Telis and Martínez-Navarrete[7] as a simple, rapid method, sensitive enough to

298   quantify the effect of water uptake on the mechanical properties of food powders that

may be related to the development of stickiness. Figure 4 shows the maximum force evaluated in the compression test carried out on borojó samples at different RH and storage times. In this figure, some of the force-distance curves obtained during the test have also been included. The analysis of these curves allowed us to detect changes in the mechanical properties which seem to be related to the caking process that characterizes the beginning of the collapse.

Force-distance curves obtained in both newly processed B and BM samples and those stored at RH lower than 43%, showed fracture peaks during the entire period under study as corresponds to a free flowing powder, with no caking problems and easy to compact. The ratio of the maximum force attained during the compression test to the sample weight (F_{max}/m) on newly processed samples was not affected by maltodextrin addition and they underwent no noticeable change as a consequence of storage time when stored at RH 23 and 33 %. Samples stored at RH of over 52% did not show these fracture peaks at any time, as occurs when the caking process is fully developed; the greater the water content, the lower the force needed to compact the liquefied sample. In B and BM samples stored at RH 68, 75 and 85 %, a sharp decrease in F_{max}/m was observed from the third storage day onwards. Force-distance curves obtained in BM samples stored at 43% RH showed fracture peaks for up to 14 days, while BM samples stored at 52% RH only showed them for up to 3 days. However, B samples under the same storage conditions did not show any fracture peak during the entire storage period under consideration. The differences observed between these samples could be associated with a protective effect of maltodextrin that slows the caking kinetic in BM samples. Caking phenomena started in B samples stored at 43 and 52% RH before 3 storage days, and progresses at a slower rate than samples stored at RH 68 %, while BM samples needed more time. The caking process starts with the formation of inter-particle

324 bridges over a certain amount of water which implies an increase of the force needed to

325 compact the sample[23]. For this reason, there was an observed increase in Fmax/m for

326 BM samples stored at 43% and 52% RH, not shown for B samples, at the beginning of

327 the storage period when compared to samples stored at 23 and 32% RH. At the end of

328 the storage period, caking was fully developed and the trend of Fmax/m was in line with

329 the rest of the BM samples.

330   From the water content calculated for each sample at each storage time, a_w and

331 T_g were predicted by applying the GAB and Gordon and Taylor fitted models,

332 respectively. The change of the mechanical parameter evaluated with a_w and with the

333 difference between the temperature at which the mechanical analysis was carried out

334 and the glass transition temperature of the sample ($\Delta T = 20 - T_g$) appears in figures 5 and

335 6, respectively. A similar trend, sigmoid in behavior, was observed in both cases. At an

336 a_w greater than CWA, which means the samples are in the rubbery state ($\Delta T > 0$), a sharp

337 decrease in Fmax/m was observed, related with a softening of the samples in this

338 physical state. The Boltzman equation was fitted to Fmax/m vs. ΔT (OriginPro 6.1

339 software) separately for samples with and without maltodextrin and to all the grouped

340 data (table 1). As no significant differences were observed between the fittings (table 2),

341 no effect of MD on the mechanical properties of borojó powder can be assumed as

342 related to glass transition temperature This was expected, since the presence of MD had

343 no observed effect on T_g. In this way, figure 6 shows the trend of the predicted behavior

344 by using the corresponding model parameters. From the fitted parameters, it was

345 possible to determine that 20% of the transition between the upper and lower

346 asymptotes occurred at a value of $\Delta T = 12.19$ ºC, whereas 80% of the transition was

347 attained at $\Delta T = 36.12$ ºC. As suggested by Foster et al.[24], this result allows us to

348 conclude that important changes in the mechanical properties of borojó powder related

349 to collapse development occur at about 10 ºC above T_g. The magnitude of the

350 temperature differences obtained in this study coincides with the results obtained by

351 Foster et al.[24], when studying the cohesiveness of different freeze–dried sugar powders.

352 The T_g of samples that led to a ΔT equal to 12.19 and 36.12 ºC were 7.81 and -16.12 ºC

353 and the corresponding a_w were 0.445 and 0.631.

354   For color measurement, CIEL*a*b* system coordinates was selected. In this

355 system, L* denotes lightness on a 0 to 100 scale from black to white; a*, (+) red or (-)

356 green; and b* (+) yellow or (-) blue. The total color difference (ΔE*) with respect to the

357 newly spray-dried borojó was obtained (Eq. 5).

358

359 $$\Delta E^* = \sqrt{(\Delta L^*)^2 + (\Delta a^*)^2 + (\Delta b^*)^2}$$ Eq. 5

360

361   Figure 7 shows the L*a*b* values for samples, with and without maltodextrin,

362 in the range of the studied relative humidity during the storage time. Color coordinates

363 of samples remained more or less stable over time when stored at relative humidities

364 lower than 43-52 %. From this value, L* and b* decreased and a* increased over time;

365 the greater the RH surrounding the sample, the greater the observed change. When the

366 data were plotted vs. a_w (figure 8), the addition of maltodextrin was observed to have an

367 effect. This involved an increase in L* and b* and a decrease in a*, related to an

368 increase in the lightness of the product and in the hue angle due to the development of

369 yellowness. In both samples, as the water activity increased, lightness and b*

370 coordinates decreased and a* increased, in a sigmoid way. The abrupt change of the

371 coordinates was observed when the a_w was in the range of 0.5 to 0.6 and it provoked a

372 darkness in the samples and an important change in the hue angle and chrome that

373 turned the samples browner. The afore mentioned a_w range was near to that established

374 when 20-80% of the change in the mechanical properties with ΔT was calculated,

375 indicating that the decrease in the viscosity which takes place at about ten degrees above

376 the glass transition favors color changes. These color changes may be attributed to

377 optimum conditions for enzymatic and non-enzymatic browning reactions. Some

378 authors have pointed out that both kinds of reactions occur mainly at intermediate water

379 activities[25-28]. The Maillard, or non-enzymatic browning reaction, is most likely to occur

380 in low-moisture systems (a_w 0.3-0.7), as the removal of water allows the solid content to

381 be concentrated and, hence, leads to an increase in the interactions between the reducing

382 sugars and amino acids in the fruit. On the other hand, water activity values of 0.430

383 have been pointed out as the limit above which the rate of food enzymatic browning

384 rises. Nevertheless, water dilution that takes place at water activity values which are too

385 high may prevent these processes.

386   The color difference with respect to newly spray-dried borojó was calculated at

387 each storage period and RH (Figure 9). As can be observed, three groups of samples can

388 be identified. The first one, with color differences lower than about six units ($\Delta E < 6$),

389 appeared at a_w values lower than 0.5. The second one was found in the range of a_w from

390 0.5 to 0.7, were a sharp increase in ΔE values from approximately 5 to 22 was observed.

391 From this water activity onwards, ΔE remained stable. Color changes that occur in

392 borojó at a_w values lower than 0.5 could be more related with the development of

393 Maillard reactions, while those which take place from a_w 0.5 could be more closely

394 related to enzymatic browning. The presence of maltodextrin does not prevent browning

395 reactions.

CONCLUSIONS

The critical water content and critical water activity for the glass transition of borojó at 20 °C was 0.046 g water/g product and 0.319, respectively. The water content of the newly spray-dried borojó powders used in this study were in the range of this CWC, so the use of high molecular weight solutes should be recommended to increase the T_g of the product and, therefore, its stability. Nevertheless, the amount of solute added must be optimized by taking both the product composition and the process used to obtain the powder into account. Otherwise, no significant effect could be detected, as occurred in this study. Changes in the mechanical properties of borojó powder related to collapse development started when the sample moved to the rubbery state and began to be significant at about 10 ºC above T_g. The increase in the molecular mobility from this point on also favors browning reactions. Maltodextrin presence slows the caking kinetics but induces color changes to spray-dried borojó powder.

References

1. L.H. Mosquera, G. Moraga, N. Martínez-Navarrete, J. Food Eng. 9, 72 (2010). doi: 10.1016/j.jfoodeng.2009.09.017

2. V. Truong, B. R. Bhandari, T. Howe, J. Food Eng. 71, 55 (2005). doi: 10.1016/j.jfoodeng.2004.10.017

3. B. Bhandari. *Glass transition in relation to stickiness during spray drying* (Academic press, Sterling Publication, London, 2001), pp 64

4. Y. Roos. *Phase transitions in foods* (Academic Press, New York, 1995), pp. 360.

419   5.   P. Saragoni, J.M. Aguilera, P. Bouchon, Food Chem. 104, 122 (2007). doi:

420   10.1016/j.foodchem.2007.11.066

421   6.   C.K. Pua, N. Sheikh Abd. Hamid, C.P. Tanm, H. Mirhosseini, R. Abd. Rahman,

422   G. Rusul, J. Food Eng. 89, 419 (2008). doi: 10.1016/j.jfoodeng.2008.05.023

423   7.   V.R.N. Telis, N. Martínez-Navarrete, LWT – Food. Sci. Technol. 43, 744 (2010).

424   doi:10.1016/j.lwt.2009.12.007

425   8.   L. Greenspan, J. Res. Nat. Inst. Stan. 81, 89 (1977). IDS: DM875

426   9.   W.E.L. Spiess, W.R. Wolf, ed. by F. Escher, B. Hallstrom, H.S. Mefert, W.E.L.

427   Spiess, G. Woss. *Physical Properties of foods* (Aplied Sci. Publisher, New York, 1983),

428   p. 65

429   10.   C. Van den Berg, S. Bruin, ed. by L.B. Rockland, G.T. Stewart. *Water Activity*

430   *and its Estimation in Food Systems: Theoretical Aspects* (Academic Press, London/New

431   York, 1981), p. 43

432   11.   M.   Gordon,   J.S.   Taylor,   J.   Appl.   Chem.   2,   493   (1952).

433   doi:10.1002/jctb.5010020901G

434   12.   V.R.N. Telis, N. Martínez-Navarrete, Food Biophysics. 4, 83 (2009) doi:

435   10.1007/s11483-003-9104-0

436   13.   G. Moraga, N. Martínez-Navarrete, A. Chiralt, J. Food Eng. 62, 315 (2004). doi:

437   10.1016/S0260-8774(03)00245-0

438   14.   C.I. Beristain, E. Azuara, E.J. Vernon-Carter, J. Food Sci. 67, 211.2002. IDS:

439   522JP

440   15.   B.R. Bandhari, R.W. Hartel, ed. by . C. Onwulata, R.P. Konstance. *Encapsulated*

441   *and food powder*. (Marcel Dekker, New York, 2005), p. 216

442   16.   N. William, *Estadística para Ingenieros y Científicos* (MacGraw-Hill, Mex.,

443   2006), pp 120

444   17.   A.L. Gabas, V.R.N. Telis., P.J.A. Sobral, J. Telis-Romero, J. Food. Eng. 82, 246

445   (2007). doi: 10.1016/j.jfoodeng.2007.02.029

446   18.   M.A. Silva, P.J.A. Sobral, T.G. Kieckbusch, J. Food. Eng. 77, 426 (2006). doi:

447   10.1016/j.jfoodeng.2005.07.009

448   19.   Md. K. Haque, Y. H. Ross, Innovative Food Science & Emergin Technologies.

449   7,1-2,(2006) doi:10.1016/j.ifset.2004.12.004

450   20.   J.M. Aguilera, J.M. del Valle., M. Karel, Trends Food Sci. Technol. 8, 149

451   (1995). doi:10.1016/S0924-2244(00)89023

452   21.   H. Levine, L. Slade, Cryoletters 9, 21 (1988) IDS: M1923

453   22.   Y.H. Ross, J. Food Eng. 24, 339 (1995b) doi:10.1016/0260-8774(95)90050-L

454   23.   G. Barbosa-Canovas, E. Ortega-Rivas, P. Juliano, & H. Yan. (2005). *Food*

455   *powders: physical properties, processing and functionality*. (Kluwer Academic/Plenum

456   Publisher New York, N.Y) p.372

457   24.   K.D. Foster, J.E. Bronlund., A.H.J. Paterson, J. Food Eng. 77, 997 (2006). doi:

458   10.1016/j.jfoodeng.2005.08.028

459   25.   E. Venir, M. Munari, A. Tonizzo, E. J. Maltini, Food Eng. 81, 27 (2007) doi:

460   10.1016/j.jfoodeng.2006.10.004

461   26.   N. C. Acevedo, C. Schebor., P. Buera, J. Food Eng. 77, 1108 (2006). doi:

462   10.1016/j.jfoodeng.2005.08.045

463   27.   N. C. Acevedo, C. Schebor., P. Buera, Food Chem. 108, 900 (2008). doi:

464   10.1016/j.foodchem.2007.11.057Ahmed, U.S. Shivhareb, P. Singhc, Food Chem. 84,

465   605 (2004). doi: 10.1016/S0308-8146(03)00285-1

466   28.   L. Hang-Ing Ling, J. Birch, M. Lim, Int. J. Food. Sci. Tech. 40, 921 (2005).

467   doi:10.1111/j.1365-2621.2005.00996

Legends

Fig.1. Amount of water adsorbed (g water/g dry solids) in function of water activity of Borojó Powder, Spray Dried (solid line) and Borojó Powder, Spray Dried (Maltodextrin) (dashed line) products (experimental points, $\bigcirc$ and $\bullet$, respectively, and predicted behavior by GAB fitted model).

Fig.2. Glass transition temperature (T_g) in function of water content of Borojó Powder, Spray Dried (solid line) and Borojó Powder, Spray Dried (Maltodextrin) (dashed line) products (experimental points, $\bigcirc$ and $\bullet$, respectively, and predicted behavior by Gordon and Taylor fitted model).

Fig.3. Glass transition temperature (T_g) – water activity (a_w) ($\blacksquare$) and water content (x_w: g water/g product)– water activity ($\square$), relationships of Borojó Powder, Spray Dried and Borojó Powder, Spray Dried (Maltodextrin) products (experimental points and predicted behavior by GAB and Gordon and Taylor model fitted to all the experimental data toghethter).

Fig.4. Maximum force attained per mass unit in the compression test carried out at different relative humidity and storage time of (a) Borojó Powder, Spray Dried and (b) Borojó Powder, Spray Dried (Maltodextrin) products.

Fig.5 Change in the maximum force attained per mass unit in the compression test carried out as a function of a_w in Borojó Powder, Spray Dried ($\bigcirc$) and Borojó Powder, Spray Dried (Maltodextrin) ($\bullet$) products. The line indicates the critical water activity.

Fig.6. Change in the maximum force attained per mass unit in the compression test carried out in Borojó Powder, Spray Dried and Borojó Powder, Spray Dried (Maltodextrin) products, as a function of T-T$_g$. Experimental points ($\bigcirc$ and $\bullet$, respectively) and predicted behavior by the fitted Boltzman equation to all the experimental data together.

Fig.7. L*a*b* color coordinates of (a) Borojó Powder, Spray Dried (Maltodextrin) and (b) Borojó Powder, Spray Dried products, at different relative humidity and storage time.

Fig.8. L*a*b* color coordinates of Borojó Powder, Spray Dried ($\bigcirc$) and Borojó Powder, Spray Dried (Maltodextrin) ($\bullet$) products, as a function of water activity.

Fig.9. Color difference of Borojó Powder, Spray Dried ($\bigcirc$) and Borojó Powder, Spray Dried (Maltodextrin) ($\bullet$) products, stored at every relative humidity with respect to newly spray-dried borojó.
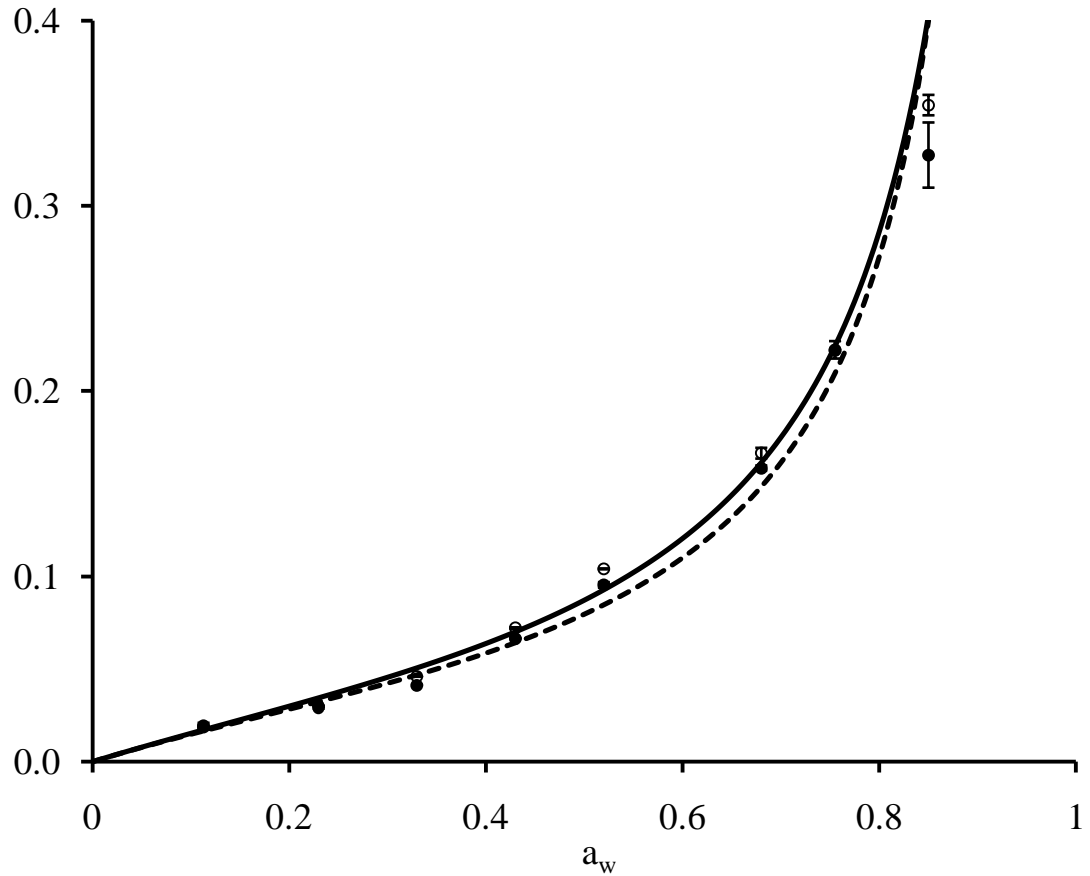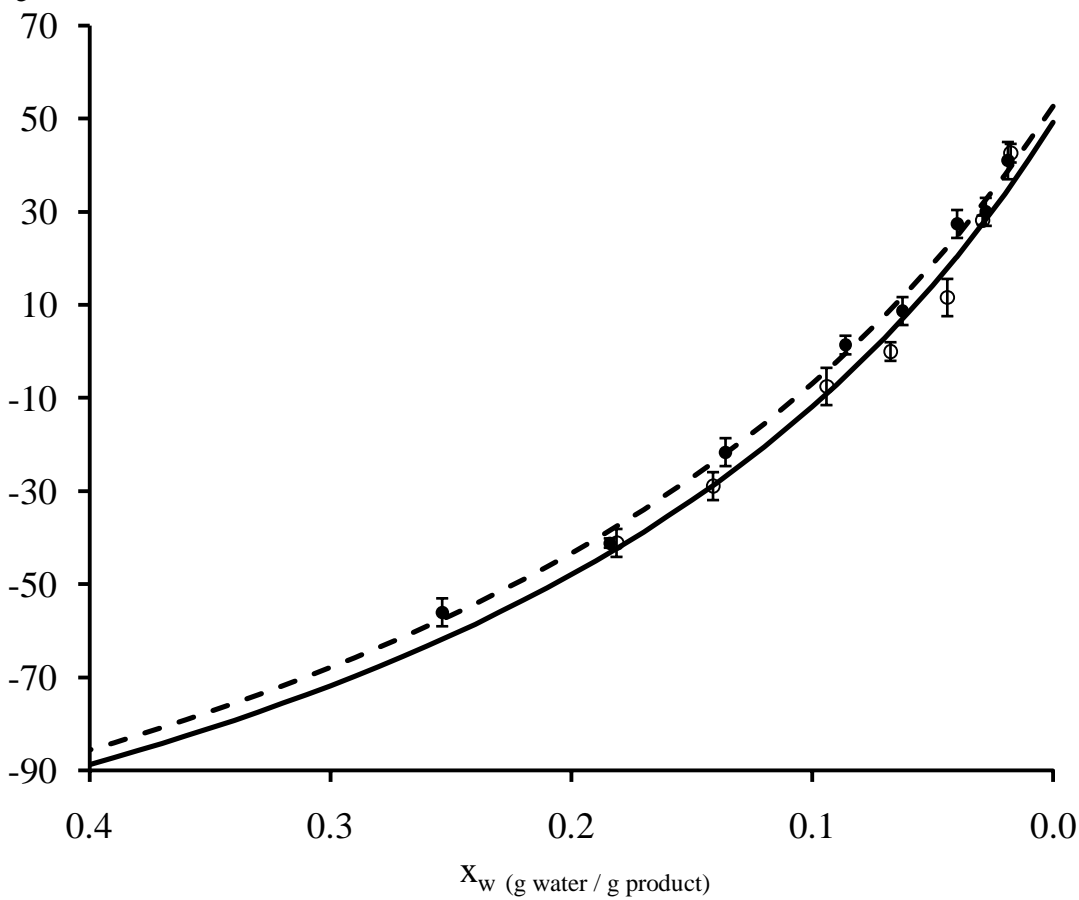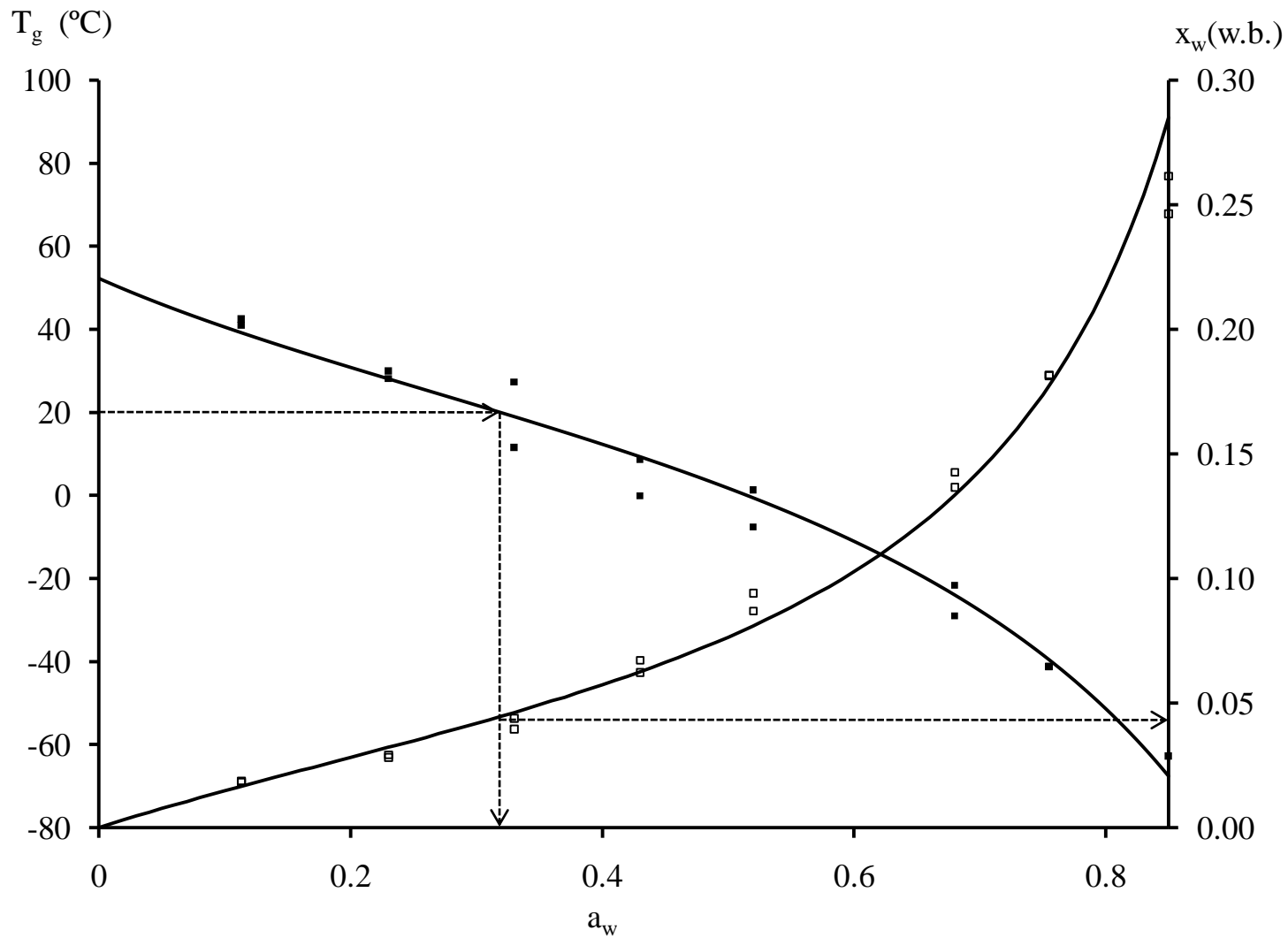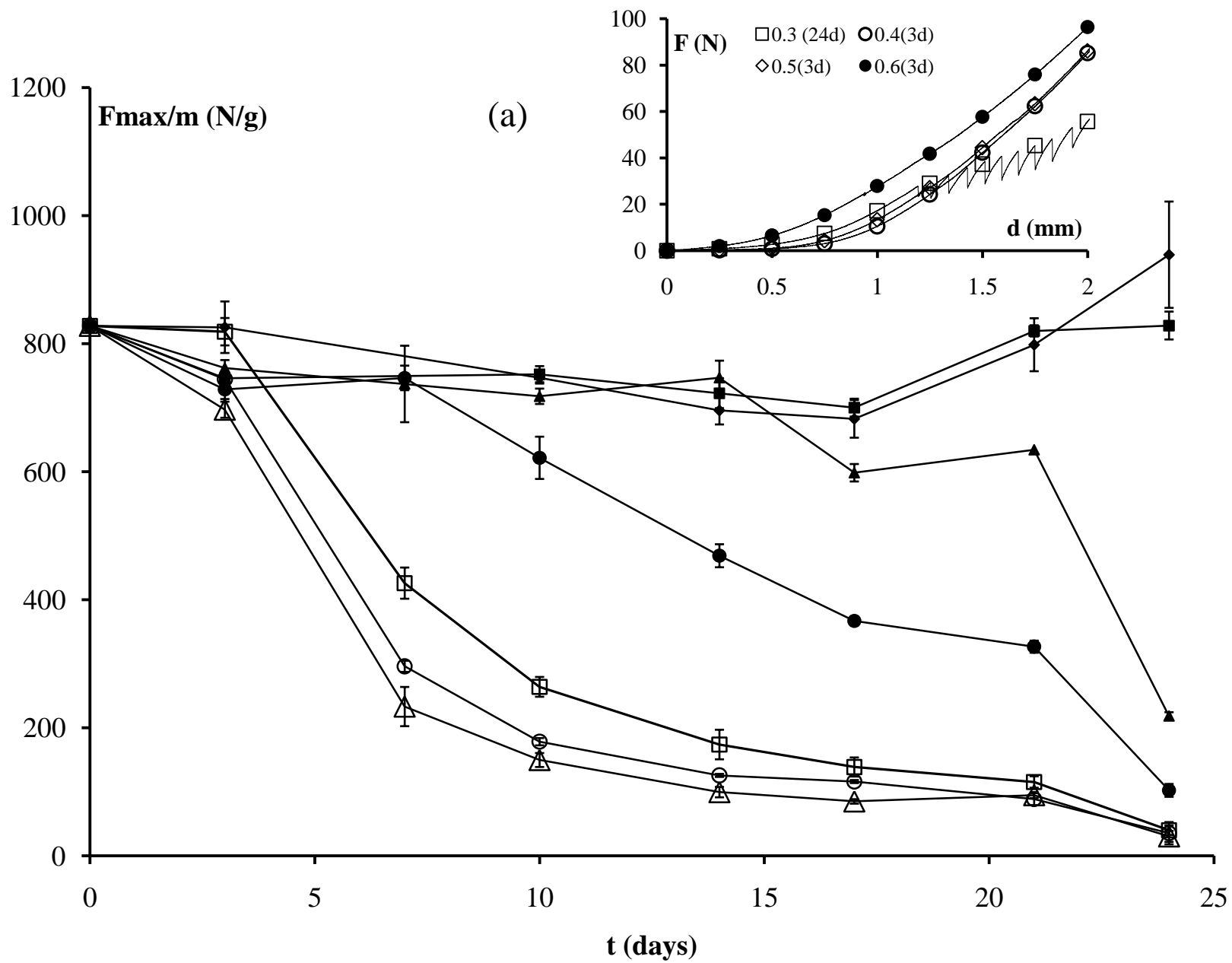
Figure 1

$w_{e\ (d.b.)}$

a_w

Figure 2

T_g (°C) plotted against x_w (g water / g product)

Figure 3

Fmax/m (N/g)

(a)

F (N)

□ 0.3 (24d) ○ 0.4(3d)
◇ 0.5(3d) ● 0.6(3d)

d (mm)

t (days)

Fmax/m (N/g)

(b)

F (N)

□0.5 (3d)   △0.4 (14d)

◆0.4 (17d)   ○0.5 (10d)

d (mm)

t (days)

Figure 5

Fmax (N/g)

a_w
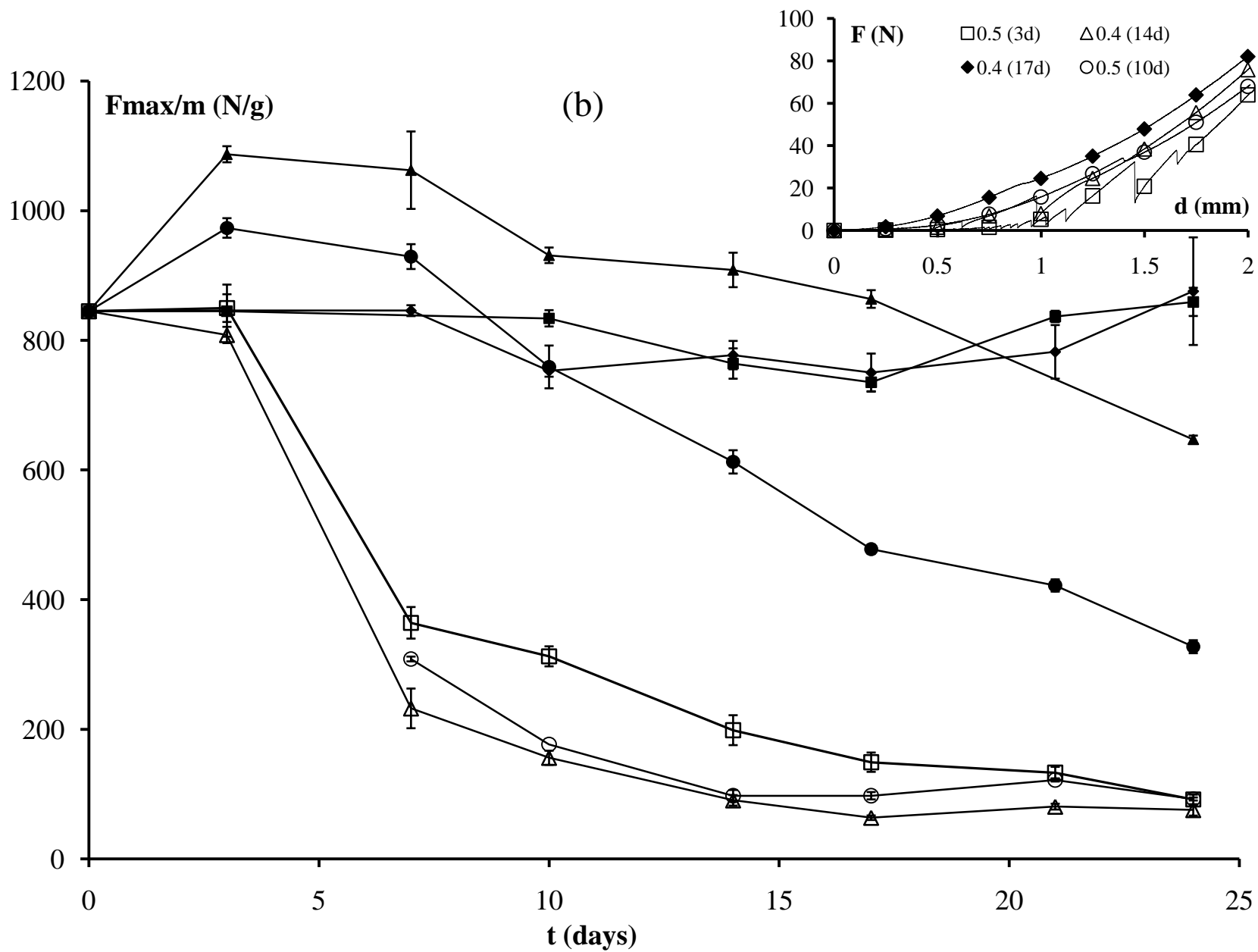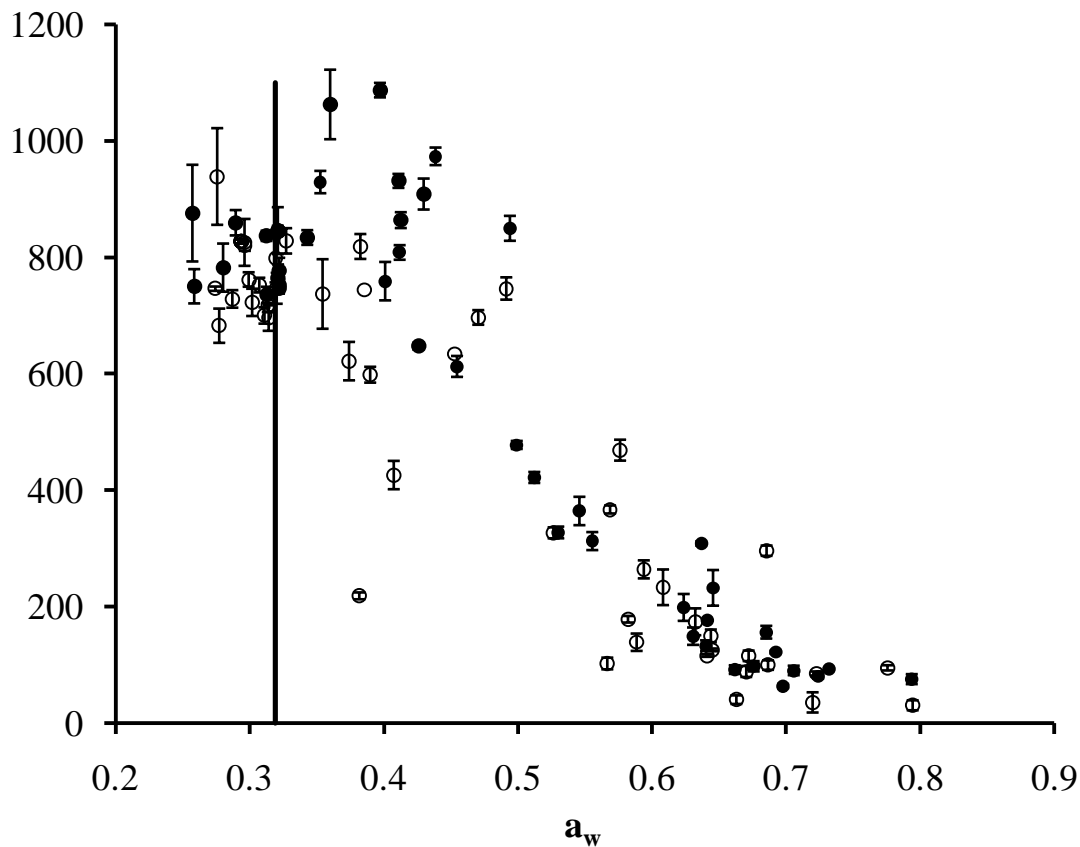
Figure 6

Fmax (N/g)
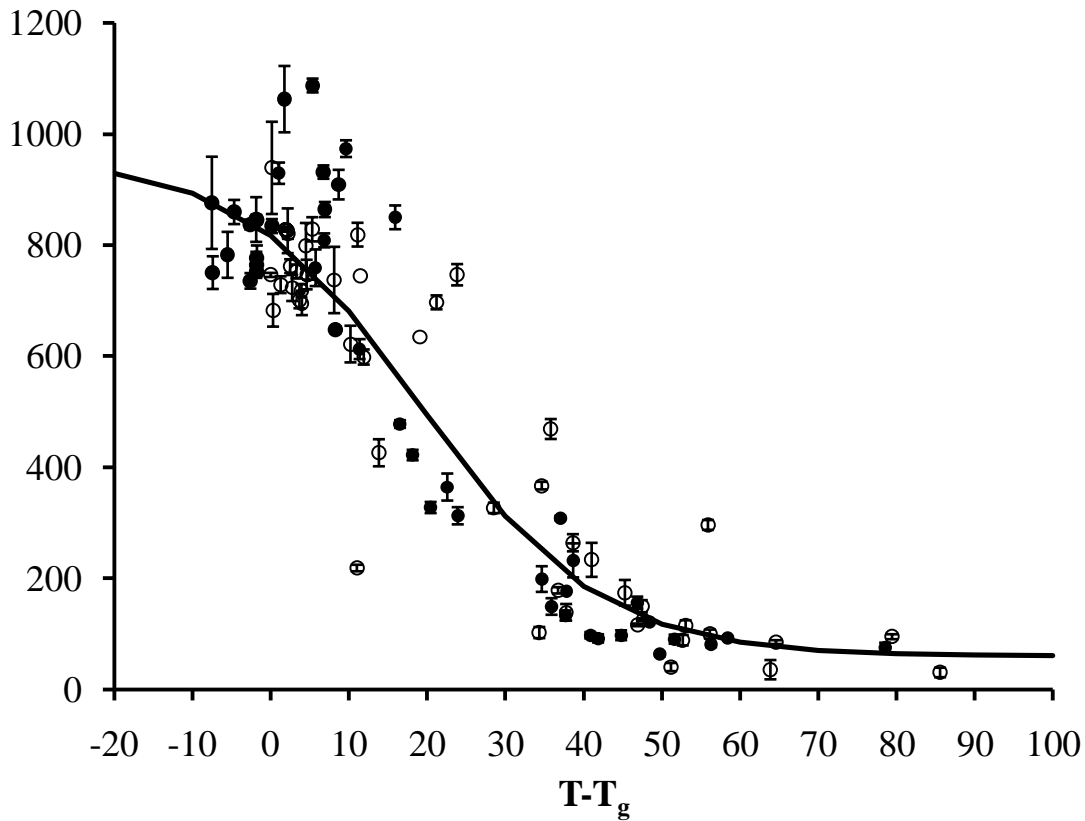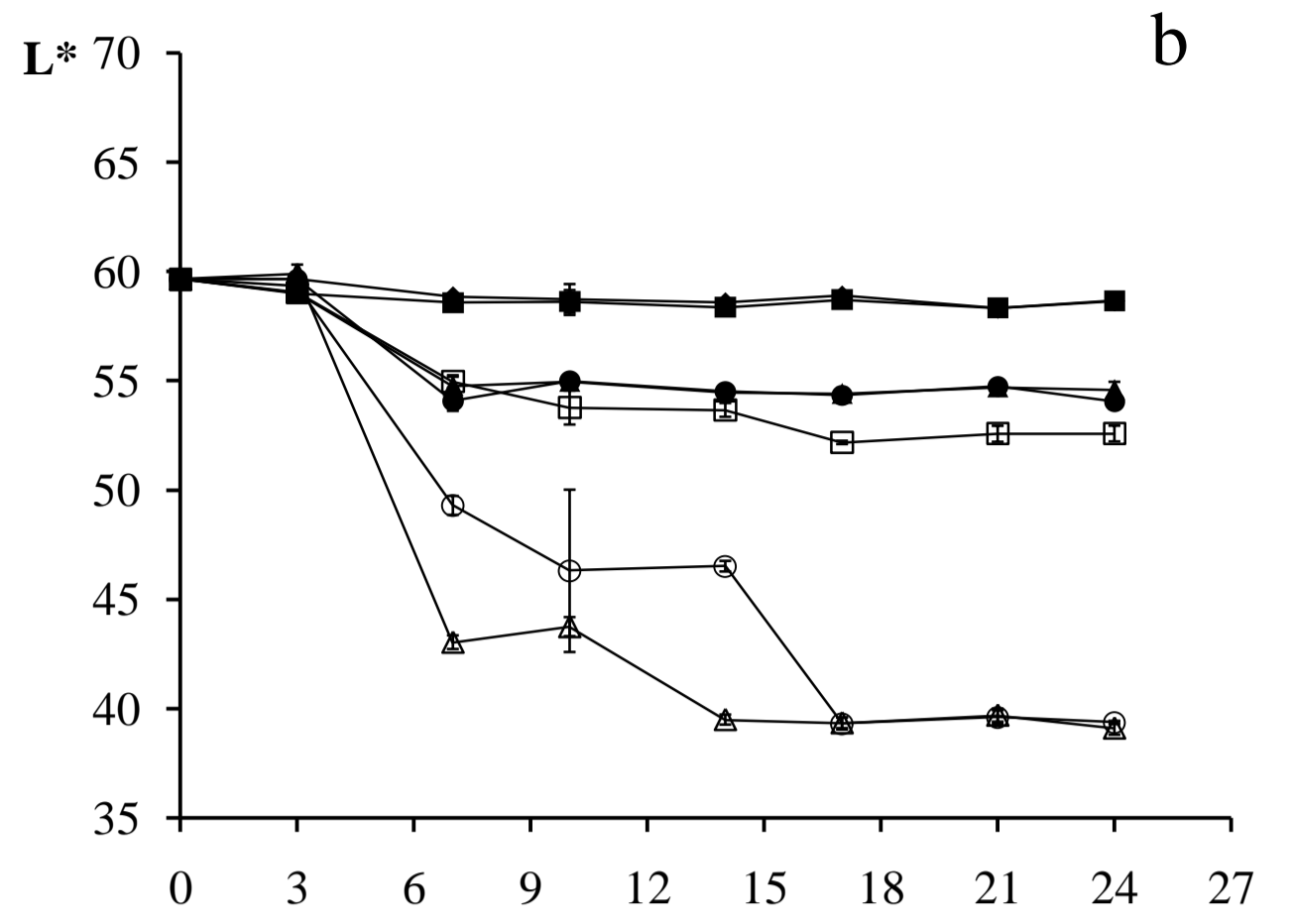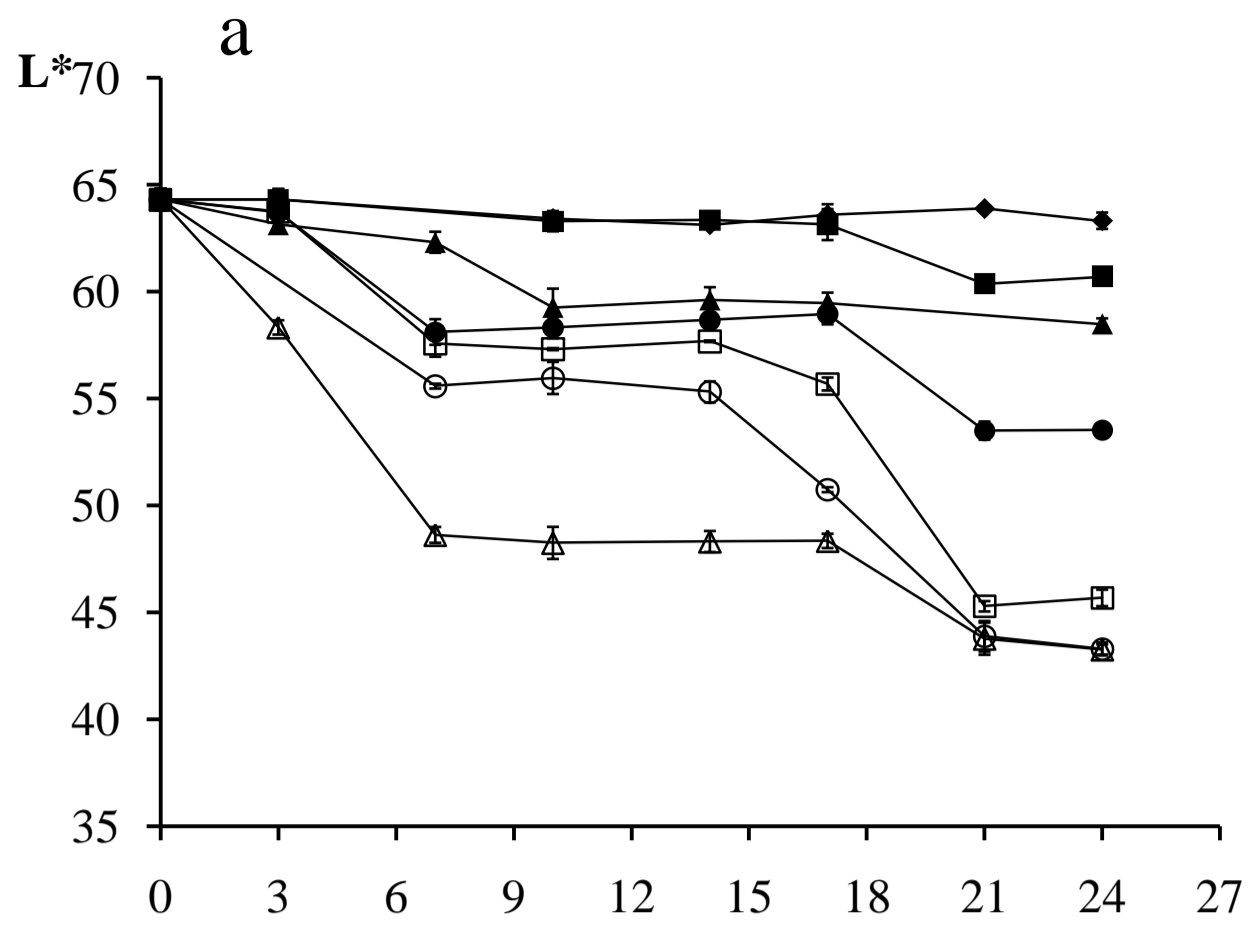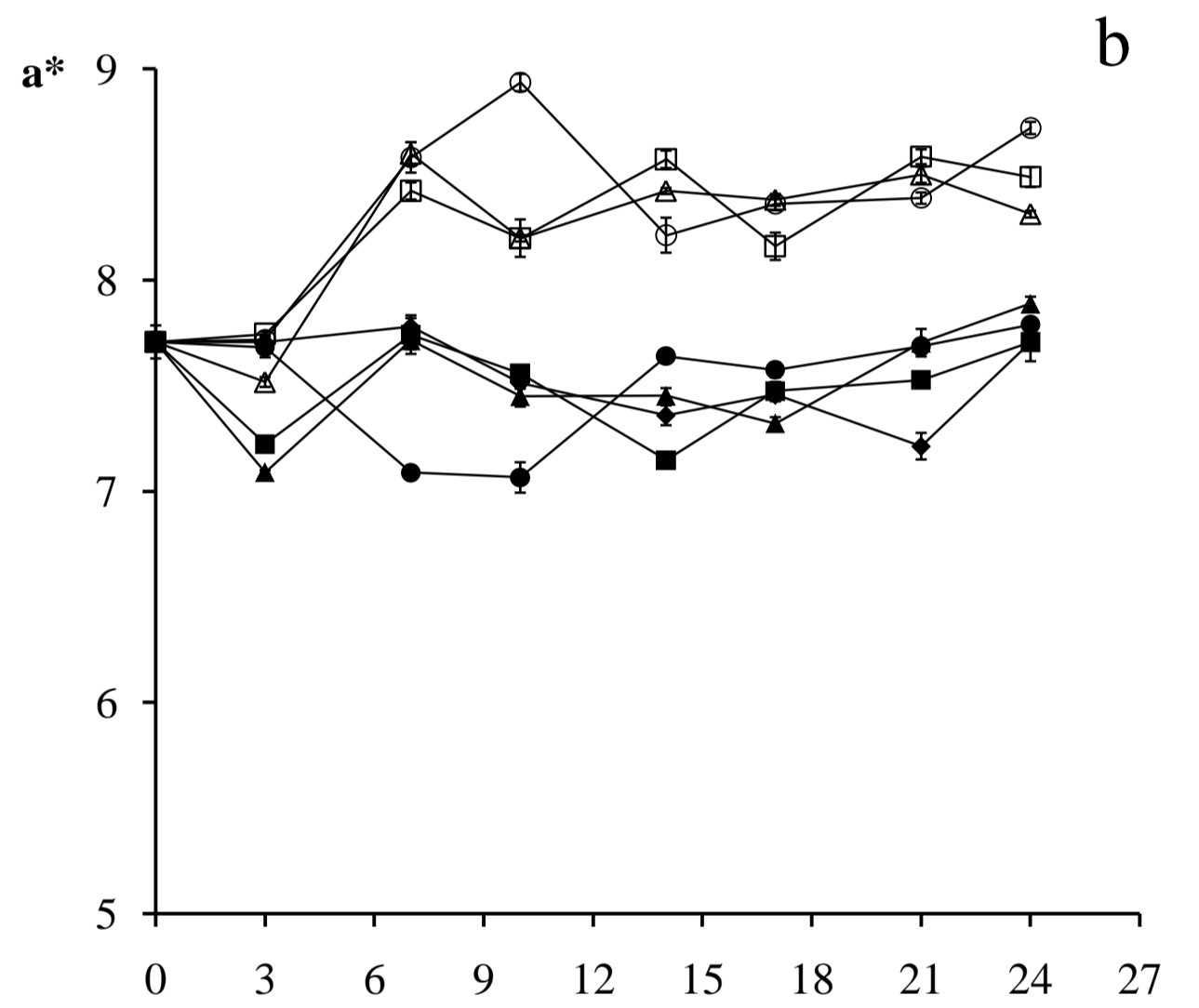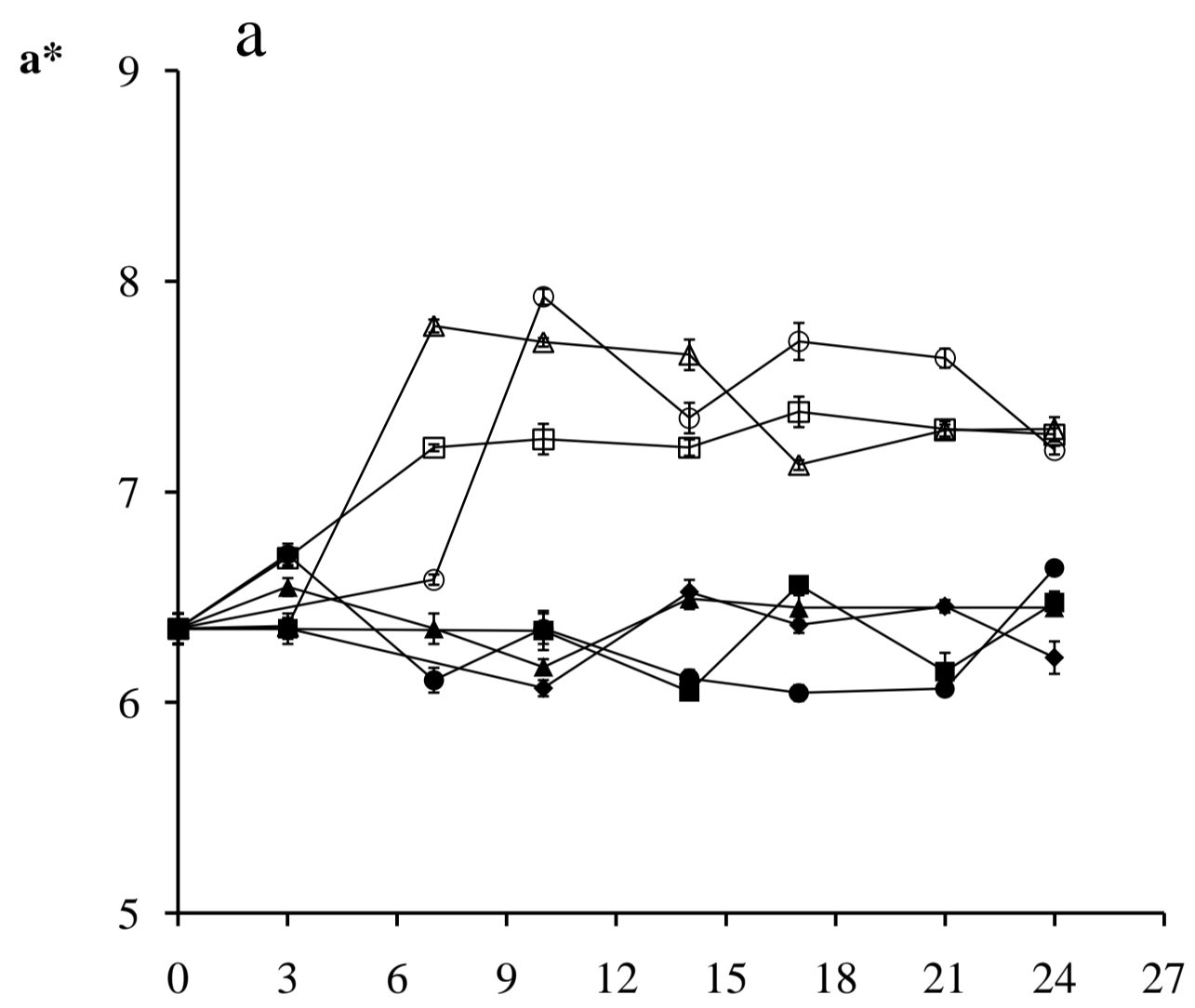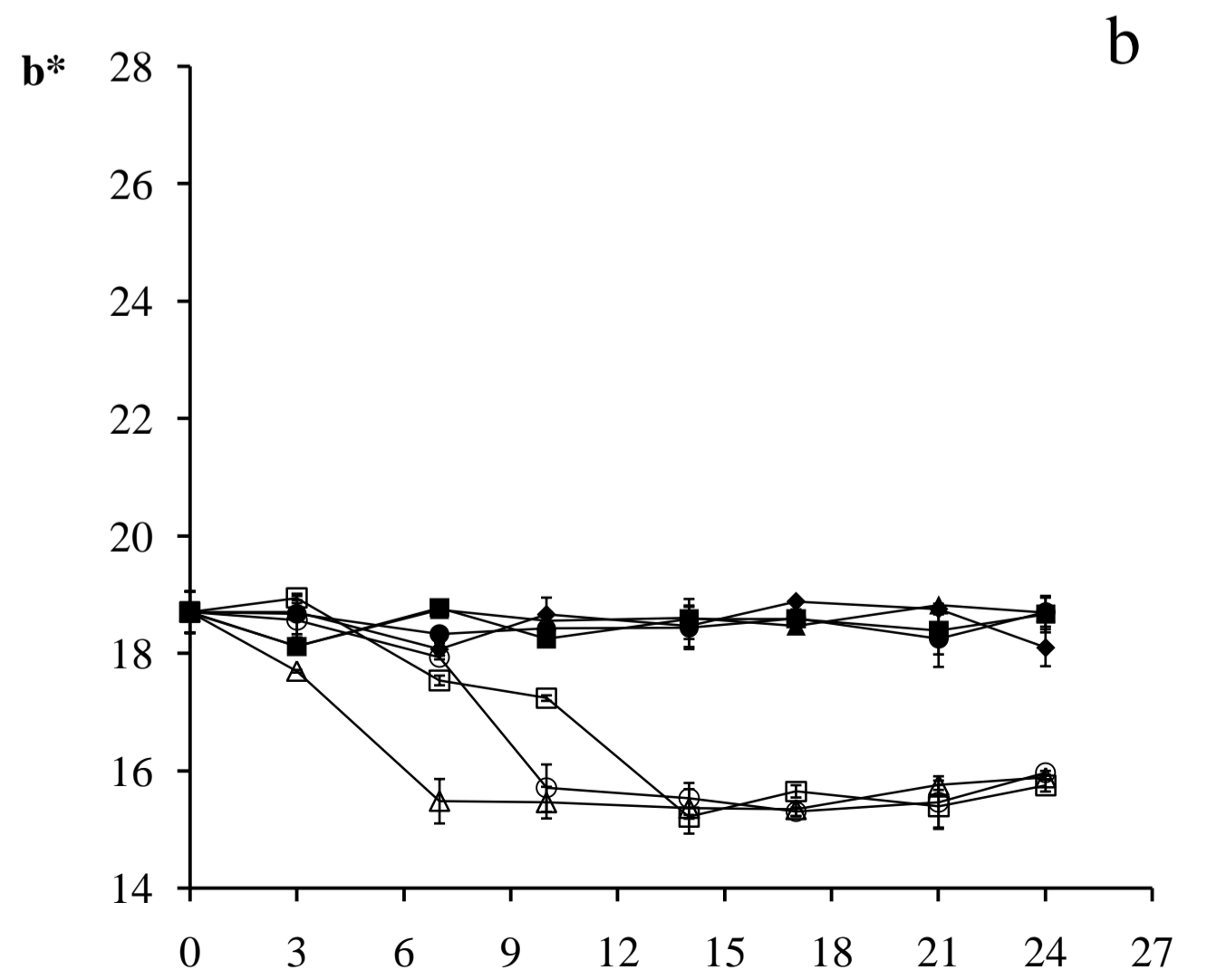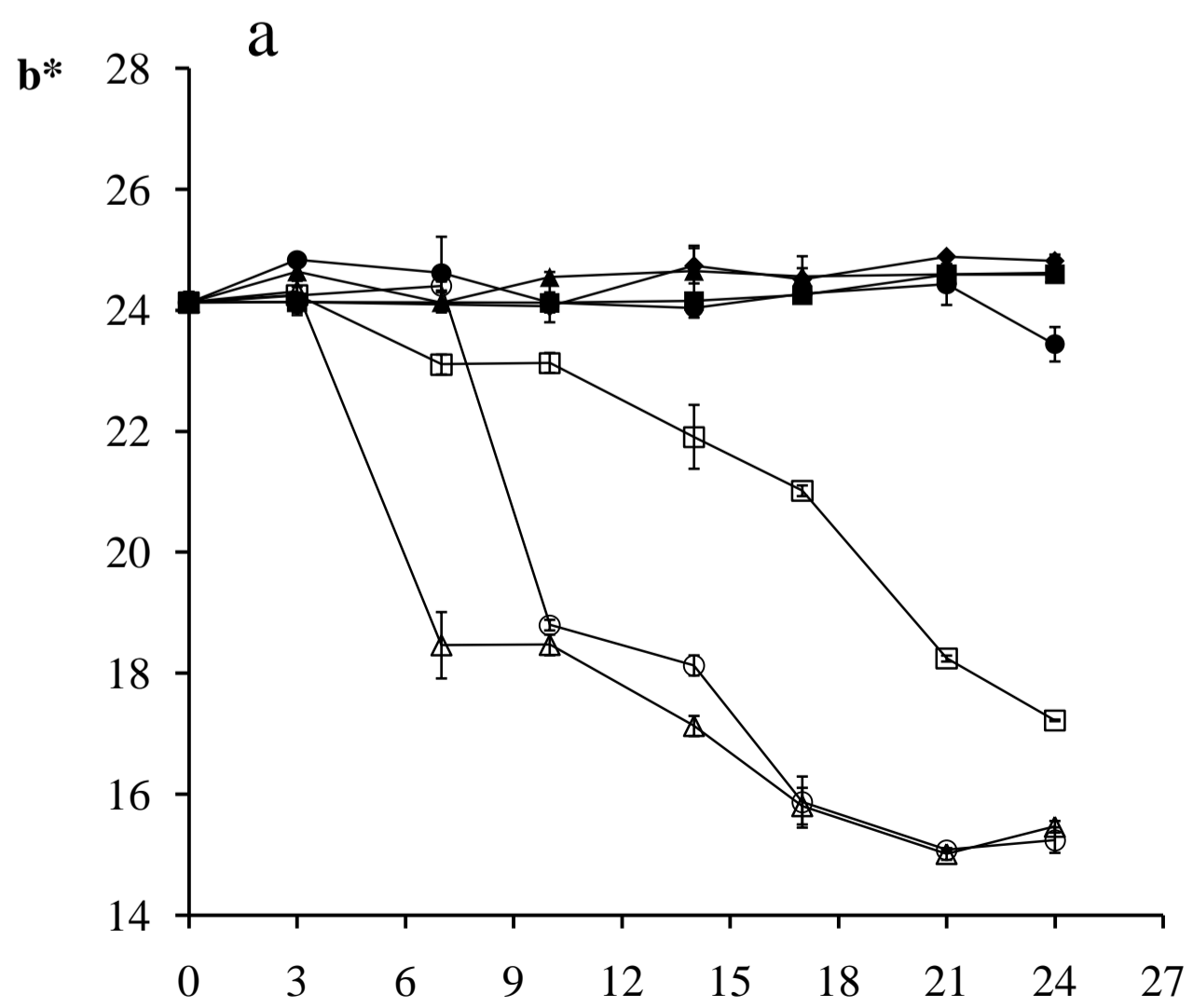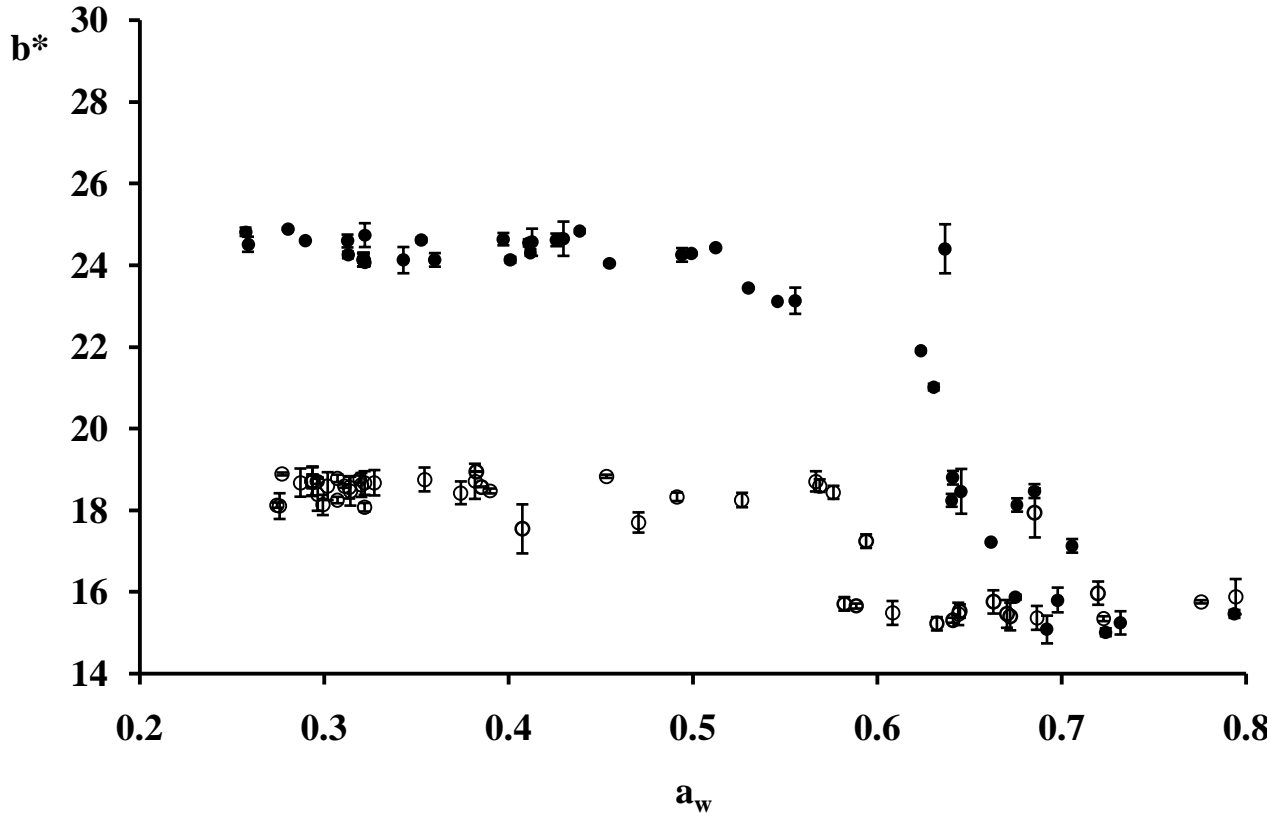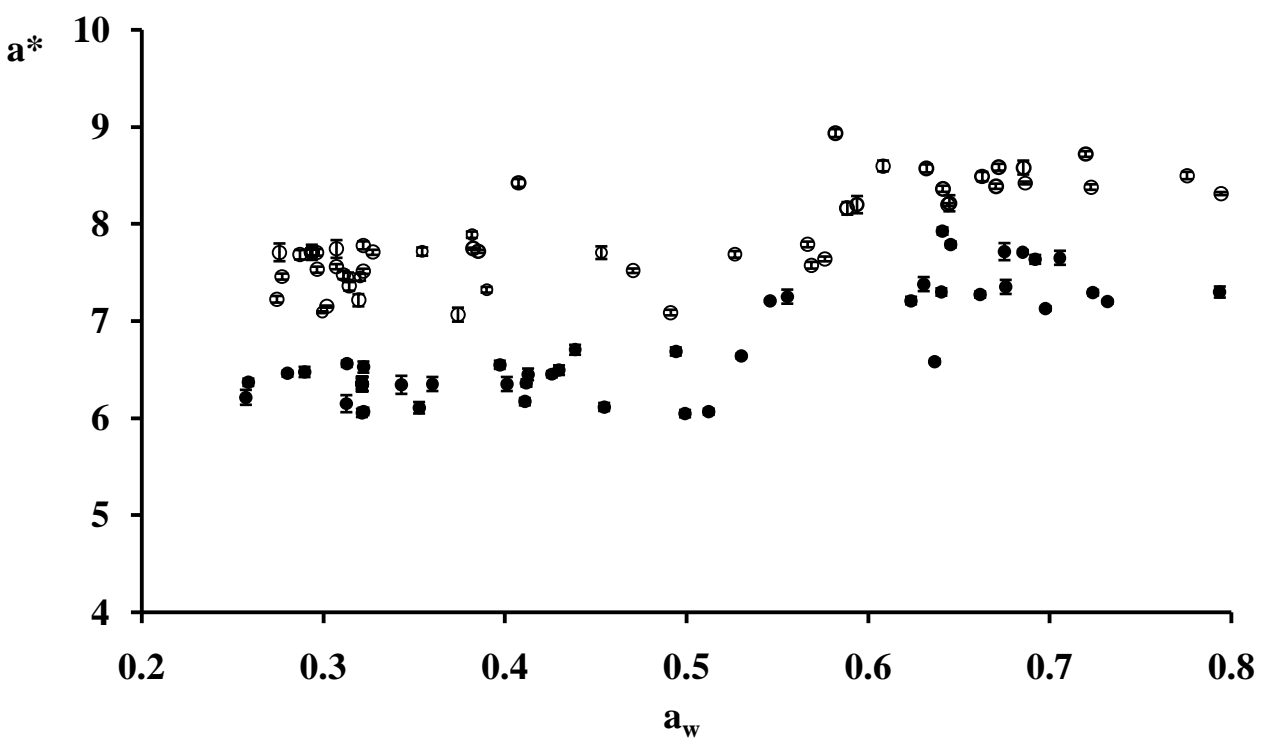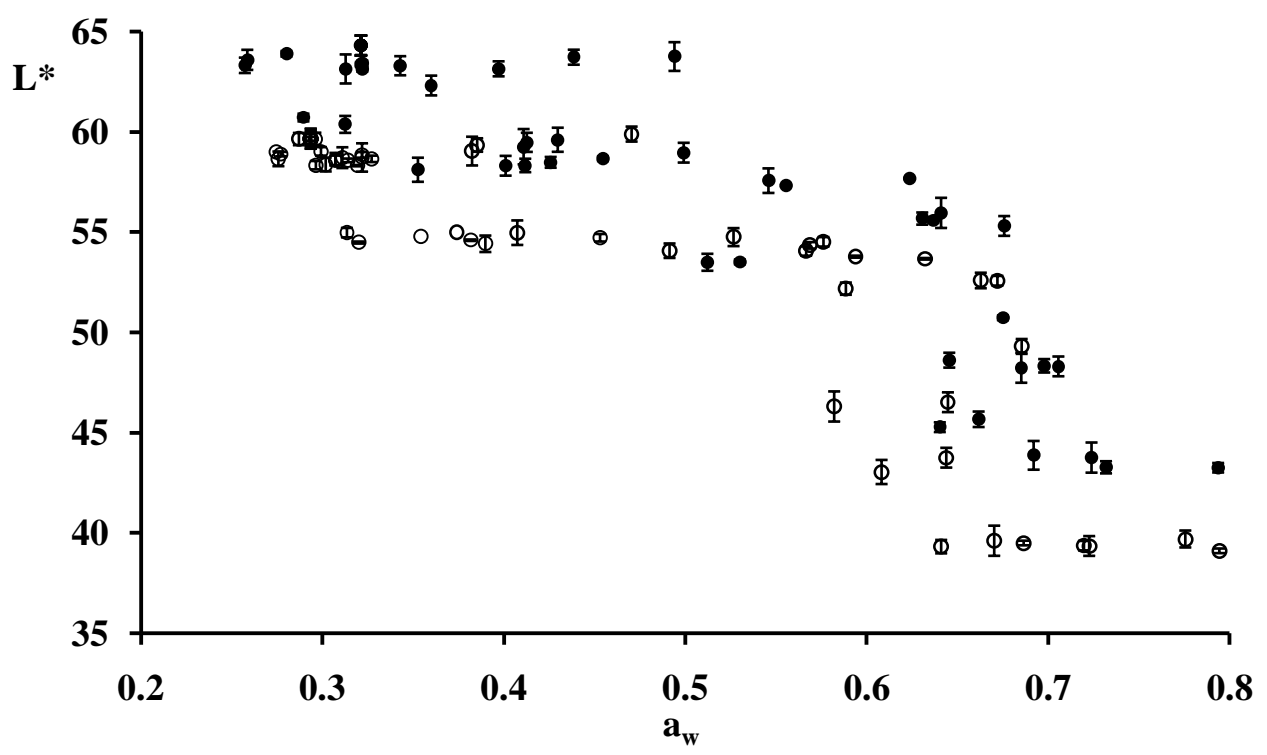
Figure 7

Figure 8

Figure 9
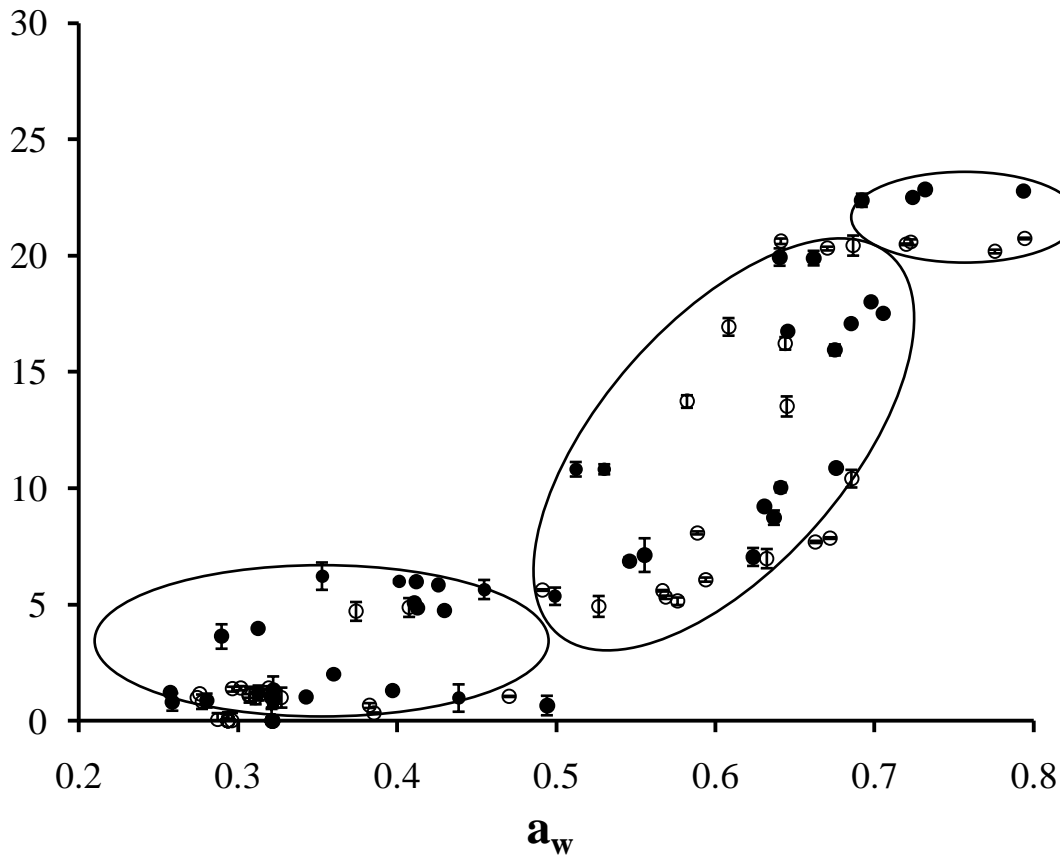
Table 1. Values of the obtained parameters when fitting experimental data to the GAB, Gordon and Taylor and Boltzman equations: of Borojó Powder, Spray Dried (B) and Borojó Powder, Spray Dried (Maltodextrin) (BM) products.

Fitting	B	BM	B + BM
GAB			
k	1.016	1.036	1.027
C	2.739	3.155	2.947
w_o	0.058	0.050	0.053
R^2	0.895	0.888	0.882
Gordon & Taylor			
T_{gs}	51.1 ±3	53.3 ±2	52.3 ±2
k	4.6 ± 0.3	4.2 ± 0.1	4.4 ± 0.2
R^2	0.987	0.995	0.986
Boltzman			
F_1	929.82	870.22	956.49
F_2	35.93	118.27	59.53
ΔT_F	23.03	17.77	19.28
λ_F	13.17	5.92	11.43
20%	28.63	9.97	12.19
80%	47.32	25.87	36.12
R^2	0.870	0.967	0.908

Table 2. Statistical comparison between Borojó Powder, Spray Dried (B) and Borojó Powder, Spray Dried (Maltodextrin) (BM) products, in terms of the fitted models.

	GAB	Gordon and Taylor	Boltzman (Fmax/m)
RSSg	12.07	420.20	901814.00
ΣRSSi	11.04	243.20	799817.00
FDRg	29	13	95
DFDR	3	2	4
ΣFDRi	26	11	91
E	0.81	4.00	2.90
F (99%)	5.53 [n.s]	7.28 [n.s]	3.95 [n.s]

[n.s] Non-significant differences ($\alpha > 0.01$)

Feature Extraction and Similarity of Movement Detection during Sleep, Based on Higher Order Spectra and Entropy of the Actigraphy Signal: Results of the Hispanic Community Health Study/Study of Latinos

Miguel Enrique Iglesias Martínez [1] , **Juan M. García-Gomez [2,*]** , **Carlos Sáez [2]** ,
Pedro Fernández de Córdoba [3] and **J. Alberto Conejero [3]**

[1]   Departamento de Telecomunicaciones, Universidad de Pinar del Río, Pinar del Río, Cuba, Martí #270,
      CP: 20100; Instituto Universitario de Matemática Pura y Aplicada, Universitat Politècnica de València (UPV),
      Camino de Vera s/n, 46022 Valencia, España; migueliglesias2010@gmail.com
[2]   Biomedical Data Science Lab (BDSLab), Instituto Universitario de Tecnologías de la Información y
      Comunicaciones (ITACA), Universitat Politècnica de València (UPV), Camino de Vera s/n,
      46022 Valencia, España; carsaesi@ibime.upv.es
[3]   Instituto Universitario de Matemática Pura y Aplicada, Universitat Politècnica de València (UPV),
      Camino de Vera s/n, 46022 Valencia, España; pfernandez@mat.upv.es (P.F.d.C.); aconejero@upv.es (J.A.C.)
*   Correspondence: juanmig@ibime.upv.es; Tel.: +34-963-877-000 (ext. 75278)

Abstract: The aim of this work was to develop a new unsupervised exploratory method of characterizing feature extraction and detecting similarity of movement during sleep through actigraphy signals. We here propose some algorithms, based on signal bispectrum and bispectral entropy, to determine the unique features of independent actigraphy signals. Experiments were carried out on 20 randomly chosen actigraphy samples of the Hispanic Community Health Study/Study of Latinos (HCHS/SOL) database, with no information other than their aperiodicity. The Pearson correlation coefficient matrix and the histogram correlation matrix were computed to study the similarity of movements during sleep. The results obtained allowed us to explore the connections between certain sleep actigraphy patterns and certain pathologies.

Keywords: actigraphy; bispectrum; entropy; feature extraction

1. Introduction

Actigraphy is now being increasingly used to explore sleep patterns in sleep laboratories. Its main advantages include its easy setup, its low cost, and the fact that prolonged records can be obtained over time, permitting patient activity in ambulatory conditions without interfering with their daily routines. It is considered to be a valuable tool for controlling and monitoring circadian alterations and insomnia, as well as avoiding false positives in the assessment of daytime sleepiness tests, such as the multiple sleep latency test, and the wakefulness maintenance test [1–5].

Many recent studies have validated the practice of actigraphy, for example, in [6] several wrist-worn sleep assessments, actigraphy devices were compared. A relationship has been found between sleep disorders and their effects on certain conditions, such as hypertension and obesity [7], and it is now even possible to analyze sleep depth by actigraphy signals [8].

A review of the current state of higher-order statistics (HOS) and their use in biosignal analysis can be found in [9]. As most of the biomedical signals are non-linear, non-stationary, and non-Gaussian

in nature, iHOS (Higher Order Statistics) analysis is preferable to second-order correlations and power spectra [9]. On this issue, several studies, such as [10] have been published on the screening of pediatric sleep apnea–hypopnea syndrome, and the automated classification of glaucoma stages in [11].

Concerning the detection of similarity of movements, in [12,13] although classification patterns were obtained from sleep/awake states according to the characteristics of the actigraphy signal, they were not based on higher order spectra. In fact, the common approach is to analyze individual actigraphy records over several days, so that the studies cited above were not focused on the analysis of the activity signal as a random process that is dependent on the movement of a certain part of the body.

The present work is based on the bispectral analysis of actigraphy signals and their relationship with bispectral entropy. The increase of movements as a form of feature extraction measurement, and the detection of similarities of movements during sleep are shown as features to be considered. The results obtained indicate the potential of this approach for the study of sleep disorders, and their connection with other conditions. The work is organized as follows: Materials and Methods are described in Section 2, the results are given in Section 3, the Discussion in Section 4, and the Conclusions and future work are outlined in Section 5.

2. Materials and Methods

2.1. Data Acquisition

The experiments were carried out on 20 samples of actigraphy signals obtained from the Hispanic Community Health Study/Study of Latinos (HCHS/SOL) Database [14–17] chosen at random, through the use of the "randi" Matlab function. The Sueño Ancillary Study recruited 2252 HCHS/SOL participants to wear wrist-worn actigraphy devices (Actiwatch Spectrum, Philips Respironics, Royal Philips, Netherlands,) between 2010 and 2013. The participants were instructed to wear the watch for a week. Records were scored by a trained technician of the Boston Sleep Reading Center [17].

2.2. Methods

Actigraphy signals have a random nature that can be visualized in terms of uniformity in the bispectrum. This uniformity depends on the non-impulsive characteristics of the signal, which are reflected in the spectrum as frequency peaks. Since the bispectrum is a function that presents unique characteristics for each signal in terms of frequency and phase it can easily be seen in a graph. This led us to explore an entire methodology based on calculating the bispectrum and the bispectral entropy, which would be able to detect similar characteristics in movement patterns during sleep. Twenty cases of actigraphy signals were analyzed to extract their characteristics, which were then used to determine similarities and differences among the signals.

The activity signals were first normalized to 1, and then segmented to determine the subjects' daily activity record. The bispectrum of the total sample of the activity signal recorded was seven days. The experiments were conducted on two age groups between 18 and 44 years old, and 45 and 64 years old.

2.3. Theoretical Foundations: Bispectrum

Let $\{x(n)\}_n$, $n = 0, \pm1, \pm2, \ldots$ be a stationary random vector, and let us also suppose that we can compute its higher order moments [18,19], where:

$$m_k^x(\tau_1, \tau_2, \ldots, \tau_{k-1}) = E(x(n) \cdot x(n + \tau_1) \ldots x(n + \tau_{k-1})) \tag{1}$$

represents the moment of order k of that vector. This moment only depends on the different time slots $\tau_1, \ldots, \tau_{k-1}$ where $\tau_i = 0, \pm1, \ldots$ for all i. The cumulants are similar to the moments, but the difference is that the moments of a random process are derived from the characteristic function of the random

variable, while the cumulant generating function is defined as the logarithm of the characteristic function of that random variable. The k-th order cumulant of a stationary random process $\{x(n)\}_n$ can be written as [20]:

$$c_k^x(\tau_1, \tau_2, \ldots, \tau_{k-1}) = m_k^x(\tau_1, \tau_2, \ldots, \tau_{k-1}) - m_k^G(\tau_1, \tau_2, \ldots, \tau_{k-1}), \tag{2}$$

where $m_k^G(\tau_1, \tau_2, \ldots, \tau_{k-1})$ is the k-th order moment of a process with an equivalent Gaussian distribution that presents the same mean value and autocorrelation function as the vector $\{x(n)\}_n$.

It is evident from (2) that a process following a Gaussian distribution has null cumulants for orders greater than 2, since $m_k^x(\tau_1, \tau_2, \ldots, \tau_{k-1}) = m_k^G(\tau_1, \tau_2, \ldots, \tau_{k-1})$, and so that $c_k^x(\tau_1, \tau_2, \ldots, \tau_{k-1}) = 0$ [20,21].

In practice, we estimate cumulants and polyspectra from a finite amount of data $\{x(n)\}_{n=0}^{N-1}$. These estimates are also random and are characterized by their bias and variance [22]. Let $\{x(n)\}_n$ denote a zero mean stationary process; we assume that all relevant statistics exist, and that they have finite values. The third order cumulant sample estimate is given by [21]:

$$C_3(\tau_1, \tau_2) = \frac{1}{N} \sum_{n=N_1}^{N_2} x(n) \cdot x(n + \tau_1) \cdot x(n + \tau_2) \tag{3}$$

where N_1 yand N_2 are chosen such that the sums only involve $x(n)$ for $n = 0, \ldots, N-1$, N being the number of samples in the cumulant region. Likewise, the bispectrum estimation is defined as the Fourier Transform of the third-order cumulant sequence [22]:

$$B_x^N(f_1, f_2) = \sum_{\tau_1=-N-1}^{N-1} \sum_{\tau_2=-N-1}^{N-1} C_3(\tau_1, \tau_2) \cdot e^{-2\pi f_1 \tau_1} \cdot e^{-2\pi f_2 \tau_2} = \frac{1}{N^2} X^*(f_1 + f_2) \cdot X(f_1) \cdot X(f_2) \tag{4}$$

where f_1 and f_2 are the spectral frequency vectors of the sequence $\{x(n)\}_{n=0}^{N-1}$, and $X(f_i)$, $i = 1, 2$, is its Fourier Transform.

2.4. Bispectral Entropy Analysis

Entropy provides a measure for quantifying the information content of a random variable in terms of the minimum number of bits per symbol that are required to encode the variable. It is an indicator of the amount of randomness or uncertainty of a discrete random process [23]. Consider a random variable Z with M states $z_1, z_2, \ldots z_M$, and state probabilities $p_1, p_2, \ldots p_M$, that is, $P(Z = z_i) = p_i$, the entropy of Z is defined as:

$$H(Z) = -\sum_{i=1}^{M} p_i \log_2(p_i) \tag{5}$$

The entropy of a discrete-valued random variable attains a maximum value for a uniformly distributed variable. In order to extend this notion from the spatial to the frequency domain, we introduce bispectral entropy as a way of measuring the uniformity of the spectrum [21]. The bispectral entropy is defined as:

$$E_{bx}^N(f_1, f_2) = -\sum_{\tau_1=-N-1}^{N-1} \sum_{\tau_2=-N-1}^{N-1} P_x^N(f_1, f_2) \cdot \log_2 P_x^N(f_1, f_2) \tag{6}$$

where the energy probability is computed in terms of the bispectrum estimation:

$$P_x^N(f_1, f_2) = \frac{B_x^N(f_1, f_2)}{\sum_{\tau_1=-N-1}^{N-1} \sum_{\tau_2=-N-1}^{N-1} B_x^N(f_1, f_2)} \tag{7}$$

3. Results

The actigraphy signals that measured the movements of individuals while sleeping were analyzed. These movements have an intrinsically random nature, since they can occur with non-specific probabilities and durations. This can be checked by analyzing the frequency spectrum of the activity signal and comparing it with a noise pattern. The probabilistic distribution function of the spectral pattern depends on the nature and uniformity of the movements, which may follow a normal distribution or another, such as a uniform distribution, depending on the random nature of the process.

3.1. Application of the Bispectrum to the Actigraphy Signal

A spectral analysis based on the one-dimensional Fourier transform is not recommended for the detection of traits in a random signal, such as the actigraphy signal. For these, this analysis only provides information relative to the magnitude-frequency or phase-frequency distribution. In other words, what is visualized in the spectrum is noise, which in our case, is in fact the useful information from which certain characteristics and features have to be extracted. The frequency spectrum of two actigraphy signals is shown in Figure 1, where it can be seen that the one-dimensional Fourier Transform is not able to identify the discriminant features in this type of signal.
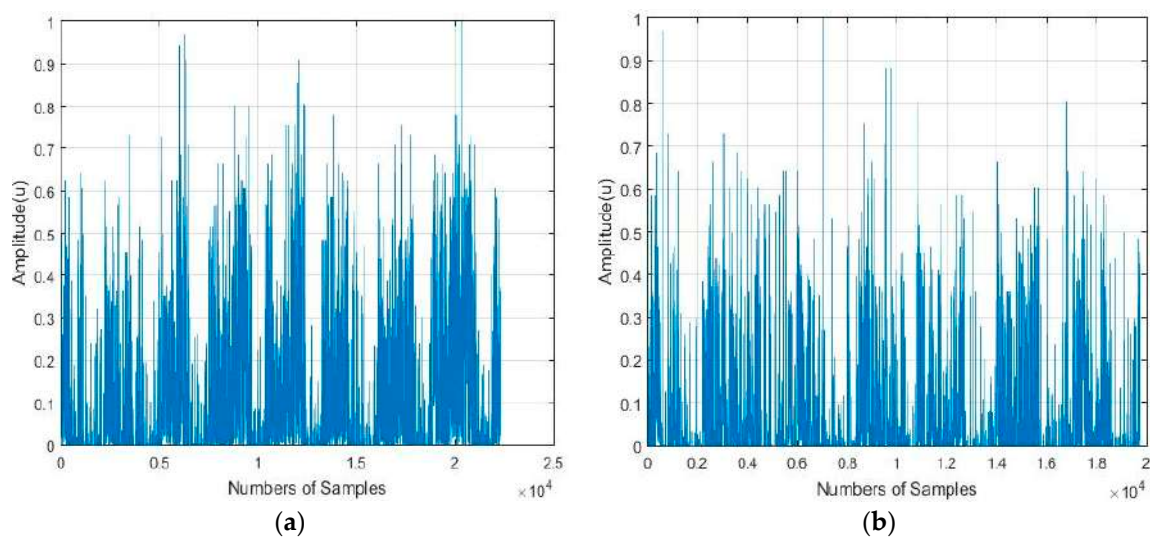
Figure 1. Ilustration of: (**a**,**b**) Examples of the frequency spectrum of two actigraphy signals obtained from their respective one-dimensional Fourier transforms.

Unlike the one-dimensional frequency spectrum, the bispectrum of an activity signal can provide information on the spatial distribution of the amplitude, and on the frequency components (see Equation (4)). This information can be represented in a matrix that can be used to obtain the particular identification features of each signal. The bispectrum of the actigraphy signal was simulated in MatLab, using the Higher Order Spectra Analysis toolbox. Figures 2 and 3 show the contours of the bispectrum surface of the actigraphy signal, where f1 and f2 are the normalized spectral frequency vectors generated from the calculation of the bidimensional Fourier Transform.

We found that the bispectrum can indicate variables that measure specific characteristics of the movement during sleep, based on the uniformity of the activity data and the disorder of the sample. Here, a greater frequency disorder at a bispectral level may imply an excess of movement during the analyzed period, which can even be an identifying feature of sleep, and be linked to patients. For the sake of completeness, we can see in Figures 2–5 that the bispectrum is a unique variable for each actigraphy signal.
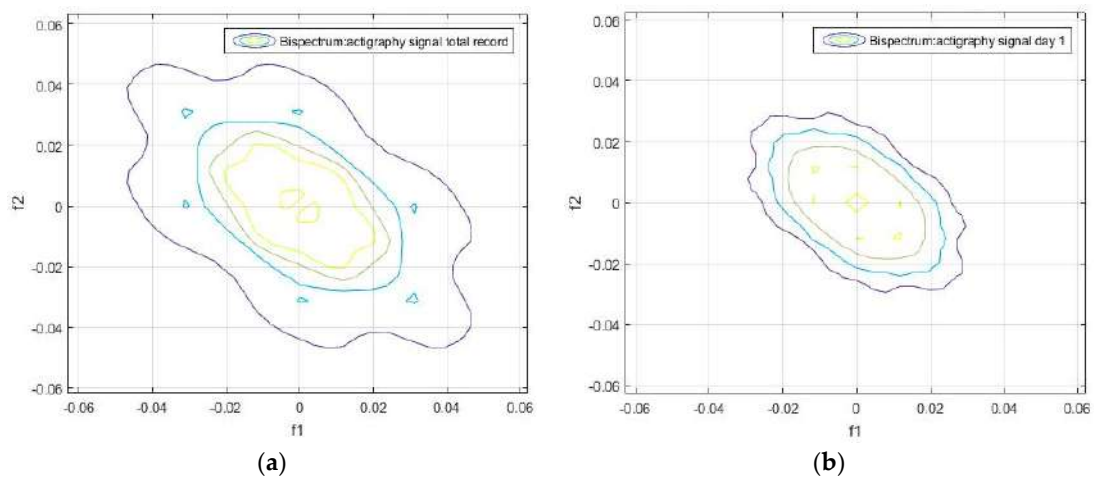
Figure 2. (**a**) Bispectrum of the activity record over seven days, and (**b**) bispectrum of the activity record on day 1 of the actigraphy data sample hchs-sol-sueno-00163225.
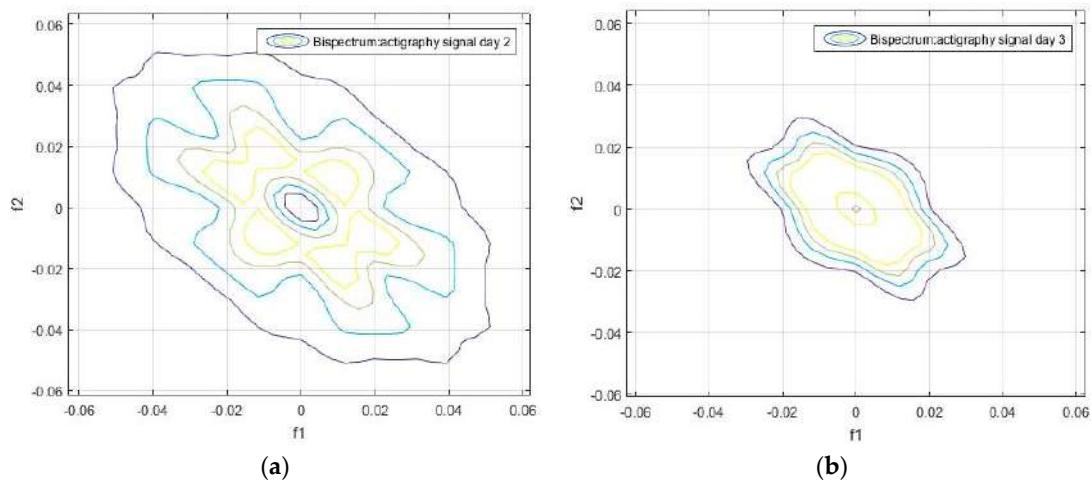
Figure 3. (**a**) Bispectrum of the activity record on day 2, and of (**b**) bispectrum of the activity record on day 3 of the actigraphy data sample hchs-sol-sueno-00163225.
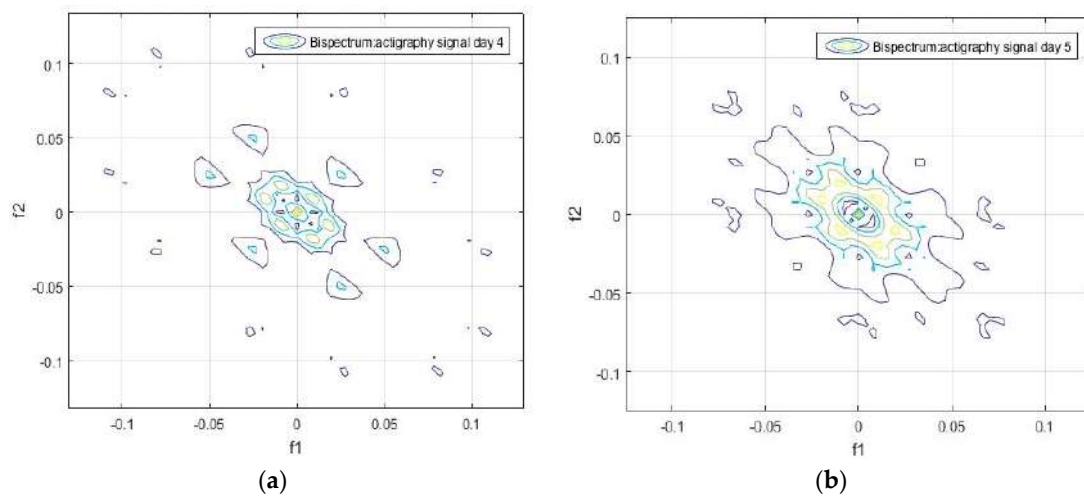
Figure 4. (**a**) Bispectrum of the activity record on day 4, and (**b**) bispectrum of the activity record on day 5 of the actigraphy data sample hchs-sol-sueno-00163225.

(**a**)　　　　　　　　　　　　　　　　　　　　　　　(**b**)
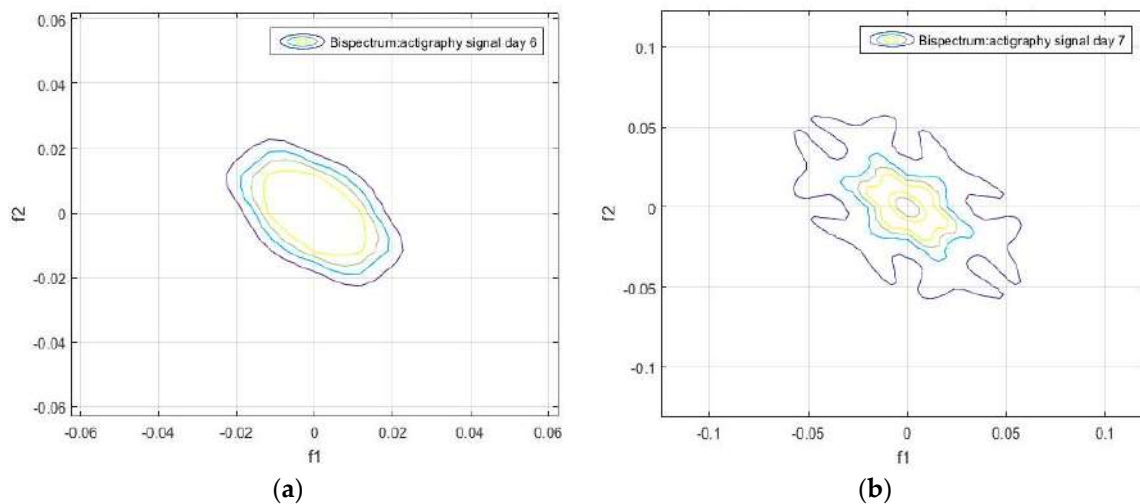
Figure 5. (**a**) Bispectrum of the activity record on day 6, and (**b**) bispectrum of the activity record on day 7 of the actigraphy data sample hchs-sol-sueno-00163225.

It can also be seen that the daily bispectrum registrations are all different from each other, showing that all these registers form an identification pattern, which we have named the bispectral pattern of the activity signal.

A bispectrum analysis was performed on 20 different activity signal records. We tried to identify each one with a specific spectral sleep pattern per day, and to find a possible relationship between an individual's movement patterns during sleep. The results obtained are shown in Figures 6–8, which give the bispectrum of the actigraphy signal for the first 10 of the 20 analyzed actigraphy signals from the HCHS/SOL database.

(**a**)　　　　　　　　　　　　　　　　　　　　　　　(**b**)
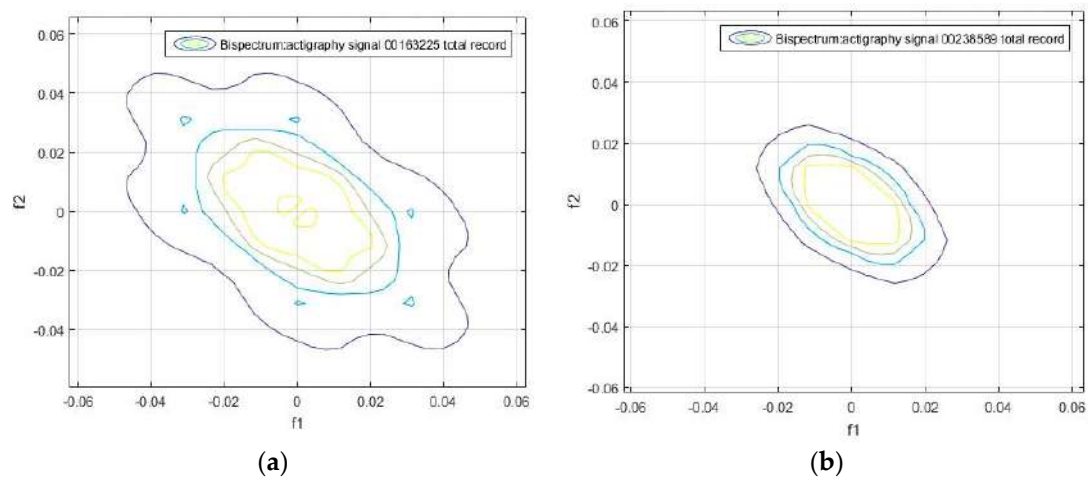
Figure 6. Bispectrum obtained from the 7-day activity record of the samples (**a**) hchs-sol-sueno-00163225and (**b**) hchs-sol-sueno-00238589.

(**a**)

(**b**)

(**c**)

(**d**)
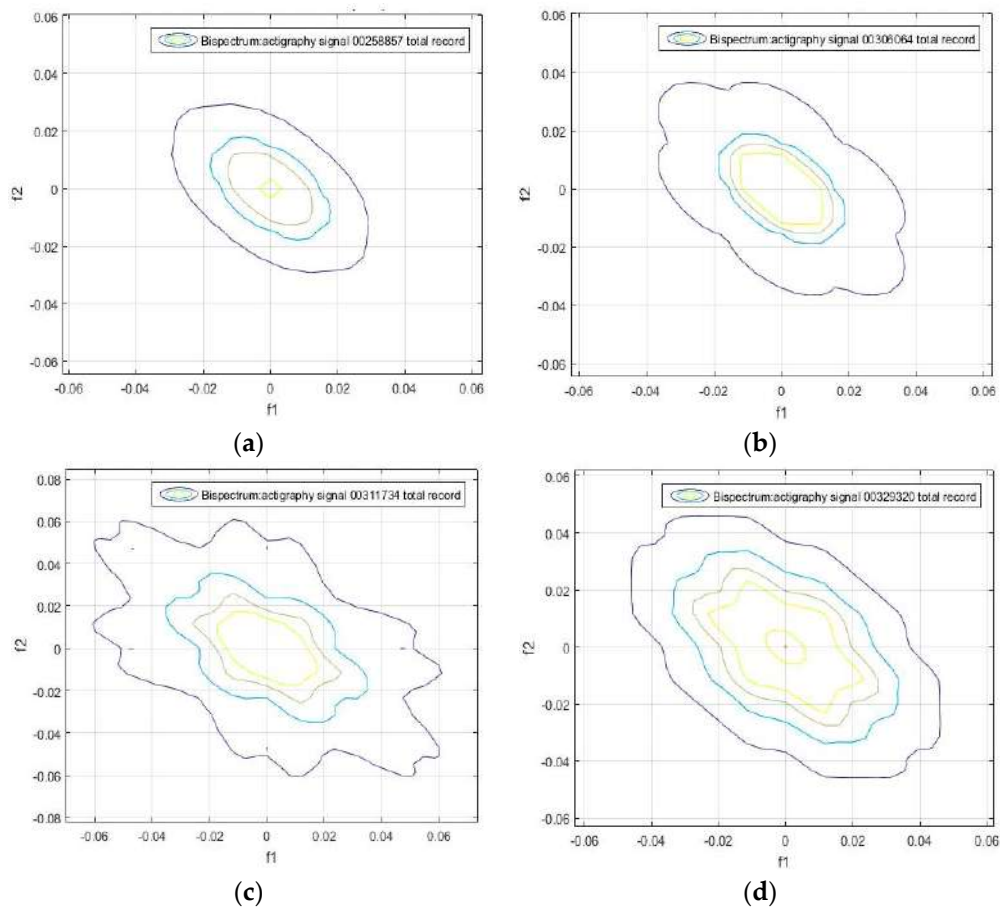
Figure 7. Bispectrum obtained from the 7-day activity record of the samples (**a**) hchs-sol-sueno-00258857, (**b**) hchs-sol-sueno-00306064, (**c**) hchs-sol-sueno-00311734, and (**d**) hchs-sol-sueno-00329320.

It can be seen that there are unique identifiable characteristic features that can be used to obtain patterns of movement during sleep. For instance, Figures 5–8 have similar contours. This means individuals can be divided into groups according to the similarity of their sleep patterns.

(**a**)

(**b**)

Figure 8. *Cont.*

(**c**) (**d**)

Figure 8. Bispectrum obtained from the 7-day activity record of the samples (**a**) hchs-sol-sueno-00349159 (**b**) hchs-sol-sueno-00358110 (**c**) hchs-sol-sueno-00496432 (**d**) hchs-sol-sueno-00504839.

To further illustrate these results, we correlated the bispectrum of the seven days of signals by computing the Pearson correlation coefficients for every pair of samples to find similarities between the two signals. The results are given in the correlation matrix R in Table 1. For example, R_{1-2} is the Pearson correlation coefficient between the bispectrum of samples 1 and 2 from hchs-sol-sueno-00163225 and hchs-sol-sueno-00238589.

In order to determine subgroups in the set of samples, and to identify the pairs of signals that give correlation values closest to 1, we selected the pairs with correlation values of greater than 0.97. This was done to satisfy the hypothesis of the similarity of the sleep movement patterns of two signals, since there must be as few differences as possible, and therefore, also minimal differences in their bispectral patterns. The results of similar pairs are shown in black in Figure 9, in which the values with the lowest correlation are indicated with red dashed lines to show different activity patterns. For this latter case, we considered values of below 0.8. Although these values are relatively high in comparison with other applications, we have considered its use for the search of dissimilar sleep patterns.

Table 1. Correlation matrix obtained from the analysis of the bispectrum comparison of the 7-day activity signal for the 20 Hispanic Community Health Study/Study of Latinos (HCHS/SOL) database samples analyzed.

0.898	0.944	0.934	0.965	0.957	0.899	0.899	0.947	0.825	0.966	0.976	0.971	0.950	0.979	0.911	0.972	0.970	0.973	0.945
0.961	0.935	0.875	0.881	0.767	0.860	0.957	0.981	0.823	0.935	0.953	0.949	0.869	0.991	0.884	0.876	0.923	0.919	-
0.965	0.944	0.914	0.837	0.911	0.961	0.909	0.892	0.970	0.976	0.970	0.917	0.970	0.937	0.925	0.959	0.933	-	-
0.931	0.886	0.860	0.899	0.949	0.887	0.886	0.949	0.954	0.950	0.895	0.945	0.920	0.916	0.936	0.885	-	-	-
0.938	0.914	0.926	0.927	0.809	0.962	0.969	0.951	0.945	0.949	0.890	0.973	0.965	0.967	0.913	-	-	-	-
0.847	0.832	0.899	0.817	0.948	0.951	0.936	0.915	0.971	0.896	0.974	0.926	0.945	0.972	-	-	-	-	-
0.849	0.844	0.688	0.889	0.892	0.854	0.864	0.870	0.773	0.889	0.888	0.863	0.799	-	-	-	-	-	-
0.908	0.799	0.887	0.929	0.911	0.904	0.862	0.867	0.881	0.921	0.920	0.849	-	-	-	-	-	-	-
0.913	0.891	0.957	0.976	0.956	0.913	0.965	0.912	0.921	0.955	0.926	-	-	-	-	-	-	-	-
0.739	0.871	0.898	0.905	0.791	0.966	0.819	0.810	0.861	0.860	-	-	-	-	-	-	-	-	-
0.946	0.924	0.892	0.964	0.841	0.960	0.960	0.941	0.922	-	-	-	-	-	-	-	-	-	-
0.977	0.964	0.958	0.942	0.964	0.963	0.976	0.953	-	-	-	-	-	-	-	-	-	-	-
0.975	0.953	0.966	0.957	0.954	0.981	0.949	-	-	-	-	-	-	-	-	-	-	-	-
0.921	0.954	0.952	0.944	0.970	0.906	-	-	-	-	-	-	-	-	-	-	-	-	-
0.888	0.970	0.961	0.960	0.957	-	-	-	-	-	-	-	-	-	-	-	-	-	-
0.899	0.886	0.937	0.931	-	-	-	-	-	-	-	-	-	-	-	-	-	-	-
0.962	0.971	0.937	-	-	-	-	-	-	-	-	-	-	-	-	-	-	-	-
0.967	0.912	-	-	-	-	-	-	-	-	-	-	-	-	-	-	-	-	-
0.938	-	-	-	-	-	-	-	-	-	-	-	-	-	-	-	-	-	-

Figure 9. Visualization of pairs with Pearson correlation coefficients greater than 0.97 (black line) and lower than 0.8 (red dashed line).

The correlation values given in Table 1 and Figure 9 show that there may be a similarity in sleep movement patterns. In Table 1, the maximum distance value is 0.3122 and the minimum is 10^{-6}, the mean is 0.0538, and the statistical mode (the most frequent value in an array) is 0.001. Figure 10 gives a comparative measurement of the values in Table 1 by rearranging the columns of the matrix into a vector, and considering it as a time series, in which the x-coordinate is the position in the vector and the y-coordinate, the corresponding value of the coefficient. In this arrangement, the groups indicate almost repetitive terms that represent signals with similar characteristics.
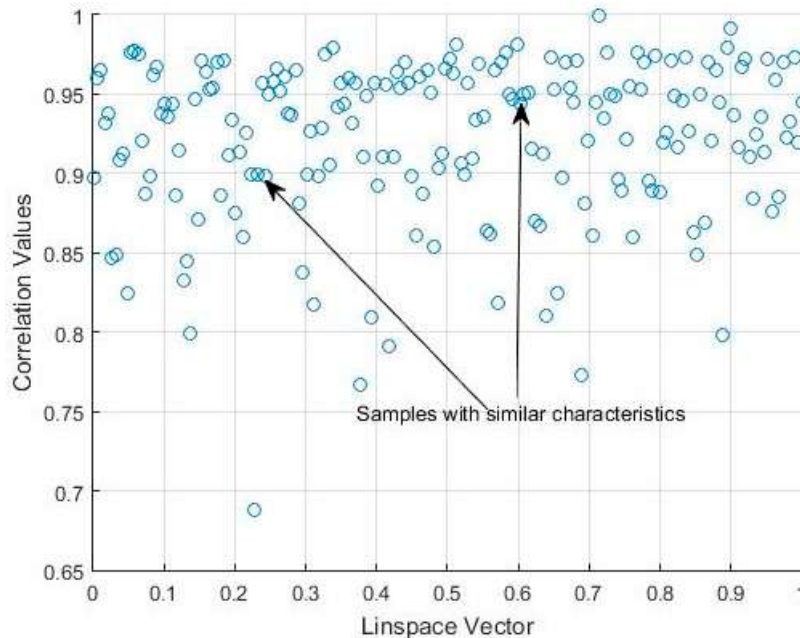
Figure 10. Scatter plot of the correlation matrix shown in Table 1.

In order to better distinguish the differences and similarities between the sleep signals, we performed another analysis using the bispectral entropy as the method of characterizing the disorder/uniformity of the processed signals.

3.2. Application of Bispectral Entropy as a Measure of Actigraphy Disorder

The experiment was based on a similarity analysis, analogous to that of the bispectrum. We calculated the bispectral entropy of each activity sample for the whole period of seven days, to obtain a measure of the degree of uniformity of the sleep movement pattern, taking the degree of randomness of the activity signal into account. We considered the maximum value of the bispectral entropy as a way of describing the degree of uniformity of a random process.

The bispectral entropy of the signals was computed in a minimum window of eight samples, to represent the temporal displacement index of the signals. The results obtained are shown in Figure 11, together with the mean value of the bispectral entropy of each actigraphy signal.
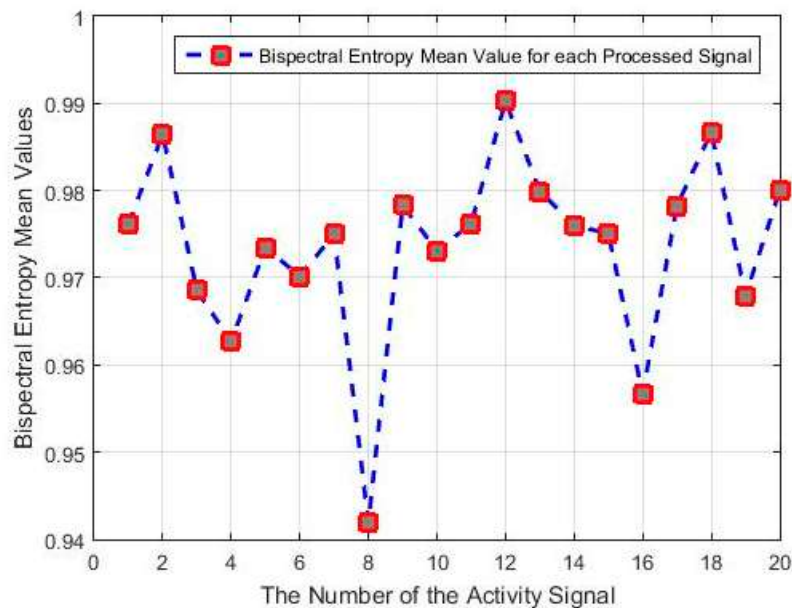
Figure 11. Mean bispectral entropy values of the 20 actigraphy signals considered.

It can be seen that signals 8 and 16 have the lowest bispectral entropy values, due to the non-uniformity of the bispectrum frequency distribution. This can also be identified in some of the previous graphs; for instance, in Figure 8b, the high-frequency components are characterized by the outer points (in blue), and the disconnected regions are the lowest frequency values.

In Figure 11 there are also samples with similar values of bispectral entropy of between 0.98 and 0.99, which indicates that they may be related to the hypothesis that activity samples with a similar correlation at the bispectral level may have the same level of uniformity of their value distributions. The opposite is also true with the minimum values of bispectral entropy, shown in Figure 11, as are those of samples 8, 10, 7, and 16, and other visible relationships, whose correlation values are under 0.8 in Table 2, and in Figure 11 are related to different uniformity patterns.

Given the analogy of the activity signal with the random process, the maximum entropy value would mean a greater uniformity of movement in the subject in the time interval studied, i.e., a high uniformity in the randomness of the movements. Conversely, occasional movements would be associated with impulsive noise, which has a non-uniform randomness, and thus, it would be associated with minimum entropy.

To also visualize the frequency of the maximum uniformity of sleep movements, histograms were made of the 7-day bispectral entropy of each activity signal. The frequencies of the entropy values for each processed sample are shown in Figures 12 and 13. These histograms provide information on the number of repetitions of the entropy values in each sample, i.e., the number of times the value in the data vector is repeated.
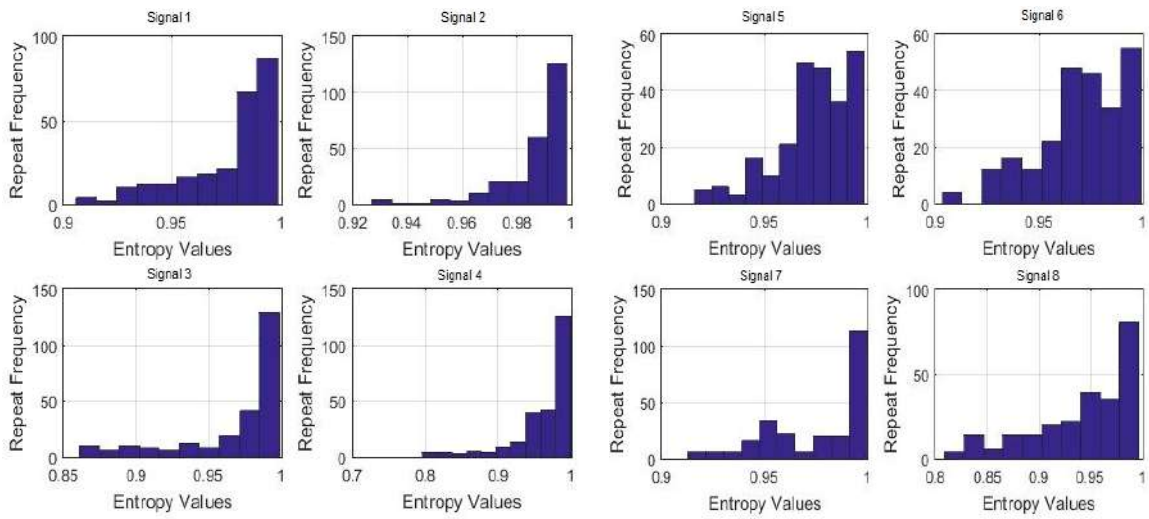
Figure 12. Histograms of the 7-day bispectral entropy of each activity signal (Signals 1 to 8, processed samples).
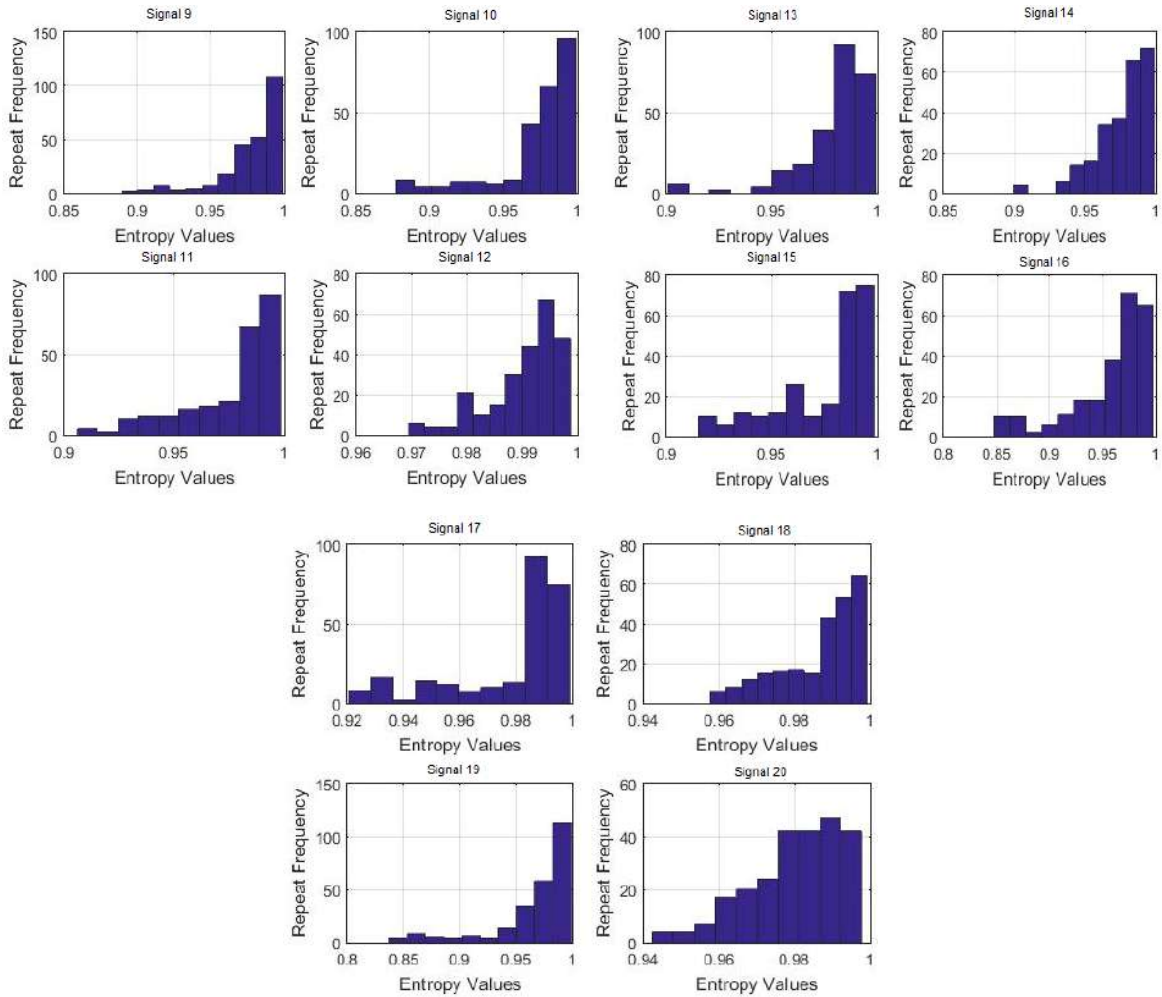
Figure 13. Histograms of the 7-day bispectral entropy of each activity signal (Signals 9 to 20, processed samples).

Although none of the histograms is repeated in Figures 12 and 13, some of them show certain similarities that could indicate similar sleep patterns. To verify this, the histograms were correlated to each other, with the criteria for the entropy values as well as for the data repetition frequency. The results are shown below in Table 2.

Table 2. Correlation matrix obtained from the analysis of the bispectral entropy histograms of the 20 analyzed samples from the HCHS/SOL database.

0.966	0.906	0.908	0.681	0.702	0.791	0.889	0.934	0.957	1.000	0.828	0.928	0.938	0.972	0.931	0.927	0.931	0.957	0.720	
0.976	0.973	0.699	0.714	0.880	0.944	0.967	0.948	0.966	0.725	0.842	0.893	0.906	0.865	0.841	0.889	0.985	0.650	-	
0.979	0.593	0.623	0.937	0.930	0.943	0.906	0.906	0.583	0.731	0.783	0.840	0.763	0.748	0.827	0.964	0.504	-	-	
0.715	0.732	0.913	0.979	0.985	0.945	0.908	0.677	0.780	0.845	0.824	0.818	0.740	0.894	0.983	0.621	-	-	-	
0.981	0.514	0.802	0.774	0.711	0.681	0.816	0.706	0.853	0.558	0.730	0.511	0.762	0.703	0.934	-	-	-	-	
0.553	0.805	0.790	0.715	0.702	0.793	0.697	0.848	0.575	0.708	0.490	0.773	0.713	0.926	-	-	-	-	-	
0.886	0.845	0.788	0.791	0.429	0.559	0.665	0.709	0.615	0.589	0.729	0.863	0.430	-	-	-	-	-	-	
0.975	0.929	0.889	0.731	0.786	0.874	0.798	0.834	0.717	0.913	0.958	0.720	-	-	-	-	-	-	-	
0.976	0.934	0.779	0.859	0.908	0.855	0.887	0.789	0.947	0.989	0.714	-	-	-	-	-	-	-	-	
0.957	0.840	0.927	0.925	0.912	0.947	0.878	0.975	0.980	0.708	-	-	-	-	-	-	-	-	-	
0.828	0.928	0.938	0.972	0.931	0.927	0.931	0.957	0.720	-	-	-	-	-	-	-	-	-	-	
0.937	0.932	0.796	0.928	0.825	0.898	0.756	0.910	-	-	-	-	-	-	-	-	-	-	-	
0.955	0.934	0.992	0.931	0.937	0.865	0.800	-	-	-	-	-	-	-	-	-	-	-	-	
0.889	0.962	0.863	0.939	0.897	0.899	-	-	-	-	-	-	-	-	-	-	-	-	-	
0.929	0.950	0.887	0.892	0.646	-	-	-	-	-	-	-	-	-	-	-	-	-	-	
0.924	0.954	0.892	0.802	-	-	-	-	-	-	-	-	-	-	-	-	-	-	-	
0.846	0.845	0.618	-	-	-	-	-	-	-	-	-	-	-	-	-	-	-	-	
0.932	0.801	-	-	-	-	-	-	-	-	-	-	-	-	-	-	-	-	-	
0.657	-	-	-	-	-	-	-	-	-	-	-	-	-	-	-	-	-	-	

Table 2 contains the results based on the histogram of the bispectral entropy of the activity signals to provide a criterion for the similarity of the data, based on the uniformity of the bispectrum. This table can be interpreted similarly to Table 1, which was based on the algorithm that describes the matrix correlation in Figure 9.

According to the previous analysis, the upper threshold was 0.97, and the lower threshold was a little lower than previously found. We considered 0.7 to distinguish between the similarities and clear differences among the signals (see Figure 14).
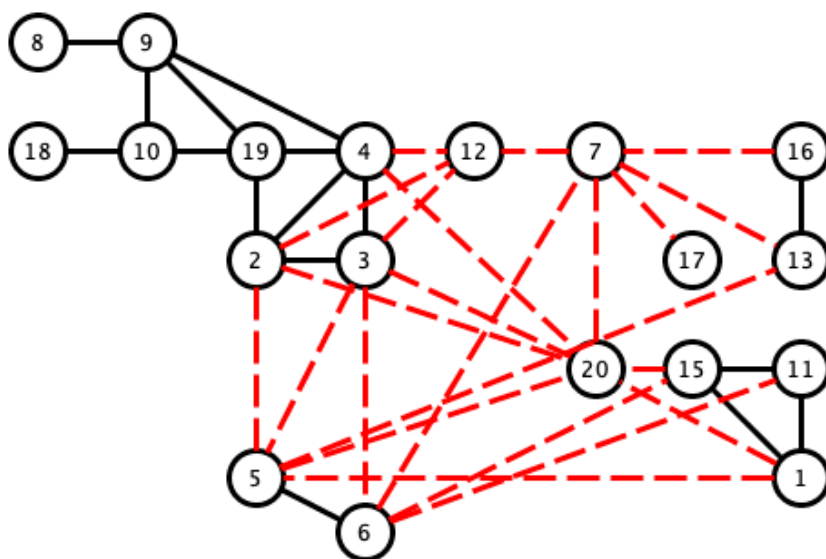
Figure 14. Visualization of pairs with Pearson correlation coefficients greater than 0.97 (black line) and lower than 0.7 (red dashed line).

It can thus be seen that several histograms are highly correlated, which indicates that this activity signal presents a high level of data uniformity, i.e., bispectral entropies with similar values, and also a high correlation value in terms of the bispectrum comparison. The dispersion graph of the correlation values obtained from Table 2 is shown in Figure 15. The data with similar values are seen to be grouped. The maximum value of the distance matrix is 0.6715, and the minimum is 10^{-5}. The mean value of the distance matrix was 0.1407, and the statistical mode was 10^{-5}, which indicates data groups with similar characteristics associated with the same type of movement, as can be seen in Figure 15.
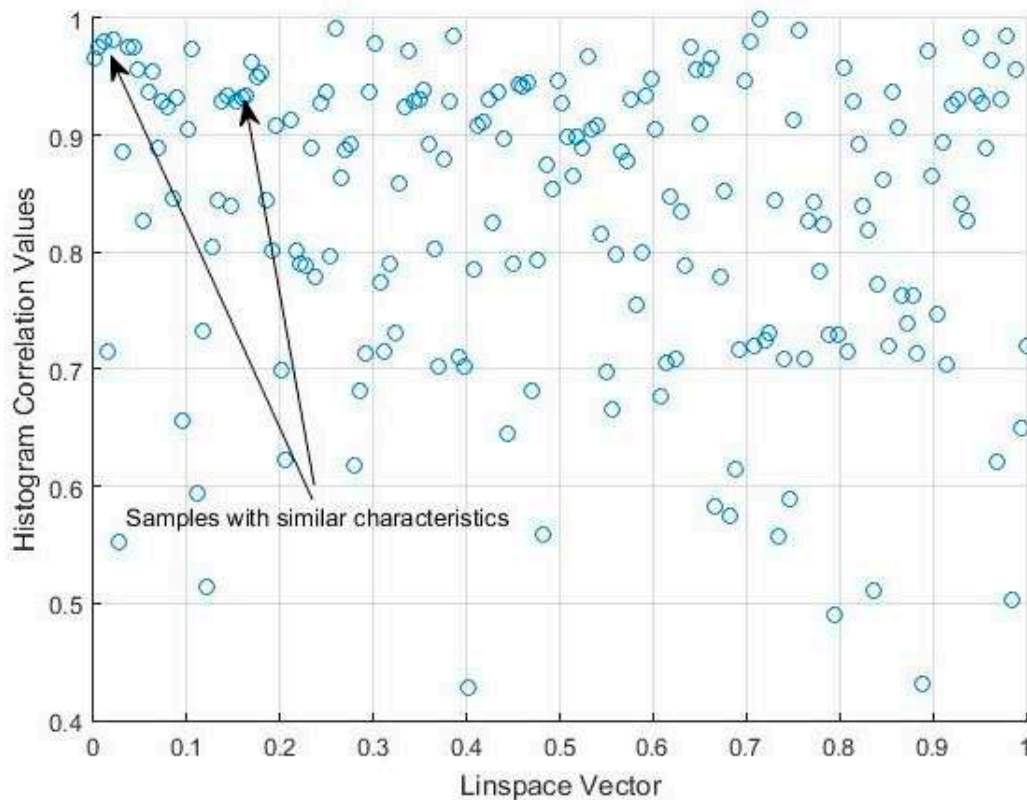
Figure 15. Scatter plot for the correlation matrix shown in Table 2.

4. Discussion

In order to associate the results with clinical diagnoses, several variables were taken from the HCHS/SOL database as the clinical characteristics of the 20 actigraphy samples. First, we considered the following variables:

CDCR_SUENO: self-report of cerebrovascular disease & carotid revascularization.
CHD_SELF_SUENO: combination of self-reports of coronary revascularization or heart attack.
DIABETES_SELF_SUENO: indicates a self-report of diabetes.
DIABETES _SUENO: indicates diabetes.
DM_AWARE_SUENO: describes the awareness of diabetes.
Hypertension_SUENO: indicates hypertension status.
STROKE_SUENO: checks for a self-report of stroke history.
 STROKE_TIA_SUENO: checks for medical history of stroke, mini-stroke or TIA (transient ischemic attack).

These variables are of the 0/1 type, i.e., '0' for a negative response and '1' for a positive. Their values for the 20 individuals whose actigraphy signals were processed can be found in Table 3.

Table 3. Clinical characteristics of each individual analyzed for each actigraphy sample.

Samples	CDCR_SUENO	CHD_SELF_SUENO	DIABETES_SELF_SUENO	DIABETES_SUENO	DM_AWARE_SUENO	HYPERTENSION_SUENO	STROKE_SUENO	STROKE_TIA_SUENO
1	0	0	0	0	0	1	0	0
2	1	1	1	1	1	1	0	0
3	0	0	0	0	0	1	0	0
4	0	0	0	0	0	0	0	0
5	0	0	0	0	0	0	0	0
6	0	0	0	0	0	0	0	0
7	0	0	0	1	0	1	0	0
8	0	0	0	0	0	1	0	0
9	0	0	0	0	0	0	0	0
10	0	0	0	0	0	1	0	0
11	0	0	0	0	0	0	0	0
12	0	0	0	0	0	0	0	0
13	0	0	0	0	0	0	0	0
14	0	0	0	0	0	0	0	0
15	0	0	0	0	0	0	0	0
16	0	0	0	0	0	1	0	0
17	0	0	0	1	0	0	0	0
18	0	1	0	0	0	1	0	0
19	0	0	1	1	1	1	0	0
20	0	0	0	0	0	1	0	0

To relate the clinical characteristics of the patients with the obtained results, the correlation was first used, which is a measure of the similarity of data. We show these results, although the obtained correlations are weak, in part, for the limited number of signals used, and for the limitations of the information content embedded in the used signals database.

We opted to consider the HYPERTENSION_SUENO variable to study relationships within the actigraphy signals, since its value varies in several samples. First, we saw that 47.62% of the pairs whose bispectrum correlates with a value greater than 0.97 share the same clinical diagnosis. However, in Figure 9, it can be seen that the pairs with the same positive or negative diagnosis tend to cluster, which indicates a stronger hidden relationship that cannot be obtained by simply correlating the bispectrum of the signals (see Figure 16).
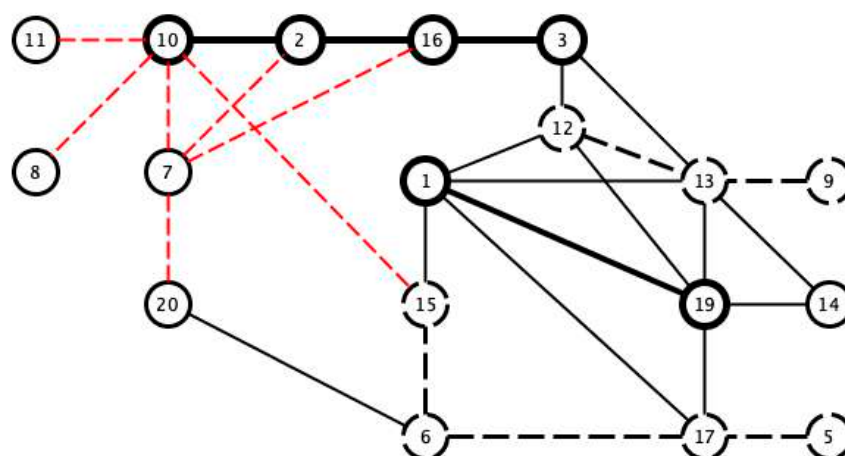
Figure 16. Pairs of bispectrum signals correlated with a coefficient that is greater than 0.97 (black lines) or lower than 0.7 (red dashed line). The thick black line indicates pairs that share a hypertension diagnosis, while the dashed black line indicates pairs in which neither has hypertension.

A similar effect was found in the comparison of the bispectral entropy histograms. Only 41.17% of the pairs correlated with a coefficient of 0.97 or higher present the same hypertension diagnoses. However, in the pairs with the same diagnosis in Figure 14 those sharing the hypertension diagnosis are seen to be connected (see Figure 17).
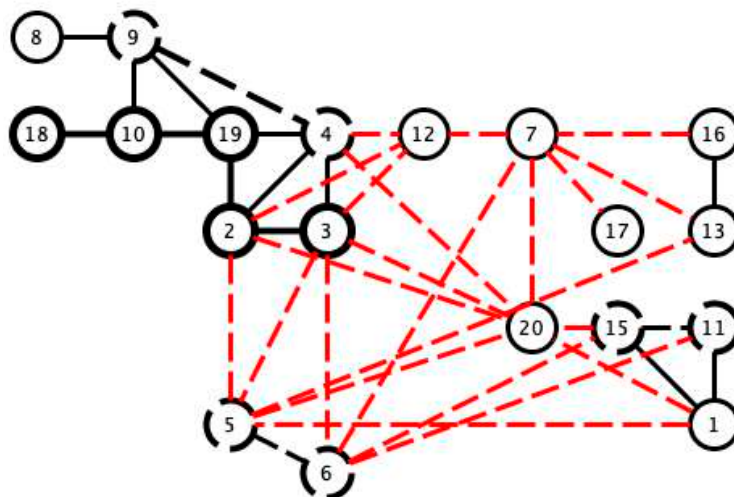
Figure 17. Pairs of bispectral entropy histograms correlated with a coefficient greater than 0.97 (black lines), and lower than 0.7 (red dashed line). The thick black line indicates pairs with a shared hypertension diagnosis, while the dashed black line indicates pairs in which neither has hypertension.

Although, the results shown in Figures 16 and 17 are not conclusive, they do suggest a further in-depth study of the characteristics of bispectrum signals that can contribute most to these similarities. It is also worth mentioning that the limited number of cases considered in this study advise a more systematic study of larger database samples.

5. Conclusions

This paper has shown that the application of higher-order statistical analysis to actigraphy signals can contribute to determining the traits and patterns of movement during sleep. These criteria can be based on part of the spatial information provided by the bispectrum and the bispectral entropy, both of which can help us to determine effective criteria for measuring the uniformity of data randomness.

The actigraphy signal experiments suggest the possible application of these criteria for the extraction and comparison of patterns of sleep movements. This would have a potential use in medicine, since similar pathologies may have similar associated movement patterns.

In future work we propose to use high-order statistical techniques, as for instance in [23]. We also want to experiment with data from chest actigraphy or other actigraphy signal measures, to corroborate the potential use of sleep actigraphy signals for purposes of diagnosis.

Our next step will be to increase the number of cases analyzed to cover the entire HCHS/SOL database, and also to experiment with other clinical characteristics in patients and pathologies associated with specific sleep disorders or brain-associated diseases.

Conflicts of Interest: The authors declare no conflict of interest. The founding sponsors had no role in the design of the study, in the collection, analyses or interpretation of data, in the writing of the manuscript, or in the decision to publish the results.

References

1. Kushida, C.A.; Chang, A.; Gadkary, C.; Guilleminault, C.; Carrillo, O.; Dement, W.C. Comparison of actigraphic, polysomnographic, and subjective assessment of sleep parameters in sleep-disordered patients. *Sleep Med.* **2001**, *2*, 389–396. [CrossRef]
2. Jean-Louis, G.; Kripke, D.F.; Mason, W.J.; Elliott, J.A.; Youngstedt, S.D. Sleep estimation from wrist movement quantified by different actigraphic modalities. *J. Neurosci. Methods* **2001**, *105*, 185–191. [CrossRef]
3. Ancoli-Israel, S.; Cole, R.; Alessi, C.; Chambers, M.; Moorcraft, W.; Pollak, C.P. The role of actigraphy in the study of sleep and circadian rhythms. *Sleep* **2003**, *26*, 342–392. [CrossRef] [PubMed]
4. de Souza, L.; Benedito, A.A.; Nogueira, M.L.; Poyares, D.; Tufik, S.; Calil, H.M. Further validation of actigraphy for sleep studies. *Sleep* **2003**, *26*, 1–5. [CrossRef]
5. Taraldsen, K.; Chastin, S.F.; Riphagen, I.I.; Vereijken, B.; Helbostad, J.L. Physical activity monitoring by use of accelerometer-based body-worn sensors in older adults: A systematic literature review of current knowledge and applications. *Maturitas* **2012**, *71*, 13–19. [CrossRef]
6. Martin, J.L.; Hakim, A.D. Wrist Actigraphy. *Chest* **2011**, *139*, 1514–1527. [CrossRef]
7. Ray, M.A.; Youngstedt, S.D.; Zhang, H.; Robb, S.W.; Harmon, B.E.; Jean Louis, G.; Bo, C.; Hurley, T.G.; Herbert, J.R.; Bogan, R.K.; et al. Examination of wrist and hip actigraphy using a novel sleep estimation procedure. *Sleep Sci.* **2014**, *7*, 74–81. [CrossRef]
8. Giménez, S.; Romero, S.; Alonso, J.F.; Mañanas, M.Á.; Pujol, A.; Baxarias, P.; Antonijoan, R.M. Monitoring sleep depth: Analysis of bispectral index (BIS) based on polysomnographic recordings and sleep deprivation. *J. Clin. Monit. Comput.* **2017**, *31*, 103–110. [CrossRef]
9. Chua, K.C.; Chandran, V.; Acharya, U.R.; Lim, C.M. Application of higher order statistics/spectra in biomedical signals: A review. *Med. Eng. Phys.* **2010**, *32*, 679–689. [CrossRef]
10. Vaquerizo-Villar, F.; Álvarez, D.; Kheirandish-Gozal, L.; Gutiérrez-Tobal, G.C.; Barroso-García, V.; Crespo, A.; Del Campo, F.; Gozal, D.; Hornero, R.G. Utility of bispectrum in the screening of pediatric sleep apnea-hypopnea syndrome using oximetry recordings. *Comput. Methods Programs Biomed.* **2018**, *156*, 141–149. [CrossRef]
11. Noronha, K.P.; Acharya, U.R.; Nayak, K.P.; Martis, R.J.; Bhandary, S.V. Automated classification of glaucoma stages using higher order cumulant features. *Biomed. Signal Process* **2014**, *10*, 174–183. [CrossRef]
12. Long, X.; Fonseca, P.; Foussier, J.; Haakma, R.; Aarts, R. Sleep and wake classification with actigraphy and respiratory effort using dynamic warping. *IEEE J. Biomed. Health* **2014**, *18*, 1272–1284. [CrossRef] [PubMed]
13. Matthews, K.A.; Patel, S.R.; Pantesco, E.J.; Buysse, D.J.; Kamarck, T.W.; Lee, L.; Hall, M.H. Similarities and differences in estimates of sleep duration by polysomnography, actigraphy, diary, and self-reported habitual sleep in a community sample. *Sleep Health* **2018**, *4*, 96–103. [CrossRef] [PubMed]
14. Dean, D.A., 2nd; Goldberger, A.L.; Mueller, R.; Kim, M.; Rueschman, M.; Mobley, D.; Sahoo, S.S.; Jayapandian, C.P.; Cui, L.; Morrical, M.G.; et al. Scaling up scientific discovery in sleep medicine: The National Sleep Research Resource. *Sleep* **2016**, *39*, 1151–1164. [CrossRef] [PubMed]
15. Zhang, G.Q.; Cui, L.; Mueller, R.; Tao, S.; Kim, M.; Rueschman, M.; Mariani, S.; Mobley, D.; Redline, S. The National Sleep Research Resource: Towards a sleep data commons. *J. Am. Med. Inform. Assoc.* **2018**, to appear. [CrossRef]

16. Redline, S.; Sotres-Alvarez, D.; Loredo, J.; Hall, M.; Patel, S.R.; Ramos, A.; Shah, N.; Ries, A.; Arens, R.; Barnhart, J.; et al. Sleep-disordered breathing in Hispanic/Latino individuals of diverse backgrounds. The Hispanic Community Health Study/Study of Latinos. *Am. J. Respir. Crit. Care Med.* **2014**, *189*, 335–344. [CrossRef]

17. Patel, S.R.; Weng, J.; Rueschman, M.; Dudley, K.A.; Loredo, J.S.; Mossavar-Rahmani, Y.; Ramirez, M.; Ramos, A.R.; Reid, K.; Seiger, A.N.; et al. Reproducibility of a standardized actigraphy scoring algorithm for sleep in a US Hispanic/Latino Population. *Sleep* **2015**, *38*, 1497–1503. [CrossRef]

18. Mendel, J.M. Tutorial on higher-order statistics (spectra) in signal processing and system theory: Theoretical results and some applications. *IEEE Proc.* **1991**, *79*, 278–305. [CrossRef]

19. Nikia, C.L.; Mendel, J.M. Signal Processsing with higher-order spectra. *IEEE Signal Process. Mag.* **1993**, *10*, 10–37. [CrossRef]

20. Swami, A.; Mendel, J.M.; Nikias, C.L. *Higher-Order Spectral Analysis Toolbox User's Guide, Version 2*; United Signals & Systems, Inc.: Ranco Palos Verde, CA, USA, 2001.

21. Vaseghi, S.V. *Advanced Digital Signal Processing and Noise Reduction*, 4th ed.; John Wiley & Sons: Hoboken, NJ, USA, 2008.

22. Bao, M.; Zheng, C.; Li, X.; Yang, J.; Tian, J. Acoustical vehicle detection based on bispectral entropy. *IEEE Signal Process. Lett.* **2009**, *16*, 378–381. [CrossRef]

23. Murua, A.; Sanz-Serna, J.M. Vibrational resonance: A study with high-order word-series averaging. *Appl. Math. Nonlinear Sci.* **2016**, *1*, 239–246. [CrossRef]

Detection of Bar Breakages in Induction Motor via Spectral Subtraction of Stray Flux Signals

Miguel E. Iglesias-Martínez, Pedro Fernández de Córdoba,
Jose A. Antonino-Daviu, and J. Alberto Conejero.

Abstract – In this paper, statistical signal processing techniques are applied to electromotive force signals captured in external coil sensors for broken bars detection in induction motors. An algorithm based spectral subtraction analysis is applied for broken bar identification, independent of the relative position of the bar breakages. Moreover, power spectrum analyses enable the discrimination between healthy and faulty conditions.

The results obtained with experimental data prove that the proposed approach provides good results for fault detectability. Moreover the identification of the faults, and the signal correlation indicator to prove the results, are also presented for different positions of the flux sensor.

Index Terms-- Fault Diagnosis, Induction Motors, Flux, Signals, Spectral Analysis.

I. INTRODUCTION

A recent trend in the electric motor condition monitoring area relies on combining the information obtained from the analyses of different machine quantities (currents, vibrations, temperatures, etc…) to reach a more reliable conclusion about its health. This is due to the fact that it has been proven that the analysis of a single quantity enables to diagnose specific faults or anomalies but it is not enough to determine the health of the whole motor. In this context, the analysis of classical quantities that are well-known in the industry, such as currents or vibrations, has shown certain problems or drawbacks for the diagnosis of certain faults [1].

With regards to the condition of the rotor, neither current nor vibration analysis have proven to be valid in all the cases that may rise in industry; it has been reported, for instance, the occasional occurrence of false indications when these techniques are used [2-5]. One of the cases where these techniques have not shown good results when detecting rotor damages is under the presence of non-adjacent bar breakages in the rotor cage. Under such situation, the effects of one bar breakage can be partially compensated by those of other

M.E. Iglesias Martínez, Universidad de Pinar del Río Hermanos Saíz Montes de Oca, Departamento de Telecomunicaciones, Martí # 270,Pinar del Río, Cuba, E-mail: migueliglesias2010@gmail.com

Pedro Fernández de Córdoba, Instituto Universitario de Matemática Pura y Aplicada, Universitat Politècnica de València, E-46022 Valencia, Spain, E-mail: pfernandez@mat.upv.es

Jose A. Antonino-Daviu, Instituto Tecnológico de la Energía, Universitat Politècnica de València, E-46022 Valencia, Spain, E-mail: joanda@die.upv.es

J. Alberto Conejero, Instituto Universitario de Matemática Pura y Aplicada, Universitat Politècnica de València, E-46022 Valencia, Spain
E-mail address: aconejero@upv.es

breakage, for certain relative positions, making difficult the identification of the fault components in the resulting spectra [6-8]. This may result in incorrect indications.

Due to these problems, other technologies are being explored by many researchers worldwide. One of these technologies relies on studying the external magnetic field in the vicinity of the motor [9-23]. Specifically in relation to rotor faults[24],eccentricity [25] and stator faults[26], It has been proven that, when certain faults are present, specific harmonics are amplified in the Fourier spectra of the electromotive force (emf) signals induced in external coil sensors installed at different positions [9,16]. More specifically, some authors have characterized the components amplified by rotor faults, eccentricities or even stator failures and have proven the potential of this technique for the detection of such faults. The simplicity, low cost and easy implementation of the technique makes it a very interesting option to complement the information obtained with other well-known technologies, especially considering the progressive reduction in price of the available flux sensors that comes together with an increase of their features [21].

Though most of the works related to flux monitoring have explored the applicability of the technique under stationary conditions [9,20], some recent works have also studied the viability of the method under transient operation, obtaining very promising results [23,27,28].

In this work, a new algorithm to detect rotor damages in induction motors based on the analysis of stray flux signals is proposed. It uses a spectral pattern recognition method based on the spectral subtraction of the power spectrum. In relation to the uses of pattern recognition [29] and spectral subtraction [30,31] techniques , some works has been made, applying different points of view, to detect de specifics fault. The proposed algorithm is applied not only to detect adjacent bar breakages, but also non-consecutive broken bars.

The results show the potential of this approach, that provides valuable information to detect rotor damages or, at least, to complement the information provided by other quantities, enhancing the performance of classical techniques.

Section II describes the considered fault as well as its related harmonics. The proposed pattern recognition method and the experimental results are shown in Section III and IV respectively. Finally, conclusions are outlined in Section V.

II. ROTOR BAR BREAKAGE DETECTION VIA ANALYSIS OF FLUX SIGNALS

Different authors have proven that the presence of certain faults in the motor amplifies some components in the stray flux spectrum [9-16]. Former works in [15-20] proposed the

use of external coil sensors for the capture of the necessary signals and the subsequent Fourier analysis of these signals to detect the components amplified by the rotor damages and other faults. With regards to the detection of bar damages, in [32] it is suggested the study of the sideband components appearing at $f \cdot (1 \pm 2 \cdot s \cdot f)$ (with s=slip and f=supply frequency) around the main frequency component in the FFT spectrum of the captured emf signals. More recent works in [33] and [9,11-12] proposed the study of other components in the low frequency region of the FFT spectrum of the emf induced in external coil sensors; according to these authors, when rotor faults are present, the components located at $s \cdot f$ and $3 \cdot s \cdot f$ are amplified in that FFT spectrum. Therefore, the study of the amplitudes of these harmonics may become a reliable indicator of the presence of the fault.

Although most of the works developed in the literature are focused on the analysis of the emf signals induced in external coil sensors at steady-state operation of the motor, some recent papers have explored the viability of the analysis of these signals under the startup, obtaining very promising results [23]. These works have proven that, during transient operation, these components follow particular trajectories that can be used as evidences of the presence of the fault.

The present work focuses on the flux-based detection of rotor faults but considering the case of non-adjacent broken bars, an issue that has been barely considered in past works.

III. THE PROPOSED ALGORITHM

To try to achieve some recognition criteria to classify the damages, a method based on spectrum descending order was applied to the signal obtained after preprocessing (output signal after noise reduction). Later, a spectral subtraction operation with respect to the signal with the healthy motor was also performed. Finally, a moving average block is used as a smoothing filter to eliminate impulsive components of the spectral subtraction. The resulting algorithm given by these processes is described in Fig. 1.

The pattern recognition algorithm is based on the use as a basic pattern of the signal of the healthy motor. This is not a serious restriction under a practical point of view, since that signal could be obtained after motor commissioning or after motor inspection, once the rotor is guaranteed to be healthy. In the method, once the actual samples have been captured, they can be compared with the healthy ones. The proposed method is based on searching for patterns, by looking at the differences in the spectrum of both signals (actual sample vs. healthy one). The use of the signal of the healthy motor as a signal reference is analogous to the schemes of adaptive systems. What is obtained at the output and in each represented pattern is a spectral pattern that identifies the number of broken bars present in the motor.
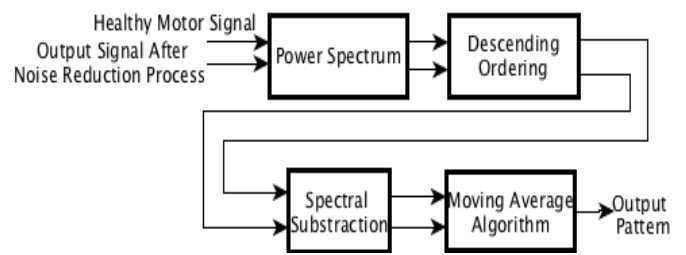
Fig. 1. The proposed algorithm for identifying broken bars.

IV. EXPERIMENTAL RESULTS

Different experiments were developed at the laboratory by using a 4-pole, 1.1 kW induction motor which was coupled to a DC machine acting as a load. Different cage rotors (28 bars in each rotor) with diverse levels of failure were available, so that each specific rotor could be assembled to test the corresponding rotor fault condition. More specifically, in this work the considered cases are: healthy rotor and rotor with two broken bars. In this latter case, different relative positions between the broken bars were tested, namely: bars 1-2 broken (adjacent broken bars), bars 1-3 broken, bars 1-4 broken, bars 1-5 broken and bars 1-6 broken.

In each test, the machine was started until it reached the steady-state regime. The emf signal induced in an external coil sensor attached to the frame of the machine was captured using a digital oscilloscope. More specifically, two different sensor locations were considered: position A (sensor attached to the lateral part of the motor frame, in the shaft side, Fig. 2 (b)) and position B (sensor attached to the center of the frame, Fig. 2(c)). Both the experimental test bench and the two considered sensor positions are shown in Fig. 2.

(a)

(b)   (c)
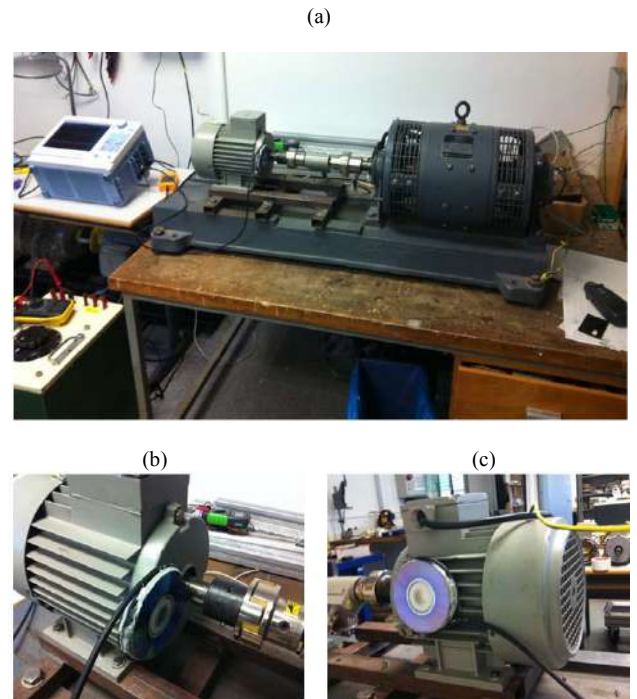
Fig. 2. a) Experimental test bench, b) Position A of the coil sensor,
c) Position B of the coil sensor.

The idea of the proposed algorithm to identify the broken bar pattern is to take as a reference the healthy state of the motor, in order to detect the corresponding faulty condition. The objective is to detect differences in the power spectrum, taking into account that a motor in a healthy state will have a certain power spectrum; if the motor is faulty, it will no longer have the same spectrum, hence the foundation based on the rearrangement of the power spectrum and spectral subtraction, to obtain an identification pattern of broken bars regardless of the relative position of the bars.

The developed algorithm was conditioned by two goals: 1) it should be able to distinguish between healthy and faulty cases based on the analyses of flux data and 2) it should be able to detect the existence of the fault regardless of the position of the bars hat break.

A. *Experimental results obtained from the measurement in position A*

Regarding the position A, the resulting pattern obtained for each sample after application of the proposed algorithm (see Fig. 1) allows us to discern when we are in the presence of a motor with two broken bars, since all the samples converge to the same line (see Fig. 3).
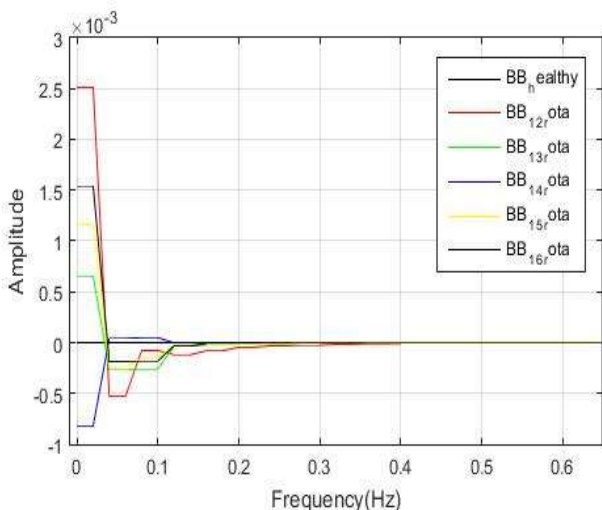
Fig. 3. Resulting spectral pattern obtained from position A.

In Fig.3 we can also see the stepped positioning of the obtained patterns from each sample according to the relative positions, whose difference lies in the amplitude, that is: first position_1_2 (red), position_1_6 (black), position_1_5 (yellow), position_1_3 (green), the above except for position_1_4 (blue) which reflects a total difference with the rest of the obtained patterns, from each sample. This result can be very useful for discrimination between the healthy and faulty cases and for the identification of the two broken bars case, regardless of the relative position of the broken bars.

To prove that we are in the presence of a motor with two broken bars, the Pearson correlation coefficient was applied between the resulting patterns obtained from the measurements carried out in position A. The correlation obtained between the resulting patterns is almost 1, except on the case of position 1_4. Table I shows the results obtained. In that table, CORRE_X_X is the correlation obtained from each pattern with respect to the resulting pattern of the bar

BB_1_2. The measurement BB_1_2 was taken as reference, but another sample could have been taken, the correlation will give similar values with the exception of position 1_4, which has a certain difference as shown in the graph of Fig.3. Now if we consider the mean value of the module of the obtained correlations, it gives as result: 0.9768

TABLE I
CORRELATION VALUES OBTAINED ACCORDING TO THE RESULTING PATTERNS.
POSITION A

CORRE_12_16 = 1.0000 0.9933 0.9933 1.0000	CORRE_12_15 = 1.0000 0.9945 0.9945 1.0000
CORRE_12_13 = 1.0000 0.9344 0.9344 1.0000	CORRE_12_14 = 1.0000 -0.9849 -0.9849 1.0000

B. *Experimental results obtained from the measurement in position B*

As for the position B, it is verified by the resulting pattern (see Fig.4) that there are two broken bars and just as in the position A, we can discern in which relative position is the position 1_4 (blue) and the position 1_6 (black) which are differentiable from the rest of the others, since their correlation value is negative as well as the results of the measurement at position A.
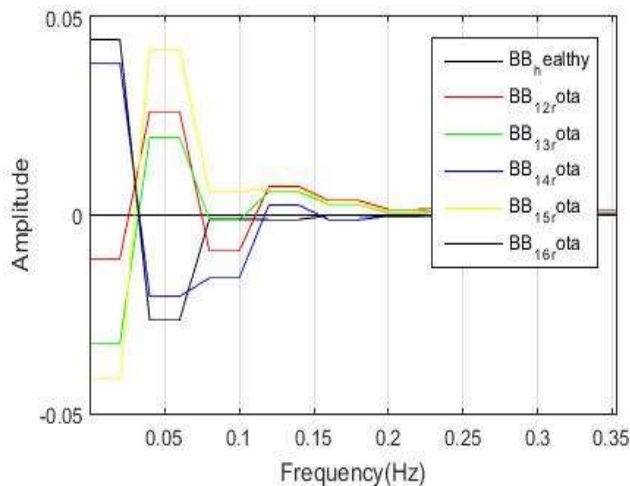
Fig. 4. Resulting spectral pattern obtained from position B.

With respect to the other positions, these follow a stepped descendently pattern as in Fig.2, although not in the same order. The correlation obtained between the resulting patterns as in position A is almost 1, except on the position 1_4 and position 1_6, whereby these two positions can be discerned. In Table 2 the results are shown. Now if we proceed in the same way as for position A, with the average value of the module of the correlations obtained, it gives as result: 0.7309. The correlation levels obtained in the measurements

made in both relative positions A and B respectively, oscillate between 0.7 and 0.98, which can be a variable indicator to identify broken bars using the flux signals.

CORRE_12_16 =	CORRE_12_15 =
1.0000 -0.7361 -0.7361 1.0000	1.0000 0.8457 0.8457 1.0000
CORRE_12_13 =	CORRE_12_14 =
1.0000 0.7875 0.7875 1.0000	1.0000 -0.5542 -0.5542 1.0000

C. Discrimination between healthy and damaged state based on the spectra.

The discrimination between healthy and faulty conditions can be carried out by simply comparing the corresponding spectra of the captured emf signals. However, this procedure may be influenced by the occurrence of non-adjacent breakages since, depending on the relative positions between the bars that break, the amplitudes of the fault harmonics may sensibly differ. However, as pointed out in previous works [8, 10, 11,26], the analyses of the FFT spectra may be helpful at least to have an evidence on if the anomaly may be present. A rough analysis of the characteristics of the FFT spectra for each one of the considered positions of the sensor is presented below.

Characteristics of the spectra for position A:

- All the analyzed signals have little external interference or noise in the spectrum; this ripple noise can come from the same data acquisition system, from the AC line or from the sensor (see Figures 5 and 6).
- The same considerations are applicable to the signals captured for the sensor at position A, although, in this case, the amplitudes of all fault harmonics are less significant. This is due to the lower portion of flux that is captured at this position (see Fig. 5).

(a)

(b)

(c)

(d)

(e)

(f)
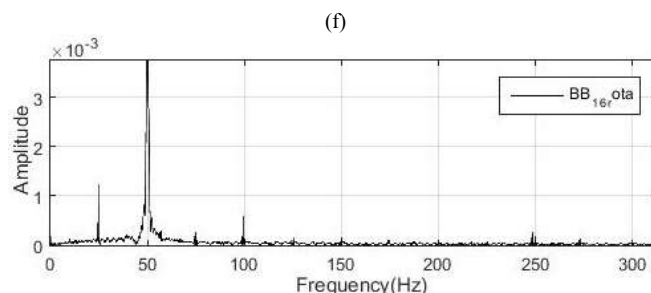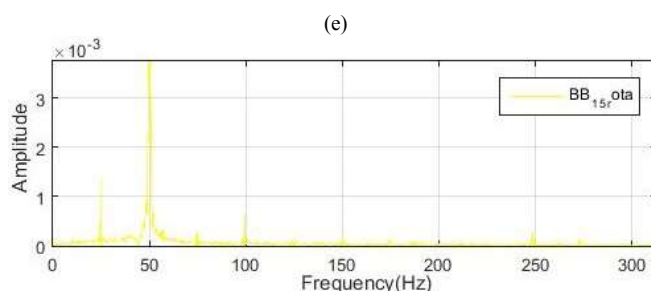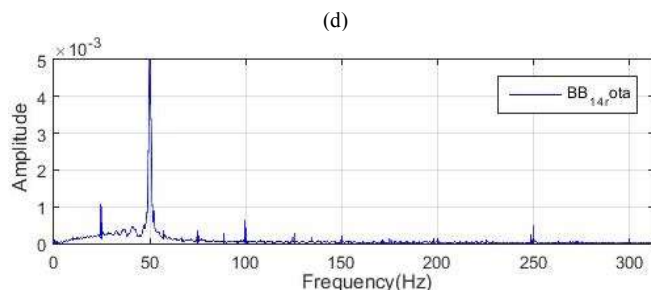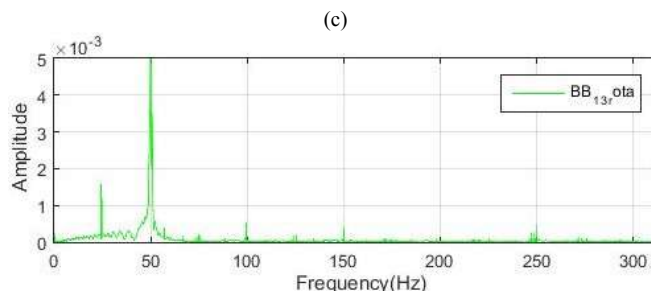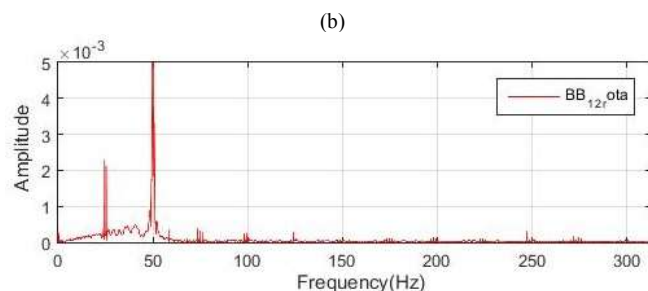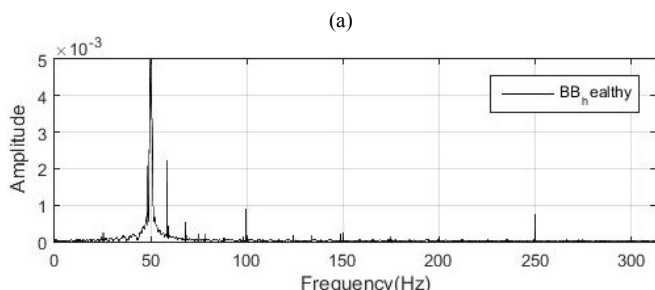
Fig. 5. Comparison of the spectrum of the healthy motor (a), with the broken bars spectrum((b) to (f)). Relative Position: A

Characteristics of the spectra for position B:

- All samples have the expected fundamental harmonic at 50Hz (see Figures 5 and 6), as well as a noticeable 150Hz component.

- Sideband components are present for all faulty cases although their amplitudes vary depending on the relative position between broken bars (maximum amplitude for adjacent bars, in agreement with previous works [8, 10, 11, 26].
- If the low frequency regions are zoomed fault harmonics are detectable at components $s \cdot f$ and $3s \cdot f$. Once again their amplitudes are influenced by the relative positions of the breakages. But their presence may be an evidence of the existence of the fault.
- The eccentricity harmonics at 25Hz and 75 Hz increase their amplitudes for all faulty cases but this is probably due to the assembly process of the rotor during the tests.
- The spectra corresponding to positions 1_6 and 1_5 are very similar. The same happens between the spectra of the position 1_3 and 1_5.

With the previously extracted characteristics, it is possible to distinguish visually between the spectrum of the healthy motor and the damaged one (see Fig.6).
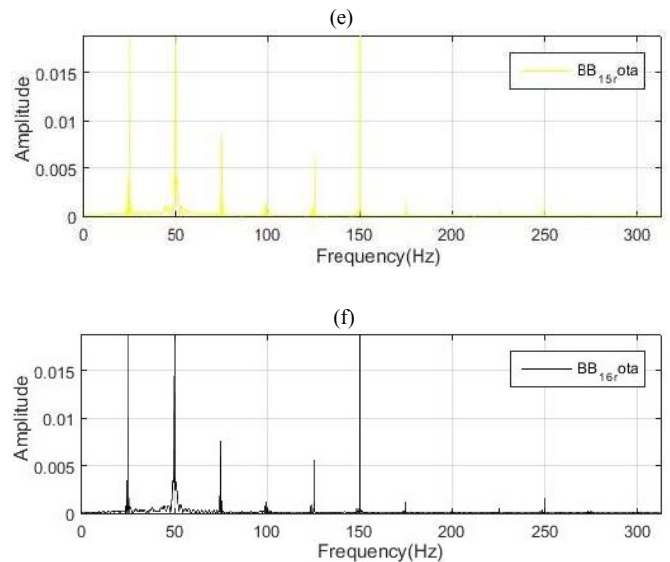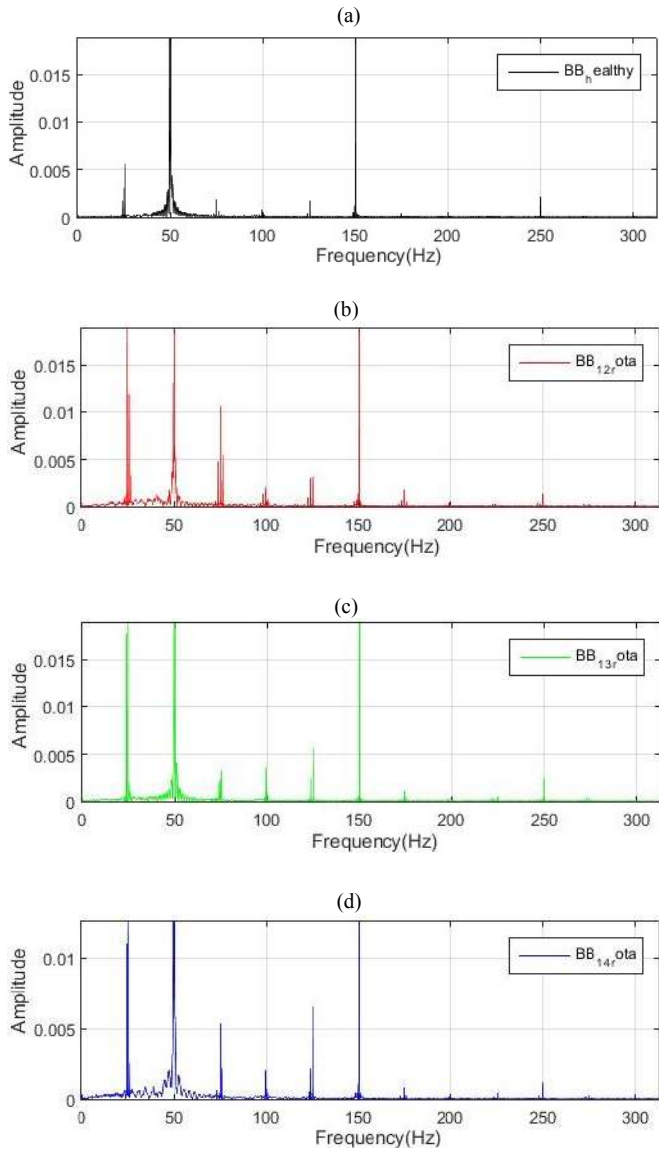
(a)

(b)

(c)

(d)

(e)

(f)

Fig. 6. Comparison of the spectrum of the healthy motor (a), with the broken bars spectrum ((b) to (f)). Relative Position: B

V. CONCLUSIONS

This work proposes the use of induction motor stray flux signals for the identification of bar breakages regardless of their relative position. During the experiments carried out, it was shown that it is possible with the proposed algorithm to detect the fault and even distinguish the relative position of the bars that break.

The proposed method is based on the frequency spectral subtraction of the power spectrum, furthermore it is use the Pearson correlation coefficient, which was applied to demonstrate the similarity of all the resulting patterns, obtained for two broken bars.

In order to identify between healthy and damaged state, the analysis of the Fourier spectrum may be sufficient; the differences between the spectrum of the healthy motor and the faulty states in both positions A and B can be noticed visually, by means of the harmonics appearing both at lower frequencies and around the main component.

VI. REFERENCES

[1] S. Nandi, H. A. Toliyat, and Xi. Li,:" Condition Monitoring and Fault Diagnosis of Electrical Motors—A Review", *IEEE Transactions on Energy Conversion*, vol. 20, no. 4, pp:719-729, December 2005.
[2] M. Riera-Guasp, J.A. Antonino-Daviu,and G.A. Capolino:"Advances in Electrical Machine, Power Electronic, and Drive Condition Monitoring and Fault Detection: State of the Art", *IEEE Transactions on Industrial Electronics*, Vol. 62, No. 3,pp:1746-1759, March 2015
[3] J. A. Antonino-Daviu, M. Riera-Guasp, J. R. Folch, and M. Pilar Molina Palomares, "Validation of a new method for the diagnosis of rotor bar failures via wavelet transform in industrial induction machines," *IEEE Trans. Ind. Appl.*, vol. 42, pp. 990-996, 2006.
[4] C. Yang, T-J. Kang, D. Hyun, S. Lee, J. Antonino-Daviu, J. Pons-Llinares, "Reliable Detection of Induction Motor Rotor Faults Under the Rotor Axial Air Duct Influence," *IEEE Trans. Ind. Appl.*, vol. 50, no. 4, pp. 2493-2502, Jul.-Aug. 2014.

[5] J. A. Antonino-Daviu, J. Pons-Llinares, Sungsik Shin, Kun Wang Lee and Sang Bin Lee, "Reliable detection of induction motor rotor faults under the influence of rotor core magnetic anisotropy," in Proc.of the 2015 IEEE 10th International Symposium on Diagnostics for Electrical Machines, Power Electronics and Drives (SDEMPED), Guarda, 2015, pp. 14-21.

[6] T. J. Sobczyk, W. Maciolek, "Does the component (1-2s)f0 in stator current is sufficient for detection of rotor cage faults?", Proc. SDEMPED 2005, Vienna, Austria, pp. 1-5, Sep. 2005.

[7] G. Y. Sizov, A. Sayed-Ahmed, C. C. Yeh and Nabeel A. O. Demerdash, "Analysis and Diagnostics of Adjacent and Nonadjacent Broken-Rotor-Bar Faults in Squirrel-Cage Induction Machines," *IEEE Trans. Ind. Elec.*, Vol. 56, No. 11, pp. 4627-4641, Nov. 2009.

[8] M. Riera-Guasp, M. F. Cabanas, J. A. Antonino-Daviu, M. Pineda-Sánchez and C. H. R. García, "Influence of Nonconsecutive Bar Breakages in Motor Current Signature Analysis for the Diagnosis of Rotor Faults in Induction Motors," in *IEEE Transactions on Energy Conversion*, vol. 25, no. 1, pp. 80-89, March 2010.

[9] R. Romary, R. Pusca, J. P. Lecointe, and J. F. Brudny, "Electrical machines fault diagnosis by stray flux analysis," in *Proc. IEEE WEMDCD*, Paris, France, Mar. 11–12, 2013, pp. 247–256.

[10] L. Frosini, A. Borin, L. Girometta, and G. Venchi, "A novel approach to detect short circuits in low voltage induction motor by stray flux measurement," in *Proc. ICEM*, Marseille, France, Sep. 2–5, 2012, pp. 1538–1544.

[11] R. Romary, R. Pusca, J. P. Lecointe, and J. F. Brudny, "Electrical machines fault diagnosis by stray flux analysis," in *Proc. IEEE WEMDCD*, Paris, France, Mar. 11–12, 2013, pp. 247–256.

[12] R. Romary, R. Pusca, J. P. Lecointe, and J. F. Brudny, "Electrical machines fault diagnosis by stray flux analysis," in *Proc. IEEE WEMDCD*, Paris, France, Mar. 11–12, 2013, pp. 247–256.

[13] L. Frosini, A. Borin, L. Girometta, and G. Venchi, "A novel approach to detect short circuits in low voltage induction motor by stray flux measurement," in *Proc. ICEM*, Marseille, France, Sep. 2–5, 2012, pp. 1538–1544.

[14] V. Kokko, "Condition monitoring of squirrel-cage motors by axial magnetic flux measurements," M.S. thesis, Dept. Elect. Eng., Optoelectron. Meas., Univ. Oulu, Oulu, Finland, 2006.

[15] H. Henao, C. Demian, and G.-A. Capolino, "A frequency-domain detection of stator winding faults in induction machines using an external flux sensor," *IEEE Trans. Ind. Appl.*, vol. 39, no. 5, pp. 1272–1279, Sep./Oct. 2003.

[16] H. Henao, G.-A. Capolino, and C. S. Mar¸ti¸s, "On the stray flux analysis for the detection of the three-phase induction machine faults," in *Conf. Rec. 38th IEEE IAS Annu. Meeting*, 2003, vol. 2, pp. 1368–1373.

[17] A. Yazidi *et al.*, "Detection of stator short-circuit in induction machines using an external leakage flux sensor," in *Proc. IEEE ICIT*, Hammamet, Tunisia, 2004, pp. 166–169.

[18] A. Yazidi, H. Henao, and G.-A. Capolino, "Broken rotor bars fault detection in squirrel cage induction machines," in *Proc. IEEE IEMDC*, San Antonio, TX, USA, 2005, pp. 741–747.

[19] S. H. Kia, H. Henao, G.-A. Capolino, and C. S. Mar¸ti¸s, "Induction machine broken bars fault detection using stray flux after supply disconnection," in *Proc. IEEE IECON*, Paris, France, 2006, pp. 1498–1503.

[20] S. M. J. Rastegar Fatemi, H. Henao, and G.-A. Capolino, "Gearbox monitoring by using the stray flux in an induction machine based electromechanical system," in *Proc. IEEE MELECON*, Ajaccio, France, 2008, pp. 484–489.

[21] Ch. Jiang, S.Li, T.G. Habetler:"A review of condition monitoring of induction motors based on stray flux", *In Energy Conversion Congress and Exposition (ECCE)*, 2017 IEEE, DOI: 10.1109/ECCE.2017.8096907

[22] S.B. Salem, M. Salah, W. Touti:"Stray Flux analysis for monitoring eccentricity faults in induction motors: Experimental study", In Control, Automation and Diagnosis (ICCAD), 2017 International Conference on, DOI:10.1109/CADIAG.2017.8075673

[23] J. A. Antonino-Daviu, Alfredo Quijano-López, Vicente Climente-Alarcon, Hubert Razik:"Evaluation of the detectability of rotor faults and eccentricities in induction motors via transient analysis of the stray flux", In *Energy Conversion Congress and Exposition (ECCE)*, 2017 IEEE, DOI: 10.1109/ECCE.2017.8096633

[24] G. Mirzaeva , K. I. Saad,:"Advanced Diagnosis of Rotor Faults and Eccentricity in Induction Motors Based on Internal Flux Measurement", *IEEE Transactions on Industry Applications*, Vol: 54, Issue: 3, pp: 2981 – 2991, May-June 2018.

[25] J. Faiz S.M.M.Moosavi,:"Eccentricity fault detection – From induction machines to DFIG—A review", *Renewable and Sustainable Energy Reviews,* Vol.55, pp: 169-179, March 2016.

[26] A. Siddique ; G.S. Yadava ; B. Singh,:"A review of stator fault monitoring techniques of induction motors", *IEEE Transactions on Energy Conversion* , Vol.: 20, Issue: 1,pp: 106 – 114, March 2005.

[27] J.A. Antonino-Daviu, H. Razik, A. Quijano-Lopez and V. Climente-Alarcon, "Detection of rotor faults via transient analysis of the external magnetic field," *IECON 2017 - 43rd Annual Conference of the IEEE Industrial Electronics Society*, Beijing, 2017, pp. 3815-3821.

[28] H. Cherif, A. Menacer, R. Romary and R. Pusca, "Dispersion field analysis using discrete wavelet transform for inter-turn stator fault detection in induction motors," *2017 IEEE 11th International Symposium on Diagnostics for Electrical Machines, Power Electronics and Drives (SDEMPED)*, Tinos, 2017, pp. 104-109.

[29] Ruonan Liu Boyuan Yang Enrico Zio Xuefeng Chen: "Artificial intelligence for fault diagnosis of rotating machinery: A review", *Mechanical Systems and Signal Processing,* Vol.108, pp 33-47, August 2018.

[30] K. C. Deekshit Kompella , M. Venu Gopala Rao , R. Srinivasa Rao:" SWT based bearing fault detection using frequency spectral subtraction of stator current with and without an adaptive filter", TENCON 2017 - 2017 IEEE Region 10 Conference Electronic ISSN: 2159-3450, DOI: 10.1109/TENCON.2017.8228277.

[31] El Houssin, El Bouchikhi , Vincent Choqueuse , Mohamed El Hachemi Benbouzid,:"Current Frequency Spectral Subtraction and Its Contribution to Induction Machines' Bearings Condition Monitoring" *IEEE Transactions on Energy Conversion* , Vol.: 28, Issue: 1, March 2013.

[32] A. Bellini, C. Concari, G. Franceschini, C. Tassoni and A. Toscani, "Vibrations, currents and stray flux signals to asses induction motors rotor conditions", IECON 2006 - 32nd Annual Conference on IEEE Industrial Electronics, Paris, 2006, pp. 4963-4968.

[33] A. Ceban, R. Pusca and R. Romary, "Study of Rotor Faults in Induction Motors Using External Magnetic Field Analysis", *IEEE Trans. Ind. Electronics*, vol. 59, no. 5, pp. 2082-2093, 2012.

VII. BIOGRAPHIES

Miguel Enrique Iglesias Martínez was born in Pinar del Río Cuba in 1984. He obtained a degree in Telecommunications and Electronics Engineering from the University of Pinar del Río (UPR), in 2008. He obtained a Master's Degree in Digital Systems at the Higher Polytechnic Institute (CUJAE), La Habana, Cuba, in 2011. He has obtained 4 scientific prizes from the Cuba Academy of Sciences in the years 2011, 2012, 2015 and 2017 respectively. He is currently doing his PhD in Mathematics at the Universitat Politècnica de València.. His areas of research interest are: Signal Processing, Noise Analysis and Blind Information Extraction, as well as the Design of Digital Systems.

Pedro Fernández de Córdoba was born in Valencia in October 1965. He obtained the degree, the M.Sc., and the Ph.D. in Theoretical Physics from the Universitat de València (UV), Valencia, Spain in 1988, 1990, and 1992, respectively. He also obtained the Ph.D. in Mathematics from the Universidad Politécnica de Valencia (UPV), Valencia, Spain, in 1997. His research work was performed at UV, UPV, the Joint Institute for Nuclear Research (Russia), the University of Tübingen (Germany) and the Istituto Nazionale di Fisica Nucleare (INFN) in Torino (Italy), among others. He is currently Professor in the Departament of Applied Mathematics at UPV. Nowadays, his research interests include the area of modelling and numerical simulation of physical and engineering problems, mainly focusing on the numerical treatment of heat and mass transfer problems. Pedro Fernández de Córdoba is Doctor Honoris Causa from University of Pinar del Rio (Cuba), member of the Colombian Academy of Exact, Physical and Natural Sciences, member of the Académie Nationale des Sciences, Arts et Lettres du Bénin, Profesor Invitado de the University of Pinar del Rio (Cuba) and Profesor Visitante "Ad Honorem" of the Universidad del Magdalena (Colombia). Furthermore, since its establishment on September 30, 2011, he has been member of the Board of the Spanish Mathematics-Industry network (www.math-in.net).

Jose A. Antonino-Daviu (S'04, M'08, SM'12) received his M.S. and Ph. D. degrees in Electrical Engineering, both from the Universitat Politècnica de València, in 2000 and 2006, respectively. He also received his Bs. in Business Administration from Universitat de Valencia in 2012. He was working for IBM during 2 years, being involved in several international projects. Currently, he is Associate Professor in the Department of Electrical Engineering of the mentioned University, where he develops his docent and research work. He has been invited professor in Helsinki University of Technology (Finland) in 2005 and 2007, Michigan State University (USA) in 2010, Korea University (Korea) in 2014 and Université Claude Bernard Lyon 1 (France) in 2015. He is IEEE Senior Member since 2012 and he has published over 160 contributions, including international journals, conferences and books. He is also Associate Editor of IEEE transactions on Industrial Informatics and has been Guest Editor in IEEE transactions on Industrial Electronics. He was General Co-Chair of IEEE SDEMPED 2013.

J. Alberto Conejero received the Ph.D. degree from the Universitat Politècnica de València (UPV), Spain, in 2004, and received the Outstanding Dissertation Award. He is currently the Chair of the Department of Applied Mathematics, UPV. His research interests are dynamical systems, partial differential equations, graph theory, and the multidisciplinary applications of mathematics to computer science and biotechnology.

Detection of Nonadjacent Rotor Faults in Induction Motors via Spectral Subtraction and Autocorrelation of Stray Flux Signals

Miguel Enrique Iglesias-Martínez [ID], Pedro Fernández de Córdoba [ID], Jose A. Antonino-Daviu [ID], *Senior Member, IEEE*, and J. Alberto Conejero [ID]

Abstract—In this paper, statistical signal processing techniques are applied to electromotive force signals captured in external coil sensors for adjacent and nonadjacent broken bars detection in induction motors. An algorithm based on spectral subtraction analysis is applied for broken bar identification, independent of the relative position of the bar breakages. Moreover, power spectrum analyses enable the discrimination between healthy and faulty conditions. The results obtained with experimental data prove that the proposed approach provides good results for fault detectability. Moreover, the identification of the faults, and the signal correlation indicator to prove the results are also presented for different positions of the flux sensor.

Index Terms—Fault diagnosis, flux, induction motors, signals, spectral analysis.

I. INTRODUCTION

A recent trend in the electric motor condition monitoring area relies on combining the information obtained from the analyses of different machine quantities (currents, vibrations, temperatures, etc.) to reach a more reliable conclusion about its health. This is due to the fact that it has been proven that the analysis of a single quantity enables to diagnose specific faults or anomalies but it is not enough to determine the health of the whole motor. In this context, the analysis of classical quantities that are well known in the industry, such as currents or vibrations, has shown some problems or drawbacks for the diagnosis of certain faults [1].

With regards to the condition of the rotor, neither current nor vibration analyses have proven to be valid in all the cases that may rise in industry; it has been reported, for instance, the occasional occurrence of false indications when these techniques are used [2]–[5]. One of the cases where these techniques have not shown good results when detecting rotor damages is under the presence of nonadjacent bar breakages in the rotor cage. In this regard, over recent decades, several works have reported problems of current-based techniques to detect such fault: in the early 1980s Hargis *et al.* already pointed out that when the broken bars are separated by $\pi/2$ electrical radians, current analysis may underestimate the number of broken bars and may even fail to detect the defect [6]. Years later, Benbouzid [7] ratified the previous statement, remarking that the lower sideband harmonic (LSH) may not be discernible when the breakages occur at specific relative locations. The statement of the problem led several authors to deepen in the physical study of the phenomenon by developing suitable electric motor models that were aimed to analyze the relation between the relative positions of the broken bars and the results of *motor current signature analysis* (MCSA). This is the case of [8], in which a model of a 22-bar, four-pole machine was built considering all the potential cases of double breakages; the authors concluded again that the amplitude of the LSH greatly depends on the relative position between the broken bars. Other physical analyses of the problem that reached analogous conclusions can be found in [9] and [10], while empirical analyses were performed in [11]. Finally, in [12], it is presented a physical analysis of the air gap magnetic anomaly for the case of any double bar breakage, including multiple experimental tests that confirmed the effect of the bar breakage location on the MCSA results. This work proved that when two broken bars are separated by a distance equal to half the pole pitch, the LSH amplitude can be significantly lower than that reached for the case of only one broken bar.

In spite of the number of works dealing with the nonadjacent broken bars issue, note that most of them are focused on presenting rigorous analyses of the problem which ratify the difficulties of classical diagnosis methods. However, none of the previous works has proposed reliable solutions to the problem, neither based on current analysis nor on analysis of other quantities.

More recently, several groups of authors have proposed novel strategies that were intended to solve the nonadjacent broken bars diagnosis issue. In this regard, Riera-Guasp *et al.* [13] proposed a method for detecting nonadjacent bar breakages, which relies on the study, both at steady-state and under starting, of high-order harmonics (located at $f \cdot (5 - 4 \cdot s)$ and $f \cdot (5 - 6 \cdot s)$, with f = supply frequency and s = slip) produced by the fault in the stator current. The problem of this approach is that these harmonics often have low amplitudes and are not always easily discernible neither on the Fourier spectrum of the steady-state current nor on the time-frequency analysis of the starting current. On the other hand, Antonino-Daviu *et al.* [14] compares the performance of MCSA and *zero sequence current* (ZSC) analysis to detect both adjacent and nonadjacent bars. This works concludes that the ZSC analysis may be promising to avoid potential false-negative indications of MCSA. However, this method requires the measurement of currents in all three motor phases (in delta configuration) for the later computation of the ZSC, which is not easy in many real industrial applications. In a more recent work, Gyftakis *et al.* [15] proposed a reliable indicator to detect nonadjacent broken bars based on the *filtered Park's/extended Park's vector approach*. This method relies on monitoring the higher harmonic index of the Park's vector. Their results were confirmed via multiple experimental tests. Once again, the problem is that measurement of all three currents is necessary, a requirement that may significantly complicate the industrial applicability of the approach.

Due to the important problems of the methods relying of current analysis to detect nonadjacent broken bars, other technologies based on alternative quantities are being explored. In this context, in [16], it is proposed the installation of a Hall effect sensor between two stator slots and the subsequent *fast Fourier transform* (FFT) analysis of the registered data. The disadvantage of this method, which proves to be effective under low slip operating conditions, is the unpractical nature of the approach due to the necessity of sensor installation during motor assembly. However, this work demonstrates the potential of the flux analysis for such diagnosis, even though it is focused on the analysis of the internal flux in the machine.

An alternative flux-based method that could have a more practical feasibility would rely on the analysis of the motor stray flux. In this regard, the study of the external magnetic field in the vicinity of the motor has been proposed as a very interesting alternative for the diagnosis of several motor faults, namely: adjacent rotor faults [17]–[19], eccentricities [20], [21], stator faults [22]–[24] or even gearbox problems [25]. It has been proven that when certain faults are present, specific harmonics are amplified in the Fourier spectra of the *electromotive force* (EMF) signals induced in external coil sensors installed at different positions. The simplicity, low cost, and easy implementation of the technique make it a very interesting option to complement the information obtained with other well-known technologies, especially considering the progressive reduction in price of the available flux sensors that comes together with an increase of their features [26]. Though most of the previous works related to flux monitoring have explored the applicability of the technique under stationary conditions, some recent works have also studied the viability of the method under transient operation, obtaining very promising results [27]–[29].

In spite of all these advances, very few works have deepened in the application of the stray-flux analysis technique to detect nonadjacent broken bars in induction motors. One of the few available papers in this topic is [30], which relies on the extraction of certain spectral flux component over time. Once again, the main constraint is that it focuses on the amplitudes of high-order harmonics that may not always be easily detectable.

In this work, a new algorithm to detect rotor damages, in induction motors based on the analysis of stray flux signals, is proposed. It uses a spectral pattern recognition method based on the spectral subtraction of the power spectrum of the captured flux signals. The proposed algorithm is applied not only to detect adjacent bar breakages, but also nonadjacent broken bars. In this paper, different positions of the considered sensor are assessed. The results, which are an extension of those already presented in [31], show the potential of this approach, which provides valuable information to detect nonadjacent rotor damages. One important advantage of the proposed approach, in comparison with other methods, is its simple implementation and practical feasibility, since only one sensor measurement is required. Moreover, this can be done in a non-invasive way, without perturbing the operation of the machine. This is a crucial advantage in industry, where non-invasive nature and simplicity are crucial requirements for the massive penetration of fault diagnosis techniques. Finally, the method relies on clear variations of the detected patterns which are discernible even for low fault severity levels and that are based on the overall flux spectrum rather than on particular harmonics that could be easily affected by other phenomena or which may have reduced amplitudes. The validity of the proposed approach is proven through several experimental tests that have been developed with the aid of an in-house built sensor that enables to measure the necessary quantity in a simple and fast way.

II. ROTOR BAR BREAKAGE DETECTION VIA ANALYSIS OF FLUX SIGNALS

Different authors have proven that the presence of certain faults in the motor amplifies some components in the stray flux spectrum [17]–[25], [32]. Most of these works proposed the use of external coil sensors for the capture of the necessary signals and the subsequent Fourier analysis of these signals to detect the components amplified by rotor damages and other faults. Regarding the detection of bar damages, in [32], it is suggested the study of the sideband components appearing at $f \cdot (1 \pm 2 \cdot s \cdot f)$ (with s stands for the *slip* and f for the supply frequency) around the main frequency component in the FFT spectrum of the captured EMF signals. More recent works such as [17] and [33] propose the study of other components in the low frequency region of the FFT spectrum of the EMF induced in external coil sensors; according to these authors, when rotor faults are present, the components located at $s \cdot f$ and $3 \cdot s \cdot f$ are amplified in that FFT spectrum. Therefore, the study of the amplitudes of these harmonics may become a reliable indicator of the presence of the fault.
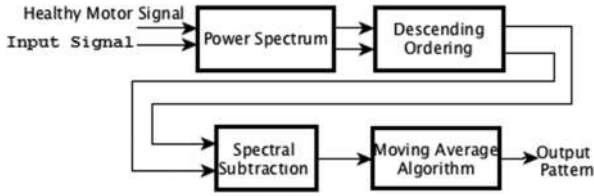
Fig. 1. Block diagram of the proposed algorithm for identifying broken bars.

Although most of the works developed in the literature are focused on the analysis of the EMF signals induced in external coil sensors at steady-state operation of the motor, some recent papers have explored the viability of the analysis of these signals under the startup, obtaining very promising results [27], [28], [34]. These works have proven that, during transient operation, the fault components follow particular trajectories that can be used as evidences of the failure.

The present work focuses on the flux-based detection of rotor faults but considering the case of nonadjacent broken bars. As commented above, despite several works have stated the difficulties that conventional methods have under this situation, very few works have tried to proposed effective solutions to the problem.

III. PROPOSED ALGORITHM

To try to achieve some recognition criteria to classify the damages, a method based on the spectrum descending order is applied to the signal obtained after preprocessing (output signal after noise reduction). Later, a spectral subtraction operation with respect to the signal of the healthy motor is also performed [35], [36]. Finally, a moving average block is used as a smoothing filter to eliminate impulsive components of the spectral subtraction. The resulting algorithm given by these processes is described in Fig. 1.

The pattern recognition algorithm is based on the use, as a basic pattern, of the signal of the healthy motor. This is not a serious restriction under a practical point of view, since that signal could be obtained after motor commissioning or after motor inspection, once the rotor is guaranteed to be healthy. In the method, once the actual samples have been captured, they can be compared with the healthy ones. The proposed method is based on searching for patterns, by looking at the differences in the spectrum of both signals (actual sample versus healthy one). The use of the signal of the healthy motor as a signal reference is analogous to the schemes of adaptive systems. What is obtained at the output, is a spectral pattern that identifies the number of broken bars present in the motor.

For finite duration discrete-time signals $\{x(n)\}_{n=0}^{N-1}$ (which represents the signal to be processed) and $\{y(n)\}_{n=0}^{N-1}$ (which represents the healthy motor signal that is taken as reference signal), both of length N samples, the classic method for estimation of the power spectrum is the periodogram. The periodogram is defined as

$$Pxx(f) = \frac{1}{N}\left|\sum_{m=0}^{N-1} x(m)e^{j2\pi fm}\right|^2 = \frac{1}{N}|X(f)|^2. \quad (1)$$
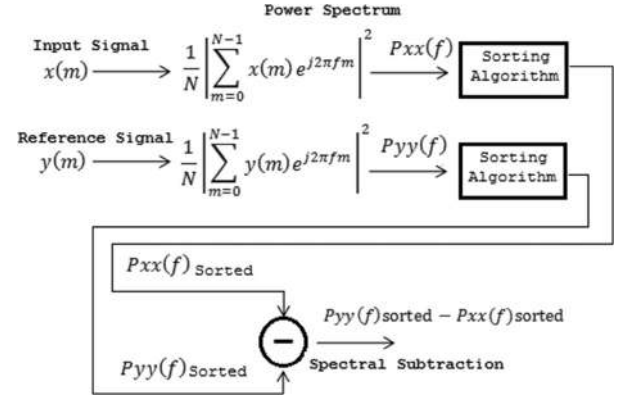
Fig. 2. Method to perform the proposed algorithm.

In our case, the algorithm is based on performing the power spectrum for both signals, namely: the input signal x and the reference signal y. Afterward, we proceed to sort the power spectrum using descend method. The obtained results for both signals after sorting the power spectrum are used for spectral subtraction. The overall process to perform the proposed algorithm is shown in Fig. 2.

As a final step, we propose the application of a moving average filter for smoothing. The novelty of this algorithm relies on the use of a reference signal which controls the entire process, in addition to the use of spectral subtraction and the ordering of the power spectrum. Computational complexity of the algorithm is low, since it is based on second-order statistics.

IV. EXPERIMENTAL RESULTS

Different experiments were developed at the laboratory by using a four-pole, 1.1-kW induction motor which was coupled to a dc machine acting as a load. The detailed characteristics of the tested motor and load can be found in the Appendix. Different cage rotors (28 bars in each rotor) with diverse levels of failure were available, so that each specific rotor could be assembled to test the corresponding rotor fault condition. More specifically, in this work, the considered cases are: healthy rotor and rotor with two broken bars. In this latter case, different relative positions between the broken bars were tested, namely: bars 1–2 broken (adjacent broken bars), bars 1–3 broken, bars 1–4 broken, bars 1–5 broken, and bars 1–6 broken.

In each test, the machine was started until it reached the steady-state regime. The EMF signal induced in an external coil sensor attached to the frame of the machine was captured using a digital YOKOGAWA DL-850 oscilloscope. The flux sensor was built in the laboratory and was based on a coil with 1000 turns with an external diameter of 80 mm and an internal diameter of 39 mm. Two different sensor locations were considered: Position A (sensor attached to the lateral part of the motor frame, in the shaft side, Fig. 3(b)) and Position B (sensor attached to the center of the frame, Fig. 3(c)). The signals were captured using a sampling rate of 5 kHz and the acquisition time for the steady-state signals was 40 s. Both the experimental test bench and the two considered sensor positions are shown in Fig. 3.

In order to detect the corresponding faulty condition, the idea of the proposed algorithm to identify the broken bar pattern
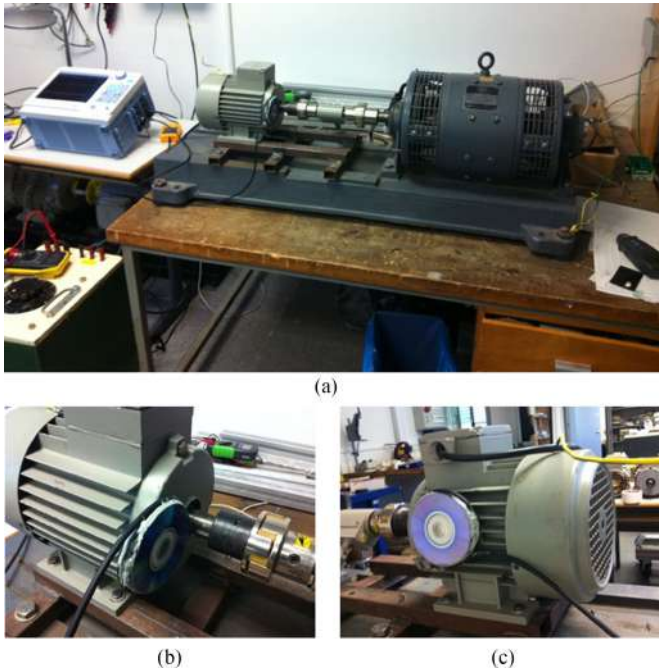
Fig. 3. (a) Experimental test bench. (b) Position A of the coil sensor. (c) Position B of the coil sensor.

Fig. 4. Resulting spectral pattern obtained from Position A.

TABLE I
CORRELATION VALUES OBTAINED ACCORDING TO THE
RESULTING PATTERNS: POSITION A

CORR_POS_1_2 & 1_6 =	CORR_POS_1_2 & 1_5 =
1.0000 0.9933 0.9933 1.0000	1.0000 0.9945 0.9945 1.0000
CORR_POS_1_2 & 1_3=	CORR_POS_1_2 & 1_4=
1.0000 0.9344 0.9344 1.0000	1.0000 -0.9849 -0.9849 1.0000

is to take, as a reference, the healthy state of the motor. The objective is to detect differences in the power spectrum, taking into account that a motor in a healthy state will have a certain power spectrum. When the motor is faulty, it will no longer have the same spectrum. Hence, our method will be based on the rearrangement of the power spectrum and spectral subtraction to obtain an identification pattern of broken bars regardless of the relative position of the bars.

The developed algorithm was conditioned by two goals: 1) it should be able to distinguish between healthy and faulty cases based on the analyses of flux data; and 2) it should be able to detect the existence of the fault regardless of the position of the bars that break.

A. Experimental Results Obtained From the Measurement in Position A

Regarding Position A, the resulting pattern obtained for each sample after the application of the proposed algorithm (see Fig. 1) allows us to discern when we are in the presence of a motor with two broken bars, since all the samples converge to the same line (see Fig. 4).

In Fig. 4, we can also see the stepped positioning of the obtained patterns from each sample according to the relative positions, whose difference lies in the amplitude, that is: first position_1_2 (red), position_1_6 (black), position_1_5 (yellow), position_1_3 (green), the above except for position_1_4 (blue) which reflects a total difference with the rest of the obtained patterns, from each sample. This result can be very useful for discrimination between the healthy and faulty cases and for the identification of the two broken bars case, regardless of the relative position of the broken bars.

To prove that we are in the presence of a motor with two broken bars, the Pearson correlation coefficient was applied between the resulting patterns obtained from the measurements carried out in Position A. The correlation obtained between the resulting patterns is almost 1, except on the case of Position 1_4. Table I shows the results obtained. In that table, CORR_POS_X_X is the correlation obtained from each pattern with respect to the resulting pattern of the bar BB_1_2. The measurement BB_1_2 was taken as reference, but another sample could have been taken; the correlation will give similar values with the exception of Position 1_4, which has a certain difference as shown in the graph of Fig. 4. Now, if we consider the mean value of the module of the obtained correlations, it gives as result: 0.9768.

B. Experimental Results Obtained From the Measurement in Position B

As for Position B, it is verified by the resulting pattern (see Fig. 5) that there are two broken bars and just as in Position A, we can discern in which relative position is Position 1_4 (blue) and Position 1_6 (black) which are differentiable from the rest of the others, since their correlation value is negative as well as the results of the measurement at Position A.
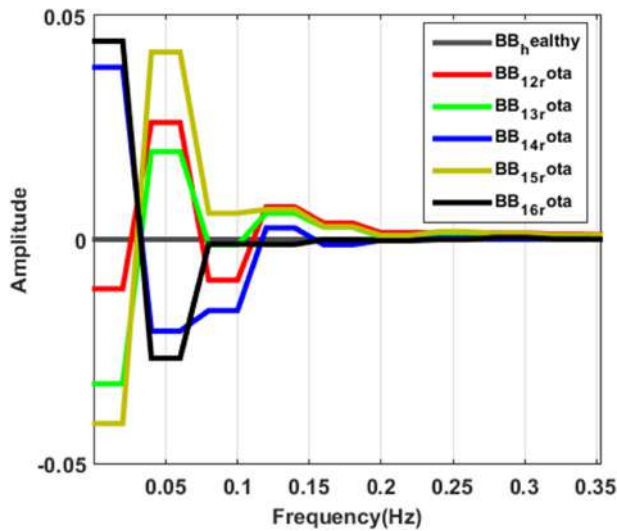
Fig. 5. Resulting spectral pattern obtained from Position B.

TABLE II
CORRELATION VALUES OBTAINED ACCORDING TO THE
RESULTING PATTERNS: POSITION B

CORR_POS_1_2 & 1_6 =	CORR_POS_1_2 & 1_5 =
1.0000 -0.7361	1.0000 0.8457
-0.7361 1.0000	0.8457 1.0000
CORR_POS_1_2 & 1_3 =	CORR_POS_1_2 & 1_4 =
1.0000 0.7875	1.0000 -0.5542
0.7875 1.0000	-0.5542 1.0000

With respect to the other broken bar relative positions (1_2, 1_3, and 1_5), these follow a stepped descendent pattern as in Fig. 2, although not in the same order. The correlation obtained between the resulting patterns as in Position A is almost 1, except on Position 1_4 and Position 1_6, whereby these two positions can be discerned. In Table II, the results are shown. Now, if we proceed in the same way as for Position A, with the average value of the module of the correlations obtained, it yields: 0.7309. The correlation levels obtained in the measurements made in both relative Positions A and B, respectively, oscillate between 0.7 and 0.98, which can be a variable indicator to identify broken bars using the flux signals.

Note that the power spectra of Figs. 4 and 5 have been sorted according to the amplitude in descending form, as a way to organize the vector to evaluate the spectral subtraction, whose objective is to obtain differences in the spectrum in relation to the healthy state. By carrying out the spectral subtraction of the spectra, only the components in the failure bands will remain, since the components of fundamental frequencies as well as the noise that may exist in the spectrum are cancelled out.

The fault components appear in the spectrum in the bands adjacent to the fundamental frequency. When the spectrum is sorted, the frequency components are placed in descending order according to their amplitude value; the amplitude values of the components where there is a fault will take a new position in

the new ordered amplitude vector, but this information is not relevant, since what is intended is to find out a common pattern for when there are two broken bars, regardless of their relative position, so, in this case, the information relative to the location in the frequency domain is not so relevant.

C. Discrimination Between Healthy and Damaged States Based on the Spectra

The discrimination between healthy and faulty conditions can be carried out by comparing the corresponding spectra of the captured EMF signals. However, this procedure is influenced by the occurrence of nonadjacent breakages since, depending on the relative positions between the bars that break, the amplitudes of the fault harmonics may sensibly differ [30]. However, as pointed out in previous works [17], [33], the analyses of the Fourier spectra may be helpful at least to have evidence that an anomaly may be present. A rough analysis of the characteristics of the Fourier spectra for each one of the considered positions of the sensor (see Figs. 6 and 7) is presented next. Table III synthesizes the conclusions of both figures and includes the case of a single broken bar for comparison purposes.

Characteristics of the spectra for Position A are as follows.
1) All the analyses show the presence of the main rotor fault component (LSH), which is typically used for diagnosing the fault and that is located at $f \cdot (1-2 \cdot s)$. However, note that there are clear differences between the amplitude of this harmonic for healthy and faulty conditions, a fact that may enable to discriminate between both conditions (see Fig. 6).
2) Note that, for the different cases of broken bars, the amplitude of the LSH significantly changes. The maximum amplitude is reached when the broken bars are consecutive (Positions 1–2), whereas the minimum amplitudes happen when the broken bars are at Positions 1–4 and 1–5. This fact clearly confirms the influence of the relative position of the broken bars on the fault component amplitude. In any case, in spite of these differences between faulty cases, the differences are evident versus healthy condition.

Characteristics of the spectra for Position B are as follows.
1) All samples have the expected fundamental harmonic at 50 Hz (see Fig. 7).
2) As in Position A, sideband components are present for all faulty cases although their amplitudes vary depending on the relative position between broken bars (maximum amplitude for adjacent bars, in agreement with the conclusions of previous works focused on current analysis [12]).
3) Again, there is a significant variation between the lower sideband amplitude for the faulty cases. In some relative positions, the compensation effect between both breakages may lead to very low amplitudes of the sideband that may lead to difficulties for discriminating versus healthy condition.
4) If the low frequency regions (not shown in the figures due to space restrictions) are studied, fault harmonics are detectable at components $s \cdot f$ and $3s \cdot f$ [33]. Once again their
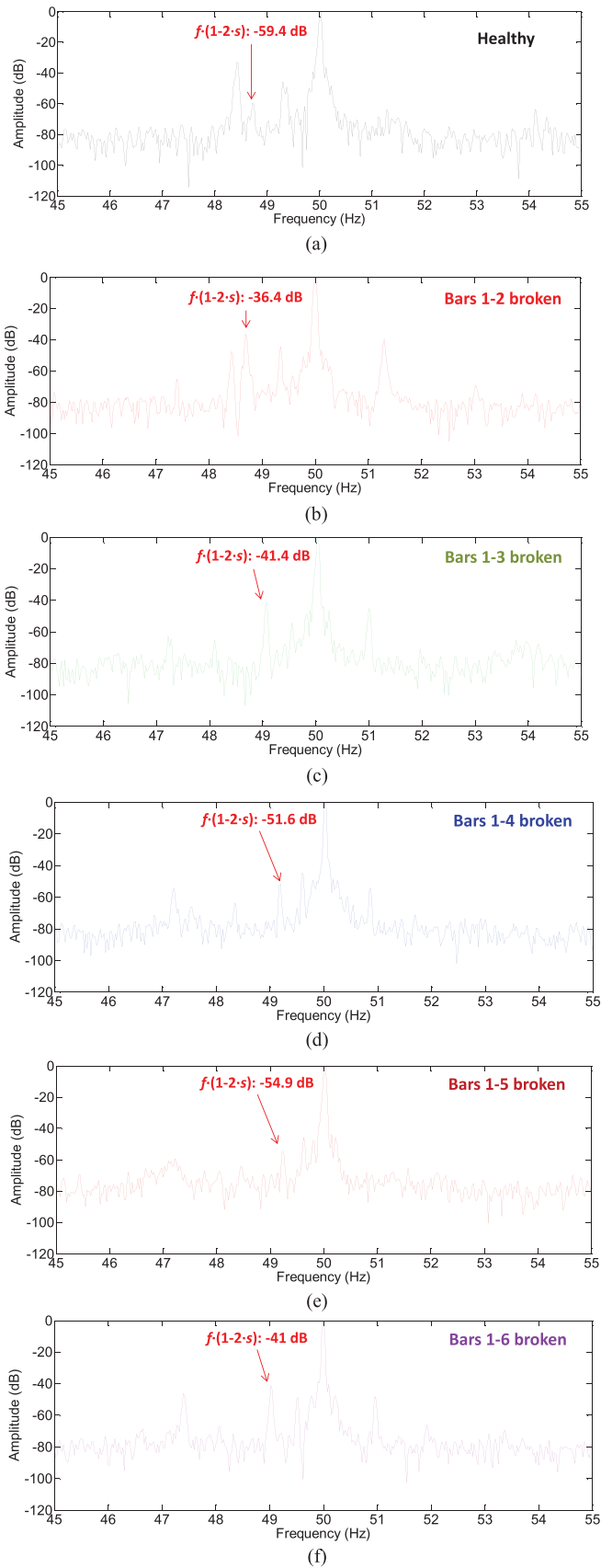
Fig. 6. Comparison of the spectrum of (a) healthy motor, with (b)–(f) broken bars spectra. Sensor Position: A.
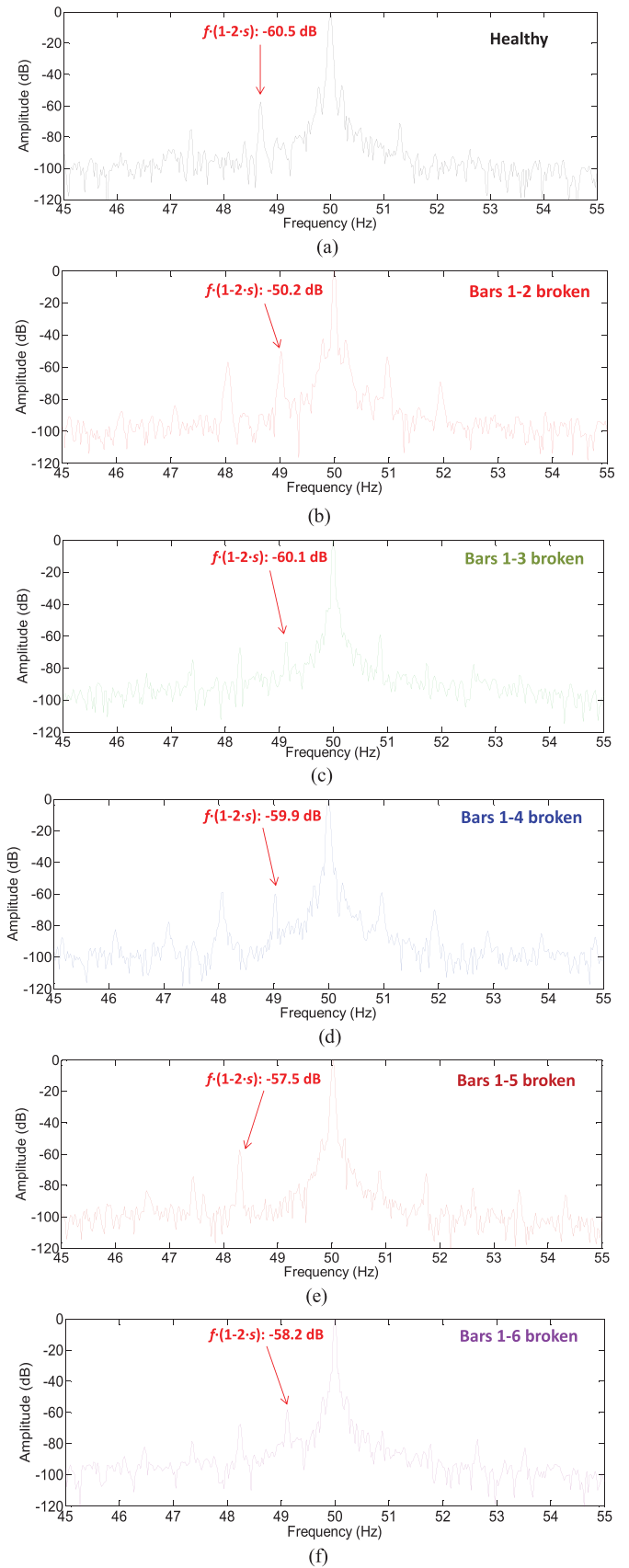
Fig. 7. Comparison of the spectrum of (a) healthy motor, with (b)–(f) broken bars spectra. Sensor Position: B.

TABLE III
LSH FREQUENCY AND AMPLITUDE FOR EACH TESTED CONDITION
AND FOR EACH SENSOR POSITION

SENSOR POSITION A			
CONDITION	SPEED (RPM)	LSH FREQUENCY (Hz)	LSH AMPLITUDE (dB)
Healthy	1481	48,73	-59,4
1 broken bar	1480	48,67	-53,2
2 broken bars (1-2)	1480	48,67	-36,4
2 broken bars (1-3)	1487	49,13	-41,4
2 broken bars (1-4)	1488	49,20	-51,6
2 broken bars (1-5)	1488	49,20	-54,9
2 broken bars (1-6)	1486	49,07	-41
SENSOR POSITION B			
CONDITION	SPEED (RPM)	LSH FREQUENCY (Hz)	LSH AMPLITUDE (dB)
Healthy	1480	48,67	-60,5
1 broken bar	1486	49,07	-54,1
2 broken bars (1-2)	1484	48,93	-50,2
2 broken bars (1-3)	1488	49,20	-60,1
2 broken bars (1-4)	1485	49,00	-59,9
2 broken bars (1-5)	1479	48,60	-57,5
2 broken bars (1-6)	1486	49,07	-58,2

Fig. 8. Comparison between: (a) indicator for healthy state condition for both sensor positions A and B and (b) indicator for broke state condition for both sensor positions A and B.

amplitudes are influenced by the relative positions of the breakages. But their presence is evidence of the existence of the fault.

In conclusion, the analyses of the spectra can enable to distinguish visually between healthy and faulty conditions but the influence of the relative position between broken bars may make the discrimination difficult in some cases. Due to this, the algorithm proposed in the first part of this paper can be especially useful to diagnose this situation and avoid false-negative indications.

D. Discrimination Between Healthy and Damaged States Based on the Autocovariance Function

From the previous results based on the information of the frequency spectrum, differences between both spectra can be visually appreciated for the healthy and damaged states. However, it is convenient to obtain an indicator that emits a constant or a variable value in a certain range when it is in the presence of a healthy motor and when the motor is damaged.

In relation to this, in this section, an algorithm based on the square value of the median of the autocovariance of the flux signal is proposed. It is decided to use the median and not the mean value so that the amplitude peak in the flux signal has no influence at the time of the calculation of the indicator. The reason for using the quadratic value of the median of the autocovariance is explained by the fact that it is necessary to obtain a quantitative indicator which clearly differs between healthy and faulty conditions. Although other quantities such as the mean value, quadratic mean of variance have been also evaluated, they have not led to so sensitive results as the proposed quantity.

The theoretical foundations of the proposed algorithm are described next: for a stationary periodic real signal, the autocovariance function of a random, stationary process $\{x(n)\}_{n=0}^{N-1}$ is a measure of the dispersion of the process around its mean value and is defined as a function dependent on the first and second-order moments as follows:

$$c_2^x(\tau) = m_2^x(\tau) - (m_1^x)^2 \tag{2}$$
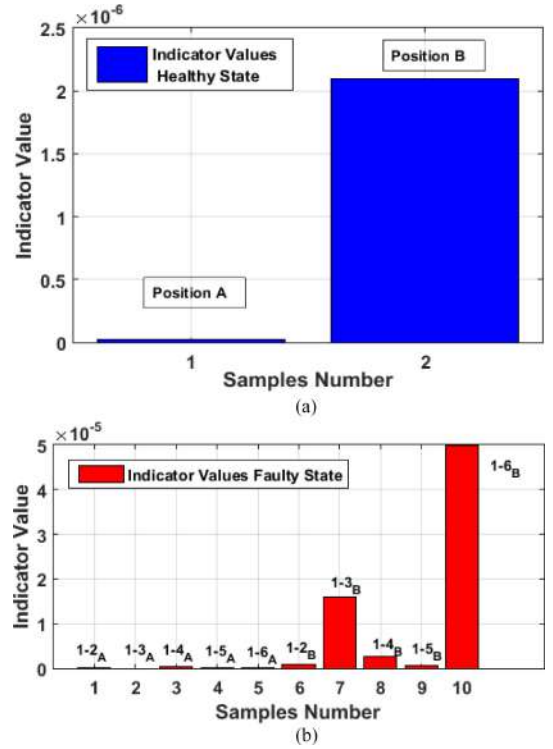
where $m_2^x(\tau_1)$ is the autocorrelation function. From the above equation, it can be noted that if the process is of value zero mean value, the autocovariance coincides with the autocorrelation function. Then, replacing in (2) and applying second-order statistics we have

$$c_2^x(\tau) = \frac{1}{N} \sum_{t=0}^{N-1-\tau} x(t) \cdot x(t+\tau). \tag{3}$$

Then, after obtaining the autocovariance function, we proceed to calculate the square value of the median, for each sample used in the experiment, which is as follows:

Let $x_1, x_2, x_3, \ldots, x_n$ be the data of a sample ordered in increasing order and designating the median M_e as: if n is odd, the median is the value occupied by the position $M_{e(c_2^x)} = \frac{c_2^x(\tau)_{(n+1)}}{2}$, then if n is not odd, the median is the arithmetic mean of the two central values. Then, it would be

$$M_{e(c_2^x)} = \frac{c_2^x(\tau)_{(\frac{n}{2})} + c_2^x(\tau)_{(\frac{n}{2}+1)}}{2}.$$

Substituting to find out the temporary indicator

$$\mathrm{Ind}_t = \left(M_{e(c_2^x)}\right)^2. \tag{4}$$

The obtained results applying the proposed algorithm as a temporary indicator for the detection of the healthy–damaged state of the motor are shown in Fig. 8, likewise these are summarized in Table IV.

As it can be observed in Table IV, there is a notable difference in the values of the indicator obtained for Position A with respect

TABLE IV
VALUES OF THE INDICATOR AND MULTIPLICATION FACTOR
FOR BOTH SENSOR POSITIONS A AND B

SENSOR POSITION	INDICATOR FOR FAULTY STATE	INDICATOR FOR HEALTHY STATE	MULTIPLICATION FACTOR
HEALTHY_A		2.7E-08	
1-2_A	6.8E-09		0.2519
1-3_A	1.7E-10		0.0063
1-4_A	4.4E-07		16.2963
1-5_A	3.4E-09		0.1259
1-6_A	4.65E-08		1.7222
HEALTHY_B		2.1E-06	
1-2_B	9.77E-07		0.4652
1-3_B	1.6E-05		7.6190
1-4_B	2.67E-06		1.2714
1-5_B	5.23E-07		0.2490
1-6_B	5E-05		23.8095

to those obtained for Position B, even for the same condition. This indicates that the sensor position plays an important role. Note also that there are important differences between the value of the indicator for healthy condition and its corresponding value for each fault condition (second and third columns). In order to obtain a measure of this difference, a multiplication factor is introduced (see fourth column); it is defined as the ratio between the value of the indicator for the corresponding faulty condition and its value for healthy state. This ratio gives an idea of the fault severity in comparison with the healthy condition.

Note that the relative Positions 1–3_A, 1–3_B, and 1–6_B, respectively, are the positions where more noticeable differences of the indicator are obtained in relation to the values obtained for the healthy condition. For the other relative positions, the differences are not so clear; a fact that indicates that, in addition to the sensor position, the relative position of the broken bar also has certain influence in the results.

V. CONCLUSION

This work proposes the use of induction motor stray flux signals for the identification of bar breakages regardless of their relative position. During the experiments carried out, it was shown that it is possible with the proposed algorithm to detect the fault and even distinguish the relative position of the bars that break.

The proposed method is based on the frequency spectral subtraction of the power spectrum and on the subsequent computation of the Pearson correlation coefficient, which was calculated to demonstrate the similarity of all the patterns obtained for the case of two broken bars [37], [38].

In order to identify between healthy and damaged states, a rough analysis of the power spectrum may be sufficient in some situations; the differences between the spectrum of the healthy motor and the faulty states in both Positions A and B can be noticed visually, by means of the harmonics appearing both at lower frequencies and around the main component.

Furthermore in relation to this, a potential indicator to evaluate the condition of the motor and discriminate between healthy and damaged states has been evaluated experimentally. This indicator is based on the calculation of the square value of the median of the autocovariance function of the stray flux signal.

It is shown that there are quantitative differences in the obtained values when evaluating the indicator for both states (healthy and faulty) and it was demonstrated that the position of the flux sensor as well as the relative position of the broken bar may have influence at the time of calculation of the indicator. According to the obtained results, the indicator evaluated when the sensor is at Position B seems to be more sensitive than when the sensor is at Position A.

APPENDIX

See Tables V and VI.

TABLE V
RATED CHARACTERISTICS OF THE TESTED MOTOR

Model 1LA2080-4AA10	
Rated power (P_N)	1.1 kW
Rated speed (n_N)	1410 rpm
Rated voltage (U_N)	400(Y)/230 (Δ)
Rated current (I_N)	2.7(Y)/4.6 (Δ)
Rated power factor (Cos φ)	0.8
Number of rotor bars	28

TABLE VI
RATED CHARACTERISTICS OF THE LOAD (D.C. MACHINE)

Rated power (P_N)	3 kW
Rated speed (n_N)	2000 -3000 rpm
Rated voltage (U_N)	220 V
Rated excitation current	0.4 A
Rated armature current	13.6 A
Number of pole pairs	1

REFERENCES

[1] S. Nandi, H. A. Toliyat, and X. Li, "Condition monitoring and fault diagnosis of electrical motors—A review," *IEEE Trans. Energy Convers.* 20, no. 4, pp. 719–729, Dec. 2005.

[2] M. Riera-Guasp, J. A. Antonino-Daviu, and G. A. Capolino, "Advances in electrical machine, power electronic, and drive condition monitoring and fault detection: State of the art," *IEEE Trans. Ind. Electron.* 62, no. 3, pp. 1746–1759, Mar. 2015.

[3] J. A. Antonino-Daviu, M. Riera-Guasp, J. R. Folch, and M. Pilar Molina Palomares, "Validation of a new method for the diagnosis of rotor bar failures via wavelet transform in industrial induction machines," *IEEE Trans. Ind. Appl.* 42, no. 4, pp. 990–996, Jul./Aug. 2006.

[4] C. Yang, T.-J. Kang, D. Hyun, S. Lee, J. Antonino-Daviu, and J. Pons-Llinares, "Reliable detection of induction motor rotor faults under the rotor axial air duct influence," *IEEE Trans. Ind. Appl.* 50, no. 4, pp. 2493–2502, Jul./Aug. 2014.

[5] J. A. Antonino-Daviu, J. Pons-Llinares, S. Shin, K. W. Lee, and S. B. Lee, "Reliable detection of induction motor rotor faults under the influence of rotor core magnetic anisotropy," in *Proc. IEEE 10th Int. Symp. Diagnostics Elect. Mach. Power Electron. Drives*, Guarda, Portugal, 2015, pp. 14–21.

[6] C. Hargis, B. G. Gaydon, and K. Kamash, "The detection of rotor defects in induction motors," in *Proc. IEE Int. Conf. Elect. Mach. Des. Appl.*, London, U.K., pp. 216–220.

[7] M. H. Benbouzid, "A review of induction motors signature analysis as a medium for fault detection," *IEEE Trans. Ind. Electron.* 47, no. 5, pp. 984–993, Oct. 2000.

[8] T. J. Sobczyk and W. Maciolek, "Does the component (1-2s)f0 in stator current is sufficient for detection of rotor cage faults?" in *Proc. IEEE 5th Int. Symp. Diagnostics Elect. Mach. Power Electron. Drives*, Vienna, Austria, Sep. 2005, pp. 1–5.

[9] J. Faiz and B. M. Ebrahimi, "Locating rotor broken bars in induction motors using finite element method," *Energy Convers. Manage.* 50, no. 1, pp. 125–131, Jan. 2009.

[10] G. Y. Sizov, A. Sayed-Ahmed, C. C. Yeh, and N. A. O. Demerdash, "Analysis and diagnostics of adjacent and nonadjacent broken-rotor-bar faults in squirrel-cage induction machines," *IEEE Trans. Ind. Electron.* 56, no. 11, pp. 4627–4641, Nov. 2009.

[11] A. Menacer, S. Moreau, G. Champenois, M. S. N. Said, and A. Benakcha, "Experimental detection of rotor failures of induction machines by stator current spectrum analysis in function of the broken rotor bars position and the load," in *Proc. Int. Conf. Comput. Tool*, Sep. 2007, pp. 1752–1758.

[12] M. Riera-Guasp, M. F. Cabanas, J. A. Antonino-Daviu, M. Pineda-Sánchez, and C. H. R. García, "Influence of nonconsecutive bar breakages in motor current signature analysis for the diagnosis of rotor faults in induction motors," *IEEE Trans. Energy Convers.* 25, no. 1, pp. 80–89, Mar. 2010.

[13] M. Riera-Guasp, J. Pons-Llinares, F. Vedreño-Santos, J. A. Antonino-Daviu, and M. Fernández Cabanas, "Evaluation of the amplitudes of high-order fault related components in double bar faults," in *Proc. 8th IEEE Symp. Diagnostics Elect. Mach. Power Electron. Drives*, Bologna, Italy, 2011, pp. 307–315.

[14] J. A. Antonino-Daviu, K. N. Gyftakis, R. Garcia-Hernandez, H. Razik, and A. J. M. Cardoso, "Comparative influence of adjacent and non-adjacent broken rotor bars on the induction motor diagnosis through MCSA and ZSC methods," in *Proc. 41st Annu. Conf. IEEE Ind. Electron. Soc.*, Yokohama, Japan, 2015, pp. 1680–1685.

[15] K. N. Gyftakis, J. A. Antonino-Daviu, and A. J. M. Cardoso, "A reliable indicator to detect non-adjacent broken rotor bars severity in induction motors," in *Proc. 22nd Int. Conf. Elect. Mach.*, Lausanne, Switzerland, 2016, pp. 2910–2916.

[16] C. G. Dias and C. M. de Sousa, "An experimental approach for diagnosis of adjacent and nonadjacent broken bars in induction motors at very low slip," in *Proc. IEEE Int. Elect. Mach. Drives Conf.*, Miami, FL, USA, 2017, pp. 1–6.

[17] R. Romary, R. Pusca, J. P. Lecointe, and J. F. Brudny, "Electrical machines fault diagnosis by stray flux analysis," in *Proc. IEEE Workshop Elect. Mach. Des. Control Diagnosis*, Paris, France, Mar. 11–12, 2013, pp. 247–256.

[18] A. Yazidi, H. Henao, and G.-A. Capolino, "Broken rotor bars fault detection in squirrel cage induction machines," in *Proc. IEEE Int. Conf. Elect. Mach. Drives*, San Antonio, TX, USA, 2005, pp. 741–747.

[19] H. Henao, G.-A. Capolino, and C. S. Martis, "On the stray flux analysis for the detection of the three-phase induction machine faults," in *Proc. Conf. Rec. 38th IEEE IAS Annu. Meeting* 2, 2003, pp. 1368–1373.

[20] G. Mirzaeva and K. I. Saad, "Advanced diagnosis of rotor faults and eccentricity in induction motors based on internal flux measurement," *IEEE Trans. Ind. Appl.* 54, no. 3, pp. 2981–2991, May/Jun. 2018.

[21] S. B. Salem, M. Salah, W. Touti, K. Bacha, and A. Chaari, "Stray flux analysis for monitoring eccentricity faults in induction motors: Experimental study," in *Proc. Int. Conf. Control Autom. Diagnosis*, 2017, pp. 292–297, doi: 10.1109/CADIAG.2017.8075673.

[22] L. Frosini, A. Borin, L. Girometta, and G. Venchi, "A novel approach to detect short circuits in low voltage induction motor by stray flux measurement," in *Proc. Int. Conf. Elect. Mach.*, Marseille, France, Sep. 2–5, 2012, pp. 1538–1544.

[23] H. Henao, C. Demian, and G.-A. Capolino, "A frequency-domain detection of stator winding faults in induction machines using an external flux sensor," *IEEE Trans. Ind. Appl.* 39, no. 5, pp. 1272–1279, Sep./Oct. 2003.

[24] A. Yazidi, D. Thailly, H. Henao, R. Romary, G.-A. Capolino, and J.-F. Brudny, "Detection of stator short-circuit in induction machines using an external leakage flux sensor," in *Proc. IEEE Int. Conf. Ind. Technol.*, Hammamet, Tunisia, 2004, pp. 166–169.

[25] S. M. J. Rastegar Fatemi, H. Henao, and G.-A. Capolino, "Gearbox monitoring by using the stray flux in an induction machine based electromechanical system," in *Proc. IEEE Mediterranean Electrotech. Conf.*, Ajaccio, France, 2008, pp. 484–489.

[26] C. Jiang, S. Li, and T. G. Habetler, "A review of condition monitoring of induction motors based on stray flux," in *Proc. IEEE Energy Convers. Congr. Expo.*, Cincinnati, OH, USA, 2017, pp. 5424–5430.

[27] J. A. Ramirez-Nunez *et al.*, "Evaluation of the detectability of electromechanical faults in induction motors via transient analysis of the stray flux," *IEEE Trans. Ind. Appl.* 54, no. 5, pp. 4324–4332, Sep./Oct. 2018.

[28] H. Cherif, A. Menacer, R. Romary, and R. Pusca, "Dispersion field analysis using discrete wavelet transform for inter-turn stator fault detection in induction motors," in *Proc. IEEE 11th Int. Symp. Diagnostics Elect. Mach. Power Electron. Drives*, Tinos, Greece, 2017, pp. 104–109.

[29] J. A. Antonino-Daviu, H. Razik, A. Quijano-Lopez, and V. Climente-Alarcon, "Detection of rotor faults via transient analysis of the external magnetic field," in *Proc. 43rd Annu. Conf. IEEE Ind. Electron. Soc.*, Beijing, China, 2017, pp. 3815–3821.

[30] P. A. Panagiotou, I. Arvanitakis, N. Lophitis, J. A. Antonino-Daviu, and K. N. Gyftakis, "Analysis of stray flux spectral components in induction machines under rotor bar breakages at various locations," in *Proc. 23rd Int. Conf. Elect. Mach.*, Alexandroupoli, Greece, 2018, pp. 2345–2351.

[31] M. E. Iglesias-Martínez, P. F. de Córdoba, J. A. Antonino-Daviu, and J. A. Conejero, "Detection of bar breakages in induction motor via spectral subtraction of stray flux signals," in *Proc. 23rd Int. Conf. Elect. Mach.*, Alexandroupoli, Greece, 2018, pp. 1796–1802.

[32] A. Bellini, C. Concari, G. Franceschini, C. Tassoni, and A. Toscani, "Vibrations, currents and stray flux signals to asses induction motors rotor conditions," in *Proc. 32nd Annu. Conf. IEEE Ind. Electron.*, Paris, France, 2006, pp. 4963–4968.

[33] A. Ceban, R. Pusca, and R. Romary, "Study of rotor faults in induction motors using external magnetic field analysis," *IEEE Trans. Ind. Electron.* 59, no. 5, pp. 2082–2093, May 2012.

[34] J. A. Antonino-Daviu, H. Razik, A. Quijano-Lopez, and V. Climente-Alarcon, "Detection of rotor faults via transient analysis of the external magnetic field," in *Proc. 43rd Annu. Conf. IEEE Ind. Electron. Soc.*, Beijing, China, 2017, pp. 3815–3821.

[35] K. C. Deekshit Kompella, M. Venu Gopala Rao, and R. Srinivasa Rao, "SWT based bearing fault detection using frequency spectral subtraction of stator current with and without an adaptive filter," in *Proc. IEEE Region 10 Conf.*, 2017, pp. 2472–2477, doi: 10.1109/TENCON.2017.8228277.

[36] E H. El Bouchikhi, V. Choqueuse, and M. El Hachemi Benbouzid, "Current frequency spectral subtraction and its contribution to induction machines' bearings condition monitoring," *IEEE Trans. Energy Convers.* 28, no. 1, pp. 135–144, Mar. 2013.

[37] H. Deborah, N. Richard, and J. Y. Hardeberg, "A comprehensive evaluation of spectral distance functions and metrics for hyperspectral image processing," *IEEE J. Sel. Topics Appl. Earth Observ. Remote Sens.* 8, no. 6, pp. 3224–3234, Jun. 2015.

[38] G. Borelli, J. Jovic Bonnet, Y. Rosales Hernandez, K. Matsuda, and J. Damerau, "Spectral-distance-based detection of EMG activity from capacitive measurements," *IEEE Sens. J.* 18, no. 20, pp. 8502–8509, Oct. 15, 2018.

Miguel Enrique Iglesias-Martínez was born in Pinar del Río Cuba in 1984. He received the B.Sc. degree in telecommunications and electronics engineering from the University of Pinar del Río, Pinar del Río, Cuba, in 2008, the master's degree in digital systems from Higher Polytechnic Institute (Ciudad Universitaria José Antonio Echeverría (CUJAE)), La Habana, Cuba, in 2011, and is currently working toward the Ph.D. degree in mathematics at the Universitat Politècnica de València, Valencia, Spain.

His research interests include signal processing, noise analysis and blind information extraction, as well as the design of digital systems.

Mr. Iglesias-Martínez was recipient of four scientific prizes from the Cuba Academy of Sciences in the years 2011, 2012, 2015, and 2017.

Pedro Fernández de Córdoba was born in Valencia in October 1965. He received the B.Sc., M.Sc., and Ph.D. degrees in physics from the Universitat de València (UV), Valencia, Spain, in 1988, 1990, and 1992, respectively. He also received the Ph.D. degree in mathematics from the Universidad Politécnica de Valencia (UPV), Valencia, in 1997.

His research work was performed at UV, UPV, the Joint Institute for Nuclear Research (Russia), the University of Tübingen (Germany), and the Istituto Nazionale di Fisica Nucleare, Torino, Italy, among others. He is currently a Professor with the Department of Applied Mathematics, UPV. His research interests include the area of modeling and numerical simulation of physical and engineering problems, mainly focusing on the numerical treatment of heat and mass transfer problems.

Dr. de Córdoba is Doctor Honoris Causa from the University of Pinar del Rio (Cuba), a member of the Colombian Academy of Exact, Physical and Natural Sciences, a member of the Académie Nationale des Sciences, Arts et Lettres du Bénin, Profesor Invitado of the University of Pinar del Rio, and Profesor Visitante "Ad Honorem" of the Universidad del Magdalena (Colombia). Furthermore, since its establishment on September 30, 2011, he has been a member of the Board of the Spanish Mathematics-Industry network (www.math-in.net).

Jose A. Antonino-Daviu (S'04–M'08–SM'12) received the M.S. and Ph.D. degrees in electrical engineering from the Universitat Politècnica de València, Valencia, Spain, in 2000 and 2006, respectively, and the B.S. degree in business administration from the Universitat de Valencia, Valencia, in 2012.

He was with IBM for two years, being involved in several international projects. He is currently an Associate Professor with the Department of Electrical Engineering of the mentioned university, where he develops his docent and research work. He was an Invited Professor with the Helsinki University of Technology, Finland, in 2005 and 2007, Michigan State University, USA, in 2010, Korea University, South Korea, in 2014, and the Université Claude Bernard Lyon 1, France, in 2015. He has authored or coauthored more than 170 contributions, including international journals, conferences, and books.

Dr. Antonino-Daviu is an Associate Editor for IEEE TRANSACTIONS ON INDUSTRIAL INFORMATICS and IEEE Industry Applications Society Distinguished Lecturer for 2019–2020. He has been the Guest Editor for IEEE TRANSACTIONS ON INDUSTRIAL ELECTRONICS. He was the General Co-Chair of IEEE International Symposium on Diagnostics for Electric Machines, Power Electronics and Drives 2013. He was recipient of the Nagamori Award from Nagamori Foundation, Kyoto, Japan, in 2018, for his contributions in electric motors transient analysis area.

J. Alberto Conejero received the M.Sc. degree in mathematics from the Universitat de València, Valencia, Spain, in 1998, and the Ph.D. degree in applied mathematics from the Universitat Politècnica de València (UPV), Valencia, in 2004, receiving the Outstanding Dissertation Award.

He has been an Associate Professor with UPV since 2009. He is currently the Director of the Department of Applied Mathematics, UPV, and responsible of the M.Sc. program on Mathematics Research at UPV. He was an Invited Researcher of Bowling Green St. University, USA; Kent St. University, USA; Università del Salento, Italy; Universität Tübingen, Germany; and Czech Academy of Sciences, Czech Republic. He is the author of more than 60 papers in international journals. His research interests include dynamical systems, partial differential equations, graph theory, and the multidisciplinary applications of mathematics to computer science, engineering, and biotechnology.

Dr. Conejero was recipient of the Teaching Excellence Prize of UPV in 2014.

Rotor Fault Detection in Induction Motors Based on Time-Frequency Analysis Using the Bispectrum and the Autocovariance of Stray Flux Signals

Miguel E. Iglesias-Martínez [1,2] , **Jose Alfonso Antonino-Daviu [3,*]** ,
Pedro Fernández de Córdoba [2] and **J. Alberto Conejero [2]**

[1] Departamento de Telecomunicaciones, Universidad de Pinar del Río, Pinar del Río, Martí #270, CP 20100, Cuba; migueliglesias2010@gmail.com

[2] Instituto Universitario de Matemática Pura y Aplicada, Universitat Politècnica de València (UPV), Camino de Vera s/n, 46022 Valencia, Spain; pfernandez@mat.upv.es (P.F.d.C.); aconejero@upv.es (J.A.C.)

[3] Instituto Tecnológico de la Energía, Universitat Politècnica de València (UPV), Camino de Vera s/n, 46022 Valencia, Spain

* Correspondence: joanda@die.upv.es; Tel.: +34-963877592

Abstract: The aim of this work is to find out, through the analysis of the time and frequency domains, significant differences that lead us to obtain one or several variables that may result in an indicator that allows diagnosing the condition of the rotor in an induction motor from the processing of the stray flux signals. For this, the calculation of two indicators is proposed: the first is based on the frequency domain and it relies on the calculation of the sum of the mean value of the bispectrum of the flux signal. The use of high order spectral analysis is justified in that with the one-dimensional analysis resulting from the Fourier Transform, there may not always be solid differences at the spectral level that enable us to distinguish between healthy and faulty conditions. Also, based on the high-order spectral analysis, differences may arise that, with the classical analysis with the Fourier Transform, are not evident, since the high order spectra from the Bispectrum are immune to Gaussian noise, but not the results that can be obtained using the one-dimensional Fourier transform. On the other hand, a second indicator based on the temporal domain that is based on the calculation of the square value of the median of the autocovariance function of the signal is evaluated. The obtained results are satisfactory and let us conclude the affirmative hypothesis of using flux signals for determining the condition of the rotor of an induction motor.

Keywords: indicator; fault diagnosis; induction motors; bispectrum; autocovariance

1. Introduction

In the electric motor condition monitoring area, there is a continuous search for new techniques that are able to enhance the performance and to avoid the drawbacks of the currently existing ones. In this context, the analysis of alternative machine quantities is being explored, as a way to complement the information provided by the well-known methods that are widespread in the industry (currents and vibrations). This is especially important, taking into consideration that no single quantity has been proved to be reliable enough to diagnose the condition of the whole machine, and that the best option seems to be to combine the information obtained from different sources [1–3].

Induction motor fault detection (FD) methods, such as stray flux data analysis [4–8], have specific advantages that make them especially attractive for certain applications. Fault diagnosis and processing techniques based on stray flux signals are completely non-invasive and their set up is relatively simple, although the application of this approach requires a specific sensor and a priori knowledge of the

distribution of the magnetic field around the electrical machine, which depends, in general, on the manufacturing characteristics of the induction motor [1].

In reference [6], fault detection from the analysis of stray flux signals is based on the variation of the amplitude versus the load of a specific harmonic for two different positions of the flux sensor. The advantage of this method is that it does not require information about the machine behavior in a healthy state. In reference [4], the use of an analytical model that allows us to determine the magnetic flux approximation under conditions of healthy and faulty states for the case of a short circuit between the stator turns and the broken bars is explained. We also refer to [7] for another method for short circuitdetection using stray flux signals.

Fault diagnosis using stray flux signals is based on spectral analysis, through statistical methods, of the harmonics signals obtained from the flux sensor at different relative positions. Compared with classical methods based on analysis of currents such as MCSA (Monte Carlo Statistical Analysis), a disadvantage is that the results may depend on the position of the sensor, and it is not possible to theoretically establish a general rule to obtain the optimum position in the measurement. Moreover, there are no defined thresholds to determine the severity of the fault based on the analysis of these quantities.

In spite of the drawbacks of stray flux data analysis, the progressive cost decrement of necessary flux sensors together with the aforementioned advantages of this technique have led to a renewed dynamism in the research devoted to the study of this technique. Recent works have even extrapolated its application to transient analysis, showing especial advantages in comparison with other methods [9]. Stray flux analysis is adequate to avoid occasional false indications appearing when other techniques are applied to rotor fault detection [10]. Moreover, the suitability of stray flux analysis for non-adjacent bar breakage detection has been explored in [11,12]. Regarding statistical analysis using stray flux signals, an algorithm has been proposed in [13] that relies on the use of the mean value and the standard deviation of the spectral components. Its performance has been tested with three levels of faults, see also [14,15].

In the present work, an algorithm to determine the rotor condition of induction motors from the analysis of stray flux signals is proposed. The detection of the healthy and faulty state conditions is based on a time-frequency analysis of the bispectrum and of the autocovariance function. The results are satisfactory and show the potential of this approach, which provides valuable information to detect the state of the rotor or, at least, to supplement the information provided by other quantities, improving the performance of classical techniques.

2. Materials and Methods

2.1. Data Acquisition

The experimental test bench was based on a 1.1 kW induction motor that was driving a direct current generator. Stray flux measurements were obtained by registering the electromotive force waveforms induced in an external coil sensor that was attached tovarious positions of the motor frame. The flux sensor was a coil with 1000 turns with an external diameter of 80 mm and an internal diameter of 39 mm.

Different operating conditions of the motor were considered. To differentiate the results by working regimes, our samples were taken during the motor startup (the motor was fed at 60% of the rated voltage) and at steady state (in this case the motor was fed 100% of the nominal voltage). We have obtained eight samples of flux signals of a healthy motor and sixteen samples of flux signals of a motor with adamaged rotor (one broken bar). All the measurements in the experiments were taken under similar characteristics in both cases, in order to facilitate subsequent comparisons. In both experiments, the sampling frequency was 5 kHz.

We show in Tables 1 and 2 the different conditions of the experiments for capturing the flux signals of the healthy and faulty motors during start-up (60% of the supply voltage), as well as the

corresponding sensor positions (see Figure 1). In these tables, NL stands for 'No load' whereas FL means 'Full Load'.

Table 1. Characteristics of the experiment for the healthy motor during start-up.

Sample	Position	Load	Speed (r/min)	Torque (Nm)	Supply Voltage (%)	Time (s)
0	DMA	NL	988	0.49	60	1
2	DM	NL	988	0.49	60	1
4	E	NL	987	0.51	60	1
6	L	NL	986	0.54	60	1

Table 2. Characteristics of the experiment for the damaged motor with a broken bar during start-up.

Sample	Position	Load	Speed (r/min)	Torque (Nm)	Supply Voltage (%)	Time (s)
0	DMA	NL	985	0.49	60	1
2	DM	NL	988	0.49	60	1
4	E	NL	987	0.49	60	1
6	L	NL	985	0.49	60	1
8	DMA	FL	755	5.1	60	1
10	DM	FL	750	5	60	1
12	E	FL	760	5	60	1
14	L	FL	765	5	60	1
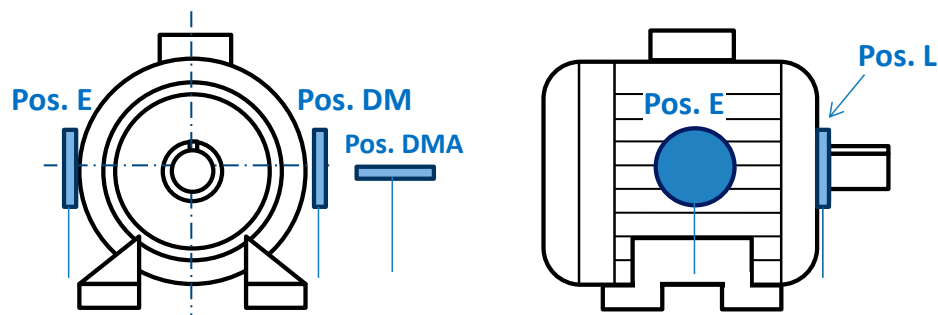
Figure 1. Different positions considering the flux sensor.

Similar experiments were carried out with the motor under permanent regime (100% of the supply voltage). We summarize in Tables 3 and 4 the experimental conditions of the motor operation at steady state.

Table 3. Characteristics of the experiments for the healthy motor at steady state.

Sample	Position	Load	Speed (r/min)	Torque (Nm)	Supply Voltage (%)	Time (s)
1	DMA	NL	994	0.49	100	8
3	DM	NL	994	0.48	100	8
5	E	NL	995	0.51	100	8
7	L	NL	995	0.5	100	8

Table 4. Characteristics of the experiment for the damaged motor with a broken bar at steady state.

Sample	Position	Load	Speed (r/min)	Torque (Nm)	Supply Voltage (%)	Time (s)
1	DMA	NL	994	0.52	100	8
3	DM	NL	994	0.53	100	8
5	E	NL	994	0.55	100	8
7	L	NL	997	0.58	100	8
9	DMA	FL	940	6.2	100	8
11	DM	FL	940	6.13	100	8
13	E	FL	940	6.1	100	8
15	L	FL	940	6.09	100	8

2.2. Analysis in the Frequency Domain: Theoretical Foundation

Let $\{x(n)\}$, $n = 0, \pm1, \pm2, \ldots$ be a stationary random vector. Let us consider the high-order moments, see [13,14],

$$m_k^x(\tau_1, \tau_2, \ldots, \tau_{k-1}) = E\{x(n)x(n + \tau_1) \ldots x(n + \tau_{k-1})\} \tag{1}$$

that represents the moment of order k of the vector, which depends only on the different time intervals $\tau_1, \tau_2, \ldots \tau_{k-1}, \tau_i = 0, \pm1, \ldots$ for all i. Since, in practice cumulants are functions dependent on the expected value, they have to be estimated, since we have a finite amount of data to process $\{x(n)\}_{n=0}^{N-1}$.

These estimators are of a stationary nature and are characterized by first- and second-order statistical functions such as the mean value and variance. Then, let $\{x(n)\}$, $n = 0, \pm1, \pm2, \ldots$ be a stationary process of zero mean value. The third ordercumulant is given by:

$$C_{3x}(\tau_1, \tau_2) = \frac{1}{N} \sum_{n=N_1}^{N_2} x(n) \cdot x(n + \tau_1) \cdot x(n + \tau_2) \tag{2}$$

where N_1 and N_2 are chosen in such a way that the summation involves only $x(n)$ with $n \in [0, N-1]$, N being the number of samples to be evaluated in the cumulant region, see [15]. Likewise, the bispectrum is defined by the Fourier Transform of the third order cumulant, which is given by:

$$B_x^N(f_1, f_2) = \sum_{\tau_1=-N-1}^{N-1} \sum_{\tau_2=-N-1}^{N-1} C_{3x}(\tau_1, \tau_2) \cdot e^{-2\pi f_1 \tau_1} \cdot e^{-2\pi f_2 \tau_2}$$
$$= \frac{1}{N^2} X(f_1, f_2) \cdot X(f_1) \cdot X(f_2) \tag{3}$$

where $X(f)$ is the Fourier Transform of the sequence $\{x(n)\}_{n=0}^{N-1}$, see [15].

For the detection of the healthy and the damaged state conditions of an induction motor, an algorithm based on the sum of the mean value of the bispectrum absolute values $(B_{x-mean}^N(f))$ of the flux signal is proposed. From (3), we can obtain its formal description, shown as follows:

$$(B_{x-mean}^N(f)) = \frac{1}{N} \sum_{i=1}^{N} \left| B_x^N(f_1, f_2) \right|_i \tag{4}$$

where N is the number of rows of the $N \times N$ square matrix obtained from the bispectrum. The obtained result in (4) is a $1 \times N$ vectorthat contains the average frequency values of the amplitude bispectrum matrix of the flux signal. From the obtained result in (4), we define an indicator variable in the frequency domain by the following expression, as the summation of every average frequency values of the amplitude bispectrum:

$$\text{Ind(f)} = \sum_{i=1}^{N} B_{x-mean}^N(f)_{(i)} \tag{5}$$

that will be used for the detection of the healthy and faulty condition of the induction motor.

2.3. Temporal Domain Analysis

First, we process the flux signals in the time domain, using the initial data of the experiment, see Tables 1–4. During the start-up, it is shown that the indicator variable in the frequency domainleads to good results and a palpable difference is observed, which enables us to discriminate between healthy and damaged state conditions of arotor. However, when the motor works at steady state, at 100% of the rated voltage, the method based on the analysis in the frequency domain is not completely effective.

Therefore, to solve the aforementioned issues and to obtain a reliable indicator to be applied in both situations, enabling the discrimination between healthy and damaged rotors, an algorithm based

on the autocovariance function of the stray flux signals is proposed. This algorithm is based on the square value of the median of the autocovariance matrix of the flux signal. The theoretical foundations of the proposed are described below:

The autocovariance function of a random stationary process $\{x(n)\}_{n=0}^{N-1}$ is a measure of its dispersion around its mean value and is defined as a function dependent on the first- and second-order moments as follows [16]:

$$C_2^x(\tau) = m_2^x(\tau) - (m_1^x)^2 \tag{6}$$

where $m_2^x(\tau)$ is the autocorrelation function and $(m_1^x)^2$ is the first order moment. From (6), it can be noted that if the process is of zero mean value, the autocovariance coincides with the autocorrelation function. Then, replacing in (6) $m_2^x(\tau)$ and applying second order statistics we have:

$$C_2^x(\tau) = \frac{1}{N} \sum_{t=0}^{N-1-\tau} x(t) \cdot x(t+\tau) \tag{7}$$

Then, after obtaining the autocovariance function, we proceed to calculate the square value of the median, for each sample used in the experiment, which is as follows [16,17]:

Let be $x_1, x_2, x_3, \ldots, x_n$ the data of an ordered sample in increasing order and designating the median as M_e, if n is odd, the median is the value that the position occupies: $M_{e(c_2^x)} = \frac{c_2^x(\tau)_{(n+1)}}{2}$, then if n is pair, the median is the arithmetic mean of the two central values. Then, $M_{e(c_2^x)}$ would be:

$$M_{e(c_2^x)} = \frac{c_2^x(\tau)_{(\frac{n}{2})} + c_2^x(\tau)_{(\frac{n}{2}+1)}}{2} \tag{8}$$

Substituting to find out the temporary indicator:

$$Ind_t = \left(M_{e(c_2^x)}\right)^2 \tag{9}$$

The obtained result in (9) will be taken as the variable of indication in the time domain for the detection of the healthy and faulty conditions in the induction motor.

3. Results

3.1. Results in the Frequency Domain

Using the data obtained in the experiments, we have applied the algorithm described in the Section 2.2 in order to obtain the indication variable in the frequency domain, based on the bispectrum of the flux signal. This enabled us to discriminate between the healthy and faulty conditions of an induction motor. The bispectrum has been calculated in a window of 1024 samples, which results in a square matrix, where the number of rows and columns coincides with the data window to be processed, i.e., 1024 × 1024.

We have used the algorithm based on the bispectruminstead of the analysis based on the one-dimensional Fourier transform. The reason is the following: when applying the proposed method using the sum of the mean of the frequency spectrum absolute value, no relative differences were observed between the healthy and the damagedstates if the one-dimensional Fourier transform is used, as mentioned above.

This statement has been checked using sample 0 (position DMA of Table 1) corresponding to the samples of flux signals of the healthy motor and comparing the results with sample 0 (position DMA of Table 2) corresponding to the samples of flux signals of the motor with one broken rotor bar. The obtained results are shown in Figure 2 and Table 5, respectively.
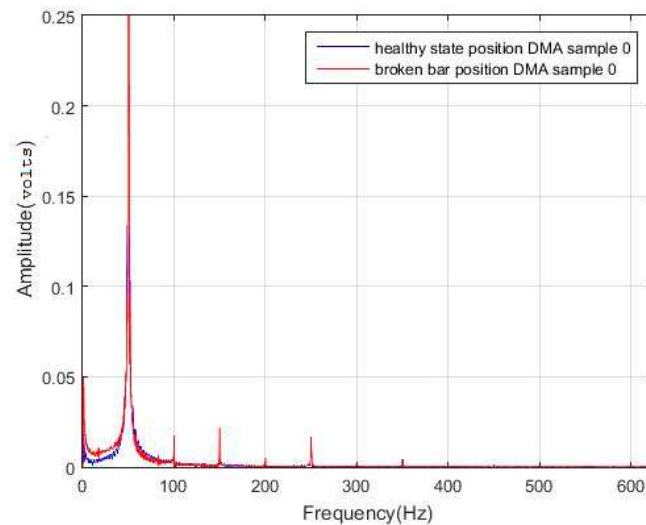
Figure 2. Comparison of the frequency spectra of the flux signals for the healthy state (blue) and for the faulty state with one broken bar (red). Sample 0, DMA position.

Table 5. Obtained results by applying the one-dimensional Fourier Transform and calculating the indicator (Equations (4) and (5)).

Sample	Obtained Indicator in Frequency Domain
0, DMA position, healthy state	$9.1160 \cdot 10^{-4}$
0, DMA position, damage state (one broken bar)	$8.8375 \cdot 10^{-4}$

In Table 5, the difference that exists between both values of the indicator is $2.7857 \cdot 10^{-5}$, which is not significant to reliably discriminate between healthy and faulty conditions. Likewise, in Figure 2, no relevant differences are clearly observed in the spectra of both samplesfor the same position (DMA).

Taking into consideration the previous results, we decided to use the bispectrum of the flux signals. The algorithm based on Equations (4) and (5) was applied to obtain an indication variable that was able to detect differences between the healthy and damaged conditions. Figure 3 shows the bispectrum of the flux signal in the healthy state (sample 0, position DMA) and faulty state (sample 0, position DMA).

As can be seen in Figure 3, the bispectrum has two circles corresponding to fundamental frequency values of the form (f_1, f_2), in this case (0.01,0.01), which corresponds to the frequency of 50 Hz (normalized to 1), depicted in Figure 2, corresponding to the frequency spectrum using the one-dimensional Fourier transform.

Similarly, around these two points there are other four circles which correspond to the frequency values, multiples of the fundamental frequency of 50 Hz. As shown in Figure 3, there are differences between the bispectrum of the flux signal of the healthy motor and of the damaged motor.

These six circles visualized in the contour of the bispectrum appear in all the analyzed samples, both in the healthy and in the faulty state conditions. This can be observed in Figures 4–9.

(**a**)

(**b**)
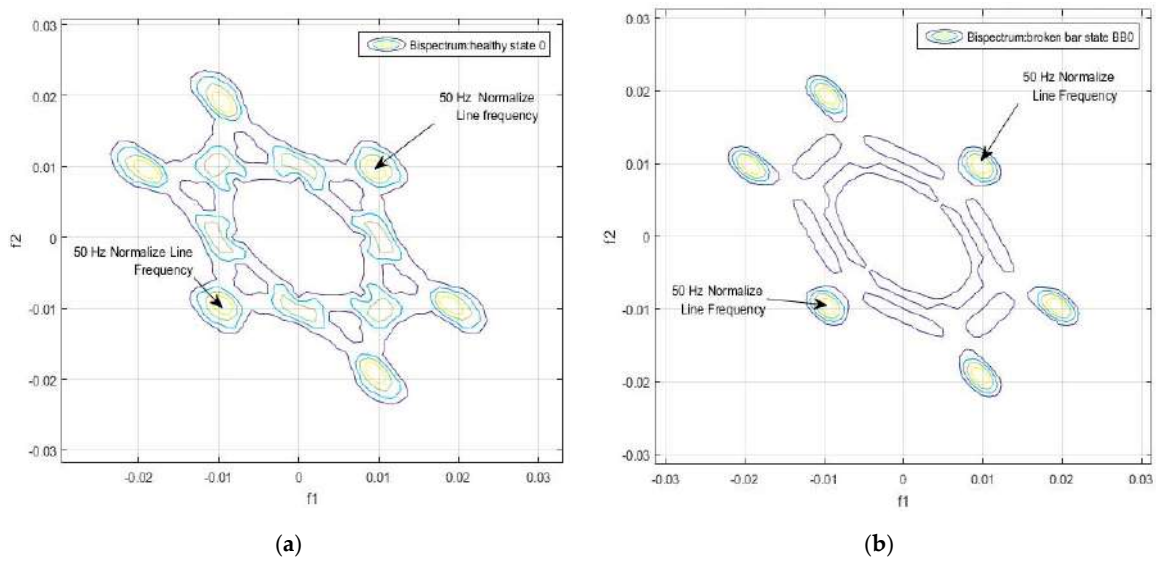
Figure 3. (**a**) Contour of bispectrum of the motor flux signal in healthy condition (sample 0, DMA position) (**b**) Contour of bispectrum of the motor flux signal in faulty condition (sample 0, DMA position).

(**a**)

(**b**)

(**c**)

(**d**)
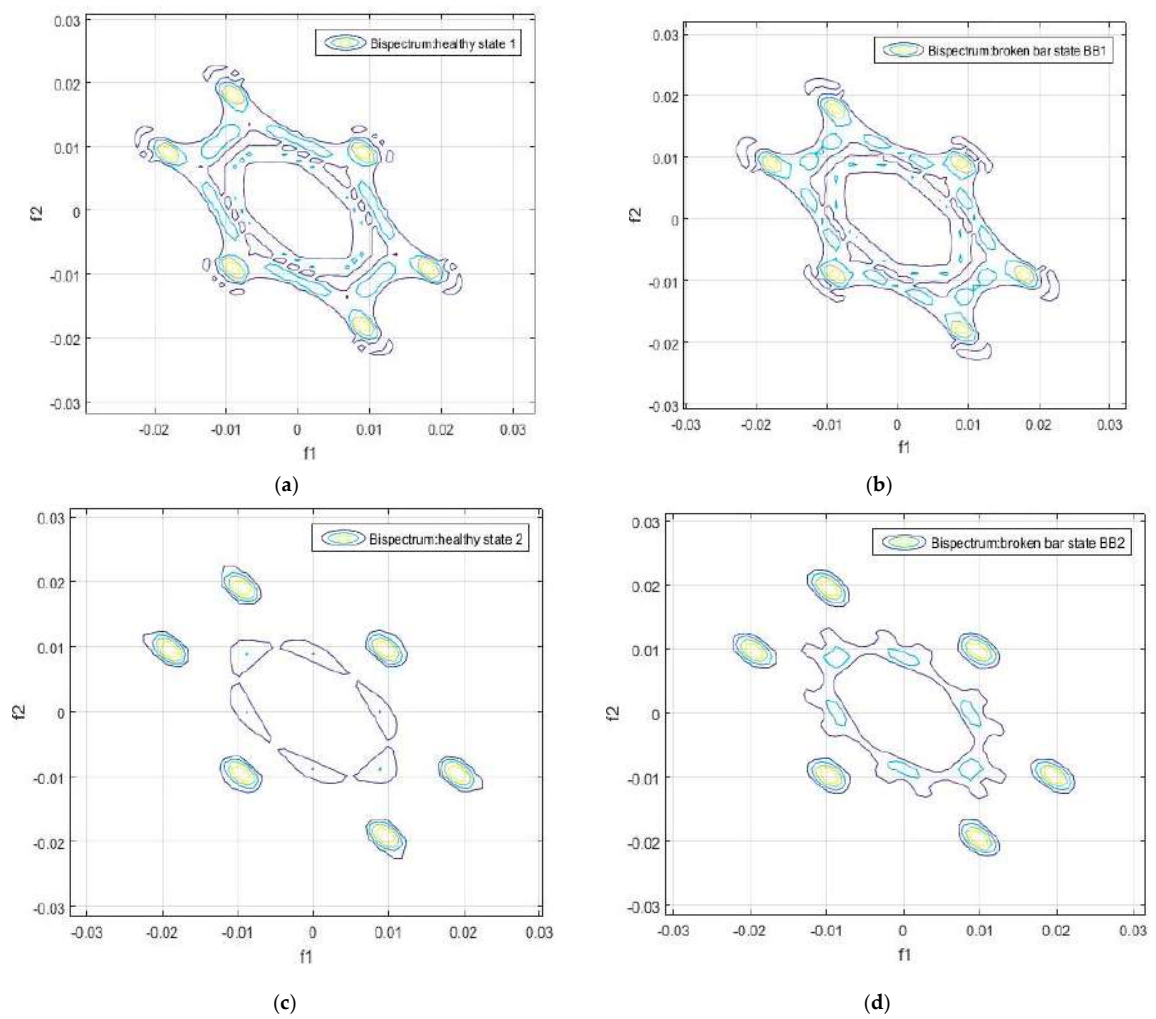
Figure 4. Contour of the bispectrum of the motor flux signal: (**a**) Sample 1 of the healthy motor, (**b**) Sample 1 of the damaged motor, (**c**) Sample 2 of the healthy motor, (**d**) Sample 2 of the damaged motor.
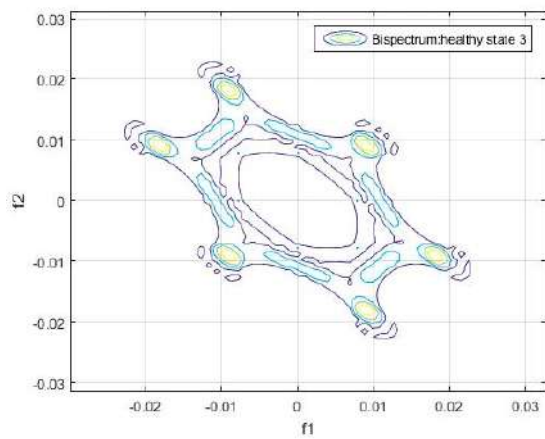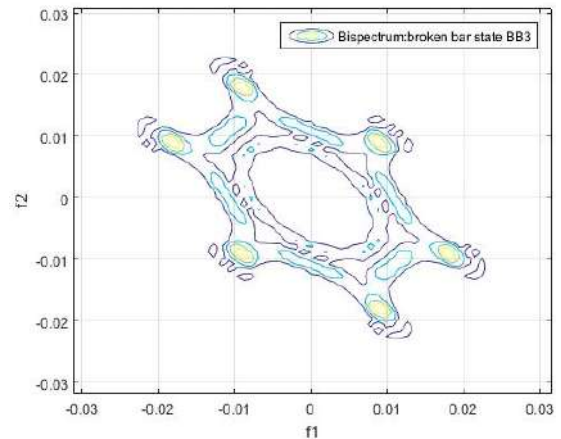
(**a**)   (**b**)

Figure 5. Contour of the bispectrum of the motor flux signal: (**a**) Sample 3 of the healthy motor and (**b**) Sample 3 of the damaged motor.
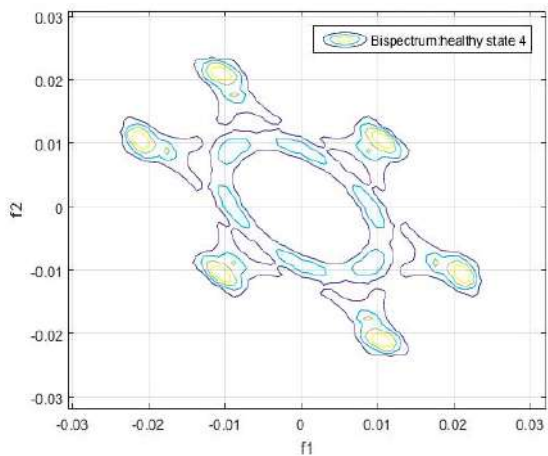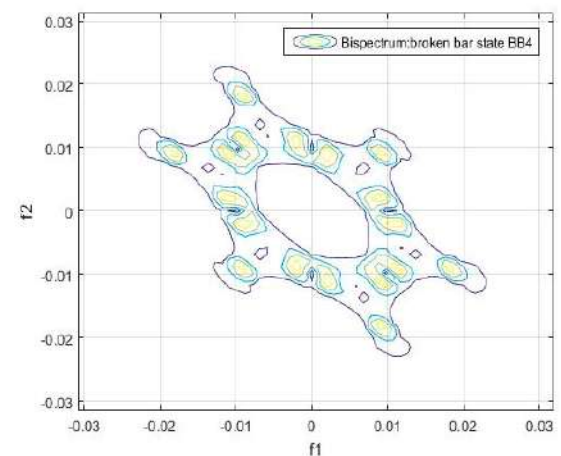
(**a**)   (**b**)

Figure 6. Contour of the bispectrum of the motor flux signal: (**a**) Sample 4 of the healthy motor, (**b**) Sample 4 of the damaged motor.
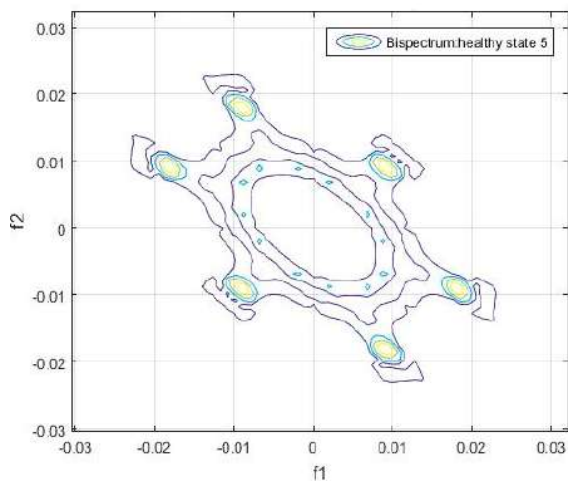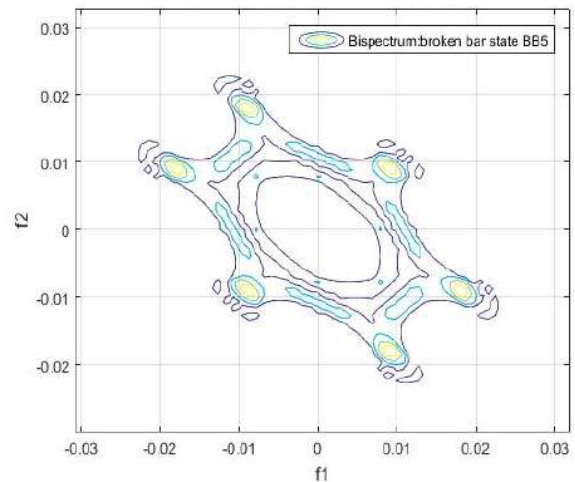
(**a**)   (**b**)

Figure 7. Contour of the bispectrum of the motor flux signal: (**a**) Sample 5 of the healthy motor and (**b**) Sample 5 of the damaged motor.
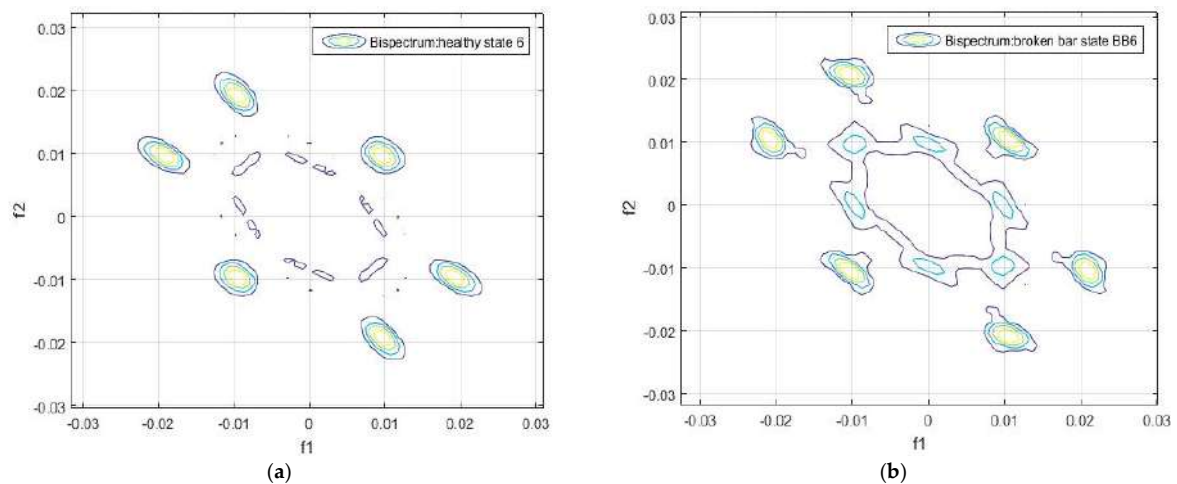
Figure 8. Contour of the bispectrum of the motor flux signal: (**a**) Sample 6 of healthy the motor, (**b**) Sample 6 of the damaged motor.
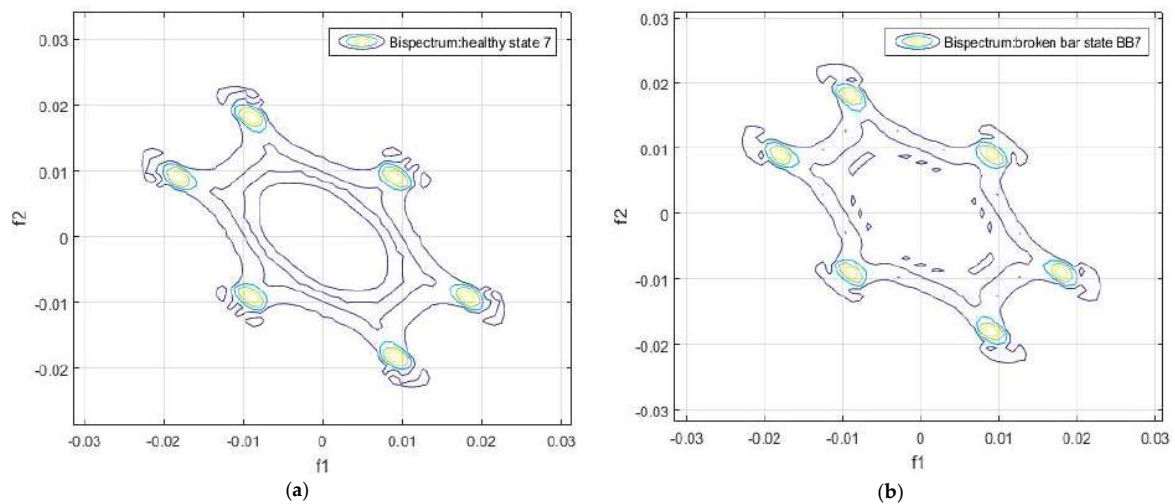
Figure 9. Contour of the bispectrum of the motor flux signal: (**a**) Sample 7 of the healthy motor, and (**b**) Sample 7 of the damaged motor

In Figures 3–6 we show the differences in the bispectrum between the healthy and the damaged motors, for the different positions at which the measurements of the flux signals were taken. Note that in some graphs there are more substantial differences, such as in Figure 3 as well as in Figure 4c,d. The differences depend on the position in which the measurement was taken, as well as on the load, and on the supply, and will also depend on obtaining a more or less significant difference in relation to the value of the indicator in the frequency domain (Equation (5)).

The calculation of the indicator in the frequency domain based on Equations (4) and (5) was performed for the data in Tables 1–4, which correspond to the motor under healthy and faulty conditions. The obtained results are shown in Tables 5 and 6.

Table 6. Results of the indicator in the frequency domain based on Equations (4) and (5) for the data of the experiment with the healthy motor during start-up.

Sample	Position	Load	Speed (r/min)	Torque (Nm)	Supply Voltage (%)	Time (s)	Indicator
0	DMA	NL	988	0.49	60	1	30.38804
2	DM	NL	988	0.49	60	1	27.28881
4	E	NL	987	0.51	60	1	28.56996
6	L	NL	986	0.54	60	1	26.75429

From the results shown in Tables 6 and 7, it can be seen that for similar operating conditions, the indicator in the frequency domain depends on the position of the sensor, as can be seen for samples 0, 4, 8 and 14. In these cases, the relative differencesare appreciable and it is possible to discern between one state and the other. On the other hand, the difference in the values of the indicator for the other positions, such as with samples 2 and 6, is not significant. In any case, the values of the indicator for the faulty condition are always greater than those of the equivalent healthy one.

Table 7. Results of the indicator in the frequency domain based on Equations (4) and (5) for the data of the experiment with the faulty motor with a broken bar, during start-up.

Sample	Position	Load	Speed (r/min)	Torque (Nm)	Supply Voltage (%)	Time (s)	Indicator
0	DMA	NL	985	0.49	60	1	38.15795
2	DM	NL	988	0.49	60	1	28.76003
4	E	NL	987	0.49	60	1	38.77947
6	L	NL	985	0.49	60	1	28.88013
8	DMA	FL	755	5.1	60	1	32.06025
10	DM	FL	750	5	60	1	25.04451
12	E	FL	760	5	60	1	23.42840
14	L	FL	765	5	60	1	41.01978

On the other hand, we show in Tables 8 and 9 show the values of the indicator when the motor works at steady-state (100% of the nominal voltage).

Table 8. Results of the indicatorin the frequency domain based on Equations (4) and (5) for the data of the experiments with the healthy motor at steady state.

Sample	Position	Load	Speed (r/min)	Torque (Nm)	Supply Voltage (%)	Time (s)	Indicator
1	DMA	NL	994	0.49	100	8	1.152108
3	DM	NL	994	0.48	100	8	1.192266
5	E	NL	995	0.51	100	8	0.597756
7	L	NL	995	0.5	100	8	0.726403

Table 9. Results of the indicator in the frequency domain based on Equations (4) and (5) for the data of the experiments with the faulty motor with a broken bar at steady state.

Sample	Position	Load	Speed (r/min)	Torque (Nm)	Supply Voltage (%)	Time (s)	Indicator
1	DMA	NL	994	0.52	100	8	0.842987
3	DM	NL	994	0.53	100	8	0.854711
5	E	NL	994	0.55	100	8	0.975386
7	L	NL	997	0.58	100	8	0.709328
9	DMA	FL	940	6.2	100	8	3.707399
11	DM	FL	940	6.13	100	8	3.254082
13	E	FL	940	6.1	100	8	3.979508
15	L	FL	940	6.09	100	8	2.998851

From the results shown in Tables 8 and 9, it is noted that the differences between the values of the indicator in the frequency domain for healthy and faulty conditionsare not significant when the motor works at steady state. This may be due to the fact that, during startup, certain harmonics vary in frequency and amplitude [9]. This does not happen under the steady state regime, during which the harmonics maintain well-defined frequencies and amplitudes, as long as the load level does not change.

From the results shown in the above tables, it can be deduced that, under the healthy condition, the indicator in the frequency domainreachesa maximum value of 30.38804, and the minimum value is 0.597756. On the other hand, the indicator for the faulty condition (motor with a broken bar) ranges between 0.709328 and 41.0198. The value of the indicator for the healthy condition never exceeds the value of 31 for all measurements.

All the comparisons related to the values of the indicator have been carried out between measurements that were obtained under similar operating conditions. This leads to the conclusion that the position of the sensor plays a crucial role and that significant differences are not obtained in every position.

3.2. Results in the Time Domain

Taking into consideration the previous results obtained in the frequency domain, a new algorithm based on the square value of the median of the autocovariance matrix of the flux signal was proposed, as described in Equation (8). This gives a fault detection indicator in the time domain. The results obtained after applying this last algorithmare shown in Figure 10, and they are summarized in Tables 10–13.
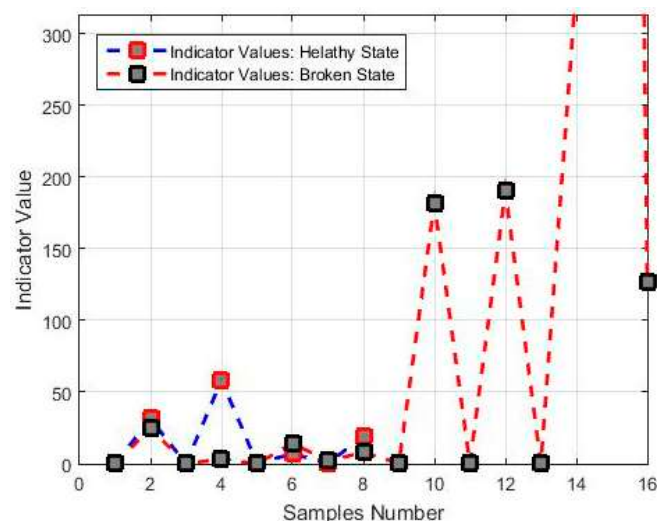
Figure 10. Values of the indicator in the time domain for all the samples used in the experiments.

Table 10. Results of the indicatorin the time domain, based on Equations (6)–(8), for the data of the experiments with the healthy motor during startup.

Sample	Position	Load	Speed (r/min)	Torque (Nm)	Supply Voltage (%)	Time (s)	Indicator
0	DMA	NL	988	0.49	60	1	0.071959
2	DM	NL	988	0.49	60	1	0.027691
4	E	NL	987	0.51	60	1	0.435514
6	L	NL	986	0.54	60	1	0.537173

The previous results show that there is a notable difference between the values of the indicator when the motor works at steady-state (100% of the rated supply), but not during the start-up, when it works at 60% of the rated supply.

Table 11. Results of the indicator in the time domain, based on Equations (6)–(8), for the data of the experiments with the motor with one broken bar during startup.

Sample	Position	Load	Speed (r/min)	Torque (Nm)	Supply Voltage (%)	Time (s)	Indicator
0	DMA	NL	985	0.49	60	1	0.003537
2	DM	NL	988	0.49	60	1	0.009451
4	E	NL	987	0.49	60	1	0.009606
6	L	NL	985	0.49	60	1	2.046191
8	DMA	FL	755	5.1	60	1	0.370122
10	DM	FL	750	5	60	1	0.033363
12	E	FL	760	5	60	1	0.005345
14	L	FL	765	5	60	1	2227.965

Table 12. Results of the indicator, based on Equations (6)–(8), for the data of the healthy motor experiments under the steady state regime.

Sample	Position	Load	Speed (r/min)	Torque (Nm)	Supply Voltage (%)	Time (s)	Indicator
1	DMA	NL	994	0.49	100	8	31.38462
3	DM	NL	994	0.48	100	8	58.30218
5	E	NL	995	0.51	100	8	6.948441
7	L	NL	995	0.5	100	8	19.03505

Table 13. Results of the indicator, based on Equations (6)–(8), for the data of the faulty motor experiments under the steady state regime.

Sample	Position	Load	Speed (r/min)	Torque (Nm)	Supply Voltage (%)	Time (s)	Indicator
1	DMA	NL	994	0.52	100	8	24.67371
3	DM	NL	994	0.53	100	8	3.342042
5	E	NL	994	0.55	100	8	14.26557
7	L	NL	997	0.58	100	8	7.897072
9	DMA	FL	940	6.2	100	8	181.7043
11	DM	FL	940	6.13	100	8	190.5501
13	E	FL	940	6.1	100	8	334.8858
15	L	FL	940	6.09	100	8	126.3791

4. Discussion

We group the previous results with respect to the flux sensor location in order to compare the indicator values obtained in the frequency and time domains, for different fault conditions and operating regimes, see Tables 14 and 15.

Table 14. Results of the time and frequency indicators for the DMA position.

Sample	Position	Load	Speed (r/min)	Torque (Nm)	Supply Voltage (%)	Time (s)	Frequency Indicator	Time Indicator	State
0	DMA	NL	988	0.49	60	1	30.38804	0.071959	Healthy
	DMA	NL	994	0.49			38.15795	0.003537	Faulty
1	DMA	NL	994	0.49	100	8	1.152108	31.38462	Healthy
	DMA	NL	994	0.52			0.842987	24.67371	Faulty

For the sample corresponding to the DMA position, the difference of the indicators values is noticeable at the startup, when working in the frequency domain. The difference in the temporal indicator between the healthy and faulty condition is preceded by a multiplication factor of 20. When the motor works at steady-state (with 100% of the rated supply), the difference in the values of the

time indicator is appreciable. At startup, the indicator in the frequency domain is always greater for the faulty state; the opposite occurs with the temporary indicator at steady-state.

Table 15. Results of the time and frequency indicators for the DM position.

Sample	Position	Load	Speed (r/min)	Torque (Nm)	Supply Voltage (%)	Time (s)	Frequency Indicator	Time Indicator	State
2	DM	NL	988	0.49	60	1	27.28881	0.027691	Healthy
	DM	NL	988	0.49			28.76003	0.009451	Faulty
3	DM	NL	994	0.48	100	8	1.192266	58.30218	Healthy
	DM	NL	994	0.53			0.854711	3.342042	Faulty

For the sample corresponding to the DM position, the difference of the indicators values at startup is not as noticeable compared to the values obtained at the DMA position, when working in the frequency domain. The difference in the time indicator between the healthy and damaged state is preceded by a multiplication factor of 3. When the motor works at steady-state, the difference of the time indicator is as significant as for the DMA position. At startup, the indicator in the frequency domain is always greater for the faulty condition; the opposite occurs with the temporal indicator at steady-state.

For the sample corresponding to the E position, there is a significant difference between the values of the indicator in the frequency domain at the startup, as with the DMA position. The difference in the temporal indicator between the healthy and the faulty condition is preceded by a multiplication factor of 45. At steady-state, with 100% of the rated voltage, the differences of the temporal indicatorsare significant. At startup, the indicator in the frequency domain is always greater for the faulty state; the same occurs in this case for the time indicator at steady-state, contrary to what happens in positions DM and DMA.

For the sample corresponding to the L position, the difference of the indicator at start-up is not clearly noticeable when working in the frequency domain as with the DMA and E sensor positions. The difference in the temporal indicator between the healthy and the faulty conditions is preceded by a multiplication factor of 4. When working at steady-state, the difference of the temporal indicator is significant. The indicator in the frequency domain is higher for the faulty state during start-up; the opposite occurs with the temporal indicator at steady-state.

From the results obtained in Tables 14–17, for the four sensor positions analyzed (DMA, DM, E, L), the following can be concluded:

- The indicator in the frequency domain for the healthy condition varies in a range of $26 \leq Ind_f \leq 30$, and for the faulty condition it varies from $28 \leq Ind_f \leq 38$ during start-up. In this regime, the values of the indicator in the frequency domain for the healthy state are always lower than the corresponding values for the faulty state.
- When the motor operates at steady state, the indicator in the time domain ranges from $6 \leq Ind_t \leq 58$ for the healthy condition, and between $3 \leq Ind_t \leq 24$ for the faulty one.
- The best results are obtained when the measurement is carried out in the DMA position, since the values of both indicators are within the limits of obtained values.
- In order to discern between the healthy and faulty conditions, the signal obtained from the flux sensor must first be evaluated during the start-up, for which the indicator is calculated based on the analysis in the frequency domain. At steady-state, the signal should be better evaluated using the time indicator.
- A diagnostic decision based on the limit values for both indicators should be finally adopted. In order to obtain a more reliable conclusion of the rotor condition, the two indicators must be evaluated.

Table 16. Results of the time and frequency indicators for the E position.

Sample	Position	Load	Speed (r/min)	Torque (Nm)	Supply Voltage (%)	Time (s)	Frequency Indicator	Time Indicator	State
4	E	NL	987	0.51	60	1	28.56996	0.435514	Healthy
	E	NL	987	0.49			38.77947	0.009606	Faulty
5	E	NL	995	0.51	100	8	0.597756	6.948441	Healthy
	E	NL	994	0.55			0.975386	14.26557	Faulty

Table 17. Results of the time and frequency indicators for the L position.

Sample	Position	Load	Speed (r/min)	Torque (Nm)	Supply Voltage (%)	Time (s)	Frequency Indicator	Time Indicator	State
6	L	NL	986	0.54	60	1	26.75429	0.537173	Healthy
	L	NL	985	0.49			28.88013	2.046191	Faulty
7	L	NL	995	0.5	100	8	0.726403	19.03505	Healthy
	L	NL	997	0.58			0.709328	7.897072	Faulty

The accuracy of the proposed method as a classification of the condition of the damaged-healthy state of the induction motor depends, to a large extent, on the relative position where the measurement is made. Although regardless of the obtained results and the relative positions of each measurement, it can be noted that the average of the indication values obtained for the indicator in the frequency domain never exceeds the value of 28.250275 for the healthy state and 33.644395 for the damaged case. Similarly, if the analysis is performed for the indicator in the time domain, we have an average value of 28.91757275 for the healthy state, and of 12.5445985 for the faulty one. That is, in an a priori analysis, a result of the indication variable greater than these values, both for the frequency and time domains, can be concluded as an affirmative diagnosis of failure, as shown for the cases of the DMA and E positions.

5. Conclusions

The spectral analysis based on the bispectrum of the flux signals captured at external positions of an induction motor was proposed in order to provide a criterion to discriminate between healthy and faulty rotor conditions in induction motors.

To this end, an algorithm based on the sum of the mean value of the bispectrum module of the induction motor flux signal was theoretically described and implemented.

To demonstrate the results experimentally, several real samples of flux signals were registered, both for healthy and faulty conditions of the rotor cage, and for different operating conditions.

The proposed algorithms are based on the sum of the mean value of the bispectrum module of the flux signal and on the square value of the median of the autocovariance function. The results have shown they can be considered as indicators that enable us to provide a criterion for the discrimination between healthy and faulty conditions of the motor.

We can also conclude that the position where the measurement of the flux signal is carried out is an important factor, as well as the operating regime of the motor.

In conclusion, the study carried out in this paper implies that, with the analysis of stray flux signals, it is possible to obtain indicator variables that discriminate between faulty and healthy motors, which is an improvement and a complementtoexisting results obtained by using classical techniques for the diagnosis of failures in electrical machines and, in the future, may be a contribution to the development of portable industrial diagnostic devices.

As future work, it is proposed to carry out an estimation analysis of the accuracy of the proposed method and to obtain an algorithm for the optimization of the relative position of the flux sensor at the time of the measurement.

Conflicts of Interest: The authors declare no conflict of interest. The funders had no role in the design of the study; in the collection, analyses, or interpretation of data; in the writing of the manuscript, or in the decision to publish the results.

References

1. Nandi, S.; Toliyat, H.A.; Li, X. Condition monitoring and fault diagnosis of electrical motors—A review. *IEEE Trans. Energy Convers.* **2005**, *20*, 719–729. [CrossRef]

2. Henao, H.; Capolino, G.-A.; Fernández-Cabanas, M.; Filippetti, F.; Bruzzese, C.; Strangas, E.; Pusca, R.; Estima, J.; Riera-Guasp, M.; Kia, S.H. Trends in fault diagnosis for electrical machines. *IEEE Ind. Electron. Mag.* **2014**, *8*, 31–42. [CrossRef]

3. Riera-Guasp, M.; Antonino-Daviu, J.A.; Capolino, G. Advances in electrical machine, power electronic, and drive condition monitoring and fault detection: State of the art. *IEEE Trans. Ind. Electron.* **2015**, *62*, 1746–1759. [CrossRef]

4. Chen, J.; Sufei, L.; Thomas, G.H. A review of condition monitoring of induction motors based on stray flux. In Proceedings of the IEEE Energy Conversion Congress and Exposition (ECCE), Cincinnati, OH, USA, 1–5 October 2017. [CrossRef]

5. Romary, R.; Pusca, R.; Lecointe, J.P.; Brudny, J.F. Electrical machines fault diagnosis by stray flux analysis. In Proceedings of the IEEE Workshop Electrical Machines Design, Control and Diagnosis (WEMDCD), Paris, France, 11–12 March 2013; pp. 245–254.

6. Cabanas, M.F.; Norniella, J.G.; Melero, M.G.; Rojas, C.H.; Cano, J.M.; Pedrayes, F.; Orcajo, G.A. Detection of Stator Winding InsulationFailures: On–line and Off–line Tests. In Proceedings of the IEEE Workshop Electrical Machines Design, Control and Diagnosis (WEMDCD), Paris, France, 11–12 March 2013; pp. 208–217.

7. Pusca, R.; Demian, C.; Mercier, D.; Lefevre, E.; Romary, R. An improvement of a diagnosis procedure for AC machines using two external flux sensors based on a fusion process with belief functions. In Proceedings of the IECON 2012—38th Annual Conference on IEEE Industrial Electronics Society, Montréal, QC, Canada, 25–28 October 2012; pp. 5096–5101.

8. Frosini, L.; Borin, A.; Girometta, L.; Venchi, G. A novel approach to detect short circuits in low voltage induction motor by stray flux measurement. In Proceedings of the 2012 XXth International Conference on Electrical Machines, Marseille, France, 2–5 September 2012; pp. 1536–1542.

9. Ramirez-Nunez, J.A.; Antonino-Daviu, J.A.; Climente-Alarcón, V.; Quijano-López, A.; Razik, H.; Osornio-Rios, R.A.; Romero-Troncoso, R.D. Evaluation of the Detectability of Electromechanical Faults in Induction Motors Via Transient Analysis of the Stray Flux. *IEEE Trans. Ind. Appl.* **2018**, *54*, 4324–4332. [CrossRef]

10. Park, Y.; Yang, C.; Kim, J.; Kim, H.; Lee, S.B.; Gyftakis, K.N.; Panagiotou, P.; Kia, S.H.; Capolino, G.A. Stray Flux Monitoring for Reliable Detection of Rotor Faults under the Influence of Rotor Axial Air Ducts. *IEEE Trans. Ind. Electron.* **2018**. [CrossRef]

11. Iglesias-Martínez, M.E.; Fernández de Córdoba, P.; Antonino-Daviu, J.A.; Conejero, J.A. Detection of Bar Breakages in Induction Motor via Spectral Subtraction of Stray Flux Signals. In Proceedings of the XIII IEEE International Conference on Electrical Machines (ICEM), Alexandroupoli, Greece, 3–6 September 2018; pp. 1796–1802. [CrossRef]

12. Panagiotou, P.A.; Arvanitakis, I.; Lophitis, N.; Antonino-Daviu, J.A.; Gyftakis, K.N. Analysis of Stray Flux Spectral Components in Induction Machines under Rotor Bar Breakages at Various Locations. In Proceedings of the XIII IEEE International Conference on Electrical Machines (ICEM), Alexandroupoli, Greece, 3–6 September 2018; pp. 2345–2351.

13. Mendel, J.M. Tutorial on higher-order statistics (spectra) in signal processing and system theory: Theoretical results and some applications. *IEEE Proc.* **1991**, *79*, 278–305. [CrossRef]

14. Nikia, C.L.; Mendel, J.M. Signal Processing with higher-order spectra. *IEEE Signal Process. Mag.* **1993**, *10*, 10–37. [CrossRef]

15. Swami, A.; Mendel, J.M.; Nikias, C.L. *Higher-Order Spectral Analysis Toolbox User's Guide, Version 2*; UnitedSignals & Systems, Inc.: Ranco Palos Verde, CA, USA, 2001.

16. Vaseghi, S.V. *Advanced Digital Signal Processing and Noise Reduction*, 4th ed.; John Wiley & Sons: Hoboken, NJ, USA, 2008.

17. Murua, A.; Sanz-Serna, J.M. Vibrational resonance: A study with high-order word-series averaging. *Appl. Math. Nonlinear Sci.* **2016**, *1*, 239–246. [CrossRef]

POSITIVE CURVATURE CAN MIMIC A QUANTUM

J.M. Isidro[1,a], **J.L.G. Santander**[2,b] and **P. Fernández de Córdoba**[1,c]

[1]Instituto Universitario de Matemática Pura y Aplicada,
Universidad Politécnica de Valencia, Valencia 46022, Spain
[2]Departamento de Ciencias Experimentales y Matemáticas,
Universidad Católica de Valencia, Valencia 46002, Spain
[a]joissan@mat.upv.es, [b]jlgonzalez@mat.upv.es,
[c]pfernandez@mat.upv.es

Abstract We elaborate on the existing idea that quantum mechanics is an emergent phenomenon, in the form of a coarse–grained description of some underlying deterministic theory. We apply the Ricci flow as a technical tool to implement dissipation, or information loss, in the passage from an underlying deterministic theory to its emergent quantum counterpart. A key ingedient in this construction is the fact that the space of physically inequivalent quantum states (either pure or mixed) has positive Ricci curvature. This leads us to an interesting thermodynamical analogy of emergent quantum mechanics.

1   Introduction

Quantum mechanics as a statistical theory has been argued to *emerge* from an underlying deterministic theory [1]. Specifically, for any quantum system there exists at least one deterministic model that reproduces all its dynamics after prequantisation. This existence theorem has been extended to include cases characterised by sets of commuting beables [2]; it has also been complemented with an explicit dynamical theory [3].

Mechanisms have been presented [1, 2, 3] to explain the passage from a deterministic theory to a probabilistic theory. Usually they are based on a dynamical system, the phase–space trajectories of which possess suitably located attractors (*e.g.*, at the eigenvalues of the given quantum Hamiltonian, or at certain configurations of the density matrix). These mechanisms can be thought of as an existence theorem, in that every quantum system (with a finite–dimensional Hilbert space) possesses at least one deterministic system underlying it.

On the other hand there are plenty of dissipation equations in physics and mathematics, equations implementing the information loss that is characteristic of the passage from classical to quantum. The heat equation immediately comes to mind.

In this contribution we develop a deterministic model exhibiting dissipation, from which quantum mechanics emerges naturally. Given a quantum mechanics with a complex d–dimensional Hilbert space, the Lie group $SU(d)$ represents classical canonical transformations on the projective space $\mathbb{CP}^{d-1}$ of quantum states. Let R stand for the Ricci flow [4] of the manifold $SU(d-1)$ down to one point, and let P denote the projection from the Hopf bundle onto its base $\mathbb{CP}^{d-1}$. Then the underlying deterministic

1

model we propose here is the Lie group $SU(d)$, acted on by the operation PR.

We would like to mention that additional quantum–mechanical applications of the Ricci flow have been reported in [5, 6, 7, 8]; deterministic models of quantum mechanics and closely related topics are dealt with at length in [9, 10, 11, 12].

2 The Ricci flow as a (nonlinear) heat flow

Given an n–dimensional manifold $\mathbb{M}$ endowed with the Riemannian metric g_{ij}, the equation governing the (unnormalised) Ricci flow reads

$$\frac{\partial g_{ij}}{\partial t} = -2R_{ij}, \qquad i,j = 1, \ldots, n, \qquad t \geq 0, \tag{1}$$

where t is an evolution parameter (not a coordinate on $\mathbb{M}$), and R_{ij} is the Ricci tensor corresponding to the metric g_{ij}. Informally one can say that Ricci–flat spaces remain unchanged under the flow, while positively curved manifolds contract and negatively curved manifolds expand under the flow. We will be interested in the particular case of Einstein manifolds, where the Ricci tensor and the metric are proportional:

$$R_{ij} = \kappa g_{ij}, \tag{2}$$

with κ a constant. Since the metric g_{ij} is assumed positive definite, the sign of κ equals the sign of the Ricci tensor. Relevant examples of positively curved Einstein manifolds are complex projective space $\mathbb{CP}^N$ and the special unitary group $SU(N)$, both of which will play an important role in what follows. Their respective metrics are the Fubini–Study metric [13] and the Killing–Cartan metric [14].

Under the Ricci flow, the contraction of a whole manifold down to a point can play the role of a dissipative mechanism. One hint that this intuition is correct comes from the following example. Consider a 2–dimensional manifold endowed with the isothermal coordinates x and y. Then the metric reads

$$\mathrm{d}s^2 = \mathrm{e}^{-f(x,y)} \left(\mathrm{d}x^2 + \mathrm{d}y^2 \right). \tag{3}$$

Allowing the metric to depend also on the evolution parameter t, the Ricci flow equation (1) becomes

$$\frac{\partial f}{\partial t} = \nabla^2 f. \tag{4}$$

The above is formally identical to the heat equation, with one important difference, however: the Laplacian ∇^2 is computed with respect to the metric (3), in which it reads

$$\nabla^2 f = \mathrm{e}^f \left(\frac{\partial^2 f}{\partial x^2} + \frac{\partial^2 f}{\partial y^2} \right). \tag{5}$$

Regardless of the nonlinearity of (5), the fact that the Ricci–flow equation can be recast as a generalisation of the heat equation is a clear hint that a dissipative mechanism is at work.

3   The deterministic model for pure states

In this section we will consider a quantum system with a finite, complex d–dimensional Hilbert space of quantum states, that we can identify with $\mathbb{C}^d$. Let $\mathcal{C}$ denote the phase space of the classical model, the quantisation of which gives the quantum system under consideration. For our purposes the precise nature of this classical model on $\mathcal{C}$ is immaterial. Now unitary transformations on Hilbert space are the quantum counterpart of canonical transformations on classical phase space $\mathcal{C}$. We may thus regard $SU(d)$ as representing classical canonical transformations, $\mathbb{C}^d$ being the carrier space of this representation. We are considering, as in ref. [1], the simplified case of a finite–dimensional Hilbert space. Without loss of generality we will restrict to those canonical transformations that are represented by unitary matrices with determinant equal to 1.

Now quantum states are unit rays rather than vectors, so in fact the true space of inequivalent quantum states is the complex projective space $\mathbb{CP}^{d-1}$. The latter can be regarded as a homogeneous manifold:

$$\mathbb{CP}^{d-1} = \frac{SU(d)}{SU(d-1) \times U(1)}. \tag{6}$$

In this picture we have $SU(d)$ as the total space of a fibre bundle with typical fibre $SU(d-1) \times U(1)$ over the base manifold $\mathbb{CP}^{d-1}$. The projection map

$$\pi : SU(d) \longrightarrow \mathbb{CP}^{d-1}, \qquad \pi(w) := [w] \tag{7}$$

arranges points $w \in SU(d)$ into $SU(d-1) \times U(1)$ equivalence classes $[w]$.

Classical canonical transformations as represented by $SU(d)$ act on the Hilbert space $\mathbb{C}^d$. This descends to an action α of $SU(d)$ on $\mathbb{CP}^{d-1}$ as follows:

$$\alpha : SU(d) \times \mathbb{CP}^{d-1} \longrightarrow \mathbb{CP}^{d-1}, \quad \alpha(u, [v]) := [uv]. \tag{8}$$

Here we have $u \in SU(d)$, $[v] \in \mathbb{CP}^{d-1}$, and uv denotes $d \times d$ matrix multiplication. One readily checks that this action is well defined on the equivalence classes under right multiplication by elements of the stabiliser subgroup $SU(d-1) \times U(1)$. This allows one to regard quantum states as equivalence classes of classical canonical transformations on $\mathcal{C}$. Physically, u in (8) denotes (the representative matrix of) a canonical transformation on $\mathcal{C}$, and $[v]$ denotes the equivalence class of (representative matrices of) the canonical transformation v or, equivalently, the quantum state $|v\rangle$.

In the picture just sketched, two canonical transformations are equivalent whenever they differ by a canonical transformation belonging to $SU(d-1)$, and/or whenever they differ by a $U(1)$–transformation. Modding out by $U(1)$ has a clear physical meaning: it is the standard freedom in the choice of the phase of the wavefunction corresponding to the matrix $v \in SU(d)$. Modding out by $SU(d-1)$ also has a physical meaning: canonical transformations on the $(d-1)$–dimensional subspace $\mathbb{C}^{d-1} \subset \mathbb{C}^d$ are a symmetry of v. Therefore the true quantum state $|v\rangle$ is obtained from $v \in SU(d)$ after modding out by the stabiliser subgroup $SU(d-1) \times U(1)$.

We conclude that this picture contains some of the elements identified as responsible for the passage from a classical world (canonical transformations) to a quantum

world (equivalence classes of canonical transformations, or unit rays within Hilbert space). This is so because some kind of dissipative mechanism is at work, through the emergence of orbits, or equivalence classes. However the projection (7) is an on/off mechanism. Instead, one would like to see dissipation occurring as a flow along some continuous parameter. To this end we need some deterministic flow governed by some differential equation.

We claim that we can render the projection (7) a dissipative mechanism governed by some differential equation. This equation will turn out to be the Ricci flow (1). Proof of this statement follows.

The Lie group $SU(d-1) \times U(1)$ is compact, but it is not semisimple due to the Abelian factor $U(1)$. Leaving the $U(1)$ factor momentarily aside, $SU(d-1)$ is semisimple and compact. As such it qualifies as an Einstein space with positive scalar curvature with respect to the Killing–Cartan metric [14]. Now eqn. (1) ensures that $SU(d-1)$ contracts to a point under the Ricci flow.

However the $U(1)$ factor renders $SU(d-1) \times U(1)$ nonsemisimple. As a consequence, the Killing–Cartan metric of $SU(d-1) \times U(1)$ has a vanishing determinant [14]. The Ricci flow can still cancel the $SU(d-1)$–factor within $SU(d)$, but not the $U(1)$ factor. After contracting $SU(d-1)$ to a point we are left with the space $U(1) \times \mathbb{CP}^{d-1}$ or, more generally, with a $U(1)$–bundle over the base manifold $\mathbb{CP}^{d-1}$. This $U(1)$–bundle over $\mathbb{CP}^{d-1}$ is the Hopf bundle, where the total space is the sphere S^{2d-1} in $2d-1$ real dimensions [13]. This sphere falls short of being the true space of quantum states by the unwanted $U(1)$–fibre, that cannot be removed by the Ricci flow. It can, however, be done away with by projection P from the total space of the bundle down to its base. The combined operation "Ricci flow R, followed by projection P" acts on the stabiliser subgroup $SU(d-1) \times U(1)$ of the initial $SU(d)$ and leaves us with $\mathbb{CP}^{d-1}$ as desired. Therefore this combined operation PR acts in the same way as the projection π in (7). As opposed to the latter, however, this combined operation PR provides us with a differential equation that implements dissipation along a continuous parameter, at least along most of the way.

4 The deterministic model for mixed states

We have so far dealt only with pure quantum states. In trying to extend our previous analysis to mixed quantum states, we must first answer the following two questions: What is the manifold of mixed quantum states, and what sign does its Ricci scalar have? Mixed states can be represented by density matrices D, expressible as

$$D = \sum_{j=1}^{n} |v_j\rangle p_j \langle v_j|, \qquad n > 1, \tag{9}$$

the $p_j > 0$ being the probability of finding the system in the pure state $|v_j\rangle$. Above we assume that $n > 1$, *i.e.*, that the state considered is not pure but truly mixed. The p_j must add up to unity,

$$\sum_{j=1}^{n} p_j = 1. \tag{10}$$

4

It turns out that the manifold of density matrices is a norm–closed (with respect to the trace norm), convex subset of the unit sphere of the space of trace–class operators (see, *e.g.*, [15]). In the finite–dimensional setup considered here, all operators are trace class, and we are left with a convex subset of the unit sphere of the space of $d \times d$ Hermitian matrices. Now the space of $d \times d$ Hermitian matrices has (real) dimension $d^2 - 1$, so its unit sphere is $d^2 - 2$ (real) dimensional. The manifold of mixed states is a convex subset of the real sphere S^{d^2-2}. In particular, the latter has positive Ricci curvature. On the other hand, the N–dimensional sphere S^N equals the homogeneous manifold $SO(N + 1)/SO(N)$, so our manifold of mixed quantum states is a convex subset of

$$S^{d^2-2} = \frac{SO(d^2 - 1)}{SO(d^2 - 2)}. \tag{11}$$

As in the case of pure states, the special orthogonal groups in the numerator and in the denominator above carry positive Ricci curvature with respect to the corresponding Killing–Cartan metric [14].

Now eqn. (11) differs very little from (6), that we discussed at length in the case of pure quantum states. One difference between these two equations is that (6) contains the unitary groups, while (11) contains the special orthogonal groups. Another difference is that the Abelian factor $U(1)$ in the denominator of (6) has disappeared from (11) (one could still mod out the right–hand side of (11) by the discrete group $\mathbb{Z}_2$ in order to obtain real projective space, but the latter is not related to the space of density matrices). One final difference between the pure and the mixed case is that the latter does not have the full left–hand side of (11) as the space of quantum states, but only a convex subset thereof.

All this notwithstanding, these three differences do not suffice to prevent the analysis (and the ensuing conclusions) of the case of pure quantum states from applying to the case of mixed quantum states as well. It is interesting to observe that mixed quantum states are actually simpler to deal with than pure states, because the absence of the Abelian factor in the denominator of (11) allows one to dispense with the projection P from the Hopf bundle—in fact, in the mixed case there is no Hopf bundle at all.

Having seen that the case of mixed quantum states does not differ substantially from that of pure states, for the rest of this contribution we will concentrate on pure quantum states.

5   Positive curvature mimics a quantum

Our starting point was the observation that canonical transformations on classical phase space are implemented quantum–mechanically as unitary transformations on the Hilbert space of quantum states. In our finite–dimensional setup, this gave rise to a natural action of $SU(d)$ on $\mathbb{C}^d$. This action provided us with the building blocks to construct the deterministic system that we take to underlie the given quantum mechanics. Next, different pieces of classical information (elements of $SU(d)$, or classical canonical transformations) were arranged into quantum equivalence classes (points on $\mathbb{CP}^d$, or quantum states): this procedure implements information loss, or dissipation. Quantum states thus arose as equivalence classes of canonical transformations on classical phase

space. However, dissipation was not implemented by means of the usual projection (7) (an on/off mechanism), but rather by means of the Ricci flow (followed by the projection P). The rationale was that the Ricci flow provided us with a a deterministic mechanism governed by a dissipative differential equation, that can be understood as a flow along a continuous parameter.

In a nutshell, our deterministic model is the group manifold $SU(d)$, acted on by the combined operation PR described above. Here R stands for the Ricci flow of $SU(d-1)$ down to one point, and P stands for the projection from the Hopf bundle with total space S^{2d-1} onto its base $\mathbb{CP}^{d-1}$.

The previous conclusions can be compactly recast, somewhat in the style of newspaper headlines, as *positive curvature mimics a quantum* [16, 17]. This raises the question, how about negative curvature? From what was said above it should be clear that the answer is negative: negative curvature *cannot* mimic a quantum, since negative curvature causes expansion, rather than contraction to a point. Temporarily abandoning our geometrical stance, let us take a brief thermodynamical detour that will lend further support to our statement concerning negative curvature. Thermodynamics is a coarse–grained version of an underlying microscopic theory, namely, statistical mechanics. Coarse–graining the notion of mechanical energy in statistical mechanics gives rise to the thermodynamical notion of heat. In our setup, the analogue of the heat equation is the Ricci flow equation. Admittedly, the classical heat equation is linear while the Ricci flow equation is not, but this difference will play no role here. In fact, the analogy between these two equations goes so far, that the Ricci flow equation (1) can actually be derived from a functional $\mathcal{F}$, called Perelman's functional [4], which happens to be a monotonically increasing function of the time t. Therefore $\mathcal{F}$ qualifies as an entropy. Now heat flow occurs from higher temperature to lower temperature; such a heat flow is accompanied by an increase in entropy. This reveals what the thermodynamical analogue of negative curvature must be: heat flowing from *lower* temperature to *higher* temperature. This is clearly unphysical. Thus thermodynamics meets geometry in the statement that negative curvature cannot mimic a quantum.

We would also like to point out that a related form of coarse–graining has been put forward [18] in order to explain the emergence of quantum mechanics from an underlying deterministic theory. In fact we can provide a dictionary between our thermodynamical analogy, on the one hand, and the requirements imposed on the operation of coarse–graining in ref. [18], on the other. Namely: probability conservation in [18] corresponds to energy conservation in our thermodynamical analogy, while dissipation in [18] is matched, in our picture, by increase in entropy.

Looking beyond, one could even pose the question: regardless of the sign, *why curvature at all?* We have seen that Ricci–flat spaces remain unchanged under the Ricci flow. In our thermodynamical analogy, this would correspond to no heat flow at all, that is, to a temperature distribution satisfying the static Laplace equation $\nabla^2 T = 0$. A nonvanishing (and, as we have argued, positive) value of the scalar curvature provides us with a natural length scale: the Ricci scalar. With it, a natural notion of a quantum comes along.

References

[1] G. 't Hooft, *Emergent quantum mechanics and emergent symmetries*, `arXiv:0707.4568 [hep-th]`.

[2] H.-T. Elze, *Note on the existence theorem in "Emergent quantum mechanics and emergent symmetries"*, J. Phys. A: Math. Theor. **41** (2008) 304020, `arXiv:0710.2765 [quant-ph]`.

[3] H.-T. Elze, *The attractor and the quantum states*, Int. J. Qu. Info. **7** (2009) 83, `arXiv:0806.3408 [quant-ph]`.

[4] P. Topping, *Lectures on the Ricci flow*, London Mathematical Society Lecture Notes Series **325**, Cambridge University Press (2006).

[5] R. Carroll, *Some remarks on Ricci flow and the quantum potential*, `arXiv:math-ph/0703065`.

[6] R. Carroll, *Ricci flow and quantum theory*, `arXiv:0710.4351 [math-ph]`.

[7] J.M. Isidro , J.L.G. Santander and P. Fernández de Córdoba, *Ricci flow, quantum mechanics and gravity*, Int. J. Geom. Meth. Mod. Phys. **6** (2009) 505, `arXiv::0808.2351 [hep-th]`.

[8] J.M. Isidro, J.L.G. Santander and P. Fernández de Córdoba, *On the Ricci flow and emergent quantum mechanics*, J. Phys. Conf. Ser. **174** (2009) 012033, `arXiv:0902.0143 [hep-th]`.

[9] H.-T. Elze (ed.), *Decoherence and Entropy in Complex Systems*, Selected Lectures from DICE 2002, Springer Lecture Notes in Physics, Berlin (2004).

[10] A. Khrennikov, *Prequantum classical statistical field theory: reconsideration of foundations*, AIP Conf. Proc. **962** (2007) 118.

[11] A. Faraggi and M. Matone, *The equivalence postulate of quantum mechanics: main theorems*, `arXiv:0912.1225 [hep-th]`.

[12] G. Bertoldi, A. Faraggi and M. Matone, *Equivalence principle, higher dimensional Mobius group and the hidden antisymmetric tensor of quantum mechanics*, Class. Quant. Grav. **17** (2000) 3965, `arXiv: hep-th/9909201`.

[13] S. Kobayashi and K. Nomizu, *Foundations of Differential Geometry*, Wiley, New York (1996).

[14] S. Helgason, *Differential Geometry, Lie Groups, and Symmetric Spaces*, Graduate Studies in Mathematics **34**, American Mathematical Society, Providence (2001).

[15] W. Thirring, *Quantum Mathematical Physics*, 2nd ed., Springer, Berlin (2003).

[16] B. Koch, *Relativistic Bohmian mechanics from scalar gravity*, `arXiv:0810.2786 [hep-th]`.

[17] B. Koch, *A geometrical dual to relativistic Bohmian mechanics: the multi particle case*, `arXiv:0901.4106 [gr-qc]`.

[18] H.-T. Elze, *Does quantum mechanics tell an atomistic spacetime?* `arXiv:0906.1101 [quant-ph]`.

ON THE NONCOMMUTATIVE EIKONAL

J.M. Isidro[1,2,a], **P. Fernández de Córdoba**[1,b], **J.M. Rivera–Rebolledo**[3,c]
and **J.L.G. Santander**[4,d]

[1]Instituto Universitario de Matemática Pura y Aplicada,
Universidad Politécnica de Valencia, Valencia 46022, Spain
[2]Max–Planck–Institut für Gravitationsphysik, Albert–Einstein–Institut,
D–14476 Golm, Germany
[3]Departamento de Física, U. P. Adolfo López Mateos, 07738 Lindavista,
México D. F., Mexico
[4]Departamento de Ciencias Experimentales y Matemáticas,
Universidad Católica de Valencia, Valencia 46002, Spain
[a]joissan@mat.upv.es, [b]pfernandez@mat.upv.es,
[c]jrivera@esfm.ipn.mx, [d]jlgonzalez@mat.upv.es

Abstract We study the eikonal approximation to quantum mechanics on the Moyal plane. Instead of using a star product, the analysis is carried out in terms of operator–valued wavefunctions depending on noncommuting, operator–valued coordinates.

1 Introduction

That spacetime must stop being a continuum once sufficiently high energies are reached is by now an old notion. Already in the 1930's, Heisenberg replaced a continuum spacetime with a lattice, in order to tame the divergences of quantum field theory. This lattice broke Lorentz invariance, which later models [1] succeeded in preserving. Attempts to quantise gravity also lead to the introduction of a fundamental length scale. This fundamental length scale, beyond which the concept of distance becomes meaningless, is called the Planck length. Replacing a continuum with some kind of discrete, or quantised, manifold, leads naturally to the conclusion that coordinates must be operator–valued quantities.

The purpose of this paper is to analyse the eikonal (or semiclassical) approximation to nonrelativistic quantum mechanics on the Moyal plane $\mathbb{R}^2_\theta$, the latter being coordinatised by operators X, Y satisfying the Heisenberg algebra $[X, Y] = XY - YX = \mathrm{i}\theta\mathbf{1}$, with $\theta > 0$. In particular we will need to write down the Hamilton–Jacobi equation, and its close cousin the Schroedinger equation, on the noncommutative plane. Two steps are involved here:
i) defining a classical mechanics on the noncommutative plane $\mathbb{R}^2_\theta$;
ii) quantising the classical mechanics so defined.
On an energy scale, quantisation ($\hbar > 0$) sets in well before noncommutativity ($\theta > 0$). In other words, in the real world one expects mechanics on a noncommutative space to be automatically quantum, rather than classical. We will see that, in fact, steps *i)* and *ii)* above are inextricably linked. However, if only methodologically, we will consider

the two steps above separately.

There are several alternative, though basically equivalent, approaches to physics on noncommutative spaces. One approach, by far the most widespread, uses number–valued coordinates and momenta (and functions thereof), while replacing the commutative pointwise product of functions with a noncommutative star product [2]. Another approach, little developed so far, uses operator–valued coordinates and momenta already from the start. Coordinates and momenta are now multiplied as matrices. In particular, operator–valued coordinates satisfy certain nontrivial commutation relations. In this paper we will further develop this second approach: we want our wavefunctions Ψ to be functions of the position operators X, Y, the latter satisfying $[X, Y] = \mathrm{i}\theta\mathbf{1}$. This will imply that the wavefunction Ψ itself will become an operator. This property is reminiscent of second–quantised theories. In fact it has been argued [3] that (yet another) approach to noncommutative quantum mechanics is provided by the 1–particle sector of noncommutative quantum field theory; then the noncommutative wavefunction, a c–number object, arises as a matrix element of a field operator[1]. However we prefer to stay within the framework of a finite number of degrees of freedom, and to try and construct wavefunctions that are operator–valued from the start, without resorting to field theory. After all, at least on commutative spaces, it is perfectly possible to formulate the quantum mechanics of a finite number of degrees of freedom, in a manner that is totally independent of quantum field theory, *i.e.*, without embedding quantum mechanics into an infinite number of degrees of freedom. We will see that noncommutative spaces also share this possibility. One surprising outcome of our approach will be that the mechanical action itself (the solution to the Hamilton–Jacobi equation) will also become an operator, without second–quantising the theory.

One can turn our argument around and analyse to what extent quantum mechanics, especially *emergent* quantum mechanics [4] and also *emergent* gravity [5, 6, 7], imply a granularity of spacetime. A comprehensive exposition of emergent physics, with extensive references, is given in the nice book [8]. The existing literature on noncommutative theories (deformation quantisation, quantum mechanics, field theory, string theory, gravity) is too vast to quote here, but we would like to mention the general refs. [9, 10, 11, 12]. Geometric treatments of quantum mechanics have also been studied in depth; for a sample see, *e.g.*, [2, 13, 14, 15, 16].

Approaches to quantum theory that are primarily based on Hamilton–Jacobi equations (and generalisations thereof) are well known; we will just mention [17] and the many references therein. For later use we recall that classical Hamilton–Jacobi theory on the commutative configuration space $\mathbb{R}^2$ coordinatised by x, y can be (extremely succinctly) summarised by the equations

$$ \mathcal{S} = -Et + \int p_x \mathrm{d}x + p_y \mathrm{d}y, \qquad p_x = \frac{\partial \mathcal{S}}{\partial x}, \qquad p_y = \frac{\partial \mathcal{S}}{\partial y} \tag{1} $$

and

$$ \frac{\partial \mathcal{S}}{\partial t} + \frac{1}{2m}\left[\left(\frac{\partial \mathcal{S}}{\partial x}\right)^2 + \left(\frac{\partial \mathcal{S}}{\partial y}\right)^2 \right] + \mathcal{U}(x, y) = 0, \tag{2} $$

---

[1]Of course, the previous statement also applies to theories on commutative spacetimes.

where $\mathcal{U}(x, y)$ is a potential function. We use the notation $\mathcal{S}$ for the *classical* action integral on the commutative plane $\mathbb{R}^2$, in order to distinguish it from the *operator–valued action* S to be introduced presently on the Moyal plane $\mathbb{R}^2_\theta$. The same notational convention applies to the classical potential function $\mathcal{U}$ and to its operator–valued analogue U, to be defined later.

This paper is organised as follows. Section 2 presents the noncommutative algebra of position and momentum operators that our construction is based upon. This algebra can be unitarily represented in a number of different ways. For reasons that will become clear presently, our favourite representation is given in terms of *noncommutative oscillator modes*. The latter can be thought of as harmonic oscillators on (an auxiliary copy of) the Moyal plane; we provide an explicit construction of these noncommutative oscillator modes, in some detail. Once position and momentum operators X, Y, P_X, P_Y are defined in terms of these modes, we need to define a mechanical action S depending on X, Y, P_X, P_Y and such that properties as close as possible to those satisfied by its commutative counterpart (1), (2) continue to hold true. This is done in section 3. By now we have an object S that plays the role of the classical mechanical action $\mathcal{S}$. However S is operator–valued, because the position and momentum variables it depends on are themselves operators. The next step, at least in a semiclassical analysis, is to consider the exponential of (i times) S, and to derive the equation satisfied by the latter, the Schroedinger equation on noncommutative space. This is done in section 4. Despite the numerous formal analogies with quantum mechanics on the commutative plane, there are some substantial differences that are pointed out along the way. Finally section 5 presents some concluding remarks concerning:
i) the role of the Bopp shift and the nonequivalent Poisson structures that it relates;
ii) the commutative limit of our model;
iii) the resolution of some apparent clashes with some classical theorems of Wigner, and of Stone and von Neumann;
iv) some speculations about a classical/quantum duality in noncommutative theories.

2 The noncommutative Poisson–Heisenberg algebra

2.1 The commutator algebra

The noncommutative plane $\mathbb{R}^2_\theta$ is defined as the algebra of functions of two generators X, Y satisfying the commutator $[X, Y] = \mathrm{i}\theta\mathbf{1}$, with $\theta > 0$. We regard $\mathbb{R}^2_\theta$ as a two–dimensional configuration space endowed with noncommuting coordinates X, Y. On the corresponding noncommutative phase space $\mathbb{R}^4_{\theta,\hbar}$ we have the operators X, Y, P_X, P_Y satisfying a commutator algebra that we postulate to be

$$[X, Y] = \mathrm{i}\theta\mathbf{1}, \quad [X, P_X] = [Y, P_Y] = \mathrm{i}\hbar\mathbf{1}, \quad [P_X, P_Y] = [X, P_Y] = [Y, P_X] = 0, \tag{3}$$

We will call the set of eqns. (3) the 2–dimensional, *noncommutative Poisson–Heisenberg algebra*. The time variable t will be taken to commute with all generators X, Y, P_X, P_Y.

It has been known for long that the *Bopp shift*

$$Y \mapsto Y - \frac{\theta}{\hbar} P_X \qquad (4)$$

reduces the noncommutative Poisson–Heisenberg algebra (3) to the usual Poisson–Heisenberg algebra in two commuting space dimensions. This notwithstanding, it is instructive to work with the algebra (3). This is so because one can think of (3) as being the commutator algebra of quantum mechanics with *two* deformation parameters—one quantum of area θ, one quantum of action $\hbar$. Standard quantum mechanics contains only the quantum of area on phase space, $\hbar$; noncommutative quantum mechanics adds a quantum of area on configuration space, θ. In the presence of the two quanta $\hbar$ and θ, and given a particle of mass m, the quantity $\hbar^2/(m\theta)$ has the dimensions of energy. We will see that the quantity $\hbar^2/(m\theta)$ plays an important role in what follows.

As usual we define the adjoint action of operator A on operator B by

$$\mathrm{ad}_A(B) = [A, B]. \qquad (5)$$

The adjoint action $\mathrm{ad}_A(B)$ behaves formally as a derivative: it is linear and satisfies the Leibniz rule

$$\mathrm{ad}_A(BC) = \mathrm{ad}_A(B)\, C + B\, \mathrm{ad}_A(C). \qquad (6)$$

We also have the Jacobi identity

$$[\mathrm{ad}_A, \mathrm{ad}_B] = \mathrm{ad}_{[A,B]}, \qquad (7)$$

which expresses a generalisation of the integrability property $\partial^2 f/\partial x \partial y = \partial^2 f/\partial y \partial x$ valid for derivatives of functions $f(x, y)$. Replacing phase–space derivatives with adjoint actions will be an essential tool in our approach to noncommutative quantum mechanics.

2.2 Commutative oscillator modes

We will first construct a Hilbert–space representation for the commutator algebra (3), in terms of *commutative* oscillator modes. This is of course trivial, but it will serve as a warmup exercise for the construction in terms of *noncommutative* oscillator modes. Consider the usual harmonic oscillator eigenstates ϕ_n in 1 dimension, where $n \in \mathbb{N}$. The space spanned by the ϕ_n is ℓ^2, the Hilbert space of complex, square–summable sequences. In two commuting dimensions x, y we have the eigenstates $\phi_{nm}(x, y) = \phi_n(x)\phi_m(y)$. The latter form an orthonormal basis for the Hilbert space $\ell^2 \times \ell^2$. Position and momentum operators X', Y', P'_X, P'_Y can be defined on the space $\ell^2 \times \ell^2$ as usual [18]: acting on the first index,

$$X'\phi_{nm} := \sqrt{\frac{\theta}{2}} \left(\sqrt{n+1}\, \phi_{n+1,m} + \sqrt{n}\, \phi_{n-1,m} \right), \qquad (8)$$

$$P'_X\phi_{nm} := \frac{\mathrm{i}\hbar}{\sqrt{2\theta}} \left(\sqrt{n+1}\, \phi_{n+1,m} - \sqrt{n}\, \phi_{n-1,m} \right). \qquad (9)$$

4

For the second index we define the action of Y', P'_Y similarly, with the sole difference that the (reverse) Bopp shift (4) must be taken into account:

$$Y'\phi_{nm} := \sqrt{\frac{\theta}{2}} \left(\sqrt{m+1}\, \phi_{n,m+1} + \sqrt{m}\, \phi_{n,m-1} \right) + \frac{\theta}{\hbar} P'_X \phi_{nm}, \qquad (10)$$

$$P'_Y \phi_{nm} := \frac{\mathrm{i}\hbar}{\sqrt{2\theta}} \left(\sqrt{m+1}\, \phi_{n,m+1} - \sqrt{m}\, \phi_{n,m-1} \right). \qquad (11)$$

One verifies that the operators X', Y', P'_X, P'_Y indeed satisfy the algebra (3). We have denoted these operators with a prime because this representation is unsatisfactory for our purposes. Indeed, there is nothing noncommutative about the eigenstates ϕ_{nm}: they are simply those of the harmonic oscillator on the commutative plane $\mathbb{R}^2$, non-commutativity being implemented in the algebra by means of the (inverse) Bopp shift. Instead one would like to have a representation space spanned by eigenstates ψ_{nm} of the harmonic oscillator on the noncommutative plane $\mathbb{R}^2_\theta$. This will be done explicitly in section 2.4.

2.3 Interlude

Before moving on to noncommutative oscillator modes we need to recall some elementary facts [19]. Consider the space F of all entire functions $f : \mathbb{C} \to \mathbb{C}$ such that

$$f(z) = \sum_{n=0}^{\infty} \frac{c_n}{\sqrt{n!}} z^n, \qquad \sum_{n=0}^{\infty} |c_n|^2 < \infty. \qquad (12)$$

This space is Hilbert with respect to the scalar product

$$\langle f | \tilde{f} \rangle := \frac{1}{2\pi\mathrm{i}} \int \mathrm{d}z^* \wedge \mathrm{d}z\, f^*(z) \tilde{f}(z) \mathrm{e}^{-|z|^2}, \qquad (13)$$

where the asterisk denotes complex conjugation, and the integral extends over all $\mathbb{R}^2$ with $z = (x + \mathrm{i}y)/\sqrt{2}$. An orthonormal basis is given by the set of all complex monomials

$$f_n(z) := \frac{z^n}{\sqrt{n!}}, \qquad n \in \mathbb{N}. \qquad (14)$$

The space F is called *Bargman–Segal space*. The f_n are in 1–to–1 correspondence with the harmonic oscillator eigenstates ϕ_n of section 2.2.

Next consider the following variant of Bargman–Segal space. Let us consider functions $g : \mathbb{R} \to \mathbb{C}$ such that

$$g(x) = \sum_{n=0}^{\infty} \frac{c_n}{\sqrt{n!}} x^n, \qquad \sum_{n=0}^{\infty} |c_n|^2 < \infty, \qquad (15)$$

the c_n being complex coefficients. Here our functions g are complex–valued analytic functions of one *real* variable x. Call G the space of all functions satisfying (15). A basis for G is given by the set of all real monomials

$$g_n(x) := \frac{x^n}{\sqrt{n!}}, \qquad n \in \mathbb{N}. \qquad (16)$$

We can define a scalar product on G by declaring these monomials to be orthonormal,

$$\langle g_n | g_m \rangle := \delta_{nm}, \qquad n, m \in \mathbb{N}, \tag{17}$$

and extending the above to all elements of G by complex linearity. This scalar product makes G a complex Hilbert space. The difference with respect to Bargman–Segal space F is that, the functions $g \in G$ depending on the real variable x instead of the complex variable z, the scalar product on G is no longer given by (13), nor by its real analogue. Indeed, given any two $g, \tilde{g} \in G$, the analogue of (13) for G would be the integral

$$\int_{-\infty}^{\infty} \mathrm{d}x \, g^*(x)\tilde{g}(x)\mathrm{e}^{-x^2}. \tag{18}$$

Although this integral does define a scalar product on G, this scalar product does not make the basis (16) orthogonal, as one readily verifies. Therefore one, and only one, of the following properties can be satisfied:

i) the space G is Hilbert with respect to the scalar product (18), but the monomial basis (16) is not orthogonal with respect to it;

ii) the space G is Hilbert with respect to the scalar product (17), and the monomial basis (16) is indeed orthonormal with respect to it, but this scalar product is not given by the integral (18).

This being the case, we settle in favour of condition *ii)* above as our choice for the Hilbert space G.

Finally, the construction given by eqns. (15)–(17) can be straightforwardly extended to complex–valued, analytic functions of *two* real variables x, y. This will be used next.

2.4   Noncommutative oscillator modes

Next we construct a unitary, Hilbert–space representation for the algebra (3), in terms of noncommutative oscillator modes. It will be based on the Hilbert space, just mentioned in section 2.3, of complex–valued, analytic functions of two real variables—but with *noncommuting, selfadjoint operators* replacing the real variables.

Consider first an auxiliary copy $\mathcal{H}$ of the Heisenberg algebra, spanned by operators $V, W, \mathbf{1}$ satisfying $[V, W] = \mathrm{i}\theta\mathbf{1}$, where both V and W have dimensions of length. The algebra $\mathcal{H}$ is realised in the standard way: V acts on auxiliary wavefunctions $h(v)$ by multiplication, $Vh(v) = vh(v)$, and W acts by differentiation, $Wh(v) = -\mathrm{i}\theta\mathrm{d}h/\mathrm{d}v$. That the dimension of θ is length squared, rather than that of an action, should not bother us, since $\mathcal{H}$ is an auxiliary construct. The corresponding Hilbert space of the wavefunctions $h(v)$, also termed auxiliary, is $L^2(\mathbb{R}, \mathrm{d}v)$. This Hilbert space, however, is *not* the carrier space of the unitary representation of the algebra (3) that we are looking for. To reiterate, the algebra $[V, W] = \mathrm{i}\theta\mathbf{1}$ just introduced, although isomorphic to the subalgebra $[X, Y] = \mathrm{i}\theta\mathbf{1}$ contained in (3), acts on the auxiliary space $L^2(\mathbb{R}, \mathrm{d}v)$, while the space on which the algebra $[X, Y] = \mathrm{i}\theta\mathbf{1}$ will act is about to be defined below.

Next let $U(\mathcal{H})$ denote the universal enveloping algebra of $\mathcal{H}$. By definition, $U(\mathcal{H})$ is the algebra of polynomials in the operators $V, W, \mathbf{1}$, of arbitrarily high degree, with

V and W satisfying $[V, W] = \mathrm{i}\theta\mathbf{1}$. Some suitable completion of $U(\mathcal{H})$, denoted $\overline{U(\mathcal{H})}$ and to be constructed presently, is the space of convergent power series in V, W. We take an arbitrary vector of $\overline{U(\mathcal{H})}$ to be an expression of the form

$$\psi(V, W) = \sum_{n,m=0}^{\infty} \frac{c_{nm}}{\sqrt{n!\,m!\,\theta^{n+m}}} V^n W^m, \tag{19}$$

where the c_{nm} are complex coefficients, such that the above series converges (in a sense to be specified presently). The factor $(\theta^{n+m})^{-1/2}$ ensures that all summands are dimensionless. From now we will prescribe all vectors of $\overline{U(\mathcal{H})}$ to be normal–ordered, *i.e.*, V will *always* be assumed to precede W, if necessary by applying the commutator $[V, W] = \mathrm{i}\theta\mathbf{1}$.

A basis for $\overline{U(\mathcal{H})}$ is given by the vectors

$$\psi_{nm}(V, W) = \frac{1}{\sqrt{n!\,m!\,\theta^{n+m}}} V^n W^m, \qquad n, m \in \mathbb{N}. \tag{20}$$

The simplest choice for a scalar product on $\overline{U(\mathcal{H})}$ is to declare the basis vectors (20) orthonormal,

$$\langle \psi_{n_1 m_1} | \psi_{n_2 m_2} \rangle := \delta_{n_1 n_2} \delta_{m_1 m_2}, \tag{21}$$

and to extend (21) to all of $\overline{U(\mathcal{H})}$ by complex linearity. Then the squared norm of the vector (19) equals $\sum_{nm} |c_{nm}|^2$:

$$\|\psi(V, W)\|^2 = \sum_{n,m=0}^{\infty} |c_{nm}|^2. \tag{22}$$

Since this norm must be finite, this identifies $\overline{U(\mathcal{H})}$ as the Hilbert space of square–summable complex sequences $\{c_{nm}\}$ in two indices n, m, *the latter taken to be normal–ordered* as in (20); this defines the completion of $U(\mathcal{H})$ referred to above. It is worthwhile to observe that, although the vectors (19) are unbounded operators in their action on the auxiliary Hilbert space $L^2(\mathbb{R}, \mathrm{d}v)$, the same vectors *do* have a finite norm as elements of the Hilbert space $\overline{U(\mathcal{H})}$. This is so because the norm of $\psi(V, W)$ in (22) is being measured by means of the complex coefficients c_{nm}, not by means of the operator norms of V, W (themselves infinite). We will henceforth call the ψ_{nm} of (20) *noncommutative oscillator modes*.

The Hilbert space $\overline{U(\mathcal{H})}$ just constructed will become the carrier space of a representation of the algebra (3). For this we need to define the action of the operators X, Y, P_X, P_Y on the noncommutative oscillator modes (20). We set

$$X\psi_{nm} := \sqrt{\frac{\theta}{2}} \left(\sqrt{n+1}\,\psi_{n+1,m} + \sqrt{n}\,\psi_{n-1,m} \right) \tag{23}$$

and

$$P_X\psi_{nm} := \frac{\mathrm{i}\hbar}{\sqrt{2\theta}} \left(\sqrt{n+1}\,\psi_{n+1,m} - \sqrt{n}\,\psi_{n-1,m} \right). \tag{24}$$

7

For the second index we define the action of Y, P_Y similarly, with the sole difference that the (reverse) Bopp shift (4) must be taken into account:

$$Y\psi_{nm} := \sqrt{\frac{\theta}{2}} \left(\sqrt{m+1}\,\psi_{n,m+1} + \sqrt{m}\,\psi_{n,m-1} \right) + \frac{\theta}{\hbar} P_X \psi_{nm} \qquad (25)$$

and

$$P_Y \psi_{nm} := \frac{i\hbar}{\sqrt{2\theta}} \left(\sqrt{m+1}\,\psi_{n,m+1} - \sqrt{m}\,\psi_{n,m-1} \right). \qquad (26)$$

Finally, the operators X, Y, P_X, P_Y so defined are Hermitian and satisfy the algebra (3) as desired. The above X, Y, P_X, P_Y are distinguished notationally from the operators X', Y', P'_X, P'_Y of (8)–(11) in order to stress the fact that they are actually different operators acting on different spaces[2], even if the two sets of operators satisfy the same algebra (3). From now on we will only work with the representation of the algebra (3) provided by (23)–(26).

Although they will not be used here, the previous results can be easily generalised to higher dimensions [20].

3 The Hamilton–Jacobi equation on the Moyal plane

Our next task is to write down the Hamilton–Jacobi equation. For this we define the following dimensionless coordinates Q_A, Q_B and momenta P_A, P_B:

$$Q_A := \frac{1}{\sqrt{\theta}} X, \quad P_A := \frac{\sqrt{\theta}}{\hbar} P_X, \quad Q_B := \frac{1}{\sqrt{\theta}} Y - \frac{\sqrt{\theta}}{\hbar} P_X, \quad P_B := \frac{\sqrt{\theta}}{\hbar} P_Y. \quad (27)$$

These operators satisfy the standard, dimensionless, Poisson–Heisenberg algebra:

$$[Q_A, P_A] = [Q_B, P_B] = i\mathbf{1}, \quad [Q_A, Q_B] = [P_A, P_B] = [Q_A, P_B] = [Q_B, P_A] = 0. \quad (28)$$

One can think of the space spanned by Q_A, Q_B, P_A, P_B as a commutative phase space, the only difference being that coordinates and momenta are operators on $\overline{U(\mathcal{H})}$. Correspondingly, phase–space derivatives will be replaced with the adjoint action (5). Our strategy will be to first write down the Hamilton–Jacobi equation on this commutative phase space. Then we will transform the result back into the noncommutative space spanned by X, Y, P_X, P_Y.

A key property of the classical mechanical action $\mathcal{S}$, when expressed as a function of the coordinates as in eqn. (1), is that it serves as a potential function for the momenta, *i.e.*, $p_x = \partial \mathcal{S} / \partial x$ and $p_y = \partial \mathcal{S} / \partial y$. This property must be maintained in the case under consideration here, where coordinates and momenta are operator–valued, and the adjoint action replaces the partial derivatives. Thus we need to find a Hermitian operator, that we will call the *operator–valued action S*, depending on Q_A, P_A, Q_B, P_B, and such that it will yield the momenta when one takes the adjoint action with respect

---

[2]All infinite–dimensional, complex, separable Hilbert spaces being unitarily isomorphic, the above statement is to be understood as *different realisations of Hilbert space*.

to the coordinates. In order to obtain a linear expression in the momenta, we need S to be a quadratic combination of the momenta. This leads one to the following operator:

$$S := -\frac{1}{\hbar}Et\mathbf{1} + \frac{1}{2}P_A^2 + \frac{1}{2}P_B^2 - U(Q_A, Q_B). \tag{29}$$

Here $U(Q_A, Q_B)$ is a dimensionless real function of Q_A, Q_B, that we can look upon as an operator–valued generalisation of the classical potential function $\mathcal{U}(x, y)$ of eqn. (2). Indeed, whatever our choice for $U(Q_A, Q_B)$ we find

$$\mathrm{i}P_A = \mathrm{ad}_{Q_A}(S), \qquad \mathrm{i}P_B = \mathrm{ad}_{Q_B}(S) \tag{30}$$

as one should; the factors of i ensure the Hermitian property. Eqns. (29), (30) are to be regarded as the noncommutative generalisation of eqn. (1). We would like to observe that the following consistency check on (30) is satisfied. The integrability condition $\partial^2 \mathcal{S}/\partial y \partial x = \partial p_x/\partial y = \partial p_y/\partial x = \partial^2 \mathcal{S}/\partial x \partial y$ holds true in eqn. (1). Therefore the operator analogue of this classical integrability condition should read

$$\mathrm{ad}_{Q_A}(P_B) = \mathrm{ad}_{Q_B}(P_A), \tag{31}$$

and, indeed, this is satisfied thanks to the Jacobi identity (7).

The operator action S is a dimensionless, Hermitian quantum operator acting on the carrier space $\overline{U(\mathcal{H})}$. Now, in order to write down the Hamilton–Jacobi equation, a Hamiltonian is needed. We will make a judicious choice for the Hamiltonian operator, followed by some consistency checks to ensure that our choice is correct. We claim that the Hamiltonian operator H corrending to (29) is given by

$$H = \frac{1}{2}P_A^2 + \frac{1}{2}P_B^2 + U(Q_A, Q_B). \tag{32}$$

The above is also a dimensionless, Hermitian operator. Replacing phase–space derivatives with adjoint actions, it is reasonable to demand that the Hamilton equations of motion be

$$\dot{P}_A = -\mathrm{ad}_{Q_A}(H), \quad \dot{Q}_A = \mathrm{ad}_{P_A}(H) \quad \dot{P}_B = -\mathrm{ad}_{Q_B}(H), \quad \dot{Q}_B = \mathrm{ad}_{P_B}(H). \tag{33}$$

We find, for the Hamiltonian (32) and the canonical pair Q_A, P_A,

$$\mathrm{ad}_{P_A}(H) = -\mathrm{i}\frac{\partial U}{\partial Q_A}, \qquad \mathrm{ad}_{Q_A}(H) = \mathrm{i}P_A. \tag{34}$$

Thus Newton's law is satisfied as it should, because

$$\ddot{Q}_A = \frac{\mathrm{d}}{\mathrm{d}t}\left(\mathrm{ad}_{P_A}(H)\right) = \mathrm{ad}_{\dot{P}_A}(H) = -[[Q_A, H], H] = -\mathrm{i}[P_A, H] = -\frac{\partial U}{\partial Q_A}. \tag{35}$$

Obviously the same holds for the other canonical pair Q_B, P_B.

We can now write down the noncommutative Hamilton–Jacobi equation for a particle of mass m on the Moyal plane, subject to the potential $U(Q_A, Q_B)$. It reads

$$\frac{\partial S}{\partial t} + \frac{\hbar}{m\theta}\left[-\frac{1}{2}\left(\mathrm{ad}_{Q_A}(S)\right)^2 - \frac{1}{2}\left(\mathrm{ad}_{Q_B}(S)\right)^2 + U(Q_A, Q_B)\right] = 0. \tag{36}$$

9

We draw attention to the negative sign preceding the squared adjoint actions, due to the imaginary units in (30); otherwise (36) is the natural operator generalisation of its classical counterpart (2). The factor $\hbar/(m\theta)$ has the dimensions of time inverse, thus making (36) dimensionally homogeneous. We will find it useful to separate out in (29) the piece that is proportional to the identity, thus leaving the reduced, or time–independent, operator action $S^{(0)}$:

$$S = -\frac{1}{\hbar}Et\mathbf{1} + S^{(0)}, \quad S^{(0)} := \frac{1}{2}P_A^2 + \frac{1}{2}P_B^2 - U(Q_A, Q_B). \tag{37}$$

Then (30) becomes

$$\mathrm{i}P_A = \mathrm{ad}_{Q_A}\left(S^{(0)}\right), \qquad \mathrm{i}P_B = \mathrm{ad}_{Q_B}\left(S^{(0)}\right), \tag{38}$$

which gives the time–independent Hamilton–Jacobi equation

$$\frac{\hbar^2}{m\theta}\left[-\frac{1}{2}\left(\mathrm{ad}_{Q_A}(S^{(0)})\right)^2 - \frac{1}{2}\left(\mathrm{ad}_{Q_B}(S^{(0)})\right)^2 + U(Q_A, Q_B)\right] = E. \tag{39}$$

Here appears the quantity $\hbar^2/(m\theta)$ mentioned in section 2.

A comment is in order. In principle one would not expect Planck's constant $\hbar$ to be present in the Hamilton–Jacobi equation, since the latter is a classical equation, which arises before quantisation. This much is true of theories on commutative spaces. However, as remarked in section 1, any theory on noncommutative space must include $\hbar$ because, on an energy scale, quantum effects set in much earlier than noncommutative effects. This being the case, the distinction between *classical* and *quantum* turns out to be rather formal.

A more mundane explanation of the same fact is provided by the following argument. The noncommutative theory depends on the dimensionful parameter θ. The latter must enter the Hamilton–Jacobi equation. Now (36) and (39) cannot be balanced dimensionally in terms of just one dimensionful parameter; at least one more dimensionful parameter is needed for homogeneity. Planck's constant $\hbar$ does precisely that job.

Using (27) we can now rewrite the operator action of (29) in terms of X, Y, P_X, P_Y:

$$S := -\frac{1}{\hbar}Et\mathbf{1} + \frac{\theta}{2\hbar^2}P_X^2 + \frac{\theta}{2\hbar^2}P_Y^2 - U(X, Y, P_X). \tag{40}$$

Some caution is necessary here since, in general, the potential function $U(Q_A, Q_B)$ suffers from ordering ambiguities once we express Q_A, Q_B in terms of X, Y, P_X, P_Y. This requires that some ordering prescription be adopted, *e.g.*, Weyl's symmetrisation[3]. We also observe that the potential U in (40) can depend on P_X, but not on P_Y, due to the Bopp shift (4). From the time–independent operator action $S^{(0)}$ of (37) we similarly obtain

$$S^{(0)} := \frac{\theta}{2\hbar^2}P_X^2 + \frac{\theta}{2\hbar^2}P_Y^2 - U(X, Y, P_X). \tag{41}$$

---

[3]This is not specific to our approach in terms of operator–valued quantities, since the same ordering ambiguities would arise if we used a star product.

For the time–dependent Hamilton–Jacobi equation (36) we find

$$\frac{\partial S}{\partial t} + \frac{\hbar}{m\theta}\left[-\frac{1}{2\theta}\left(\mathrm{ad}_X(S)\right)^2 - \frac{1}{2\theta}\left(\mathrm{ad}_Y(S) - \frac{\theta}{\hbar}\mathrm{ad}_{P_X}(S)\right)^2 + U\right] = 0, \quad (42)$$

while its time–independent version (39) becomes

$$\frac{\hbar^2}{m\theta}\left[-\frac{1}{2\theta}\left(\mathrm{ad}_X(S^{(0)})\right)^2 - \frac{1}{2\theta}\left(\mathrm{ad}_Y(S^{(0)}) - \frac{\theta}{\hbar}\mathrm{ad}_{P_X}(S^{(0)})\right)^2 + U\right] = E. \quad (43)$$

Altogether, eqns. (42) and (43) above reexpress the Hamilton–Jacobi equations (36) and (39) in terms of the noncommutative variables X, Y, P_X, P_Y. However, in general one should stop short of calling (42) and (43) Hamilton–Jacobi equations in the strict sense of the word. For such to be the case, one should be able to replace any possible occurrence of P_X with its expression in terms of $\mathrm{ad}_X(S)$. One such occurrence happens within the potential U. This makes the replacement impossible, as we see from (40), because one has $P_X = \hbar\,\mathrm{ad}_X(S+U)/(\mathrm{i}\theta)$: in trying to eliminate P_X in favour of $\mathrm{ad}_X(S)$, the offending term in the potential U reappears! Moreover, P_X also shows up in the terms $\mathrm{ad}_{P_X}(S)$ and $\mathrm{ad}_{P_X}(S^{(0)})$, where it should also be replaced.

A moment's reflection shows that, in fact, things are exactly as they should. Let us go back to eqns. (1), (2), where it is implicitly understood that x, y, p_x, p_y satisfy the standard Poisson algebra $\{x, y\} = 0 = \{p_x, p_y\}$, $\{x, p_y\} = 0 = \{y, p_x\}$, $\{x, p_x\} = 1 = \{y, p_y\}$, which is isomorphic to that in (28). All these variables are canonical. This fact guarantees that the replacements $p_x = \partial S/\partial x$ and $p_y = \partial S/\partial y$, as well as their operator–valued analogues $\mathrm{i}P_A = \mathrm{ad}_{Q_A}(S)$, $\mathrm{i}P_B = \mathrm{ad}_{Q_B}(S)$, can be performed. Thus (36) and (39) are *bona fide* Hamilton–Jacobi equations. However, neither the Bopp shift (4) nor its inverse is a canonical transformation, because the algebra satisfied by X, Y, P_X, P_Y differs from that satified by Q_A, Q_B, P_A, P_B. The latter are canonical variables, while the former are not.

To summarise, we have written down the Hamilton–Jacobi equation using a set of (operator–valued) canonical variables Q_A, Q_B, P_A, P_B, and we have then transformed the resulting equation using a set of noncanonical variables X, Y, P_X, P_Y, by means of a diffeomorphism (the Bopp shift) that does *not* qualify as a canonical transformation. There is no way the Moyal phase space $\mathbb{R}^4_{\theta,\hbar}$ can be *canonically* transformed into the standard phase space $\mathbb{R}^4_\hbar$. Physically this is so because the quantum of area θ that is present in $\mathbb{R}^4_{\theta,\hbar}$ is absent in $\mathbb{R}^4_\hbar$. The Bopp shift respects the quantum of action $\hbar$, but not the quantum of area θ.

4 The Schroedinger equation on the Moyal plane

In order to write down the Schroedinger equation on the Moyal plane, we will follow the same strategy of section 3. Namely, we will first work with the canonical variables Q_A, Q_B, P_A, P_B of (27), in terms of which we will write down the Schroedinger equation; only then will we transform back to the noncommutative variables X, Y, P_X, P_Y.

The Schroedinger equation we will arrive at will turn out to be valid only semi-classically. We first need explain what one understands as the semiclassical limit of

noncommutative quantum mechanics. In the commutative case, the semiclassical limit is obtained as $\hbar \to 0$, when the Schroedinger equation reduces to the Hamilton–Jacobi equation. Since noncommutative quantum mechanics contains two deformation parameters $\hbar, \theta$, we ask what the precise regime of these parameters is that corresponds to the eikonal approximation. We claim that the eikonal approximation corresponds to the limit $\hbar \to 0$ and $\theta \to 0$ while holding $\hbar^2/(m\theta)$ fixed. Obviously $\hbar$ must go to zero. However, as mentioned in the introduction, noncommutative effects set in (on an energy scale) much later than quantum effects, so $\hbar \to 0$ enforces $\theta \to 0$ as well. Since the ratio $\hbar^2/(m\theta)$ must be held fixed for the Hamilton–Jacobi equation (36) (or its reexpression (42)) to be well defined, this proves our claim.

To begin with, let us consider the free case, $U = 0$. We expect a time–independent, semiclassical wavefunction $\Phi^{(0)}$ to be given by the exponential of (i times) the reduced action of eqn. (37):

$$\Phi^{(0)} = \exp\left(\mathrm{i} S^{(0)}\right) = \exp\left(\frac{\mathrm{i}}{2} P_A^2 + \frac{\mathrm{i}}{2} P_B^2\right). \tag{44}$$

Using the algebra (28) we find

$$\mathrm{ad}_{Q_A} \Phi^{(0)} = -P_A \Phi^{(0)}, \qquad \mathrm{ad}_{Q_B} \Phi^{(0)} = -P_B \Phi^{(0)} \tag{45}$$

and

$$\mathrm{ad}_{Q_A}^2 \Phi^{(0)} = \left(P_A^2 - \mathrm{i}\mathbf{1}\right) \Phi^{(0)}, \quad \mathrm{ad}_{Q_B}^2 \Phi^{(0)} = \left(P_B^2 - \mathrm{i}\mathbf{1}\right) \Phi^{(0)}. \tag{46}$$

Remembering (38) we arrive at

$$\frac{1}{2}\left(\mathrm{ad}_{Q_A}^2 + \mathrm{ad}_{Q_B}^2 + 2\mathrm{i}\right) \Phi^{(0)} = -\frac{1}{2}\left[\left(\mathrm{ad}_{Q_A}(S^{(0)})\right)^2 + \left(\mathrm{ad}_{Q_B}(S^{(0)})\right)^2\right] \Phi^{(0)}. \tag{47}$$

Now eqn. (39) suggests equating the right–hand side to $Em\theta\Phi^{(0)}/\hbar^2$:

$$\frac{1}{2}\left(\mathrm{ad}_{Q_A}^2 + \mathrm{ad}_{Q_B}^2 + 2\mathrm{i}\right) \Phi^{(0)} = \frac{Em\theta}{\hbar^2} \Phi^{(0)}. \tag{48}$$

Setting $\Phi := \Phi^{(0)} \exp\left(-\mathrm{i}Et/\hbar\right)$ we can finally write

$$\frac{\hbar^2}{2m\theta}\left(\mathrm{ad}_{Q_A}^2 + \mathrm{ad}_{Q_B}^2 + 2\mathrm{i}\right) \Phi = \mathrm{i}\hbar\frac{\partial\Phi}{\partial t}. \tag{49}$$

Let us take stock. The expression $\mathrm{ad}_{Q_A}^2 + \mathrm{ad}_{Q_B}^2$ on the left–hand side can be interpreted as an operator–valued analogue of the standard Laplacian $\partial^2/\partial x^2 + \partial^2/\partial x^2$. The term $2\mathrm{i}\mathbf{1}$ can be interpreted as a constant potential, and can therefore be dropped. As it stands, (49) is strictly equivalent to the Hamilton–Jacobi equation (36) when $U = 0$, and we can declare

$$\frac{\hbar^2}{2m\theta}\left(\mathrm{ad}_{Q_A}^2 + \mathrm{ad}_{Q_B}^2\right) \Phi = \mathrm{i}\hbar\frac{\partial\Phi}{\partial t} \tag{50}$$

to be the Schroedinger equation for a free particle on the Moyal plane. Modulo the factor $\hbar^2/2m\theta$, eqn. (50) is formally identical to the standard Schrodinger equation. However it must be borne in mind that its structure is substantially different. Eqn. (50) is

not the expression of an operator acting on a vector, to produce another vector. Rather, it expresses an equality between operators. By the same token, its time–independent form (48) is not a eigenvalue equation for a vector, but an eigenvalue equation for the eigen*operator* $\Phi^{(0)}$. (This is the operator analogue of the star–eigenvalue equations; see, *e.g.*, ref. [21]). Last but not least, we recall that no approximation has been made in order to reproduce the Hamilton–Jacobi equation from the Schroedinger equation, as (50) and (36) are strictly equivalent when $U = 0$. We will see presently that this equivalence will also remain in the interacting case, at least in the semiclassical limit.

In the presence of a potential U, the natural generalisation of (50) is

$$\frac{\hbar^2}{2m\theta}\left[\mathrm{ad}_{Q_A}^2 + \mathrm{ad}_{Q_B}^2 + U(Q_A, Q_B)\right]\Psi = \mathrm{i}\hbar\frac{\partial\Psi}{\partial t}. \tag{51}$$

We look for semiclassical solutions to (51) in the form $\Psi := \Psi^{(0)}\exp\left(-\mathrm{i}Et/\hbar\right)$, where $\Psi^{(0)}$ is suggested by (37):

$$\Psi^{(0)} := \exp\left(\mathrm{i}S^{(0)}\right) = \exp\left[\frac{\mathrm{i}}{2}P_A^2 + \frac{\mathrm{i}}{2}P_B^2 - \mathrm{i}U(Q_A, Q_B)\right]. \tag{52}$$

Unfortunately there is no neat expression for the analogues of (45) and (46) when U is nontrivial. One can power–expand the exponential (52) and act with ad_{Q_A}, ad_{Q_B} term by term, but the presence of a nonconstant $U(Q_A, Q_B)$ prevents a tidy rearrangement of the result into any manageable expression. This is ultimately due to the fact that, when U is nonconstant, (52) does *not* factorise as

$$\exp\left(\frac{\mathrm{i}}{2}P_A^2 + \frac{\mathrm{i}}{2}P_B^2\right)\exp\left[-\mathrm{i}U(Q_A, Q_B)\right]. \tag{53}$$

In turn, the impossibility of the factorisation (53) is due to the nonvanishing of the following commutators:

$$[P_A^2, U] = -\mathrm{i}P_A\frac{\partial U}{\partial Q_A} - \mathrm{i}\frac{\partial U}{\partial Q_A}P_A, \qquad [P_B^2, U] = -\mathrm{i}P_B\frac{\partial U}{\partial Q_B} - \mathrm{i}\frac{\partial U}{\partial Q_B}P_B. \tag{54}$$

However, we should remember that the commutators (54) have been computed using the dimensionless algebra (28). When one reinstates powers of $\hbar$, one immediately sees that the right–hand sides of (54) are $O(\hbar)$. In the semiclassical limit considered throughout in this paper, one may drop terms of order $\hbar$ while keeping $\hbar^2/(m\theta)$ fixed. We may thus approximate the right–hand sides of (54) by zero. In this limit, the wavefunction (52) can be approximated by its factorised form (53):

$$\Psi^{(0)} \simeq \exp\left(\frac{\mathrm{i}}{2}P_A^2 + \frac{\mathrm{i}}{2}P_B^2\right)\exp\left[-\mathrm{i}U(Q_A, Q_B)\right]. \tag{55}$$

Using the semiclassical wavefunction (55), one sees that the reasoning from eqn. (45) to eqn. (50) continues to hold true in the presence of the potential $U(Q_A, Q_B)$. In this way one establishes that the operator wavefunction $\Psi := \Psi^{(0)}\exp\left(-\mathrm{i}Et/\hbar\right)$ satisfies the Schroedinger equation (51). For the latter we claim validity within the semiclassical

regime only, given the approximation made in (55). Moreover, as was already the case for the free particle, the Schroedinger equation (51) in the presence of a potential U is strictly equivalent to the Hamilton–Jacobi equation (36). In this sense, the difference between these two equations lies in the choice one makes for the quantity one works with, *i.e.*, either the action S or its exponential. We should also add that the reverse order for the factors in (55) would be justified just as well in the semiclassical limit. Within the accuracy of this limit, it is actually a matter of choice which exponential appears on the left and which one on the right.

As a final step, we need to recast the Schroedinger equation (51) in terms of the noncommutative variables X, Y, P_X, P_Y. This is readily done: using (27) we perform the replacement

$$\mathrm{ad}_{Q_A}^2 + \mathrm{ad}_{Q_B}^2 = \frac{1}{\theta}\mathrm{ad}_X^2 + \frac{1}{\theta}\mathrm{ad}_Y^2 - \frac{2}{\hbar}\mathrm{ad}_{P_X}\mathrm{ad}_Y + \frac{\theta}{\hbar^2}\mathrm{ad}_{P_X}^2 \tag{56}$$

in (51). This gives

$$\frac{\hbar^2}{2m\theta}\left[\frac{1}{\theta}\mathrm{ad}_X^2 + \frac{1}{\theta}\mathrm{ad}_Y^2 - \frac{2}{\hbar}\mathrm{ad}_{P_X}\mathrm{ad}_Y + \frac{\theta}{\hbar^2}\mathrm{ad}_{P_X}^2 + U(X,Y,P_X)\right]\Psi = \mathrm{i}\hbar\frac{\partial\Psi}{\partial t}. \tag{57}$$

The same *caveat* discussed at length after eqn. (43) applies to (57) as well.

5 Discussion

In this paper we have taken some first steps towards a head–on approach to quantum mechanics on noncommutative spaces, an approach that has been demanded and studied to some extent in the literature [22]. The novelty lies in the attempt to express wavefunctions purely in terms of operator–valued coordinates, rather than in terms of c–valued functions that are multiplied together by means of a star product. The underlying logic is as follows. Coordinates X, Y on the Moyal plane are operators satisfying $[X,Y] = \mathrm{i}\theta\mathbf{1}$. This implies that wavefunctions Ψ, as functions of X, Y, must also be operators. This represents a radical departure from the viewpoint of deformation quantisation, where noncommutativity lies hidden under the star product of c–valued wavefunctions. Not only wavefunctions, but the mechanical action itself (the solution to the Hamilton–Jacobi equation) must become an operator. This is totally natural since, at least in the semiclassical limit, one expects the mechanical action to be proportional to the logarithm of the wavefunction. If the latter is an operator, so must be the former.

The strategy followed in writing down the Hamilton–Jacobi and the Schroedinger equations on the Moyal plane involves three steps. The first step is to use the Bopp shift (4), in order to transform the original noncommutative variables X, Y, P_X, P_Y (satisfying the algebra (3)) into dimensionless variables Q_A, Q_B, P_A, P_B (satisfying the algebra (28)). In terms of the latter there is a well–defined procedure for writing down the Hamilton–Jacobi equation. The second step is to pass therefrom to the Schroedinger equation. This second step involves some generally accepted guesswork[4]. The third,

---

[4]This guesswork is sometimes summarised in the statement that *first quantisation is a mystery, second quantisation is a functor*.

and final, step, is to undo the Bopp shift and transform the equations so obtained back into the original noncommutative variables X, Y, P_X, P_Y. The Bopp shift is a diffeomorphism that does *not* qualify as a canonical transformation. However we need canonical variables in order to first write down the Hamilton–Jacobi equation, which one later uses as a bridge to the Schroedinger equation. As explained in detail towards the end of section 3, it is impossible to *canonically* transform the Moyal phase space $\mathbb{R}^4_{\theta,\hbar}$ into the standard phase space $\mathbb{R}^4_\hbar$. Physically this is so because the quantum of area θ that is present in $\mathbb{R}^4_{\theta,\hbar}$ is absent in $\mathbb{R}^4_\hbar$. The existence of the two quanta $\hbar$ and θ leads to the existence of a natural energy scale $\hbar^2/(m\theta)$ (for any given particle mass m), which is absent in standard quantum mechanics.

A key element in our construction is provided by the noncommutative oscillator modes ψ_{nm} of section 2.4. The ψ_{nm} are quantum mechanical wavefunctions of a harmonic oscillator defined on (an auxilary copy of) the Moyal plane. As $\theta \to 0$, the ψ_{nm} must be replaced with the commutative oscillator modes ϕ_{nm} of section 2.2 (the ϕ_{nm} are standard oscillator modes on $\mathbb{R}^2$). Finally setting $\theta = 0$ but $\sqrt{\theta} = 1$ (as befits the fact that $\sqrt{\theta} > \theta$ when $\theta \to 0$) we see that eqns. (23) to (26) respectively become eqns. (8) to (11): this is the commutative limit.

The symmetry algebra (the commutator algebra of section 2.1) is realised unitarily on the Hilbert space $\overline{U(\mathcal{H})}$ spanned by the noncommutative oscillator modes ψ_{nm}. The latter are not to be confused with the true quantum states Ψ of the theory. We thus meet a situation in which the quantum states Ψ of the theory do *not* support a representation of the symmetry algebra—in apparent violation of Wigner's theorem. There is however no violation, because Wigner's theorem implicitly assumes a commutative space. The states ψ_{nm} that support a representation of the symmetry algebra are intermediate states in our construction, while the true quantum states Ψ, being operator–valued and thus noncommutative, are not bound by Wigner's theorem to furnish a representation. Similar arguments apply to the Stone–von Neumann theorem as applied to the subalgebra $[X, P_X] = \mathrm{i}\hbar = [Y, P_Y]$. This latter theorem is also not violated since it too presupposes a commutative space.

The following thoughts, of a somewhat speculative nature, are collected here to conclude. It was mentioned in the introduction, and also right after the Hamilton–Jacobi equation (39) that, in the presence of noncommutativity, the distinction between *classical* and *quantum* turns out to be somewhat formal, devoid of physical content. This is so because, in principle, one does not expect Planck's constant to arise at the level of the classical Hamilton–Jacobi equation—but the fact is, it does arise. There is also no way one can have a *purely classical* noncommutative theory because quantum effects set in much earlier, on an energy scale, than noncommutative effects. Moreover, when the potential is constant on the Moyal plane, the Schroedinger equation (for the exponential of the action operator) and the Hamilton–Jacobi equation (for the action operator alone) are actually equivalent. This is in marked contrast with the case of commutative quantum mechanics, where the same equivalence holds only semiclassically. In the interacting case on the Moyal plane this equivalence (between Schroedinger and Hamilton–Jacobi) is generally lost (of course, it continues to hold in the semiclassical limit). One is thus tempted to call this state of affairs a *classical/quantum duality* of noncommutative quantum mechanics. It is interesting to observe that analogous ef-

fects have been reported in [7, 8, 23]. Although the latter refer to somewhat different contexts, they are by no means totally different from ours. One is also reminded of the UV/IR mixing of noncommutative field theories [24]. Altogether, we find these similarities very suggestive.

References

[1] H.S. Snyder, *Quantized Space–Time*, Phys. Rev. **71** (1947) 38.

[2] G. Giachetta, L. Mangiarotti and G. Sardanashvily, *Geometric and Algebraic Topological Methods in Quantum Mechanics*, World Scientific, Singapore (2005).

[3] V. Nair and A. Polychronakos, *Quantum Mechanics on the Noncommutative Plane and Sphere*, Phys. Lett. **B505** (2001) 267, `arXiv:hep-th/0011172`.

[4] H.-T. Elze, *The attractor and the quantum states*, Int. J. Qu. Info. **7** (2009) 83, `arXiv:0806.3408 [quant-ph]`;
Symmetry Aspects in Emergent Quantum Mechanics, J. Phys. Conf. Ser. **171** (2009) 012034;
Does Quantum Mechanics Tell an Atomistic Spacetime?, J. Phys. Conf. Ser. **174** (2009) 012009, `arXiv:0906.1101 [quant-ph]`;
Spacetime and Matter — a Duality of Partial Orders, `arXiv:1001.3964 [gr-qc]`.

[5] N. Seiberg, *Emergent Spacetime*, `arXiv: hep-th/0601234`.

[6] T. Padmanabhan, *Thermodynamical Aspects of Gravity: New Insights*, Rept. Prog. Phys. **73** (2010) 046901, `arXiv:0911.5004 [gr-qc]`.

[7] T. Singh, *Quantum Theory, Noncommutative Gravity, and the Cosmological Constant Problem*, `arXiv:0901.0978 [gr-qc]`.

[8] R. Carroll, *On the Emergence Theme of Physics*, World Scientific, Singapore (2010).

[9] J. Madore, *An Introduction to Noncommutative Differential Geometry and its Physical Applications*, London Mathematical Society Lecture Note Series **257**, Cambridge University Press, Cambridge (1999).

[10] R. Szabo, *Quantum Field Theory on Noncommutative Spaces*, Phys. Rep. **378** (2003) 207;
Quantum Gravity, Field Theory, and Signatures of Noncommutative Spacetime, `arXiv:0906.2913 [hep-th]`.

[11] R. Banerjee, B. Chakraborty, S. Ghosh, P. Mukherjee and S. Samanta, *Topics in Noncommutative Geometry Inspired Physics*, `arXiv:0909.1000 [hep-th]`.

[12] B. Chakraborty, S. Gangopadhyay, A. Saha, *Seiberg–Witten Map and Galilean Symmetry Violation in a Non–commutative Planar System*, Phys. Rev.**D70** (2004) 107707, `arXiv:hep-th/0312292`;
F. Scholtz, B. Chakraborty, S. Gangopadhyay, A. Hazra, *Dual Families of Non–commutative Quantum Systems*, Phys. Rev. **D71** (2005) 085005, `arXiv:hep-th/0502143`;
B. Chakraborty, S. Gangopadhyay, A. Hazra, F. Scholtz*Twisted Galilean Symmetry and the Pauli Principle at Low Energies*, J. Phys. **A39** (2006) 9557-9572, `arXiv:hep-th/0601121`;
S. Gangopadhyay, F. Scholtz, *Path–Integral Action of a Particle in the Noncommutative Plane*, Phys. Rev. Lett.**102** (2009) 241602.

[13] R. Carroll, *Fisher, Kähler, Weyl, and the quantum potential*, `arXiv: quant-ph/0406210`;
Some remarks on Ricci flow and the quantum potential, `arXiv:math-ph/0703065`;
Remarks on Weyl geometry and quantum mechanics, `arXiv:0705.3921 [gr-qc]`;
Ricci flow and quantum theory, `arXiv:0710.4351 [math-ph]`.

[14] N. Costa Dias, M. de Gosson, F. Luef and J. Nuno Prata, *A Deformation Quantization Theory for Non–Commutative Quantum Mechanics*, `arXiv:0911.1209 [math-ph]`.

[15] J.M. Isidro, J.L.G. Santander, P. Fernández de Córdoba, *Positive Curvature Can Mimic a Quantum*, American Institute of Physics Conference Series **1232** (2010) 86 (ed. A. Khrennikov), `arXiv:0912.1535 [hep-th]`.

[16] B. Koch, *Quantizing Geometry or Geometrizing the Quantum?*, `arXiv:1004.2879 [hep-th]`;
B. Koch, *Geometrizing the Quantum — A Toy Model*, `arXiv:1004.3240 [gr-qc]`.

[17] A. Faraggi and M. Matone, *The Equivalence Postulate of Quantum Mechanics: Main Theorems*, `arXiv:0912.1225 [hep-th]`;
G. Bertoldi, A. Faraggi and M. Matone, *Equivalence Principle, Higher Dimensional Mobius Group and the Hidden Antisymmetric Tensor of Quantum Mechanics*, Class. Quant. Grav. **17** (2000) 3965, `arXiv: hep-th/9909201`.

[18] L. Landau and E. Lifshitz, *Quantum Mechanics*, vol. 3 of *Course of Theoretical Physics*, Butterworth–Heinemann, Oxford (2000).

[19] W. Thirring, *Quantum Mathematical Physics*, 2nd ed., Springer, Berlin (2003).

[20] J.M. Isidro, P. Fernández de Córdoba, J.M. Rivera–Rebolledo and J.L.G. Santander, *Remarks on the Representation Theory of the Moyal Plane*, `arXiv:1007.4687 [hep-th]`.

[21] C. Zachos, D. Fairlie and T. Curtwright, eds., *Quantum Mechanics in Phase Space*, World Scientific, Singapore (2005).

[22] F. Scholtz, L. Gouba, A. Hafver and C. Rohwer, *Formulation, Interpretation and Application of Non–Commutative Quantum Mechanics*, J. Phys. **A42** (2009) 175303, `arXiv:0812.2803 [math-ph]`;
C. Rohwer, K. Zloshchastiev, L. Gouba and F. Scholtz, *Noncommutative Quantum Mechanics — a Perspective on Structure and Spatial Extent*, `arXiv:1004.1984 [math-ph]`.

[23] J.M. Isidro and M. de Gosson, *Abelian Gerbes as a Gauge Theory of Quantum Mechanics on Phase Space*, J. Phys. **A40** (2007) 3549, `arXiv:hep-th/0608087`.

[24] A. Fischer and R. Szabo, *UV/IR Duality in Noncommutative Quantum Field Theory*, `arXiv:1001.3776 [hep-th]`.

Research Article

Remarks on the Representation Theory of the Moyal Plane

J. M. Isidro,[1,2] P. Fernández de Córdoba,[1] J. M. Rivera-Rebolledo,[3] and J. L. G. Santander[4]

[1] *Instituto Universitario de Matemática Pura y Aplicad, Universidad Politécnica de Valencia, 46022 Valencia, Spain*
[2] *Max-Planck-Institut für Gravitationsphysik (Albert-Einstein-Institut), 14476 Golm, Germany*
[3] *Departamento de Física, Escuela Superior de Física y Matemáticas, Instituto Politécnico Nacional, U. P. Adolfo López Mateos, 07738 Lindavista, D F, Mexico*
[4] *Cátedra Energesis de Tecnología Interdisciplinar, Universidad Católica de Valencia, C/Guillem de Castro 94, Valencia 46003, Spain*

Correspondence should be addressed to J. M. Isidro, joissan@mat.upv.es

We present an explicit construction of a unitary representation of the commutator algebra satisfied by position and momentum operators on the Moyal plane.

1. Introduction

There has been a lot of activity recently around physics on noncommutative spaces (for reviews see, e.g., [1, 2] and references therein). Quite naturally, this has been accompanied by research into the foundations of quantum mechanics on noncommutative spaces. As was already the case in the early days of quantum mechanics, one key question is how to represent the symmetry algebra of the problem under consideration. The symmetry algebra encodes the kinematics, regardless of the dynamics. Classically the kinematics is summarised by the Poisson brackets $\{q_i, q_j\} = 0$, $\{p_i, p_j\} = 0$, $\{q_i, p_j\} = \delta_{ij}$, while quantum-mechanically the latter become commutators for the operators Q_i, P_j,

$$[Q_i, Q_j] = 0, \qquad [P_i, P_j] = 0, \qquad [Q_i, P_j] = i\hbar\delta_{ij}. \tag{1.1}$$

A celebrated theorem of Stone and von Neumann [3] establishes that all unitary representations of the commutator algebra (1.1) are unitarily equivalent to that given by (complex infinite-dimensional, separable) Hilbert space, with position operators Q_i acting multiplicatively on the wavefunctions and momentum operators P_j acting by differentiation of the same wavefunctions.

When space becomes noncommutative, the commutators $[Q_i, Q_j] = 0$ develop nonzero terms on their right-hand sides. For simplicity let us restrict our attention to the 2-dimensional case. We will also assume the simplest form of noncommutativity, namely, that given by the Moyal plane: $[X, Y] = i\theta \mathbf{1}$, with $\theta > 0$. The corresponding symmetry algebra that replaces (1.1) above is expressed in (2.1) below. Then a natural question to ask is what becomes of the Stone-von Neumann theorem on the Moyal plane. Although this issue has been addressed in the literature [4], here we offer an alternative viewpoint. Specifically, we provide an explicit construction of a unitary representation of the symmetry algebra (2.1) on the Moyal plane, in terms of noncommutative oscillator modes. This representation will be used in an approach to quantum mechanics on the Moyal plane [5], an approach that has been demanded in the literature [6] and developed to some extent [7–11]. The idea underlying this approach is the following. Coordinates X, Y on the Moyal plane are actually self-adjoint operators on Hilbert space. Now one expects quantum-mechanical wavefunctions to depend on the space coordinates. If the latter are operators, then wavefunctions too must be operators. This requires one to first identify a unitary representation on which X, Y, as selfadjoint operator-valued coordinates, act and satisfy the symmetry algebra (2.1). In this paper we tackle this problem, leaving the construction of operator-valued wavefunctions for a forthcoming publication [5].

2. The Noncommutative Poisson-Heisenberg Algebra

2.1. The Commutator Algebra

The noncommutative plane $\mathbb{R}^2_\theta$ is defined as the algebra of functions of two generators X, Y satisfying the commutator $[X, Y] = i\theta \mathbf{1}$, with $\theta > 0$. We regard $\mathbb{R}^2_\theta$ as a two-dimensional configuration space endowed with noncommuting coordinates X, Y. On the corresponding noncommutative phase space $\mathbb{R}^4_{\theta, \hbar}$ we have the operators X, Y, P_X, P_Y satisfying a commutator algebra that we postulate to be

$$[X, Y] = i\theta \mathbf{1}, \qquad [X, P_X] = [Y, P_Y] = i\hbar \mathbf{1}, \quad [P_X, P_Y] = [X, P_Y] = [Y, P_X] = 0. \qquad (2.1)$$

We will call the set of (2.1) the 2-dimensional, *noncommutative Poisson-Heisenberg algebra*. The time variable t will be taken to commute with all generators X, Y, P_X, P_Y. We would like to observe that positing the above algebra amounts to positing the symplectic structure first derived in [12]. One can then show that choosing the standard (quadratic in momentum) Hamiltonian, the system will carry the so-called *exotic* Galilean symmetry (for a recent review see [13]).

It has been known for long that the *Bopp shift*

$$Y \longmapsto Y - \frac{\theta}{\hbar} P_X \qquad (2.2)$$

reduces the noncommutative Poisson-Heisenberg algebra (2.1) to the usual Poisson-Heisenberg algebra in two commuting space dimensions.

2.2. Commutative Oscillator Modes

We will first construct a Hilbert-space representation for the commutator algebra (2.1), in terms of *commutative* oscillator modes. This is of course trivial, but it will serve as a warmup exercise for the construction in terms of *noncommutative* oscillator modes. Consider the usual harmonic oscillator eigenstates ϕ_n in 1 dimension, where $n \in \mathbb{N}$. The space spanned by the ϕ_n is ℓ^2, the Hilbert space of complex, square-summable sequences. In two commuting dimensions x, y we have the eigenstates $\phi_{nm}(x, y) = \phi_n(x)\phi_m(y)$. The latter form an orthonormal basis for the Hilbert space $\ell^2 \times \ell^2$. Position and momentum operators X', Y', P'_X, P'_Y can be defined on the space $\ell^2 \times \ell^2$ as usual [14]: acting on the first index,

$$X'\phi_{nm} := \sqrt{\frac{\theta}{2}}\left(\sqrt{n+1}\phi_{n+1,m} + \sqrt{n}\phi_{n-1,m}\right),$$

$$P'_X\phi_{nm} := \frac{i\hbar}{\sqrt{2\theta}}\left(\sqrt{n+1}\phi_{n+1,m} - \sqrt{n}\phi_{n-1,m}\right). \tag{2.3}$$

For the second index we define the action of Y', P'_Y similarly, with the sole difference that the (reverse) Bopp shift (2.2) must be taken into account:

$$Y'\phi_{nm} := \sqrt{\frac{\theta}{2}}\left(\sqrt{m+1}\phi_{n,m+1} + \sqrt{m}\phi_{n,m-1}\right) + \frac{\theta}{\hbar}P'_X\phi_{nm},$$

$$P'_Y\phi_{nm} := \frac{i\hbar}{\sqrt{2\theta}}\left(\sqrt{m+1}\phi_{n,m+1} - \sqrt{m}\phi_{n,m-1}\right). \tag{2.4}$$

One verifies that the operators X', Y', P'_X, P'_Y indeed satisfy the algebra (2.1). We have denoted these operators with a prime because this representation is unsatisfactory for our purposes. Indeed, there is nothing noncommutative about the eigenstates ϕ_{nm}: they are simply those of the harmonic oscillator on the commutative plane $\mathbb{R}^2$, noncommutativity being implemented in the algebra by means of the (inverse) Bopp shift. Instead one would like to have a representation space spanned by eigenstates ψ_{nm} of the harmonic oscillator on the noncommutative plane $\mathbb{R}^2_\theta$. This will be done explicitly in Section 2.4.

2.3. Interlude

Before moving on to noncommutative oscillator modes we need to recall some elementary facts [3]. Consider the space F of all entire functions $f : \mathbb{C} \to \mathbb{C}$ such that

$$f(z) = \sum_{n=0}^{\infty} \frac{c_n}{\sqrt{n!}} z^n, \qquad \sum_{n=0}^{\infty} |c_n|^2 < \infty. \tag{2.5}$$

This space is Hilbert with respect to the scalar product

$$\left\langle f \mid \tilde{f} \right\rangle := \frac{1}{2\pi i} \int dz^* \wedge dz \, f^*(z) \tilde{f}(z) e^{-|z|^2}, \tag{2.6}$$

where the asterisk denotes complex conjugation, and the integral extends over all $\mathbb{R}^2$ with $z = (x + iy)/\sqrt{2}$. An orthonormal basis is given by the set of all complex monomials

$$f_n(z) := \frac{z^n}{\sqrt{n!}}, \quad n \in \mathbb{N}. \tag{2.7}$$

The space F is called *Bargmann-Segal space*. The f_n are in 1-to-1 correspondence with the harmonic oscillator eigenstates ϕ_n of Section 2.2.

Next consider the following variant of Bargmann-Segal space. Let us consider functions $g : \mathbb{R} \to \mathbb{C}$ such that

$$g(x) = \sum_{n=0}^{\infty} \frac{c_n}{\sqrt{n!}} x^n, \qquad \sum_{n=0}^{\infty} |c_n|^2 < \infty, \tag{2.8}$$

the c_n being complex coefficients. Here our functions g are complex-valued analytic functions of one *real* variable x. Call G the space of all functions satisfying (2.8). A basis for G is given by the set of all real monomials

$$g_n(x) := \frac{x^n}{\sqrt{n!}}, \quad n \in \mathbb{N}. \tag{2.9}$$

We can define a scalar product on G by declaring these monomials to be orthonormal,

$$\left\langle g_n \mid g_m \right\rangle := \delta_{nm}, \quad n, m \in \mathbb{N}, \tag{2.10}$$

and extending the above to all elements of G by complex linearity. This scalar product makes G a complex Hilbert space. The difference with respect to Bargmann-Segal space F is that, the functions $g \in G$ depending on the real variable x instead of the complex variable z, the scalar product on G is no longer given by (2.6), nor by its real analogue. Indeed, given any two $g, \tilde{g} \in G$, the analogue of (2.6) for G would be the integral

$$\int_{-\infty}^{\infty} dx \, g^*(x) \tilde{g}(x) e^{-x^2}. \tag{2.11}$$

Although this integral does define a scalar product on G, this scalar product does not make the basis (2.9) orthogonal, as one readily verifies. Therefore one, and only one, of the following properties can be satisfied:

(i) the space G is Hilbert with respect to the scalar product (2.11), but the monomial basis (2.9) is not orthogonal with respect to it;

    (ii) the space G is Hilbert with respect to the scalar product (2.10), and the monomial basis (2.9) is indeed orthonormal with respect to it, but this scalar product is not given by the integral (2.11).

This being the case, we settle in favour of condition (ii) above as our choice for the Hilbert space G.

    Finally, the construction given by (2.8)–(2.10) can be straightforwardly extended to complex-valued, analytic functions of *two* real variables x, y. This will be used next.

2.4. Noncommutative Oscillator Modes

Next we construct a unitary, Hilbert-space representation for the algebra (2.1), in terms of noncommutative oscillator modes. It will be based on the Hilbert space, just mentioned in Section 2.3, of complex-valued, analytic functions of two real variables—but with *noncommuting, selfadjoint operators* replacing the real variables.

    Consider first an auxiliary copy $\mathcal{H}$ of the Heisenberg algebra, spanned by operators V, W, $\mathbf{1}$ satisfying $[V, W] = i\theta\mathbf{1}$, where both V and W have dimensions of length. The algebra $\mathcal{H}$ is realised in the standard way: V acts on auxiliary wavefunctions $h(v)$ by multiplication, $Vh(v) = vh(v)$, and W acts by differentiation, $Wh(v) = -i\theta\mathrm{d}h/\mathrm{d}v$. That the dimension of θ is length squared, rather than that of an action, should not bother us, since $\mathcal{H}$ is an auxiliary construct. The corresponding Hilbert space of the wavefunctions $h(v)$, also termed auxiliary, is $L^2(\mathbb{R}, \mathrm{d}v)$. This Hilbert space, however, is *not* the carrier space of the unitary representation of the algebra (2.1) that we are looking for. To reiterate, the algebra $[V, W] = i\theta\mathbf{1}$ just introduced, although isomorphic to the subalgebra $[X, Y] = i\theta\mathbf{1}$ contained in (2.1), acts on the auxiliary space $L^2(\mathbb{R}, \mathrm{d}v)$ while the space on which the algebra $[X, Y] = i\theta\mathbf{1}$ will act is about to be defined below.

    Next let $U(\mathcal{H})$ denote the universal enveloping algebra of $\mathcal{H}$. By definition, $U(\mathcal{H})$ is the algebra of polynomials in the operators V, W, $\mathbf{1}$, of arbitrarily high degree, with V and W satisfying $[V, W] = i\theta\mathbf{1}$. Some suitable completion of $U(\mathcal{H})$, denoted $\overline{U(\mathcal{H})}$ and to be constructed presently, is the space of convergent power series in V, W. We take an arbitrary vector of $\overline{U(\mathcal{H})}$ to be an expression of the form

$$\psi(V, W) = \sum_{n,m=0}^{\infty} \frac{c_{nm}}{\sqrt{n!m!}\; \theta^{n+m}} V^n W^m, \tag{2.12}$$

where the c_{nm} are complex coefficients, such that the above series converges (in a sense to be specified presently). The factor $(\theta^{n+m})^{-1/2}$ ensures that all summands are dimensionless. From now we will prescribe all vectors of $\overline{U(\mathcal{H})}$ to be normal-ordered, that is, V will *always* be assumed to precede W, if necessary by applying the commutator $[V, W] = i\theta\mathbf{1}$.

    A basis for $\overline{U(\mathcal{H})}$ is given by the vectors

$$\psi_{nm}(V, W) = \frac{1}{\sqrt{n!m!}\; \theta^{n+m}} V^n W^m, \quad n, m \in \mathbb{N}. \tag{2.13}$$

The simplest choice for a scalar product on $\overline{U(\mathcal{H})}$ is to declare the basis vectors (2.13) ortho-normal,

$$\langle \psi_{n_1 m_1} \mid \psi_{n_2 m_2} \rangle := \delta_{n_1 n_2} \delta_{m_1 m_2}, \tag{2.14}$$

and to extend (2.14) to all of $\overline{U(\mathcal{H})}$ by complex linearity. Then the squared norm of the vector (2.12) equals $\sum_{nm} |c_{nm}|^2$:

$$\left\| \psi(V, W) \right\|^2 = \sum_{n,m=0}^{\infty} |c_{nm}|^2. \tag{2.15}$$

Since this norm must be finite, this identifies $\overline{U(\mathcal{H})}$ as the Hilbert space of square-summable complex sequences $\{c_{nm}\}$ in two indices n, m, *the latter taken to be normal-ordered* as in (2.13); this defines the completion of $U(\mathcal{H})$ referred to above. It is worthwhile to observe that, although the vectors (2.12) are unbounded operators in their action on the auxiliary Hilbert space $L^2(\mathbb{R}, \mathrm{d}v)$, the same vectors *do* have a finite norm as elements of the Hilbert space $\overline{U(\mathcal{H})}$. This is so because the norm of $\psi(V, W)$ in (2.15) is being measured by means of the complex coefficients c_{nm}, not by means of the operator norms of V, W (themselves infinite). We will henceforth call the ψ_{nm} of (2.13) *noncommutative oscillator modes*.

The Hilbert space $\overline{U(\mathcal{H})}$ just constructed will become the carrier space of a representation of the algebra (2.1). For this we need to define the action of the operators X, Y, P_X, P_Y on the noncommutative oscillator modes (2.13). We set

$$X\psi_{nm} := \sqrt{\frac{\theta}{2}} \left(\sqrt{n+1}\psi_{n+1,m} + \sqrt{n}\psi_{n-1,m} \right),$$

$$P_X\psi_{nm} := \frac{i\hbar}{\sqrt{2\theta}} \left(\sqrt{n+1}\psi_{n+1,m} - \sqrt{n}\psi_{n-1,m} \right). \tag{2.16}$$

For the second index we define the action of Y, P_Y similarly, with the sole difference that the (reverse) Bopp shift (2.2) must be taken into account:

$$Y\psi_{nm} := \sqrt{\frac{\theta}{2}} \left(\sqrt{m+1}\psi_{n,m+1} + \sqrt{m}\psi_{n,m-1} \right) + \frac{\theta}{\hbar} P_X\psi_{nm},$$

$$P_Y\psi_{nm} := \frac{i\hbar}{\sqrt{2\theta}} \left(\sqrt{m+1}\psi_{n,m+1} - \sqrt{m}\psi_{n,m-1} \right). \tag{2.17}$$

Finally, the operators X, Y, P_X, P_Y so defined are Hermitian and satisfy the algebra (2.1) as desired. The above X, Y, P_X, P_Y are distinguished notationally from the operators X', Y', P'_X, P'_Y of (2.3)–(2.4) in order to stress the fact that they are actually different operators acting on different spaces (all infinite-dimensional, complex, separable Hilbert spaces being unitarily isomorphic, the above statement is to be understood as *different realisations of Hilbert space*), even if the two sets of operators satisfy the same algebra (2.1).

It is worth pointing out that the oscillator representation given above bears a close similarity with the one constructed in [15] from the nonrelativistic limit of anyons.

3. Higher Dimensions

The previous results can be easily generalised to higher-dimensional Moyal spaces. Let us outline the main results in dimension 3. Here the noncommutative Poisson-Heisenberg algebra reads

$$[X, Y] = [Y, Z] = [Z, X] = i\theta\mathbf{1}, \qquad [X, P_X] = [Y, P_Y] = [Z, P_Z] = i\hbar\mathbf{1}, \qquad (3.1)$$

all other commutators vanishing identically. For simplicity we have assumed the generators so normalised that there is just one independent noncommutativity parameter θ. The Bopp shift that reduces (3.1) to the standard Poisson-Heisenberg algebra is

$$Y \longmapsto Y - \frac{\theta}{\hbar}P_X, \qquad Z \longmapsto Z + \frac{\theta}{\hbar}P_X - \frac{\theta}{\hbar}P_Y. \qquad (3.2)$$

The algebra (3.1) contains three independent copies of the noncommutative plane. Therefore we will need three auxiliary copies $\mathcal{H}_1$, $\mathcal{H}_2$, and $\mathcal{H}_3$ of the Heisenberg algebra of Section 2.4, the jth copy having generators V_j, W_j satisfying

$$[V_j, W_j] = i\theta\mathbf{1}, \quad j = 1, 2, 3. \qquad (3.3)$$

We convene to associate the index values $j = 1, 2, 3$ with the respective commutators $[X, Y] = i\theta\mathbf{1}$, $[Y, Z] = i\theta\mathbf{1}$, and $[Z, X] = i\theta\mathbf{1}$, each one of which spans a copy of the Moyal plane. Following (2.13), the noncommutative oscillator modes $\psi_{n_j m_j}$ corresponding to the jth copy of the Moyal plane are

$$\psi_{n_j m_j} := \frac{1}{\sqrt{n_j! m_j! \theta^{n_j + m_j}}} V_j^{n_j} W_j^{m_y}, \quad n_j, m_j \in \mathbb{N}, \ j = 1, 2, 3. \qquad (3.4)$$

The above $\psi_{n_j m_j}$ provide a complete orthonormal set for the space $\overline{U(\mathcal{H}_j)}$. Position and momentum operators $X^{(1)}$, $Y^{(1)}$, $P_{X^{(1)}}$, $P_{Y^{(1)}}$ can be defined on $\overline{U(\mathcal{H}_1)}$ as in Section 2.4; by the same token we define the action of $Y^{(2)}$, $Z^{(2)}$, $P_{Y^{(2)}}$, $P_{Z^{(2)}}$ on $\overline{U(\mathcal{H}_2)}$, and the action of $Z^{(3)}$, $X^{(3)}$, $P_Z^{(3)}$, $P_X^{(3)}$ on $\overline{U(\mathcal{H}_3)}$.

Next consider the tensor product space

$$\overline{U(\mathcal{H}_1)} \otimes \overline{U(\mathcal{H}_2)} \otimes \overline{U(\mathcal{H}_3)}. \qquad (3.5)$$

A complete orthonormal set on this product space is given by the tensor product states

$$\psi_{\mathbf{nm}} := \psi_{n_1 m_2} \otimes \psi_{n_2 m_2} \otimes \psi_{n_3 m_3}, \quad \mathbf{n}, \mathbf{m} \in \mathbb{N}^3, \qquad (3.6)$$

where $\mathbf{n} = (n_1, n_2, n_3)$ and $\mathbf{m} = (m_1, m_2, m_3)$. We can extend the above position and momentum operators to act on all of $\overline{U(\mathcal{H}_1)} \otimes \overline{U(\mathcal{H}_2)} \otimes \overline{U(\mathcal{H}_3)}$ in the obvious way. Namely,

$X^{(1)}$ on $\overline{U(\mathcal{H}_1)}$ is extended as $X^{(1)} \mapsto X^{(1)} \otimes \mathbf{1}_2 \otimes \mathbf{1}_3$, while $Y^{(2)}$ on $\overline{U(\mathcal{H}_2)}$ it is extended as $Y^{(2)} \mapsto \mathbf{1}_1 \otimes Y^{(2)} \otimes \mathbf{1}_3$ and so forth. In this way all 3 sets of position and momentum operators

$$X^{(1)}, Y^{(1)}, P_X^{(1)}, P_Y^{(1)}, \qquad Y^{(2)}, Z^{(2)}, P_Y^{(2)}, P_Z^{(2)}, \qquad Z^{(3)}, X^{(3)}, P_Z^{(3)}, P_X^{(3)}, \tag{3.7}$$

each one of them initially defined to act only on the correponding space $\overline{U(\mathcal{H}_j)}$, is now defined on the tensor product space (3.5). We will not distinguish notationally between the operators (3.7) and their extensions to the tensor product space (3.5). On the latter we finally define

$$
\begin{aligned}
X &:= \frac{1}{\sqrt{2}}\left(X^{(1)} + X^{(3)}\right), & P_X &:= \frac{1}{\sqrt{2}}\left(P_X^{(1)} + P_X^{(3)}\right), \\
Y &:= \frac{1}{\sqrt{2}}\left(Y^{(1)} + Y^{(2)}\right), & P_Y &:= \frac{1}{\sqrt{2}}\left(P_Y^{(1)} + P_Y^{(2)}\right), \\
Z &:= \frac{1}{\sqrt{2}}\left(Z^{(2)} + Z^{(3)}\right), & P_Z &:= \frac{1}{\sqrt{2}}\left(P_Z^{(2)} + P_Z^{(3)}\right).
\end{aligned}
\tag{3.8}
$$

One verifies that the operators (3.8), acting on the tensor product states (3.6), indeed satisfy the algebra (3.1) as desired.

We would like to remark that the commutator relations (3.1) break rotation invariance. However, the latter can be restored if the constant parameter θ is promoted to a vector-valued function of the momentum, whenever this function is divergence-free in momentum space [13, 16].

4. Discussion

In this paper we have constructed a unitary representation for the symmetry algebra (2.1). This latter algebra encodes the kinematics of quantum mechanics on the Moyal plane, regardless of whatever specific dynamics one wishes to consider. This representation has noncommutative oscillator modes as its building blocks. Such oscillator modes are the noncommutative analogues of ordinary harmonic oscillators on the commutative plane $\mathbb{R}^2$. We have also sketched how to generalise these noncommutative oscillator modes to higher dimensions, provided that the space noncommutativity is always of the Heisenberg-algebra type.

As stated in the introduction, the purpose of these noncommutative oscillator modes is to use them in a novel approach to quantum mechanics on noncommutative spaces. This approach does not make use of c-number valued wavefunctions that are multiplied together by means of a star-product. Rather, one looks for operator-valued wavefunctions already from the start [6]. Once space coordinates are operators, since wavefunctions will be functions of the coordinates, wavefunctions themselves will become operator-valued. The analysis carried out here is a necessary first step towards that goal.

Looking beyond, a feature of emergent phenomena is that they arise as some form of coarse-grained, or thermodynamical, description of some microscopic physics that one does not have complete control of [17]. This much is true in general, and also of quantum mechanics in particular [18–21], even before introducing noncommutativity. Now

space noncommutativity also introduces a form of coarse graining, due to the existence of the quantum of area θ—not on phase space, but on configuration space. In this sense, noncommutative quantum mechanics also falls within the category of emergent physics.

Acknowledgments

References

[1] R. J. Szabo, "Quantum field theory on noncommutative spaces," *Physics Reports A*, vol. 378, no. 4, pp. 207–299, 2003.

[2] R. J. Szabo, "Quantum gravity, field theory and signatures of noncommutative spacetime," *General Relativity and Gravitation*, vol. 42, no. 1, pp. 1–29, 2009.

[3] W. Thirring, *Quantum Mathematical Physics*, Springer, Berlin, Germany, 2nd edition, 2002.

[4] L. Gouba and F. G. Scholtz, "On the uniqueness of unitary representations of the non-commutative Heisenberg-Weyl algebra," *Canadian Journal of Physics*, vol. 87, no. 9, pp. 995–997, 2009.

[5] J. M. Isidro, P. Fernández de Córdoba, J. M. Rivera-Rebolledo, and J. L. G. Santander, "Remarks on the representation theory of the Moyal plane," *High Energy Physics—Theory*. In preparation.

[6] R. Banerjee, B. Chakraborty, S. Ghosh, P. Mukherjee, and S. Samanta, "Topics in noncommutative geometry inspired physics," *Foundations of Physics*, vol. 39, no. 12, pp. 1297–1345, 2009.

[7] B. Chakraborty, S. Gangopadhyay, and A. Saha, "Seiberg-Witten map and Galilean symmetry violation in a noncommutative planar system," *Physical Review D*, vol. 70, no. 10, p. 107707, 4, 2004.

[8] F. G. Scholtz, B. Chakraborty, S. Gangopadhyay, and A. G. Hazra, "Dual families of noncommutative quantum systems," *Physical Review D*, vol. 71, no. 8, Article ID 085005, p. 11, 2005.

[9] B. Chakraborty, S. Gangopadhyay, A. G. Hazra, and F. G. Scholtz, "Twisted Galilean symmetry and the Pauli principle at low energies," *Journal of Physics A*, vol. 39, no. 30, pp. 9557–9572, 2006.

[10] S. Gangopadhyay and F. G. Scholtz, "Path-integral action of a particle in the noncommutative plane," *Physical Review Letters*, vol. 102, no. 24, Article ID 241602, p. 4, 2009.

[11] F. G. Scholtz, L. Gouba, A. Hafver, and C. M. Rohwer, "Formulation, interpretation and application of non-commutative quantum mechanics," *Journal of Physics A*, vol. 42, no. 17, Article ID 175303, p. 13, 2009.

[12] C. Duval and P. A. Horváthy, "The exotic Galilei group and the "Peierls substitution"," *Physics Letters B*, vol. 479, no. 1–3, pp. 284–290, 2000.

[13] P. A. Horváthy, L. Martina, and P. C. Stichel, "Exotic Galilean symmetry and non-commutative mechanics," *SIGMA*, vol. 6, p. 26, 2010.

[14] L. Landau and E. Lifshitz, *Quantum Mechanics*, vol. 3, Butterworth Heinemann, Oxford, UK, 2000.

[15] P. A. Horváthy and M. S. Plyushchay, "Anyon wave equations and the noncommutative plane," *Physics Letters B*, vol. 595, no. 1–4, pp. 547–555, 2004.

[16] A. Bérard and H. Mohrbach, "Monopole and Berry phase in momentum space in noncommutative quantum mechanics," *Physical Review D*, vol. 69, no. 12, Article ID 127701, p. 4, 2004.

[17] R. Carroll, *On the Emergence Theme of Physics*, World Scientific, Hackensack, NJ, USA, 2010.

[18] H. -T. Elze, "The attractor and the quantum states," *International Journal of Quantum Information*, vol. 7, no. 1, supplement, pp. 83–96, 2009.

[19] H. -T. Elze, "Symmetry aspects in emergent quantum mechanics," *Journal of Physics: Conference Series*, vol. 171, no. 1, Article ID 012034, 2009.

[20] H.-T. Elze, "Does quantum mechanics tell an atomistic spacetime?" *Journal of Physics: Conference Series*, vol. 174, Article ID 012009, 2009.

[21] A. E. Faraggi and M. Matone, "The equivalence postulate of quantum mechanics," *International Journal of Modern Physics A*, vol. 15, no. 13, pp. 1869–2017, 2000.
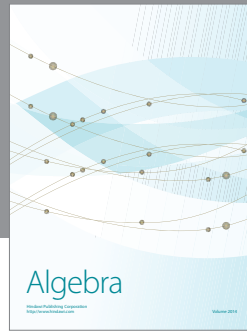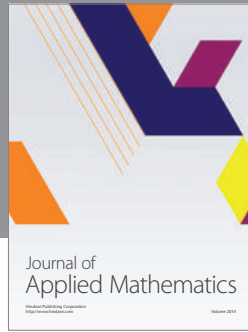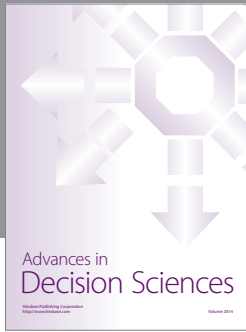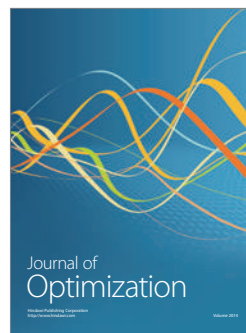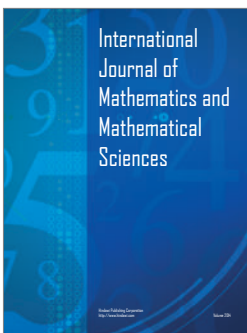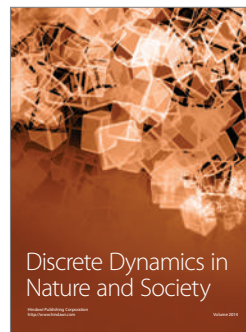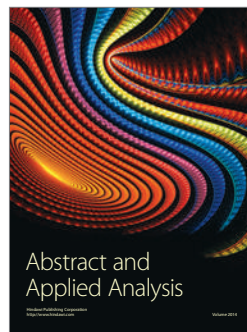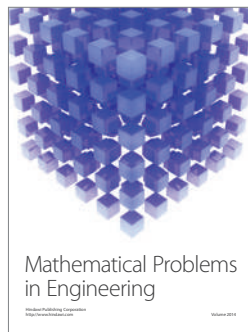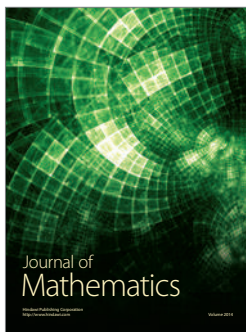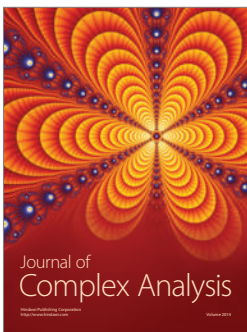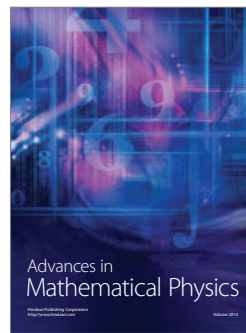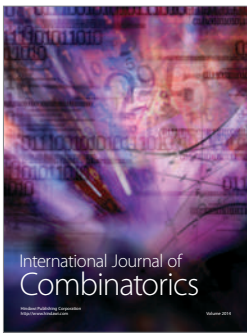
On the Contact Geometry and the Poisson Geometry of the Ideal Gas

J. M. Isidro *,† 🆔 **and P. Fernández de Córdoba** † 🆔

Instituto Universitario de Matemática Pura y Aplicada, Universidad Politécnica de Valencia, Valencia 46022, Spain; pfernandez@mat.upv.es

* Correspondence: joissan@mat.upv.es
† The two authors contributed equally to this work.

Abstract: We elaborate on existing notions of contact geometry and Poisson geometry as applied to the classical ideal gas. Specifically, we observe that it is possible to describe its dynamics using a 3-dimensional contact submanifold of the standard 5-dimensional contact manifold used in the literature. This reflects the fact that the internal energy of the ideal gas depends exclusively on its temperature. We also present a Poisson algebra of thermodynamic operators for a quantum-like description of the classical ideal gas. The central element of this Poisson algebra is proportional to Boltzmann's constant. A Hilbert space of states is identified and a system of wave equations governing the wavefunction is found. Expectation values for the operators representing pressure, volume and temperature are found to satisfy the classical equations of state.

Keywords: ideal gas; poisson geometry

1. Introduction

The link between differential geometry and thermodynamics has provided deep insights. Motivated by the theory of relativity, early treatises presenting a geometric approach to thermodynamics appeared already in the 1930s [1]. More recently we have witnessed the use of Riemannian geometry [2–7], contact geometry [8–11], Poisson and symplectic formulations [12], Finsler geometry [3], symmetric spaces [13] and generalised complex geometry [14], among others.

Conversely, the theory of gravity, a paradigmatic example of a physical theory drawing heavily on differential geometry, has achieved remarkable breakthroughs recently thanks to its extensive use of a thermodynamic approach [15–17]; for topical reviews and more extensive references see, e.g., [18,19].

In this paper we touch upon issues related to the contact geometry and to the Poisson geometry of the classical ideal gas. Concerning contact geometry [20], we make the observation that its standard 5-dimensional contact manifold $\mathcal{M}$ can be reduced to a 3-dimensional contact submanifold. Concerning Poisson geometry [20], we propose that classical thermodynamic variables be regarded as operators on a Hilbert space of quantum-like states.

(i) The contact geometry of the classical ideal gas is usually described using a 5-dimensional contact manifold $\mathcal{M}$ that can be endowed with the local coordinates U (internal energy), S (entropy), V (volume), T (temperature) and p (pressure). This description corresponds to a choice of the fundamental equation, in the energy representation, in which U depends on the two extensive variables S and V, i.e., $U = U(S,V)$, the conjugate variables being

$$T = \frac{\partial U}{\partial S}, \qquad -p = \frac{\partial U}{\partial V}. \tag{1}$$

Then the standard contact form on $\mathcal{M}$ reads

$$\alpha = \mathrm{d}U + T\mathrm{d}S - p\mathrm{d}V. \tag{2}$$

It is however well known that the internal energy of the ideal gas can be taken to depend only on the temperature T. This is achievable by means of a Legendre transformation, but it does not account for the reduction in the number of variables that U depends on. In this paper we show that, in the particular case of the ideal gas, a change of variables can be identified in configuration space (coordinatised by S, V) that reduces the fundamental equation to an expression $U = U(x)$, where $x = x(S, V)$ is a single coordinate. Supplemented with its corresponding conjugate variable p_x, the contact form on this 3-dimensional contact submanifold $\mathcal{S}$ (coordinatised by x, p_x, U) now reads

$$\beta = \mathrm{d}U + p_x\mathrm{d}x. \tag{3}$$

(ii) Concerning the Poisson geometry of the ideal gas, we propose that *classical* thermodynamic variables be regarded as operators on a Hilbert space of *quantum-like* states. Promoting functions to operators is in fact a natural thing to do, once fluctuations have been described using path integrals [21] in the spirit of [22]. We call our analysis *quantum-like*, by which we mean that *a quantum formalism is being used in order to analyse classical thermostatics*. Indeed we will see that Planck's quantum of action $\hbar$ is absent altogether, its role being played instead by Boltzmann's constant k_B.

2. The PDE's of State of the Ideal Gas

Let us consider a number N of particles of ideal gas (monoatomic for simplicity). Its fundamental equation in the energy representation $U = U(S, V)$ reads [23]

$$U(S, V) = U_0 \exp\left(\frac{2S}{3Nk_B}\right)\left(\frac{V_0}{V}\right)^{2/3}, \tag{4}$$

with U_0, V_0 certain fiducial values. Each one of the two equations defining the conjugate variables in Equation (1) qualifies as an equation of state. One can introduce Poisson brackets on the 4-dimensional Poisson manifold $\mathcal{P}$ (a submanifold of $\mathcal{M}$) spanned by the coordinates S, V and their conjugate variables T, $-p$, the nonvanishing brackets being

$$\{S, T\} = 1, \qquad \{V, -p\} = 1. \tag{5}$$

(Our definition of the Poisson brackets $\{\cdot, \cdot\}$ follows that of ref. [20]). Given now an equation of state

$$f(p, T, \ldots) = 0, \tag{6}$$

we will substitute the canonical variables (1) into it, in order to obtain

$$f\left(-\frac{\partial U}{\partial V}, \frac{\partial U}{\partial S}, \ldots\right) = 0. \tag{7}$$

We call (7) *a partial differential equation of state* (for short, *PDE of state*).

There are two independent conjugate variables, hence two independent equations of state. The definition of the pressure $p = -\partial U/\partial V$, plus Equation (9) below, yield the well-known law

$$pV = Nk_BT, \tag{8}$$

while the relation $T = \partial U/\partial S$ yields the equipartition theorem,

$$U = \frac{3}{2}Nk_BT. \tag{9}$$

In turn, Equations (8) and (1) yield the first PDE of state,

$$V\frac{\partial U}{\partial V} + Nk_B\frac{\partial U}{\partial S} = 0, \tag{10}$$

while Equations (9) and (1) yield the second PDE of state

$$U - \frac{3}{2}Nk_B\frac{\partial U}{\partial S} = 0. \tag{11}$$

One readily integrates the system (10) and (11) to obtain the fundamental Equation (4) we started off with.

The successive changes of variables

$$v := \ln\left(\frac{V}{V_0}\right), \quad s := \frac{S}{Nk_B} \tag{12}$$

and

$$x := s - v, \quad y := s + v, \tag{13}$$

transform the PDE's of state (10) and (11) into

$$\frac{\partial U}{\partial y} = 0 \tag{14}$$

and

$$U - \frac{3}{2}\frac{\partial U}{\partial x} = 0 \tag{15}$$

respectively. The solution to (14) and (15) reads

$$U = U(x) = U_0\exp\left(\frac{2x}{3}\right). \tag{16}$$

In particular, U does not depend on y. This reflects the well-known fact that the internal energy of an ideal gas can be taken to depend exclusively on the temperature T. It must be realised, though, that the change to T as *the one* independent variable involves a Legendre transformation in phase space, which is not the case in (12), (13). Instead, the above change of variables can be performed without exiting configuration space. Computing the conjugate variable p_x corresponding to the variable x we find

$$p_x = \frac{\partial U}{\partial x} = \frac{2}{3}U. \tag{17}$$

Since x is dimensionless, p_x has the dimensions of energy. Now comparing to the temperature T as computed from Equation (4),

$$T = \frac{\partial U}{\partial S} = \frac{2}{3Nk_B}U, \tag{18}$$

we arrive at the equality of the two variables p_x and T, modulo Boltzmann's constant to correct the different dimensionalities:

$$p_x = Nk_BT. \tag{19}$$

The other canonical variable, $p_y = \partial U/\partial y$, vanishes identically by virtue of the PDE of state (14).

We are thus left with a 3-dimensional contact submanifold $\mathcal{S}$ (coordinatised by x, p_x and U) of the initial 5-dimensional contact manifold $\mathcal{M}$ (coordinatised by U, S, V, T and $-p$). The contact form

β on $\mathcal{S}$ given in Equation (3) can be readily shown to equal the restriction, to the submanifold $\mathcal{S}$, of the contact form α on $\mathcal{M}$ given in Equation (2):

$$\alpha = \beta \text{ on } \mathcal{S}. \tag{20}$$

3. The Wave Equations of the Ideal Gas

Application of the canonical quantisation rules to the PDE (7) will produce a quantum-like wave equation. Initially, this canonical quantisation will be carried out on a 2-dimensional Lagrangian submanifold (the configuration space spanned by S and V) of the 5-dimensional contact manifold $\mathcal{M}$. At a later stage we will apply the changes of variables (12) and (13) in order to directly quantise a 1-dimensional Lagrangian submanifold (the configuration space spanned by x) of the 3-dimensional contact manifold $\mathcal{S}$. The two procedures (quantisation and reduction) will be seen to commute.

3.1. Quantum Commutators

Promoting the real functions S, V, T, p to Hermitian operators on a Hilbert space, the Poisson algebra of Functions (5) becomes the Poisson-Lie algebra of operator commutators

$$[S, T] = q\mathbf{1}, \qquad [V, -p] = q\mathbf{1}, \qquad q \in \mathbb{C}, \tag{21}$$

where $[X, Y] := XY - YX$ by definition. The right-hand side contains a quantum of energy q and the identity operator $\mathbf{1}$. For reasons that will soon become apparent we will assume our ideal gas to be in thermal equilibrium with a bath kept at a constant temperature T_B, so we can write

$$q = zNk_BT_B, \tag{22}$$

where k_B is Boltzmann's constant and $z \in \mathbb{C}$ a free parameter.

Assume that S and V are represented as multiplication operators on quantum-like wavefunctions $\psi(S, V)$. Then the conjugate variables act on ψ by differentiation,

$$T = -q\frac{\partial}{\partial S}, \qquad p = q\frac{\partial}{\partial V}. \tag{23}$$

Modulo operator-ordering ambiguities, substituting the variables (23) into the equations of state (8) and (9) produces two time-independent wave equations that quantum-like states $\psi(S, V)$ must satisfy. As we will prove, the solutions to these wave equations will automatically be L^2-integrable on configuration space $[S_0, S_1] \times [V_0, V_1]$. Square integrability of ψ ensures that $|\psi(S, V)|^2$ belongs to $L^1([S_0, S_1] \times [V_0, V_1])$, as befits a thermodynamic probability distribution.

3.2. Thermodynamic Wave Equations

Next we apply the quantum rules (23) to the equations of state (8) and (9). Three possible orderings for the operators V and p are Vp, pV and Weyl's $(Vp + pV)/2$; the simplest one, that we will use here, is Vp. Therefore quantum-like states will be simultaneous solutions to

$$\left(V\frac{\partial}{\partial V} + Nk_B\frac{\partial}{\partial S} \right) \psi(S, V) = 0 \tag{24}$$

and

$$\left(U(S, V) + \frac{3q}{2}Nk_B\frac{\partial}{\partial S} \right) \psi(S, V) = 0. \tag{25}$$

The above system is solved by

$$\psi_q(S, V) = \exp\left(-\frac{1}{q}U(S, V) \right) \tag{26}$$

with an arbitrary value of the parameter $q = zNk_BT_B$; equivalently z runs over the whole complex plane $\mathbb{C}$.

Some particular choices of z in (26) deserve attention. The value $z = 1$ leads to the real exponential

$$\psi_{z=1}(S, V) := \exp\left(-\frac{U(S, V)}{Nk_BT_B}\right),\tag{27}$$

while $z = \mathrm{i}$ yields the complex exponential

$$\psi_{z=\mathrm{i}}(S, V) := \exp\left(\mathrm{i}\frac{U(S, V)}{Nk_BT_B}\right).\tag{28}$$

The above states are distinguished in the sense that they are reminiscent of analogous exponentials arising in statistical mechanics and quantum mechanics, respectively.

3.3. The Wave Equations on the Reduced Phase Space

At the quantum-like level, the reduction of the phase space from the 5-dimensional $\mathcal{M}$ to the 3-dimensional $\mathcal{S}$ takes place exactly as at the classical level. Namely, the change of variables (12), (13) transforms the system (24), (25) into

$$\frac{\partial\psi}{\partial y} = 0\tag{29}$$

and

$$\left(U(x) + \frac{3q}{2}\frac{\partial}{\partial x}\right)\psi = 0,\tag{30}$$

where $U(x)$ was already identified in Equation (16). The above is solved by

$$\psi_q(x) = \exp\left(-\frac{1}{q}U(x)\right),\tag{31}$$

in agreement with our previous result (26). In particular, the y-dependence drops out as before. Now the internal energy is defined modulo the addition of a real constant,

$$U(x) \to U(x) + C, \qquad C \in \mathbb{R}.\tag{32}$$

This symmetry reflects the global invariance of the (unnormalised) wavefunction ψ_q under the action of $\mathbb{C}^*$, the multiplicative group of nonzero complex numbers:

$$\psi_q(x) \to \exp(-C/q)\psi_q(x).\tag{33}$$

As announced above the two procedures, *quantisation* and *reduction*, commute in our case.

4. Discussion

Classical thermostatics is governed by a system of partial differential equations of state, the integral of which yields the fundamental equation of the thermodynamic system under consideration. In the case of the ideal gas, the PDEs of state are Equations (10) and (11), their solution being given by Equation (4).

In this work we have established that the classical PDEs of state for the ideal gas have a set of quantum-like counterparts, the wave Equations (24) and (25). Their integral, Equation (26), is the wavefunction of a quantum-like description of the ideal gas. Summarising, one can say that *the quantum-like wavefunction is the exponential of the classical fundamental equation of the ideal gas*. This is in perfect analogy with corresponding notions in WKB quantum mechanics.

One can find a coordinate change that transforms the relevant equations into a reduced form. Under *reduced* we understand that the equations *involve the least number of variables*; geometrically this corresponds to the reduction from the initial 5-dimensional phase space $\mathcal{M}$ to a 3-dimensional subspace $\mathcal{S}$. For the classical PDEs of state this reduced form is (15); its corresponding quantum-like equation is (30). Instead of two real coordinates S, V one is left with just one coordinate x that the fundamental equation $U = U(x)$ and the wavefunction $\psi_q = \psi_q(x)$ depend on. We have succeeded in finding a coordinate transformation *without exiting configuration space* (see Equations (12) and (13)) that reduces the number of independent variables the internal energy depends on. So the phase space of the classical ideal gas is a 3-dimensional contact submanifold $\mathcal{S}$ of the standard 5-dimensional contact manifold $\mathcal{M}$. This reduction is a feature of the classical ideal gas that need not (and generally will not) hold for other thermodynamic systems. We should stress, however, that this dimensional reduction from 5 to 3 implies information loss. Inverting this dimensional reduction (i.e., returning from 3 to 5 dimensions) cannot be done without prior knowledge of the equation of state.

The quantum commutators (21) lead to the uncertainty relations $\Delta S \Delta T \geq |q|/2$, $\Delta p \Delta V \geq |q|/2$. As opposed to the quantum-mechanical uncertainty relation $\Delta x \Delta p \geq \hbar/2$, the quantum q carries the dimensions of energy (Boltzmann's constant k_B multiplied by the temperature T_B of the bath). Moreover, since T_B is arbitrary, the quantum q may be taken to be arbitrarily small. This is a fundamental difference with respect to quantum mechanics. A model containing both Planck's constant $\hbar$ and Boltzmann's constant k_B has been considered in ref. [24].

For any fixed value of the central element q in the quantum Poisson algebra, the space of solutions to the wave equation is a 1-dimensional subspace of the Hilbert space $L^1([S_0, S_1] \times [V_0, V_1])$. Moreover, there is a whole $\mathbb{C}$'s worth of central elements q for the quantum Poisson algebra (21). In quantum theory, the Hilbert space $L^2([S_0, S_1] \times [V_0, V_1])$ provides a *unitary* representation of the quantum Poisson algebra (21); for this it is necessary (though not sufficient) that the quantum q be pure imaginary [25]. Unitarity of this representation implies that observable quantities are represented by Hermitian operators. Thus unitarity is ruled out for the quantum states with $q \in \mathbb{R}$, such as the state (27). How does the the state (28) fare?

Let us recall [25] that periodic boundary conditions on the wavefunction, $\psi(a) = \psi(b)$, ensure hermiticity of $-i\partial/\partial x$ on $L^2([a, b])$. In the absence of periodicity, the Hermitian property is generally not guaranteed. However the state (28) is not periodic on $[S_0, S_1] \times [V_0, V_1]$. The inevitable conclusion is that, whatever the value of q, we are forced to deal with a non-Hermitian theory. Now the Hermitian property of operators is a sufficient (but not a necessary) condition to ensure that expectation values are real [25]. Fortunately, the relevant expectation values in the states (26) are all real. This follows by taking the scalar product of Equations (24) and (25) with ψ_q. In this way classicality is recovered in the form of Eherenfest's theorem [26] for the expectation values of the relevant operators entering the equations of state.

In the presence of a gravitational field, thermal fluctuations have been argued to be indistinguishable from quantum fluctuations [27]. Admittedly, *quantum* is Hermitean while *thermal* is not, and the loss of unitarity reported above reflects this fact. In this work we have shown that, in the thermodynamics of the ideal monoatomic gas, one can go a long way replacing *thermal* with *quantum* without noticing the difference.

Author Contributions: The two authors contributed equally to this work.

Conflicts of Interest: The authors declare no conflict of interest.

References

1. Tolman, R. *Relativity, Thermodynamics and Cosmology*; Dover: New York, NY, USA, 1987.
2. Mrugala, R. Geometric Formulation of Equilibrium Phenomenological Thermodynamics. *Rep. Math. Phys.* **1978**, *14*, 419–427.

3.   Mrugala, R. Riemannian and Finslerian Geometry in Thermodynamics. *Open Sys. Inf. Dyn.* **1992**, *1*, 379–396.

4.   Quevedo, H.; Vázquez, A. The Geometry of Thermodynamics. *AIP Conf. Proc.* **2008**, *977*, 165–172.

5.   Quevedo, H.; Sánchez, A.; Taj, S.; Vázquez, A. Curvature as a Measure of the Thermodynamic Interaction. *arXiv* **2010**, arXiv:1011.0122.

6.   Ruppeiner, G. Thermodynamics: A Riemannian Geometric Model. *Phys. Rev.* **1979**, *A20*, 1608.

7.   Ruppeiner, G. Riemannian Geometry in Thermodynamic Fluctuation Theory. *Rev. Mod. Phys.* **1995**, *67*, 605.

8.   Bravetti, A. Contact Hamiltonian Dynamics: The Concept and its Use. *Entropy* **2017**, *19*, 535.

9.   Mrugala, R.; Nulton, J.; Schön, J.; Salamon, P. Statistical Approach to the Geometric Structure of Thermodynamics. *Phys. Rev.* **1990**, *A41*, 3156.

10.   Mrugala, R.; Nulton, J.; Schön, J.; Salamon, P. Contact Structure in Thermodynamic Theory. *Rep. Math. Phys.* **1991**, *29*, 109–121.

11.   Rajeev, G. Quantization of Contact Manifolds and Thermodynamics. *Ann. Phys.* **2008**, *323*, 768–782.

12.   Rajeev, G. A Hamilton-Jacobi Formalism for Thermodynamics. *Ann. Phys.* **2008**, *323*, 2265–2285.

13.   Bravetti, A.; López-Monsalvo, C.; Quevedo, H. Maximally Symmetric Spacetimes Emerging from Thermodynamic Fluctuations. *arXiv* **2015**, arXiv:1503.08358.

14.   de Córdoba, P.F.; Isidro, J.M. Generalised Complex Geometry in thermodynamic Fluctuation Theory. *Entropy* **2015**, *17*, 5888–6902.

15.   Padmanabhan, T. Thermodynamic Aspects of Gravity: New Insights. *Rep. Prog. Phys.* **2010**, *73*, 046901.

16.   Padmanabhan, T. General Relativity from a Thermodynamic Perspective. *Gen. Relativ. Gravit.* **2014**, *46*, 1673.

17.   Padmanabhan, T. Gravity and/is Thermodynamics. *Curr. Sci.* **2015**, *109*, 2236.

18.   Linnemann, N.; Visser, M. Hints towards the Emergent Nature of Gravity. *arXiv* **2017**, arXiv:1711.10503.

19.   Moustos, D. Gravity as a Thermodynamic Phenomenon. *arXiv* **2017**, arXiv:1701.08967.

20.   Arnold, V. Mathematical Methods of Classical Mechanics. In *Graduate Texts in Mathematics*; Springer: Berlin, Germany, 1989.

21.   Ruppeiner, G. New Thermodynamic Fluctuation Theory Using Path Integrals. *Phys. Rev. A* **1983**, *27*, 1116–1133.

22.   Onsager, L.; Machlup, S. Fluctuations and Irreversible Processes. *Phys. Rev.* **1953**, *91*, 1505.

23.   Callen, H. *Thermodynamics*; Wiley: New York, NY, USA, 1960.

24.   Sasa, S.; Yokokura, Y. Thermodynamic Entropy as a Noether Invariant. *Phys. Rev. Lett.* **2016**, *116*, 140601.

25.   Thirring, W. *Quantum Mathematical Physics*; Springer: Berlin, Germany, 2003.

26.   Landau, L.; Lifshitz, E. Quantum Mechanics. In *Course of Theoretical Physics*; Butterworth-Heinemann: Oxford, UK, 2000; Volume 3.

27.   Kolekar, S.; Padmanabhan, T. Indistinguishability of Thermal and Quantum Fluctuations. *Class. Quantum Gravity* **2015**, *32*, 202001.

On the Holographic Bound in Newtonian Cosmology

José M. Isidro * [ID] **and Pedro Fernández de Córdoba** [ID]

Instituto Universitario de Matemática Pura y Aplicada, Universidad Politécnica de Valencia,
46022 Valencia, Spain; pfernandez@mat.upv.es
* Correspondence: joissan@mat.upv.es; Tel.: +34-96-3877000

Abstract: The holographic principle sets an upper bound on the total (Boltzmann) entropy content of the Universe at around $10^{123}k_B$ (k_B being Boltzmann's constant). In this work we point out the existence of a remarkable duality between nonrelativistic quantum mechanics on the one hand, and Newtonian cosmology on the other. Specifically, nonrelativistic quantum mechanics has a quantum probability fluid that exactly mimics the behaviour of the cosmological fluid, the latter considered in the Newtonian approximation. One proves that the equations governing the cosmological fluid (the Euler equation and the continuity equation) become the very equations that govern the quantum probability fluid after applying the Madelung transformation to the Schroedinger wavefunction. Under the assumption that gravitational equipotential surfaces can be identified with isoentropic surfaces, this model allows for a simple computation of the gravitational entropy of a Newtonian Universe. In a first approximation, we model the cosmological fluid as the quantum probability fluid of free Schroedinger waves. We find that this model Universe saturates the holographic bound. As a second approximation, we include the Hubble expansion of the galaxies. The corresponding Schroedinger waves lead to a value of the entropy lying three orders of magnitude below the holographic bound. Current work on a fully relativistic extension of our present model can be expected to yield results in even better agreement with empirical estimates of the entropy of the Universe.

Keywords: Boltzmann entropy; holographic bound; Newtonian cosmology

1. Introduction

There is a widespread belief that the continuum description of spacetime as provided by general relativity must necessarily break down at very short length scales and/or very high curvatures. A number of very different approaches to an eventual theory of quantum gravity have been presented in the literature; these candidate theories are too varied and too extensive to summarise here. Suffice it to say that whatever the *atoms of spacetime* may turn out to be, at the moment there exists a large body of well-established knowledge concerning the *thermodynamics of spacetime*. For recent advances in this direction, as well as a more detailed bibliography, we refer the reader to the original articles [1–4] as well as the review papers [5,6].

The overall picture that emerges is that of a continuum description after some appropriate coarse-graining of some underlying degrees of freedom (the atoms of spacetime mentioned above). Even if the precise nature of the latter is unknown as of yet, one can still make progress following a thermodynamical approach: one ignores large amounts of detailed knowledge (e.g., the precise motions followed by the atoms of a gas) while concentrating only on a few coarse-grained averages (e.g., the overall pressure exerted by the atoms of a gas on the container walls). This way of approaching the problem has come to be called *the emergent approach*.

In the emergent approach to spacetime presented in Reference [7], gravity qualifies as an entropic force. Roughly speaking, this is the statement that we do not know the fundamental degrees of freedom underlying gravity, but their overall macroscopic effect is that of driving the system under

consideration in the direction of increasing entropy. If gravitational forces are entropy gradients, then gravitational equipotential surfaces can be identified with isoentropic surfaces. This insight justifies identifying the gravitational potential and the entropy function (up to dimensional factors).

Recalling the arguments of Reference [7], a classical point particle approaching a holographic screen causes the entropy of the latter to increase by one quantum k_B. We will replace the classical particle of Reference [7] with a density of particles representing the (baryonic and dark) matter contents of a hypothetical Newtonian Universe. This volume density will be identified with the squared modulus of a nonrelativistic wavefunction ψ satisfying the Schroedinger equation. Let U denote the gravitational potential. Once dimensions are corrected (using $\hbar$ and k_B), the expectation value $\langle\psi|U|\psi\rangle$ becomes the quantum-mechanical analogue of the entropy increase caused by a classical particle approaching a holographic screen in Reference [7]. Therefore, *the expectation value $\langle\psi|U|\psi\rangle$ becomes a measure of the gravitational entropy of the Universe when the matter of the Universe is described by the wavefunction ψ.*

The next question is to determine the Newtonian potential U governing the Universe as a whole. Of course, even within the Newtonian approximation, U necessarily appears as a very rough average. We can, however, find guidance in the Hubble expansion of the Universe [8–10], which holds reasonably well over cosmological distances. This receding behaviour of the galaxies can be easily modelled by a phenomenological potential; namely, an isotropic harmonic potential carrying a negative sign:

$$U_{\text{Hubble}}(\mathbf{r}) = -\frac{H_0^2}{2}\mathbf{r}^2. \tag{1}$$

As the angular frequency, we take the current value of Hubble's constant H_0 (thus, U_{Hubble} has the dimensions of energy per unit mass, or velocity squared). The potential U_{Hubble} encodes the combined effect of the gravitational attraction, and of the repulsion caused by the dark energy on the matter content of the Universe (baryonic and dark matter). We can therefore identify the Hubble potential U_{Hubble} of Equation (1) with the gravitational potential U in the previous paragraph.

Following Reference [11], let us briefly recall why U_{Hubble} in fact combines a Newtonian gravitational attraction plus a harmonic repulsion (See Equation (9.14 b) of Reference [11]), the right-hand side of which is the force that one would obtain by differentiation of our Equation (1). The fact that Reference [11] defended the steady state theory—the rival that lost against the currently accepted big bang theory—has no bearing on this discussion, as the Newtonian limit is the same). In the Newtonian limit considered throughout this paper, the gravitational attraction is computed by applying Gauss' law to a sphere filled with a homogeneous, isotropic density of matter. Then, the gravitational field *within the sphere* turns out to be proportional to the position vector, so the corresponding potential becomes a quadratic function of the position. Altogether, the total potential at any point within the cosmological fluid is the sum of two harmonic potentials; Hubble's constant H_0 is the frequency of this total harmonic potential.

In this way, the Newtonian space $\mathbb{R}^3$ is foliated by a continuous succession of concentric spheres with growing radii. Each one of these spheres qualifies as a gravitational equipotential surface. By what was said above, these surfaces are also isoentropic surfaces, the gradients thereto pointing in the direction of the gravitational force. The negative sign in Equation (1) expresses the essential fact that this net force is repulsive instead of attractive. Already at the classical level, this potential possesses no state of least energy—a problem that resurfaces at the quantum level, as the nonexistence of a stable vacuum state [12]. What saves the day is the crucial observation that, in fact, *our observable Universe is finite in size*, instead of extending over all of $\mathbb{R}^3$. The current value R_0 of the radius of the observable Universe provides us with a natural cutoff. In this way, a stable vacuum state is guaranteed to exist.

2. Newtonian Cosmology as a Quantum Mechanics

The Poisson equation satisfied by the nonrelativistic gravitational potential U created by a mass density ρ,

$$\nabla^2 U = 4\pi G\rho, \tag{2}$$

arises naturally in the weak-field limit of Einstein's field equations. In this limit (also called the *Newtonian approximation*), the (baryonic and dark) matter contents of the Universe are modelled as an ideal fluid (see, e.g., [13]) satisfying the Poisson Equation (2) as well as the continuity equation

$$\frac{\partial \rho}{\partial t} + \nabla \cdot (\rho\mathbf{v}) = 0 \tag{3}$$

and the Euler equation

$$\frac{\partial \mathbf{v}}{\partial t} + (\mathbf{v} \cdot \nabla)\,\mathbf{v} + \frac{1}{\rho}\nabla p - \mathbf{F} = 0. \tag{4}$$

In Equations (3) and (4), ρ is the volume density of fluid mass, p is the pressure, $\mathbf{v}$ is the velocity field within the cosmological fluid, and $\mathbf{F}$ the force per unit volume acting on the fluid. The cosmological principle requires that the velocity $\mathbf{v}$ be everywhere proportional to the position vector $\mathbf{r}$. This latter statement is nothing but Hubble's law, which one can mimic by means of the phenomenological potential (1). Indeed, the latter satisfies the Poisson Equation (2),

$$\nabla^2 U_{\text{Hubble}} = -3H_0^2, \tag{5}$$

the right-hand side corresponding to a *negative* mass density $\rho = -3mH_0^2/(4\pi G)$.

In Reference [14], we have pointed out the existence of a remarkable *duality between nonrelativistic quantum mechanics on the one hand, and Newtonian cosmology on the other* (we thank a referee for drawing our attention to Reference [15]). Specifically, nonrelativistic quantum mechanics has a quantum probability fluid that exactly mimics the behaviour of the cosmological fluid—the latter considered in the Newtonian approximation. One proves that Equations (3) and (4)—which govern the cosmological fluid—become the very equations that govern the quantum probability fluid after applying the Madelung transformation. The inclusion of the Hubble potential as an external force acting on the quantum system then yields Equation (2).

The duality just mentioned can be used to *compute thermodynamical quantities of the Universe using standard quantum mechanics*. In the introduction, we have argued that the operator $\mathbf{R}^2 = X^2 + Y^2 + Z^2$—which is proportional to the Hubble potential (1)—is a measure of the amount of gravitational entropy enclosed by the Universe. Correcting dimensions by means of the appropriate physical constants, the operator

$$\mathcal{S} := \mathcal{N}\frac{k_B m H_0}{\hbar}\mathbf{R}^2 \tag{6}$$

qualifies as a Boltzmann entropy. Above m is the total mass (baryonic and dark) of the observable Universe. A *dimensionless* factor $\mathcal{N}$ is left undetermined by these simple arguments; we generally expect $\mathcal{N}$ to be of order unity. We call $\mathcal{S}$ the gravitational entropy operator.

The present paper is a continuation of—and an improvement on—our previous article [14]. Let us examine this point in more detail. Within the scope of the approximations considered here, the effective Hamiltonian operator H_{eff} acting on the wavefunction $\psi(\mathbf{r})$ that models the cosmological fluid is

$$H_{\text{eff}} = -\frac{\hbar^2}{2m}\nabla^2 - \frac{k_{\text{eff}}}{2}\mathbf{r}^2, \qquad k_{\text{eff}} = mH_0^2. \tag{7}$$

Above, we have defined the effective elastic constant k_{eff} corresponding to the Hubble potential (1). The amount of mass m_V contained within a volume V equals $m_V = m\int_V \mathrm{d}^3x|\psi|^2$; the whole observable Universe is a sphere of radius R_0 (we collect our cosmological data m, H_0, R_0 from Reference [16]).

Considering the Universe as a sphere with finite radius has the advantage that the instabilities [12] due to the negative sign of the potential are avoided naturally. Although the Hamiltonian (7) can be diagonalised and its exact eigenfunctions can be obtained explicitly [14,17], the latter are extremely cumbersome for explicit computations. As a first step, for the sake of simplicity, in Reference [14] we obtained the expectation value $\langle S \rangle$ using a set of eigenfunctions of the *free* Hamiltonian $-\hbar^2 \nabla^2 / (2m)$.

The analysis performed in this paper uses the exact eigenfunctions of the effective Hamiltonian (7); this improves on the results of our calculation of Reference [14]. The values thus obtained will be closer to actual (empirical) estimates for the entropy of the Universe [18], so the upper bound $S_{\max} \sim 10^{123} k_B$ set by the holographic principle will no longer be saturated. Specifically, we will refine the results of our previous Reference [14] by three orders of magnitude; see Equations (20) and (26) below. Further work is required in order to extend our results beyond the Newtonian limit [19]; this extension will hopefully yield values in even better agreement with existing estimates.

3. Estimate of the Entropy

Let us separate variables in the effective Hamiltonian (7) using spherical coordinates. The standard factorisation $\psi(\mathbf{r}) = R(r) Y_{lm}(\theta, \varphi)$ leads to a radial wave equation

$$\frac{1}{r^2} \frac{\mathrm{d}}{\mathrm{d}r} \left(r^2 \frac{\mathrm{d}R}{\mathrm{d}r} \right) - \frac{l(l+1)}{r^2} R + \frac{2m}{\hbar^2} \left(E + \frac{k_{\mathrm{eff}}}{2} r^2 \right) R = 0. \tag{8}$$

The choice $l = 0$ imposed by the cosmological principle leads to

$$r^2 \frac{\mathrm{d}^2 R}{\mathrm{d}r^2} + 2r \frac{\mathrm{d}R}{\mathrm{d}r} + \frac{2m}{\hbar^2} \left(Er^2 + \frac{mH_0^2}{2} r^4 \right) R = 0. \tag{9}$$

As shown in References [14,17], two linearly independent solutions of (9) turn out to be

$$R_\alpha^{(1)}(r) = \exp \left(\frac{\mathrm{i}\beta^2 r^2}{2} \right) {}_1F_1 \left(\frac{3}{4} - \frac{\mathrm{i}\alpha}{4}, \frac{3}{2}; -\mathrm{i}\beta^2 r^2 \right) \tag{10}$$

and

$$R_\alpha^{(2)}(r) = \frac{1}{r} \exp \left(\frac{\mathrm{i}\beta^2 r^2}{2} \right) {}_1F_1 \left(\frac{1}{4} - \frac{\mathrm{i}\alpha}{4}, \frac{1}{2}; -\mathrm{i}\beta^2 r^2 \right), \tag{11}$$

where ${}_1F_1(a, b; z)$ is the confluent hypergeometric function [20], and the parameters α, β take on the values

$$\alpha := \frac{2E}{\hbar H_0}, \qquad \beta^4 := \frac{m^2 H_0^2}{\hbar^2}. \tag{12}$$

To begin with, the complete wavefunction corresponding to the radial wavefunction (10) reads

$$\psi_\alpha^{(1)}(r, \theta, \varphi) = \frac{N_\alpha^{(1)}}{\sqrt{4\pi}} \exp \left(\frac{\mathrm{i}\beta^2 r^2}{2} \right) {}_1F_1 \left(\frac{3}{4} - \frac{\mathrm{i}\alpha}{4}, \frac{3}{2}; -\mathrm{i}\beta^2 r^2 \right); \tag{13}$$

the radial normalisation factor $N_\alpha^{(1)}$ will be determined presently. The eigenfunction $\psi_\alpha^{(1)}$ is singularity free over the entire interval $[0, R_0]$. A numerical estimate yields $\beta \simeq 1.1 \times 10^{35}$ m^{-1}. Given that $R_0 \simeq 4.4 \times 10^{26}$ m, the dimensionless product $(\beta r)^2$ in Equation (13) quickly drives the function ${}_1F_1$ into its asymptotic regime, where it can be approximated as [20]

$$ {}_1F_1(a, b; z) \simeq \frac{\Gamma(b)}{\Gamma(b-a)} \mathrm{e}^{-\mathrm{i}\pi a} z^{-a} + \frac{\Gamma(b)}{\Gamma(a)} \mathrm{e}^z z^{a-b}, \quad |z| \to \infty, \tag{14}$$

whenever $|\arg(z)| < \pi$ and $b \neq 0, -1, -2, \dots$ We will also need Stirling's formula

$$\Gamma(t) \simeq \exp\left[\left(t - \frac{1}{2}\right) \ln t - t + \frac{1}{2} \ln 2\pi\right],\tag{15}$$

valid for $|t| \to \infty$ whenever $|\arg(t)| < \pi$. When applying Stirling's approximation, we will select the main branch of the complex logarithm. Another order-of-magnitude estimate yields $\alpha \simeq 10^{52} E$, with the energy E expressed in Joules; this fact allows the first summand in (14) to be dropped in favour of the second. Then, a lengthy calculation based on Equations (14) and (15) yields the desired asymptotic expression of the confluent hypergeometric function in (13):

$$\begin{aligned}
{}_1F_1\left(\tfrac{3}{4} - \tfrac{i\alpha}{4}, \tfrac{3}{2}; -i\beta^2 r^2\right) &\simeq \tfrac{1}{2\sqrt{2}} \exp\left(\tfrac{3}{4} - i\pi\right) \exp\left(\tfrac{\pi\alpha}{2}\right) \exp\left(\tfrac{i\alpha}{4} \ln \tfrac{\alpha}{4}\right) \\
&\times \exp\left\{-i\left[\beta^2 r^2 + \tfrac{\alpha}{2} \ln(\beta r)\right]\right\} \exp\left(-\tfrac{3}{2} \ln \beta r\right), \qquad r \to \infty.
\end{aligned}\tag{16}$$

Finally, substituting Equation (16) into Equation (13), and absorbing an irrelevant constant within the normalisation factor $N_\alpha^{(1)}$, we obtain the following asymptotic wavefunction:

$$\begin{aligned}
\psi_\alpha^{(1)}(r, \theta, \varphi) &\simeq \tfrac{N_\alpha^{(1)}}{\sqrt{4\pi}} \exp\left(\tfrac{\pi\alpha}{2}\right) \exp\left(\tfrac{i\alpha}{4} \ln \tfrac{\alpha}{4}\right) \\
&\times \exp\left\{-\tfrac{i}{2}\left[\alpha \ln(\beta r) + \beta^2 r^2\right]\right\} (\beta r)^{-3/2}, \qquad r \to \infty.
\end{aligned}\tag{17}$$

We observe that the asymptotic expression (17) is singular at $r = 0$ while the original wavefunction (13) was not. This is just a consequence of having replaced the exact wavefunction with its asymptotic approximation for large r. Therefore, Equation (17) applies at most over the interval $[\epsilon, R_0]$, where $\epsilon > 0$ is small but nonvanishing. We need to determine a suitable ϵ and the wavefunction $\psi_\alpha^{(1)}$ over $[0, \epsilon]$.

A natural choice to make is $\epsilon = \beta^{-1}$. This is sufficiently small, while at the same time, values of $r > \beta^{-1}$ fall well within the asymptotic regime (14) of the confluent hypergeometric function. Over the interval $[0, \beta^{-1}]$, we will approximate ${}_1F_1$ by its Taylor expansion ${}_1F_1(a, b; z) \simeq 1 + az/b$ [20]. Altogether, the normalised approximate wavefunction for the matter contents of the Universe

$$\begin{aligned}
\psi_\alpha^{(1)}(r, \theta, \varphi) &= \sqrt{\tfrac{\beta^3}{4\pi \ln(\beta R_0)}} \exp\left(\tfrac{i\alpha}{4} \ln \tfrac{\alpha}{4}\right) \\
&\times \begin{cases} \exp\left(-i/2\right), & r \in [0, \beta^{-1}] \\ \exp\left\{-\tfrac{i}{2}\left[\alpha \ln(\beta r) + \beta^2 r^2\right]\right\} (\beta r)^{-3/2}, & r \in [\beta^{-1}, R_0] \end{cases}
\end{aligned}\tag{18}$$

is regular over the entire interval $[0, R_0]$. With the wavefunction (18), we obtain

$$\langle \psi_\alpha^{(1)} | \mathbf{R}^2 | \psi_\alpha^{(1)} \rangle = \frac{R_0^2}{2 \ln(\beta R_0)},\tag{19}$$

after dropping subleading terms in β. Substituted back into Equation (6), this produces a value of the entropy

$$\langle \psi_\alpha^{(1)} | \mathcal{S} | \psi_\alpha^{(1)} \rangle = 6\mathcal{N} \times 10^{120} k_B\tag{20}$$

which, taking $\mathcal{N} = 1/6$, is three orders of magnitude below the upper bound $\mathcal{S}_{\max} \sim 10^{123} k_B$ set by the holographic principle. This is a considerable improvement upon the results of Reference [14], where the holographic bound was saturated.

In the case of the second, linearly-independent radial wavefunction (11), we have the complete eigenfunction

$$\psi_\alpha^{(2)}(r, \theta, \varphi) = \frac{N_\alpha^{(2)}}{\sqrt{4\pi}} \frac{1}{r} \exp\left(\frac{i\beta^2 r^2}{2}\right) {}_1F_1\left(\frac{1}{4} - \frac{i\alpha}{4}, \frac{1}{2}; -i\beta^2 r^2\right).\tag{21}$$

As opposed to $\psi_\alpha^{(1)}$, the wavefunction $\psi_\alpha^{(2)}$ is singular at $r = 0$. Again applying Equations (14) and (15), one finds the asymptotics

$$
\begin{aligned}
{}_1F_1\left(\tfrac{1}{4} - \tfrac{\mathrm{i}\alpha}{4}, \tfrac{1}{2}; -\mathrm{i}\beta^2 r^2\right) &\simeq \tfrac{1}{\sqrt{2}} \exp\left(\tfrac{1}{4} - \tfrac{\mathrm{i}\pi}{2}\right) \exp\left(\tfrac{\pi\alpha}{2} + \tfrac{\mathrm{i}\alpha}{4} \ln \tfrac{\alpha}{4}\right) \\
&\times \exp\left[-\mathrm{i}\left(\tfrac{\alpha}{2} \ln \beta r + \beta^2 r^2\right)\right] \exp\left(-\tfrac{1}{2} \ln \beta r\right), \quad r \to \infty.
\end{aligned}
\tag{22}
$$

Next, substituting (22) into (21) produces, after absorbing an irrelevant constant within the normalisation factor,

$$
\begin{aligned}
\psi_\alpha^{(2)}(r, \theta, \varphi) &\simeq \tfrac{N_\alpha^{(2)}}{\sqrt{4\pi}} \tfrac{1}{r} \exp\left(\tfrac{\pi\alpha}{2} + \tfrac{\mathrm{i}\alpha}{4} \ln \tfrac{\alpha}{4}\right) \\
&\times \exp\left[-\tfrac{\mathrm{i}}{2}\left(\alpha \ln \beta r + \beta^2 r^2\right)\right] (\beta r)^{-1/2}, \quad r \to \infty.
\end{aligned}
\tag{23}
$$

Finally, arguments similar to those leading up to Equation (18) produce the following normalised approximate wavefunction over the complete interval $[0, R_0]$:

$$
\begin{aligned}
\psi_\alpha^{(2)}(r, \theta, \varphi) &= \sqrt{\tfrac{\beta}{4\pi \ln(\beta R_0)}} \exp\left(\tfrac{\mathrm{i}\alpha}{4} \ln \tfrac{\alpha}{4}\right) \\
&\times \begin{cases} \tfrac{1}{r} \exp\left(-\mathrm{i}/2\right), & r \in [0, \beta^{-1}] \\ \tfrac{1}{r} \exp\left\{-\tfrac{\mathrm{i}}{2}\left[\alpha \ln(\beta r) + \beta^2 r^2\right]\right\} (\beta r)^{-1/2}, & r \in [\beta^{-1}, R_0]. \end{cases}
\end{aligned}
\tag{24}
$$

We observe that the approximate wavefunction (24) remains singular at $r = 0$, as imposed by the exact wavefunction (21). With the above, one computes

$$
\langle \psi_\alpha^{(2)} | \mathbf{R}^2 | \psi_\alpha^{(2)} \rangle = \frac{R_0^2}{2 \ln(\beta R_0)},
\tag{25}
$$

coincident with the corresponding result (19) for the regular wavefunction. Therefore

$$
\langle \psi_\alpha^{(2)} | \mathcal{S} | \psi_\alpha^{(2)} \rangle = 6\mathcal{N} \times 10^{120} k_B,
\tag{26}
$$

in complete agreement with the entropy already found in (20) for the regular wavefunction.

4. Discussion

The holographic principle sets an upper bound of approximately $10^{123} k_B$ on the entropy content of the Universe. Some phenomenological estimates [18] place the actual value at around $10^{104} k_B$, gravitational entropy (and in particular, black holes) representing the largest single contributors to the entropy budget of the Universe. Although Newtonian cosmology does allow for black holes [21], the many simplifications made by our elementary model necessarily leave out some essential physics of the Universe. Nevertheless, our toy model succeeds in capturing some key elements of reality. For example, the upper bound set by the holographic principle is always respected, even by such a crude approximation as the free waves [14]. The Hubble waves (18) and (24) represent a considerable improvement on the free waves, as they reduce the expectation value of the entropy by three orders of magnitude. We hope that a fully general-relativistic treatment [19] will yield results in even better agreement with existing empirical estimates.

Admittedly, solutions (10) and (11) violate the cosmological principle. In fact, any solution to the (interacting) Schroedinger equation will violate the cosmological principle. Only free wave solutions to the free wave equation (i.e., with zero potential) satisfy the cosmological principle. However, the free wavefunctions of our previous Reference [14] saturate the holographic principle, while our improved Hubble wavefunctions (10) and (11) no longer saturate it. This is essential for the very existence of life in the Universe. Given that the cosmological principle itself is an idealisation, we believe the improved entropy results obtained using Hubble wavefunctions outweigh the violation of the cosmological principle.

Since α in Equation (12) is the (dimensionless) energy eigenvalue in $H_{\text{eff}}\psi = E\psi$, the parameter α plays the same role that the quantum number $n \in \mathbb{N}$ plays in the standard harmonic oscillator, where the potential energy is positive definite. Our negative definite harmonic potential does not have quantised energy levels, but continuous energy levels α instead. However, the range of values covered by α, while unbounded above, is bounded below by the existence of the radius of the Universe: a classical particle at rest at $r = R_0$ would carry an energy

$$E_0 = -\frac{1}{2}mH_0^2R_0^2. \tag{27}$$

This configuration can be regarded as the classical vacuum state. In terms of the dimensionless eigenvalue α, this energy equals

$$\alpha_0 = -\frac{mH_0R_0^2}{\hbar} = -2.6 \times 10^{123}. \tag{28}$$

The vacuum energy (28) has been determined by a classical argument; although the uncertainty principle will shift the minimum energy (28) by a positive amount, this correction can be discarded for our purposes, as it will be negligible compared to (28) itself. The negative sign in (28) is due to the Hubble potential (1), while the dimensionless factor 2.6 is of order unity. Thus, the vacuum energy (28) yields the approximate equality

$$|\alpha_0| \simeq \frac{\mathcal{S}_{\text{max}}}{k_B} \simeq 10^{123}. \tag{29}$$

The above numerical coincidence is in fact a consistency check on all our previous arguments. It confirms once again that the holographic bound is never exceeded, since both the energy and the entropy grow quadratically with the distance.

We have seen in Section 3 that the linearly-independent wavefunctions $\psi_\alpha^{(1)}$ and $\psi_\alpha^{(2)}$ coalesce asymptotically in r. This occurs despite the fact that $\psi_\alpha^{(1)}$ is regular at $r = 0$ while $\psi_\alpha^{(2)}$ is singular. In turn, this implies that issues of regularity of the wavefunction at $r = 0$ are irrelevant for our purposes. Our estimate of the entropy remains valid regardless of the precise wavefunction used in a neighbourhood of $r = 0$; this neighbourhood is $[0, \beta^{-1}]$.

The constant β arises naturally when diagonalising the effective Hubble Hamiltonian (7); see Equation (12). It turns out that $\beta^{-1} \simeq 10^{-35}$ m, which is close to the value of the Planck length L_P,

$$\beta^{-1} = \sqrt{\frac{\hbar}{mH_0}} \simeq L_P = \sqrt{\frac{\hbar G}{c^3}}. \tag{30}$$

Our toy model of the Universe thus possesses an intrinsic length scale, β^{-1}, which numerically equals the Planck length. This approximate equality is no coincidence (we thank a referee for pointing this out to us): the value of m is that of the mass enclosed by the Hubble horizon for a critical Universe, $m \simeq 1/(H_0 G)$, hence $\beta \simeq 1/\sqrt{G} = 1/L_P$.

Our analysis is rooted in previous studies [22,23] on the emergent property of quantum mechanics. According to the hypothesis of emergence, quantum mechanics as we know it should be the effective theory of some underlying mechanics, the coarse graining of which would yield our current quantum models. Important recent work in general relativity [1–4] also points in the same direction: gravity appears to be the *thermodynamics* of some underlying degrees of freedom—a continuous spacetime emerging only as their low-energy limit. That seemingly unrelated fields such as quantum theory and general relativity might share fundamental common features [24] is an intriguing possibility worthy of future study.

Author Contributions: The two authors contributed equally to this article

Conflicts of Interest: The authors declare no conflict of interest.

References

1. Padmanabhan, T. General Relativity from a Thermodynamic Perspective. *Gen. Relativ. Grav.* **2014**, *46*, 1673.
2. Padmanabhan, T. Emergent Gravity Paradigm: Recent Progress. *Mod. Phys. Lett. A* **2015**, *30*, 1540007.
3. Padmanabhan, T. Gravity and/is Thermodynamics. *Curr. Sci.* **2015**, *109*, 2236.
4. Padmanabhan, T. The Atoms of Space, Gravity and the Cosmological Constant. *Int. J. Mod. Phys.* **2016**, *D25*, 1630020.
5. Linnemann, N.; Visser, M. Hints towards the Emergent Nature of Gravity. *arXiv* **2017**, arXiv:1711.10503.
6. Moustos, D. Gravity as a Thermodynamic Phenomenon. *arXiv* **2017**, arXiv:1701.08967.
7. Verlinde, E. On the Origin of Gravity and the Laws of Newton. *J. High Energy Phys.* **2011**, *1104*, 29.
8. Hubble, E. A Relation between Distance and Radial Velocity among Extra–Galactic Nebulae. *Proc. Natl. Acad. Sci. USA* **1929**, *15*, 168–173.
9. Perlmutter, S.; Aldering, G.; Deustua, S.; Fabbro, S.; Goldhaber, G.; Groom, D.E.; Kim, A.G.; Kim, M.Y.; Knop, R.A.; Nugent, P.; et al. Cosmology from Type Ia Supernovae. *Bull. Am. Astron. Soc.* **1997**, *29*, 1351.
10. Riess, A.; Filippenko, A.V.; Challis, P.; Clocchiatti, A.; Diercks, A.; Garnavich, P.M.; Gilliland, R.L.; Hogan, C.J.; Jha, S.; Kirshner, R.P.; et al. Observational Evidence from Supernovae for an Accelerating Universe and a Cosmological Constant. *Astron. J.* **1998**, *116*, 1009.
11. Bondi, H. *Cosmology*; Dover: New York, NY, USA, 2010.
12. Broadbridge, P.; Zulkowski, P. Dark Energy States from Quantization of Boson Fields in a Universe with Unstable Modes. *Rep. Math. Phys.* **2006**, *57*, 27–40.
13. Weinberg, S. *Cosmology*; Oxford University Press: Oxford, UK, 2008.
14. Cabrera, D.; de Córdoba, P.F.; Isidro, J.M. Boltzmann Entropy of a Newtonian Universe. *Entropy* **2017**, *19*, 212.
15. Widrow, L.; Kaiser, N. Using the Schrödinger Equation to Simulate Collisionless Matter. *Astrophys. J. Lett.* **1993**, *416*, L71.
16. Planck Collaboration. Planck 2015 Results. XIII. Cosmological Parameters. *Astron. Astrophys.* **2016**, *594*, A13.
17. Finster, F.; Isidro, J.M. L^p–Spectrum of the Schrödinger Operator with Inverted Harmonic Oscillator Potential. *J. Math. Phys.* **2017**, *58*, 092104.
18. Egan, C.; Lineweaver, C. A Larger Estimate of the Entropy of the Universe. *Astrophs. J.* **2010**, *710*, 1825.
19. De Córdoba, P.F.; Isidro, J.M. Boltzmann Entropy of the FLRW Universe. **2018**, in preparation.
20. Lebedev, N. *Special Functions and Their Applications*; Dover Publications: New York, NY, USA, 1972.
21. Martínez-Merino, A.; Obregón, O.; Ryan, M. Newtonian Black Holes: Particle Production, "Hawking" Temperature, Entropies and Entropy Field Equations. *arXiv* **2016**, arXiv:1611.09654.
22. Elze, H.T. Symmetry Aspects in Emergent Quantum Mechanics. *J. Phys. Conf. Ser.* **2009**, *171*, 012034.
23. Torromé, R.G. A Theory of Emergent Quantum Mechanics and Classical Emergent Gravity. *arXiv* **2014**, arXiv:1402.5070.
24. Matone, M. Equivalence Postulate and Quantum Origin of Gravitation. *Found. Phys. Lett.* **2002**, *15*, 311–328.

Experimental and Modeling Analysis of *Synechocystis* sp. PCC 6803 Growth

Miguel Lopo[a] Arnau Montagud[e] Emilio Navarro[d] Isabel Cunha[a]
Andrea Zille[a] Pedro Fernández de Córdoba[e] Pedro Moradas-Ferreira[a, b]
Paula Tamagnini[a, c] Javier F. Urchueguía[e]

[a]IBMC – Instituto de Biologia Molecular e Celular, [b]Instituto de Ciências Biomédicas Abel Salazar (ICBAS), and [c]Departamento de Biologia, Faculdade de Ciências, Universidade do Porto, Porto, Portugal; [d]Departamento de Lenguajes y Ciencias de la Computación, Campus de Teatrinos, Universidad de Málaga, Málaga, and [e]Instituto de Matemática Pura y Aplicada, Universidad Politécnica de Valencia, Valencia, Spain

Key Words

Cyanobacteria · Dynamic flux balance analysis · Growth · pH · *Synechocystis*

Abstract

Background/Aims: The influence of different parameters such as temperature, irradiance, nitrate concentration, pH, and an external carbon source on *Synechocystis* PCC 6803 growth was evaluated. ***Methods:*** 4.5-ml cuvettes containing 2 ml of culture, a high-throughput system equivalent to batch cultures, were used with gas exchange ensured by the use of a Parafilm™ cover. The effect of the different variables on maximum growth was assessed by a multi-way statistical analysis. ***Results:*** Temperature and pH were identified as the key factors. It was observed that *Synechocystis* cells have a strong influence on the external pH. The optimal growth temperature was 33°C while light-saturating conditions were reached at 40 μE·m^{-2}·s^{-1}. ***Conclusion:*** It was demonstrated that *Synechocystis* exhibits a marked difference in behavior between autotrophic and glucose-based mixotrophic conditions, and that nitrate concentrations did not have a significant influence, probably due to endogenous nitrogen reserves. Furthermore, a dynamic metabolic model of *Synechocystis* photosynthesis was developed to gain insights on the underlying mechanism enabling this cyanobacterium to control the levels of external pH. The model showed a coupled effect between the increase of the pH and ATP production which in turn allows a higher carbon fixation rate.

Copyright © 2012 S. Karger AG, Basel

Introduction

Cyanobacteria are a large and widespread group of photoautotrophic microorganisms that combine the ability to perform an oxygenic photosynthesis with typical prokaryote features. As a group, cyanobacteria are known to survive a wide spectrum of environmental stresses, such as temperature shock [Waterbury, 2006], photo-oxidation, nutrient deficiency, pH changes [Blanco-Rivero et al., 2005], salinity, osmotic stress, and ultraviolet light [Mullineaux, 2001]. The unicellular non-nitrogen fixing *Synechocystis* sp. PCC 6803 was the first photosynthetic autotroph to have its genome sequenced [Kaneko et al., 1996]; it has been used in a variety of global gene expression [Gill et al., 2002; Hihara et al., 2001; Singh et al., 2003] and metabolomic studies [Bricker et al., 2004; Yang et al., 2002]. Additionally, data on genomics and pro-

Paula Tamagnini
IBMC – Instituto de Biologia Molecular e Celular
Universidade do Porto, Rua do Campo Alegre 823
PT-4150-180 Porto (Portugal)
Tel. +351 226 074 900, E-Mail pmtamagn@ibmc.up.pt

teomics of this microorganism accounts for the majority of the information available on cyanobacteria [Burja et al., 2003]. At present, there is probably no other cyanobacterium which has been investigated in such detail, making it suitable for many biotechnological applications [Gutthann et al., 2007; Vermaas, 1996]. It can grow under photoautotrophic conditions, mixotrophic conditions with glucose as a carbon source, and heterotrophic conditions with a daily short pulse of light. However, there is some controversy whether *Synechocystis* sp. PCC 6803 can grow under strict heterotrophic conditions [Anderson and McIntosh, 1991; Bricker et al., 2004]. According to Vermaas [1996] the following growth modes can be considered for *Synechocystis* sp. PCC 6803: photoautotrophic (CO_2, light and active PS II and PS I); photoheterotrophic (glucose and active PS II or PS I); photomixotrophic (glucose and active PS II and PS I); heterotrophic (glucose; 5 min of light per day), and anaerobic (glucose or other fixed carbon source).

Recently, modeling efforts have been made in order to gain insight into this unicellular cyanobacterium metabolism [Navarro et al., 2009; Shastri and Morgan, 2005; Yang et al., 2002], but these models lack accuracy regarding photosynthesis description, bundling together photosynthetic pathways into a reduced set of reactions. On the other hand, many physiological studies have addressed the effects of environmental factors affecting cyanobacteria growth and *Synechocystis* sp. PCC 6803 in particular. However, multifactorial studies are scarce.

Light plays a crucial role in all photosynthetic organisms by regulating growth, altering gene expression, and resetting circadian rhythms, among others [Gill et al., 2002; Mullineaux, 2001, Montagud et al., 2010], but it can also be harmful to the photosynthetic machinery. It has been observed in *Synechocystis* sp. PCC 6803 that visible light might play a double role, inducing damage to PS II when it is strong and inducing repair of the photodamaged PS II when it is weak [Allakhverdiev and Murata, 2004].

Cyanobacteria are found in environments with quite different temperature ranges. Most cyanobacteria are mesophilic and live on environments where temperature may range from freezing to 40°C [Waterbury, 2006]. They typically have growth optima between 20 and 35°C; however, organisms that can grow up to 75°C have been found [Castenholtz, 1969].

Nitrate is the most common nitrogen source used by cyanobacteria, it is widely utilized for their growth and its limitation induces a well-characterized set of cellular responses such as: visible chlorosis or 'yellowing' [Allen

and Smith, 1969], degradation of phycobiliproteins [Collier and Grossman, 1992], alteration of the ratio of phycocyanin to allophycocyanin [Yamanaka and Glazer, 1980], degradation of thylakoid membranes, a decrease in chlorophyll, an increase in carotenoid content or carotenoid/chlorophyll ratio, as well as an increase in glycogen content [Stevens et al., 1981].

Under laboratory conditions, cyanobacteria have generally been reported to prefer neutral to slightly alkaline media [Kratz and Myers, 1955]. In the natural environments, however, cyanobacteria extend their distribution to pH values as low as 4 [Kurian et al., 2006; Steinberg et al., 1998]. Kallas and Castenholz [1982] analyzed cytoplasmic pH homeostasis in cyanobacteria and observed that the growth rate of *Synechococcus* sp. was inhibited at pH 7.0 and below, and no sustained growth took place at pH 6.0. However, even when these cells were exposed to pH 4.8, they retained a higher intracellular pH, suggesting that there are other factors involved in the acid tolerance mechanisms of these photosynthetic microorganisms to maintain homeostasis within the cell [Summerfield and Sherman, 2008]. It has also been shown that acid-tolerant cyanobacteria maintain a neutral cytoplasmic pH, although how they keep a strong transmembrane pH gradient is still unknown [Steinberg et al., 1998]. As well as being acid-tolerant, cyanobacteria are among the most alkaliphilic microbes and frequently dominate alkaline environments such as soda lakes and microbial mats [Summerfield and Sherman, 2008].

All the factors mentioned above affect *Synechocystis* sp. PCC 6803 metabolism in a variety of manners and to different extents, which are only partially understood. Therefore, a holistic analysis is needed in order to take into account the complete metabolism and the factors that perturb it. Since flux balance analysis (FBA) was published [Varma and Palsson, 1994], it became possible to unveil characteristics and potentials of cell metabolism with only the bare knowledge of reactions stoichiometry and optimization criteria. Nevertheless, this algorithm has the underlying assumption that biological systems work under a pseudo-steady state. Therefore, under perturbed conditions this premise does not stand and other approximations have been developed to gain metabolic insights. Among them, dynamic flux balance analysis (DFBA) [Mahadevan et al., 2002], based on the optimal control theory, allows the study of transition states when, for instance, the environment conditions change. However, this analysis is computationally expensive, and is mainly used when one is interested in a part of the whole organism or in processes in which a reduced effective

Table 1. Experimental matrix with conditions/parameters to be tested on *Synechocystis* sp. PCC 6803 growth

	States				
Heterotrophic	1 × light (0)	3 × temperature (25, 30, 33)	3 × glucose (2, 5, 7)	3 × nitrate (0.1, 0.75, 1.5)	7 × pH (7.5, 8, 8.5, 9, 10, 10.5, 11)
Autotrophic and mixotrophic	3 × light (20, 40, 60)	5 × temperature (25, 27, 30, 33, 35)	4 × glucose (0, 2, 5, 7)	3 × nitrate (0.1, 0.75, 1.5)	7 × pH (7.5, 8, 8.5, 9, 10, 10.5, 11)

Light in $\mu E \cdot m^{-2} \cdot s^{-1}$; temperature in °C; glucose in mM and nitrate in g/l.

model can be developed to reproduce it. The DFBA algorithm was recently extended to include the Minimization of Metabolic Adjustment [Segre et al., 2002] hypothesis, being named Minimization of Metabolic Adjustment Dynamic Flux Balance Analysis (M-DFBA) [Luo et al., 2006]. Even without complete system parameters, these methods can find the optimal state of a system or process by searching for the optimal solution using stoichiometric information for specific reactions.

In the present study, different environmental parameters such as temperature, irradiance, nitrate concentration, pH, and an external carbon source, in the form of glucose, were analyzed simultaneously to unveil their influence in *Synechocystis* sp. PCC 6803 growth, using a high-throughput system equivalent to batch cultures. Statistical analysis of this set of non-homogeneous data was performed to compare these time series and to retrieve undercover governing factors. Additionally, an effective dynamic model of *Synechocystis* sp. PCC 6803 metabolism was developed in order to elucidate the basis behind the pH increase during growth. This multivariable analysis will contribute to the understanding of *Synechocystis* sp. PCC 6803 metabolism and will establish the basis for its utilization as a photoautotrophic *chassis* for synthetic biology projects.

Results

Autotrophic Growth

Out of all the possible combinations described in table 1, a subset of 72 autotrophic conditions was selected. 2,221 optical density (OD) measurements were performed for the 254 samples (3 technical replicates). At least three independent experiments (biological replicates) were also performed. Each experiment run in average during 8 days and the measurements were performed

daily. The data were statistically analyzed. A four-way ANOVA, where a model with all the effects and interactions up to the third order was tested, showed that initial pH, temperature, and level of irradiance are the main factors affecting maximum autotrophic growth, with highly significant p values ($p < 10^{-16}$). Nitrate levels initially present in the culture showed p values close to 0.4, which clearly discards any influence in growth results. Among the possible two- and three-way interaction terms in the model, there are two that showed a clear statistical influence in growth ($p < 10^{-16}$): the interaction between initial pH and illumination level and between temperature and pH. In other words, illumination and temperature modify the way in which pH affects growth.

To reveal the pairwise differences between the experimental sets obtained at different levels of the main parameters, a Student t-distribution analysis was performed to represent the confidence regions of maximum specific growth at the different conditions (using a confidence level of $\alpha = 0.05\%$). Figure 1 depicts experimental results representing the sample mean of maximum specific growth, μ_{max}, at different levels of nitrate, an initial pH of 8.5 (HEPES buffer) and 20 $\mu E \cdot m^{-2} \cdot s^{-1}$ irradiance. The grey-shaded area represents the range of the confidence region ($\alpha = 5\%$) of the maximum specific growth at the different temperatures after data are averaged over the different levels of nitrate. The dashed curve and isolated data markers represent maximum specific growth results at particular values of initial nitrate (0.1, 0.75 and 1.5 g/l). As it can be observed, growth reaches a maximum value around 30°C and decreases at higher temperatures whilst results at particular levels of nitrate fall within the confidence region of the nitrate-averaged curve. Again this shows that, from the statistical point of view, nitrate concentrations did not have a noticeable influence on *Synechocystis* sp. PCC 6803 growth (online supplementary fig. S1; for all online supplementary material, see www.
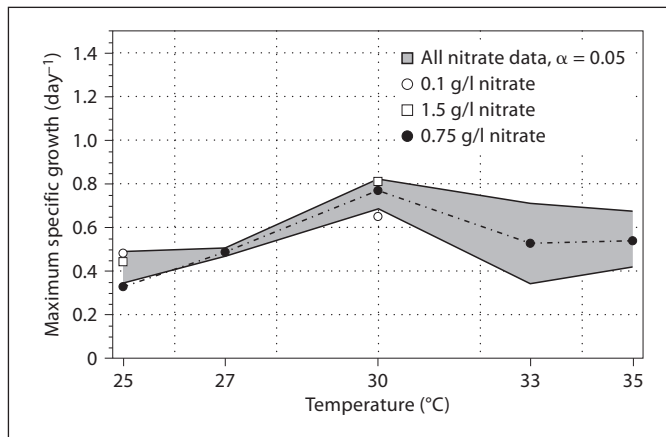
Fig. 1. Temperature profile of maximum specific autotrophic growth with different initial nitrate concentrations. The grey-shaded area corresponds, at the 95% confidence level, to the region of maximum growth if all nitrate levels (0.1, 0.75, and 1.5 g/l) are averaged. Data markers show the result for specific levels of nitrate: hollow circles correspond to 0.1 g/l, hollow squares correspond to 1.5 g/l, and black circles (and dashed line) to 0.75 g/l. In all tests irradiance was 20 μE·m^{-2}·s^{-1} and HEPES buffer was used for cultivation with an initial pH of 8.5.
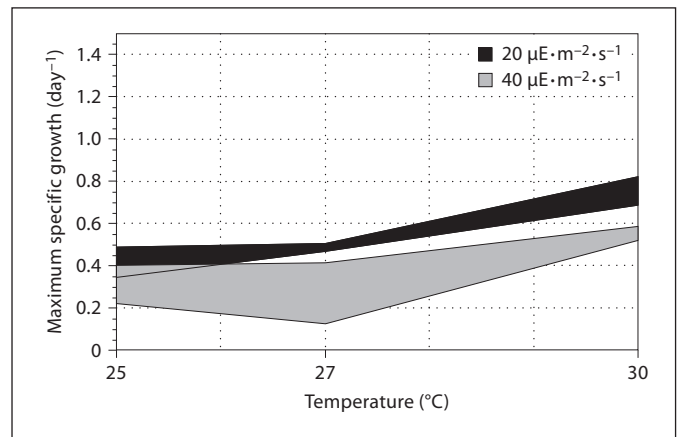
Fig. 2. Temperature profiles of the 95% level confidence regions of maximum specific autotrophic growth at different irradiance levels. The upper black filled area corresponds to experiments with a level of irradiance of 20 μE·m^{-2}·s^{-1}, and the lower grey area to experiments with a level of 40 μE·m^{-2}·s^{-1}. Results of experiments at different nitrate concentrations were averaged and HEPES buffer was used for cultivation with an initial pH of 8.5.

karger.com/doi/10.1159/000336850), not even with values as low as 0.1 g/l (1.2 mM) which is reported in the literature as N-limited conditions [Schmitz et al., 2002]. However, one should bear in mind that the endogenous nitrogen reserves build up during the maintenance growth in BG11 medium might fulfill the organism needs.

Figure 2 compares autotrophic maximum specific growth at the two tested illumination levels (20 and 40 μE·m^{-2}·s^{-1}) with an initial pH of 8.5 (online suppl. fig. S2). Results obtained at the lower level of illumination, 20 μE·m^{-2}·s^{-1}, are significantly above those measured at 40 μE·m^{-2}·s^{-1}, indicating that, in the case of such small cuvette volumes, light-saturating conditions were probably reached already at 20 μE·m^{-2}·s^{-1}, with bleaching becoming noticeable at 40 μE·m^{-2}·s^{-1}. This effect is not so clear at lower initial pH values, when maximum growth is also lower.

From these first observations, it was rather apparent that initial pH is strongly affecting culture growth. pH values rose considerably during cultivation time in the buffered conditions with lower pHs, as well as in the 'no buffer' conditions, stabilizing around pH 10 (data not shown). As expected, the increase in pH was faster in the absence of any buffer, but occurred nonetheless in HEPES-buffered medium reaching similar equilibrium values. This observation brought about the idea of using

different buffers to sustain higher values of pH. Representative results of these measurements are shown in figure 3, where the maximum growth results, (μ_{max}), are compared for different types of buffers and initial pH conditions. A very significant increase in maximum growth was obtained at initial pHs of 9 and 10 in CHES-buffered medium and 33°C. Results obtained with CAPS-buffered medium and without buffer, also exposed in figure 3, clearly confirm this trend in growth and increase in the optimum growth temperatures. Values of growth reach up to about 1.8 day^{-1} in optimum conditions (CAPS buffer, pH 11 and 33°C) compared to a typical value of 0.7 day^{-1} in CHES-buffered conditions taken as reference (online suppl. fig. S4).

To complete the description of pH-related behavior, in figure 4 the relative maximum growth versus relative cell density evolution of three representative samples has been compared. The left curve corresponds to high growth conditions (CHES buffer, initial pH 9), whereas the curves with maxima located at the center and right represent HEPES growth conditions at pH 8.5 and 7.5, respectively. With CHES buffer, maximum growth is reached already in the 0–1st day of cultivation and decreases rapidly afterwards. At a relative cell density of about 70% (with respect to cell density at the end of cultivation) a second growth maximum arises in what ap-
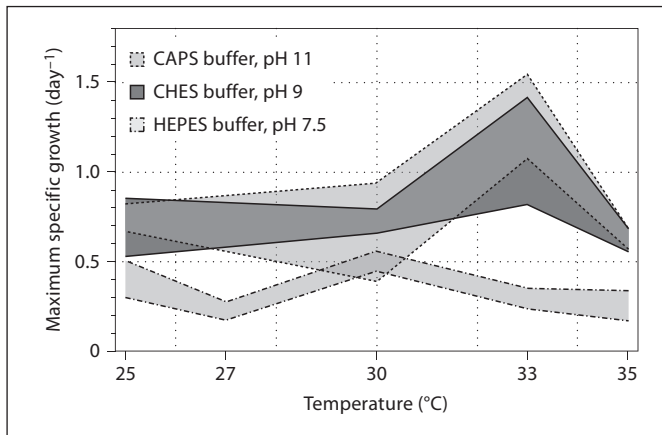
Fig. 3. Temperature profiles of the 95% level confidence regions of maximum specific autotrophic growth at different levels of initial pH. Cultures grown with different buffers: CAPS (initial pH 11) upper dashed limited grey area, CHES (pH 9) dark grey area, and HEPES (pH 7.5) lower light grey area. In all tests irradiance was 20 $\mu E \cdot m^{-2} \cdot s^{-1}$.

Fig. 4. Relative growth vs. relative cell density in autotrophic growth samples in different buffer/initial pHs. The horizontal axis represents cell concentration relative to maximum cell concentration (at the end of batch growth) and the vertical axis growth values relative to maximum growth. In all tests irradiance was 20 $\mu E \cdot m^{-2} \cdot s^{-1}$, temperature 30°C, and initial nitrate concentration 0.75 g/l. Dark circles correspond to CHES buffer pH 9, hollow squares and hollow circles represent HEPES at pHs 8.5 and 7.5, respectively.

pears to be a diauxic type of growth profile. This type of profile is also found in CAPS-buffered conditions, where even episodes of 'negative growth' (cell death/OD decrease) appear (data not shown). This phenomenon can also be observed in some mixotrophic conditions with HEPES or CHES buffer.

In contrast, HEPES-buffered growth curve displays maximum growth in the 3rd–4th day of cultivation. Diauxic growth features seem to appear, but only at the very end of the experiment.

Summarizing, from these data, it seems clear that cells find their optimum growth conditions at high pH values (between 9 and 11) and at temperatures close to 33°C (online suppl. fig. S3). In media with higher starting pHs, with CHES or CAPS buffer, optimum growth conditions are reached in an earlier stage of cultivation, followed by a decay in growth and then another growth burst at higher cell density values (fig. 4). This diauxic growth dynamic points to some metabolic shift which, as will be explained in the next section, could be connected to the carbon dioxide and carbonate assimilation mechanisms of the cell.

Furthermore, results from a 'scale-up' (see online suppl. fig. S5a and S6a) showed no significant differences between growth in our cuvettes system and 100-ml cultures in Erlenmeyer flasks, showing that we are dealing with a reliable high-throughput system to evaluate *Synechocystis* sp. PCC 6803 growth.

Mixo- and Heterotrophic Growth

For mixotrophic samples, irradiation was held constant at 20 $\mu E \cdot m^{-2} \cdot s^{-1}$. A subset of 86 conditions was selected giving a total of 258 samples and 2,154 OD measurements. As before, four-way ANOVA results showed that temperature, initial pH, and glucose concentration are the main factors affecting maximum mixotrophic growth. Of all possible interactions, the one with a clearer significant statistical influence (p value $<10^{-3}$) on growth is the interaction between the glucose concentration and temperature. As in autotrophic growth, nitrate concentration initially present in the culture can be discarded as having an effect on growth (with a non-significant p value of 0.32).

Results regarding mixotrophic maximum growth are shown in figure 5, where maximum specific growth results at different temperature levels for the three different glucose concentrations (2, 5 and 7 mM) are presented. Autotrophic maximum growth values, with the same initial pH and buffers, are shown for comparison. Significantly higher growth values are always observed in mixotrophic growth. At 25°C, maximum specific growth is 2–2.5 times larger in mixotrophic than in autotrophic condi-
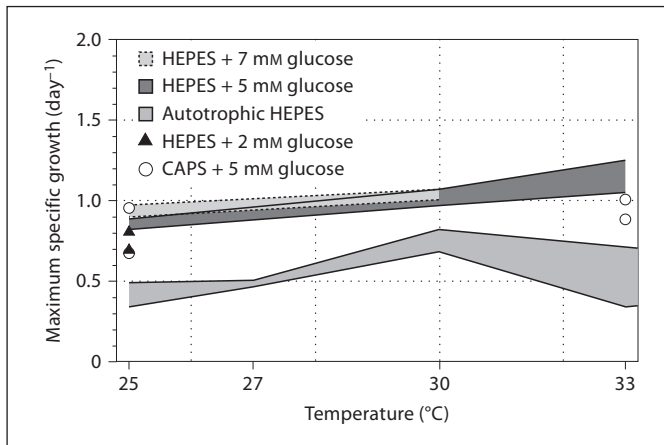
Fig. 5. Maximum specific growth vs. temperature profile of the 95% confidence regions in mixotrophic vs. autotrophic growth. Irradiance was 20 μE·m^{-2}·s^{-1}, glucose concentration 2, 5, or 7 mM, and initial pH 8.5 or 10. Light grey area with dashed lines depicts maximum specific mixotrophic growth with 7 mM glucose, dark grey area corresponds to 5 mM glucose, and filled triangles correspond to 2 mM glucose, all with HEPES buffer pH 8.5. Hollow circles correspond to mixotrophic growth with 5 mM glucose and CAPS buffer pH 10, the lower light grey area shows autotrophic growth with HEPES buffer pH 8.5 (used as reference).
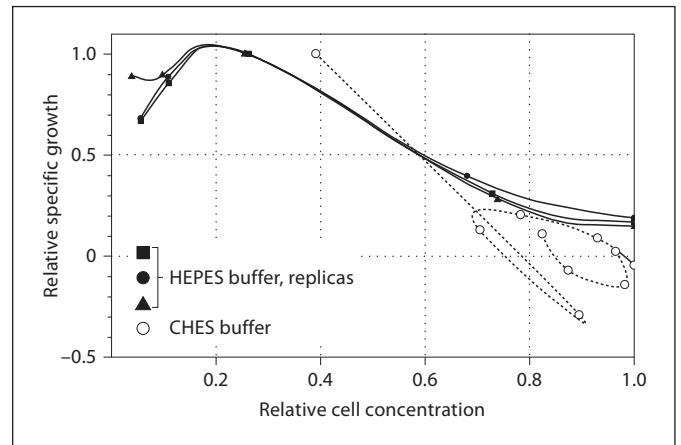
Fig. 6. Relative growth vs. relative cell concentrations curves of mixotrophic growth (5 mM glucose) at 30°C and an initial pH of 8.5 with two different buffers. The three replicates of the same sample with HEPES buffer are represented by filled symbols: squares, triangles, and circles. The dashed curve with hollow circles corresponds to one replica with CHES buffer.

tions and there is a steady increase with higher glucose concentration. The results at 30°C depict a smaller relative difference between growth in mixo- versus autotrophic conditions (1.5-fold) and also between records with different glucose concentrations.

The use of CHES buffer, with a higher initial pH, offered what seemed to be at first sight an unexpected result. It was observed that, irrespective of pH, differences between growths of different replicas with CHES buffer became systematically quite large, i.e. the confidence intervals of maximum specific growth broadened substantially. Another noticeable effect was the shortening of the lag phase, whereby the number of days to reach maximum growth shifted from 3–4 days with HEPES buffer to 0–1 days with CHES buffer. This behavior is exemplified in figure 6, in which curves displaying relative growth versus relative cell concentrations in mixotrophic growth under 30°C and an initial pH of 8.5 are presented for three replicas of one HEPES buffer culture (full symbols) and one replica of a CHES-buffered culture (hollow circles). The curves corresponding to HEPES cultivation show the same general profile, which is completely different from the CHES curve. In the latter, clear phases of cell death (relative cell concentration drops from one day to

the other) and diauxic growth can be observed. The growth profile of the rest of CHES-buffered cultures consistently displays this type of irregularities with large quantitative differences between replicas grown under the same conditions. These observations suggest that, in conditions in which light-based and glucose-based cell growth mechanisms have a similar potential (as in CHES conditions near 30°C) the resulting growth may become unstable. On the contrary, if one mechanism is predominant, culture growth becomes regular.

Additionally, the 'scale-up' performed (see online suppl. fig. S5b and S6b) showed that growth in mixotrophic conditions is consistently higher than in autotrophic conditions.

Finally, to study heterotrophic growth, 12 different conditions were selected totalizing 36 samples and 324 OD measurements. Glucose level was held constant at 5 mM and temperature was kept at 30°C in all tests. ANOVA results show that neither nitrate concentration nor initial pH substantially affect maximum specific growth within the confidence level chosen. The overall averaged maximum heterotrophic growth value of 0.42 day^{-1} can be compared to the value of around 0.8 day^{-1} obtained for autotrophic growth and around 1.1 day^{-1} in mixotrophic

growth under equivalent conditions. Furthermore, the analysis of growth profiles indicates that, systematically, after reaching the stationary phase (about the 5th–6th day), cell cultures undergo a noticeable decrease in population with cell death rates that reach up to one half of maximum specific growth rate (data not shown).

Discussion

The multifactorial and wide set of experiments shown in this study were developed to highlight the importance and effect of the main variables relevant for *Synechocystis* sp. PCC 6308 metabolism, and to establish the optimum growth conditions for the use of this organism as a model for future molecular biology developments. Additionally, a dynamic modeling framework is proposed to elucidate some basic questions that relate to the very significant pH alteration processes observed during the experiments.

Following the results from previous authors [Anderson and McIntosh, 1991; Bricker et al., 2004; Vermaas, 1996], and confirmed by this work, *Synechocystis* sp. PCC 6803 can grow photoautotrophically, a condition requiring both photosystems to be functional, mixotrophically, photoheterotrophically (without the need for a functional PS II) and heterotrophically, using glucose as carbon source and with a daily pulse of light.

Reports from the literature are arguably consensual regarding optimum light intensity for *Synechocystis* sp. PCC 6803 or cyanobacteria in general. Depending on the culture volume, flask geometry and inoculum, *Synechocystis* sp. PCC 6803 is able to withstand higher light intensities, for instance, Anderson and McIntosh [1991] exposed 75-ml cultures to 40 μE·m^{-2}·s^{-1}, whereas Bricker et al. [2004] grew 150-ml cultures at the same light intensity. However, some studies point out that *Synechocystis* sp. PCC 6803 cells can grow under a wide range of light intensities, up to approximately 1,000 μE·m^{-2}·s^{-1} or even more. Hihara et al. [2001] exposed 50-ml cultures of this cyanobacterium to a shift of light intensity from what they considered low light: 20 μE·m^{-2}·s^{-1}, to high light: 300 μE·m^{-2}·s^{-1}, and concluded that the higher intensity was sufficient to induce large changes in the gene expression profile. In their environmental study, Allakhverdiev and Murata [2004] grew *Synechocystis* PCC 6803 cells in 120-ml glass tubes at 70 μE·m^{-2}·s^{-1}. Subsequently, to assess the photodamage-repair cycle of PS II, the cells were exposed to various light intensities in 4.5-ml cuvettes for short periods, never exceeding 90 min. These light intensities were: 250, 500, 750, 1,000, 1,500 and 2,000 μE·m^{-2}·s^{-1} and the authors considered values up to 1,000 μE·m^{-2}·s^{-1} as weak light and from then onwards strong light. They concluded that the rate of photodamage was proportional to light intensity and that the rate of repair also depended on light intensity: it was high under weak light and reached a maximum at 300 μE·m^{-2}·s^{-1}. However, according to Vermaas [1996], *Synechocystis* sp. PCC 6803 cells grow best at 40–70 μE·m^{-2}·s^{-1} and are photoinactivated easily at higher light intensity. Our results show that for small volumes (2 ml) and our cuvette's geometry, 20 μE·m^{-2}·s^{-1} is closer to the optimum light intensity than the second irradiance chosen (40 μE·m^{-2}·s^{-1}), an indication that saturated light condition regimen may have been reached at this higher intensity. It seems clear for us that the debate regarding optimum light intensity for *Synechocystis* sp. PCC 6803 is still open, and researchers need to realize how important it is to clarify, describe and consider all the parameters involved such as: culture volume, flask geometry, cell density, and time of exposure, to name just a few.

Previous observations [Berry and Bjorkman, 1980] have shown that *Synechocystis* sp. PCC 6803 cells seem to suffer from low- and high-temperature stress <25 and >40°C, respectively, an effect associated to PS II sensitivity, with a complete stop of growth at 15 and 45°C. In another study, regarding growth temperature acclimation and high-temperature effects on PS II of *Synechocystis* sp. PCC 6803, Inoue et al. [2001] observed that maximum growth was obtained at 30°C, but that this cyanobacterium grew at a quite similar rate in temperatures ranging from 25 to 40°C, which agrees with the rate of photosynthesis at these temperatures.

While growth limitation at high temperatures seems to be due to limitation of PS II activity, acclimation to low temperatures takes place in parallel with an increase in the desaturation level of thylakoid membranes fatty acids [Los et al., 1993]. A rise in the desaturation level of fatty acids in the thylakoid galactolipids increases the resistance of the cyanobacterial cells to low temperatures [Wada et al., 1994]. However, Sakamoto and Bryant [1998], demonstrated that *Synechocystis* sp. PCC 6803 cells grown at 15°C aggregate and undergo chlorosis, and that this may be due to nitrogen limitation.

Our results indicate that *Synechocystis* sp. PCC 6803 growth holds critical temperature dependence: in autotrophic growth with HEPES-buffered cultures (pH between 7.5 and 9), maximum growth is observed around 30°C, while with CHES buffer (pH between 9 and 11) it occurs at 33°C. Temperature is an asymmetric factor.

Growth rate at 25°C was about half the value when compared to the optimum temperature, while at the highest temperature tested (35°C) the decrease was not so patent (75% of the maximum value).

The presence of an exogenous carbon (i.e. glucose) source has proven to be a very important factor in *Synechocystis* sp. PCC 6803 growth. In our experiments, the exact same culture was grown in media where the only difference was the amount of glucose concentration: autotrophic (without glucose) and mixotrophic (2, 5 and 7 mM glucose). Mixotrophic growth was approximately 2–2.5 times larger than autotrophic growth at 30°C at a concentration of 5 mM. A further increase of concentration between 5 and 7 mM does show a further effect, though non-significant, on growth (fig. 5). Yoo et al. [2007] obtained similar results when growing *Synechocystis* sp. PCC 6803 cells with and without 5 mM glucose. Experiments by other authors [Williams, 1988] show the same type of trends.

In our set of experiments the influence of nitrate on specific growth was below the statistical significance threshold. This behavior may be explained by the fact that during maintenance growth in BG11 medium (1.5 g/l of $NaNO_3$), the organism acquired sufficient nitrogen reserves to endure the time-span (about 1 week) of low concentrations it was subjected. It is known that growth under nitrogen-limiting conditions favors glycogen production in *Synechocystis* sp. PCC 6803. Yoo et al. [2007] observed, using transmission electron microscopy, that in these conditions, glycogen particles accumulate in large amounts and fill the cytosol of the cells.

In order to shed light on the role of pH in *Synechocystis* sp. PCC 6308 growth, a simplified modeling scheme was used to explain and give insight on the basic mechanism behind pH response of the cells, considering its particular difficulty and dynamic nature.

On the one hand, cyanobacteria are among the most alkalotolerant or alkalophilic microbes and preferably grow at pHs ranging from neutral to 11 [Langworthy, 1978; Lopez-Archilla et al., 2004]. On the other hand, there is a well-documented connection between the action and effects of the photosynthesis machinery of the cells and their ability to increase the surrounding pH [Becking et al., 1960]. In normal laboratory conditions, *Synechocystis* sp. PCC 6308 cells increase their surrounding pH by 1–2 units over several days. However, when placed in acid stress situation at a tolerable pH (≥4.4), this organism's cells are able to increase their surrounding pH to 6 and above within a few minutes. *Synechocystis* sp. PCC 6308 exhibits predictable physiological responses to acid stress but it is incapable of growing in media with a pH <4.4. This capability is cell density-dependent, as high cell concentration cultures have been able to withstand pH shock as low as 3.5 [Huang et al., 2002]. The ability of cyanobacteria to grow at alkaline pH implies the presence of mechanisms for the maintenance of an intracellular pH more acidic than that of the external environment [Miller et al., 1984]. Indeed, an increase in the external pH of 2 units results only in an increase of 0.2 units in both the cytosol and the thylakoid lumen. Such changes alter the CO_2/HCO_3^- ratio within the cell, and regulation of CO_2/HCO_3^- concentration is essential for maintaining the carboxylase activity of Rubisco [Summerfield and Sherman, 2008]. Halophilic or halotolerant cyanobacteria are thought to possess a membrane-associated Na^+/H^+ antiport system that could participate in pH homeostasis. This could be the case of *Synechocystis* sp. PCC 6803, since its genome contains information for such potential pumps [Maestri and Joset, 2000].

In the present work, *Synechocystis* sp. PCC 6803 cultures (initial pH 8.5) were grown in continuous light under pH-unstressed conditions. The pH increase observed (up to 10.5) in the buffered (after 10 days) and unbuffered (after 5 days) systems may be attributable to carbon fixation through photosynthesis, which can shift the most common pH-buffering mechanism in freshwater systems – the carbon dioxide/bicarbonate/carbonate equilibrium. This light-dependent increase of external pH can be observed in nature [Pierson et al., 1999], and is particularly remarkable in hypereutrophic systems, as a consequence of a very high primary production [Lopez-Archilla et al., 2004]. Photosynthesis is favored under more alkaline conditions, since alkaline systems act as a trap for atmospheric carbon dioxide [Imhoff et al., 1978] which, in turn, is more available for primary production. Moreover, at high pHs, nutrients such as phosphorous become more soluble [Talling and Talling, 1965]. Evidence that *Synechocystis* sp. PCC 6308 cells must photosynthesize to increase external pH is provided by the fact that cells placed in the dark do not grow and do not increase the external pH, even with a carbon source (glucose) added to the media as it was observed in our experiments. In addition, if an autotrophic culture is switched to dark, pH tends to decrease to the initial level. This effect is not observed in heterotrophic conditions. An alternative explanation for the external pH increase is that ammonia may be excreted into the medium by pH-stressed *Synechocystis* sp. PCC 6803 cells [Huang et al., 2002]. However, in the present work, no ammonia was detected in the high pH medium (data not shown), indicating that if there was
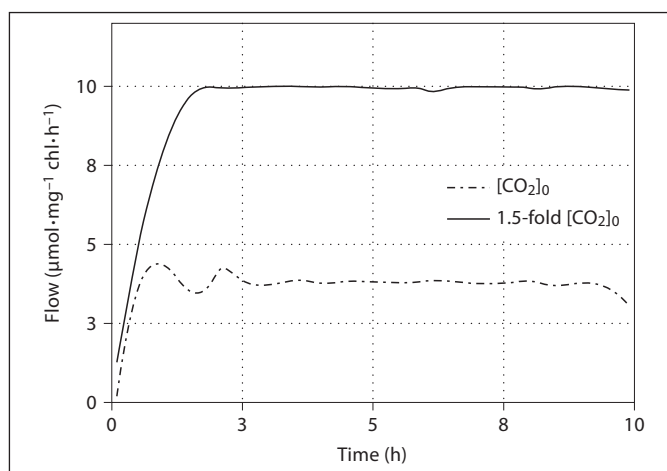
Fig. 7. Flux of ATP production for the normal condition (dashed line) and 1.5-fold $[CO_2]_0$ (continuous line).

Fig. 8. High-throughput experimental design. Four clear-side cuvettes with 2 ml of *Synechocystis* sp. PCC 6803 culture on acrylic rack inside growth chamber (for details, see Experimental Procedures).

any trace of ammonia, it would be consumed by the cells within a short time [Sakamoto et al., 1999].

On account of these observations, we have developed a modeling scheme based on the connection between pH changes and photosynthesis-related metabolic activity, taking into consideration that, even though some models have been developed for *Escherichia coli* and other organisms [Reed et al., 2003; Senger and Papoutsakis, 2008], a comprehensive metabolic scheme taking into account protons in the frame of a photosynthetic organism is not yet available. The model's scheme, explained with more detail in the online supplementary material, is based on the following three assumptions: (1) the cells are able to take up carbon in the form of HCO_3^-, which is indeed a more efficient way to concentrate it in the carboxisomes; (2) the solubility of carbon dioxide increases with pH, and (3) due to the solubility and pH effect on the different solved carbon species, the pH at which HCO_3^- turns to be the dominant carbon source solved in water is around 10.3.

Upon culture illumination, some protons are removed from the medium, as a consequence of the tight pH control in the cytoplasm [Miller et al., 1984], and pumped into the thylakoid membrane to produce NADPH and ATP from light. This phenomenon produces an increase of pH in the medium which, consequently, increases the amount of carbon solved. Using the M-DFBA model (see online suppl. material for detailed description) we monitored the dynamic short-term reaction of the cells to a perturbation in CO_2 concentration. The initial conditions of the system were obtained from literature [Bays-

dorfer and Robinson, 1985; Goyal and Tolbert, 1996; Luttge, 2002; Rutter and Cobb, 1983; Sharkey et al., 1986; Smith and Griffiths, 1996; Takeuchi et al., 2002; Vu and Yelenosky, 1988]. Our algorithm follows the *medium scale algorithm* as implemented in the *fmincon* function in the MATLAB® software platform.

The resulting time evolution is depicted in figure 7, where, depending on the increase in CO_2 concentration, a subsequent increase in ATP production within some hours is observed. According to our results, when $[CO_2]_0$ increases 1.5-fold, ATP production experiences a 2.5 times increase. As ATP production is positively correlated with the voltage in the membrane [Kaim and Dimroth, 1999; Nagel et al., 1995], the direct consequence is an increase in the number of protons removed from the medium and stored inside the thylakoid membrane. Hence, a feedback loop begins which causes an increase of pH up to 10.3. At this pH level, the predominant form of carbon (bicarbonate) in the media changes to a form that is less suitable for cell growth and the system reaches a state of equilibrium which agrees with the pH steady values observed at the end of our autotrophic growth experiments.

Conclusions

A multifactorial set of experiments, with over 3,000 individual measurements, was conducted to highlight the effect of the main variables relevant for *Synechocystis* sp. PCC 6308 growth and to establish the optimum con-

ditions for its use as a model *chassis* for biotechnological applications. It was demonstrated that *Synechocystis* sp. PCC 6803 can grow photoautotrophically, mixotrophically, photoheterotrophically (without the need for a functional PS II) and heterotrophically, using glucose as carbon source and a daily pulse of light.

Irradiance, glucose presence, and temperature were found to be the major governing factors. In our experiments the influence of nitrate was too small to be detected within our statistical significance threshold and growth was meaningfully larger at a light intensity of 20 $\mu E \cdot m^{-2} \cdot s^{-1}$ than for the second irradiance chosen (40 $\mu E \cdot m^{-2} \cdot s^{-1}$), where, for small volumes (2 ml) and our cuvette's geometry, damaging effects may appear.

In autotrophic growth, there is a significant effect and interaction of pH and temperature; in HEPES-buffered cultures (pH between 7.5 and 9), maximum growth is observed around 30°C, while CHES- or CAPS-buffered (pH between 9 and 11) and no-buffer cultures show a very marked peak in growth at 33°C. Maximum growth of 1.8 day^{-1} was obtained in the latter, high pH, conditions, being 2.5–3 times larger than growth in lower pH media.

In mixotrophic conditions growth, around 1 day^{-1}, is much more insensitive to pH and temperature. Opposite to autotrophism, mixotrophic growth is smaller in high pH media compared to lower pH media.

To explain the above results, a modeling scheme by means of an adapted M-DFBA method is proposed in which photosynthetic activity is related to pH and cell growth. The model predicts that pH around the cells increases, as a consequence of photosynthetic activity, up to a value of 10.3. This pH value is in accordance with our observations and is explained by the solubility curve of different carbonate species in water and their ability to be metabolized by *Synechocystis* sp. PCC 6308.

Experimental Procedures

Organisms and Standard Growth Conditions
The unicellular non-N_2-fixing cyanobacterium *Synechocystis* sp. PCC 6803 (obtained from the Pasteur Culture Collection, Paris, France) was maintained in BG11 medium [Stanier et al., 1971] at 25°C, and 16 h light (20 $\mu E \cdot m^{-2} \cdot s^{-1}$)/8 h dark cycles.

Growth Experiments
Inoculums of 200 µl from the maintenance culture grown under standard conditions (transferred 24 h before to fresh BG11 medium) with an $OD_{730} \approx 1.0$, were added to sterile 4.5-ml cuvettes containing 1,800 µl of medium with given concentrations of glucose, nitrate, and pH values. Each experiment was per-

formed in triplicate and under aseptic conditions. The cuvettes were closed with sterilized Parafilm™, and placed in acrylic racks specially designed for this experiment (fig. 8). This constitutes a high-throughput system, equivalent to batch cultures with the Parafilm cover allowing gas exchanges. The racks were placed in a chamber with constant temperature and irradiance (20 or 40 $\mu E \cdot m^{-2} \cdot s^{-1}$ with Osram L18W/765 cool white daylight bulbs). Table 1 shows the initial experimental matrix with all the conditions to be tested. Not all the combinations of this matrix were tested. As the workflow moved along and new results were obtained, some combinations were abandoned and more relevant ones were introduced, notably other temperatures (33 and 35°C), and pHs (9.0, 10.0, 10.5 and 11.0). For the control of the pH several buffers (HEPES, CHES and CAPS) were used, according to their pKa, with a concentration of 10 mM (or 10, 20, 30, 50 and 100 mM for HEPES, see online suppl. fig. S7). Growth in normal BG11 media without controlled pH was also tested. OD at 730 nm was recorded daily.

Statistical Analysis of the Specific Growth
The quantitative analysis of *Synechocystis* sp. PCC 6308 growth in various conditions was based on the OD measurements (see above). For each bin, i, a specific growth parameter, representing the exponent of (assumed) exponential growth within the given time interval is calculated as:

$$\mu_i = \frac{\log\left[x_{i+1} / x_i\right]}{t_{i+1} - t_i}$$

where t_i is time, in units of days running from day 0 to $t_{i_{max}}$ and x_i is the corresponding measured OD.

In order to work with a statistic that does not depend rather arbitrarily on test duration, particularly if in some particular conditions stationary growth is reached sooner than in others, we chose not to work with the mean specific growth rate but rather the maximum specific growth rate:

$$\mu_{max} = \text{Max}\{\mu_i\}\big|_{i=0,\cdots,i_{max}}$$

In addition we can obtain the time $t_{i_{max}}$ at which maximum specific growth is reached and the corresponding OD record, $x_{i_{max}}$.

From the three replicas of any of the experimental samples with a given level of light, nitrate and glucose, it was possible to calculate confidence intervals for the sample growth parameters, corrected by means of the Student t distribution. The usual confidence level of 95% was selected and used to represent solid areas in figures 1–3 and 5.

References

Allakhverdiev SI, Murata N: Environmental stress inhibits the synthesis de novo of proteins involved in the photodamage-repair cycle of photosystem II in *Synechocystis* sp. PCC 6803. Biochim Biophys Acta 2004;1657: 23–32.

Allen MM, Smith AJ: Nitrogen chlorosis in blue-green algae. Arch Mikrobiol 1969;69:114–120.

Anderson SL, McIntosh L: Light-activated heterotrophic growth of the cyanobacterium *Synechocystis* sp. strain PCC 6803: a blue-light-requiring process. J Bacteriol 1991;173: 2761–2767.

Bailey J, Ollis D: Biochemical Engineering Fundamentals, ed 2. New York, McGraw-Hill, 1986.

Baysdorfer C, Robinson JM: Metabolic interactions between spinach leaf nitrite reductase and ferredoxin-NADP reductase: competition for reduced ferredoxin. Plant Physiol 1985;77:318–320.

Becking LGMB, Kaplan IR, Moore D: Limits of the natural environment in terms of pH and oxidation-reduction potentials. J Geol 1960; 68:243–284.

Berry J, Bjorkman O: Photosynthetic response and adaptation to temperature in higher plants. Annu Rev Plant Physiol Plant Molec Biol 1980;31:491–543.

Blanco-Rivero A, Leganes F, Fernandez-Valiente E, Calle P, Fernandez-Pinas F: MRPA, a gene with roles in resistance to Na^+ and adaptation to alkaline pH in the *Cyanobacterium anabaena* sp. Pcc7120. Microbiology 2005; 151:1671–1682.

Bricker TM, Zhang S, Laborde SM, Mayer PR 3rd, Frankel LK, Moroney JV: The malic enzyme is required for optimal photoautotrophic growth of *Synechocystis* sp. strain PCC 6803 under continuous light but not under a diurnal light regimen. J Bacteriol 2004;186: 8144–8148.

Burja AM, Dhamwichukorn S, Wright PC: Cyanobacterial postgenomic research and systems biology. Trends Biotechnol 2003;21: 504–511.

Castenholtz RW: Thermophilic blue-green algae and the thermal environment. Bacteriol Rev 1969;33:476–504.

Collier JL, Grossman AR: Chlorosis induced by nutrient deprivation in *Synechococcus* sp. strain PCC 7942: not all bleaching is the same. J Bacteriol 1992;174:4718–4726.

Gill RT, Katsoulakis E, Schmitt W, Taroncher-Oldenburg G, Misra J, Stephanopoulos G: Genome-wide dynamic transcriptional profiling of the light-to-dark transition in *Synechocystis* sp. strain PCC 6803. J Bacteriol 2002;184:3671–3681.

Goyal A, Tolbert NE: Association of glycolate oxidation with photosynthetic electron transport in plant and algal chloroplasts. Proc Natl Acad Sci USA 1996;93:3319–3324.

Gutthann F, Egert M, Marques A, Appel J: Inhibition of respiration and nitrate assimilation enhances photohydrogen evolution under low oxygen concentrations in *Synechocystis* sp. PCC 6803. Biochim Biophys Acta 2007; 1767:161–169.

Hihara Y, Kamei A, Kanehisa M, Kaplan A, Ikeuchi M: DNA microarray analysis of cyanobacterial gene expression during acclimation to high light. Plant Cell 2001;13:793–806.

Huang JJ, Kolodny NH, Redfearn JT, Allen MM: The acid stress response of the cyanobacterium *Synechocystis* sp. strain PCC 6308. Arch Microbiol 2002;177:486–493.

Imhoff JF, Sahl HG, Soliman GSH, Truper HG: The Wadi Natrum – chemical composition and microbial mass developments in alkaline brines of eutrophic desert lakes. Geomicrobiol J 1978;1:219–234.

Inoue N, Taira Y, Emi T, Yamane Y, Kashino Y, Koike H, Satoh K: Acclimation to the growth temperature and the high-temperature effects on photosystem II and plasma membranes in a mesophilic cyanobacterium, *Synechocystis* sp. PCC 6803. Plant Cell Physiol 2001;42:1140–1148.

Kaim G, Dimroth P: ATP synthesis by F-type ATP synthase is obligatorily dependent on the transmembrane voltage. EMBO J 1999; 18:4118–4127.

Kallas T, Castenholz RW: Internal pH and ATP-ADP pools in the cyanobacterium *Synechococcus* sp. during exposure to growth-inhibiting low pH. J Bacteriol 1982;149:229–236.

Kaneko T, Sato S, Kotani H, Tanaka A, Asamizu E, Nakamura Y, Miyajima N, Hirosawa M, Sugiura M, Sasamoto S, Kimura T, Hosouchi T, Matsuno A, Muraki A, Nakazaki N, Naruo K, Okumura S, Shimpo S, Takeuchi C, Wada T, Watanabe A, Yamada M, Yasuda M, Tabata S: Sequence analysis of the genome of the unicellular cyanobacterium *Synechocystis* sp. strain PCC 6803. II. Sequence determination of the entire genome and assignment of potential protein-coding regions. DNA Res 1996;3:109–136.

Konak AR: Equation for batch bacterial growth. Biotechnol Bioeng 1975;17:271–272.

Kratz WA, Myers J: Photosynthesis and respiration of three blue-green algae. Plant Physiol 1955;30:275–280.

Kurian D, Phadwal K, Maenpaa P: Proteomic characterization of acid stress response in *Synechocystis* sp. PCC 6803. Proteomics 2006;6:3614–3624.

Langworthy TA: Microbial Life in Extreme Environments. London, Academic Press, 1978.

Lopez-Archilla AI, Moreira D, Lopez-Garcia P, Guerrero C: Phytoplankton diversity and cyanobacterial dominance in a hypereutrophic shallow lake with biologically produced alkaline pH. Extremophiles 2004;8:109–115.

Los D, Horvath I, Vigh L, Murata N: The temperature-dependent expression of the desaturase gene desa in *Synechocystis* PCC 6803. FEBS Lett 1993;318:57–60.

Luo R, Wei H, Ye L, Wang K, Chen F, Luo L, Liu L, Li Y, Crabbe MJ, Jin L, Zhong Y: Photosynthetic metabolism of c3 plants shows highly cooperative regulation under changing environments: a systems biological analysis. Proc Natl Acad Sci USA 2009;106:847–852.

Luo RY, Liao S, Tao GY, Li YY, Zeng S, Li YX, Luo Q: Dynamic analysis of optimality in myocardial energy metabolism under normal and ischemic conditions. Mol Syst Biol 2006; 2:2006.0031.

Luttge U: CO_2-concentrating: consequences in crassulacean acid metabolism. J Exp Bot 2002;53:2131–2142.

Maestri O, Joset F: Regulation by external pH and stationary growth phase of the acetolactate synthase from *Synechocystis* PCC 6803. Mol Microbiol 2000;37:828–838.

Mahadevan R, Edwards JS, Doyle FJ 3rd: Dynamic flux balance analysis of diauxic growth in *Escherichia coli*. Biophys J 2002; 83:1331–1340.

Miller AG, Turpin DH, Canvin DT: Na^+ requirement for growth, photosynthesis, and pH regulation in the alkalotolerant cyanobacterium *Synechococcus leopoliensis*. J Bacteriol 1984;159:100–106.

Montagud A, Navarro E, Fernandez de Cordoba P, Urchueguia JF, Patil KR: Reconstruction and analysis of genome-scale metabolic model of a photosynthetic bacterium. BMC Syst Biol 2010;4:156.

Mullineaux CW: How do cyanobacteria sense and respond to light? Mol Microbiol 2001;41: 965–971.

Nagel G, Mockel B, Buldt G, Bamberg E: Functional expression of bacteriorhodopsin in oocytes allows direct measurement of voltage dependence of light induced H^+ pumping. FEBS Lett 1995;377:263–266.

Navarro E, Montagud A, de Cordoba PF, Urchueguia JF: Metabolic flux analysis of the hydrogen production potential in *Synechocystis* sp. PCC 6803. Int J Hydrogen Energy 2009;34:8828–8838.

Pierson BK, Parenteau MN, Griffin BM: Phototrophs in high-iron-concentration microbial mats: physiological ecology of phototrophs in an iron-depositing hot spring. Appl Environ Microbiol 1999;65:5474–5483.

Reed JL, Vo TD, Schilling CH, Palsson BO: An expanded genome-scale model of *Escherichia coli* K-12 (iJR904 GSM/GPR). Genome Biol 2003;4:R54.

Rutter JC, Cobb AH: Translocation of ortho-phosphate and glucose-6-phosphate in codium fragile chloroplasts. New Phytol 1983; 95:559–568.

Sakamoto T, Bryant DA: Growth at low temperature causes nitrogen limitation in the cyanobacterium *Synechococcus* sp. PCC 7002. Arch Microbiol 1998;169:10–19.

Sakamoto T, Inoue-Sakamoto K, Bryant DA: A novel nitrate/nitrite permease in the marine cyanobacterium *Synechococcus* sp. Strain PCC 7002. J Bacteriol 1999;181:7363–7372.

Schmitz O, Boison G, Salzmann H, Bothe H, Schutz K, Wang SH, Happe T: HoxE – a subunit specific for the pentameric bidirectional hydrogenase complex (HoxEFUYH) of cyanobacteria. Biochim Biophys Acta 2002; 1554:66–74.

Segre D, Vitkup D, Church GM: Analysis of optimality in natural and perturbed metabolic networks. Proc Natl Acad Sci USA 2002;99: 15112–15117.

Senger RS, Papoutsakis ET: Genome-scale model for clostridium acetobutylicum. II. Development of specific proton flux states and numerically determined sub-systems. Biotechnol Bioeng 2008;101:1053–1071.

Sharkey TD, Stitt M, Heineke D, Gerhardt R, Raschke K, Heldt HW: Limitation of photosynthesis by carbon metabolism: II. O_2-insensitive CO_2 uptake results from limitation of triose phosphate utilization. Plant Physiol 1986;81:1123–1129.

Shastri AA, Morgan JA: Flux balance analysis of photoautotrophic metabolism. Biotechnol Prog 2005;21:1617–1626.

Singh AK, McIntyre LM, Sherman LA: Microarray analysis of the genome-wide response to iron deficiency and iron reconstitution in the cyanobacterium *Synechocystis* sp. PCC 6803. Plant Physiol 2003;132:1825–1839.

Smith EC, Griffiths H: The occurrence of the chloroplast pyrenoid is correlated with the activity of a CO_2-concentrating mechanism and carbon isotope discrimination in lichens and bryophytes. Planta 1996;198:6–16.

Stanier RY, Kunisawa R, Mandel M, Cohen-Bazire G: Purification and properties of unicellular blue-green algae (order Chroococcales). Bacteriol Rev 1971;35:171–205.

Steinberg CEW, Schafer H, Beisker W: Do acid-tolerant cyanobacteria exist? Acta Hydrochim Hydrobiol 1998;26:13–19.

Stevens SE, Balkwill DL, Paone DAM: The effects of nitrogen limitation on the ultrastructure of the cyanobacterium agmeneilumquadruplicatum. Arch Microbiol 1981;130: 204–212.

Summerfield TC, Sherman LA: Global transcriptional response of the alkali-tolerant cyanobacterium *Synechocystis* sp. strain PCC 6803 to a pH 10 environment. Appl Environ Microbiol 2008;74:5276–5284.

Takeuchi A, Yamaguchi T, Hidema J, Strid A, Kumagai T: Changes in synthesis and degradation of rubisco and LHCII with leaf age in rice (*Oryza sativa* L.) growing under supplementary UV-B radiation. Plant Cell Environment 2002;25:695–706.

Talling JF, Talling IB: The chemical composition of African lake waters. Int Rev Ges Hydrobiol Hydrograph 1965;50:421–463.

Varma A, Palsson BO: Stoichiometric flux balance models quantitatively predict growth and metabolic by-product secretion in wildtype *Escherichia coli* W3110. Appl Environ Microbiol 1994;60:3724–3731.

Vermaas W: Molecular genetics of the cyanobacterium *Synechocystis* sp. PCC 6803: principles and possible biotechnology applications. J Appl Phycol 1996;8:263–273.

Vu JC, Yelenosky G: Water deficit and associated changes in some photosynthetic parameters in leaves of 'Valencia' orange (*Citrus sinensis* [L.] Osbeck). Plant Physiol 1988;88:375–378.

Wada H, Gombos Z, Murata N: Contribution of membrane lipids to the ability of the photosynthetic machinery to tolerate temperature stress. Proc Natl Acad Sci USA 1994;91: 4273–4277.

Waterbury J: The prokaryotes: a handbook on the biology of bacteria: bacteria – firmicutes, cyanobacteria; in Dworkin M, Falkow S, Rosenberg E, Schleifer KH, Stackebrandt E (eds): Cyanobacteria. New York, Springer Science, 2006, vol 4, p 1140.

Williams JGK: Construction of specific mutations in photosystem II photosynthetic reaction center by genetic engineering methods in *Synechocystis* 6803. Meth Enzymol 1988; 167:766–778.

Yamanaka G, Glazer AN: Dynamic aspects of phycobilisome structure. Phycobilisome turnover during nitrogen starvation in *Synechococcus* sp. Arch Microbiol 1980;124:39–47.

Yang C, Hua Q, Shimizu K: Metabolic flux analysis in *Synechocystis* using isotope distribution from ^{13}C-labeled glucose. Metab Eng 2002;4:202–216.

Yoo SH, Keppel C, Spalding M, Jane JL: Effects of growth condition on the structure of glycogen produced in cyanobacterium *Synechocystis* sp. PCC 6803. Int J Biol Macromol 2007;40:498–504.

BMC
Systems Biology

RESEARCH ARTICLE

Open Access

Reconstruction and analysis of genome-scale metabolic model of a photosynthetic bacterium

Arnau Montagud[1,3*], Emilio Navarro[2], Pedro Fernández de Córdoba[1], Javier F Urchueguía[1], Kiran Raosaheb Patil[3]

Abstract

Background: *Synechocystis* sp. PCC6803 is a cyanobacterium considered as a candidate photo-biological production platform - an attractive cell factory capable of using CO_2 and light as carbon and energy source, respectively. In order to enable efficient use of metabolic potential of *Synechocystis* sp. PCC6803, it is of importance to develop tools for uncovering stoichiometric and regulatory principles in the *Synechocystis* metabolic network.

Results: We report the most comprehensive metabolic model of *Synechocystis* sp. PCC6803 available, *i*Syn669, which includes 882 reactions, associated with 669 genes, and 790 metabolites. The model includes a detailed biomass equation which encompasses elementary building blocks that are needed for cell growth, as well as a detailed stoichiometric representation of photosynthesis. We demonstrate applicability of *i*Syn669 for stoichiometric analysis by simulating three physiologically relevant growth conditions of *Synechocystis* sp. PCC6803, and through *in silico* metabolic engineering simulations that allowed identification of a set of gene knock-out candidates towards enhanced succinate production. Gene essentiality and hydrogen production potential have also been assessed. Furthermore, *i*Syn669 was used as a transcriptomic data integration scaffold and thereby we found metabolic hot-spots around which gene regulation is dominant during light-shifting growth regimes.

Conclusions: *i*Syn669 provides a platform for facilitating the development of cyanobacteria as microbial cell factories.

Background

Cyanobacteria, which have been model organisms since the early 70s of the past century [1], are a widespread group of photoautotrophic microorganisms, which originated, evolved, and diversified early in Earth's history [2]. It is commonly accepted that cyanobacteria played a crucial role in the Precambrian phase by contributing oxygen to the atmosphere [3]. All cyanobacteria combine the ability to perform an oxygenic photosynthesis (resembling that of chloroplasts) with typical prokaryotic features, like performing anoxygenic photosynthesis by using hydrogen sulfide (H_2S) as the electron donor or fixing atmospheric dinitrogen (N_2) into ammonia (NH_3). Relevance of this phylum covers from evolutionary studies [4] to biotechnological applications, including bio-fuel production [5]. *Synechocystis* sp. PCC6803 is a cyanobacterium that is considered as a good candidate

for developing a photo-biological cell factory towards production of a variety of molecules of socio-economic interest, with CO_2 (and/or sugars) as carbon source and light (and/or sugars) as energy source [6]. The diversity of potential applications in this sense is broad. Works have been published on heterologous production of metabolites such as isoprene [6], poly-beta-hydroxybutyrate [7], biofuels [8] and bio-hydrogen [9,10] - an energy vector of global interest [11].

Synechocystis sp. PCC6803 is capable of growing under three different growth conditions as marked by the utilized carbon source (/s) [12]. This causes that three distinct modes of operation are interweaved over the same metabolic network, *viz.*, i) photoautotrophy, where energy comes from light and carbon from CO_2; ii) heterotrophy, where energy and carbon source is a saccharide, for instance glucose; and, iii) mixotrophy, a combination of the above two, where light is present as well as a combination of two carbon sources: glucose and CO_2. Reconstruction of a genome-scale metabolic model for this model photo-synthetic bacterium is one

* Correspondence: armontag@mat.upv.es
[1]Instituto Universitario de Matemática Pura y Aplicada, Universidad Politécnica de Valencia, Camino de Vera 14, 46022 Valencia, Spain
Full list of author information is available at the end of the article

BioMed Central

of the main goals of the current study. Genome-scale metabolic network reconstruction is, in essence, a systematic assembly and organization of all the reactions which build up the metabolism of a given organism; and has been of great interest in the post-genomic era. The variety of applications of such a metabolic model [13] includes the possibility of assessing projects for the production and optimization of an added value metabolite. If a model is formulated properly, it is expected to allow simulating environmental and genetic perturbations in the metabolic network. Thus, together with appropriate constraints, a metabolic model would partially represent a virtual organism - an *in silico* model that allows probing possible flux distributions inside the cell under different environmental conditions and for a given genetic make-up. Towards this end, a variety of tools/algorithms are available [14], including flux balance analysis (FBA) [15,16], minimization of metabolic adjustments (MOMA) [17], regulatory on-off minimization (ROOM) [18] and metabolic control analysis (MCA) [19,20].

Synechocystis sp. PCC6803 genome was sequenced, annotated and made publicly available in 1996 [21,22] and has been the target of some metabolic modeling effort, especially for central carbon metabolic reconstructions [23,24]. The work from Yang *et al* [23] focused on a metabolic model of glycolysis, tricarboxylic acid cycle and pentose phosphate pathway that was simulated under heterotrophic and mixotrophic conditions. Shastri and Morgan [24] studied a metabolic model with the same pathways under autotrophic conditions and compared their results to the ones from Yang *et al*. These two works considered one lumped reaction for the photosynthesis of the system. More recently, an uncurated reaction list with a biomass composition represented by central carbon metabolites has been published [25]. This model, however, is not suitable for simulations due to lack of proper biomass equation, lumped nature of some key reactions and missing reactions.

The large quantity of information featured in public databases, like details about genomes [26], pathways [27], enzymes [28] or proteins [29] can be used from different databases to gather all published data for one specific organism. However, the lack of quality must be considered as a major drawback of some of the databases: false positives, false negatives as well as wrongly annotated objects may hinder efforts of collecting accurate data [30]. Consequently, manual reconstruction by detailed inspection of each and every reaction, biomass equation based on metabolic building blocks (such as amino acids and nucleotides), consistency and integrity of the network is a pre-requisite for creating a high quality and useful metabolic model [31]. The current study presents such manually curated reconstruction for

Synechocystis sp. PCC6803 and demonstrates some of its potential applications.

The present model features a detailed biomass equation which encompasses all the building blocks that are needed for a flux distribution simulation that reflects observed phenotype. No lumped reactions are present and photosynthesis is described as a set of 19 reactions, thus enabling the tracing of the corresponding fluxes. Furthermore, different analyses are performed by using this metabolic reconstruction, including reaction knock-out simulations, flux variability analysis and identification of transcriptional regulatory hotspots. Overall, *i*Syn669 is a valuable tool towards the development of a photo-biological production platform. The model will also contribute to the existing set of genome-scale models with a virtue of being one of the first stoichiometric models that account for photosynthesis.

Results and Discussion
Genome-scale metabolic network reconstruction
A complete literature examination, including databases, biochemistry textbooks and the annotated genome sequence, was needed in order to extract the current state of the art on known metabolic reactions within the metabolic network of *Synechocystis* sp. PCC6803. For a thorough overview of the process of metabolic model reconstruction, refer to very instructive work by Forster *et al* [32] as well as review by Feist *et al* [31]. In detail, the reconstruction started with the annotation and genomic sequence files of *Synechocystis* sp. PCC6803 [21,22]. These files were used with Pathway Tools software [33] in order to build a database of all the genes, proteins and metabolites presents in the organism. The list of reactions was then retrieved from Pathway Tools; EC numbers and stoichiometry of the reactions were checked and verified with the help of the Enzyme nomenclature database [34] and KEGG pathway database [27]. Reactions were elementally balanced except for protons, so that chemical conversions were coherent. In some of the reactions present in these databases, metabolites were reported in a non-specific form (e.g. 'an alcohol'). This is insufficient for metabolic model simulation and, so, corresponding organism-specific metabolites had to be identified [32]. Additionally, in a large number of reactions cofactors were not completely clarified: an enzyme being capable of using NADH or NADPH or both. In the latter, two reactions were included in the reconstructed metabolic network. Determination of reversibility of the reactions was assisted by specific enzyme databases, like BRENDA [28]. If no conclusive evidence was reported, reactions were set to be reversible.

In the reconstruction of the metabolic model, many reactions (a total of 79 reactions, see Table 1) were

Table 1 Distribution of the model reactions as per cognate genes

Number of reactions	882
-With assigned genes	669
·Protein-mediated transport	78
-With no cognate gene	221
·Chemical conversion	47
·Transport reactions	20
·EC reactions not annotated	79
·Needed for biomass simulation	75

found to be necessary for the production of the monomers, precursors or building blocks, that are considered in the biomass equation but which have no corresponding enzyme coding gene assigned. In consequence, many genes that were not annotated before should be considered, as they code for enzymes that should be present to allow the formation of biomass. For instance, enzymes malyl-CoA lyase and isocitrate lyase were not allocated in the annotation of the genome albeit their activities have been measured [35,36] and their presence is necessary to complete the glyoxylate shunt; consequently, they were included in the model.

The product of this reconstruction process was a set of reactions that encompass all the known metabolite conversions that take place in *Synechocystis* sp. PCC6803. The resulting network, *i*Syn669, consists of 882 metabolic reactions and 790 metabolites (see Table 1 for more information). A total of 669 genes were included, to which 639 reactions were assigned (see Additional file 1 for details); the difference between the number of genes and assigned reactions is due to the presence of considerable number of protein complexes (e.g. photosynthetic or respiratory activities) and isoenzymes. Reactions with no cognate genes are also present in *i*Syn669, 20 passive transport reactions and 47 chemical conversions (not mediated by enzymes) were included. Additionally, a total of 79 reactions were included on the basis of biochemical evidence or physiological considerations, but currently with no annotated Open Reading Frame (ORF). *i*Syn669 genome-scale metabolic model is available in Additional file 2 (in OptGene [37] format).

*i*Syn669 spans all the biologically relevant flux nodes in the *Synechocystis* metabolism. Pyruvate, phosphoenol-pyruvate (PEP), 3-phosphoglycerate, erythrose-4-phosphate and 2-oxoglutarate are main flux nodes for amino acids biosynthesis. Acetyl-CoA is an important flux node for fatty acids production, with high relevance for metabolic engineering towards biofuel production. Biosynthesis of nucleic acids comes from different metabolites, namely, ribose-5-phosphate, 5-phospho-beta-D-

ribosyl-amine, L-histidine and L-glutamine. Moreover, with the information publicly available on databases, we can conclude that *Synechocystis* sp. PCC6803 bears an incomplete tricarboxylic acid cycle (TCA cycle), as it lacks 2-ketoglutarate dehydrogenase (EC 1.2.4.2). It has been published that glyoxylate shunt completes this cycle [35], permitting the recycling of TCA metabolites. Alternatively, aspartate transaminase (reaction *2.6.1.1a* in *i*Syn669) can interconvert 2-ketoglutarate and oxaloacetate, thus bridging the gap of 2-ketoglutarate dehydrogenase, but short-circuiting TCA cycle.

From the network topology perspective, *i*Syn669 displays the connectivity distribution pattern similar to that of the other microbial genome-scale networks, e.g. yeast [32] and *Escherichia coli* [38] (Table 2). While most of the metabolites have few connections, few metabolites are involved in very many reactions and are often referred to as metabolic hubs. Homeostasis of such highly connected metabolites will affect globally the metabolic phenotype (as reflected in metabolite levels and fluxes) and therefore of interest for studying the organization of regulatory mechanisms on the genome-wide scale. Most connected metabolites include those related to energy harvesting (e.g. ATP, NADP+, oxygen), a key metabolite in the porphyrin and chlorophyll metabolism (S-adenosyl methionine), a couple of amino acids

Table 2 Most connected metabolites in the iSyn669 metabolic network

Metabolite	Neighbors	Neighbors in E. coli	Neighbors in yeast
H2O	213	697	-
ATP	144	338	166
phosphate	108	81	113
ADP	103	253	131
diphosphate	97	28	-
H+	74	923	188
CO2	72	53	66
NADP+	64	39	61
NADPH	63	66	57
NAD+	46	79	58
L-glutamate	45	52	56
NADH	42	75	52
AMP	36	86	48
oxygen O2	36	40	31
ammonia	28	22	-
S-adenosyl-L-methionine	25	18	19
glutathione	25	17	10
a malonyl-ACP	23	15	10
L-glutamine	22	18	23
coenzyme A	21	71	39

and its precursors (L-glutamate, L-glutamine and glutathione) and a key metabolite in the lipid biosynthesis pathway (malonyl-ACP). High connectivity of these metabolites hints to their potential central role in the re/adjustments of fluxes following environmental changes/perturbations. In order to discover the corresponding regulatory mechanisms, additional studies should be done - e.g. putative regulatory sequence motifs associated with the neighbors of these highly connected metabolites [39]. Furthermore, most connected metabolites with filtered cofactors can be found in Additional file 3.

Simulations of the three metabolic modes

*i*Syn669, together with appropriate physiological constraints, was used as a stoichiometric simulation model by using FBA algorithm [40]. The FBA model simulates steady state behavior by enforcing mass balances constraints for the all metabolic intermediates (Methods). Biomass synthesis, a theoretical abstraction for cellular growth, is considered as a drain of some of these intermediates, i.e. building blocks, into a general biomass component. Different studies have reported that the simulation results do not usually vary drastically when using a common biomass equation for different growth condition [15,24]. Nevertheless, experimental efforts should be directed at the depiction of the best precursors and composition that could characterize, at least, the three main growth modes, *viz.*, autotrophy, heterotrophy and mixotrophy, in the scope of recent results [41]. Due to the lack of such data, the present work uses one single biomass equation in the simulations of all three metabolic states (Table 3). Presence of photosynthesis allows *i*Syn669 to "grow" under the all three metabolic states (*i.e.*, FBA with biomass formation as an objective function results in a feasible solution): carbon dioxide and light (autotrophic), sugars (heterotrophic), carbon dioxide, light and sugars (mixotrophic).

Growth under pure heterotrophy, or dark heterotrophy (in the absence of light) is a subject under study [42,43], being the regular experimental design to give a short light pulse prior to the pure heterotrophic phase (light-activated heterotrophy). Nevertheless, the theoretical flux distribution under heterotrophic conditions is interesting by itself - especially in comparison with the flux distribution in a light-fed energy metabolism. Moreover, fluxes in the heterotrophy mode may help in obtaining insight into the variations under the mixotrophic condition, which is of high relevance for industrial applications [9].

All FBA simulations were carried out under the appropriate constraints so as to match an autotrophic specific growth rate of 0.09 h^{-1}. This growth rate corresponds to a light input of 0.8 mE g_{DW}^{-1} h^{-1} and to a net

Table 3 *i*Syn669 Biomass composition

Metabolite	mmole/g DCW	Metabolite	mmole/g DCW
Amino acids [38]		**Deoxyribonucleotides [58]**	
Alanine	0.499149	dATP	0.0241506
Arginine	0.28742	dTTP	0.0241506
Aspartate	0.234232	dGTP	0.02172983
Asparagine	0.234232	dCTP	0.02172983
Cysteine	0.088988	**Ribonucleotides** [1]	
Glutamine	0.255712	AMP	0.14038929
Glutamate	0.255712	UMP	0.14038929
Glycine	0.595297	GMP	0.12374585
Histidine	0.092056	CMP	0.12374585
Isoleucine	0.282306	**Lipids** [59]	
Leucine	0.437778	16C-lipid	0.20683718
Lysine	0.333448	(9Z)16C-lipid	0.01573412
Methionine	0.149336	18C-lipid	0.00351776
Phenylalanine	0.180021	(9Z)18C-lipid	0.03188596
Proline	0.214798	(9Z,12Z)18C-lipid	0.03568367
Serine	0.209684	(9Z,12Z,15Z)18C-lipid	0.01797109
Threonine	0.246506	(6Z,9Z,12Z)18C-lipid	0.05031906
Tryptophan	0.055234	(6Z,9Z,12Z,15Z)18C-lipid	0.01448179
Tyrosine	0.133993	**Antenna chromophores** [60]	
Valine	0.411184	Chlorophyll a	0.02728183
Carbohydrates [61]		Carotenoids	0.00820225
Glycogen	0.01450617		

Biomass composition description with references where the information was retrieved from. All this building blocks with their respective stoichiometric coefficient is converted into one gram of dry cell weight. Biomass equation is reaction *Biomass* in Additional files 2 and 4.

carbon flux of 3.4 mmol g_{DW}^{-1} h^{-1} into the cell, with HCO_3^- and CO_2 as carbon sources. For the sake of comparison across the different conditions, uptake rates for the corresponding carbon sources were matched based on normalization per number of carbon atoms (this does not affect mono-carbon compounds like carbon dioxide and carbonic acid, but has importance in glucose feeding). Results of the subsequent FBA simulations for the three different growth conditions are presented in the following. Some of the reactions that are physiologically relevant for each of the conditions are summarized in Table 4 and Figure 1. Flux values for the rest of the reactions, including the upper and lower bounds are provided in Additional file 4.

Heterotrophy

Heterotrophy was simulated by considering glucose as the sole carbon source with uptake rate of 0.567 mmol g_{DW}^{-1} h^{-1}, entering the system through *glcP* glucose transporter (reaction *TRANS-RXN59G-152* in *i*Syn669). With the purpose of having a *pure* heterotrophic state,

Table 4 Comparison of selected fluxes across different growth conditions

Reaction name	Autotrophy	Minimum flux	Maximum flux	Mixotrophy	Minimum flux	Maximum flux	Dark Heterotrophy	Minimum flux	Maximum flux	Light Heterotrophy	Minimum flux	Maximum flux	Reaction description
2.7.1.2a	0	0	0	0.567	0.566	0.567	0.567	0.566	0.567	0.567	0.566	0.567	beta-D-glucose + ATP → beta-D-glucose-6-phosphate + ADP
4.2.1.2	12.67	12.667	+∞	14.67	14.657	+∞	0.905	0.884	+∞	2.148	1.836	+∞	malate ↔ fumarate + H2O
5.3.1.6	1.201	1.2	+∞	1.269	1.269	+∞	-0.054	-0.051	-0.055	0.066	0.067	+∞	D-ribose-5-phosphate ↔ D-ribulose-5-phosphate
_UQ	0.8	0	0.8	0.8	0	0.8	0	0	0	0.8	0	0.8	PSII* + UQ + 2 H+ → PSII + UQH2
_1.6.5.3	0	0	+∞	0	0	+∞	2.134	0	+∞	0	0	+∞	NADH + UQ + 7 H+ → NAD+ + UQH2 + 4 H+_peribac
_3.6.3.14	38.348	15.7	+∞	21.727	21.7	+∞	4.98	4.95	+∞	6.292	6.281	+∞	3 H+_peribac + phosphate O4P + ADP ↔ 3 H+ + H2O + ATP
6.2.1.1	0.008	-∞	+∞	-30.017	-∞	+∞	-2.124	-∞	+∞	-4.635	-∞	+∞	coenzyme A + acetate + ATP ↔ acetyl-CoA + diphosphate + AMP

Units in mmol g_{DW}^{-1} h^{-1}. 2.7.1.2a, glucokinase, is the reaction that phosphorylates beta-D-glucose upon entrance in the cell, marking the start of the glycolysis. The flux direction changes can be seen in reaction 4.2.1.2, fumarate hydratase, from TCA cycle and 5.3.1.6, ribose-5-phosphate isomerase, from the pentose phosphate pathway. _UQ and _1.6.5.3 are reactions that reduce UQH2 from photosystem II or NADH oxidation, respectively, causing a pumping of protons to the thylakoid. _3.6.3.14 is the ATP synthase that forms ATP shuttling protons from the thylakoid to the cytosol. 6.2.1.1, acetate-CoA ligase, is the reaction that generates acetyl-CoA from acetate and coenzyme A, that would be a major flux hub in an ethanol-producing strain, standing as the first step of fermentation.

Figure 1 Selected reactions in *i*Syn669 network that display flux changes across the four studied growth modes. Flux values (in mmol g_{DW}^{-1} h^{-1}) for selected reactions in the *Synechocystis* sp. PCC6803 metabolism. These reactions mark changes across four growth modes, *viz.*, autotrophy, mixotrophy and light and dark heterotrophy. Corresponding flux ranges can be found in Table 4 and in Additional file 4 for all the reactions in *i*Syn669.

photon uptake rate was constrained to 0; this caused photosynthesis fluxes to be shut down. In this case, glucose will be the source for the formation of carbon backbones for the building blocks of the cell, depicted in the biomass equation. The glycolytic and the oxidative mode of the pentose phosphate pathway were found to be active. Oxidative pentose phosphate pathway is the major pathway for glucose catabolism as was reported in reference [44]. PEP carboxylase (reaction *4.1.1.31* in *i*Syn669) is the main anaplerotic flux to the TCA cycle. Carbon fixation efficiency is around 60%, the rest being released in the form of CO_2, as reported in our previous work [9].

In contrast to dark heterotrophy, if a light-activated heterotrophy simulation is run, light enters the system and RuBisCO enzyme is active (reaction *4.1.1.39*), fixing all the CO_2 that was released in dark heterotrophy, boosting carbon efficiency to a theoretical 100%. In this case, global flux distribution as well as flux ranges resemble that of autotrophy more than that of the dark heterotrophy. Carbon skeletons are still produced through glycolysis and NAD(P)H is reduced along the glycolysis, pyruvate metabolism and TCA cycle. On the other hand, pentose phosphate pathway has shifted to the reductive mode due to RuBisCO activation and the corresponding flux is increased in magnitude. Carbon fixation happens at the RuBisCO level, thereby assimilating the CO_2 produced by the glucose metabolism, and

the production of ATP and NADPH through photosynthesis relieves the oxidative phosphorylation from draining NADPH to generate ATP.

Autotrophy

Photoautotrophy was initially simulated considering an illumination of 0.15 mE m^{-2} s^{-1}. Assuming that the mass of a typical *Synechocystis* sp. PCC6803 cell is 0.5 pg [45] and its radius is 1.75 µm [46], we estimated that the theoretical maximum illumination is 41563.26 mE g_{DW}^{-1} h^{-1}. An additional optimization step was performed in order to estimate physiologically meaningful photon uptake values that are closer to the experimental measurements [24]. First, carbon uptake rate was found that resulted in a specific growth rate of 0.09 h^{-1}, while the light intake was unconstrained. Next, the growth rate was constrained to this value and the second optimization problem was solved where light uptake was minimized. This minimization resulted in photon uptake for photosystem I (reaction *_lightI*) and photosystem II (reaction *_lightII*) being 0.8 mE g_{DW}^{-1} h^{-1}. Carbon sources used in simulating photoautotrophy conditions were carbon dioxide and carbonic acid, and its entrance to the system was mediated by RuBisCO (reaction *4.1.1.39* in *i*Syn669) and carbonic anhydrase (reaction *4.2.1.1b*) respectively. As *i*Syn669 biomass equation encompasses all essential metabolite precursors, these will be the sinks of our network, while photons, carbon dioxide and/or carbonic acid will be the sources. Thus

autotrophic fluxes will flow in the gluconeogenic direction and through the Calvin cycle, which is the reductive mode of the pentose phosphate pathway. PEP carboxylase is the main anaplerotic flux to the TCA cycle and glyoxylate shunt is inactive.

Mixotrophy

Photons, carbon dioxide and glucose are independent feed fluxes in this simulation. These fluxes entered the system through the same reactions as described for the previous growth modes. Carbon source presents, in this case, one more degree of freedom than in the rest of the conditions. In order to keep a comparative criterion across conditions, we normalized CO_2 and glucose inputs to the same carbon uptake flux as in the case of the autotrophy and the heterotrophy. Photon uptake rates were also normalized in a similar manner to match the autotrophic state. Having the same metabolic sinks as the two previous modes and the sources from the both of them, it is logical to think that the resulting flux distribution will be a mixture of the autotrophic and heterotrophic simulations. Indeed, we observed that the mixotrophic flux distribution lies in-between the previous two states, being a bit closer to the heterotrophy. Glycolysis is present and glyoxylate is shut down; an active photosynthesis is present, oxidative phosphorylation is less stressed than in heterotrophy as the energy can be produced from the photon uptake; and Calvin cycle is active, as carbon sources are CO_2 and glucose.

Flux variability analysis

Flux balance analysis presented above guarantees to find the optimal objective function value (biomass formation rate). However, the predicted intra-cellular flux distribution is not necessarily unique due to the presence of multiple pathways that are equivalent in terms of their overall stoichiometry. Thus, often the system exhibits multiple optimal solutions and further elucidation requires additional constraints based on experimental evidences (e.g. carbon labeling data). Alternatively, physiological insight can be still obtained by studying the variability at each flux node given the objective function value - a procedure referred to as flux variability analysis. In order to gain insight into the flux changes underlying the changes in the *Synechocystis* metabolism due to (un)availability of light, we have compared the autotrophic growth with the other two by using flux variability analysis (Figure 2). Interestingly, autotrophy permits an overall broader flux landscape than heterotrophy (let it be dark or light-activated). On the other hand autotrophic flux ranges are in general narrower than the mixotrophic ranges. Figure 1 and Table 4 depict some of the physiologically relevant reactions for which the feasible flux range differs across conditions. These include glucokinase from glycolysis, fumarate hydratase from TCA cycle, ribose-5-phosphate isomerase from pentose phosphate pathway, NADH dehydrogenase from oxidative phosphorylation or photosystem II oxidation. These reactions mark the key nodes in the metabolism network that must be appropriately regulated in order to adapt in response to the available energy/carbon source. Mechanisms underlying such changes will be of particular interest not only for biotechnological applications but also from the biological point of view. As a glimpse of the detailed flux (re-) distributions in each of the studied growth conditions, Additional file 5 describes fluxes in the pyruvate metabolism.
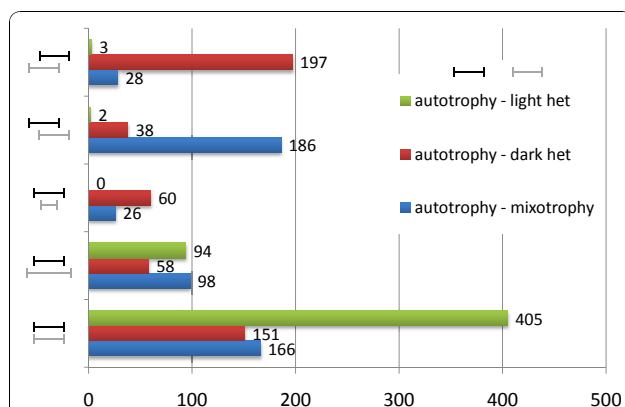
Figure 2 Overview of the flux adjustments between different growth conditions. Comparison of flux variability between autotrophy *vs.* mixotrophy, autotrophy *vs.* dark heterotrophy and autotrophy *vs.* light-activated heterotrophy. Minimum and maximum flux ranges were compared for each reaction, 378 reactions were found blocked in all the studied conditions.
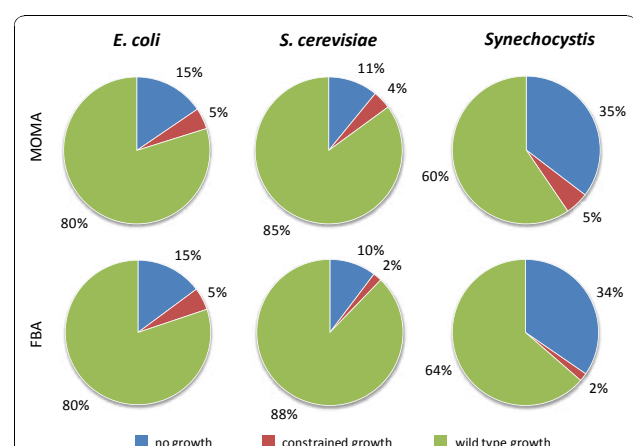
Figure 3 Essential genes in *Synechocystis* sp. PCC6803. Distribution of gene knock-out results for three model organisms, simulated by using FBA and MOMA algorithm, classified as wild-type growth, constrained growth and no growth.

Gene/Reaction knock-out analysis

The comprehensive set of reconstructed biochemical equations of iSyn669 and FBA simulations enabled us to further analyze the characteristics and potential of the *Synechocystis* metabolic network. This can be oriented towards the study of the reactions (and thereby the corresponding genes) that are necessary for the growth, or to *in silico* metabolic engineering for identification of targets for maximization of a given metabolite of socio-economic interest.

Essential Genes

iSyn669 network consists of 790 metabolites and 882 reactions. Among these, 350 genes (36% of the total, Figure 3) were found to be necessary for the formation of the biomass under the mixotrophic growth conditions by using FBA and MOMA algorithms. This set of genes can be divided in to two categories: i) essential genes, deletion of which completely inhibits biomass growth (304 genes, 34% of the total, with FBA): and ii) genes deletion of which causes a reduced growth rate (46 genes, 2% of the total, with FBA). The set of 304 essential genes can be understood as the core of the metabolism, as deleting them would produce an unviable organism. The results based on MOMA algorithm essentially tally these numbers: 311 essential genes, 35% of the total, and 45 that cause a reduced growth rate, 5% of the total, (Additional file 6).

Interestingly, if we compare the proportion of the essential genes under FBA simulation in the metabolic networks of *E. coli* (187 genes, 15% of the total) [38] and *Saccharomyces cerevisiae* (148, 10% of the total) [32] with iSyn669, we find that *Synechocystis* has a significantly larger fraction of metabolic genes whose deletion obliterates biomass formation (304 genes, 34% of the total). One possible explanation for the difference in the relative proportion of essential genes in these three organisms would be an incomplete/incorrect annotation of the genome of *Synechocystis* sp. PCC6803. For example, if only one of the isoenzymes corresponding to a reaction is annotated, the corresponding *in silico* knock-out will result in a false negative prediction. It is important to note that the computational predictions of gene essentiality based on FBA are highly dependent on the growth medium used for the simulations. Thus, the comparison across different species may not be straightforward. Moreover, it is also possible that the natural growth conditions of *Synechocystis* may have dictated selection for a relatively high proportion of essential genes. Such hypotheses need careful consideration of several factors and are beyond the scope of this work.

Production of value-added compounds

Synechocystis sp. PCC6803 is considered as a candidate photobiological production platform - it can potentially produce molecules of interest by using CO_2 and light

[6]. To this end, iSyn669 can be used to perform simulations, not only for assessing the feasibility of producing a given compound, but also to identify potential metabolic engineering targets towards improved productivity. For example, FBA simulations can help in estimating maximum theoretical yields for the products/intermediates of interest. A product of obvious interest is hydrogen. In our previous work [9], we have estimated maximum theoretical hydrogen production values that are far from the current state of experimental reports. *In silico* studies can direct the efforts and counsel the scientists towards a hydrogen producing cyanobacteria that could be of impact. iSyn669 predicts, in autotrophic conditions, a theoretical H_2 evolution rate of 0.17 mmol g_{DW}^{-1} h^{-1} obliterating biomass growth. Else, the stoichiometry permits the evolution of 0.156 mmol g_{DW}^{-1} h^{-1} of hydrogen with a biomass growth of 10% of the wild type (0.007 mmol g_{DW}^{-1} h^{-1}).

Succinate is an important metabolite for its biotechnological applications as well as for being a metabolite that bridges the TCA cycle with the electron transfer chain. As an example of the usefulness of the present metabolic model we have designed an *in silico* metabolic engineering strategy to improve the production of succinate. The underlying idea is to design a succinate over-producing metabolic network (through reaction knock-out simulations), whereas the intracellular fluxes are distributed so as to maximize the biological objective function (e.g. growth) [47]. To this end, OptGene algorithm [37] was used together with Minimization Of Metabolic Adjustment (MOMA) [17] as a biological objective function. MOMA has been reported to provide better description of flux distributions in mutants or under un-natural growth conditions as opposed to FBA. A *design objective function* which copes with the metabolite of interest, succinate, has been determined maintaining the *biological objective function* as the biomass formation.

OptGene simulations for single, double and triple knock-out strategies were performed to obtain solutions with improved succinate production, but without drastically diminishing the biomass production. We used mixotrophic conditions, for which wild type optimal growth rate was 0.17909 mmol g_{DW}^{-1} h^{-1}. The best single knock-out was found to be the mutant of pyruvate kinase (reaction *2.7.1.40c* in iSyn669 and genes *sll0587* and *sll1275*) that has a succinate evolution of 0.5695 mmol g_{DW}^{-1} h^{-1} with a growth rate of 0.0714 mmol g_{DW}^{-1} h^{-1}. Blocking this reaction, preventing pyruvate and phosphoenolpyruvate from using GTP and GDP would drive a high increase in succinate production. The flux between pyruvate and phosphoenolpyruvate can still be accomplished with reactions *2.7.1.40a* and *2.7.9.2*, but using ATP and ADP as cofactors. Double

deletion did not improve the results from the single knock-out strain, evolving the same succinate production with the same growth rate. The best triple knock-out was found to be the combination of pyruvate kinase (reaction *2.7.1.40c* in *i*Syn669 and genes *sll0018* and *sll0587*), fructose-bisphosphate aldolase (reaction *4.1.2.13b* in *i*Syn669 and genes *slr0943* and *sll1275*) and succinate dehydrogenase (reaction *_1.3.99.1* in *i*Syn669 and genes *sll0823*, *sll1625* and *slr1233*). This simulated strain has a succinate evolution of 0.6999 mmol g_{DW}^{-1} h^{-1} with a growth rate of 0.0688 mmol g_{DW}^{-1} h^{-1}. This design combines the blocking of the oxidation of succinate on the electron chain transfer through succinate dehydrogenase with the prevention of using GTP between pyruvate and phosphoenolpyruvate and the lack of an aldolase needed in the reductive mode of the pentose phosphate pathway. This leads to a situation where flux is directed to TCA cycle in order to meet with an overproduction of succinate.

These studies on knock-outs are reaction centered, even though the *in vivo* knock-out building will ultimately be through gene manipulations. This is the reason underlying the fact that we found *2.7.1.40c* knock-out as the best result. This design would hint at the idea of selection of a mutated pyruvate kinase protein specific for ATP cofactor. This may be difficult to achieve on the bench, but has high biotechnological expectations.

*i*Syn669 as a data integration scaffold

Apart from the flux simulations, another important problem in the field of metabolic systems biology that can be addressed by using reconstructed genome-scale models is the integration of the different genome-wide biomolecular abundance datasets, i.e. *omics* datasets, such as transcriptome and metabolome. An example of algorithms for carrying out such an integrative analysis through the use of genome-scale metabolic networks is Reporter Features [48,49]. Reporter algorithm allows integration of *omics* data with bio-molecular interaction networks, thereby allowing identification of cellular regulatory focal points (i.e. *reporter features*), for instance *reporter metabolites* as regulatory hubs in the metabolic network.

In this work, Reporter Features software was used to integrate transcriptional information over the reconstructed *Synechocystis* sp. PCC6803 network allowing us to infer regulatory principles underlying metabolic flux changes following shifts in growth mode. In particular, we analyzed the data from a work [50] that reports the transcriptional changes caused in *Synechocystis* sp. PCC6803 by shifts from darkness to illumination conditions and back. As it can be understood from the rationale beneath the metabolic capabilities of this cyanobacterium, the presence or absence of light drives big changes in the flux distribution through the network, as discussed in the previous sections. We have focused our study on the relationship between the transcription of *Synechocystis* sp. PCC6803 genes and the reactions of the metabolic network. Associations between genes and reactions were identified, listing all the genes that performed or were involved in a specific reaction. With this information and the metabolic model, Reporter Features analysis was carried out. In brief, the analysis helped to identify metabolites around which the transcriptional changes are significantly concentrated. These metabolites are termed reporter metabolites as they represent key regulatory nodes in the network.

Gill *et al* [50] designed the experiment so that *Synechocystis* was grown to mid-exponential phase (A_{730} = 0.6 to 0.8). Then, the lights were extinguished and RNA samples were taken after 24 h in the dark (full dark). Illumination was then turned back on for 100 min (transient light), followed immediately by an additional 100 min in the dark (transient dark).

We were interested in two aspects of this study: i) to identify metabolites around which regulation is centered during the light regime transitions; and ii) to find the metabolic genes that were collectively significantly co-regulated across these transitions [49].The analysis was divided in three parts: an analysis of the data arrays from the whole experimental profile ("all time points"), an analysis of the shift from darkness to a light environment ("dark to light") and from light back to dark ("light to dark"). For a study of the overall genome and its light regulation, refer to Gill *et al* [50]. In this study, as the relationship between the metabolism and this regulation was investigated, genes with no direct relationship to a metabolic reaction were not considered. Distributions of the genes across KEGG Orthologies related to the metabolism altered with the light shift are depicted in Table 5.

All time points

When all seven arrays were used, *reporter metabolites* were found to be quite scattered across the metabolism spanning several metabolic pathways, and thus offering a global view of the transcriptional response in the metabolic network (see Figure 4a and Table 6a). Presence of some amino acids (*L-tyrosine, L-isoleucine*), nucleic acids and its precursors (*GTP, dihydroorotate*), carbon metabolism metabolites (*D-ribulose-5-phosphate, succinyl-CoA*), lipids precursors (*myo-inositol, D-myo-inositol 3-monophosphate*), cofactors (*thioredoxin, p-aminobenzoate*) and photosynthesis metabolites (*plastocyanin*) pictures a scenario of a global regulation throughout the different metabolic pathways.

By using the metabolic sub-network search algorithm, we found 212 genes that have their expression changed

Table 5 KEGG orthology groups for the metabolic genes altered with the light shift.

	All time points		Dark to Light		Light to Dark	
	Number of genes	%	Number of genes	%	Number of genes	%
Energy Metabolism	128	60.38	128	51.82	127	61.65
Amino Acid Metabolism	25	11.79	31	12.55	24	11.65
Carbohydrate Metabolism	24	11.32	28	11.33	23	11.16
Metabolism of Cofactors and Vitamins	13	6.13	26	10.53	12	5.83
Nucleotide Metabolism	12	5.66	23	9.32	12	5.83
Lipid Metabolism	7	3.3	5	2.02	6	2.91
Membrane Transport	3	1.42	4	1.63	2	0.97
Biosynthesis of Secondary Metabolites	0	0	1	0.4	0	0
Biosynthesis of Polyketides and Nonribosomal Peptides	0	0	1	0.4	0	0
Total	212	100	247	100	206	100

across the arrays and that have a relationship with the metabolites of *i*Syn669 network. Furthermore, 50 genes were identified that are strongly co-regulated all along the profile of the experiment (Additional File 7, section a). This set of genes is characterized in two groups. The first set consists of the genes from photosynthesis (93.85%) and oxidative phosphorylation (6.15%). The second set is representative of a variety of genes from different pathways such as amino acid metabolism

Figure 4 *Reporter metabolites* **under light/dark regime**. a) *Reporter metabolites* for *all time points* set of arrays depicted on the *i*Syn669 network. b) Light/dark-shift profiles and localization of the genome arrays for the work from Gill *et al.* [47].

(39%), carbohydrate metabolism (22%), nucleotide metabolism (13%), nitrogen metabolism (13%) and metabolism of cofactors (9%) that globally regulates the entire metabolic network (see Table 5 for further details).

It can be expected that an experimental design like the one we have based our work on, which combines a shift from dark to light with a shift back to darkness, will encompass an important part of the regulatory changes the cell is undergoing in its natural habitat. In a glucose-deficient environment, the presence or absence of light is the main condition around which the *Synechocystis* metabolism gravitates [9]. Indeed, one of the co-regulated sets consists of the genes coding for the proteins that work on, and around, the thylakoid membrane, let it be photosynthesis or oxidative phosphorylation genes.

Dark to light

Next, we considered the arrays that represent the shift from darkness to light, the first three arrays (from "24 hours of darkness" array to "60 minutes of light" array). *Reporter metabolites* were found to be largely within the nucleotide and amino acid metabolism (Table 6b). Some cofactors were also identified as regulation hubs like *tetrahydrofolate*, *thioredoxin* and *adenosylcobinamide*.

Sub-network search yielded set of 247 genes that have their expression changed across the first three arrays and that are related with *i*Syn669 reactions. Furthermore, 84 genes were identified that are strongly co-regulated across the three arrays (Additional File 7, section b). This set of genes cover photosynthesis (25%), oxidative phosphorylation (24%), amino acid metabolism (11%), carbohydrate metabolism (11%), nucleotide metabolism (10%) and metabolism of cofactors (10%).

This set of data arrays are indeed a good example of a cell's metabolic machinery starting up. After a 24 hour period in darkness where cell density did not

Table 6 Reporter metabolites for the light shift experiment.

a)		b)		c)	
Metabolite	*Number of neighbors*	*Metabolite*	*Number of neighbors*	*Metabolite*	*Number of neighbors*
All time points		**Dark to Light**		**Light to Dark**	
L-tyrosine	4	N-carbamoyl-L-aspartate	3	5-phosphoribosyl-N-formylglycineamidine	3
N-carbamoyl-L-aspartate	3	dihydroorotate	3	diphosphate	76
dTDP	4	5-phosphoribosyl 1-pirophosphate	9	a 1,4-alpha-D-glucan_n	2
L-isoleucine	3	L-valine	3	a 1,4-alpha-D-glucan_n1	2
D-ribulose-5-phosphate	4	5-phospho-ribosyl-glycineamide	3	UDP-N-acetylmuramoyl-L-alanyl-D-glutamyl-meso-2,6-diaminoheptanedioate	2
D-myo-inositol (3)-monophosphate	2	O-phospho-L-homoserine	2	pyridoxine-5'-phosphate	2
myo-inositol	2	peptidylproline (omega = 180)	4	(E, E)-farnesyl diphosphate	3
L-valine	3	peptidylproline (omega = 0)	4	GMP	6
succinyl-CoA	3	indole-3-glycerol-phosphate	2	phosphoribosylformiminoAICAR-phosphate	2
adenosine	2	5-aminoimidazole ribonucleotide	3	L-aspartyl-4-phosphate	2
GTP	13	tetrahydrofolate cofactors	8	pantothenate	2
thioredoxin	11	GTP	13	undecaprenyl-diphospho-N-acetylmuramoyl-L-alanyl-D-glutamyl-meso-2,6-diaminopimeloyl-D-alanyl-D-alanine	2
thioredoxin disulfide	11	L-glutamate gamma-semialdehyde	2	MurAc(oyl-L-Ala-D-gamma-Glu-L-Lys-D-Ala-D-Ala)-diphospho-undecaprenol	2
p-aminobenzoate	2	inosine-5'-phosphate	5	undecaprenyl-diphospho-N-acetylmuramoyl-L-alanyl-D-glutamyl-L-lysyl-D-alanyl-D-alanine	2
acetylphosphate	2	pantetheine 4'-phosphate	2	L-aspartate-semialdehyde	2
glycine	7	UDP-N-acetylmuramoyl-L-alanyl-D-glutamate	2	5-phospho-ribosyl-glycineamide	3
succinate	7	phytoene	2	5'-phosphoribosyl-N-formylglycineamide	4
dihydroorotate	3	thioredoxin	11	sulfur	2
PC	12	thioredoxin disulfide	11	glycine	7

Reporter metabolites for each set of arrays analysed with Reporter Features software.

change (see Figure 1 in Gill *et al* [50]), light enters the system and the cell starts to synthesize new bio-molecules, mostly nucleotides so it can copy its genetic material and amino acids to build up proteins.

Light to dark

Finally, we considered the arrays that represent the shift from light to dark, data from "90 minutes of light" array to "60 minutes of dark" array. Similar to the previous case study, reporter metabolites were found to be focused on the nucleotide and amino acid metabolism (Table 6c). Additionally, the presence of metabolite *a 1,4-alpha-D-glucan_n* and its cognate *a 1,4-alpha-D-glucan_n1* also stands out as they are involved in carbon reserves catabolism and anabolism.

With the help of the sub-network search, 133 genes were identified as being significantly co-regulated across those three arrays (Additional File 7, section c). This set comprises of the genes from photosynthesis (34%), oxidative phosphorylation (26%), amino acid metabolism (12%), carbohydrate metabolism (12%), nucleotide metabolism (7.5%) and metabolism of cofactors (4.5%).

This last set of data array is a scenario where metabolism is being shut down, as a consequence of the darkness and lack of carbohydrate source. Without light, photosynthesis is blocked and carbon fixation is nearly obliterated. Cells strive to build up carbon reserves (hence the presence of *a 1,4-alpha-D-glucan_n* as a *reporter metabolite*) and oxidative phosphorylation is the

main energy pathway that remains present. Regulation is centered on the energy metabolism shift (60% of the total co-regulated sub-network), withholding amino acids and nucleotide precursors and keeping the cofactors available in a low-profile metabolism.

Conclusions

We have successfully reconstructed a genome-scale metabolic network for *Synechocystis* sp. PCC6803, called *i*Syn669, which allows simulating production of all the metabolic precursors of the organism. The metabolic reconstruction represents an up-to-date database that encompasses all knowledge available in public databases, scientific publications and textbooks on the metabolism of this cyanobacterium.

From the annotation publicly available, our metabolic network includes 882 metabolic reactions and 790 metabolites, as well as the information from 669 genes that have some relationship with the metabolic reactions. This model is the most complete and comprehensive work for *Synechocystis* sp. PCC6803 to date, which has its potential as the photosynthetic model organism. Interestingly, the reconstruction identified 79 reactions that should be present in the metabolism but with no cognate gene discovered yet; this should direct experimental work at the discovery of these genes. Topological characteristics of the network resemble those of other reconstructed microbial metabolic networks and thus provide an additional input for the analysis of their structural and organizational properties from evolutionary perspective.

Applicability of *i*Syn669 metabolic model was demonstrated by using a variety of computational analyses. Flux balance analysis was applied in order to simulate the three physiologically important growth conditions of cyanobacteria, *viz.*, heterotrophic, mixotrophic and autotrophic. Our metabolic model was capable of simulating the production of the monomers or building blocks that build up the cells, in the range that is in agreement with the reported growth experiments. Our photosynthetic metabolic model includes all of the central metabolic pathways that previous works [23-25] considered. Regarding the parts from our model that overlap with the previous works (part of the central carbon metabolism), the predictions for the flux directionality changes following light shift match between those models and *i*Syn669. In fact, *i*Syn669 expands the flux study to all the pathways described in the *Synechocystis* sp. PCC6803 genome annotation. Further work should be directed at the definition of a detailed and descriptive biomass cell composition, so as to have a better representation of the biomass equation for simulation purposes.

Single reaction/gene knock-out simulations revealed 311 genes that are essential for the survival. Bearing in mind the distance from the efforts taken in the annotation of the genome of the bacteria and yeast models to that of the cyanobacterium, our study shows that *Synechocystis* sp. PCC6803 has a larger fraction of genes that are essential for producing biomass, as opposed to *Escherichia coli* and *Saccharomyces cerevisiae*. Further investigation of the causes for this difference will be of definite interest in understanding the genome annotation and/or the evolution of the metabolic network of *Synechocystis*.

Evaluation of the theoretical potential of this organism to produce hydrogen was assessed, in support of the efforts directed to this direction from several groups and scientific council initiatives. Present hydrogen production projects are far from the theoretical potential, but efforts in this field can trigger a very significant increase of the present hydrogen evolution rates in *Synechocystis* sp. PCC6803 or other photobiological production platforms candidates, e.g. *Chlamydomonas reinhardtii*, *Nostoc punctiforme* and *Synechococcus* species.

Suitability of the presented model for performing *in silico* metabolic engineering analysis was demonstrated by using OptGene software framework. Furthermore, we also show that *i*Syn669 can be used as a scaffold to integrate network-wide *omics* data. As a case study, we identified key *reporter metabolites* around which regulation during light shifts is organized, as well as gene sub-networks that were co-regulated across the light conditions.

Altogether, the genome-scale metabolic network of *Synechocystis* sp. PCC6803 (*i*Syn669) will be a valuable tool for the applied and fundamental research of *Synechocystis* sp. PCC6803, as well as for the broad field of metabolic systems biology. *i*Syn669 represents an important step for the integration of tools and knowledge from different disciplines towards development of photo-biological cell factories.

Methods
Metabolic network reconstruction

Pathway Tools software [33] was used to construct a *Synechocystis*-specific database of genes, proteins, enzymes and metabolites. *Synechocystis* sp. PCC6803 genome and annotation files were downloaded from NCBI Entrez Genome repository as of date 10 of September of 2008 [51]. Pathway tools retrieved a first version of the network, which had to be checked with different kinds of databases depending on the information they bear. Databases used towards this purpose included Enzyme nomenclature database [34], KEGG pathway database [27], BioCyc genome database [26],

BRENDA Enzyme database [28] and UniProt protein database [29].

Parts that characterize *Synechocystis* network, like the incomplete TCA cycle [52,53], the presence of the glyoxylate shunt [35], the interconnected photosynthesis and oxidative phosphorylation [54] or the cyclic and non-cyclic electron transport related to these latter processes [55-57], were accounted for in detail.

At the end of the reconstruction process, four kinds of relationships were present in the database: reaction with cognate genes, reactions that needed to be included in the model in order to have metabolic precursors in the network (with no assigned genes), non-enzymatic reactions that have no related gene, and genes described in the annotations but with no assigned function. For an overview of the underlying process, please refer to Fortser *et al* [32] work on the reconstruction of *Saccharomyces cerevisiae* metabolic network.

Linear programming for Flux Balance Analysis

The set of biochemical reactions of the genome-scale metabolic model were formulated as a steady state stoichiometric model:

$$S \cdot v = 0$$

The details are described elsewhere, for example in Stephanopoulos *et al* [40]. This model describes cellular behavior under pseudo steady-state conditions, where S is stoichiometric matrix that contains the stoichiometric coefficients corresponding to all internal (balanced) metabolites. v is flux vector that corresponds to the columns of S. Given a set of experimentally-driven constraints, former equation was solved by using linear programming, the approach known as flux balance analysis, or FBA [16].

Since the number of reactions is typically larger than the number of metabolites, the system becomes underdetermined. In order to obtain a feasible solution for the intracellular fluxes, an optimization criterion on metabolic balances has to be imposed. This can be formulated by maximizing one of the biochemical reactions, e. g. biomass equation, subject to the mass balance and the capacity constraints.

For instance,

$$\text{Max}\left(v_i\right) \qquad \text{subject to } S \cdot v_j = 0 \quad \forall j \in N$$

$$v_{j,irr} \in R^+$$

$$v_{j,rev} \in R$$

$$v_{j,const} \in R, v_{min} < v_{j,const} < v_{max}$$

$$v_{j,uptake} \in R, v_{min} < v_{j,uptake} < v_{max}$$

where v_j is the rate of the jth reaction. The elements of the flux vector v were constrained for the definition of reversible and irreversible reactions, $v_{j,rev}$ and $v_{j,irr}$, respectively. Additionally, two set of equations were established, $v_{j,const}$, constrained metabolic reactions, and $v_{j,uptake}$, uptake reactions, which were bound by experimentally determined values from the literature. Biomass synthesis was considered as a drain of precursors or building blocks into a hypothetical biomass component. Flux through biomass synthesis reaction, being the biomass formation rate, is directly related to growth of the modeled organism [40]. Table 3 shows the biomass composition that was considered in the *i*Syn669 metabolic model.

Simulations were performed with the OptGene software [37]. Some capacity constraints had to be added in order to have a feasible solution for the linear programming problem. As an example, maximum uptake rates were determined as follows: maximum glucose uptake rate under heterotrophic conditions was found to be 0.85 mmol glucose g_{DW}^{-1} h^{-1} [23]. Maximum CO_2 uptake rate was found to be 3.7 mmol CO_2 g_{DW}^{-1} h^{-1} [24]. Additionally, we fixed the maintenance requirement for the heterotrophic case to be 1.67 ATP moles per mole of glucose consumed as was determined by ref [24], and was maintained for autotrophic and mixotrophic growth.

MOMA algorithm

Segre *et al* [17] introduced the method of minimization of metabolic adjustment (MOMA) to better understand the flux states of mutants. MOMA is based on the same stoichiometric constraints as FBA, but relaxes the assumption of optimal growth flux for the mutants, testing the hypothesis that the corresponding flux distribution is better approximated by the flux minimal response to the perturbation than by the optimal one.

MOMA algorithm searches for a point in the feasible space of the solutions space of the knock-out (Φ^j) that has minimal distance from a given flux vector w. The goal is to find the vector $x \in \Phi^j$ such that the Euclidean distance

$$D(w,x) = \sqrt{\sum_{i=1}^{N}(w_i - x_i)^2}$$

is minimized. For details, please address to Segre *et al* [17].

Reporter Features algorithm

Reporter Features software [48] works on three kinds of information - network, *omics* data and association between genes and the nodes in the network. We have used Reporter Features for a transcriptomic analysis, so our three files were *p-values* file, resulting from a Student t-test run on transcriptomic data, interaction file, where reactions are connected to the corresponding substrates and products, and association file, where gene

are associated to reactions they are involved in, either by coding for the enzyme or by regulating the gene that codes for the enzyme.

In brief, Reporter algorithm converts the p-value for a given node to a z-score by using the inverse normal cumulative distribution function (cdf^{-1}).

$$z_{gene\ i} = cdf^{-1}\left(1 - p_{gene\ i}\right)$$

After scoring each non-feature node in this fashion, we need to calculate the score of each feature j, $z_{feature\ j}$. We used the scoring method based on distribution of the means, which is a test for the null hypothesis "genes adjacent to feature j display their normalized average response by chance". In particular, the score of each feature j is defined as the average of the scores of its neighbour N_j nodes (genes), i.e.:

$$z_{feature\ j} = \frac{1}{N_j}\sum_{k=1}^{N_j} z_{gene\ k}$$

To evaluate the significance of each $z_{feature\ j}$, this value should be corrected for the background distribution of z scores in the data, by subtracting the mean (m_N) and dividing by the standard deviation (s_N) of random aggregates of size N.

$$z_{feature\ j}^{corrected} = \frac{\left(z_{feature\ j} - m_N\right)}{s_N}$$

Additional material

Additional file 1: *i*Syn669 reactions to gene connections. Excel file with the list of *i*Syn669 reactions and its cognate list of genes.

Additional file 2: *i*Syn669 genome-scale metabolic model in OptGene format. Text file with the stoichiometric model, in OptGene [37] format, with all the constraints needed for its simulation with FBA algorithm.

Additional file 3: Most connected metabolites with filtered cofactors. Supplementary table with most connected metabolites once the cofactors have been filtered.

Additional file 4: *i*Syn669 metabolic fluxes simulated under four conditions. Excel file with all the reactions simulations and resulting flux ranges from the model simulated under four growth conditions: autotrophy, dark o pure heterotrophy, light-activated heterotrophy and mixotrophy.

Additional file 5: Fluxes of reactions around pyruvate. Flux values (in mmol/g DCW/h) for reactions that produce or drain pyruvate in *Synechocystis* sp. PCC6803 metabolism. Negative sign in bidirectional reactions means pyruvate consumption. Reactions names can be traced in reaction list in Additional files 2 and fluxes can be found in Additional file 4.

Additional file 6: FBA and MOMA simulation values for biomass growth in *Synechocystis* sp. PCC6803, *Escherichia coli* and *Saccharomyces cerevisiae* genome-scale metabolic models. Excel file

with the growth values under MOMA simulation for *Synechocystis* sp. PCC6803, *Escherichia coli* and *Saccharomyces cerevisiae*. Data for *Synechocystis* is original from present work, data for *Escherichia coli* has been obtained from metabolic model from reference 18 and data for *Saccharomyces cerevisiae* is from reference 30.

Additional file 7: *i*Syn669 groups of correlated genes in the three sets of arrays of light shift experiments. Word file with the list of *i*Syn669 correlated genes in "All time points", "Dark to light" and "Light to dark" analyses.

Abbreviations
BM: biomass; DCW: dry cell weight; FBA: flux balance analysis; MCA: metabolic control analysis; MOMA: minimization of metabolic adjustments; ORF: Open Reading Frame; PEP: phosphoenolpyruvate; ROOM: regulatory on-off minimization of metabolic fluxes; RuBisCO: Ribulose-1,5-bisphosphate carboxylase oxygenase; TCA cycle: tricarboxylic acid cycle

Author details
[1]Instituto Universitario de Matemática Pura y Aplicada, Universidad Politécnica de Valencia, Camino de Vera 14, 46022 Valencia, Spain. [2]Departamento de Lenguajes y Ciencias de la Computación, Campus de Teatrinos, Universidad de Málaga, 29071 Málaga, Spain. [3]Structural and Computational Biology Unit, European Molecular Biology Laboratory, Meyerhofstrasse 1, D-69117 Heidelberg, Germany.

Authors' contributions
AM and EN conducted the reconstruction and the different analyses. PF and JFU conceived of the study and participated in its design. AM and KRP designed the study and wrote the manuscript. All authors contributed to, read and approved the final manuscript.

References
1. Allen MM, Smith AJ: **Nitrogen chlorosis in blue-green algae.** *Arch Mikrobiol* 1969, **69**:114-120.
2. Tamagnini P, Axelsson R, Lindberg P, Oxelfelt F, Wunschiers R, Lindblad P: **Hydrogenases and hydrogen metabolism of cyanobacteria.** *Microbiol Mol Biol Rev* 2002, **66**:1-20, table of contents.
3. Schopf J: **The Fossil Record: Tracing the Roots of the Cyanobacterial Lineage.** In *The ecology of cyanobacteria.* Edited by: Whitton B, Potts M. Dordrecht: Kluwer Academic Publishers; 2000:13-35.
4. Shi T, Falkowski PG: **Genome evolution in cyanobacteria: the stable core and the variable shell.** *Proc Natl Acad Sci USA* 2008, **105**:2510-2515.
5. Tamagnini P, Leitao E, Oliveira P, Ferreira D, Pinto F, Harris DJ, Heidorn T, Lindblad P: **Cyanobacterial hydrogenases: diversity, regulation and applications.** *FEMS Microbiol Rev* 2007, **31**:692-720.
6. Lindberg P, Park S, Melis A: **Engineering a platform for photosynthetic isoprene production in cyanobacteria, using Synechocystis as the model organism.** *Metab Eng* 2010, **12**:70-79.
7. Wu GF, Wu QY, Shen ZY: **Accumulation of poly-beta-hydroxybutyrate in cyanobacterium Synechocystis sp. PCC6803.** *Bioresour Technol* 2001, **76**:85-90.
8. Liu X, Curtiss R: **Nickel-inducible lysis system in Synechocystis sp. PCC 6803.** *Proc Natl Acad Sci USA* 2009, **106**:21550-21554.
9. Navarro E, Montagud A, Fernández de Córdoba P, Urchueguía JF: **Metabolic flux analysis of the hydrogen production potential in Synechocystis sp. PCC6803.** *Int J Hydrogen Energy* 2009, **34**:8828-8838.
10. McHugh K: *Hydrogen production methods* Alexandria, Virginia: MPR Associates, Inc; 2005.

11. Turner J, Sverdrup G, Mann M, Maness P, Kroposki B, Ghirardi M, Evans R, Blake D: **Renewable hydrogen production.** *International Journal Energy Research* 2008, **32**:379-407.

12. Herrero A, Flores E: *The cyanobacteria: molecular biology, genomics, and evolution* Norfolk, UK: Caister Academic Press; 2008.

13. Oberhardt MA, Palsson BO, Papin JA: **Applications of genome-scale metabolic reconstructions.** *Mol Syst Biol* 2009, **5**:320.

14. Patil KR, Akesson M, Nielsen J: **Use of genome-scale microbial models for metabolic engineering.** *Curr Opin Biotechnol* 2004, **15**:64-69.

15. Varma A, Palsson BO: **Metabolic capabilities of Escherichia coli: II. Optimal growth patterns.** *J Theor Biol* 1993, **165**:503-522.

16. Edwards J, Ramakrishna R, Schilling C, Palsson B: **Metabolic flux balance analysis.** In *Metabolic engineering.* Edited by: Lee S, Papoutsakis E. New York: Marcel Dekker Inc; 1999.

17. Segre D, Vitkup D, Church GM: **Analysis of optimality in natural and perturbed metabolic networks.** *Proc Natl Acad Sci USA* 2002, **99**:15112-15117.

18. Shlomi T, Berkman O, Ruppin E: **Regulatory on/off minimization of metabolic flux changes after genetic perturbations.** *Proc Natl Acad Sci USA* 2005, **102**:7695-7700.

19. Rapoport TA, Heinrich R, Jacobasch G, Rapoport S: **A linear steady-state treatment of enzymatic chains. A mathematical model of glycolysis of human erythrocytes.** *Eur J Biochem* 1974, **42**:107-120.

20. Kacser H, Burns JA: **The control of flux.** *Symp Soc Exp Biol* 1973, **27**:65-104.

21. Kaneko T, Sato S, Kotani H, Tanaka A, Asamizu E, Nakamura Y, Miyajima N, Hirosawa M, Sugiura M, Sasamoto S, *et al*: **Sequence analysis of the genome of the unicellular cyanobacterium Synechocystis sp. strain PCC6803. II. Sequence determination of the entire genome and assignment of potential protein-coding regions (supplement).** *DNA Res* 1996, **3**:185-209.

22. Kaneko T, Nakamura Y, Sasamoto S, Watanabe A, Kohara M, Matsumoto M, Shimpo S, Yamada M, Tabata S: **Structural analysis of four large plasmids harboring in a unicellular cyanobacterium, Synechocystis sp. PCC 6803.** *DNA Res* 2003, **10**:221-228.

23. Yang C, Hua Q, Shimizu K: **Metabolic flux analysis in Synechocystis using isotope distribution from 13C-labeled glucose.** *Metab Eng* 2002, **4**:202-216.

24. Shastri AA, Morgan JA: **Flux balance analysis of photoautotrophic metabolism.** *Biotechnol Prog* 2005, **21**:1617-1626.

25. Fu P: **Genome-scale modeling of Synechocystis sp. PCC6803 and prediction of pathway insertion.** *Journal of Chemical Technology & Biotechnology* 2009, **84**:473-483.

26. Karp PD, Ouzounis CA, Moore-Kochlacs C, Goldovsky L, Kaipa P, Ahren D, Tsoka S, Darzentas N, Kunin V, Lopez-Bigas N: **Expansion of the BioCyc collection of pathway/genome databases to 160 genomes.** *Nucleic Acids Res* 2005, **33**:6083-6089.

27. Kanehisa M, Araki M, Goto S, Hattori M, Hirakawa M, Itoh M, Katayama T, Kawashima S, Okuda S, Tokimatsu T, Yamanishi Y: **KEGG for linking genomes to life and the environment.** *Nucleic Acids Res* 2008, **36**: D480-484.

28. Chang A, Scheer M, Grote A, Schomburg I, Schomburg D: **BRENDA, AMENDA and FRENDA the enzyme information system: new content and tools in 2009.** *Nucleic Acids Res* 2009, **37**:D588-592.

29. **The universal protein resource (UniProt).** *Nucleic Acids Res* 2008, **36**: D190-195.

30. Weise S, Grosse I, Klukas C, Koschutzki D, Scholz U, Schreiber F, Junker BH: **Meta-All: a system for managing metabolic pathway information.** *BMC Bioinformatics* 2006, **7**:465.

31. Feist AM, Herrgard MJ, Thiele I, Reed JL, Palsson BO: **Reconstruction of biochemical networks in microorganisms.** *Nat Rev Microbiol* 2009, **7**:129-143.

32. Forster J, Famili I, Fu P, Palsson BO, Nielsen J: **Genome-scale reconstruction of the Saccharomyces cerevisiae metabolic network.** *Genome Res* 2003, **13**:244-253.

33. Karp PD, Paley S, Romero P: **The Pathway Tools software.** *Bioinformatics* 2002, **18**(Suppl 1):S225-232.

34. Bairoch A: **The ENZYME database in 2000.** *Nucleic Acids Res* 2000, **28**:304-305.

35. Yang C, Hua Q, Shimizu K: **Quantitative analysis of intracellular metabolic fluxes using GC-MS and two-dimensional NMR spectroscopy.** *J Biosci Bioeng* 2002, **93**:78-87.

36. Pearce J, Carr NG: **The metabolism of acetate by the blue-green algae, Anabaena variabilis and Anacystis nidulans.** *J Gen Microbiol* 1967, **49**:301-313.

37. Patil KR, Rocha I, Forster J, Nielsen J: **Evolutionary programming as a platform for in silico metabolic engineering.** *BMC Bioinformatics* 2005, **6**:308.

38. Feist AM, Henry CS, Reed JL, Krummenacker M, Joyce AR, Karp PD, Broadbelt LJ, Hatzimanikatis V, Palsson BO: **A genome-scale metabolic reconstruction for Escherichia coli K-12 MG1655 that accounts for 1260 ORFs and thermodynamic information.** *Mol Syst Biol* 2007, **3**:121.

39. Zelezniak A, Pers TH, Soares S, Patti ME, Patil KR: **Metabolic network topology reveals transcriptional regulatory signatures of type 2 diabetes.** *PLoS Comput Biol* 2010, **6**:e1000729.

40. Stephanopoulos G, Aristidou AA, Nielsen JH: *Metabolic engineering: principles and methodologies* San Diego: Academic Press; 1998.

41. Schuetz R, Kuepfer L, Sauer U: **Systematic evaluation of objective functions for predicting intracellular fluxes in Escherichia coli.** *Mol Syst Biol* 2007, **3**:119.

42. Anderson SL, McIntosh L: **Light-activated heterotrophic growth of the cyanobacterium Synechocystis sp. strain PCC 6803: a blue-light-requiring process.** *J Bacteriol* 1991, **173**:2761-2767.

43. Carr NG, Whitton BA: *The Biology of cyanobacteria* Berkeley: University of California Press; 1982.

44. Pelroy RA, Rippka R, Stanier RY: **Metabolism of glucose by unicellular blue-green algae.** *Arch Mikrobiol* 1972, **87**:303-322.

45. Loferer-Krossbacher M, Klima J, Psenner R: **Determination of bacterial cell dry mass by transmission electron microscopy and densitometric image analysis.** *Appl Environ Microbiol* 1998, **64**:688-694.

46. Lawrence BA, Suarez C, DePina A, Click E, Kolodny NH, Allen MM: **Two internal pools of soluble polyphosphate in the cyanobacterium Synechocystis sp. strain PCC 6308: an in vivo 31P NMR spectroscopic study.** *Arch Microbiol* 1998, **169**:195-200.

47. Stephanopoulos G, Alper H, Moxley J: **Exploiting biological complexity for strain improvement through systems biology.** *Nat Biotechnol* 2004, **22**:1261-1267.

48. Oliveira AP, Patil KR, Nielsen J: **Architecture of transcriptional regulatory circuits is knitted over the topology of bio-molecular interaction networks.** *BMC Syst Biol* 2008, **2**:17.

49. Patil KR, Nielsen J: **Uncovering transcriptional regulation of metabolism by using metabolic network topology.** *Proc Natl Acad Sci USA* 2005, **102**:2685-2689.

50. Gill RT, Katsoulakis E, Schmitt W, Taroncher-Oldenburg G, Misra J, Stephanopoulos G: **Genome-wide dynamic transcriptional profiling of the light-to-dark transition in Synechocystis sp. strain PCC 6803.** *J Bacteriol* 2002, **184**:3671-3681.

51. **NCBI Entrez Genome for Synechocystis sp. PCC6803.** [http://www.ncbi. nlm.nih.gov/sites/entrez?Db=genome&Cmd=ShowDetailView&TermToSearch = 112].

52. Pearce J, Leach CK, Carr NG: **The incomplete tricarboxylic acid cycle in the blue-green alga Anabaena variabilis.** *J Gen Microbiol* 1969, **55**:371-378.

53. Vazquez-Bermudez MF, Herrero A, Flores E: **Uptake of 2-oxoglutarate in Synechococcus strains transformed with the Escherichia coli kgtP gene.** *J Bacteriol* 2000, **182**:211-215.

54. Peschek GA, Löffelhardt W, Schmetterer G: *The phototrophic prokaryotes* New York: Kluwer Academic/Plenum; 1999.

55. Rubio FC, Camacho FG, Sevilla JM, Chisti Y, Grima EM: **A mechanistic model of photosynthesis in microalgae.** *Biotechnol Bioeng* 2003, **81**:459-473.

56. Albertsson P: **A quantitative model of the domain structure of the photosynthetic membrane.** *Trends Plant Sci* 2001, **6**:349-358.

57. Allen J: **Photosynthesis of ATP-electrons, proton pumps, rotors, and poise.** *Cell* 2002, **110**:273-276.

58. Herdman M, Janvier M, Waterbury J, Rippka R, Stanier R: **Deoxyribonucleic Acid Base Composition of Cyanobacteria.** *Journal of General Microbiology* 1979, **111**:63-71.

59. Tasaka Y, Gombos Z, Nishiyama Y, Mohanty P, Ohba T, Ohki K, Murata N: **Targeted mutagenesis of acyl-lipid desaturases in Synechocystis: evidence for the important roles of polyunsaturated membrane lipids in growth, respiration and photosynthesis.** *EMBO J* 1996, **15**:391-396.

60. Miao X, Wu Q, Wu G, Zhao N: **Changes in photosynthesis and pigmentation in an agp deletion mutant of the cyanobacterium Synechocystis sp.** *Biotechnol Lett* 2003, **25**:391-396.

61. Burrows EH, Chaplen FW, Ely RL: **Optimization of media nutrient composition for increased photofermentative hydrogen production by Synechocystis sp. PCC6803.** *International Journal of Hydrogen Energy* 2008, **33**:6092-6099.

Research Article

Flux coupling and transcriptional regulation within the metabolic network of the photosynthetic bacterium *Synechocystis* sp. PCC6803

Arnau Montagud[1,2], Aleksej Zelezniak[2,3], Emilio Navarro[4], Pedro Fernández de Córdoba[1], Javier F Urchueguía[1], Kiran Raosaheb Patil[2]

[1] Instituto Universitario de Matemática Pura y Aplicada, Universidad Politécnica de Valencia, Spain.
[2] Structural and Computational Biology Unit, European Molecular Biology Laboratory, Heidelberg, Germany.
[3] Department of Systems Biology, Technical University of Denmark, Denmark.
[4] Departamento de Lenguajes y Ciencias de la Computación, Universidad de Málaga, Spain.

Synechocystis sp. PCC6803 is a model cyanobacterium capable of producing biofuels with CO_2 as carbon source and with its metabolism fueled by light, for which it stands as a potential production platform of socio-economic importance. Compilation and characterization of *Synechocystis* genome-scale metabolic model is a pre-requisite toward achieving a proficient photosynthetic cell factory. To this end, we report *i*Syn811, an upgraded genome-scale metabolic model of *Synechocystis* sp. PCC6803 consisting of 956 reactions and accounting for 811 genes. To gain insights into the interplay between flux activities and metabolic physiology, flux coupling analysis was performed for *i*Syn811 under four different growth conditions, *viz.*, autotrophy, mixotrophy, heterotrophy, and light-activated heterotrophy (LH). Initial steps of carbon acquisition and catabolism formed the versatile center of the flux coupling networks, surrounded by a stable core of pathways leading to biomass building blocks. This analysis identified potential bottlenecks for hydrogen and ethanol production. Integration of transcriptomic data with the *Synechocystis* flux coupling networks lead to identification of *reporter flux coupling pairs* and *reporter flux coupling groups* – regulatory hot spots during metabolic shifts triggered by the availability of light. Overall, flux coupling analysis provided insight into the structural organization of *Synechocystis* sp. PCC6803 metabolic network toward designing of a photosynthesis-based production platform.

Supporting information available online

1 Introduction

In recent years, the need for a clean, sustainable, and efficient chemical production platform has trapped considerable interest of the society. Future energy requirements demand a sustainable alternative for the use of fossil fuels, to restrict further global warming and pollution. For instance, advances have been achieved in the design and implementation of microbial processes for the first, second, and third generation biofuels. However, the design of a clean industrial production platform stands as a cornerstone for the next step in green biotechnology, focused on getting energy from light source, and relieving air of CO_2. Such a strategy offers the much-needed avoidance of diversion of energy from human food chain or the recollection of vegetal left-over from the fields. One of the best places to search for such alternative solutions is

Correspondence: Dr. Kiran Raosaheb Patil, Structural and Computational Biology Unit, European Molecular Biology Laboratory, Meyerhofstrasse 1, D-69117 Heidelberg, Germany
E-mail: patil@embl-heidelberg.de

naturally occurring micro-organisms, where the goal of trapping light and CO_2 has already been achieved several millennia back. Photoautotrophs harvest energy from photons through the photosynthesis and shape carbon skeletons out of atmospheric CO_2 through Calvin cycle's carbon fixation. Nowadays, the capability of taming such organisms to the production of energy-rich compounds for use as biofuels, *e.g.*, alcohols or hydrogen, is a goal that is within our reach [1].

In the search for such an ideal system, focus has been set on algae and cyanobacteria. These unicellular organisms have been targeted due to their ease of cultivation, little nutritional demands and tolerance – its wide range of habitats include aquatic (saltwater and freshwater), terrestrial, and extreme environments (including frigid lakes of the Antarctic or hot springs). Additionally, they would not suffer from the disadvantages encountered with the current strategies, being capable of producing biofuels in an essentially continuous process [2]. *Synechocystis* sp. PCC6803 is a cyanobacteria model organism for its robust growth characteristics, is naturally transformable [3], with its genome sequenced, and annotated [4]. At present, there is probably no other cyanobacterium which has been investigated in such detail, making it an interesting organism for biotechnological applications [5] such as heterologous production of metabolites like isoprene [6], poly-beta-hydroxybutyrate [7], alcohols [2], biofuels [8], and bio-hydrogen [1]. *Synechocystis* is thus an attractive candidate for developing a clean and sustainable platform for biotechnological processes aimed at value-added products formation.

Metabolic models at the genome-scale are one of the pre-requisites for rational metabolic engineering approaches as well as for eventually developing synthetic cell factories [9–11]. Genome-scale metabolic models also offer an opportunity to systematically analyze *omics* datasets in the context of cellular metabolic phenotypes and thereby to gain insights into the operational principles of the cell factories. Genome-scale metabolic modeling approach has been applied to a diversity of organisms in a variety of conditions in the context of metabolic engineering, pathway re-routing, and systems biology in general. In this sense, previous works on *Synechocystis* metabolic models [12–14] are a good start to use these *in silico* design approaches toward creating a photosynthetic bio-refinery. One of the interesting approaches for understanding the operating principles and capabilities of a micro-organism is to analyze the stoichiometric links between the metabolic reactions at the steady state – an approach termed flux coupling analysis. Flux

coupling analysis, first presented by Burgard *et al.* [15], has been used to study flux capabilities of *Saccharomyces cerevisiae* and *Escherichia coli* [16] and has facilitated metabolic flux analysis [17].

In this study, we present an upgraded and updated *Synechocystis* sp. PCC6803 genome-scale metabolic model (*i*Syn811). The updated model is used to gain insights into the organization and operational principles of the *Synechocystis* metabolic network. Four growth conditions were investigated in *i*Syn811: (i) autotrophy, where light enters the system to feed energy needs and molecular CO_2 to build carbon skeletons; (ii) pure, *dark* heterotrophy (DH), where glucose is the only source of carbon and energy; (iii) LH, where in addition to glucose light enters the system as a source of energy; and (iv) mixotrophy, where CO_2, glucose, and light enter the cell. We show the usefulness of the flux coupling analysis by identifying flux connectivity characteristics in the above four growth conditions of physiological relevance for industrial production. Flux coupling networks were further analyzed by applying the reporter features algorithm [18, 19] and thereby revealing some of the key transcriptional regulatory patterns prevailing in the *Synechocystis* sp. PCC6803 metabolic network.

2 Material and methods

2.1 Genome-scale metabolic model and database

Genomic, metabolic, and bibliomic data were compiled with *i*Syn669 [14] model at the center, resulting in an up-to-date *Synechocystis* sp. PCC6803-specific database of genes, proteins, enzymes, and metabolites. This database was built with the aid of Pathway Tools software [20] and is available upon request.

Starting with this database, genes and reactions were manually curated and assembled in order to obtain a flux balance model that could simulate the known characteristics of *Synechocystis* metabolism. Functionality and model usefulness were checked through a variety of algorithms such as FBA, MOMA, and Reporter Features [18, 19]. This model bears four kinds of gene-reaction relationships: reaction with cognate genes, reactions that needed to be included in the model in order to have metabolic precursors in the network (with no assigned genes), non-enzymatic reactions that have no related gene, and genes described in the annotations but with no assigned function. The new version of *Synechocystis* sp. PCC6803 genome-scale metabolic model has been named *i*Syn811 and is available at http://www.sysbio.se/BioMet.

2.2 Constraints used for flux balance simulations

FBA simulations were constrained so as to match an autotrophic specific growth rate of 0.09 h^{-1} which corresponds to a light input of 0.8 mE g$_{DW}$$^{-1}$ h^{-1} and to a net carbon flux of 3.4 mmol g$_{DW}$$^{-1}$ h^{-1} into the cell, with HCO$_3^-$ and CO$_2$ as carbon sources. These parameters were maintained for comparative purposes in the heterotrophic condition, glucose being the sole carbon source and blocking photons input in the DH. Some of the constraints were altered in the mixotrophic conditions in order to simulate the characteristic flux distribution of this growth mode. Phosphate, water, sulfate, nitrate, ammonia as well as carbon monoxide and hydrogen peroxide transport across the membrane were considered and properly bounded. Some of the reversible reactions involving NADH and NADPH were constrained to be irreversible so that spurious transhydrogenation was controlled. All the relevant constraints used in this study can be found in Supplementary information (Table 1, file 1).

2.3 Flux coupling analysis

We adapted the flux coupling finder procedure developed by Burgard *et al.* [15] to analyze the functional associations between the reactions of the genome-scale metabolic network of *Synechocystis* sp. PCC6803 across the four different simulated growth conditions. This constraint-based modeling approach relies on minimization and maximization of the intra-cellular flux ratios to determine the extent of the dependency between any two reactions within the network, given the mass-balance constraints and the exchange fluxes with the environment. The difference between our implementation and the original algorithm [15] is that we did not create coupled reaction sets; instead, we examined each of the reaction pairs for the type of flux coupling relationship. Computational requirements were on the order of minutes for the complete genome-scale model. The algorithm was imple-

mented in Matlab® (MathWorks®) by using GLPK as linear programming solver (http://www.gnu.org/software/glpk/) and is available upon request.

Four types of flux coupling relationships were considered: (i) fully coupled: non-zero flux in one reaction implies non-zero and fixed flux through the other reaction, and *vice versa*; (ii) partially coupled: non-zero flux in one reaction implies non-zero but variable flux in the other reaction; (iii) directionally coupled: non-zero flux in one reaction implies non-zero flux in the other, but not necessarily the reverse; and (iv) uncoupled: presence of flux through one reaction does not bound flux through the other and *vice versa* (reactions are stoichiometrically independent at steady-state) [15]. The flux-coupling results shown here are from the calculations run without including a biomass formation reaction (description of the constraints used can be found in Supplementary Table 1, file 1, and coupled reactions can be found in Supplementary information, file 2). The biomass equation was excluded in order to avoid coupling of a large number of fluxes to the biomass formation reaction. However, all biomass components were allowed to be drained independent of one another. Calculations performed with the biomass formation reaction present retrieved similar coupling patterns within the rest of the reactions (data not shown).

2.4 Transcriptome data analysis

Reporter features algorithm [18, 21] was used to integrate this data in the flux coupling networks. This algorithm works with three kinds of information: (i) *p-values* for genes, resulting from, for example, Student's *t*-test run on transcriptomic data, (ii) interaction file, where genes/reactions are connected to the corresponding features, in this case the sets of coupled reactions, and (iii) association file, where genes are linked to the corresponding reactions.

In the present case, the interaction file was the list of coupled reactions and the association file

Table 1. Relative distribution of reactions among different flux coupling relationships. Percentages of reactions falling within each coupling type are Highlighted in italics. A reaction can participate in more than one coupling set and hence the number of reactions in a coupled group do not necessarily sum up to the total number of reactions.

	E. coli		*S. cerevisiae*		*Synechocystis* autotrophic		*Synechocystis* mixotrophic		*Synechocystis* LH		*Synechocystis* DH	
Directionally	421	*35.8*	473	*39.3*	527	*41.3*	517	*39.4*	517	*40*	512	*39.6*
Fully coupled	353	*30*	265	*22*	214	*16.8*	226	*16.4*	227	*16*	213	*15.7*
Partially coupled	–		44	*3.6*	113	*8.8*	111	*8.7*	111	*8.7*	111	*8.7*
Reactions in model	1176		1204		1275		1275		1275		1275	

linked gene symbols in the *p-values* file to the reaction names as used in the interaction file. We retrieved the transcriptomic data from a contribution that studied clusters of genes differentially expressed with and without light [22]. In this work, *Synechocystis* sp. PCC6803 was grown under 24 h of darkness, followed by 100 min of light and 100 min of darkness. Seven genome-wide transcriptional analyses were performed over the length of the experiment.

3 Results

We first present an updated genome-scale metabolic model that has been thoroughly tested for the use with the steady state metabolic simulation algorithms. This model has been the basis of flux coupling analysis which uncovers coupling potential among reactions, as well as for integration of transcriptome data toward revealing regulation patterns among these coupled reactions.

3.1 Updated genome-scale model of *Synechocystis* sp. PCC6803

Our previous genome-scale metabolic model, *i*Syn669, was updated to *i*Syn811, which bears 956 reactions, 866 of them with cognate genes, 911 metabolites and 811 genes. When bidirectional reactions are converted to unidirectional, a pre-requisite of flux coupling analysis algorithm used in this study, the number of reactions is extended to 1245 reactions. Methods were used as described previously [14] in order to cope with unspecificity with respect to cofactor or metabolite usage, unbalanced reactions and reversibility. Biomass equation used was the same as the *i*Syn669 model [14], which takes into account amino acids, nucleic acids, lipids, carbohydrates, ribonucleotides, deoxyribonucleotides, and antenna chromophores. This model has been compiled in OptGene [21] format in order to be readily usable with this software and is available at BioMet webpage (http://www.sysbio.se/BioMet).

In order to further facilitate the use of the *Synechocystis* sp. PCC6803 model, we have also compiled our work as a Pathway Tools Tier 2 Pathway-Genome Database (PGDB) (available upon request). Searches for genes, reactions, proteins, pathways, and regulations can be performed on this service. Our *Synechocystis* sp. PCC6803 database consists of 3622 genes, 3572 proteins, 58 transport reactions, 701 compounds, 43 tRNAs, and 889 enzymatic reactions distributed among 180 Meta-Cyc pathways.

3.2 Blocked reactions

Reactions that could not carry steady state flux for a given set of environmental constraints [autotrophic, mixotrophic, dark heterotrophic (DH), or, light-activated heterotrophic (LH)] were identified as blocked reactions.

*i*Syn811 blocked reactions range between 39.45% under autotrophy to 41.25% under DH, some more than *E. coli* (28%) [23] and similar to *S. cerevisiae* (39.2%) [24] both under aerobic heterotrophy (Supplementary information, Table 2, file 3). Focusing on the different growth conditions of *Synechocystis*, mixotrophy stands as the condition with the least number of blocked reactions, but not far from the other conditions. Autotrophy has the import of glucose and the phosphorylation of glucose blocked. Many of the folate biosynthesis reactions, photosynthesis reactions, and Calvin cycle (CO_2 fixation) can have non-zero steady state flux only under autotrophic and mixotrophic conditions. DH has most of the photosynthesis pathway blocked and, as LH and mixotrophy, allows flux in the upper part of the glycolysis and the import of glucose. Mixotrophy, as the condition with least blocked reactions, stands in between autotrophy and heterotrophy: flux is feasible through folate biosynthesis, Calvin cycle, photosynthesis as well as all the glycolysis; additionally, many coenzyme A biosynthesis reactions have potential non-zero flux only in this condition.

3.3 Flux coupling

As reported by Burgard *et al.* [15], an imposed constant stoichiometry biomass composition leads to the generation of one large coupled reaction set that is mostly fully coupled. This biomass reaction serves simulation purpose of draining the compounds necessary for cell growth (*e.g.* amino acids and nucleotides) in a pre-specified stoichiometry. We have seen that the coupling sets of networks with and without biomass-coupled reaction are essentially the same in terms of diversity and relative fraction of different types of couplings (data not shown). In fact only one set of reactions, which is the drain of monomers to the biomass reaction, is additionally present in the latter (set that represents 67 reactions, 5.25% of the total reactions in *i*Syn811). As the biomass reaction is an abstraction of growth and has purely simulation purposes, we here present only the results of networks with independent biomass monomer drains under the four studied growth modes.

*i*Syn811 presents similar relative distribution of coupling patterns as *E. coli* and *S. cerevisiae*, with

twice more directionally coupled sets than fully coupled and almost one-fifth of partially coupled groups (Table 1). Furthermore, the *Synechocystis* model portrays less fully coupled reactions and two-fold more partially coupled reactions than *S. cerevisiae* model. The distribution of coupled reactions is shown in Table 1 and the complete sets of coupled reactions are provided in Supplementary information (file 2).

3.3.1 Autotrophy

In this growth condition, light is the source of energy and molecular CO_2 of carbon skeletons. Photosynthesis is essential in this mode in order to fulfil the cellular needs of ATP and redox potential. Looking at the effect of growth conditions on flux coupling analysis, we observed that the autotrophy has slightly less fully coupled sets and a few more directionally coupled reactions (Figure 1A). An interpretation of the different coupling cases from a biological perspective can be found in Figure 2.

Most coupled reactions are directionally coupled, with the corresponding reactions spanning all functional pathways in the *Synechocystis* metabolic model. Directionally coupled reactions are relationships where activity in one reaction obliges another to have activity but not the other way around. The carbon fixation and the entrance of CO_2 to the cell stand in the center of the network together with ATP production in the thylakoid membrane (which is the node with the highest degree, 254), leaving the rest of the coupling sets to stem from them. Notably, almost all the fatty acid biosynthesis is directionally coupled to many central pathways as glycolysis, pentose phosphate pathway, and Calvin cycle. Almost all reactions from photosynthesis are directionally coupled (only five couplings are left to be fully coupled) and in such a way that follows the photosynthesis pathway structure, as they are coupled also with the oxidative phosphorylation.

In the fully coupled reaction network there is one big cluster, several medium size clusters (with four or more reactions) and many 2- and 3-mer sets. Fully coupled reactions are reactions whose flux ratios have a constant value, thus activity of one reaction forces another one to have a specific, unique, value. Interestingly, the large cluster (highly interconnected with 102 reactions and 5151 connections) is made up of most of the reactions (11 out of 13) of the chlorophyll pathway interconnected between them and connected with reactions from fatty acid biosynthesis, from carotenoid biosynthesis, and several amino acids (aspartate, histidine, and glutamate, among others). Medium-sized clusters are an 8-mer set for the of NAD(P)
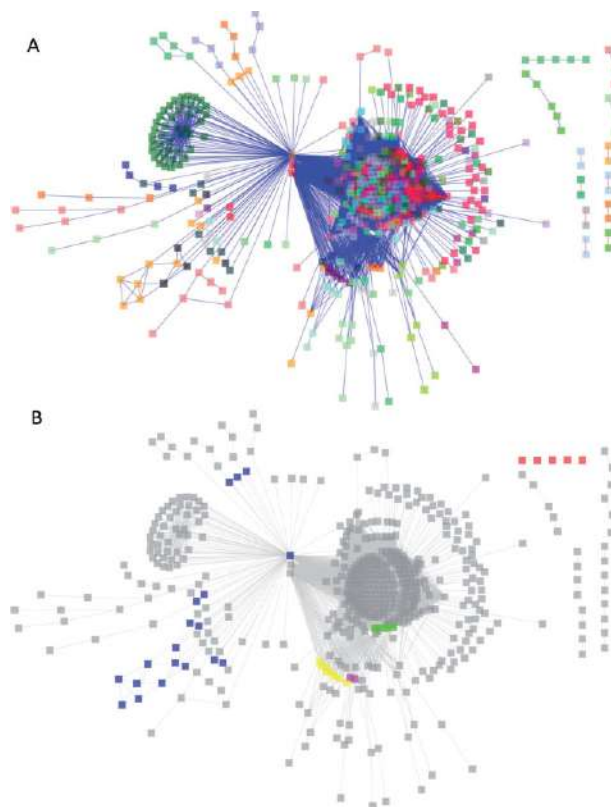
Figure 1. Flux coupling network for autotrophic growth condition. A) Global network topology. Nodes represent reactions and are colored according to the pathway they belong to (for instance, orange is photosynthesis, dark gray is oxidative phosphorylation, dark pink is Calvin cycle, dark green is glutathione metabolism, red is fatty acids, and different grades of green are different amino acids syntheses). Edges represent flux coupling and are colored according to the type of interaction (blue – directionally, red – fully and green – partially coupled). B) *Reporter flux coupling groups* for dark-light-dark shifts under autotrophic growth conditions. Pyrimidine fully coupled set (*ful16*) in light purple, blue color represents the photosynthesis and oxidative phosphorylation cluster of *dir1* coupling group. These groups are *reporter couplings* in all the studied conditions: *all time points* and in the light shifts from *dark to light* and *light to dark*. Purine fully coupled biosynthesis (*ful4*) in green color highlights regulation in *all time points* and during the shift from *light to dark*. Glutamate directionally coupled metabolism (*dir2*) in red is identified to be a regulatory hub on *all time points*. Fully coupled set of NAD(P)H turnover (*ful3*), depicted in yellow, is a regulatory center in *dark to light* environmental shift.

metabolism, an 8-mer set for biosynthesis of steroids, and a 5-mer for purine metabolism.

Finally, partially coupled reactions are the reactions that are mutually needed, but whose fluxes can have a range of values. In partially coupled reactions sets, we have found two noteworthy groups. First, a complex of 111 reactions made up of a core of 11 reactions part of the porphyrin and chlorophyll metabolism (specifically, *S*-adenosyl methionine, or SAM, formation) and 17 reactions part of the fatty acid biosynthesis (malonyl-CoA formation
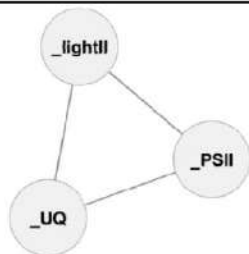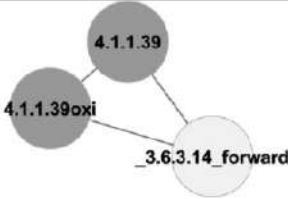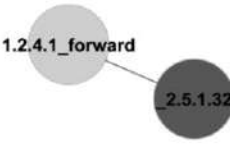
Analysis	Remarks	Example	
Fully coupled reactions	Suitable for the application of metabolic control analysis for the identification of rate controlling step (/s).	_lightII _PSII _UQ	If photosystem II could be engineered to be more efficient in using photons (_PSII), this would foster the initial step of linear photosynthesis (_UQ).
Directionally coupled reactions	Engineering of a target flux should be co-ordinated with the source flux.	4.1.1.39 4.1.1.39oxi _3.6.3.14_forward	ATP synthase is needed to have RuBisCo carboxylase and oxidase activities, but then increased ATP synthase activity may not direct an increased carboxylase activity.
Partially coupled reactions	Metabolic control analysis, as well as independent manipulation of nodes, may be necessary	4.1.1.39 — 2.7.1.19	Phosphoribulokinase activity has to have flux in a window of values compatible to that of RuBisCO carboxylase. Upper limit is fixed by other constraints, like CO_2 supply.
Reporter pair	Transcriptional co-regulation of the corresponding enzymes under the studied perturbation response. May involve (known or unknown) transcription factors.	1.2.4.1_forward 2.5.1.32	Provides clues for the discovery of new regulatory mechanisms. Engineering of the corresponding fluxes should take into account the co-regulatory patterns (esp. under non-steady state conditions)

Figure 2. Examples of potential applications of *i*Syn881 flux coupling analysis for metabolic engineering.

and its union with acyl carrier protein are coupled with the oligomerization reaction of lipids). The second group is made of the carboxylative reaction of the ribulose-1,5-bisphosphate carboxylase oxygenase (RuBisCO) and the phosphoribulokinase reaction, this is, the reaction that fixes the atmospheric carbon and the one that generates the substrate in which CO_2 will be fixed. These sets are a good example of partially coupled reactions. For example, flux ratios between SAM formation and chlorophyll synthesis have a minimum value (as chlorophyll *a* needs SAM and is also needed for the cell composition), but the activity on reaction 2.5.1.6 (formation of SAM) is not the only reaction where SAM can be produced and, thus, has a range of possible values in order to fulfil the need of chlorophyll.

3.3.2 Heterotrophy
In this growth condition, energy and carbon come from glucose or other carbohydrates. Cyanobacteria researchers identify this condition as "dark heterotrophy" (DH), in order to differentiate it from a "light-activated heterotrophy" (LH) condition where photons are permitted to enter the system, hence activating photosynthesis, but with no CO_2 fixation. Little differences in the coupling distribution or network clustering have been found across these two conditions (Table 1). The only difference comparing both conditions is that the LH network has a complete photosynthesis cluster, which embeds the reactions from the oxidative phosphorylation, while the DH network has only the photosynthetic reactions needed for a proper oxidative phosphorylation pathway, as both share some elements in the thylakoid membrane.

Directional coupling is a predominant characteristic in this network, even though as a major difference to autotrophic condition, glucose entering the cell and its phosphorylation are centrally located in the network together with ATP synthase, which is again the most connected reaction with a

degree of 251. This change alters the networks in such a way that all other groups and cluster are arranged around these reactions. Nonetheless, as in the autotrophic case, almost all of the fatty acid biosynthesis, NAD(P) metabolism and porphyrin and chlorophyll metabolism reactions are directionally coupled between themselves and connected to these two reactions. Moreover, purine and pyrimidine biosynthesis and glutamate and proline pathways are coupled together in a linear way, but independent of the core of the network.

Fully coupled reactions sets in DH are analogous to autotrophic. The highly-connected big cluster is also found (with 102 reactions and 5151 connections inter and intra pathways), made out of chlorophyll pathway, fatty acid biosynthesis, carotenoid biosynthesis, and several amino acids reactions. The similarity in the smaller sets is notable: medium clusters are present, like the ones with reactions of the steroids biosynthesis, NAD(P) metabolism, and fatty acid biosynthesis and several smaller like most of the glutathione metabolism (forming 2-mers) as well as groups of reactions from fatty acid biosynthesis and amino acids. Nevertheless some small sets stand out as different, like some reactions from pyruvate metabolism and pentose phosphate pathway, a few reactions from photosynthesis, as well as the appearance of the oxidative reaction of the RuBisCO enzyme that works as a source of glycolate, needed for the glyoxylate shunt.

Heterotrophic partially coupled reactions are different from the ones in the autotrophic: SAM coupled to all the reactions of chlorophyll metabolism and fatty acid biosynthesis are present, but the partial coupling of ribulose-1,5-bisphosphate production and use is no more present. If there is no carbon fixation, it is clear that ribulose-1,5-bisphosphate will not be drained at RuBisCO carboxylase reaction.

3.3.3 Mixotrophy

This condition is a blend of the previous two conditions. Glucose, molecular CO_2, and photons are present in the system; hence, carbon and energy have more than one source. Interestingly, we see a different network topology of coupling networks from the previous conditions: fewer clusters and less connectivity are found in this condition, due to the fact that the mixotrophic condition has more feeding sources and is, thus, more flexible in the flux distribution, i.e., with more degrees of freedom. Molecular carbon fixation and glucose transport and phosphorylation are coupled, but only connected to the ATP production which is the reaction at the core of the network. This coupling permits the mixed flux behavior that was observed in previous work [13, 14]. Photosynthesis cluster is present analogously to the autotrophic condition. In our mixotrophic coupling network, ATP synthase is the most connected reaction with a degree of 256. Furthermore, mixotrophy is the condition with fewer couplings, which is due to the increase in the degrees of freedom of the flux distribution.

As it happens with the other two conditions, directionally coupled reactions are the largest set of coupling pairs in the network. In this case, though, carbon entering the system is detached from the nucleus of the network, leaving that place to the ATP production from which the biomolecular-building pathways stem. Fatty acid biosynthesis, NAD(P) metabolism, pyrimidine and purine biosynthesis, porphyrin and chlorophyll metabolism, sucrose metabolism, and TCA cycle reactions are directionally coupled inter pathways, and some of them also intra pathway.

Fully coupled reactions follow the trend of the other conditions. The highly-connected big cluster is present with 102 reactions (and 5151 connections inter and intra pathways): fatty acid biosynthesis, porphyrin, and chlorophyll metabolism are included, as well as several amino acids. As in the previous cases, the medium-sized sets include clusters for the biosynthesis of steroids, NAD(P) metabolism, and purine metabolism. Smaller sets include 2-mers from Calvin cycle, glycolysis, pentose phosphate pathway, photosynthesis, porphyrin, and chlorophyll metabolism and almost all the glutathione metabolism.

Mixotrophic partially coupled reactions are the same as in the heterotrophic case. Feeding of ribulose-1,5-bisphosphate is not found in partial couplings and has gone to the less restrictive directional coupling set due to the increase in the degrees of freedom of the mixotrophic network.

3.4 Reporter couplings

Reporter features is a method designed to, given a bio-molecular abundance data, discover major regulatory players in a biological network [14, 18, 19]. Reporter features algorithm was applied to the coupling network in order to identify regulatory hubs – *reporter flux coupling pairs* and *reporter flux coupling groups*. In particular, we address the task of identification of flux coupling reaction pairs or groups that are differentially regulated during light shifts: from 24 h of darkness to 100 min of light to 100 min of darkness. Genome-wide transcription data were taken from the study by Gill *et al.*[22].

3.4.1 Reporter coupling pairs

A coupling characterizes functional relationship between the two reactions, *viz.* directional, full or partial coupling. Each coupling pair was independently studied across the transcription data arrays of a light-shift experiment discovering regulatory hubs – *reporter coupling pairs* (Supplementary information, file 4).

All time points

Using all seven transcription arrays as input, we covered two light shifts: turning on the photosynthesis and metabolic machinery and shutting it down. We looked for couplings with significant coregulation among all seven arrays. Most statistically significant pairs were the ones covering the connection between pathways from the central carbon metabolism (purine metabolism, coenzyme A biosynthesis) or biological building blocks (fatty acid biosynthesis, porphyrin, and chlorophyll metabolism, biosynthesis of steroids) to amino acid pathways (glutamate, threonine).

Dark to light

In this analysis, we focused on the shift from darkness to the growth in the presence of light. RuBisCO (reaction 4.1.1.39 in the model) stands as the most influential regulatory hub in this set and most significant pairs bear this vital reaction. Additionally, the core carbon metabolism (Calvin cycle, TCA cycle) is significantly paired to building block synthesis pathways (carotenoid biosynthesis, porphyrin, and chlorophyll metabolism, fatty acid biosynthesis) as well as to amino acid biosynthesis (histidine, aspartate). Photosynthesis reactions are scarcely present in seven pairs, which are not the most significant.

Light to dark

Finally, we analyzed the shift from an illuminated condition to darkness. Most statistically significant pairs cover pathway from the central carbon metabolism (sucrose metabolism, glycolysis, pentose phosphate pathway) links to biosynthesis pathways (biosynthesis of steroids, purine metabolism, porphyrin, and chlorophyll metabolism, fatty acid biosynthesis) and to amino acids (aspartate, isoleucine). Interestingly, photosynthesis reactions are predominant in this set (93 out of 586), even though they are not present in the most significant pairs. Additionally, carboxylative reaction from RuBisCO is not significant.

3.4.2 Reporter coupling groups

Groups of coupled reactions were compiled by connecting reactions coupled to each other. This way,

we were able to identify higher order regulatory hubs – *reporter coupling groups* for the light shift dataset (Supplementary information, file 5).

All time points

We looked for coupling groups with significant corregulation among all the seven arrays, which covered both light shifts. Glutamate directionally coupled metabolism (*dir2*), purine fully coupled biosynthesis (*ful4*), and pyrimidine fully coupled set (*ful16*) were identified as *reporter coupling groups* (their knitting over the *i*Syn811 coupling network can be seen in Figure 1B).

Dark to light

We found three *reporter coupling groups* that were significant during the start-up of metabolism following the availability of light. Reporter couplings were glutamate directionally coupled metabolism (*dir2*) and two fully coupled sets: pyrimidine (*ful16*) and NAD(P) metabolism (*ful3*).

Light to dark

Two fully coupled groups were revealed as *reporter coupling groups*: pyrimidine (*ful16*) and purine biosynthesis (*ful4*).

Finally, as *dir1* coupling group conveys 388 reactions (32.7% of the total) we have used clustering methods [25] (http://clusterviz.sourceforge.net/) to identify significantly coregulated subsets. The cluster made up of all directionally coupled reactions from the photosynthesis and the oxidative phosphorylation from *dir1* set was discovered as such in all three data sets, even though the 388-mer *dir1* set, as a whole, is not.

4 Discussion

We have hereby described the flux coupling landscape in the *Synechocystis* sp. PCC6803 genome-scale metabolism, affirming the use of this methodology to gain insight into the capabilities of genome-scale metabolic network reconstructions, and into the regulatory principles underlying the adaptation to a major environmental alteration, *viz.* light shift.

4.1 Blocked reactions

Blocked reactions in *i*Syn811 are in comparable numbers to that of *E. coli* and *S. cerevisiae* (Supplementary information, Table 2, file 3). Altogether, almost 40% of the known metabolic reactions in those genome-scale models cannot carry flux under commonly used growth conditions. Among the

main reasons for this apparent dispensability are: (i) incomplete description of the biomass composition, and (ii) medium composition used in simulation. Nevertheless, a large number of metabolic reactions are possibly active only under environmental conditions not typically used in laboratory studies. Differences observed between the different growth modes of *Synechocystis* sp. PCC6803 are in accordance with the physiological information and previous modeling studies [13]: autotrophy has glucose transport and catabolism blocked; in heterotrophy blocked reactions are among photons usage and carbon fixation. Mixotrophy stands as the growth mode in which less blocked reaction are present. In fact, this mode has more uptake freedom degrees than the previous: glucose and CO_2 can be used as carbon source and glucose and photons as energy source.

4.2 Coupling networks across growth conditions

In all three conditions directionally coupled reactions are dominant. Fully coupled reactions follow and partially coupled reactions are far behind (Table 1). Even though there are significant differences, the network of coupled reactions has quite similar topology: metabolic precursors needed for cell growth stem out of the reactions responsible of ATP production and carbon transport and metabolism (Calvin cycle in autotrophy, upper part of glycolysis in heterotrophy). Apart from the central nodes of the network, topology is almost identical. This suggests the idea that, once carbon has been metabolized by the cell and energy has been drained from it, the coupling of the anabolic part of the metabolism is independent of the growth condition. Metabolic flux coupling of *Synechocystis* sp. PCC6803 has evolved around the need to be flexible in the acquisition of skeletons for building blocks, but is conservative on the construction of these building blocks (fatty acids, amino acids, nucleic acids, *etc*) as well as on the ATP production. Following the "bow tie" description of metabolism [26] *Synechocystis* appears flexible to growth conditions on the first half of the metabolism (catabolism of environmental molecules to construct precursors), but conservative on the anabolism of polymers and complex assemblies. This characteristic helps to explain the wide range of living conditions in which *Synechocystis* sp. PCC6803 is found in nature and the scarce needs it has for its growth on the bench [27].

4.3 Photosynthesis couplings

Apart from direct biotechnological designs, iSyn881 model and present analyses can also be of use for the study of biochemical questions, like the functioning of the photosynthesis pathway (Figure 3). Photosynthesis, present in autotrophy, mixotrophy and LH, is mostly directionally coupled intra pathway and with the reactions from oxidative phosphorylation, embedding four fully coupled clusters following the entrance of photons to photosystem I and II, the ADP recycling and the NADP+ reduction to NADPH. Photosynthesis and oxidative phosphorylation clusters are directionally coupled to the rest of the network through only one reaction – ATP synthase, which plays a central role in the network as it is the most connected one in all the conditions and is coupled to reactions from almost all the pathways present in the cell metabolism.

Photosynthesis can work in a linear manner (that includes photosystem I and II) or in a cyclic manner (around photosystem I). These different routes produce different products: linear evolves ATP and NADPH and cyclic produces solely ATP. In our coupling network _PSI and _PSII (reactions for photosystem I and II excitation, respectively) are independently directionally coupled to ATP synthase. Thus, PSI and PSII are uncoupled between them, meaning that there is no fixed flux ratio, or fixed ratio values window, between the two reactions. This ratio can be calculated as a result of the photons that actually enter each photosystem (in fact, usually studies look to the *easier* to measure electrons that flow on each photosystem), but the potentialities of the network do not constraint the values of that ratio.

Additionally, neither PSI, PSII or ATP synthase are coupled to NADPH reduction in thylakoid membranes (reaction _1.18.1.2, Figure 3). This reaction is fully coupled to _FNR, reaction that links ferredoxin oxidation to NADPH reduction. The scarce couplings of _1.18.1.2 can be interpreted as that there are many reactions that reduce NADPH among the metabolism or that reduce NADH and then this is converted to NADPH.

4.4 Biofuels and flux coupling

Hydrogen production is fully coupled to NADPH formation as well as directionally coupled to different pathways linking to the metabolic potential of the cell, like carbon fixation through RuBisCO reaction, 1,3-diphosphateglycerate production in glycolysis and NADP metabolism. This indicates that those reactions may be bottlenecks for boosting the
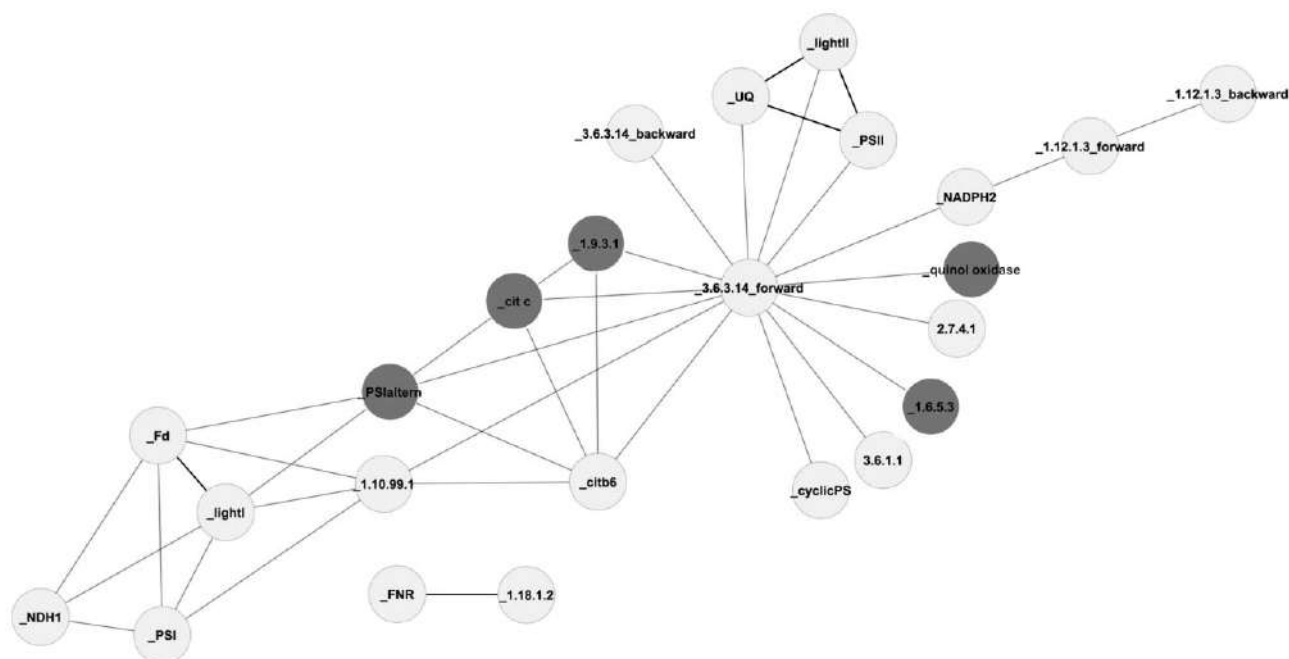
Figure 3. Flux coupling network of photosynthesis and oxidative phosphorylation. Photosynthesis is depicted in light gray and oxidative phosphorylation in dark gray. Directional couplings are fine edges and full couplings are indicated by thick edges.

H_2 production in this organism and should be considered as genetic targets when aiming at increased hydrogen production strains. Theoretical limit on the productivity of hydrogen was also probed by solving a series of linear optimization problems. Using autotrophic growth conditions, and fixing carbon and light feeds, H_2 evolution was studied as a function of minimal demand on biomass formation (Figure 4). Maximum hydrogen productivity was observed at specific growth rate 0.0448 h^{-1} with corresponding maximum H_2 production rate 0.085 mmol g_{DW}^{-1} h^{-1}.

Another interesting compound of socio-economic importance that can be a potential product of *Synechocystis* cell factory is ethanol. Ethanol production is directionally coupled to the pyruvate metabolism and to ATP synthase, as well as to some reactions from the central carbon metabolism, *e.g.* glycolysis and pentose phosphate pathway. Additionally, it is partially coupled to Calvin cycle under autotrophic condition. In order to increase the ethanol yield, the central carbon metabolism must be engineered –fluxes around pyruvate must be rerouted so as to increase alcohol production. Uptake fluxes of carbon and photons are also predicted targets for interesting genetic modifications. These findings will be useful in exploiting the photo-fermentative metabolism – so called *photanol* strategy [2]. As in case of hydrogen, theoretical productivity of ethanol was simulated by using FBA. Using au-

totrophic, mixotrophic and dark heterotrophic growth conditions, and fixing carbon and light feeds, theoretical ethanol production rate vs. growth was studied (Figure 5). Under autotrophy, maximum ethanol productivity was reached at specific growth rate of 0.0448 h^{-1} with 0.85 mmol g_{DW}^{-1} h^{-1} of ethanol production flux. Under DH, maximum ethanol productivity was reached at 0.0402 h^{-1} with 0.567 mmol g_{DW}^{-1} h^{-1} yield of ethanol. Values of LH are comparable to DH. Under mixotrophy, maximum ethanol productivity was reached at 0.0895 h^{-1} with production rate of 1.7 mmol g_{DW}^{-1} h^{-1}.

4.5 Reporter flux couplings

Reporter flux coupling pairs identified regulatory hubs among the coupling pairs. Most statistically significant pairs, across all analyses, were the ones connecting amino acid pathways with either central carbon metabolism, from which they drain precursors, or biological building blocks to which they are the source. Pairs in which RuBisCO was present were identified as major reporter coupling pairs in *dark to light* shift, leading the most statistically significant pairs. Photosynthesis is predominantly present in *light to dark* shift, even though pairs with reactions from central carbon metabolism to amino acids biosynthesis are most significant.
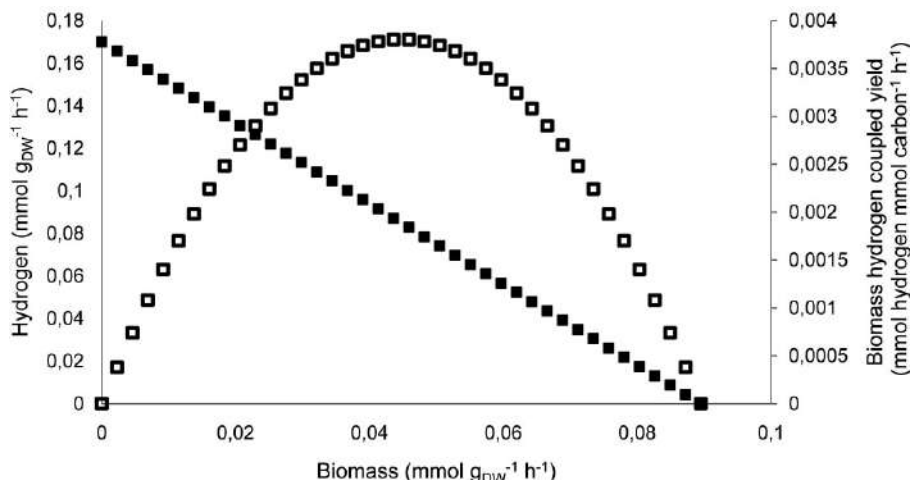
Figure 4. Theoretical productivity of hydrogen as per *i*Syn811. Productivity of hydrogen was studied by maximizing H_2 evolution at different minimal demand constraints on biomass formation under autotrophic growth condition. Full squares represent the value of hydrogen evolution, while empty squares represent biomass hydrogen coupled yield (a measure of productivity of hydrogen) – product of hydrogen and biomass production rates.
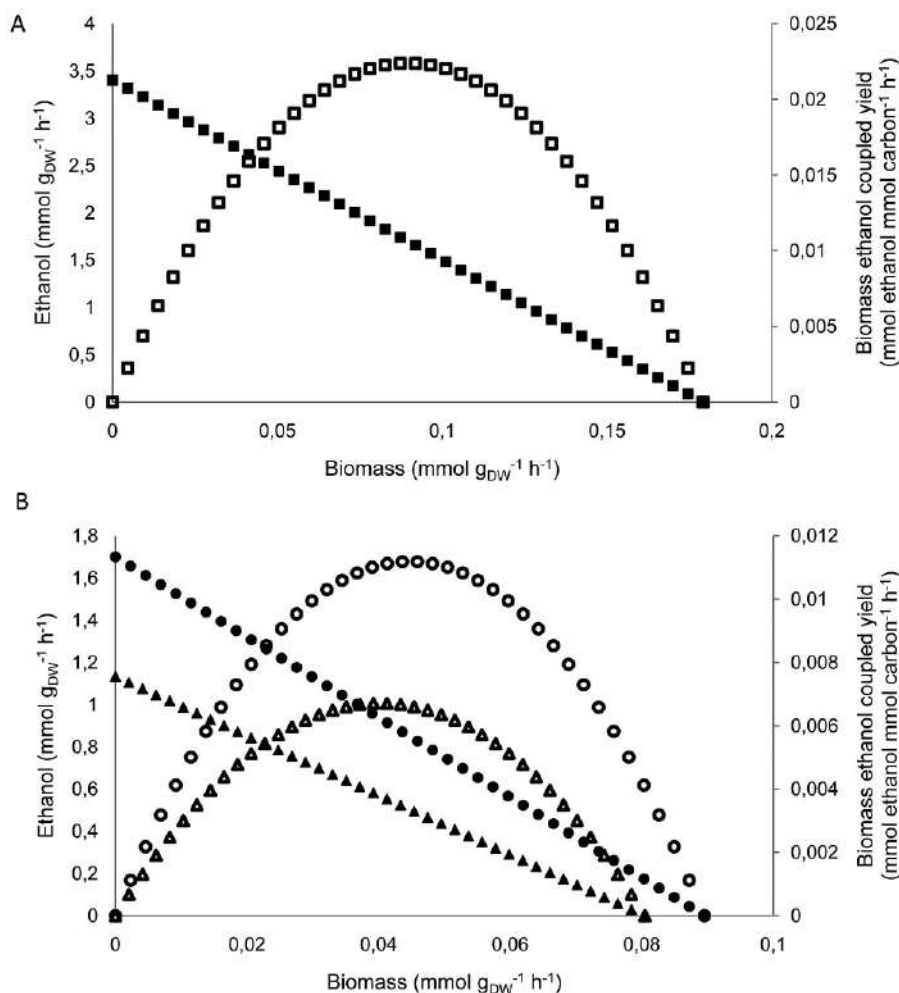
Figure 5. Theoretical productivity of ethanol as predicted by using *i*Syn811. Maximum ethanol production rate and biomass-product coupled yield are shown as a function of minimal demand on biomass formation under A) mixotrophic growth and B) autotrophic and heterotrophic growth. A) Full squares represent ethanol formation rate. Empty squares represent biomass ethanol coupled yield (a measure of productivity). B) Full circles represent the ethanol production rate as a function of growth under autotrophy, full triangles the same under DH. Empty circles represent biomass ethanol coupled yield under autotrophy. Empty triangles represent productivity of ethanol under dark heterotrophy.

Reporter flux coupling groups analysis identified higher-order regulatory hubs among the flux coupled reactions of the *Synechocystis* metabolic network. Some of the sets have been identified as reporters in all of the case studies: pyrimidine fully coupled set (*ful16*) (this set is the entrance of biomass to the pyrimidine nucleic acids: uracil, cytosine and thymine production) and photosynthesis and the oxidative phosphorylation cluster from *dir1* fully coupled set (this cluster makes up the reactions needed for the ATP and NADPH production). Additionally, NAD(P)H production fully coupled set (*ful3*) is notable as a *reporter coupling* in *dark to light* shift. From *light to dark* shift we can emphasize purine biosynthesis fully coupled set. Unfortunately, reporter features algorithm retrieved only scarce *reporter couplings* due to the incomplete information on the gene-reaction association: out of the 1275 unidirectional reactions of the *i*Syn811 model, 541 are found in some coupled set and, in turn, 416 of these reactions have one, or more, associated gene.

In summary, we have demonstrated the use of steady-state flux coupling analysis to gain insight into the metabolic potential and regulatory patterns of *Synechocystis* sp. PCC6803. The first steps of carbon acquisition and catabolism have been identified as the versatile center of the coupling network, having a stable core of biological building blocks built around. Hydrogen production is entangled to NADPH production and ethanol to the central carbon metabolism. From that couplings, potential bottlenecks for hydrogen and ethanol optimised strains production were identified. Finally, the first steps to pyrimidine biosynthesis and the photosynthesis and oxidative phosphorylation were identified as *reporter couplings*, regulatory hubs around which transcriptional changes are organized during environmental variability in light. This work will be useful for direct biotechnological applications as well as identifying misunderstanding in the model or finding weaknesses in knowledge like annotation and transcriptomic regulations. These results will be valuable for designing and implementing fine-tuned *Synechocystis* sp. PCC6803 strains and will thereby help toward building of an economically viable and environment-friendly biofuel production platform.

5 References

[1] Tamagnini, P., Leitao, E., Oliveira, P., Ferreira, D*., et al.*, Cyanobacterial hydrogenases: diversity, regulation and applications. *FEMS Microbiol. Rev.* 2007, *31*, 692–720.

[2] Angermayr, S. A., Hellingwerf, K. J., Lindblad, P., Teixeira de Mattos, M. J., Energy biotechnology with cyanobacteria. *Curr. Opin. Biotechnol.* 2009, *20*, 257–263.

[3] Kufryk, G. I., Sachet, M., Schmetterer, G., Vermaas, W. F., Transformation of the cyanobacterium Synechocystis sp. PCC 6803 as a tool for genetic mapping: optimization of efficiency. *FEMS Microbiol. Lett.* 2002, *206*, 215–219.

[4] Kaneko, T., Sato, S., Kotani, H., Tanaka, A*., et al.*, Sequence analysis of the genome of the unicellular cyanobacterium Synechocystis sp. strain PCC6803. II. Sequence determination of the entire genome and assignment of potential protein-coding regions. *DNA Res.* 1996, *3*, 109–136.

[5] Gutthann, F., Egert, M., Marques, A., Appel, J., Inhibition of respiration and nitrate assimilation enhances photohydrogen evolution under low oxygen concentrations in Synechocystis sp. PCC 6803. *Biochim. Biophys. Acta* 2007, *1767*, 161–169.

List of Supplementary files

Supplementary information, file 1 (Table 1): Table with all relevant constraints that change across the growth conditions used in this study.

Supplementary information, file 2: XLS file with description of coupled reactions in all four growth modes. Each Excel sheet can be easily converted to a SIF file to view the corresponding network in Cytoscape (http://www.cytoscape.org). Finally, an Excel sheet with the reactions differently coupled across different growth conditions is provided.

Supplementary information, file 3 (Table 2): Blocked reactions description.

Supplementary information, file 4: XLS file with the results of the *reporter coupling pairs* analysis

Supplementary information, **file 5:** XLS file listing the reporter coupling groups.

[6] Lindberg, P., Park, S., Melis, A., Engineering a platform for photosynthetic isoprene production in cyanobacteria, using Synechocystis as the model organism. *Metab. Eng.* 2010, *12*, 70–79.

[7] Wu, G. F., Wu, Q. Y., Shen, Z. Y., Accumulation of poly-beta-hydroxybutyrate in cyanobacterium Synechocystis sp. PCC6803. *Bioresour. Technol.* 2001, *76*, 85–90.

[8] Liu, X., Brune, D., Vermaas, W., Curtiss, R., 3rd, Production and secretion of fatty acids in genetically engineered cyanobacteria. *Proc. Natl. Acad. Sci. U S A* 2010.

[9] Patil, K. R., Akesson, M., Nielsen, J., Use of genome-scale microbial models for metabolic engineering. *Curr. Opin. Biotechnol.* 2004, *15*, 64–69.

[10] Barrett, C. L., Kim, T. Y., Kim, H. U., Palsson, B. O., Lee, S. Y., Systems biology as a foundation for genome-scale synthetic biology. *Curr. Opin. Biotechnol.* 2006, *17*, 488–492.

[11] Morange, M., A new revolution? The place of systems biology and synthetic biology in the history of biology. *EMBO Rep.* 2009, *10 Suppl 1*, S50–53.

[12] Shastri, A. A., Morgan, J. A., Flux balance analysis of photoautotrophic metabolism. *Biotechnol. Prog.* 2005, *21*, 1617–1626.

[13] Navarro, E., Montagud, A., Fernández de Córdoba, P., Urcheguía, J. F., Metabolic flux analysis of the hydrogen production potential in Synechocystis sp. PCC6803. *Int. J. Hydrogen Energy* 2009, *34*, 8828–8838.

[14] Montagud, A., Navarro, E., Fernández de Córdoba, P., Urcheguía, J. F., *et al.*, Reconstruction and analysis of genome-scale metabolic model of a photosynthetic bacterium. *BMC System Biology* 2010, *4*, 156.

[15] Burgard, A. P., Nikolaev, E. V., Schilling, C. H., Maranas, C. D., Flux coupling analysis of genome-scale metabolic network reconstructions. *Genome Res.* 2004, *14*, 301–312.

[16] Notebaart, R. A., Teusink, B., Siezen, R. J., Papp, B., Co-regulation of metabolic genes is better explained by flux coupling than by network distance. *PLoS Comput. Biol.* 2008, *4*, e26.

[17] Suthers, P. F., Chang, Y. J., Maranas, C. D., Improved computational performance of MFA using elementary metabolite units and flux coupling. *Metab. Eng.* 2010, *12*, 123–128.

[18] Oliveira, A. P., Patil, K. R., Nielsen, J., Architecture of transcriptional regulatory circuits is knitted over the topology of bio-molecular interaction networks. *BMC Syst. Biol.* 2008, *2*, 17.

[19] Patil, K. R., Nielsen, J., Uncovering transcriptional regulation of metabolism by using metabolic network topology. *Proc. Natl. Acad. Sci. U S A* 2005, *102*, 2685–2689.

[20] Karp, P. D., Paley, S. M., Krummenacker, M., Latendresse, M., *et al.*, Pathway Tools version 13.0: integrated software for pathway/genome informatics and systems biology. *Brief Bioinform* 2010, *11*, 40–79.

[21] Cvijovic, M., Olivares-Hernandez, R., Agren, R., Dahr, N., *et al.*, BioMet Toolbox: genome-wide analysis of metabolism. *Nucleic Acids Res.* 2010, *38*, w144–w149.

[22] Gill, R. T., Katsoulakis, E., Schmitt, W., Taroncher-Oldenburg, G., *et al.*, Genome-wide dynamic transcriptional profiling of the light-to-dark transition in Synechocystis sp. strain PCC 6803. *J. Bacteriol.* 2002, *184*, 3671–3681.

[23] Edwards, J. S., Palsson, B. O., Metabolic flux balance analysis and the in silico analysis of *Escherichia coli* K-12 gene deletions. *BMC Bioinformatics* 2000, *1*, 1.

[24] Forster, J., Famili, I., Fu, P., Palsson, B. O., Nielsen, J., Genome-scale reconstruction of the *Saccharomyces cerevisiae* metabolic network. *Genome Res.* 2003, *13*, 244–253.

[25] Bader, G. D., Hogue, C. W., An automated method for finding molecular complexes in large protein interaction networks. *BMC Bioinformatics* 2003, *4*, 2.

[26] Csete, M., Doyle, J., Bow ties, metabolism and disease. *Trends Biotechnol.* 2004, *22*, 446–450.

[27] Whitton, B. A., Potts, M., *The ecology of cyanobacteria: their diversity in time and space*, Kluwer Academic, Boston 2000.

REVIEW ARTICLE

Synechocystis sp. PCC6803 metabolic models for the enhanced production of hydrogen

Arnau Montagud[1,2], Daniel Gamermann[1,3], Pedro Fernández de Córdoba[1], and Javier F. Urchueguía[1]

[1]Instituto Universitario de Matemática Pura y Aplicada, Universitat Politècnica de València, Valencia, Spain, [2]Instituto Universitario de Medio Ambiente y Ciencia Marina, Universidad Católica de Valencia "San Vicente Mártir", Valencia, Spain, and [3]Cátedra Energesis de Tecnología Interdisciplinar, Universidad Católica de Valencia "San Vicente Mártir", Valencia, Spain

Abstract

In the present economy, difficulties to access energy sources are real drawbacks to maintain our current lifestyle. In fact, increasing interests have been gathered around efficient strategies to use energy sources that do not generate high CO_2 titers. Thus, science-funding agencies have invested more resources into research on hydrogen among other biofuels as interesting energy vectors. This article reviews present energy challenges and frames it into the present fuel usage landscape. Different strategies for hydrogen production are explained and evaluated. Focus is on biological hydrogen production; fermentation and photon-fuelled hydrogen production are compared. Mathematical models in biology can be used to assess, explore and design production strategies for industrially relevant metabolites, such as biofuels. We assess the diverse construction and uses of genome-scale metabolic models of cyanobacterium *Synechocystis* sp. PCC6803 to efficiently obtain biofuels. This organism has been studied as a potential photon-fuelled production platform for its ability to grow from carbon dioxide, water and photons, on simple culture media. Finally, we review studies that propose production strategies to weigh this organism's viability as a biofuel production platform. Overall, the work presented in this review unveils the industrial capabilities of cyanobacterium *Synechocystis* sp. PCC6803 to evolve interesting metabolites as a clean biofuel production platform.

Biofuels and biohydrogen

Today, 83% of the United States of America's energy mix (U.S. Energy Information Administration, 2011a) and 78% of Europe's (European Commission, 2011a) comes from carbon-rich fossil fuels: oil, natural gas and coal. With energy demand increasing worldwide, existing oil reserves could peak within 20 years (Zucchetto and National Research Council, 2006), followed by natural gas and coal sources. This limitation on the availability of fossil fuels does not come alone and energy dependence amongst countries as well as political turmoil in geographical areas with such fossil fuels reserves has compelled science-funding agencies to sponsor research into alternative energies. As it was outlined in the "Clean development mechanisms" of the "Kyoto Protocol" (United Nations, 1998), several alternatives of CO_2 emission-free energy production are already available, such as nuclear and renewable energy sources (Figures 1 and 2). Sadly, these solutions have been greatly developed in industrial and residential sectors, but not as much in transportation where energy is required to be in most cases in the form of a fuel. The transition from our dependence on oil for transportation

to a cleaner and more efficient energy source is an issue of great importance. In fact, studies show that oil consumption in the transportation sector accounts for up to 66% of the net oil consumption in the USA (U.S. Energy Information Administration, 2011b) with similar figures in Europe (European Commission, 2011b).

Biotechnology is a promising area in order to find a clean, wireless, transportation sector-friendly energy carrier. This area has gained importance in recent years due to a set of factors, such as consolidation of genome-scale sequencing, high-throughput techniques, increased applied focuses and multidisciplinary education programs. Several biotechnological candidates have been proposed to partially substitute oil as an energy demand. In fact, biofuels such as biodiesel or bioethanol seem to be in the short term suitable candidates to partially substitute the oil demand. They share distribution systems with conventional fuel and current engines that are compatible with them after some modifications (Atadashi et al., 2010; Wang et al., 2000). However, even if all the USA's corn and soybean production were dedicated to biofuels production, this would only meet 12% of gasoline and 6% diesel demand one (Hill et al., 2006).

Nevertheless, if we are to satisfy the increasing energy demand, producing energy with lower environmental impact, even more resources have to be invested in biotechnology and alternatives have to be found in the medium or long term.

Address for correspondence: Arnau Montagud, Instituto Universitario de Matemática Pura y Aplicada, Universitat Politècnica de València, Camí de Vera, s/n, València, Spain. Tel: 963879495. E-mail: armontag@mat.upv.es

RIGHTS LINK

Figure 1. Distribution of energy consumption in the transportation sector.   Data from USA and European countries members of OECD from *BP Review of World Energy* (BP p.l.c., 2011).
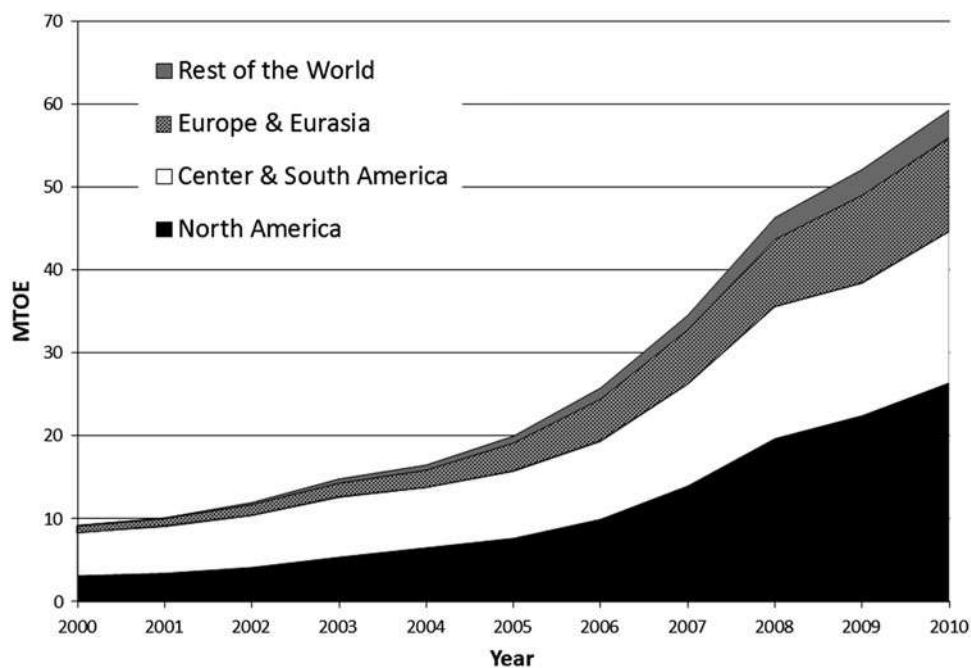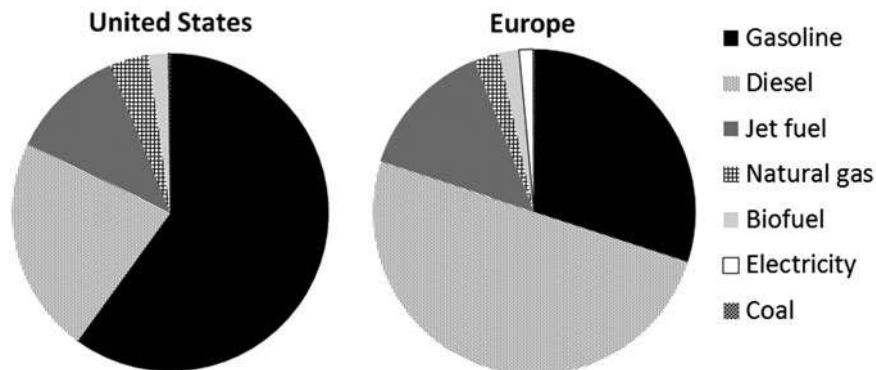
Figure 2. Biofuels production in millions of tonnes oil equivalent (MTOE). Data from USA and European countries members of OECD from *BP Review of World Energy* (BP p.l.c., 2011).

At this point, hydrogen appears as a promising future energy vector. It is relevant to all energy sectors, like transportation, residential and industrial (Momirlan & Veziroglu, 2005). Hydrogen can be produced from renewable sources and used in a wireless manner so it can provide storage options for base-load (geothermal), seasonal (hydroelectric) and intermittent (photovoltaic and wind) renewable resources. When combined with emerging decarbonization technologies, it can reduce the climate impact of continued fossil fuel utilization (Elam et al., 2003). Additionally, it has a clean combustion and an extraordinary energy density ($142\,MJ\,kg^{-1}$ for H_2 against $42\,MJ\,kg^{-1}$ for oil) which allows weight reduction per heat unit when compared to other biofuels.

USA and Europe are investing large amounts of resources on this clean alternative. In fact, the ''Committee on Alternatives and Strategies for Future Hydrogen Production and Use'' of the USA's National Research Council recommended in 2004 increased funding emphasis on ''Carbon dioxide-free energy technologies'', which includes fundamental research on hydrogen production by photobiological processes (Committee and National Research Council, 2004).

Reports set the horizon of a clean hydrogen-based economy in 2015 at the soonest, that is to start introducing production facilities, adapting distribution networks and developing novel engines. In spite of these efforts, the goal is to have a fully developed market by 2025 (United States Government, 2011). This is mainly due to two factors. One, the lack of competitiveness of fuel cell vehicles and hydrogen compared to conventional (e.g. gasoline and diesel) fuel vehicles and hybrid gasoline electric vehicles. Second, fuel cells costs are still a factor of 10–20 times too expensive, have short durability, and low energy efficiency for light-duty-vehicle applications (Committee and National Research Council, 2004). An additional technical problem is the fact that hydrogen gas is the lightest gas known in nature ($0.08988\,g\,L^{-1}$ at $0\,°C$ and $101.325\,kPa$), making it difficult to store large volumes of it.

Hydrogen is being produced currently at the industrial level, mainly by steam reforming natural gas (Das & Veziroglu, 2008). This process is costly efficient, but is neither renewable nor clean, as it has associated sulfur and CO_2 emissions. This process, as with most of the

hydrogen-producing processes from fossil fuels, generates approximately twice as many moles of CO_2 per hydrogen produced (Agrawal et al., 2007). Therefore, society would benefit if we could use renewable and clean sources to produce hydrogen. In order to reach that primary goal, several alternatives are under development.

- *Electrolysis from a renewable source of energy:*

Electrolysis using carbon-free electricity generated by energy sources like wind or solar is one of the simplest ways of producing hydrogen and is currently the only way to produce large quantities of hydrogen without emitting the traditionally undesirable by-products associated to fossil fuels. Wide use of this strategy remains a technological challenge and many research efforts are currently being carried out (Laguna-Bercero, 2012; Pregger et al., 2009). The main limiting factor is the overall electricity cost for its production from renewable sources (Department of Energy, 2007).

- *Reforming biomass and wastes:*

This efficient hydrogen-producing process can be achieved by three methods: gasification, pyrolysis/reforming and high-pressure water (Kroposki et al., 2006). It has been demonstrated that this is cost effective and is the most promising economic route for converting *syngas* into transportation fuels (Milne et al., 2002). Nevertheless, major limitations of this application are the availability of feedstock, the need of efficient and durable catalysts for gas conditioning and an efficient integration of processes.

- *Solar thermal water splitting:*

This generation process probably represents the most efficient way to produce hydrogen as solar energy is directly used to split water molecules (Greene et al., 2009; Perret, 2005). The main drawback of this technology is the requirement of very high temperatures (around 2500 °C), even though this need can be reduced using some additional chemical transformations that generates minimal residues. Currently, commercial plants of this kind are under development in order to make it costly efficient (Greene et al., 2009).

- *Photoelectrochemical water splitting:*

This strategy allows hydrogen production from light in a one-step process splitting water with an illuminated semiconductor immersed in an aqueous solution (Carty et al., 1981; Fujishima & Honda, 1972). The potential efficiency of this process is 10%–20% of the light irradiation on the semiconductor but a greater disadvantage is that the required combination of physical, chemical, structural and economic properties of the semiconductor is so restricted that no known material satisfies all of them in order to trigger industrial production (Department of Energy, 2007).

- *Photobiological water splitting:*

This biotechnological alternative is based on light absorption and charge separation reactions in the photosynthesis performed by some organisms, with an absorbance capacity of 40%–45% of solar energy (Das & Veziroglu, 2001, 2008). Such an efficiency is industrially relevant as theoretical estimations state that a cultivation surface of 500 km² would suffice to produce enough energy to fulfil the world's transportation needs (Turner et al., 2008). Recent work has obtained transient efficiencies of up to 13% by using a combination of processes (Melis, 2011). If this production

could be sustained in time, this hydrogen production strategy would be cost efficient. Therefore, the reliability of this method strongly depends on the future development of this area. A more extended review of the different biological hydrogen production strategies has been published (Hallenbeck & Benemann, 2002).

Biological hydrogen production by some microorganisms was first chartered in 1970 (Postgate, 1970). It involves two kinds of enzymes: hydrogenases and nitrogenases, involved in the nitrogen fixation metabolism (Tamagnini et al., 2002). The main bio-hydrogen production mechanisms can be grouped into two categories.

- *Fermentation:*

Many anaerobic organisms like *Thermotoga maritima* (Schröder et al., 1994), *Enterobacter aerogenes* (Fabiano & Perego, 2002), *Bacillus licheniformis* (Kalia et al., 1994), *Rhodopseudomonas palustris* P4 (Oh et al., 2002) or *Clostridium* sp. (Taguchi et al., 1996) are able to produce hydrogen as a by-product of the dark fermentation of sugars, amino acids and fatty acids. The process can be direct, anaerobically consuming sugars, or stepwise, firstly generating sugar complexes from other carbon sources like CO_2 and then fermenting them anaerobically. Fermentation has the advantage that it can use a wide range of substrates and that can be coupled to other industrial processes, like agricultural activities. This strategy is being successfully applied for industrial hydrogen production (Chou et al., 2008; Eriksen et al., 2010; Maniatis, 2010; Solazyme Inc., 2012).

However, this mechanism has two drawbacks that need to be addressed. The first is the cost of the substrates used as an energy source for hydrogen. The most energetically suitable sugar is glucose, but its cost is a limiting factor to be a cost-efficient alternative. Nevertheless, this problem can be tackled in the same way as it has been solved for ethanol production and extending suitable sources to agricultural residues like lignocelluloses. This could provide a sustainable feedstock, would reduce prices and would not divert stocks from the human food chain. The second problem is related to the stoichiometry of fermentation metabolism. Fermentation has a low efficiency in terms of hydrogen production from glucose. In fact, from a metabolic analysis of the reactions involved in the process each molecule of glucose can theoretically produce four molecules of hydrogen, while 2–3 molecules are produced under laboratory conditions (Thauer, 1976) even though higher yields have been reached by hyperthermophilic bacteria *Thermotoga maritima* (Schröder et al., 1994). This represents that, in terms of standard enthalpy of combustion, just 40% of the glucose energy input can be recovered in the form of hydrogen as a theoretical maximum, and only 20%–30% has been achieved experimentally. The rest of the energy is stored in cell's biomass, meaning growth of the organism, and other fermentation products such as acetic acid, alcohols and/or lactic acid.

- *Photon-fuelled hydrogen production:*

Photosynthetic organisms are able to use solar energy to make their own feedstock to live. Among them, cyanobacteria and some algae are able to use this energy to produce hydrogen as a transient by-product. The process of hydrogen production is based on the photosynthetic electron transport chain, which is shown in Figure 3. Schematically, the process
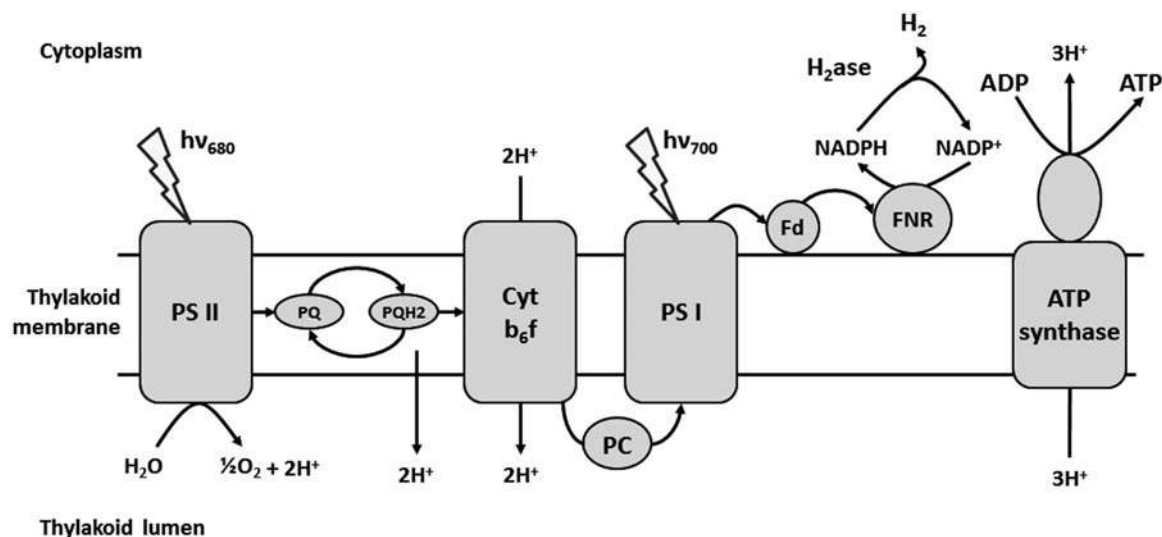
Figure 3. Photosynthetic electron transport chain. In cyanobacteria, photosynthetic transport chain share several enzymes with the respiratory transport chain (Figure 4), this fact allows the possibility of using electrons from glucose or other substrates in order to produce hydrogen. Abbreviations stand for: PS II, photosystem II; PQ, plastoquinone; PQH2, plastoquinol; cytochrome b_6f, cyt b_6f; PS I, photosystem I; Fd, ferredoxin and FNR, Ferredoxin-NADP+ reductase.

consists of the absorption of photons by the photosystem II (PSII), whose energy is used to split the water molecules into two protons and oxygen releasing two electrons to the electron transport chain. This electron transport chain leads, through a set of redox reactions, these electrons to the photosystem I (PSI) which can route them back through plastoquinone (PQ) into the *cyclic electron flow* or can drive the electrons to a NADPH dehydrogenase (FNR) into the *non-cyclic electron flow.* In several steps of the photosynthesis pathway, protons accumulate in the thylakoid lumen: in PSII water oxidation takes place in this lumen and protons are released. Also, in PQ oxidation and cytochrome *b6-f,* complex protons are pumped from the cytoplasm to the thylakoid lumen. From here, protons can be transported back to the cytoplasm, dissipating the proton gradient through ATP synthase, which uses this energy to phosphorylate ADP to ATP. The cyclic process generates a proton gradient (thus ATP) and the non-cyclic process generates proton gradient and NADPH reduction. Furthermore, depending on the cell requirements of NADPH (also known as redox potential of the cell) and ATP (major energy vector of the organism) the ratio of cyclic-to-non-cyclic photosynthesis is controlled by the cell metabolic regulation.

Cyanobacteria have a [Ni–Fe] hydrogenase, which produces hydrogen with electrons from NADPH (Tamagnini et al., 2002). Green algae commonly have a [Fe–Fe] hydrogenase, which is linked to a ferredoxin enzyme of PSI taking the electrons directly from the electron transport chain and producing hydrogen (Stripp et al., 2009a,b). Recently, there have been some efforts on heterologous hydrogenases' cloning in cyanobacteria. For instance, bacterial [Fe–Fe] hydrogenase from *Clostridium acetobutylicum* has been expressed in the cyanobacterium *Synechococcus elongatus* together with the necessary maturation systems and, under anoxic conditions, the resulting light-dependent H_2 evolution increased over 500 times compared to H_2 evolution from the endogenous [Ni–Fe] hydrogenase (Ducat et al., 2011a).

However, the main limitation in order to have cost-effective hydrogen production by photosynthesis is the fact that hydrogenases' activity is highly repressed by the oxygen, which is an inherent product of photosynthesis. Several studies (Barstow et al., 2011; Stapleton & Swartz, 2010) have attempted to solve this by trying to find a naturally-occurring oxygen-tolerant hydrogenase, like the one from *Ralstonia eutropha* H16 (Burgdorf et al., 2005), or to design a synthetic one and expressing it in cyanobacteria or green algae, as in many projects like BioModularH2 (2005). In nature, this problem has been addressed by some cyanobacteria in which the region where oxygen is produced and the one where hydrogen is generated are spatially separated. For instance, in *Nostoc*, a filamentous cyanobacteria genus made of two types of cells (vegetatives and heterocysts), hydrogen is produced as a residual product of nitrogen fixation by a nitrogenase in the heterocyst. In order to use this cyanobacterium for industrial use, the main problem is that efficiencies are limited as nitrogen fixation is energetically expensive. Nevertheless, a review of studies in this area can be found in Lopes Pinto et al. (2002).

Additional to the oxygen hindrance, efforts have been oriented to increase the electron flow that feeds the hydrogenase, circumventing NADPH formation. Cournac et al. (2004) found one of the best hydrogen producers in *Synechocystis* sp. PCC 6803 by knocking out the NADPH-dehydrogenase complex. Also, in the work from Ducat et al. (2011a) in which they improved the hydrogen production in *Synechococcus elongatus,* the linking of H_2 production to a heterologous ferredoxin bypassing the production of NADPH, considerably increased the production of a *Clostridium acetobutylicum*'s [Fe–Fe] hydrogenase.

An alternative to this problem has been to temporally separate hydrogen and oxygen production. One of the most successful strategies following this alternative has been developed by Melis et al. (2000). Their strategy is based on sulfur deprivation of algae, in such a way that the organism will not be able to normally repair the structural units of
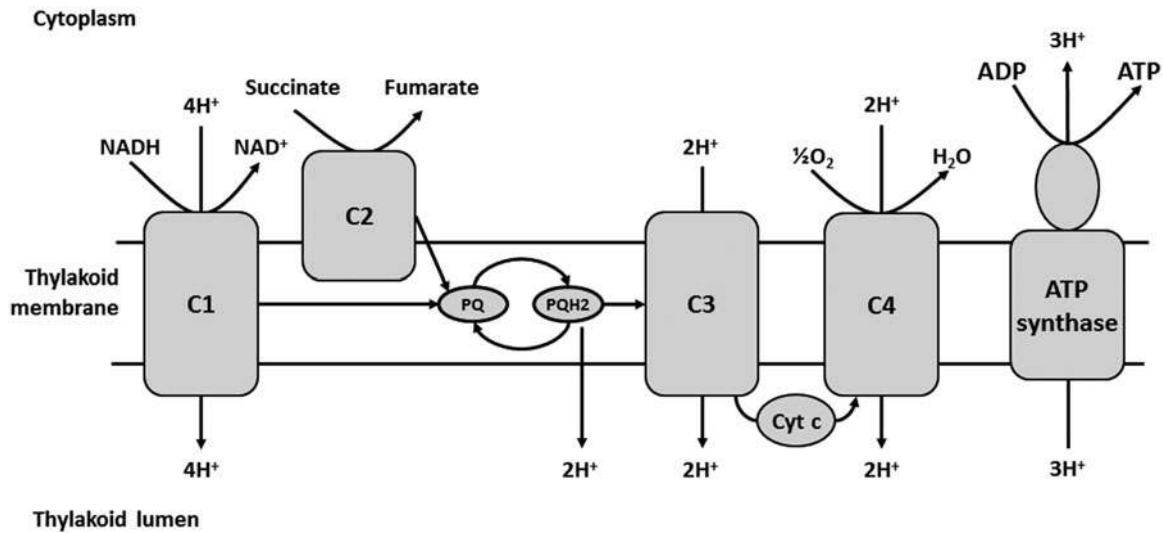
Figure 4. Oxidative phosphorylation.   In cyanobacteria, photosynthetic electron transport chain share several enzymes with the respiratory transport chain, such as *PQ* and *cyt b₆f* that performs respiratory complex 3 functions. Other abbreviations are: C1, respiratory complex I or NADH dehydrogenase; C2, respiratory complex II or succinate dehydrogenase; C3, respiratory complex III and C4, respiratory complex IV or cytochrome *c* oxidase.

photosystem II, namely D1, which is a protein that requires a fast turnover of approximately 30 min (Melis, 1991; Melis et al., 2000; Yokthongwattana & Melis, 2008). This effect produces a decrease of water splitting, and, thus, a reduction in the O_2 production associated to photosynthesis to a level that is lower than (or, at least, much closer to) the oxygen consumed by the respiration system, the oxidative phosphorylation (Figure 4). This mechanism is able to produce an anaerobic environment, which activates the hydrogenase enzyme producing hydrogen during a relatively long time span if we are to compare it with previous results. This mechanism, however, relies on the availability of a substrate, such as succinate, NADH, acetate and the like, to be able to reduce the oxygen produced by photosynthesis and provide electrons for hydrogen generation.

There is another possibility consisting on a combination of both basic strategies, called *photofermentation*. In this alternative, a co-cultivation of different organisms is designed so that the residues from the fermentation of one organism are used to feed photosynthetic bacteria in anaerobic media, resulting in continuous hydrogen production. The co-cultivation of green algae *Chlamydomonas reinhardtii* and photosynthetic purple bacteria *Rhodospirillum rubrum* are possible (Melis & Melnicki, 2006). One could consider that a sulfur deprivation strategy is closer in design to photo-fermentation, reducing O_2 production with photosynthesis to a closer level to O_2 consumption with respiration (Melis et al., 2000). These approaches would allow a continuous, or at least sustained, hydrogen production, as opposed to a stepwise coupling of biomass generation and hydrogen production, which would come from a more classical fermentation strategy.

Microbial pathway engineering has been applied to industrial processes for the biosynthesis of products of high economic value, which is not yet the case for hydrogen. Mathematical modeling of hydrogen metabolism has therefore been important to evaluate maximum theoretical product yield and to understand the interactions between biochemical energy, carbon fixation and assimilation pathways from a system-wide perspective, as will be explained in the following sections. Hopefully, these efforts will pave the way to a hydrogen-related pathway microbial engineering.

Systems biology, metabolic models and fluxes

Systems biology is the scientific area of biology that tries to exploit, gather, organize and, finally, understand as much information as possible from a given biological system (Sauer et al., 2007; Snoep & Westerhoff, 2005). Systems biology prefers all-inclusive explanations rather than local knowledge (Kitano, 2002; Palsson, 2000) allowing researchers to understand metabolic physiology quantitatively. This allows, among other goals, the design and optimization of biofuel-production bioprocesses using mathematical models. A model is a simplified description, especially a mathematical one, of a system or process, to assist calculations and predictions (Soanes & Stevenson, 2010). This simplification is achieved defining relevant factors that will be included and others that will be de-emphasized. The criteria for selecting factors are chosen in accordance to the purpose of the model, so that different purposes will need different models.

Metabolism of an organism can be modeled into a network of metabolites and enzymes. This should integrate all biochemical reactions for which we have proof and/or evidence of presence in the desired cell. This information can be retrieved from different databases, genomic annotations and literature surveys. First studies (Fell & Small, 1986; Mavrovouniotis et al., 1992; Savinell & Palsson, 1992a) did not take into account all reactions in the metabolism, mostly because in the previous years of intense genome sequencing having a whole genome sequenced was very rare. This caused researchers to denote them as *genome-scale metabolic models* when all the reactions from a genome annotation were included in a model. Additionally, the advent of metabolic studies of *Escherichia coli* (Varma & Palsson, 1993a,b), *Haemophilus influenzae* Rd (Edwards & Palsson, 1999) and
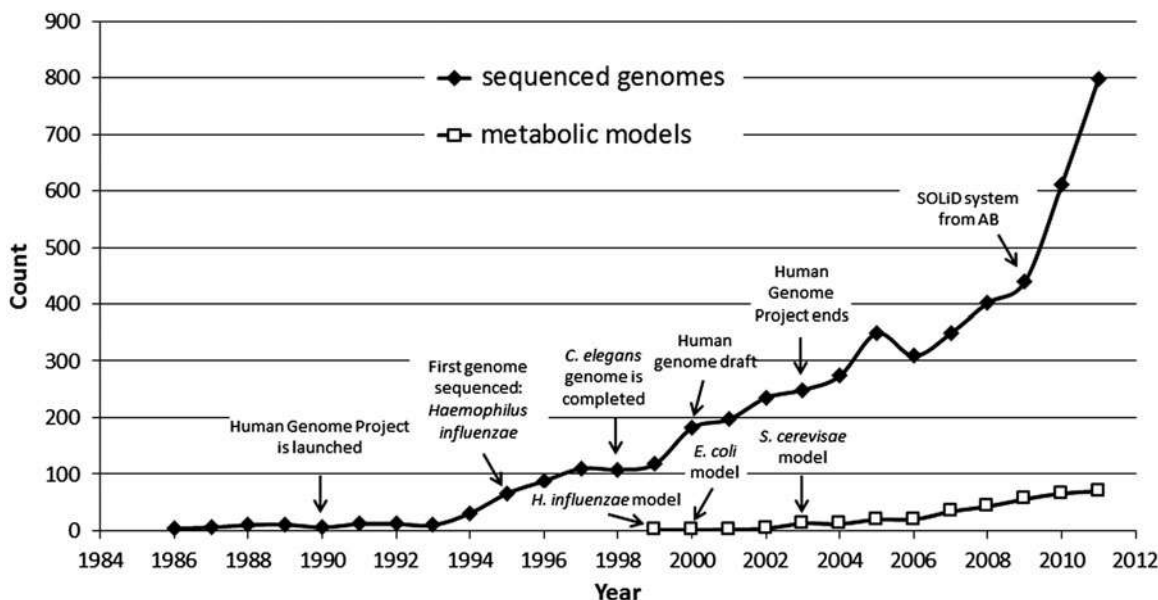
Figure 5. Publications of sequenced genomes and publications of genome-scale metabolic models.   Hits count in Scopus database of terms ''genome sequencing'' and ''genome-scale metabolic model OR network''. Major milestones are depicted. Note that between 2008 and end of 2011 genome sequencing costs per megabase of DNA dropped 1000 times (Wetterstrand, 2012). For a complete review, see Metzker (2010).

Saccharomyces cerevisiae (Förster et al., 2003) as well as the dissemination of *genome-sequencing projects* (and the huge cut on sequencing prices) established a context where it was feasible to build a genome-scale metabolic model of a desired organism (Figure 5).

A proper metabolic reconstruction project usually starts with the annotated genome. This information should be processed collating all reactions that are documented and additional experimental evidences on this organism. For an instructive discussion of this, see Förster et al. (2003). This draft has to be iteratively corrected with information from several databases, experiments, publications and from the study of the network in order to avoid the presence of false positive (and false negative) reactions. Recently, some studies have described this correction process in detail, trying to establish a common protocol (Feist et al., 2009; Thiele & Palsson, 2010). This process concludes with a network of metabolites and enzymes that encode biochemical reactions taking place within the cell. Researchers differentiate between internal fluxes as reactions occurring within cells and exchange fluxes as exchanges between cells and their environment (like drains of substrates and the formation of products). It is important to gather information on these exchange fluxes, which act as boundary parameters, in order to be able to model this set of reactions. Therefore, the physiological requirements, under which there is relevant growth of the organism, need to be gathered. This information usually comes from deep diving into the *bibliomic information* on this organism. That is, searching for experiments where growth substrates are controlled and, ideally, where the cell's products are measured.

Once the metabolic model is curated, this network can be the departing point of several other studies such as: network connectivity (Alon, 2003), comparative evolutionary studies to find patterns among organisms (Milo et al., 2002), phenotypic phase plane analyses (Reed et al., 2003), strain improvement (gene deletions and additions) (Famili et al.,

2003), network robustness studies (Stelling et al., 2002), evaluation of regulatory constraints (Patil & Nielsen, 2005), and reaction flux analysis and variability (Burgard et al., 2004).

In order to design and understand mutant strains with increased production of an industrially-interesting metabolite, researchers are interested in simulating the organism's metabolic behavior, which is to know each reaction's flux. The set of flux values, also defined as flux vector, characterizes the metabolic state of cells, i.e. the metabolism's behavior at a given time. Metabolic flux is a fundamental determinant of cell physiology and the most critical parameter of a metabolic pathway (Orth et al., 2010; Stephanopoulos & Stafford, 2002). Accurate quantification of pathway fluxes is therefore an important goal in metabolic engineering, especially where the aim is to convert as much substrate as possible to the desired metabolic product via strain improvement.

In order to have a genome-scale metabolic model able to simulate flux landscapes, attention has been drawn on constraint-based stoichiometric models (Llaneras & Picó, 2008). These models can obtain complete flux information making a set of assumptions. One of the algorithms researchers work with constraint-based stoichiometric models is the flux balance analysis (FBA), described hereafter.

Constraint-based stoichiometric description of metabolism is not new. It dates from 1986 (Fell & Small, 1986) and 1988 (Clarke, 1988), and peaked in the mid-1990s (Mavrovouniotis et al., 1992; Savinell & Palsson, 1992a,b; Schuster & Schuster, 1993; Stephanopoulos et al., 1998; Varma et al., 1993a,b; Varma & Palsson, 1993a,b, 1994a), when several studies paved the way to describe metabolic flux distributions and cell growth. This approach has yielded accurate and valuable information about how microbial cells utilize their metabolic fluxes and optimize their growth rates. These initiatives have helped researchers gain information about metabolic physiology of the culture in a quantitative manner

(Bonarius et al., 1997; Schilling et al., 1999; Stephanopoulos et al., 1998; Varma & Palsson, 1994b).

Flux balance analysis (FBA) is a widely used approach for studying biochemical networks, in particular the genome-scale metabolic network reconstructions. FBA retrieves information on reactions' fluxes and is, thus, very insightful in locating pathways and reactions where flux has changed upon genetic or environmental variation. Hence, it is a valuable tool to study flux landscapes. FBA assumes steady-state dynamics of intracellular reactions, uses knowledge of biological constraints, mainly of exchange reactions, and optimizes biomass formation rates, which is directly related to the growth of the modeled organism (Orth et al., 2010; Stephanopoulos et al., 1998). Nowadays, there are a number of software tools that ease the work with this algorithm (Cvijovic et al., 2010; Gamermann et al., 2012; Latendresse et al., 2012; Patil et al., 2005; Rocha et al., 2010; Schellenberger et al., 2011).

Furthermore, a study of flux landscapes is only one of the several applications of genome-scale metabolic models. Other uses include flux capability analysis (Burgard et al., 2004), media composition optimization (Diamant et al., 2009) and studies of environmental and genetic variations (Segrè et al., 2002). Complete reviews of those applications can be found elsewhere (Nookaew et al., 2011; Patil et al., 2004).

Metabolic models of *Synechocystis* sp. PCC6803

Cyanobacterium *Synechocystis* sp. PCC6803 was the first strain sampled in a freshwater lake in California, USA, in 1968 and is part of Pasteur Culture Collection (Gugger and Biological Resource Center of Institut Pasteur, 2011; Rippka et al., 1979; Stanier et al., 1971). Cyanobacteria are commonly accepted to have played a crucial role in the Precambrian phase by contributing oxygen to the atmosphere (Schopf, 2000). This strain of a somewhat diverse genus (Swingley & Blankenship, 2008) has been a good candidate for biotechnology uses and molecular biology studies not only for its ability to be naturally transformed by exogenous DNA (Kufryk et al., 2002), but also for its ability to grow photoautotrophically (out of light and CO_2) or due to its potential as a hydrogen producer (Houchins, 1984; Tamagnini et al., 2007), among other reasons. Interestingly, cyanobacteria are held to be the evolutionary ancestors of chloroplasts under the endosymbiont hypothesis (Douglas, 1998; Raven & Allen, 2003) and since these organisms are believed to be the ones that changed the ancient anoxygenic environment to oxygenic by means of photosynthesis (Kim et al., 2008; Schopf, 2000). Many scientists have also used cyanobacteria as an ideal model organism to study adaptation to various abiotic environmental conditions (Douglas, 1998).

Studies on this organism had a boost when molecular tools started to be developed for it (Houmard & Tandeau de Marsac, 1988; Thiel, 1994). Since then, *Synechocystis* sp. PCC6803 has become a cyanobacterial model organism. At present, there is probably no other cyanobacterium that has been investigated in such detail, making it an interesting organism for biotechnological applications (Gutthann et al., 2007), such as heterologous production of metabolites like isoprene (Lindberg et al., 2010), poly-beta-hydroxybutyrate

(Wu et al., 2001), alcohols (Angermayr et al., 2009), bio-hydrogen (Tamagnini et al., 2007) and other biofuels (Liu et al., 2010). *Synechocystis* sp. PCC6803 is consequently an attractive candidate for developing a clean and sustainable platform for biotechnological processes aimed at value-added product formation (Ducat et al., 2011b).

The *Synechocystis* sp. PCC6803 genome was sequenced and annotated in 1995 (Kaneko et al., 1995, 1996). Genome-wide transcriptional microarrays were developed in 2001 (Hihara et al., 2001; Suzuki et al., 2001) and studies have been published since then using this transcriptomic technique (Foster et al., 2007; Gill et al., 2002; Hihara et al., 2003; Huang et al., 2002; Hübschmann et al., 2005; Kanesaki et al., 2002; Schmitt & Stephanopoulos, 2003; Singh et al., 2003, 2009; Summerfield & Sherman, 2008; Suzuki et al., 2006; Wang et al., 2004; Yamaguchi et al., 2002; Zhang et al., 2008). Finally, and following the work of pioneering metabolic studies on *Haemophilus influenzae* Rd (Edwards & Palsson, 1999), *Escherichia coli* (Edwards & Palsson, 2000) and *Saccharomyces cerevisiae* (Förster et al., 2003), several groups have developed metabolic models for this organism that are described below.

These metabolic models have been used for several goals; particularly, database building, growth simulation and production yield evaluation. They have broadened the knowledge on *Synechocystis* sp. PCC6803 metabolism and have helped researchers focus on this organism's potential.

Synechocystis sp. PCC6803 metabolic models are hereby gathered and described. We have classified the models between *genome-scale metabolic models* and *central carbon metabolic models*:

(a) *Genome-scale metabolic models* are the ones that:
    (1) include all reactions annotated in the genome and
    (2) incorporate a biomass equation that encompasses all building blocks in the cell metabolism.
(b) *Central carbon metabolic models* are the ones that:
    (1) include reactions from glycolysis, tricarboxylic acid cycle and pentose phosphate pathway and, in some cases, an additional set of reactions that connect some metabolites to amino acids and/or
    (2) a biomass equation without all building blocks.

We have described all metabolic models published to this date on this cyanobacterium and outlined their characteristics, which are also depicted in Table 1. For further details, refer to the corresponding paper.

● *Yang et al. central model (2002b):*

The seminal work published in 2002 was the first time a metabolic model was developed for *Synechocystis* sp. PCC6803. The authors present results of NMR and GC-MS analysis of a cultivation fed with 13 C-glucose that were used to build the model. Researchers build a metabolic network and simulated it under heterotrophic and mixotrophic growth conditions. Photosynthesis (only working under mixotrophy) was represented as one consolidated reaction. The authors present analyses on C_1 metabolism, PEP carboxylase and malic enzyme and energy metabolism. This model includes 20 reactions and 15 metabolites and was used as a central-carbon scaffold for transcriptomic, metabolomic and fluxomic data produced by the same group (Yang et al., 2002a,c).

Table 1. Comparison of *Synechocystis* sp. PCC6803 metabolic models.

Metabolic models	Genome-scale or central	Genes	Reactions	Metabolites	Growth conditions	Compartments	Other characteristics
Yang et al. (2002a,b,c)	Central	20	20	15	Heterotrophy, mixotrophy	Cytoplasm	Integration of transcriptomic and fluxomic
Shastri & Morgan (2005)	Central	70	70 + 23	50	Autotrophy, heterotrophy, mixotrophy	Cytoplasm, extracellular	Use of biomass equation as objective function
Kun et al. (2008)	Genome-scale	–	916	879	Autotrophy, heterotrophy	Cytoplasm, extracellular	Identify autocatalytic components
Fu (2008)	Central	633	831	704	Autotrophy, heterotrophy, mixotrophy	Cytoplasm, extracellular	Metabolic phenotypic phase planes to study usage of substrates
Navarro et al. (2009)	Central	90	90	56	Autotrophy, anoxia, heterotrophy, mixotrophy	Cytoplasm, extracellular	Strategies for improved biohydrogen
Knoop et al. (2010)	Genome-scale	337	380	291	Autotrophy, heterotrophy, mixotrophy	Cytoplasm, extracellular	Insights into biomass' synthesis routes and photorespiration
Montagud et al. (2010)	Genome-scale	669	1045	790	Autotrophy, heterotrophy, mixotrophy, photoheterotrophy	Cytoplasm, extracellular, thylakoid	Identification of metabolic regulatory hubs, environmental and genetic perturbations, strategies for improved succinate
Montagud et al. (2011)	Genome-scale	811	1245	922	Autotrophy, heterotrophy, mixotrophy, photoheterotrophy	Cytoplasm, extracellular, thylakoid	Flux coupling analysis, blocked reactions identification, reporter features study
Yoshikawa et al. (2011)	Genome-scale	376	493	465	Autotrophy, heterotrophy, mixotrophy	Cytoplasm, extracellular, thylakoid	Evaluation of ethanol production
Nogales et al. (2012)	Genome-scale	678	863	795	Autotrophy, heterotrophy, mixotrophy	Cytoplasm, thylakoid, periplasm, extracellular	Energy buffers identified in electron flow pathways, photorespiration is found as an adaptive system, genetic perturbations
Saha et al. (2012)	Genome-scale	731	1156	996	Heterotrophy, mixotrophy, photoheterotrophy	Carboxysome, cytoplasm, periplasm, thylakoid	Emphasis on lipid biosynthesis, model predictions versus gene essentiality data, novel amino acids and pigments biomass quantification

- *Shastri and Morgan central model (2005):*

This model, published in 2005, extended the simulations to autotrophic growth and compared their results to the ones reported by Yang et al. (2002c). Authors use modeling assumptions that have been considered by many following reports like: maximum uptake rates, maintenance requirements, selection of objective function, two-step optimization strategy and biomass composition. Metabolic flux topologies under different environments are presented, and the authors focus their analysis on the role of a variety of pathways and reactions, such as glyoxylate shunt, transhydrogenase, cofactor balances, cyclic and non-cyclic photosynthesis. The reaction connecting the tricarboxylic acid cycle (oxoglutarate dehydrogenase complex) is included in the simulation and its effects on biomass generation are evaluated. Interestingly, six years later Zhang & Bryant (2011) shed light on the completeness of tricarboxylic acid cycle in the cyanobacterium *Synechococcus* sp. PCC 7002 through a novel 2-oxoglutarate decarboxylase and succinic semialdehyde dehydrogenase. A list of reactions is presented that connects amino acid production to central carbon metabolites and photosynthesis is represented as a single reaction. This model includes 70 reactions (plus 23 for amino acids' formation reactions) and 50 metabolites.

- *Kun et al. genome-scale model (2008):*

This model, published in 2008, has its main sources on the automated reconstruction generated from the annotated genome and deposited in the MetaCyc database (Caspi et al., 2006; Krieger et al., 2004) and on the previous Shastri and Morgan central model (2005). Authors focused their study on a series of autocatalytic molecules, not on the analysis of flux behavior or the integration of different levels of biological information. They find that metabolic replicators are apparently common and potentially both are of universal and ancestral importance in biotechnological endeavors. This model includes 916 reactions and 879 metabolites.

- *Fu central model (2008):*

Published in August 2008, this model claims to be genome-scale but fails in having a proper biomass equation that includes all molecular building blocks in the cell metabolism. Its list of reactions are from all the genome, meaning not only from a selected set of pathways, but this list is uncurated, featuring key reactions (like the reactions for the generation of NADPH and ATP, reaction 732 in Supplementary materials) and missing transport reactions. This model is not suitable for genome-scale simulations due to a lack of proper biomass equations, as a drain of all cellular building blocks. This research takes the biomass equation formulation from Shastri & Morgan (2005), so simulation results do not give more information than the ones already published. Despite that, phenotypic phase planes were performed to study usage of substrates to optimize cell growth and ethanol production strategies were assessed. This model has 831 reactions and 704 metabolites.

- *Navarro et al. central model (2009):*

Published in 2009, this central carbon metabolic model simulates all three growth conditions on the same metabolic network. Results were compared to that of Yang et al. (2002c) and Shastri & Morgan (2005). Studies are focused on oxygen evolution, carbon assimilation efficiency and growth

simulation. The model was used to determine maximum hydrogen production titers and to propose improved hydrogen producing strategies, with a special insight into anoxic conditions' benefits. The authors found potential improvements in flux distribution and oxygen evolution, this is of greater importance in a photosynthetic bacterium that has an oxygen-tolerant hydrogenase. This model has 90 reactions and 56 metabolites.

- *Knoop et al. genome-scale model (2010):*

Published in 2010, this model reconstructs *Synechocystis* sp. PCC6803 mainly from annotation files and KEGG database information, even though a selected core set of reactions is required to produce biomass. The authors studied flux behavior under different growth conditions using the FBA algorithm with special focus on the objective function biomass and its synthesis routes. Gene and nutrient regime shifts, from glycogen-utilizing dark metabolism to phototrophic growth, are also analyzed. Interestingly, the authors shed light on the function of the oxidative reaction of the RuBisCO enzyme under photorespiration. This model has 380 reactions and 291 metabolic compounds.

- *Montagud et al. genome-scale model (2010):*

The genome-scale metabolic model published in 2010 was named *i*Syn669. This metabolic model was obtained from public databases and literature in order to be able to simulate all possible growth modes under which this organism can grow. A detailed biomass equation which encompassed all elementary building blocks and a detailed stoichiometric representation of photosynthesis was published in a *Synechocystis* metabolic model. *i*Syn669 was used to perform flux balance analysis of one genome-scale metabolic model under four growth conditions. This allowed the authors to study flux adjustments between these different conditions in order to gain insights into flux adaptation when the organism shifts from one growth mode to another. Additionally, environmental and genetic perturbations were also studied to define an optimal succinate production strategy. Essential genes were analyzed and transcription data integration was achieved with the Reporter Features algorithm (Oliveira et al., 2008) with transcriptomics data in a light regime shift (Gill et al., 2002). This model has 882 reactions (1045 unidirectional) and 790 metabolites.

- *Montagud et al. genome-scale model (2011):*

The genome-scale metabolic model published in 2011 is named *i*Syn811 in this review. An update of *i*Syn669, increased information stemmed from enlarging the reaction set with isoenzymes and complexes as well as reactions that were disconnected to the rest of the network. Major changes were also made on the gene-reaction correspondence. Blocked reactions were identified and compared to *Escherichia coli* and *Saccharomyces cerevisiae* values. Over this model, an interesting study of flux capabilities under the main three growth conditions was studied and applied, termed *flux coupling analysis* (Burgard et al., 2004). The Reporter features algorithm (Oliveira et al., 2008) was applied to flux couplings' transcriptomics in a light regime shift (Gill et al., 2002). Biofuels productivity analysis was also performed, focusing on hydrogen and ethanol. This model has 976 reactions (1245 unidirectional) and 922 metabolites.

- *Yoshikawa et al. genome-scale model (2011):*

This work presents a genome-scale metabolic model of *Synechocystis* sp. PCC6803 published in 2011. The authors compare their model with that of Knoop et al. (2010) and with *i*Syn669 (Montagud et al., 2010) as to their accuracy to experimental fluxes obtained by Yang et al. (2002b) under heterotrophy and mixotrophy. Production of ethanol by *Synechocystis* sp. PCC6803 was evaluated, which enabled to a quantitative estimate of how its productivity depends on the environmental conditions, namely nitrate and photons uptake rates. This model has 493 reactions and 465 metabolites.

- *Nogales et al. genome-scale model (2012):*

This work presents yet another genome-scale metabolic model of *Synechocystis* sp. PCC6803 published in 2012. In their study, they focus on the flux analysis of photosynthesis unveiling the use of alternative electron flow pathways as energy buffers and photorespiration as a process of high-light acclimation. The authors classify two main states of the photosynthetic apparatus: a carbon-limited state and a light-limited state. Furthermore, they make predictions of possible mutants that would have a given phenotype and find some of them in published papers. This reconstruction had a follow-up publication where the authors studied metabolic features that affected biotechnological capabilities of this cyanobacteria (Nogales et al., 2013). This model includes 863 reactions and 795 metabolites.

- *Saha et al. genome-scale model (2012):*

This work presents a genome-scale metabolic model of *Synechocystis* sp. PCC6803, termed as iSyn731, published in 2012. Published models of *Synechocystis* sp. PCC6803 and *Cyanothece* sp. ATCC 51142 and drew comparisons among them and to previous data (Knoop et al., 2010; Nogales et al., 2012; Vu et al., 2012). All reactions were elementally and charge balanced and were localized into four different intracellular compartments. Biomass descriptions are derived based on experimental measurements, with new experimental data on amino acids and pigments. The authors identify all thermodynamically infeasible loops. Comparisons of model predictions against gene essentiality data picture the iSyn731 model as a very sensitive model for deletion prediction. The model contains 1156 reactions and 996 metabolites.

- *Other cyanobacteria metabolic models:*

Together with *Synechocystis* sp. PCC6803, other organisms have been targets for metabolic model reconstructions, such as *Synechococcus* sp. PCC 7002 (Hamilton & Reed, 2012), *Cyanothece* sp. ATCC 51142 (Saha et al., 2012; Vu et al., 2012), *Spirulina platensis* C1 (Klanchui et al., 2012) and new tools have reconstructed 36 cyanobacteria metabolic models for which genomic data are available (Vitkin & Shlomi, 2012).

Synechocystis sp. PCC6803 as a production platform

The *Synechocystis* sp. PCC6803 metabolic model can be used to study flux capabilities and potentials, as well as to study possible mutants to have an enhanced production of a given metabolite. The above-mentioned studies have demonstrated the utilization of FBA to estimate metabolic behavior. One of the bottlenecks of these simulations is the need to determine the several biological constraints of substrate usage and

by-products generation. Nonetheless, the amount of information generated in this study, that only needs the network configuration and these constraint-based flux simulations, is considerably higher than the input information required.

As for mutant studies, in various works (Ducat et al., 2011b; Montagud et al., 2010, 2011; Nogales et al., 2013), sets of deletion mutants have been identified with increased production of succinate, ethanol and hydrogen, among other metabolites (Ducat et al., 2011b). This work presents design strategies that range from the more classical ones, such as closing flux diverging routes from objective metabolite or the triple deletion proposal for improved production of ethanol, to the more synthetic biology ones like improved succinate production by means of the design of a new pyruvate kinase protein specific for an ATP cofactor.

Furthermore, theoretical maxima of production for ethanol and hydrogen have been identified. These values are far from what is currently produced in the literature. For hydrogen, an estimated specific growth rate of $0.0448\,h^{-1}$ with a corresponding maximum H_2 production rate of $0.085\,\mathrm{mmol\,gDW^{-1}\,h^{-1}}$ (Montagud et al., 2011) can be compared to typical $3.149 \times 10^{-4}\,\mathrm{mmol\,g\,DW^{-1}\,h^{-1}}$ (Baebprasert et al., 2011). Additionally, in Table 2, retrieved from Navarro et al. (2009), one can gather valuable information of hydrogen production with different methods. As for ethanol, Joule Unlimited has identified a genetically engineered strain of *Synechocystis* sp. PCC6803 in the patent literature to secrete ethanol at a rate of $1\,\mathrm{mg\,L^{-1}\,h^{-1}}$ ($2.171 \times 10^{-2}\,\mathrm{mmol\,gDW^{-1}\,h^{-1}}$) (Devroe et al., 2010), whereas the academic literature reports typical levels of $0.2\,\mathrm{mg\,L^{-1}\,day^{-1}}$ ($6.029 \times 10^{-4}\,\mathrm{mmol\,gDW^{-1}\,h^{-1}}$) (Deng & Coleman, 1999). Yoshikawa et al. (2011) estimated a theoretical maximum of ethanol production under autotrophy of $2\,\mathrm{mmol\,gDW^{-1}\,h^{-1}}$. Montagud et al. (2011) estimated that under autotrophy, the maximum ethanol productivity was $0.85\,\mathrm{mmol\,gDW^{-1}\,h^{-1}}$ and under mixotrophy the production value reached $1.7\,\mathrm{mmol\,gDW^{-1}\,h^{-1}}$. For a comprehensive review of the economic relevance of cyanobacteria production of interesting metabolites, such as sugars, isoprene, alcohols, alkanes and hydrogen, refer Ducat et al. (2011b).

Flux landscape studies can shed light on the capabilities of this network. Flux coupling analysis is employed in order to uncover non-straight forward functional links among fluxes (Burgard et al., 2004). Flux coupling analysis tries to uncover part of the effects that hinder mutant generation, allowing researchers to explain mutant phenotypes that were not considered because no prior knowledge was known or

Table 2. Hydrogen production rates obtained by different methods from Navarro et al. (2009).

Process	Production rate	References
Biophotolysis	$0.07\,\mathrm{mmol\,L^{-1}\,h^{-1}}$	(Kosourov et al., 2002; Melis et al., 2000)
Indirect biophotolysis*	$0.35\,\mathrm{mmol\,L^{-1}\,h^{-1}}$	(Sveshnikov et al., 1997)
Photo-fermentation	$145–160\,\mathrm{mmol\,L^{-1}\,h^{-1}}$	(Levin et al., 2004)
Dark-fermentation	$77\,\mathrm{mmol\,L^{-1}\,h^{-1}}$	(Akkerman et al., 2002)
Two stage processes	$3.37–7.2\,\mathrm{mol\,H_2\,mol\,C_6^{-1}}$	(Kumar & Das, 2001)

*Experimental values shown for photolytic methods corresponds mainly with algae, although some relevant works for cyanobacteria can be found in Levin et al. (2004).

because connectivity was not straightforward. It was found that in terms of feasibility, it seemed easier to tinker flux couplings to have increased ethanol production than an increased hydrogen production. Hydrogen is interwoven with photosynthesis and oxidative phosphorylation, making it difficult to design strategies that increase hydrogen, but do not affect growth capabilities considerably (Montagud et al., 2011).

Researchers are seduced by the idea of using this cyanobacterium due to its capability of producing metabolites autonomously from carbon dioxide, water and photons, thus photoautotrophically. In this growth mode, photosynthesis provides electrons and oxygen from water, using photons as energy donors, pumping protons that can be used to generate ATP. Hydrogenase is fed from NADPH that, in turn, is fed from these electrons. Additionally, hydrogenase is inhibited even by low levels of oxygen (Tamagnini et al., 2002). The higher photosynthetic activity, the more electron flow and consequently the more hydrogen-inhibiting oxygen is produced. Hence, photosynthesis, oxidative phosphorylation and hydrogen production are metabolic pathways that have to be system-wide engineered if we want to be successful. In this sense, efforts are being drawn to engineer an increased electron flow that feeds the hydrogenase (Cournac et al., 2004). Alternatively, oxygen production has been limited in some photosynthetic cells with an improved effect on hydrogen production (Melis et al., 2000). In fact, the inclusion of an oxygen-tolerant hydrogenase has been targeted by many projects, and researchers are beginning to publish papers on this topic (Ducat et al., 2011a).

In a recent study, production yields for isoprene and hydrogen were calculated (Saha et al., 2012). It was calculated that the maximum isoprene yield using *i*Syn731 to be 3.63×10^{-5} mole isoprene per mole of fixed carbon upon adding isoprene synthase activity to the model and simulating under maximum biomass production. Hydrogen fermentation is also estimated and the authors report that *i*Syn731 predicts a maximum hydrogen theoretical yield of 2.28 mole per mole of glycogen consumed while *i*JN678 (Nogales et al., 2012) yields a value of 2.00 mole per mole of glycogen consumed. Experimental results for *Synechocystis* sp. PCC6803 support up to 4.24 mole of hydrogen per mole of glycogen consumed (Antal & Lindblad, 2005; Bandyopadhyay et al., 2010).

In another recent study, the authors have identified the bottlenecks that may hinder the use of *Synechocystis* sp. PCC6803 as a production platform (Nogales et al., 2013). They showed that light-driven metabolism and its unique metabolic features are the main bottlenecks in harnessing its growth-coupled biotechnological potential. Main mutation targets were genes deleted in alternate electron flow pathways, which had increased hydrogen production, but reduced photosynthetic robustness (Nogales et al., 2013). They give a computational rational explanation to the evidence that, in contrast to the carbon flux, the electron flux can be manipulated more easily, especially in autotrophy (Baebprasert et al., 2011; Cournac et al., 2004; Ducat et al., 2011a).

Finally, if we are to live in a hydrogen economy several years from now, there are a series of milestones that need to be accomplished. In this direction, the US National Research Council commissioned a study to identify these efforts in 2004. This Committee on Alternatives and Strategies for Future Hydrogen Production and Use (Committee on Alternatives and Strategies for Future Hydrogen Production and Use and National Research Council, 2004) considered that, first of all, the hydrogen system must be cost-competitive, safe and appealing to the consumer, and it should preferably offer advantages from the perspectives of energy security and CO_2 emissions. Change to a clean economy based on hydrogen implies addressing several questions related to its production strategy and methods. Specifically for the transportation sector, dramatic progress in the development of fuel cells, storage devices and distribution systems is especially critical (Turner et al., 2008).

The Committee on Alternatives and Strategies for Future Hydrogen Production and Use concluded that, in order to have a hydrogen-fuelled transportation as a beachhead of a clean hydrogen economy, the four most fundamental technological and economic challenges are:

- To develop and introduce cost-effective, durable, safe, and environmentally desirable fuel cell systems and hydrogen storage systems.
- To develop the infrastructure in order to provide hydrogen for the light-duty-vehicle user.
- To reduce sharply the costs of hydrogen production from renewable energy sources, over decades.
- To capture and store (''sequester'') the carbon dioxide by-product of hydrogen production from coal.

Biotechnology can help overcome the last two challenges. Hydrogen production and carbon sequestration through biomass generation are objectives of cyanobacterial genome-scale metabolic models. Theoretical maxima, flux capabilities and mutant analysis can be studied with such models and have been reviewed. For instance, mutant generation is one of the tools of biotechnological advances and these mutants, be they knock outs, knock ins, or knock downs, etc., have a holistic effect on different parts of the metabolism. Researchers are not blind to this fact, and their habit of ignoring this has more to do with the lack of tools to cope with this complexity and uncertainty of data rather than with their willingness to overlook these systemic effects. Thus, it is of critical importance to pave the way to a situation where holistic analyses are possible and quantitative studies are conceivable. Better, more accurate, metabolic models will help us lower biofuel costs and increase its benefits. The widespread use of genome-scale metabolic models is allowing researchers to think widely and the reconstruction of genome-scale metabolic models is a process that can be streamlined and executed through a series of check-points and controls (Feist et al., 2009; Thiele & Palsson, 2010). The quality of a model mainly lies on the quality of the data. In the case of metabolic models, this starts with a detailed, high-quality genome annotation. Additionally, a metabolic model also needs very well designed experiments that retrieve conclusive data leading to relevant scientific discoveries. These experimental data should be easily interpreted with the metabolic model and should help researchers to identify targets to knock out, knock in, limiting reactions, flux-diverting pathways that could be directed to a metabolite of interest, etc.

Alas, integrating genome-scale metabolic information, i.e. *omics* data, into genome-scale metabolic models was a very promising task (Nielsen & Oliver, 2005), but has proved to be more challenging than expected (Montagud et al., 2011). In spite of this, simplifications (Szallasi et al., 2006), abstractions (Oliveira et al., 2008) and tools from foreign areas (Pérez-Escudero et al., 2009) have been used in this field. All of those tools are valid and useful if they allow us to become closer to a world where quantitative, all-inclusive approaches are possible and let us infer more efficient ways to use the biology to our needs.

Declaration of interest

References

Agrawal R, Singh NR, Ribeiro FH, Delgass WN. (2007). Sustainable fuel for the transportation sector. Proc Natl Acad Sci USA, 104, 4828–33.

Akkerman I, Janssen M, Rocha J, et al. (2002). Photobiological hydrogen production: photochemical efficiency and bioreactor design. Int J Hydrogen Energy, 27, 1195–208.

Alon U. (2003). Biological networks: the tinkerer as an engineer. Science, 301, 1866–7.

Angermayr SA, Hellingwerf KJ, Lindblad P, De Mattos MJT. (2009). Energy biotechnology with cyanobacteria. Curr Opin Biotechnol, 20, 257–63.

Antal TK, Lindblad P. (2005). Production of H2 by sulphur-deprived cells of the unicellular cyanobacteria *Gloeocapsa alpicola* and *Synechocystis* sp. PCC 6803 during dark incubation with methane or at various extracellular pH. J Appl Microbiol, 98, 114–20.

Atadashi IM, Aroua MK, Aziz AA. (2010). High quality biodiesel and its diesel engine application: a review. Renew Sustainable Energy Rev, 14, 1999–2008.

Baebprasert W, Jantaro S, Khetkorn W, et al. (2011). Increased H$_2$ production in the cyanobacterium *Synechocystis* sp. strain PCC 6803 by redirecting the electron supply via genetic engineering of the nitrate assimilation pathway. Metab Eng, 13, 610–16.

Bandyopadhyay A, Stöckel J, Min H, et al. (2010). High rates of photobiological H$_2$ production by a cyanobacterium under aerobic conditions. Nat Commun, 1, 139.

Barstow B, Agapakis CM, Boyle PM, et al. (2011). A synthetic system links FeFe-hydrogenases to essential *E. coli* sulfur metabolism. J Biol Eng, 5, 7.

BioModularH2. (2005). Engineered Modular Bacterial Photoproduction of Hydrogen (BioModularH2), FP6-2005-NEST-PATH-SYN, PATHFINDER STREP, contract no. 043340.

Bonarius HPJ, Schmid G, Tramper J. (1997). Flux analysis of underdetermined metabolic networks: the quest for the missing constraints. Trends Biotechnol, 15, 308–14.

BP p.l.c. (2011). BP statistical review of world energy, June 2011.

Burgard AP, Nikolaev E V, Schilling CH, Maranas CD. (2004). Flux coupling analysis of genome-scale metabolic network reconstructions. Genome Res, 14, 301–12.

Burgdorf T, Lenz O, Buhrke T, et al. (2005). [NiFe]-hydrogenases of *Ralstonia eutropha* H16: modular enzymes for oxygen-tolerant biological hydrogen oxidation. J Mol Microbiol Biotechnol, 10, 181–96.

Carty RH, Mazumder MM, Schreiber JD, Pangborn JB. (1981). Thermochemical hydrogen production, Report GRI-80/0023.4. Ed. Gas Research Institute. Chicago, IL.

Caspi R, Foerster H, Fulcher CA, et al. (2006). MetaCyc: a multi-organism database of metabolic pathways and enzymes. Nucleic Acids Res, 34, D511–16.

Chou C-J, Jenney FE, Adams MWW, Kelly RM. (2008). Hydrogenesis in hyperthermophilic microorganisms: implications for biofuels. Metab Eng, 10, 394–404.

Clarke BL. (1988). Stoichiometric network analysis. Cell Biophys, 12, 237–53.

Committee on Alternatives and Strategies for Future Hydrogen Production and Use, National Research Council, National Academy of Engineering. (2004). The hydrogen economy: opportunities, costs, barriers, and R&D needs. Washington, USA: National Academy Press, 1–256.

Cournac L, Peltier G, Vignais PM, et al. (2004). Sustained photoevolution of molecular hydrogen in a mutant of *Synechocystis* sp. Strain PCC 6803 deficient in the type I NADPH-dehydrogenase complex. J Bacteriol, 186, 1737–46.

Cvijovic M, Olivares-Hernández R, Agren R, et al. (2010). BioMet Toolbox: genome-wide analysis of metabolism. Nucleic Acids Res, 38, 144–9.

Das D, Veziroglu TN. (2001). Hydrogen production by biological processes: a survey of literature. Int J Hydrogen Energy, 26, 13–28.

Das D, Veziroglu TN. (2008). Advances in biological hydrogen production processes. Int J Hydrogen Energy, 33, 6046–57.

Deng MD, Coleman JR. (1999). Ethanol synthesis by genetic engineering in cyanobacteria. Appl Environ Microbiol, 65, 523–8.

Department of Energy. (2007). Hydrogen production – Hydrogen, Fuel Cells and Infrastructure Technologies Program. Department of Energy. Available from: www.eere.energy.gov/hydrogenandfuelcells/mypp/pdfs/production.pdf [last accessed 19 Aug 2013].

Devroe EJ, Kosuri S, Berry DA, et al. (2010). Hyperphotosynthetic organisms. US Patent 7785861.

Diamant I, Eldar YC, Rokhlenko O, et al. (2009). A network-based method for predicting gene-nutrient interactions and its application to yeast amino-acid metabolism. Mol Biosyst, 5, 1732–9.

Douglas SE. (1998). Plastid evolution: origins, diversity, trends. Curr Opin Genet Dev, 8, 655–61.

Ducat DC, Sachdeva G, Silver PA. (2011a). Rewiring hydrogenase-dependent redox circuits in cyanobacteria. Proc Natl Acad Sci USA, 108, 3941–6.

Ducat DC, Way JC, Silver PA. (2011b). Engineering cyanobacteria to generate high-value products. Trends Biotechnol, 29, 95–103.

Edwards JS, Palsson BØ. (1999). Systems properties of the *Haemophilus influenzae* Rd metabolic genotype. J Biol Chem, 274, 17410–16.

Edwards JS, Palsson BØ. (2000). The *Escherichia coli* MG1655 in silico metabolic genotype: its definition, characteristics, and capabilities. Proc Natl Acad Sci USA, 97, 5528–33.

Elam CC, Gregoire-Padró C, Sandrock G, et al. (2003). Realizing the hydrogen future: the International Energy Agency's efforts to advance hydrogen energy technologies. Int J Hydrogen Energy, 28, 601–7.

Eriksen NT, Riis ML, Holm NK, Iversen N. (2010). H$_2$ synthesis from pentoses and biomass in *Thermotoga* spp. Biotechnol Lett, 33, 293–300.

European Commission. (2011a). Energy and transport factsheets 2010. Available from: http://ec.europa.eu/energy/observatory/statistics/statistics_en.htm [last accessed 19 Aug 2013].

European Commission. (2011b). Europe 2020: a strategy for competitive, sustainable and secure energy. Luxembourg: Publications Office of the European Union.

Fabiano B, Perego P. (2002). Thermodynamic study and optimization of hydrogen production by *Enterobacter aerogenes*. Int J Hydrogen Energy, 27, 149–56.

Famili I, Forster J, Nielsen J, Palsson BØ. (2003). *Saccharomyces cerevisiae* phenotypes can be predicted by using constraint-based analysis of a genome-scale reconstructed metabolic network. Proc Natl Acad Sci USA, 100, 13134–9.

Feist AM, Herrgård MJ, Thiele I, et al. (2009). Reconstruction of biochemical networks in microorganisms. Nat Rev Microbiol, 7, 129–43.

Fell DA, Small JR. (1986). Fat synthesis in adipose tissue. An examination of stoichiometric constraints. Biochem J, 238, 781–6.

Förster J, Famili I, Fu P, et al. (2003). Genome-scale reconstruction of the *Saccharomyces cerevisiae* metabolic network. Genome Res, 13, 244–53.

Foster JS, Singh AK, Rothschild LJ, Sherman LA. (2007). Growth-phase dependent differential gene expression in *Synechocystis* sp. strain PCC 6803 and regulation by a group 2 sigma factor. Arch Microbiol, 187, 265–79.

Fu P. (2008). Genome-scale modeling of *Synechocystis* sp. PCC 6803 and prediction of pathway insertion. J Chem Technol Biot, 84, 473–83.

Fujishima A, Honda K. (1972). Electrochemical photolysis of water at a semiconductor elctrode. Nature, 238, 37–8.

Gamermann D, Montagud A, Jaime Infante RA, et al. (2012). PyNetMet: Python tools for efficient work with networks and metabolic models. Molecular Networks. arXiv preprint arXiv:1211.7196, 1–19.

Gill RT, Katsoulakis E, Schmitt W, et al. (2002). Genome-wide dynamic transcriptional profiling of the light-to-dark transition in *Synechocystis* sp. Strain PCC 6803. J Bacteriol, 184, 3671–81.

Greene SR, Flanagan GF, Borole AP. (2009). Integration of biorefineries and nuclear cogeneration power plants – a preliminary analysis. ORNL/TM-2008/102. Oak Ridge, TN: Oak Ridge National Laboratory.

Gugger M, Biological Resource Center of Institut Pasteur. (2011). Catalogue data sheet of Synechocystis PCC 6803. Available from: http://www.crbip.pasteur.fr/fiches/fichecata.jsp?crbip=PCC%206803 [last accessed 19 Aug 2013].

Gutthann F, Egert M, Marques A, Appel J. (2007). Inhibition of respiration and nitrate assimilation enhances photohydrogen evolution under low oxygen concentrations in *Synechocystis* sp. PCC 6803. Biochim Biophys Acta, 1767, 161–9.

Hallenbeck P, Benemann JR. (2002). Biological hydrogen production: fundamentals and limiting processes. Int J Hydrogen Energy, 27, 1185–93.

Hamilton JJ, Reed JL. (2012). Identification of functional differences in metabolic networks using comparative genomics and constraint-based models. Ed. Franca Fraternali. PLoS One, 7, e34670.

Hihara Y, Kamei A, Kanehisa M, et al. (2001). DNA microarray analysis of cyanobacterial gene expression during acclimation to high light. Plant Cell, 13, 793–806.

Hihara Y, Sonoike K, Kanehisa M, Ikeuchi M. (2003). DNA microarray analysis of redox-responsive genes in the genome of the cyanobacterium *Synechocystis* sp. strain PCC 6803. J Bacteriol, 185, 1719–25.

Hill J, Nelson E, Tilman D, et al. (2006). Environmental, economic, and energetic costs and benefits of biodiesel and ethanol biofuels. Proc Natl Acad Sci USA, 103, 11206–10.

Houchins JP. (1984). The physiology and biochemistry of hydrogen metabolism in cyanobacteria. BBA Bioenergetics, 768, 227–55.

Houmard J, Tandeau de Marsac N. (1988). Cyanobacterial genetic tools: current status. Methods Enzymol, 167, 808–47.

Huang L, McCluskey MP, Ni H, LaRossa RA. (2002). Global gene expression profiles of the cyanobacterium *Synechocystis* sp. strain PCC 6803 in response to irradiation with UV-B and white light. J Bacteriol, 184, 6845–58.

Hübschmann T, Yamamoto H, Gieler T, et al. (2005). Red and far-red light alter the transcript profile in the cyanobacterium *Synechocystis* sp. PCC 6803: impact of cyanobacterial phytochromes. FEBS Lett, 579, 1613–18.

Kalia VC, Jain SR, Kumar A, Joshi AP. (1994). Frementation of biowaste to H$_2$ by *Bacillus licheniformis*. World J Microbiol Biotechnol, 10, 224–7.

Kaneko T, Sato S, Kotani H, et al. (1996). Sequence analysis of the genome of the unicellular cyanobacterium *Synechocystis* sp. strain PCC6803. II. Sequence determination of the entire genome and assignment of potential protein-coding regions (supplement). DNA Res, 3, 185–209.

Kaneko T, Tanaka A, Sato S, et al. (1995). Sequence analysis of the genome of the unicellular cyanobacterium *Synechocystis* sp. strain PCC6803. I. Sequence features in the 1 Mb region from map positions 64% to 92% of the genome. DNA Res, 2, 153–66, 191–8.

Kanesaki Y, Suzuki I, Allakhverdiev SI, et al. (2002). Salt stress and hyperosmotic stress regulate the expression of different sets of genes in *Synechocystis* sp. PCC 6803. Biochem Biophys Res Commun, 290, 339–48.

Kim W-Y, Kang S, Kim B-C, et al. (2008). SynechoNET: integrated protein-protein interaction database of a model cyanobacterium *Synechocystis* sp. PCC 6803. BMC Bioinf, 9, S20.

Kitano H. (2002). Computational systems biology. Nature, 420, 206–10.

Klanchui A, Khannapho C, Phodee A, et al. (2012). iAK692: a genome-scale metabolic model of *Spirulina platensis* C1. BMC Syst Biol, 6, 71.

Knoop H, Zilliges Y, Lockau W, Steuer R. (2010). The metabolic network of *Synechocystis* sp. PCC 6803: systemic properties of autotrophic growth. Plant Physiol, 154, 410–22.

Kosourov S, Tsygankov A, Seibert M, Ghirardi ML. (2002). Sustained hydrogen photoproduction by *Chlamydomonas reinhardtii*: Effects of culture parameters. Biotechnol Bioeng. 78, 731–40.

Krieger CJ, Zhang P, Mueller LA, et al. (2004). MetaCyc: a multiorganism database of metabolic pathways and enzymes. Nucleic Acids Res, 32, D438–42.

Kroposki B, Levene J, Harrison K, et al. (2006). Electrolysis: information and opportunities for electric power utilities. NREL – Technical report.

Kufryk GI, Sachet M, Schmetterer G, Vermaas WFJ. (2002). Transformation of the cyanobacterium *Synechocystis* sp. PCC 6803 as a tool for genetic mapping: optimization of efficiency. FEMS Microbiol Lett, 206, 215–19.

Kumar N, Das D. (2001). Continuous hydrogen production by immobilized *Enterobacter cloacae* IIT-BT 08 using lignocellulosic materials as solid matrices. Enzyme Microb Technol, 29, 280–87.

Kun A, Papp B, Szathmáry E. (2008). Computational identification of obligatorily autocatalytic replicators embedded in metabolic networks. Genome Biol, 9, R51.

Laguna-Bercero MA. (2012). Recent advances in high temperature electrolysis using solid oxide fuel cells: a review. J Power Sources, 203, 4–16.

Latendresse M, Krummenacker M, Trupp M, Karp PD. (2012). Construction and completion of flux balance models from pathway databases. Bioinformatics, 28, 388–96.

Levin D, Pitt L, Love M. (2004). Biohydrogen production: prospects and limitations to practical application. Int J Hydrogen Energy, 29, 173–85.

Lindberg P, Park S, Melis A. (2010). Engineering a platform for photosynthetic isoprene production in cyanobacteria, using Synechocystis as the model organism. Metab Eng, 12, 70–9.

Liu X, Brune D, Vermaas W, Curtiss R. (2010). Production and secretion of fatty acids in genetically engineered cyanobacteria. Proc Natl Acad Sci USA, 6803, 2–7.

Llaneras F, Picó J. (2008). Stoichiometric modelling of cell metabolism. J Biosci Bioeng, 105, 1–11.

Lopes Pinto F, Troshina O, Lindblad P. (2002). A brief look at three decades of research on cyanobacterial hydrogen evolution. Int J Hydrogen Energy, 27, 1209–15.

Maniatis K. (2010). Biofuels from algae: results of the 2010 FP7 Call. Available from: http://www.biofuelstp.eu/downloads/presentations/2010_KM_Algae_BTP.pdf [last accessed 19 Aug 2013].

Mavrovouniotis ML, Stephanopoulos G, Stephanopoulos G. (1992). Synthesis of biochemical production routes. Comput Chem Eng, 16, 605–19.

Melis A. (1991). Dynamics of photosynthetic membrane composition and function. Biochimica et Biophysica Acta (BBA) – Bioenergetics, 1058, 87–106.

Melis A. (2011). Maximizing light utilization efficiency and hydrogen production in microalgal cultures. Department of Energy – Hydrogen Program.

Melis A, Melnicki M. (2006). Integrated biological hydrogen production. Int J Hydrogen Energy, 31, 1563–73.

Melis A, Zhang L, Forestier M, et al. (2000). Sustained photobiological hydrogen gas production upon reversible inactivation of oxygen evolution in the green alga *Chlamydomonas reinhardtii*. Plant Physiol, 122, 127–36.

Metzker ML. (2010). Sequencing technologies – the next generation. Nat Rev Genet, 11, 31–46.

Milne TA, Elam CC, Evans RJ. (2002). Hydrogen from biomass – state of the art and research challenges. IEA/H2/TR-02/001. Golden, USA: National Renewable Energy Laboratory Golden.

Milo R, Shen-Orr S, Itzkovitz S, et al. (2002). Network motifs: simple building blocks of complex networks. Science, 298, 824–7.

Momirlan M, Veziroglu TN. (2005). The properties of hydrogen as fuel tomorrow in sustainable energy system for a cleaner planet. Int J Hydrogen Energy, 30, 795–802.

Montagud A, Navarro E, Fernández de Córdoba P, et al. (2010). Reconstruction and analysis of genome-scale metabolic model of a photosynthetic bacterium. BMC Syst Biol, 4, 156.

Montagud A, Zelezniak A, Navarro E, et al. (2011). Flux coupling and transcriptional regulation within the metabolic network of the photosynthetic bacterium *Synechocystis* sp. PCC6803. Biotechnol J, 6, 330–42.

Navarro E, Montagud A, Fernández de Córdoba P, Urchueguía JF. (2009). Metabolic flux analysis of the hydrogen production potential in *Synechocystis* sp. PCC6803. Int J Hydrogen Energy, 34, 8828–38.

Nielsen J, Oliver S. (2005). The next wave in metabolome analysis. Trends Biotechnol, 23, 544–6.

Nogales J, Gudmundsson S, Knight EM, et al. (2012). Detailing the optimality of photosynthesis in cyanobacteria through systems biology analysis. Proc Natl Acad Sci USA, 109, 2678–83.

Nogales J, Gudmundsson S, Thiele I. (2013). Toward systems metabolic engineering in cyanobacteria: opportunities and bottlenecks. Bioengineered, 4, 5–4.

Nookaew I, Olivares-Hernández R, Bhumiratana S, Nielsen J. (2011). Genome-scale metabolic models of *Saccharomyces cerevisiae*. Methods Mol Biol, 759, 445–63.

Oh Y-K, Seol E-H, Lee EY, Park S. (2002). Fermentative hydrogen production by a new chemoheterotrophic bacterium *Rhodopseudomonas Palustris* P4. Int J Hydrogen Energy, 27, 1373–9.

Oliveira AP, Patil KR, Nielsen J. (2008). Architecture of transcriptional regulatory circuits is knitted over the topology of bio-molecular interaction networks. BMC Syst Biol, 2, 17.

Orth JD, Thiele I, Palsson BØ. (2010). What is flux balance analysis? Nat Biotechnol, 28, 245–8.

Palsson B. (2000). The challenges of in silico biology. Nat Biotechnol, 18, 1147–50.

Patil KR, Akesson M, Nielsen J. (2004). Use of genome-scale microbial models for metabolic engineering. Curr Opin Biotechnol, 15, 64–9.

Patil KR, Nielsen J. (2005). Uncovering transcriptional regulation of metabolism by using metabolic network topology. Proc Natl Acad Sci USA, 102, 2685–9.

Patil KR, Rocha I, Förster J, Nielsen J. (2005). Evolutionary programming as a platform for in silico metabolic engineering. BMC Bioinf, 6, 308.

Pérez-Escudero A, Rivera-Alba M, De Polavieja GG. (2009). Structure of deviations from optimality in biological systems. Proc Natl Acad Sci USA, 106, 20544–9.

Perret R. (2005). Solar hydrogen generation research – high-temperature thermochemical. Department of Energy – Hydrogen Program. Available from: http://www.hydrogen.energy.gov/pdfs/progress05/iv_i_1_perret.pdf [last accessed 19 Aug 2013].

Postgate JR. (1970). Biological nitrogen fixation. Nature, 226, 25–7.

Pregger T, Graf D, Krewitt W, et al. (2009). Prospects of solar thermal hydrogen production processes. Int J Hydrogen Energy, 34, 4256–67.

Raven JA, Allen JF. (2003). Genomics and chloroplast evolution: what did cyanobacteria do for plants? Genome Biol, 4, 209.

Reed JL, Vo TD, Schilling CH, Palsson BO. (2003). An expanded genome-scale model of *Escherichia coli* K-12 (iJR904 GSM/GPR). Genome Biol, 4, R54.

Rippka R, Deruelles J, Waterbury JB, et al. (1979). Generic assignments, strain histories and properties of pure cultures of cyanobacteria. J General Microbiol, 111, 1–61.

Rocha I, Maia P, Evangelista P, et al. (2010). OptFlux: an open-source software platform for in silico metabolic engineering. BMC Syst Biol, 4, 45.

Saha R, Verseput AT, Berla BM, et al. (2012). Reconstruction and comparison of the metabolic potential of cyanobacteria *Cyanothece* sp. ATCC 51142 and *Synechocystis* sp. PCC 6803. Ed. John Parkinson. PLoS One, 7, e48285.

Sauer U, Heinemann M, Zamboni N. (2007). Getting closer to the whole picture. Science, 316, 550–1.

Savinell JM, Palsson BØ. (1992a). Network analysis of intermediary metabolism using linear optimization. II. Interpretation of hybridoma cell metabolism. J Theor Biol, 154, 421–54.

Savinell JM, Palsson BØ. (1992b). Network analysis of intermediary metabolism using linear optimization. I. Development of mathematical formalism. J Theor Biol, 154, 421–54.

Schellenberger J, Que R, Fleming RMT, et al. (2011). Quantitative prediction of cellular metabolism with constraint-based models: the COBRA Toolbox v2.0. Nat Protoc, 6, 1290–307.

Schilling CH, Schuster S, Palsson BØ, Heinrich R. (1999). Metabolic pathway analysis: basic concepts and scientific applications in the post-genomic era. Biotechnol Prog, 15, 296–303.

Schmitt WA, Stephanopoulos G. (2003). Prediction of transcriptional profiles of *Synechocystis* PCC6803 by dynamic autoregressive modeling of DNA microarray data. Biotechnol Bioeng, 84, 855–63.

Schopf JW. (2000). The fossil record: tracing the roots of the cyanobacterial lineage. In: Whitton BA, Potts M, eds. The ecology of cyanobacteria. Dordrecht, The Netherlands: Kluwer Academic Publishers, 13–35.

Schröder C, Selig M, Schönheit P. (1994). Glucose fermentation to acetate, CO_2 and H_2 in the anaerobic hyperthermophilic eubacterium *Thermotoga maritima*: involvement of the Embden-Meyerhof pathway. Arch Microbiol, 161, 460–70.

Schuster R, Schuster S. (1993). Refined algorithm and computer program for calculating all non-negative fluxes admissible in steady states of biochemical reaction systems with or without some flux rates fixed. CABIOS, 9, 79–85.

Segrè D, Vitkup D, Church GM. (2002). Analysis of optimality in natural and perturbed metabolic networks. Proc Natl Acad Sci USA, 99, 15112–17.

Shastri AA, Morgan JA. (2005). Flux balance analysis of photoautotrophic metabolism. Biotechnol Prog, 21, 1617–26.

Singh AK, Bhattacharyya-Pakrasi M, Elvitigala T, et al. (2009). A systems-level analysis of the effects of light quality on the metabolism of a cyanobacterium. Plant Physiol, 151, 1596–608.

Singh AK, McIntyre LM, Sherman LA. (2003). Microarray analysis of the genome-wide response to iron deficiency and iron reconstitution in the cyanobacterium *Synechocystis* sp. PCC 6803. Plant Physiol, 132, 1825–39.

Snoep JL, Westerhoff HV. (2005). From isolation to integration, a systems biology approach for building the Silicon Cell. Top Curr Gen, 13, 13–30.

Soanes C, Stevenson A. (2010). The New Oxford Dictionary of English. 3rd ed. Oxford: Oxford University Press.

Solazyme Inc. (2012). Web page: http://www.solazyme.com/technology.

Stanier RY, Kunisawa R, Mandel M, Cohen-Bazire G. (1971). Purification and properties of unicellular blue-green algae (order Chroococcales). Bacteriol Rev, 35, 171–205.

Stapleton JA, Swartz JR. (2010). Development of an in vitro compartmentalization screen for high-throughput directed evolution of [FeFe] hydrogenases. PLoS ONE, 5, e15275.

Stelling J, Klamt S, Bettenbrock K, et al. (2002). Metabolic network structure determines key aspects of functionality and regulation. Nature, 420, 190–3.

Stephanopoulos G, Aristidou A, Nielsen J. (1998). Metabolic engineering: principles and methodologies. San Diego: Academic Press.

Stephanopoulos G, Stafford DE. (2002). Metabolic engineering: a new frontier of chemical reaction engineering. Chem Eng Sci, 57, 2595–602.

Stripp S, Sanganas O, Happe T, Haumann M. (2009a). The structure of the active site H-cluster of [FeFe] hydrogenase from the green alga *Chlamydomonas reinhardtii* studied by X-ray absorption spectroscopy. Biochemistry, 48, 5042–9.

Stripp ST, Goldet G, Brandmayr C, et al. (2009b). How oxygen attacks [FeFe] hydrogenases from photosynthetic organisms. Proc Natl Acad Sci USA, 106, 17331–6.

Summerfield TC, Sherman LA. (2008). Global transcriptional response of the alkali-tolerant cyanobacterium *Synechocystis* sp. strain PCC 6803 to a pH 10 environment. Appl Environ Microbiol, 74, 5276–84.

Suzuki I, Kanesaki Y, Mikami K, et al. (2001). Cold-regulated genes under control of the cold sensor Hik33 in Synechocystis. Mol Microbiol, 40, 235–44.

Suzuki I, Simon WJ, Slabas AR. (2006). The heat shock response of *Synechocystis* sp. PCC 6803 analysed by transcriptomics and proteomics. J Exp Bot, 57, 1573–8.

Sveshnikov DA, Sveshnikova NV, Rao KK, Hall DO. (1997). Hydrogen metabolism of mutant forms of *Anabaena variabilis* in continuous cultures and under nutritional stress. FEMS Microbiol Lett, 147, 297–301.

Swingley WD, Blankenship RE. (2008). Insights into cyanobacterial evolution from comparative genomics. In: Herrero A, Flores E, eds. The cyanobacteria: molecular biology, genomics, and evolution. Norfolk, UK: Horizon Scientific Press, 21–43.

Szallasi Z, Stelling J, Periwal V. (2006). System modeling in cellular biology: from concepts to nuts and bolts. Cambridge, USA: The MIT Press.

Taguchi F, Yamada K, Hasegawa K, et al. (1996). Continuous hydrogen production by *Clostridium* sp. strain no. 2 from cellulose hydrolysate in an aqueous two-phase system. J Ferment Bioeng, 82, 80–3.

Tamagnini P, Axelsson R, Lindberg P, et al. (2002). Hydrogenases and hydrogen metabolism of cyanobacteria. Microbiol Mol Biol Rev, 66, 1–20.

Tamagnini P, Leitão E, Oliveira P, et al. (2007). Cyanobacterial hydrogenases: diversity, regulation and applications. FEMS Microbiol Rev, 31, 692–720.

Thauer R. (1976). Limitation of microbial H_2-formation via fermentation. In: Schlegel HG, Barnea J, eds. Microbial energy conversion. Göttingen: E. Goltze KG, 201–14.

Thiel T. (1994). Genetic analysis of cyanobacteria. In: Bryant DA, ed. Molecular biology of cyanobacteria, Chapter 19. Dordrecht, Netherlands: Kluwer Academic Publishers, 581–611.

Thiele I, Palsson BØ. (2010). A protocol for generating a high-quality genome-scale metabolic reconstruction. Nat Protoc, 5, 93–121.

Turner J, Sverdrup G, Mann MK, et al. (2008). Renewable hydrogen production. Int J Energ Res, 32, 379–407.

U.S. Energy Information Administration. (2011a). webpage [http://www.eia.gov/].

U.S. Energy Information Administration. (2011b). August 2011 monthly energy review.

United Nations. (1998). Kyoto Protocol to the United Nations framework convention on climate change. Available from: http://unfccc.int/resource/docs/convkp/kpeng.pdf [last accessed 19 Aug 2013].

United States Government. (2011). Hydrogen and Fuel Cells Interagency Working Group [http://www.hydrogen.gov/].

Varma A, Boesch BW, Palsson BØ. (1993a). Biochemical production capabilities of *Escherichia coli*. Biotechnol Bioeng, 42, 59–73.

Varma A, Boesch BW, Palsson BØ. (1993b). Stoichiometric interpretation of *Escherichia coli* glucose catabolism under various oxygenation rates. Appl Environ Microbiol, 59, 2465–73.

Varma A, Palsson BØ. (1993a). Metabolic capabilities of *E. coli* I. Synthesis of biosynthetic precursors and cofactors. J Theor Biol, 165, 477–502.

Varma A, Palsson BØ. (1993b). Metabolic capabilities of *E. coli* II. Optimal growth patterns. J Theor Biol, 165, 503–22.

Varma A, Palsson BØ. (1994a). Metabolic flux balancing: basic concepts, scientific and practical use. Nature, 12, 994–8.

Varma A, Palsson BØ. (1994b). Stoichiometric flux balance models quantitatively predict growth and metabolic by-product secretion in wild-type *Escherichia coli* W3110. Appl Environ Microbiol, 60, 3724–31.

Vitkin E, Shlomi T. (2012). MIRAGE: a functional genomics-based approach for metabolic network model reconstruction and its application to cyanobacteria networks. Genome Biol, 13, R111.

Vu TT, Stolyar SM, Pinchuk GE, et al. (2012). Genome-scale modeling of light-driven reductant partitioning and carbon fluxes in diazotrophic unicellular cyanobacterium *Cyanothece* sp. ATCC 51142. Ed. Daniel Segrè. PLoS Comput Biol, 8, e1002460.

Wang H-L, Postier BL, Burnap RL. (2004). Alterations in global patterns of gene expression in *Synechocystis* sp. PCC 6803 in response to inorganic carbon limitation and the inactivation of ndhR, a LysR family regulator. J Biol Chem, 279, 5739–51.

Wang WG, Lyons DW, Clark NN, et al. (2000). Emissions from nine heavy trucks fueled by diesel and biodiesel blend without engine modification. Environ Sci Technol, 34, 933–9.

Wetterstrand K. (2012). DNA sequencing costs: data from the NHGRI large-scale genome sequencing program. Available from: www.genome.gov/sequencingcosts [last accessed 21 Jan 2012].

Wu GF, Wu QY, Shen ZY. (2001). Accumulation of poly-beta-hydroxybutyrate in cyanobacterium *Synechocystis* sp. PCC6803. Bioresour Technol, 76, 85–90.

Yamaguchi K, Suzuki I, Yamamoto H, et al. (2002). A two-component Mn 2-sensing system negatively regulates expression of the mntCAB Operon in Synechocystis. Plant Cell, 14, 2901–13.

Yang C, Hua Q, Shimizu K. (2002a). Integration of the information from gene expression and metabolic fluxes for the analysis of the regulatory mechanisms in *Synechocystis*. Appl Microbiol Biotechnol, 58, 813–22.

Yang C, Hua Q, Shimizu K. (2002b). Metabolic flux analysis in synechocystis using isotope distribution from 13C-Labeled glucose. Metab Eng, 4, 202–16.

Yang C, Hua Q, Shimizu K. (2002c). Quantitative analysis of intracellular metabolic fluxes using GC-MS and two-dimensional NMR spectroscopy. J Biosci Bioeng, 93, 78–87.

Yokthongwattana K, Melis A. (2008). Photoinhibition and recovery in oxygenic photosynthesis: mechanism of a photosystem II damage. In: Demmig-Adams B, Adams WW, Mattoo AK, eds. Photoprotection, photoinhibition, gene regulation, and environment. Berlin: Springer Science, 175–91.

Yoshikawa K, Kojima Y, Nakajima T, et al. (2011). Reconstruction and verification of a genome-scale metabolic model for *Synechocystis* sp. PCC6803. Appl Microbiol Biotechnol, 92, 1–5.

Zhang S, Bryant D. (2011). The tricarboxylic acid cycle in cyanobacteria. Science, 334, 1551–3.

Zhang Z, Pendse ND, Phillips KN, et al. (2008). Gene expression patterns of sulfur starvation in *Synechocystis* sp. PCC 6803. BMC Genom, 9, 344.

Zucchetto J, (ed.), National Research Council. (2006). Trends in oil supply and demand, potential for peaking of conventional oil production, and possible mitigation options: a summary report of the workshop. Washington, USA: National Academy Press.

The effects of age and emotional valence on recognition memory: An ex-Gaussian components analysis

CARMEN MORET-TATAY,[1] AMPARO MORENO-CID,[2] IRANI IRACEMA DE LIMA ARGIMON,[3] TATIANA QUARTI IRIGARAY,[3] MARCIN SZCZERBINSKI,[4] MIKE MURPHY,[4] ANDREA VÁZQUEZ-MARTÍNEZ,[2] JOAN VÁZQUEZ-MOLINA,[5] BEGOÑA SÁIZ-MAULEÓN,[5] ESPERANZA NAVARRO-PARDO[2] and PEDRO FERNÁNDEZ DE CÓRDOBA CASTELLÁ[5]

[1]*Universidad Católica de Valencia "San Vicente Mártir", Spain*
[2]*Universitat de València, Spain*
[3]*Pontifícia Universidade Católica do Rio Grande do Sul, Brazil*
[4]*University College Cork, Ireland*
[5]*Universitat Politécnica de València, Spain*

The aim of this work was to study the effects of valence and age on visual image recognition memory. The International Affective Picture System (IAPS) battery was used, and response time data were analyzed using analysis of variance, as well as an ex-Gaussian fit method. Older participants were slower and more variable in their reaction times. Response times were longer for negative valence pictures, however this was statistically significant only for young participants. This suggests that negative emotional valence has a strong effect on recognition memory in young but not in old participants. The s parameter, often related to attention in the literature, was smaller for young than old participants in an ex-Gaussian fit. Differences on the s parameter might suggest poorer attentional performance in old participants.

Key words: Ex-Gaussian components, age, emotional valence, recognition.

Moret-Tatay, C., Facultad de Psicología, Magisterio y Ciencias de la Educación, Universidad Católica de Valencia 'San Vicente Mártir', Sede de San Juan Bautista, Avenida Guillem de Castro 175, 46008, Valencia, Spain. E-mail: carmenmoret@gmail.com

INTRODUCTION

Humans regularly face emotionally charged stimuli. Thus, not surprisingly, the study of the impact of valence on memory has attracted the interest of cognitive psychology in the last decades. A useful tool regarding the nature of the stimuli is the International Affective Picture System, developed by Peter J. Lang at Florida University (1999). The success of this battery is determined by its high reliability in terms of emotional valence (the pleasantness of the stimulus), arousal (the intensity of emotion provoked by the stimulus), and dominance (the degree of control exerted by the stimulus). Most of the research that has employed the IAPS battery has analyzed response times (RTs) and percentage of errors or correct responses as the dependent variable (Borg, Leroy, Favre, Laurent & Thomas-Antérion, 2011; Charles, Mather & Carstensen, 2003; Gordillo Leon, Arana, Mestas *et al.*, 2010).

RT usually shows a high sensitivity to cognitive processes, but its distribution is often positively skewed, which is problematic for some methods of statistical analysis. However, skewed RTs can be described adequately by use of an ex-Gaussian distribution. The advantage of this analysis lies in the fact that its three parameters may map onto different cognitive processes, although the functional interpretation of those parameters is still debated in the literature (Matzke & Wagenmakers, 2009). The parameter that arguably attracts the greatest research interest is s. It has been described as a perceptual aspect of a RT (Hohle, 1965), a decision component (Luce, 1986) and more recently, an

attentional component or a defective effort control mechanism (Leth-Steensen, King Elbaz & Douglas, 2000).

Mathematically, the ex-Gaussian probability density function is the result of a combination of two random variables, a Gaussian distribution (described by its l and r parameters), and an exponential distribution (described by its s parameter). Thereby, an ex-Gaussian distribution is perfectly defined with three parameters: the first two (l and r), are the mean and standard deviation of the Gaussian component, while the third parameter (s) is the rate parameter of the exponential component. When analyzing the results from an ex-Gaussian fit, one must be careful because the parameters that describe the mean distribution are l + s. Ratcliff and Murdock (1976) and Luce (1986) showed that the ex-Gaussian function provides a good fit to several empirical reaction times distributions and it continues to be used as a tool for the analysis of RT data (Epstein, Langberg, Rosen *et al.*, 2011; Navarro-Pardo, Navarro-Prados, Gamermann & Moret-Tatay, 2013). While many researchers have related ex-Gaussian components to underlying cognitive processes, the literature is limited in terms of how the processing of emotional valence of stimuli may affect the three parameters of the ex-Gaussian distribution.

Several studies employing traditional methods (Buchanan & Adolphs, 2002; Reisberg & Heuer, 2004) have shown evidence that emotional content of visual stimuli has an impact on recognition. Rozin and Royzman (2001) stated that given positive and negative stimuli of equal objective magnitude, negative emotion is more potent. This idea is supported by Wright, Busnello,

Buratto and Stein (2012), who found more accurate responses with negative valence when studying a memory conformity effect. However, this emotional modulation of memory processes may be age-dependent. Charles *et al.* (2003) carried out two experiments where the valence of stimuli was manipulated. They found age-related reduction in memory for negative images. The reduction affected both kinds of stimuli, but it was more prominent for the negative ones. Moreover, attempts have been made to examine interactions between cognitive processes such as attention and emotion through the presentation of visual material. Some researchers concluded that such interactions could activate visual processing (Keil, Bradley, Hauk, Rockstroh, Elbert & Lang, 2005; Schupp, Stockburger, Codispoti, Junghofer, Weike & Hamm, 2007).

In the current study, we employ an alternative methodology to estimate the role of valence in terms of ex-Gaussian components and aging. To this end, a picture recognition task was conducted. Young and old participants were first exposed to different IAPS images (hereafter called target images) selected for their valence, and after a distracting interval, they were requested to differentiate the target images from other images (hereafter called distracting images). The aim of the study is to examine the impact of two factors: emotional valence of stimuli, and participants' age, on recognition memory. The data are analyzed using an ex-Gaussian components method, since it allows for appropriate modeling of skewed data, as well as modeling of distinct cognitive processes affecting RT performance.

METHOD

Participants

A sample of 40 young university students volunteered to take part in experiment 1 (32 women and 8 men with mean age of 22.23 years and SD = 2.12).

In experiment 2, a sample of 40 senior university students from a program for aged students, volunteered to take part (29 women and 11 men, mean age of 67.29 years and SD = 6.19).

Six participants in experiment 2 were replaced due to an error rate of higher than 40%. All participants had normal or corrected to normal vision, were native Spanish speakers and did not report cognitive impairment or neurological disorders. The sample selected for both groups has a female majority, but there is no reason to believe that processes addressed in this research might be gender dependent.

Materials

The stimuli used were a selection of photographs from the International Affective Picture System (IAPS, CSEA-NIMH, 1999; Lang, Bradley & Cuthbert, 1999) in the Spanish adaptation of Moltó, Montañés, Poy *et al.* (1999). We selected a total of 120 photographs divided into three sets of 40 photographs based on their scores on valence (positive, negative or neutral). For the purpose of the recognition task, from the 120 images selected, 60 were selected as the target images and 60 as distracting ones. In each set, 20 were neutral images, 20 images were negative and 20 were positive images (see Table 1).

Procedure

Participants were tested in a quiet room, in groups of three or four people. The presentation of stimuli and recording of response times were

Table 1. *Mean valence and arousal values for the selected images in the different sets from the Spanish adaptation of Moltó et al. (1999)*

		Neutral	Negative	Positive
Target	Valence	5 (0.45)	2.82 (0.75)	7.2 (0.6)
	Arousal	5 (0.46)	6.1 (0.77)	4.8 (1.2)
Distracting	Valence	5.05 (0.58)	2.82 (0.65)	7.2 (0.5)
	Arousal	4 (0.82)	5.9 (0.91)	5.1 (1.3)
Total	Valence	5.03 (0.51)	2.82 (0.69)	7.2 (0.54)
	Arousal	4 (0.66)	6 (0.84)	5 (1.2)

Note: Standard deviation in parenthesis.

controlled by a Windows operating system through DMDX software (Forster & Forster, 2003). The experiment consisted of two phases. In the first phase, the 60 target stimuli were presented randomly (20 stimuli for each of the three valence categories) with short exposures of 2 seconds each. In the second phase (15 minutes after the participants were distracted by performing visual search tasks), the 60 target stimuli plus the 60 distracting stimuli were randomly presented to the participants. Each image was presented until the participant gave a response or 2000 ms passed. The participants were instructed to press a button (labelled "Yes") to indicate whether the stimulus was a target stimulus, and press another button (labelled "No") if the stimulus was a distracting stimulus (did not appear in the first phase).

The participants were also instructed to respond as quickly as possible while maintaining a reasonable level of accuracy. The session lasted approximately 40 minutes.

Design and data analysis

Two different analyses were carried out. A classical analysis of variance (ANOVA) explored the impact of stimulus identity (target or distractor), emotional valence (neutral, positive and negative) and participants' age on response latency. The same procedure was employed for error rates. This was followed by the fitting of RT data to an ex-Gaussian distribution function. For the latter analysis, data sets were distributed in intervals in order to create a histogram. Differences between parameters from the ex-Gaussian fit were analyzed regarding their uncertainties (errors) as confidence interval lengths for each parameter.

RESULTS

The statistical analysis was performed using SPSS statistical software version 20 (IBM, Armonk, NY). Table 2 presents the reaction times average (ms), error rates and standard deviations for each group of images.

The ANOVAs were performed after reaction times below 250 ms and above 1800 ms were excluded. The 1800 ms cut-off point was adopted for consistency with earlier studies in the field (Moret-Tatay & Perea, 2011; Navarro-Pardo *et al.*, 2013). This excluded data constituted 3.3% and 5.6% of responses for young and old participants, respectively. The ex-Gaussian distribution characterization used all data. Reaction times corresponding to incorrect responses were excluded from all analyses.

The classical analysis of variance (ANOVA) was performed using a $2 \times 2 \times 3$ mixed design, with a between-subject factor of Age (young vs old) and within-subject factors of stimulus Identity (target vs distractor) and Valence (neutral positive and negative).

The ANOVA carried out on RT data showed a main effect of Age: $F(1,78) = 6.690$, MSE = 112284.91, $\eta^2 = 0.08$, $p < 0.05$, Identity: $F(1,78) = 128.311$, MSE = 8106.68, $\eta^2 = 0.62$,

Table 2. *Response time averages (ms), error rates for each experimental condition*

Group	Stimulus identity		Stimulus valence		
			Neutral	Negative	Positive
Young	Target	M	808.08	834.71	806.62
		SD	78.65	82.53	69.11
		Errors	16%	17%	19%
	Distracting	M	854.01	917.25	899.58
		SD	98.62	111.95	100.23
		Errors	3%	5%	4%
Old	Target	M	871.57	890.49	866.82
		SD	197.72	207.29	178.10
		Errors	16%	19%	20%
	Distracting	M	968.49	1004.46	993.12
		SD	186.45	184.84	179.81
		Errors	11%	14%	17%

$p < 0.001$, and Valence: $F(2,77) = 15.460$, MSE = 3623.77, $g^2 = 0.17$, $p < 0.001$. Old participants were slower than the young ones (M = 932 and 853 ms, respectively), target (previously presented) stimuli were responded to faster than the distractors (M = 846 and 939 ms, respectively). Bonferroni pairwise comparisons indicated that the negative images (M = 912 ms) were responded to significantly more slowly ($p < 0.01$) than the positive ones (M = 892 ms) and the neutral ones (M = 876 ms), while the difference between the latter two was approaching significance ($p = 0.053$). These main effects were qualified by the interactions between stimulus Identity and Age: $F(1,78) = 5.511$, $p = 0.021$, $g^2 = 0.07$, as well as Identity and Valence: $F(2,77) = 5.339$, $p = 0.007$, $g^2 = 0.07$.

The ANOVA carried out on accuracy showed a main effect of Age: $F(1,78) = 7.49$, MSE = 2613.33, $g^2 = 0.08$, $p < 0.05$, and Identity: $F(1,78) = 18.19$, MSE = 6348.01, $g^2 = 0.18$, $p < 0.001$, however, Valence did not reach the significance level ($F < 1$).

In order to explore those interactions, 2 9 3 Identity 9 Valence ANOVAs were carried out, separately for young and old participants.

Young

The ANOVA on RT data of young participants revealed main effects of Identity: $F(1,39) = 39.205$; MSE = 8336.86; $g^2 = 0.50$; $p < 0.001$, as well as Valence: $F(2,78) = 25.687$; MSE = 1586.29; $g^2 = 0.40$; $p < 0.001$. Target stimuli were processed faster (M = 816 ms) than distractors (M = 890 ms), and Bonferroni pairwise comparisons indicated that negative stimuli (M = 876 ms) were processed more slowly than positive ones (M = 853 ms), which in turn were processed more slowly than neutral ones (M = 831 ms) (all ps < 0.01). The interaction between Valence and Identity was significant: $F(2,78) = 8.588$, MSE = 1528.50; $g^2 = 0.18$; $p < 0.001$. Bonferroni pairwise comparisons indicated that, for the target stimuli, negative ones (M = 835 ms) were processed more slowly ($p < 0.05$) than both positive (M = 808 ms) and neutral ones (M = 807 ms), with no significant difference ($p > 0.50$) between the latter two categories. For the distractor stimuli, negative ones (M = 917 ms) were also processed more slowly ($p < 0.01$) than neutral ones ($p = 0.854$ ms), but not significantly more slowly ($p > 0.10$) than positive ones (M = 900 ms). Error differences did not reach statistical significance for valence ($F < 1$) but it did for distracting and target conditions: $F(1,39) = 60.79$, MSE = 11.21, $g^2 = 0.60$; $p < 0.001$.

Old

The ANOVA on the latencies of old participants also revealed significance for the main factor of Identity: $F(1,39) = 96.236$; MSE = 7876.49; $g^2 = 0.71$; $p < 0.001$, but it fell just short of significance for the main factor of emotional Valence: $F(2,78) = 2.95$; MSE = 5905.85; $g^2 = 0.07$; $p = 0.058$. The interaction between Identity and Valence was not significant, either: $F(2,78) = 1.103$, MSE = 4074.59, $g^2 = 0.03$. Thus, the target stimuli were processed faster than the distractors (M = 876 vs. 989 ms, respectively), but there was no significant differences between the processing of negative (M = 947 ms), positive (M = 930 ms) and neutral (M = 920 ms) stimuli − albeit the direction of those differences was the same as in the young group. Thus, the impact of valence on RT appears to be much more prominent in the young group. Error differences did not reach statistical significance for distracting and target conditions ($F < 1$) but it did for valence: $F(2,78) = 5.41$; MSE = 428.22; $g^2 = 0.12$; $p < 0.05$. Bonferroni pairwise comparisons indicated that positive stimuli (M = 81.31) were processed more accurately than neutral ones (M = 85.93), ps < 0.05.

Table 3. *l, r, s parameters with their uncertainty (standard error), dfs (degrees of freedom) and the ratio between v2/df for each condition*

Group	Stimulus identity	Stimulus valence	l	r	s	df	v2/df
Young	Target	Neutral	620.06 T 6.47	52.61 T 4.97	181.50 T 10.08	22	1.01
		Negative	640.33 T 6.50	60.91 T 5.41	185.55 T 10.14	25	0.84
		Positive	639.14 T 6.22	64.01 T 4.45	159.96 T 8.39	28	0.73
	Distractor	Neutral	656.34 T 8.67	74.71 T 6.59	186.11 T 11.84	27	1.26
		Negative	710.03 T 11.02	95.15 T 10.01	197.07 T 15.03	27	1.34
		Positive	681.10 T 8.04	81.91 T 6.04	215.66 T 11.22	30	0.89
Old	Target	Neutral	597.68 T 7.20	58.54 T 6.72	257.81 T 13.29	34	0.87
		Negative	611.46 T 9.43	57.43 T 8.24	248.48 T 18.26	32	1.45
		Positive	604.42 T 9.32	61.42 T 8.45	235.51 T 16.55	32	1.37
	Distractor	Neutral	660.12 T 10.26	97.11 T 8.83	307.96 T 16.62	37	0.85
		Negative	704.45 T 11.55	91.72 T 9.39	308.46 T 18.25	37	1.06
		Positive	680.65 T 12.73	104.6 T 10.01	315.33 T 19.1	36	1.01

Finally, we proceeded to characterize the reaction times by an ex-Gaussian fit. One should keep in mind that l and r are not the average and standard deviation of the ex-Gaussian distribution, which should be calculated via the three parameters that describe the distribution: the mean is in fact $M = l + s$.

Fitting the distribution means finding the optimal values for the parameters l, s and r that best describe the experimental data. For this purpose, we used the fitting function of the open-source software Gnuplot. With this software, the fit of any mathematical function to any data set can be obtained straightforwardly by a single function, but given the amount of data in the present work, the need to prepare the data (distribute it in intervals) and

the fact that many different datasets had to be fitted, a python script was programmed. This script automatically reads a set of data (reaction times), groups this data in intervals, creating a histogram and interacts with the Gnuplot software in order to fit an ex-Gaussian function to the data points. Distribution fits and graphics were both executed by the command-line program GNU plot 4.2 (via Navarro-Pardo *et al.*, 2013). The Gnuplot software employs the Levenberg-Marquardt algorithm, also known as dumped least-square method (Marquardt, 1963). The algorithm finds the optimal parameters that minimize the square of the difference between a given data set (x_i, y_i) and a target function $f(x_i)$.

Fig. 1. Reaction times for each target condition, together with the ex-Gaussian fit. Left side: Young participants. Right side: Old participants. Top: neutral condition. Middle: negative condition. Bottom: positive condition.

The algorithm is an iterative procedure that readjusts the set of parameters in each iteration. First of all, a goodness of fit function has to be defined in order to reflect the quality of the fit. The goodness of fit can be evaluated through the residual variance (the most widely used method in behavioral sciences, V^2/degrees of freedom). Smaller values are preferable as they reflect a better fit. Table 3 shows the different parameters obtained by the fitting procedure and Figs. 1 and 2 show the graphical representation of the histograms, together with fit, for each condition.

The uncertainties (errors) presented in Table 3, allow us to compare the parameters for the different conditions, regarding the uncertainties as a confidence interval length for each parameter. If we compare the distribution averages ($M = I + S$), in the younger group, we notice that the differences between neutral and negative conditions for distractor stimuli (64.65) is much bigger than the uncertainties sum (46.56), indicating a significant statistical difference. The same pattern can be found for the differences between neutral and positive condition (54.31), which is much higher than the uncertainties sum (39.77).

Regarding the S parameter, the differences between neutral and positive condition (29.55) is slightly higher than the uncertainties sum (23.06). However, for the older participants neither the distribution average, nor the S parameter are higher than the
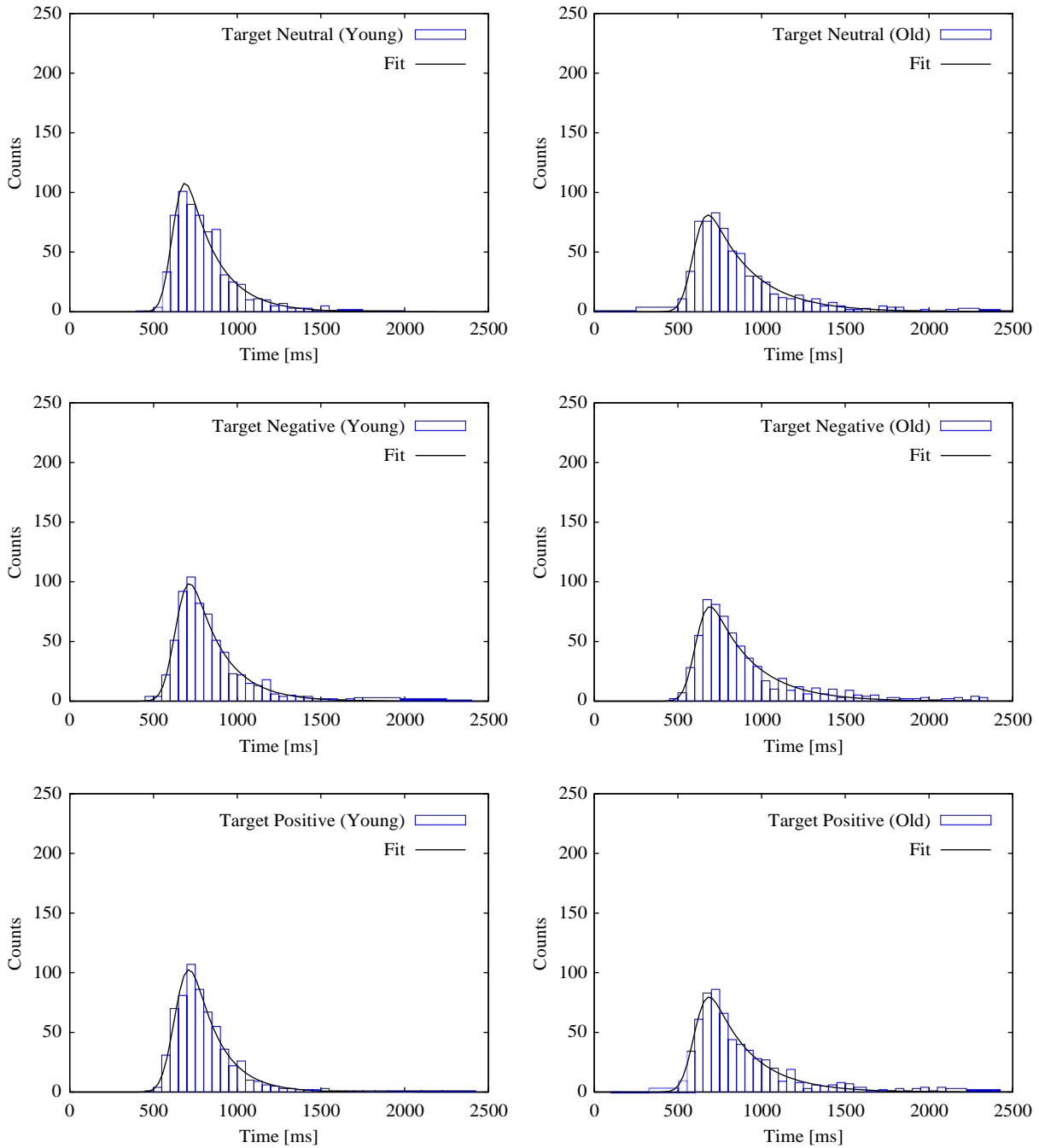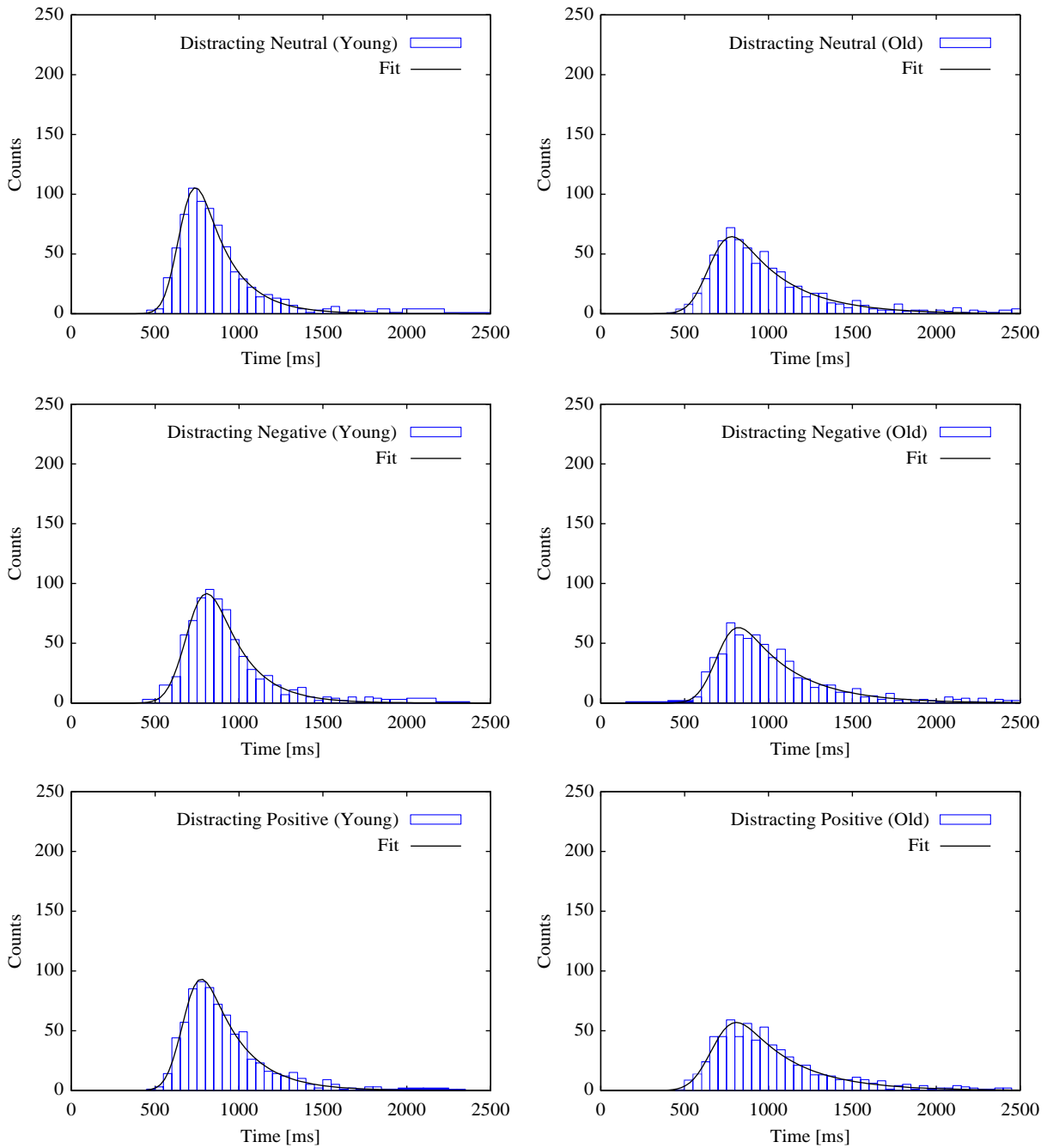

Fig. 2. Reaction times for each distracting condition, together with the ex-Gaussian fit. Left side: Young participants. Right side: Old participants. Top: neutral condition. Middle: negative condition. Bottom: positive condition.

corresponding uncertainties sums. Finally, when we compare the parameters for older and younger participants, we notice that older participants present much higher distribution average and s parameter than the young younger participants.

DISCUSSION AND CONCLUSIONS

The aim of this study was to examine the influence of emotional valence and age on visual recognition, while controlling for the level of arousal and employing a short retention interval. This recognition task was analyzed not only by the classical analysis of variance, but also through the characterization of the reaction times via an ex-Gaussian fit which allows the analysis of the conditions in terms of parameters. The present work not only presents conclusions drawn from the classical ANOVA analysis, it also presents a study on the underlying cognitive processes that cannot be tackled by conventional techniques and so presents some of the advantages of the ex-Gaussian fit. This innovative technique does not depend on the same suppositions as the classical ANOVA, nor does it require the removal of outliers, which may exclude important information.

While the main aim of this study was to show the advantages of an ex-Gaussian fit analysis, the impact of age and emotional valence on recognition memory was evaluated as well. The impact of valence on RT appears to be much more prominent in the young group. We also found slower RTs towards negative stimuli, replicating Gordillo Leon et al.'s (2010) study. Carretié, Martin-Loeches, Hinojosa and Market (2001), postulated that there is a tendency to direct attention to negative stimuli, supporting the notion that the processing of the negative emotional charge could have had an essential role in our evolution. These results were clear for young participants, but differences did not reach statistical significance for the old ones. This evidence supports the explanation offered by Charles et al. (2003) about age-related reductions in memory for negative images.

Another point to highlight is the relation between memory and attention. In traditional models, memory involves attention, encoding, storage, and retrieval. In our experiment, both age groups were slower for negative images than others; however, the s parameter cannot explain valence-linked age differences in memory. One alternative explanation, as Pôrto, Bertolucci, Bueno (2011) indicated, is that the old participant's assessment might be biased due to the nature of emotional valence. They claimed that older participants might focus more on picture details than valence. More research about this issue is necessary.

Addressing the question of RT parameters, the greater differences were found between age groups. Generally, RTs lower for young than old participants, indicating that old participants were slower. Furthermore, in light of the literature on the relation between the s parameter and attention, old participants appear to show poorer attentional performance.

Future studies may include a series of experiments that examine the role of the s parameter in the context of negative images, which try to explain if such pictures attract attention more readily or just hold attention for a longer period of time. Our data do not allow the disentangling between these explanations. Furthermore, it would also be interesting to evaluate the level of arousal, interactions between arousal and valence, and their relation to the s parameter. It would also be interesting to examine developmental changes through the study of the parameters, and also to explore the role of mood.

REFERENCES

Balota, D. A. & Spieler, D. H. (1999). Word frequency, repetition, and lexicality effects in word recognition tasks: Beyond measures of central tendency. *Journal of Experimental Psychology: General*, *128*, 32‒55.

Borg, C., Leroy, N., Favre, E., Laurent, B. & Thomas-Antérion, C. (2011). How emotional pictures influence visuospatial binding in short-term memory in ageing and Alzheimer's disease? *Brain and cognition*, *76*, 20‒25.

Buchanan, T. W. & Adolphs, R. (2002). The role of the human amygdala in emotional modulation of long‒term declarative memory. *Advances in Consciousness Research*, *44*, 9‒34.

Carretié, L., Martín-Loeches, M., Hinojosa, J. A. & Mercado, F. (2001). Emotion and attention interaction studied through event-related potentials. *Journal of Cognitive Neuroscience*, *13*, 1109‒1128.

Charles, S. T., Mather, M. & Carstensen, L. L. (2003). Aging and emotional memory: The forgettable nature of negative images for older adults. *Journal of Experimental Psychology: General*, *132*, 310‒324.

CSEA-NIMH. (1999). *International affective picture system: Digitized photographs*. Gainesville, FL: Center for Research in Psychophysiology, University of Florida.

Epstein, J. N., Langberg, J. M., Rosen, P. J., Graham, A., Narad, M. E., Antonini, T. N., *et al.* (2011). Evidence for higher reaction time variability for children with ADHD on a range of cognitive tasks including reward and event rate manipulations. *Neuropsychology*, *25*, 427‒441.

Forster, K. I. & Forster, J. C. (2003). DMDX: A windows display program with millisecond accuracy. *Behavior Research Methods, Instruments, and Computers*, *35*, 116‒124.

Gordillo León, F., Arana, J. M., Mestas, L., Salvador, J., Meilán, J. J. G., Carro, J. Y. & Pérez, E. (2010). Emocion y memoria de reconocimiento: La discriminacion de la informacion negativa como un proceso adaptativo. *Psicothema*, *22*, 765‒771.

Hohle, R. H. (1965). Inferred components of reaction times as functions of foreperiod duration. *Journal of Experimental Psychology*, *69*, 382‒386.

Keil, A., Bradley, M. M., Hauk, O., Rockstroh, B., Elbert, T. & Lang, P.J. (2002). Large-scale neural correlates of affective picture processing. *Psychophysiology*, *39*, 641‒649.

Lang, P. J. (1995). The emotion probe: Studies of motivation and attention. *American Psychologist*, *50*, 372‒385.

Lang, P. J. T., Bradley, M. M. Y. & Cuthbert, B. N. (1999). *International affective picture system (IAPS): Technical manual and affective ratings*. Gainesville, FL: The Center for Research in Psychophysiology, University of Florida.

Leth-Steensen, C., King Elbaz, Z. & Douglas, V. (2000). Mean response times, variability, and skew in the responding of ADHD children: A response time distributional approach. *Acta Psychologica*, *104*, 167‒190.

Luce, R. D. (1986). *Response times: Their role in inferring elementary mental organization*. New York: Oxford University Press.

Marquardt, D. (1963). An algorithm for least-squares estimation of nonlinear parameters. *SIAM Journal on Applied Mathematics*, *11*, 431‒441.

Matzke, D. & Wagenmakers, E.-J. (2009). Psychological interpretation of ex-Gaussian and shifted Wald parameters: A diffusion model analysis. *Psychonomic Bulletin and Review*, *16*, 798‒817.

Moltó, J., Montañés, S., Poy, R., Segarra, P., Pastor, M. C., Irún, M. P. T., *et al.* (1999). Un método para el estudio experimental de las emociones: El International Affective Picture System (IAPS). Adaptación española. *Revista de psicología general y aplicada: Revista de la Federación Española de Asociaciones de Psicología*, *52*, 55‒87.

Moret-Tatay, C. & Perea, M. (2011). Is the go/no-go lexical decision task preferable to the yes/no task with developing readers? *Journal of experimental child psychology*, *110*, 125–132.

Navarro-Pardo, E., Navarro-Prados, A., Gamermann, D. & Moret-Tatay, C. (2013). Differences between young and old university students on lexical decision task: Evidence through an ex–Gaussian approach. *Journal of General Psychology*, *140*, 251–268.

Pôrto, W. G., Bertolucci, P. H. F. & Bueno, O. F. A. (2011). The paradox of age: An analysis of responses by aging Brazilians to the International Affective Picture System (IAPS). *Revista Brasileira de Psiquiatria*, *33*, 10–15.

Ratcliff, R. & Murdock, B. B. (1976). Retrieval processes in recognition memory. *Psychological Review*, *83*, 190–214.

Reisberg, D. & Heuer, F. (2004). *Memory for emotional events*. In D. Reisberg, & P. Hertel (Eds.), *Memory and emotion* (pp. 272–307). New York: Oxford University Press.

Rozin, P. & Royzman, E. B. (2001). Negativity bias, negativity dominance, and contagion. *Personality and Social Psychology Review*, *5*, 296–320.

Schupp, H. T., Stockburger, J., Codispoti, M., Junghofer, M., Weike, A. I. & Hamm, A. O. (2007). Selective visual attention to emotion. *Journal of Neuroscience*, *27*, 1082–1089.

Wright, D. B., Busnello, R. H. D., Buratto, L. G. & Stein, L. M. (2012). Are valence and social avoidance associated with the memory conformity effect? *Acta Psychologica*, *141*, 78–85.

Psychologica Belgica

RESEARCH ARTICLE

The Effect of Corrective Feedback on Performance in Basic Cognitive Tasks: An Analysis of RT Components

Carmen Moret-Tatay[*], Craig Leth-Steensen[†],
Tatiana Quarti Irigaray[‡], Irani I. L. Argimon[‡], Daniel Gamermann[§],
Diana Abad-Tortosa[‖], Camila Oliveira[‡], Begoña Sáiz-Mauleón[¶],
Andrea Vázquez-Martínez[‖], Esperanza Navarro-Pardo[‖] and
Pedro Fernández de Córdoba Castellá[¶]

The current work examines the effect of trial-by-trial feedback about correct and error responding on performance in two basic cognitive tasks: a classic Stroop task ($n = 40$) and a color-word matching task ($n = 30$). Standard measures of both RT and accuracy were examined in addition to measures obtained from fitting the ex-Gaussian distributional model to the correct RTs. For both tasks, RTs were faster in blocks of trials with feedback than in blocks without feedback, but this difference was not significant. On the other hand, with respect to the distributional analyses, providing feedback served to significantly reduce the size of the tails of the RT distributions. Such results suggest that, for conditions in which accuracy is fairly high, the effect of corrective feedback might either be to reduce the tendency to double-check before responding or to decrease the amount of attentional lapsing.

Keywords: feedback; stroop; matching task; ex-Gaussian components

[*] Department of Neuropsychology, Methodology and Social Psychology, Universidad Católica de Valencia "San Vicente Mártir" C/Guillem de Castro, 175. Valencia 46008, ES

[†] Department of Psychology, Carleton University, 1125 Colonel By Drive, Ottawa, ON, Canada, CA

[‡] Universidade Católica do Rio Grande do Sul, Faculdade de Psicologia, Programa de Pós-Graduação em Psicologia, BR

[§] Instituto de Física, Universidade Federal do Rio Grande do Sul (UFRGS), Av. Bento Gonçalves 9500, CP 15051, 91501-970 Porto Alegre RS, BR

[‖] Facultat de Psicologia, Universitat de València, Avinguda Blasco Ibáñez, 21, ES

[¶] Universitat Politècnica de València, Departamento de expresión gráfica arquitectónica and IUMPA Camino de Vera s/n, 46022, Valencia, ES

Corresponding author: Carmen Moret-Tatay
(carmenmorettatay@gmail.com)

Introduction

An important aspect of experimentation within cognitive psychological paradigms is whether or not to provide participants with trial-by-trial corrective feedback regarding the accuracy of their performance on cognitive tasks. As noted by Krenn, Würth, and Hergovich (2013), the provision of feedback can make individuals aware of any discrepancies between actual states of performance and target states, thus allowing for an evaluation of previous performance in relation to a specific standard.

Not surprisingly, the effect of feedback on human behavior has attracted the interest of cognitive researchers. A large number of studies have examined its effect on different variables such as motivation (Deci, Koestner, & Ryan, 1999; Jussim, Sofaleta, Brown, Law, & Kohlhepp, 1992) and learning (Goodman & Wood, 2004; Wulf, Shea, and Lewthwaite, 2010). However, not as much research has been directed at determining the role that corrective accuracy feedback plays in shaping performance on tasks that involve fairly basic perceptual- or cognitive-based decision making. Hence, such work is the focus of the current study.

Some potential effects of feedback

One view of the effect of accuracy feedback on performance in basic cognitive tasks can be found in Starns and Ratcliff (2010). In their Experiment 2, participants saw a 10 × 10 grid of characters with some of the cells blank and others randomly filled by asterisks. The task was to quickly but accurately decide whether the number of asterisks displayed was either more or less than 50. The actual number of asterisks displayed on any trial ranged uniformly from 31 to 70. In a feedback condition, a post-trial correct or error message was displayed for 600 ms, and separate groups took part in feedback and no feedback conditions (i.e., the presence of feedback was manipulated in a between-participants fashion). When fitting the Ratcliff diffusion model to the obtained response time (RT) results, Starns and Ratcliff (2010) found that the major effect of providing feedback (for the college students but, interestingly, not for the aged 60+ seniors in their sample) was to lower the response criteria (i.e., the decision boundaries). In such a model, response criteria represent the amount of sequentially sampled evidence that must be accumulated in order to make a response (where the strength of the sampled evidence signal itself is referred to as the drift rate). Starns and Ratcliff (2010) conjectured that the provision of feedback helped the younger participants to be more aware of the potential for a balance between speed and accuracy, thus motivating them to make adjustments which then led to more optimal responding (i.e., lowering their response criteria which allowed them to respond faster with what could be regarded as minimal losses in accuracy). Indeed, follow-up analyses by these researchers indicated that the younger group were invoking response criteria when given feedback that were much closer to what Starns and Ratcliff (2010) referred to as the "reward-rate optimal boundary" than were the younger group who were not given feedback. Note that an analogous empirical result can be found in work by Appelgren, Penny, and Bengtsson (2014) involving the n-back memory task. In that study, accuracy-feedback-induced reductions in both RT and accuracy were observed but only for conditions in which feedback was provided after each correct response.

A second related view of the role of accuracy feedback on performance in basic cognitive tasks is that it affects strategy choice. Namely, that it aids participant's determination of the optimality of the various possible processing strategies that could be applied to the current task. For example, Touron and Hertzog (2014) had participants perform a task that, after some degree of practice, could be solved using either a more time-consuming but highly accurate visual search strategy or a fast but occasionally error-prone memory retrieval strategy. They observed an increase in the trial-by-trial, self-reported use of memory retrieval for a group provided

with accuracy feedback compared to a group with no feedback (although mainly for their older participants given that the younger participants were already employing quite high levels of memory retrieval). With respect to simple choice tasks involving highly over-learned and unbiased stimulus-response associations, such as the color-naming and matching tasks examined in the present study, one tempting but quite inefficient processing strategy would be to periodically double-check the stimulus display before making a response. Given that accuracy is typically fairly high to begin with in tasks of this nature, the provision of accuracy feedback could signal that such double-checking is not enhancing performance that much and, hence, could perhaps be dropped (which would then serve to speed up the RTs for all of the trials in which such double-checking would have occurred but didn't and also to potentially reduce accuracy somewhat, given less double-checking).

A third related view of the role of accuracy feedback on performance in basic cognitive tasks is that it affects the amount and focus of the effort devoted to a task (Krenn et al., 2013). In the context of the current research, in the first upcoming study, performance on the classic Stroop task is examined. In a Stroop task, more mistakes are generally made on incongruent Stroop trials. Hence, the provision of corrective feedback when performing such a task could make participants more aware of the fact that the irrelevant stimulus attribute is having an effect on responding and that more effort needs to then be devoted to minimizing the processing of it (either by focusing more intently on selecting the relevant attribute or by attempting to supress all processing of the irrelevant one). Such a view is also in line with the conflict-monitoring account of cognitive control (Botvinick, Braver, Barch, Carer, & Cohen, 2001) which posits that the presence of enhanced stimulus-response conflict in a task such as the Stroop task signals the need for greater cognitive control. Such control can be envisioned in terms of a top-down

attentional biasing of the relevant stimulus attribute that would then serve to enhance the strength of the evidence signal (i.e., drift rate) resulting in faster and, potentially also, more accurate responding. This account is able to provide an explanation for the finding that Stroop interference is reduced in blocks of trials containing a greater proportion of incongruent trials. With respect to the role of corrective feedback in the Stroop task, such feedback could be assumed to provide an explicit signal for the need for greater cognitive control (Bugg & Smallwood, 2014). Moreover, with respect to other types of basic cognitive tasks that do not involve such conflict, note that it would not generally be that hard to envision conditions under which an enhanced marshalling of attentional resources would lead to stronger evidence signals.

A fourth related view of the role of accuracy feedback on performance in basic cognitive tasks is that it affects the deployment of attentional resources more generally. On one hand, the provision of feedback could serve to divert attention away from the performance of the task by capturing limited attentional resources (MacLeod & MacDonald, 2000). Under such conditions, though, it could then be assumed that both accuracy and RT performance would suffer (i.e., lower accuracy accompanied by slower RTs when feedback has been provided). On the other hand, also in line with the notion that feedback enhances effort, the provision of feedback might serve to prompt participants to cut down on the number of attentional lapses that can occur when repeatedly performing such simple tasks either by enhancing motivation or increasing arousal/activation levels (for a related view see Kole, Healy, & Bourne, 2008). Cutting down on attentional lapses would reduce the number of both very slow correct responses and attentional-based errors (although note that if such errors are rather infrequent to begin with, increases in accuracy due to reductions in the number of attentional lapses might not actually turn out to be that substantial).

One bit of evidence for this view can actually also be found in the RT modeling work done by Starns and Ratcliff (2010) on the results from their Experiment 2 (detailed above). Namely, the version of the diffusion model that they used to fit the RTs also contained, what was referred to as, a "proportion of RT contaminants" parameter (i.e., p_o) which was specifically assumed by them to represent lapses in attention. On the proportion of trials indicated by the value of this parameter, an additional response delay, taken from a uniform probability distribution, was assumed to be added to the corresponding diffusion model latency. Interestingly, although never actually addressed by Starns and Ratcliff (2010), the estimated value of this parameter was lower when feedback was provided than when it was not (i.e., 0.2% vs. 1.8% of trials, respectively).

Ex-Gaussian distributional model

At this point, it is important to focus on the dependent variables that might serve to best shed light on feedback effects. Of course, measures of performance accuracy and RT will be key in this respect. However, one important way to extend typical analyses of proportion correct (PC) and mean RT is to examine the distributions of RTs obtained as a whole by fitting distributional models such as the ex-Gaussian (Balota & Spieler, 1999; Heathcote et al., 1991). The ex-Gaussian function represents the convolution of two probability distribution functions: A Gaussian (i.e., normal) and an exponential. This function generally serves to capture, quite adequately, the positively skewed shapes of most RT distributions and it can be quantified using three parameters: μ (the mean of the normal component), σ (the standard deviation of the normal component), and τ (both the mean and standard deviation of the exponential component). In a more intuitive vein, the first two parameters (i.e., μ and σ) serve to summarize the location of the leading edge of a distribution of RTs, whereas the third parameter (i.e., τ)

provides summary information related to the size of the tail of such distributions.

Importantly, like RT itself, the μ and τ parameters have been shown to be remarkably sensitive to the effects of various types of cognitive-based experimental manipulations (for a review see Matze & Wagenmakers, 2009; and see also Kristjánsson, & Jóhannesson, 2014; Leth-Steensen, 2009; Moreno-Cid et al., 2015; Moret-Tatay et al., 2014; Navarro-Pardo, Navarro-Prados, Gamermann, & Moret-Tatay, 2013). However, as extensively discussed by Matzke and Wagenmakers (2009), the substantive interpretation of the ex-Gaussian parameters is still being debated and varies considerably among researchers and theories. The key issue in this regard is the extent to which changes in individual ex-Gaussian parameters can exclusively be attributed to the effects of experimental manipulations on specific cognitive processes such as decisional versus sensory/motor processes or automatic versus controlled processes (Matze & Wagenmakers, 2009).

Nonetheless, the accounts mentioned above regarding the potential effects of providing accuracy feedback do provide some testable predictions regarding changes in the ex-Gaussian parameters μ and τ that would be expected due to the provision of feedback. First, if providing feedback leads to downwards adjustments of decision criteria to achieve a more optimal balance between the speed and accuracy of responding such adjustments, as clearly demonstrated by Matzke and Wagenmakers (2009; see also Smith & Mewhort, 1998), would be expected to lead to decreases in both μ and τ for conditions in which feedback has been provided in comparison to conditions in which it has not. Second, if providing feedback leads to attentional-based strengthening of evidence signals due to enhancements in cognitive control, then such strengthening would also be expected to lead to decreases in both μ and τ for conditions in which feedback has been provided in comparison to conditions in which it has not (Matzke & Wagenmakers,

2009; Smith & Mewhort, 1998; Spieler, Balota, & Faust, 2000; although one caveat is that, as demonstrated by Smith & Mewhort, the effect of increased signal strength, i.e., drift rate, on μ is not that dramatic for cases in which decision criteria are set fairly low).

Third, if the provision of feedback serves to induce a reduction in the number of trials in which a double-checking strategy might have been employed, such reductions would likely be expected to be reflected mainly in smaller values of the ex-Gaussian τ parameter. Such an expectation is in line with work by Penner-Wilger, Leth-Steensen, and LeFevre (2002) who found that the RT distributions obtained from Canadian graduate students when solving single-digit multiplication problems differed from those of Chinese graduate students mostly with respect to the size of τ (much larger for the Canadians). They concluded that this result was consistent with the fact that Canadian students are much more likely to report periodically using less efficient, non-retrieval solution strategies (as opposed to direct memory retrieval) than are Chinese students.

Finally, if the provision of feedback serves to induce a reduction in the number of attentional lapses, such reductions would also be expected to be reflected mainly, if not exclusively, in smaller values of the ex-Gaussian τ parameter. For example, Leth-Steensen, King Elbaz, and Douglas (2000) found that differences in the choice RTs obtained from ADHD and control children were reflected mainly in the tails of the RT distributions (i.e., in τ). They then conjectured that this effect was the result of an enhanced tendency for attentional lapsing in ADHD children (which would then lead to a larger proportion of very slow responses present in the tails of their RT distributions). In this same vein, for a sample of ADHD and typically developing adolescents, Gu, Gau, Tzang, and Hu (2016) found that, with respect to performance on the Connors continuous performance task, the ex-Gaussian parameter τ was highly positively correlated with the number of omission errors (i.e., misses) made by their participants. Such errors were higher for the ADHDs and high rates of such errors were regarded by Gu et al. (2016) as representing markers of attentional impairment. Finally, Spieler, Balota, and Faust (1996) observed enhanced Stroop effects for older adults that were due mostly to increases in tau. They then specifically attributed this result to the possibility that older adults might be more susceptible to experiencing attentional lapses on a greater proportion of trials than young adults.

The current study

In the current work, RT and accuracy performance in both a Stroop color-word task (in Study I) and a subsequent color-word matching task (in Study II) is examined under conditions in which accuracy feedback is provided after each trial and under conditions in which no accuracy feedback is provided. The first task is one of the most broadly applied paradigms in cognitive psychology (Heathcote, Popiel, & Mewhort, 1991), and it has been related to selective attention, processing speed, cognitive flexibility, and executive functions (Howieson, Lezak, & Loring, 2004; Servant, Montagnini, & Burle, 2014). In its standard set up, the Stroop paradigm requires participants to identify the font color of presented color words while trying to ignore congruent and incongruent color names. For the second task, the element of potential conflict between irrelevant aspects of the stimuli and the responses was eliminated by having participants perform a color-word matching task. Namely, they were simply asked to indicate if word names were congruent or not with the color of the font that the words were presented in. One important key aspect of the current work is that in addition to standard analyses involving mean RT and PC, RT distributional analyses are also performed by fitting the ex-Gaussian distributional model to the distributions of RTs obtained from individual participants in each condition of Studies I and II.

Method
Participants
A sample of 40 University students volunteered to take part in Study I (29 women and 11 men with an average age of 20.02 years and SD = 1.22). A sample of 30 students, from the same University, volunteered to take part in Study II (26 women and 4 men with an average age of 20.27 years and SD = 1.26). All the participants had normal vision or corrected to normal, were native Spanish speakers, and did not report any cognitive or neurological disorders

Materials
The presentation of the stimuli and recording of RT and PC were controlled by computers through the Windows software DMDX (Forster & Forster, 2003). On each trial, a fixation point (+) was presented for 500 ms in the center of the screen. Then the target stimulus was presented until the participants responded, with a maximum of 2500 ms given to respond. Word stimuli in Study I were *rojo* (which means red), *azul* (which means blue), and *xxxx*. Word stimuli in Study II were *rojo* and *azul*. The stimuli were presented in lowercase 14-pt Courier.

Design
In Study I, a 2 (presence and absence of feedback) × 3 (congruent, incongruent, and control Stroop conditions) factorial design was used. Participants were required to identify the color red by pressing one key and the color blue by pressing another. The stimuli was presented in either red or blue uppercase letters, and there were three presentation conditions: i) Congruent - red word displayed in red or blue word displayed in blue, ii) incongruent - red word displayed in blue or blue word displayed in red, and iii) neutral - xxxx in red or blue. Participants performed 18 practice trials and 240 experimental trials.

In Study II, a 2 (presence and absence of feedback) × 2 (congruent and incongruent matching conditions) factorial design was used. Participants were required to identify

if the font color was congruent with the written word by pressing one key, or not, by pressing another key. This is why condition iii) from Study I was not possible for Study II. The stimuli were presented in either red or blue lowercase letters, and there were two presentation conditions: i) Matching - red word displayed in red or blue word displayed in blue, and ii) nonmatching - red word displayed in blue or blue word displayed in red. Participants performed 18 practice trials and 160 experimental trials.

For both studies, the stimuli were presented in a randomized fashion within blocks. Furthermore, participants from each study were divided into two groups. The first group started with a block which provided immediately informative feedback and a following block which did not. The second group performed the task with the order of these blocks reversed. Informative feedback was provided immediately after each participant's response that indicated whether it was *Correcto* (correct) or *Error* (error). RTs to perform the task on each trial were recorded in milliseconds. Each session lasted about 20 minutes.

Analysis
The dependent measures to be analysed in each study were the (arcsine-transformed) PCs, mean correct RTs, and the values of each of the three ex-Gaussian parameters μ, σ, and τ. Values for each of these measures were obtained for each participant individually for each condition in the corresponding designs (i. e., the ex-Gaussian model was fit separately for each participant to the sets of correct RTs obtained in each of the six conditions of Study I and the four conditions of Study II). Any correct RTs shorter than 150 ms or more than 4 SDs above the mean in each condition (Leth-Steensen et al., 2000) were removed before running the RT analyses (i.e., 0.7% of the Study I correct RTs and 0.9% of the Study II correct RTs).

The software used to perform the ex-Gaussian fits made use of quantile maximum probability estimation (QMPE; Heathcote,

Brown, & Cousineau, 2004). QMPE fits the ex-Gaussian distribution to a set of quantile values that have been estimated from a set of RT data. Directly analogous to percentile values, quantiles represent the RT value for which a certain proportion of observed RTs fall below it. Essentially, what QMPE is doing is invoking a search for the values of μ, σ, and τ that result in ex-Gaussian-based quantile values that most closely match the actual quantile values in a set of RT data. This search is undertaken using maximum likelihood techniques. More specifically, the best fitting ex-Gaussian curve is associated with the three ex-Gaussian parameter values for which the likelihood of the observed set of actual quantile values is a maximum. For the present fits, the number of quantiles used was set at 10.

Results
Study I
Average RTs for correct responses and PCs are presented in **Table 1**. A 2 (feedback condition) × 3 (Stroop condition) fully repeated measures ANOVA was performed on both the RTs and PCs.

As expected, RT showed Stroop effects: $F(2, 78) = 21.00$, $p < .001$, $MSE = 888$, $\eta_p^2 = .350$. On the other hand, although RTs were faster for the feedback condition than for the no-feedback condition for all three Stroop conditions, this difference was not significant at the conventional .05 level: $F(1, 39) = 3.08$, $p < .10$, $MSE = 5940$, $\eta^2 = .073$. With respect to the PCs, significant Stroop effects were also

present: $F(2, 78) = 11.70$, $p < .001$, $MSE = 0.018$, $\eta_p^2 = .231$. However, neither the main effect of the feedback conditions nor its interaction with the Stroop conditions were statistically significant ($Fs < 1$).

With respect to the three ex-Gaussian parameters, analogous ANOVAs were performed on each of them as well (plots of the effects present in μ and τ are given in (**Figure 1A**). For μ, no main effects or interactions involving it were statistically significant (all $ps > .10$). For σ, as well, no main effects or interactions involving it were statistically significant (all $ps > .10$). For τ, however, both the main effect of the Stroop conditions, $F(2, 78) = 12.29$, $p < .001$, $MSE = 1412$, $\eta_p^2 = .240$, and the main effect of the feedback conditions, $F(1, 39) = 11.66$, $p < .01$, $MSE = 1930$, $\eta^2 = .230$, were significant. Note, as well, that when the order in which the feedback was provided (i.e., first or second) was entered as a factor in the design, no significant main effects or interactions involving it were present for analyses involving either μ or τ (all $ps > .05$).

Study II
Average RTs for correct responses and PCs are presented in **Table 2**. A 2 (feedback condition) × 2 (matching condition) fully repeated measures ANOVA was performed on both the RTs and PCs.

As expected, RT showed matching effects: $F(1, 29) = 167.07$, $p < .001$, $MSE = 1670$, $\eta_p^2 = .852$. On the other hand, although RTs were faster for the feedback condition

	Congruent	Incongruent	Neutral
RT			
Feedback	443	468	447
No Feedback	462	490	459
PC			
Feedback	0.983	0.954	0.976
No Feedback	0.974	0.959	0.976

Table 1: Mean RTs (in ms) and PCs for the Stroop and Feedback Conditions in Study I.

than for the no-feedback condition for each matching conditions, this difference was again not significant at the conventional .05 level: $F(1, 29) = 3.96$, $p < .10$, $MSE = 10554$, $\eta^2 = .120$. With respect to the PCs, no main effects or interactions were statistically significant (all $ps > .05$).

With respect to the three ex-Gaussian parameters, analogous ANOVAs were performed on each of them as well (plots of the effects present in μ and τ are given in (**Figure 1B**). For μ, only the main effect of matching conditions was significant, $F(1, 29) = 37.47$, $p < .001$, $MSE = 2800$, $\eta_p^2 = .564$. For σ, no main effects or interactions involving it were statistically significant (all $ps > .05$). For τ, both the main effect of the matching conditions, $F(1, 29) = 10.04$, $p < .01$, $MSE = 4398$, $\eta_p^2 = .257$, and the main effect of the feedback conditions, $F(1, 29) = 8.90$, $p < .01$, $MSE = 7767$, $\eta^2 = .235$, were significant. Note, as well, that when the order in which the feedback was provided (i.e., first or second) was entered as a factor in the design, no significant main effects or interactions involving it were present for analyses involving either μ or τ (all $ps > .10$).

	Match	No match
RT		
Feedback	693	787
No Feedback	728	827
PC		
Feedback	0.940	0.953
No Feedback	0.961	0.953

Table 2: Mean RTs (in ms) and PCs for the Matching and Feedback Conditions in Study II.

Discussion

The present results are clear in demonstrating that, for the two basic cognitive tasks examined here, providing accuracy feedback served to significantly reduce the size of the tails of the RT distributions only. That is, in both Studies I and II, although decreases in τ
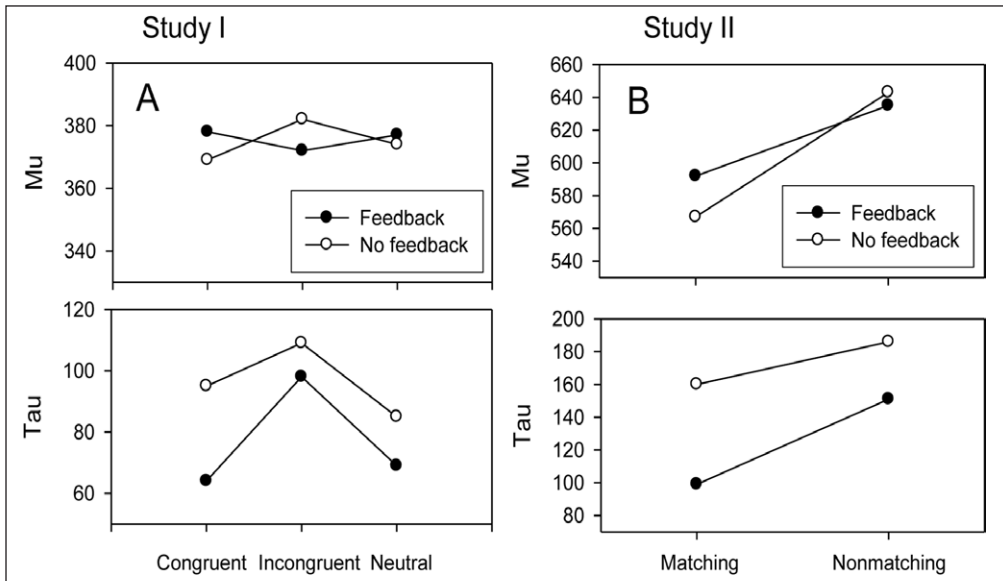

Figure 1: Values of the ex-Gaussian parameters μ (i.e., mu) and τ (i.e., tau) at each feedback by Stroop condition in Study I **(1A)** and at each feedback by matching condition in Study II **(1B)**.

were observed when feedback was given, no such decreases in μ occurred. Highlighting the importance of obtaining a more detailed description of RT through an examination of the separate ex-Gaussian RT components, in both studies, the effect of feedback on overall RT was not significant at the .05 level. Hence, if only RTs had been examined here, any conclusions concerning the effect of providing feedback on the speed of responding would have to have been regarded as being somewhat tentative. Moreover, in neither study did the provision of such feedback serve to significantly affect the accuracy of responding (for further discussion of the potential effects of corrective feedback on overall accuracy see Appelgren et al., 2014, and for a demonstration of the fact that corrective feedback does not seem to affect post-error slowing see Houtman, Castellar, Notebaert, & Nu, 2012).

Importantly, the presence of feedback effects in τ but not in μ is somewhat diagnostic regarding the different views of the potential effects of such feedback discussed earlier. Namely, such a result is highly suggestive of the fact that providing feedback served to reduce either the tendency to double-check before responding or the amount of attentional lapsing. Given such possibilities, one aspect of future research might be to examine the role that various kinds individual difference variables such as anxiety (Bishop, Duncan, Brett, & Lawrrence, 2004; Henderson, Synder, Gupta, & Banich, 2012), might have in determining this feedback effect. Although the possibility that the present changes in τ with feedback were due to stronger evidence signals cannot be completely ruled out note that, as discussed earlier, small or negligible effects in μ under such conditions would only be expected if decision thresholds were set quite low (as they would be if participants had been instructed to emphasize speed), and there is no indication in either the RTs or the PCs from either Study I or II that this would have been the case here.

With respect to the first view regarding the potential effect of feedback discussed earlier,

it seems that participants in the present studies were likely already performing quite optimally in terms of balancing out the speed and accuracy of their responding. Note that in Starns and Ratcliff's (2010) Experiment 2, the discrimination task was actually rather difficult on some trials (e.g., deciding whether a display with 49 asterisks had either more or less than 50 asterisks) leading to an overall observed accuracy of around 85% correct that was much lower than in the present studies (as was also the case for the n-back memory task of Appelgren et al., 2014). Hence, such circumstances may have induced an overly cautious response set that was then subject to adjustments when feedback was provided (at least for their younger participants).

Finally, what might the results of this study have to say to cognitive researchers in general with respect to the issue of whether corrective accuracy feedback should or should not be included as part of their experimental procedures? Well, for studies that are concerned mainly with examining RT for which accuracy is typically quite high (i.e., > 90%), the current results suggest that providing such feedback would indeed tend to reduce the size of the tails of the RT distributions (hence, serving to lower both the RT means and standard deviations of individual participants). However, as is also evident in the current results, the effect of providing feedback did not interact with either of the other experimental manipulations (i.e., Stroop congruency or color-word match). If it is indeed the case that such feedback effects do not serve to moderate any other effects then, perhaps, the slight increases in the tails of the RT distributions that would occur when not providing such feedback might be something that could easily be tolerated. On the other hand, for those researchers who might then be interested in going on to fit parameterized process-based models, such as the diffusion model, to their RT data, reducing the possibility of either double-checking or attentional lapses (both of which could actually be regarded as RT contaminants) by

providing corrective accuracy feedback might indeed be helpful with respect to achieving the best possible parameter estimates from those model fits.

Competing Interests

The authors have no competing interests to declare.

References

Appelgren, A., Penny, W., & Bengtsson, S. L. (2014). Impact of feedback on three phases of performance monitoring. *Experimental Psychology*, *61*, 224–233. DOI: http://dx.doi.org/10.1027/1618-3169/a000242

Balota, D. A., & Spieler, D. H. (1999). Word frequency, repetition, and lexicality effects in word recognition tasks: Beyond measures of central tendency. *Journal of Experimental Psychology: General*, *128*, 32–55. DOI: http://dx.doi.org/10.1037/0096-3445.128.1.32

Bishop, S., Duncan, J., Brett, M., & Lawrence, A. D. (2004). Prefrontal cortical function and anxiety: controlling attention to threat-related stimuli. *Nature Neuroscience*, *7*, 184–188. DOI: http://dx.doi.org/10.1038/nn1173

Botvinick, M. M., Braver, T. S., Barch, D. M., Carer, C. S., & Cohen, J. D. (2001). Conflict monitoring and cognitive control. *Psychological Review*, *108*, 624–652. DOI: http://dx.doi.org/10.1037/0033-295X.108.3.624

Deci, E. L., Koestner, R., & Ryan, R. M. (1999). A meta-analytic review of experiments examining the effects of extrinsic rewards on intrinsic motivation. *Psychological Bulletin, 125,* 627–668. DOI: http://dx.doi.org/10.1037/0033-2909.125.6.627

Goodman, J. S., & Wood, R. E. (2004). Feedback specificity, learning opportunities, and learning. *Journal of Applied Psychology, 89,* 809–821. DOI: http://dx.doi.org/10.1037/0021-9010.89.5.809

Heathcote, A., Brown, S., & Cousineau, D. (2004). QMPE: Estimating Lognormal, Wald, & Weibull RT distributions with a parameter-dependent lower bound. *Behavior Research Methods, Instruments, & Computers*, *36*, 277–290. DOI: http://dx.doi.org/10.3758/BF03195574

Heathcote, A., Popiel, S. J., & Mewhort, D. J. K. (1991). Analysis of response time distributions: An example using the Stroop task. *Psychological Bulletin, 109,* 340–347. DOI: http://dx.doi.org/10.1037/0033-2909.109.2.340

Henderson, R. K., Snyder, H. R., Gupta, T., & Banich, M. T. (2012). When does stress help or harm? The effects of stress controllability and subjective stress response on Stroop performance. *Frontiers in Psychology, 3.* DOI: http://dx.doi.org/10.3389/fpsyg.2012.00179

Houtman, F., Castellar, E. N., Notebaert, W., & Nu, E. (2012). Orienting to errors with and without immediate feedback. *Journal of Cognitive Psychology*, *24*, 37–41. DOI: http://dx.doi.org/10.1080/20445911.2011.617301

Howieson, D. B., Lezak, M. D., & Loring, D. W. (2004). *Orientation and attention.* Neurological Assessment, 3365–3367.

Jussim, L., Soffin, S., Brown, R., Ley, J., & Kohlhepp, K. (1992). Understanding reactions to feedback by integrating ideas from symbolic interactionism and cognitive evaluation theory. *Journal of Personality and Social Psychology, 62,* 402–421. DOI: http://dx.doi.org/10.1037/0022-3514.62.3.402

Kole, J. A., Healy, A. F., & Bourne Jr., L. E. (2008). Cognitive complications moderate the speed-accuracy tradeoff in data entry: A cognitive antidote to inhibition. *Applied Cognitive Psychology*, *22*, 917–937. DOI: http://dx.doi.org/10.1002/acp.1401

Kristjánsson, Á., & Jóhannesson, Ó. I. (2014). How priming in visual search affects response time distributions: Analyses with ex-Gaussian fits. *Attention, Perception, & Psychophysics, 76,* 2199–2211. DOI: http://dx.doi.org/10.3758/s13414-014-0735-y

Leth-Steensen, C. (2009). Lengthening fixed preparatory durations within a

digit magnitude classification task serves mainly to shift distributions of response times upwards. *Acta Psychologica, 130,* 72–80. DOI: http://dx.doi.org/10.1016/j.actpsy.2008.10.003

Leth-Steensen, C., King Elbaz, Z., & Douglas, V. I. (2000). Mean response times, variability, and skew in the responding of ADHD children: a response time distributional approach. *Acta Psychologica, 104,* 167–190. DOI: http://dx.doi.org/10.1016/S0001-6918(00)00019-6

MacLeod, C., & MacDonald, P. (2000). Interdimensional interference in the Stroop effect: Uncovering the cognitive and neural anatomy. *Trends in Cognitive Sciences, 4,* 383–391. DOI: http://dx.doi.org/10.1016/S1364-6613(00)01530-8

Matzke, D., & Wagenmakers, E.-J. (2009). Psychological interpretation of ex-Gaussian and shifted Wald parameters: A diffusion model analysis. *Psychonomic Bulletin & Review, 16,* 798–817. DOI: http://dx.doi.org/10.3758/PBR.16.5.798

Moreno-Cid, A., Moret-Tatay, C., Irigaray, T. Q., Argimon, I. I., Murphy, M., Szczerbinski, M., Fernández, P. et al. (2015). The Role of Age and Emotional Valence in Word Recognition: An Ex-Gaussian Analysis. *Studia Psychologica, 57,* 83–94.

Moret-Tatay, C., Argimon, I., Quarty, T., Moreno, A., Szczerbinski, M., Murphy, M., Vázquez-Molina, J., Vázquez-Martínez, A., Saíz-Mauleon, B., Navarro-Pardo, E., & Fernández de Córdoba Castellá, P. (2014). The effects of age and emotional valence on recognition memory: ex-Gaussian components analysis. *Scandinavian Journal of Psychology, 55,* 420–426. DOI: http://dx.doi.org/10.1111/sjop.12136

Navarro-Pardo, E., Navarro-Prados, A. B., Gamermann, D., & Moret-Tatay, C. (2013). Differences between young and old university students on lexical decision task: evidence through an ex-Gaussian approach. *Journal of General Psychology, 140,* 251–268. DOI: http://dx.doi.org/10.1080/00221309.2013.817964

Penner-Wilger, M., Leth-Steensen, C., & LeFevre, J. (2002). Decomposing the problem-size effect: A comparison of response time distributions across cultures. *Memory & Cognition, 30,* 1160–1167. DOI: http://dx.doi.org/10.3758/BF03194333

Servant, M., Montagnini, A., & Burle, B. (2014). Conflict tasks and the diffusion framework: Insight in model constraints based on psychological laws. *Cognitive Psychology, 72,* 162–195. DOI: http://dx.doi.org/10.1016/j.cogpsych.2014.03.002

Smith, D. G., & Mewhort, D. J. K. (1998). The distributions of latencies constrains theories of decision time: A test of the random-walk model using numeric comparison. *Australian Journal of Psychology, 50,* 149–156. DOI: http://dx.doi.org/10.1080/00049539808258791

Spieler, D., Balota D., & Faust, M. (1996) Stroop performance in healthy younger and elder adults and in individuals with dementia of the Alzheimer's type. *Journal of Experimental Psychology: Human Perception and Performance, 22,* 461–479. DOI: http://dx.doi.org/10.1037/0096-1523.22.2.461

Spieler, D. H., Balota, D. A., & Faust, M. E. (2000). Levels of selective attention revealed through analyses of response time distributions. *Journal of Experimental Psychology: Human Perception and Performance, 26,* 506–526. DOI: http://dx.doi.org/10.1037/0096-1523.26.2.506

Starns, J. J., & Ratcliff, R. (2010). The effects of aging on the speed-accuracy compromise: Boundary Optimality in the Diffusion Model. *Psychology and Aging, 25,* 377–390. DOI: http://dx.doi.org/10.1037/a0018022

Touron, D. R., & Hertzog, C. (2014). Accuracy and speed feedback: Global and local effects on strategy usage. *Experimental Aging Research, 40,* 332–356. DOI: http://dx.doi.org/10.1080/0361073X.2014.897150

Wulf, G., Shea, C., & Lewthwaite, R. (2010). Motor skill learning and performance: a review of influential factors. *Medical Education, 44,* 75–84. DOI: http://dx.doi.org/10.1111/j.1365-2923.2009.03421.x

ExGUtils: A Python Package for Statistical Analysis With the ex-Gaussian Probability Density

Carmen Moret-Tatay[1]*, Daniel Gamermann[2], Esperanza Navarro-Pardo[3] and Pedro Fernández de Córdoba Castellá[4]

[1] Department of Neuropsychology, Methodology, Basic and Social Psychology, Faculty of Psychology, Universidad Católica de Valencia San Vicente Mártir, Valencia, Spain, [2] Instituto de Física, Universidade Federal do Rio Grande do Sul (UFRGS), Porto Alegre, Brazil, [3] Department of Developmental and Educational Psychology, Faculty of Psychology, Universitat de Valencia, Valencia, Spain, [4] Grupo de Modelización Interdisciplinar, Instituto Universitario de Matemática Pura y Aplicada, InterTech, Universitat Politècnica de València, Valencia, Spain

The study of reaction times and their underlying cognitive processes is an important field in Psychology. Reaction times are often modeled through the ex-Gaussian distribution, because it provides a good fit to multiple empirical data. The complexity of this distribution makes the use of computational tools an essential element. Therefore, there is a strong need for efficient and versatile computational tools for the research in this area. In this manuscript we discuss some mathematical details of the ex-Gaussian distribution and apply the ExGUtils package, a set of functions and numerical tools, programmed for python, developed for numerical analysis of data involving the ex-Gaussian probability density. In order to validate the package, we present an extensive analysis of fits obtained with it, discuss advantages and differences between the least squares and maximum likelihood methods and quantitatively evaluate the goodness of the obtained fits (which is usually an overlooked point in most literature in the area). The analysis done allows one to identify outliers in the empirical datasets and criteriously determine if there is a need for data trimming and at which points it should be done.

Keywords: response times, response components, python, ex-Gaussian fit, significance testing

1. INTRODUCTION

The reaction time (RT) has become one of the most popular dependent variables in cognitive psychology. Over the last few decades, much research has been carried out on problems focusing exclusively on success or fail in trials during the performance of a task, emphasizing the importance of RT variables and their relationship to underlying cognitive processes (Sternberg, 1966; Wickelgren, 1977; McVay and Kane, 2012; Ratcliff et al., 2012). However, RT has a potential disadvantage: its skewed distribution. One should keep in mind that in order to perform data analysis, it is preferable that the data follow a known distribution. If the distribution is not symmetrical, it is possible to carry out some data transformation techniques (e.g., the Tukey scale for correcting skewness distribution), or to apply some trimming techniques, but with these techniques, statistics may be altered (in other words a high concentration of cases in a given range

may be favored and as a result, statistics can appear biased). Moreover, transformations can affect the absolute value of the data or modify the relative distances between data. When conducting trimming it is not easy to distinguish noisy data from valid information, or in other words, to set the limits between outliers and extreme data (Heathcote et al., 1991). Whether we include or exclude outliers often depends on the reason why they might occur, dealing with the decision to classify them as variability in the measurement or as an experimental error. Another option, for the analysis of skewed data, is to characterize them with a known skewed distribution. This procedure allows one to determine the probability of an event based on the statistical model used to fit the data. A common problem with this approach is to estimate the parameters that characterize the distribution. In practice, when one wants to find out the probability for an event numerically, a quantified probability distribution is required.

Going back to the point on characterizing data with a specific distribution, there is one distribution that has been widely employed in the literature when fitting RT data: the exponentially modified Gaussian distribution (West, 1999; Leth-Steensen et al., 2000; West and Alain, 2000; Balota et al., 2004; Hervey et al., 2006; Epstein et al., 2011; Gooch et al., 2012; Navarro-Pardo et al., 2013). This distribution is characterized by three parameters, μ, σ and τ. The first and second parameters (μ and σ), correspond to the average and standard deviation of the Gaussian component, while the third parameter (τ) is the decay rate of the exponential component. This distribution provides good fits to multiple empirical RT distributions (Luce, 1986; Lacouture and Cousineau, 2008; Ratcliff and McKoon, 2008), however there are currently no published statistical tables available for significance testing with this distribution, though there are softwares like S-PLUS (Heathcote, 2004) or PASTIS (Cousineau and Larochelle, 1997) and programming language packages available for R, MatLab or Methematica.

In this article we present a package, developed in Python, for performing statistical and numerical analysis of data involving the ex-Gaussian function. Python is a high-level interpreted language. Python and R are undoubtedly two of the most widespread languages, as both are practical options for building data models with a lot of community support. However, the literature seems to be rather scarce in terms of computations with the ex-Gaussian function in Python. The package presented here is called ExGUtils (from ex-Gaussian Utilities), it comprises functions for different numerical analysis, many of them specific for the ex-Gaussian probability density.

The article is organized as follows: in the next section we present the ex-Gaussian distribution, its parameters and a different way in which the distribution can be parameterized. Following this, we discuss two fitting procedures usually adopted to fit probability distributions: the least squares and the maximum likelihood. In the third section we present the ExGUtils module and we apply it in order to fit experimental data, evaluate the goodness of the fits and discuss the main differences in the two fitting methods. In the last section we present a brief overview.

2. THE ex-GAUSSIAN DISTRIBUTION AND ITS PROBABILITY DENSITY

Given a randomly distributed X variable that can assume values between minus infinity and plus infinity with probability density given by the gaussian distribution,

$$g(x) = \frac{1}{\sigma\sqrt{2\pi}} \exp\left(-\frac{1}{2}\left(\frac{x-\mu}{\sigma}\right)^2\right), \quad (1)$$

and a second random Y variable that can assume values between zero and plus infinity with probability density given by an exponential distribution,

$$h(x) = \frac{1}{\tau}e^{-\frac{x}{\tau}}, \quad (2)$$

let's define the Z variable as the sum of the two previous random variables: $Z = X + Y$.

The gaussian distribution has average μ and standard deviation σ, while the average and standard deviation of the Y variable will be both equal to τ. The Z variable will also be a random variable, whose average will be given by the sum of the averages of X and Y and whose variance will be equal to the sum of the variances of X and Y:

$$M = \mu + \tau \quad (3)$$
$$S^2 = \sigma^2 + \tau^2 \quad (4)$$

Defined as such, the variable Z has a probability density with the form (Grushka, 1972):

$$f(x) = \frac{1}{2\tau} \exp\left(\frac{1}{2\tau}\left(2\mu + \frac{\sigma^2}{\tau} - 2x\right)\right) \operatorname{erfc}\left(\frac{\mu + \frac{\sigma^2}{\tau} - x}{\sqrt{2}\sigma}\right) \quad (5)$$

which receives the name of ex-Gaussian distribution (from exponential modified gaussian distribution). The erfc function is the complementary error function. One must be careful, for μ and σ are NOT the average and standard deviation for the ex-Gaussian distribution, instead the average and variance of the ex-Gaussian distribution is given by Equations (3)–(4): $M = \mu + \tau$ and $S^2 = \sigma^2 + \tau^2$. On the other hand, a calculation of the skewness of this distribution results in:

$$K = \int_{-\infty}^{\infty} \left(\frac{x-M}{S}\right)^3 f(x)\mathrm{d}x = \frac{2\tau^3}{(\sigma^2 + \tau^2)^{\frac{3}{2}}}, \quad (6)$$

While the gaussian distribution has null skewness, the skewness of the exponential distribution is exactly equal to two. As a result the skewness of the ex-Gaussian has an upper bound equal to two in the limit $\sigma \ll \tau$ (when the exponential component dominates) and a lower bound equal to zero in the limit $\sigma \gg \tau$ (when the gaussian component dominates).

Let's parameterize the ex-Gaussian distribution in terms of its average M, standard deviation S and a new skewness parameter

$\lambda = \sqrt[3]{\frac{K}{2}}$. Defined in this way, the λ parameter can have values between 0 and 1. Now, defining the standard coordinate z ($z = \frac{x-M}{S}$) one can have the ex-Gaussian distribution normalized for average 0 and standard deviation 1 in terms of a single parameter, its asymmetry λ:

$$f_\lambda(z) = \frac{1}{2\lambda} \exp\left(\frac{1}{2\lambda^2}(-2z\lambda - 3\lambda^2 + 1)\right) \text{erfc}\left(\frac{-z + \frac{1}{\lambda} - 2\lambda}{\sqrt{2}\sqrt{1-\lambda^2}}\right).$$
(7)

in this case, in terms of λ, the parameters μ, σ and τ are given by:

$$\mu = -\lambda$$
(8)

$$\sigma = \sqrt{1-\lambda^2}$$
(9)

$$\tau = \lambda.$$
(10)

Thus, the ex-gaussian represents a family of distributions that can be parametrized in terms of their assymmetry. Ranging from the

FIGURE 1 | ex-Gaussian distributions for different values of the λ asymmetry parameter.

exponential (maximum assymmetry in the limit when $\lambda = 1$) to a gaussian (symmetrical distribution in the limit when $\lambda = 0$).

In **Figure 1**, we show plots for the ex-Gaussian function for different values of the parameter λ. We should note that for very small values of λ (less than around 0.2), the ex-Gaussian is almost identical to the gaussian function (see **Figure 2**)[1].

Given a probability density, an important function that can be calculated from it is its cumulative distribution (its left tail), which is the result of the integral

$$F(z) = \int_{-\infty}^{z} f(x)\mathrm{d}x.$$
(11)

The importance of this function is that given the cumulative distribution one is able to calculate the probability of an event. For the ex-gaussian, the expression for its cumulative distribution is given by:

$$F(x) = \frac{1}{2}\text{erfc}\left(-\frac{x-\mu}{\sqrt{2}\sigma}\right) - \frac{1}{2}\exp\left(\frac{\sigma^2}{\tau^2} - \frac{x-\mu}{\tau}\right)$$
$$\text{erfc}\left(-\frac{\frac{x-\mu}{\sigma} - \frac{\sigma}{\tau}}{\sqrt{2}}\right)$$
(12)

Let's also define z_α, the value of z for which the right tail of the distribution has an area equal to α:

$$\alpha = \int_{z_\alpha}^{\infty} f(x)\mathrm{d}x.$$
(13)

$$1 - F(z_\alpha) = \alpha$$
(14)

so, solving the Equation (14), one is able to obtain the value of z_α for any given α.

---

[1] In this cases, the numerical evaluation of the ex-Gaussian distribution in Equation (5) becomes unstable and one can without loss (to a precision of around one part in a million) approximate the ex-Gaussian by a gaussian distribution.
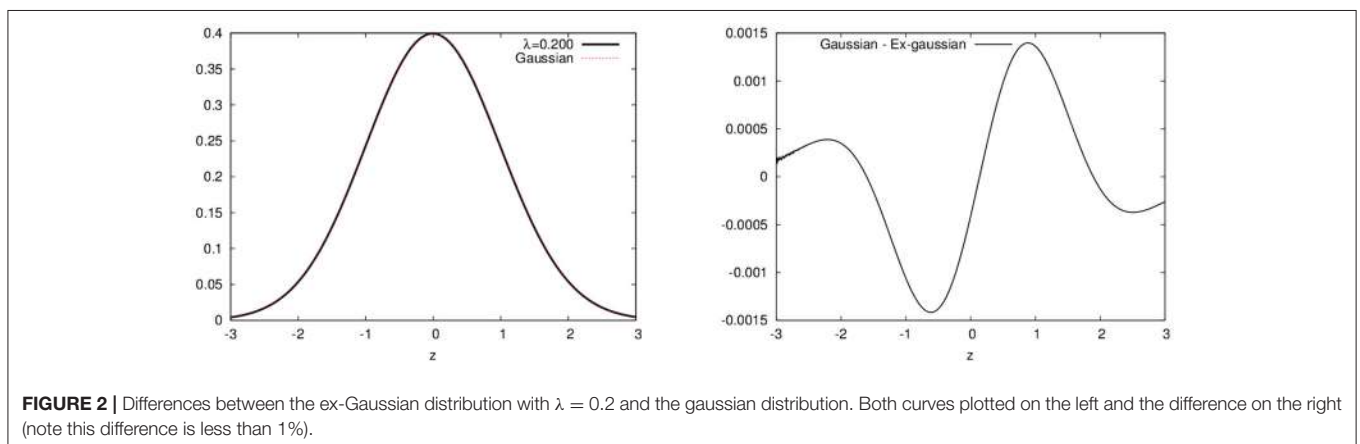
FIGURE 2 | Differences between the ex-Gaussian distribution with $\lambda = 0.2$ and the gaussian distribution. Both curves plotted on the left and the difference on the right (note this difference is less than 1%).

3. FITTING THE PROBABILITY DISTRIBUTION

We are interested in the following problem: given a dataset, to estimate the parameters μ, σ and τ that, plugged into Equation (5), best fit the data.

We must now define what it means to best fit the data. Different approaches here will result in different values for the parameters. The most trivial approach would be to say that the best parameters are those that result in the fitted ex-Gaussian distribution with the same statistical parameters: average (M), standard deviation (S) and asymmetry (K or λ). So, one can take the dataset, calculate M, S, and K and use the relations between them and the parameters μ, σ and τ:

$$M = \mu + \tau \tag{15}$$

$$S = \sqrt{\sigma^2 + \tau^2} \tag{16}$$

$$\lambda = \sqrt[3]{\frac{K}{2}} = \frac{\tau}{\sqrt{\sigma^2 + \tau^2}} \tag{17}$$

$$\mu = M - S\lambda \tag{18}$$

$$\sigma = S\sqrt{1 - \lambda^2} \tag{19}$$

$$\tau = S\lambda \tag{20}$$

This method of evaluating the parameters from the statistic (*momenta*) is know as the method of the moments as is usually the worst possible approach given the resulting bias. For instance, in some experiments, one finds the K parameter bigger than 2 (or $\lambda > 1$) and from Equation (17) one sees that, in order to have $K > 2$, σ cannot be a real number.

Another approach is to find the parameters that minimize the sum of the squared differences between the observed distribution and the theoretical one (least squares). In order to do that, one must, from the dataset, construct its distribution (a histogram), which requires some parametrization (dividing the whole range of observations in fixed intervals). Since a potentially arbitrary choice is made here, the results might be dependent on this choice. When analyzing data, we will study this dependency and come back to this point.

The last approach we will study is the maximum likelihood method. The function in Equation (5) is a continuous probability distribution for a random variable, which means that $f(x)dx$ can be interpreted as the probability that a observation of the random variable will have the x value (with the infinitesimal uncertainty dx). So, given a set of N observations of the random variable, $\{x_i\}$, with $i = 1, 2, ..., N$, the likelihood $\mathcal{L}$ is defined as the probability of such a set, given by:

$$\mathcal{L} = \prod_{i=1}^{N} f(x_i; \mu, \sigma, \tau) \tag{21}$$

$$\ln \mathcal{L} = \sum_{i=1}^{N} \ln \left(f(x_i; \mu, \sigma, \tau) \right) \tag{22}$$

The maximum likelihood method consists in finding the parameters μ, σ and τ that maximize the likelihood $\mathcal{L}$ (or its

logarithm[2] $\ln \mathcal{L}$). Note that in this approach, one directly uses the observations (data) without the need of any parametrization (histogram).

In both approaches, least squares and maximum likelihood, one has to find the extreme (maximum or minimum) of a function. The numerical algorithm implemented for this purpose is the steepest descent/ascent (descent for the minimum and ascent for the maximum). The algorithm consists in interactively changing the parameters of the function by amounts given by the gradient of the function in the parameter space until the gradient falls to zero (to a certain precision). There are other optimization methods, like the simplex (Van Zandt, 2000; Cousineau et al., 2004), which also iteratively updates the parameters (in the case of the simplex without the need to compute the gradients). We chose to implement steepest ascent in order to gain in efficiency: since one is able to evaluate the gradients, this greedy algorithm should converge faster than the sample techniques used by simplex. But in any case, both algorithms (steepest descent and simplex) should give the same results, since both search the same maximum or minimum.

4. THE EXGUTILS MODULE

ExGUtils is a python package with two modules in its 3.0 version: one purely programmed in python (`pyexg`) and the other programmed in C (`uts`). The advantage of having the functions programmed in C is speed, stability and numerical precision.

As mentioned, the package has two modules: `pyexg` and `uts`. The first one comprises all functions with source code programed in python, some of which depend on the `numpy`, `scipy` and `random` python packages. On the other hand, the module `uts` contains functions with source code programmed in C. In **Table 1** one can find a complete list of all functions contained in both modules and the ones particular to each one. The source distribution of the ExGUtils module comes with a manual which explains in more detail and with examples the functions.

5. APPLICATIONS

We use here the ExGUtils package in order to analyze data from the experiment in Navarro-Pardo et al. (2013). From this work, we analyse the datasets obtained for the reaction times of different groups of people in recognizing different sets of words in two possible experiments (yes/no and go/nogo). In the Appendix B we briefly explain the datasets analyzed here (which are provided as Supplementary Material for download).

In our analysis, first each dataset is fitted to the ex-Gaussian distribution through the three different approaches aforementioned:

- moments $\rightarrow$ Estimating the parameters through the sample statistics Equations (18–20).

[2]Note that, since the logarithm is an monotonically increasing function, the maximal argument will result in the maximum value of the function as well.

TABLE 1 | Functions present in the package modules.

Module	Function	Brief description
Present	drand	Returns a random number with homogeneous distribution between 0 and 1
in	exp_rvs	Returns a random number with exponential distribution between 0 and infinity
both	gauss_rvs	Returns a random number with gaussian distribution between minus infinity and infinity
modules	exg_rvs	Returns a random number with ex-Gaussian distribution between minus infinity and infinity
	gauss_pdf	Evaluates the gaussian distribution at a given point
	gauss_cdf	Evaluates the gaussian cumulative distribution at a given point
	exg_pdf	Evaluates the ex-Gaussian distribution at a given point
	exg_cdf	Evaluates the ex-Gaussian cumulative distribution at a given point
	exg_lamb_pdf	Evaluates the ex-Gaussian distribution parameterized in terms of its asymmetry at a given point
	exg_lamb_cdf	Evaluates the ex-Gaussian cumulative distribution parameterized in terms of its asymmetry at a given point
	pars_to_stats	Given the parameters μ, σ and τ, evaluates the corresponding statistics M, S, and K
	stats_to_pars	Given the statistics M, S and K, evaluates the corresponding parameters μ, σ and τ
	histogram	Given a set of observations, produces an histogram
	stats	Given a set of observations, returns the statistics M, S, and K
	stats_his	Given a set of observations, presented as a histogram, returns the statistics M, S, and K
	correlation	Given a set of points, returns the linear correlation coefficient for the points
	minsquare	Given a set of points, fits a polynomial to the data using the least square method
	exgLKHD	Evaluates the likelihood and its gradient in the parameter space for a dataset in a given point of the parameter space
	maxLKHD	Evaluates the parameters μ, σ and τ that maximize the likelihood for a given dataset
	exgSQR	Evaluates the sum of squared differences and its gradient in the parameter space for an histogram in a given point of the parameter space
	minSQR	Evaluates the parameters μ, σ and τ that minimize the sum of squared differences for a given histogram
Only	int_points_gauss	Creates a point partition of an interval for evaluating a gaussian integral
in	intsum	Evaluates the gaussian integral for a function calculated at the points in a gaussian partition
uts		
Only	zero	Finds the zero of an equation
in	ANOVA	Performs an ANOVA test
pyexg	integral	Evaluates an integral

In python type `help(FUNC)` *(where* `FUNC` *should be the name of a given function), in order to obtain the list of arguments that each function should receive and in which order.*

- minSQR → Estimation through least square method, using as initial point in the steepest descent algorithm the μ, σ and τ obtained from the method of moments above[3].
- maxLKHD → Estimation through maximum likelihood method, using as initial point in the steepest ascent algorithm the μ, σ and τ obtained from the method of moments[3].

In **Table 2**, one can see the estimated parameters and the corresponding statistics for the different experiments. From the table, one sees that in the case of the experiments performed with young people, the value of the skewness, K, is bigger than two. This happens because of a few atypical measurements far beyond the bulk of the distribution. In fact, many researches opt for trimming extreme data, by "arbitrarly" choosing a cutoff and removing data points beyond this cutoff. One must, though, be careful for the ex-Gaussian distribution does have a long right tail, so we suggest a more criterious procedure:

Having the tools developed in `ExGUtils`, one can use the parameters obtained in the fitting procedures (either minSQR or maxLKHD) in order to estimate a point beyond which one should find no more than, let's say, 0.1% of the distribution. In the Appendix A (Supplementary Material), the Listing 1 shows a quick python command line in order to estimate this point in the case of the young_gng experiment. The result informs us that, in principle, one should not expect to have more than 0.1% measurements of reaction times bigger than 1472.84 ms if the parameters of the distribution are the ones adjusted by maxLKHD for the young_gng empirical data. In fact, in this experiment, one has 2396 measurements of reaction times, from those, 8 are bigger than 1472.8 ms (0.33%). If one now calculates the statistics for the data, removing these 8 outliers, one obtains:

$$\text{moments:} \quad M = 593.80 \; S = 154.30 \; K = 1.91 \; \mu = 441.82$$
$$\sigma = 26.67 \; \tau = 151.98$$
$$\text{minSQR:} \quad M = 590.11 \; S = 142.44 \; K = 1.67 \; \mu = 455.96$$
$$\sigma = 47.89 \; \tau = 134.14$$
$$\text{maxLKHD:} \quad M = 593.80 \; S = 148.44 \; K = 1.69 \; \mu = 453.52$$
$$\sigma = 48.52 \; \tau = 140.29$$

In **Figure 3** one can see the histogram of data plotted along with three ex-Gaussians resulting from the above parameters.

Now, one might ask, having these different fits for the same experiment, how to decide which one is the best? Accepting the parameters of a fit is the same as accepting the null hypothesis that the data measurements come from a population with an ex-Gaussian distribution with the parameters given by the ones obtained from the fit. In Clauset et al. (2009) the authors suggest a procedure in order to estimate a p-value for this hypothesis when the distribution is a power-law. One can generalize the procedure for any probability distribution, like the ex-Gaussian, for example:

---

[3] In the cases where K was bigger than 2, the inicial parameters were calculated as if $K = 1.9$. Note that the final result of the search should not depend on the inicial search point if it starts close to the local maximum/minimum.

TABLE 2 | Parameters and statistics obtained with the three fitting methods.

Experiment	Moments						minSQR						maxLKHD					
	M	S	K	μ	σ	τ	M	S	K	μ	σ	τ	M	S	K	μ	σ	τ
elder_gng	831.14	318.95	1.75	526.06	93.02	305.08	841.45	334.97	1.85	515.16	75.76	326.29	831.14	318.39	1.79	524.49	85.67	306.65
elder_hfgng	798.55	310.00	1.94	491.52	42.78	307.03	803.42	308.32	1.82	504.66	76.18	298.76	796.63	312.32	1.90	489.39	56.11	307.24
elder_hfyn	826.15	278.61	1.62	566.56	101.16	259.59	810.03	256.41	1.68	568.03	84.74	242.00	826.15	275.10	1.75	563.06	80.40	263.08
elder_lfgng	863.73	324.53	1.60	562.65	121.14	301.08	887.69	371.88	1.90	522.22	68.76	365.46	863.73	339.88	1.87	531.43	71.38	332.30
elder_lfyn	884.53	315.93	1.59	591.97	119.27	292.55	882.16	310.04	1.77	584.33	86.12	297.84	884.53	308.13	1.62	597.54	112.18	286.98
elder_pseudo	1189.64	416.92	0.88	872.59	270.73	317.05	1233.90	518.22	1.79	734.21	137.33	499.69	1189.64	447.89	1.60	773.74	166.24	415.90
elder_yn	854.88	298.93	1.63	575.78	107.04	279.11	846.94	286.75	1.75	572.77	84.01	274.17	854.88	292.72	1.68	578.59	96.69	276.29
young_gng	597.90	169.90	2.71	–	–	–	590.36	142.94	1.66	455.98	48.71	134.38	597.90	154.25	1.72	451.09	47.33	146.81
young_hfgng	562.94	141.88	3.04	–	–	–	555.47	115.19	1.54	449.84	45.93	105.63	562.94	126.30	1.65	444.47	43.77	118.47
young_hfyn	621.16	176.99	3.88	–	–	–	610.51	128.15	1.53	493.32	51.86	117.19	621.16	148.38	1.65	482.08	51.70	139.08
young_lf	632.96	187.61	2.46	–	–	–	625.36	161.43	1.65	473.80	55.61	151.55	632.96	173.23	1.71	468.51	54.43	164.45
young_lfgng	632.96	187.61	2.46	–	–	–	625.36	161.43	1.65	473.80	55.61	151.55	632.96	173.23	1.71	468.51	54.43	164.45
young_lfyn	668.57	184.88	2.10	–	–	–	660.23	165.16	1.60	507.06	61.77	153.18	668.58	176.56	1.70	501.24	56.31	167.34
young_pseudo	722.53	190.36	2.37	–	–	–	718.60	175.25	1.64	554.66	61.92	163.94	722.53	180.58	1.68	552.03	59.47	170.50
young_yn	644.37	182.41	2.90	–	–	–	635.20	148.99	1.62	496.41	54.18	138.78	644.37	164.31	1.69	488.96	53.34	155.42

For each one of the three procedures, we present the obtained parameters and the correspondent statistics. Note that for the method of the moments, the statistics is directly obtained from the dataset and the parameters are evaluated based on this statistic from Equations (18–20), while the other methods obtain the parameters from the dataset and the statistics presented in the table is evaluated based on these parameters from the expressions in eqs. Some conditions were not estimated because of a few atypical measurements far beyond the bulk of the distribution (K larger than 2). (15–17).
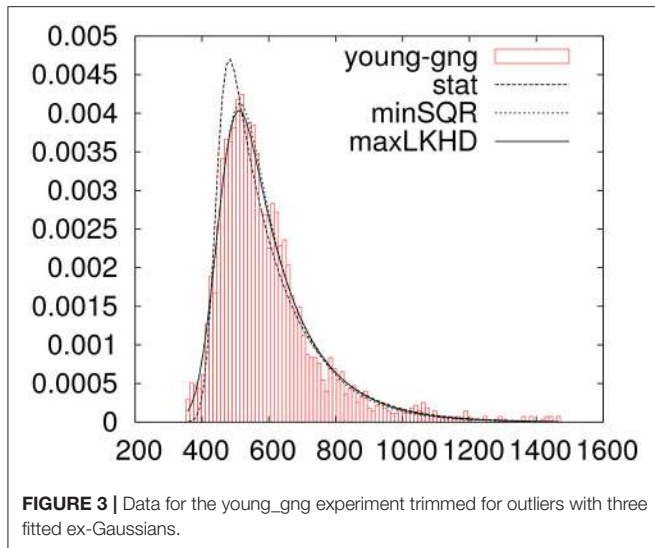
FIGURE 3 | Data for the young_gng experiment trimmed for outliers with three fitted ex-Gaussians.

TABLE 3 | Probabilities p1 and p2 for the fits.

Experiment	minSQR		maxLKHD	
	KS	p2 ($\bar{KS} \pm sd$)	KS	p1 ($\bar{KS} \pm sd$)
elder_gng	64.52	0.001 (29.47 ± 8.12)	38.89	0.096 (29.96 ± 12.54)
elder_hfgng	44.32	0.001 (20.85 ± 5.73)	49.61	0.003 (21.33 ± 5.86)
elder_hfyn	34.10	0.019 (20.10 ± 5.35)	35.30	0.021 (20.44 ± 7.49)
elder_lfgng	42.83	0.005 (21.73 ± 5.98)	31.70	0.043 (20.96 ± 5.94)
elder_lfyn	17.25	0.634 (19.76 ± 5.18)	29.00	0.028 (19.15 ± 5.63)
elder_pseudo	62.79	0.000 (26.12 ± 6.81)	53.10	0.009 (25.69 ± 10.41)
elder_yn	32.87	0.258 (28.77 ± 7.42)	62.72	0.012 (29.00 ± 14.16)
young_gng	35.92	0.136 (28.60 ± 7.39)	69.38	0.003 (28.66 ± 8.36)
young_hfgng	21.33	0.305 (19.70 ± 4.99)	34.11	0.016 (20.13 ± 6.16)
young_hfyn	29.75	0.049 (19.59 ± 5.04)	45.20	0.009 (19.83 ± 7.03)
young_lf	22.06	0.318 (20.39 ± 5.81)	37.78	0.015 (20.67 ± 7.82)
young_lfgng	22.06	0.299 (20.08 ± 5.25)	37.78	0.012 (20.27 ± 6.52)
young_lfyn	23.62	0.182 (19.66 ± 5.03)	17.66	0.542 (19.56 ± 7.43)
young_pseudo	20.35	0.867 (27.86 ± 7.20)	28.48	0.386 (28.44 ± 10.87)
young_yn	38.34	0.097 (28.07 ± 7.03)	54.20	0.003 (28.13 ± 8.66)

KS is the Kolmogorov-Smirnov statistic calculated between the data and its fitted ex-Gaussian. In columns p1 and p2, one finds the probabilities that a randomly generated dataset has a bigger KS statistic than the empirical data. In parenthesis, the average KS statistic and standard deviation for the generated random samples.

- Take a measure that quantifies the distance between the data and the fitted theoretical distribution. One could use $\ln \mathcal{L}$ or χ^2, but, as our fitting procedures maximize or minimize these measures, as the authors in Clauset et al. (2009) suggest, in order to avoid any possible bias, we evaluate the Kolmogorov-Smirnov statistic, which can be calculated for reaction-time data without the need of any parametrization.
- Randomly generate many data samples of the same size as the empirical one using the theoretical distribution with the parameters obtained from the fit to the empirical data.
- Fit each randomly generated data sample to the theoretical distribution using the same fit procedure used in the case of the empirical data.
- Evaluate the Kolmogorov-Smirnov statistic between the random sample and its fitted theoretical distribution.

Following this procedure, one can evaluate the probability that a random data sample, obtained from the fitted distribution, has a bigger distance to the theoretical curve than the distance between the empirical data and its fitted distribution. If this probability is higher than the confidence level one is willing to work with, one can accept the null hypothesis knowing that the probability that one is committing a type I error if one rejects the null hypothesis is p.

In the Appendix A (Supplementary Material) we provide listings with the implementation, in python via the `ExGUtils` package, of the functions that evaluate this p probability and the Kolmogorov-Smirnov statistic. In **Table 3** we provide the values of p obtained for the experiments, using minSQR and maxLKHD approaches (p1 and p2, respectively).

We can see that there are some discrepancies in **Table 3**. Sometimes minSQR seems to perform better, sometimes maxLKHD. One might now remember that the minSQR method depends on a parametrization of the data. In order to perform the fit, one needs to construct a histogram of the data, and there is an arbitrary choice in the number of intervals one divides the data into. In the fits performed till now, this number is set to be the

default in the `histogram` function of the `ExGUtils` package, namely two times the square root of the number of measurements in the data.

In order to study the effect of the number of intervals in the values for the parameters and of p2, we performed the procedure of fitting the data through minSQR after constructing the histogram with different number of intervals. In **Figure 4** we show the evolution of the p2 probability, along with the values for μ, σ, and τ obtained by minSQR for the histograms constructed with a different number of intervals for the young_hfgng experiment.

From the figure one sees that while the number of intervals is unreasonably small compared to the size of the empirical dataset, the values for the fitted ex-Gaussian parameters fluctuate, while the p probability is very small, but, once the number of intervals reaches a reasonable value, around 40, the values for the parameters stabilize and the value of p also gets more stable. So the question remains, why the values for the probability obtained with maxLKHD method is so small in the case of this experiment? The fact is that the likelihood of the dataset is very sensible to outliers. For the value of the probability [$f(x)$ in Equation 5] gets very small for the extreme values. Therefore, in these cases, it might be reasonable to make some criterious data trimming. So we proceed as follows: Given a dataset, we first perform a pre-fitting by maxLKHD. Using the parameters obtained in this fit, we estimate the points where the distribution has a left and right tails of 0.1% and remove measurements beyond these points. With the trimmed dataset, removed of outliers, we perform fits again and evaluate the p1 and p2 probabilities. In **Table 4**, we show the results for this new round of fitting and probability evaluations. In more than half of the experiments where one could see a big
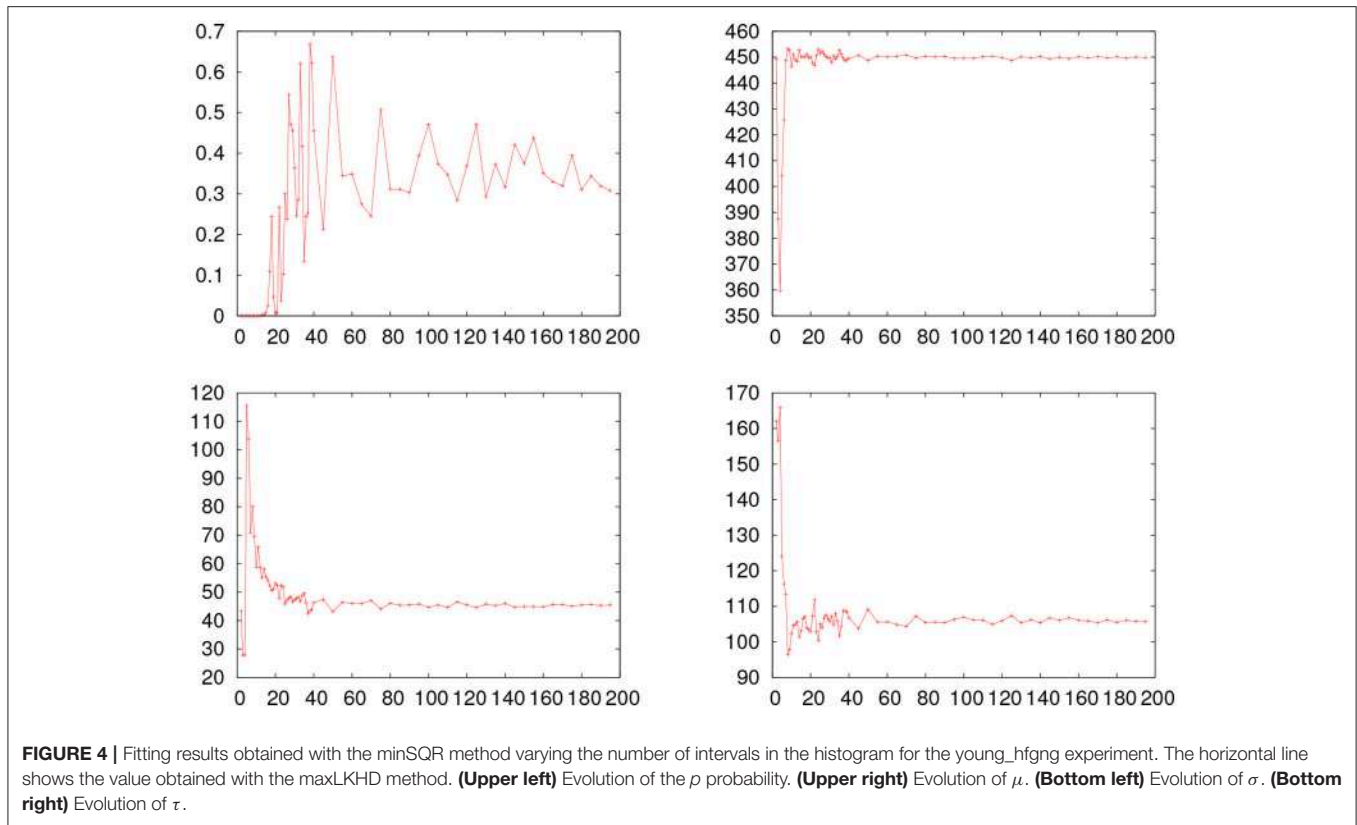
FIGURE 4 | Fitting results obtained with the minSQR method varying the number of intervals in the histogram for the young_hfgng experiment. The horizontal line shows the value obtained with the maxLKHD method. **(Upper left)** Evolution of the p probability. **(Upper right)** Evolution of μ. **(Bottom left)** Evolution of σ. **(Bottom right)** Evolution of τ.

TABLE 4 | The p1 and p2 probabilities for the fits.

Experiment	N	N' (%)	minSQR		maxLKHD	
			KS	p2 ($\bar{KS} \pm sd$)	KS	p1 ($\bar{KS} \pm sd$)
elder_gng	2,348	2 (0.09)	66.58	0.000 (28.92 ± 7.32)	50.24	0.040 (30.98 ± 17.55)
elder_hfgng	1,174	8 (0.68)	34.20	0.040 (20.67 ± 5.70)	32.64	0.010 (20.66 ± 5.83)
elder_hfyn	1,175	2 (0.17)	32.09	0.040 (20.01 ± 4.86)	24.76	0.090 (19.22 ± 6.69)
elder_lfgng	1,174	1 (0.09)	43.49	0.000 (21.47 ± 5.83)	33.22	0.030 (20.57 ± 6.90)
elder_lfyn	1,139	4 (0.35)	19.97	0.550 (20.55 ± 6.37)	19.71	0.620 (19.97 ± 6.11)
elder_pseudo	1,910	5 (0.26)	57.26	0.000 (26.91 ± 6.64)	57.11	0.010 (26.61 ± 10.06)
elder_yn	2,314	5 (0.22)	36.83	0.240 (28.57 ± 7.46)	29.72	0.230 (30.54 ± 14.33)
young_gng	2,396	10 (0.42)	38.93	0.250 (27.82 ± 6.32)	43.11	0.020 (30.19 ± 17.07)
young_hfgng	1,200	8 (0.67)	23.28	0.780 (19.25 ± 4.39)	17.82	0.430 (18.07 ± 4.13)
young_hfyn	1,180	9 (0.76)	27.97	0.050 (19.68 ± 4.91)	28.93	0.010 (20.74 ± 7.71)
young_lf	1,196	5 (0.42)	25.11	0.310 (20.09 ± 5.21)	25.32	0.020 (19.69 ± 4.29)
young_lfgng	1,196	5 (0.42)	25.11	0.280 (20.51 ± 5.08)	25.32	0.080 (20.55 ± 5.05)
young_lfyn	1,132	3 (0.27)	25.20	0.230 (19.42 ± 5.40)	16.60	0.780 (20.72 ± 8.53)
young_pseudo	2,326	10 (0.43)	23.33	0.940 (27.59 ± 7.05)	25.85	0.870 (28.45 ± 12.48)
young_yn	2,312	12 (0.52)	46.10	0.130 (27.80 ± 7.87)	28.58	0.210 (31.21 ± 19.74)

KS is the Kolmogorov-Smirnov statistic calculated between the data and its fitted ex-Gaussian. N is the number of data points in each empirical dataset, N' in the number of points removed by the trimming and in brackets next to it its proportion in relation to the total data. In columns p1 and p2, one finds the probabilities that a randomly generated dataset has a bigger KS statistic than the empirical data. In parenthesis, the average KS statistic and standard deviation for the generated random samples.

discrepancy between p1 and p2 in **Table 3**, the trimmed data do show better results. For some datasets, the trimming had no impact on the discrepancy. In any case, one might wonder

about the impact of the trimming in the obtained parameters. Therefore, in **Table 5**, we show the results obtained with different trimming criteria.

TABLE 5 | Results for different trimming on the data.

Experiment	%	minSQR				maxLKHD			
		μ	σ	τ	p2	μ	σ	τ	p1
elder_gng	0.1	513.52	73.00	329.54	0.001	518.71	75.02	313.04	0.026
elder_gng	0.5	516.62	76.61	319.50	0.002	521.83	70.31	299.00	0.011
elder_gng	1.0	516.04	76.80	317.93	0.000	523.84	66.32	291.17	0.014
elder_hfgng	0.1	509.10	84.96	285.05	0.043	504.96	65.26	297.06	0.012
elder_hfgng	0.5	509.39	89.51	277.28	0.020	511.19	65.09	277.33	0.020
elder_hfgng	1.0	508.40	83.49	279.35	0.016	512.79	59.89	272.67	0.005
elder_hfyn	0.1	564.82	82.19	246.63	0.052	558.93	71.17	266.45	0.148
elder_hfyn	0.5	565.70	83.88	242.73	0.036	559.98	68.60	261.73	0.143
elder_hfyn	1.0	566.73	87.05	235.38	0.006	561.88	65.77	255.95	0.094
elder_lfgng	0.1	521.64	62.39	368.34	0.006	530.64	68.95	333.51	0.041
elder_lfgng	0.5	523.29	67.46	359.50	0.006	530.25	60.81	329.35	0.011
elder_lfgng	1.0	523.37	67.70	356.20	0.002	533.09	59.45	318.33	0.008
elder_lfyn	0.1	583.03	84.58	301.15	0.562	581.72	76.56	305.56	0.577
elder_lfyn	0.5	584.32	86.07	296.15	0.524	584.60	78.19	296.28	0.329
elder_lfyn	1.0	586.72	85.93	287.48	0.470	589.73	77.85	278.47	0.027
elder_pseudo	0.1	735.04	133.55	498.90	0.001	755.81	134.79	436.48	0.012
elder_pseudo	0.5	733.65	135.57	499.00	0.001	754.68	132.25	438.02	0.017
elder_pseudo	1.0	732.54	135.87	498.14	0.000	752.31	124.65	442.19	0.014
elder_yn	0.1	572.16	81.99	275.26	0.251	567.87	73.30	288.63	0.280
elder_yn	0.5	573.64	84.34	270.01	0.373	570.72	72.30	278.01	0.378
elder_yn	1.0	573.82	84.87	266.60	0.246	573.48	72.59	268.80	0.159
young_gng	0.1	456.35	48.59	133.40	0.292	453.37	47.60	140.66	0.013
young_gng	0.5	456.95	47.02	132.15	0.177	456.29	43.54	134.00	0.167
young_gng	1.0	457.70	46.28	130.55	0.096	457.63	40.37	131.00	0.013
young_hfgng	0.1	449.79	45.31	105.15	0.707	448.42	44.89	109.02	0.565
young_hfgng	0.5	450.77	44.72	103.91	0.500	449.62	40.74	107.45	0.704
young_hfgng	1.0	451.94	44.75	101.09	0.208	451.50	37.51	103.23	0.226
young_hfyn	0.1	493.66	50.92	116.16	0.032	487.17	51.93	126.49	0.009
young_hfyn	0.5	494.62	50.74	114.27	0.054	488.97	51.00	122.73	0.025
young_hfyn	1.0	495.77	50.10	111.55	0.083	493.08	49.40	114.69	0.170
young_lf	0.1	473.36	54.44	151.84	0.287	471.09	54.85	157.76	0.037
young_lf	0.5	474.18	55.22	148.96	0.207	474.72	51.93	148.93	0.117
young_lf	1.0	475.03	54.10	147.35	0.067	475.22	45.69	148.46	0.019
young_lfgng	0.1	473.36	54.44	151.84	0.290	471.09	54.85	157.76	0.054
young_lfgng	0.5	474.18	55.22	148.96	0.201	474.72	51.93	148.93	0.119
young_lfgng	1.0	475.03	54.10	147.35	0.068	475.22	45.69	148.46	0.021
young_lfyn	0.1	508.16	61.53	151.83	0.228	503.17	57.27	162.27	0.776
young_lfyn	0.5	508.79	62.11	148.82	0.306	506.82	56.33	153.58	0.713
young_lfyn	1.0	508.92	59.52	148.67	0.278	508.72	51.89	151.43	0.545
young_pseudo	0.1	555.42	63.03	161.81	0.951	555.36	60.57	162.27	0.858
young_pseudo	0.5	556.11	63.54	159.16	0.364	556.92	57.17	158.77	0.194
young_pseudo	1.0	557.18	62.50	157.25	0.096	559.57	54.06	153.59	0.021
young_yn	0.1	497.56	54.59	136.65	0.141	492.23	53.69	146.70	0.144
young_yn	0.5	498.05	54.18	135.23	0.374	495.25	52.33	139.85	0.605
young_yn	1.0	498.17	53.86	134.10	0.556	496.97	50.70	136.71	0.494

The column % indicates the amount of tail trimmed to the left and right of the data.

Now, having the full picture, one can realize that some values of p are indeed small, indicating that either the ex-Gaussian distribution is not that good a model in order to fit the empirical results, or there is still some systematic error in the analysis of the experiments. Most of these empirical datasets where one sees very low values of p are with elderly people. These have the τ parameter much bigger than the σ which indicates a very asymmetric distribution with a long right tail. Indeed, a careful analysis of the histograms will show that the tail in these empirical distributions seems to be cut short at the extreme of the plots, so that the limit time in the experiment should be bigger than 2,500 ms in order to get the full distribution. One might argue that the trimming actually was removing data, but most of the removed points in the trimming of elderly data, was from the left tail and not from the right. This issue will result in the wrong evaluation of the KS statistics, since it assumes that one is dealing with the full distribution. This kind of analysis might guide better experimental designs.

6. OVERVIEW

The ex-Gaussian fit has turned into one of the preferable options when dealing with positive skewed distributions. This technique provides a good fit to multiple empirical data, such as reaction times (a popular variable in Psychology due to its sensibility to underlying cognitive processes). Thus, in this work we present a python package for statistical analysis of data involving this distribution.

This tool allows one to easily work with alternative strategies (fitting procedures) to some traditional analysis like trimming. This is an advantage given that an ex-Gaussian fit includes all data while trimming may result in biased statistics because of the cuts.

Moreover, this tool is programmed as Python modules, which allow the researcher to integrate them with any other Python resource available. They are also open-source and free software which allows one to develop new tools using these as building blocks.

7. AVAILABILITY

ExGUtils may be downloaded from the Python Package index (https://pypi.python.org/pypi/ExGUtils/3.0) for free along with the source files and the manual with extended explanations on the functions and examples.

AUTHOR CONTRIBUTIONS

CM-T participated in the conception, design, and interpretation of data, and in drafting the manuscript. DG participated in the design, and analysis and interpretation of data, and in drafting the manuscript. EN-P and PF participated in revising the manuscript.

FUNDING

SUPPLEMENTARY MATERIAL

The Supplementary Material for this article can be found online at: https://www.frontiersin.org/articles/10.3389/fpsyg.2018.00612/full#supplementary-material

REFERENCES

Balota, D. A., Cortese, M. J., Sergent-Marshall, S. D., Spieler, D. H., and Yap, M. (2004). Visual word recognition of single-syllable words. *J. Exp. Psychol. Gen.* 133:283. doi: 10.1037/0096-3445.133.2.283

Clauset, A., Shalizi, C. R., and Newman, M. E. J. (2009). Power-Law distributions in empirical data. *SIAM Rev.* 51, 661–703. doi: 10.1137/070710111

Cousineau, D., Brown, S., and Heathcote, A. (2004). Fitting distributions using maximum likelihood: methods and packages. *Behav. Res. Methods Instrum. Comput.* 36, 742–756. doi: 10.3758/BF03206555

Cousineau, D., and Larochelle, S. (1997). Pastis: a program for curve and distribution analyses. *Behav. Res. Methods Instrum. Comput.* 29, 542–548. doi: 10.3758/BF03210606

Epstein, J. N., Langberg, J. M., Rosen, P. J., Graham, A., Narad, M. E., Antonini, T. N., et al. (2011). Evidence for higher reaction time variability for children with adhd on a range of cognitive tasks including reward and event rate manipulations. *Neuropsychology* 25:427. doi: 10.1037/a0022155

Gooch, D., Snowling, M. J., and Hulme, C. (2012). Reaction time variability in children with adhd symptoms and/or dyslexia. *Dev. Neuropsychol.* 37, 453–472. doi: 10.1080/87565641.2011.650809

Grushka, E. (1972). Characterization of exponentially modified gaussian peaks in chromatography. *Anal. Chem.* 44, 1733–1738. doi: 10.1021/ac60319a011

Heathcote, A. (2004). Fitting wald and ex-wald distributions to response time data: an example using functions for the s-plus package. *Behav. Res. Methods Instrum. Comput.* 36, 678–694. doi: 10.3758/BF03206550

Heathcote, A., Popiel, S. J., and Mewhort, D. (1991). Analysis of response time distributions: an example using the stroop task. *Psychol. Bull.* 109:340.

Hervey, A. S., Epstein, J. N., Curry, J. F., Tonev, S., Eugene Arnold, L., Keith Conners, C., et al. (2006). Reaction time distribution analysis of neuropsychological performance in an adhd sample. *Child Neuropsychol.* 12, 125–140. doi: 10.1080/09297040500499081

Lacouture, Y., and Cousineau, D. (2008). How to use matlab to fit the ex-gaussian and other probability functions to a distribution of response times. *Tutor. Quant. Methods Psychol.* 4, 35–45. doi: 10.20982/tqmp.04.1.p035

Leth-Steensen, C., King Elbaz, Z., and Douglas, V. I. (2000). Mean response times, variability, and skew in the responding of adhd children: a response time distributional approach. *Acta Psychol.* 104, 167–190. doi: 10.1016/S0001-6918(00)00019-6

Luce, R. D. (1986). *Response Times: Their Role in Inferring Elementary Mental Organization.* Oxford psychology series. New York, NY; Oxford: Oxford University Press; Clarendon Press.

McVay, J. C., and Kane, M. J. (2012). Drifting from slow to "D'oh!": working memory capacity and mind wandering predict extreme reaction times and executive control errors. *J. Exp. Psychol. Learn. Mem. Cogn.* 38:525. doi: 10.1037/a0025896

Navarro-Pardo, E., Navarro-Prados, A. B., Gamermann, D., and Moret-Tatay, C. (2013). Differences between young and old university students on a lexical decision task: evidence through an ex-Gaussian approach. *J. Gen. Psychol.* 140, 251–268. doi: 10.1080/00221309.2013.817964

Ratcliff, R., Love, J., Thompson, C. A., and Opfer, J. E. (2012). Children are not like older adults: a diffusion model analysis of developmental changes in speeded responses. *Child Dev.* 83, 367–381. doi: 10.1111/j.1467-8624.2011.01683.x

Ratcliff, R., and McKoon, G. (2008). The diffusion decision model: theory and data for two-choice decision tasks. *Neural Comput.* 20, 873–922. doi: 10.1162/neco.2008.12-06-420

Sternberg, S. (1966). High-speed scanning in human memory. *Science* 153, 652–654. doi: 10.1126/science.153.3736.652

Van Zandt, T. (2000). How to fit a response time distribution. *Psychon. Bull. Rev.* 7, 424–465. doi: 10.3758/BF03214357

West, R. (1999). Age differences in lapses of intention in the stroop task. *J. Gerontol. Ser. B Psychol. Sci. Soc. Sci.* 54, P34–P43. doi: 10.1093/geronb/54B.1.P34

West, R., and Alain, C. (2000). Age-related decline in inhibitory control contributes to the increased stroop effect observed in older adults. *Psychophysiology* 37, 179–189. doi: 10.1111/1469-8986.3720179

Wickelgren, W. A. (1977). Speed-accuracy tradeoff and information processing dynamics. *Acta Psychol.* 41, 67–85. doi: 10.1016/0001-6918(77)90012-9